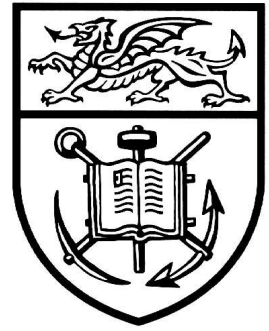


UNIVERSITY OF WALES SWANSEA  
SCHOOL OF ENGINEERING



FINITE ELEMENT MODELLING OF FLUID FLOW  
WITH MOVING FREE SURFACES AND INTERFACES  
INCLUDING FLUID-SOLID INTERACTION

Wulf Georg Dettmer  
Dipl.-Ing. (Hannover), M.Sc. (Swansea)

Thesis submitted to  
the University of Wales in Candidature  
for the Degree of Doctor of Philosophy

September 2004



# Declarations

1. This work has not previously been accepted in substance for any degree and is not being concurrently submitted in candidature for any degree.

Signed ..... (candidate)

Date .....

2. This work is the result of my own work and investigation, except where otherwise stated. Other sources have been acknowledged by giving explicit references. A bibliography is appended.

Signed ..... (candidate)

Date .....

3. I hereby give consent for my thesis, if accepted, to be available for photocopying and for inter-library loan, and for the title and summary to be made available to outside organisations.

Signed ..... (candidate)

Date .....



# Acknowledgements

I would like to thank Prof. Djordje Perić, my supervisor, for his invaluable guidance, support and encouragement during all stages of this work.

The financial support, which I received from the Engineering and Physical Sciences Research Council (EPSRC) of the United Kingdom, is gratefully acknowledged. This work was carried out under grant number GR/R92318/01. My special thanks go to Prof. Perić for making this possible.

I would like to thank the Department of Civil Engineering, later the School of Engineering, of the University of Wales Swansea as a whole for providing a very supportive and encouraging research environment.

I am especially grateful to my colleagues Andreas Rippl, Antonio and Mariela Orlando, Chenfeng Li, Francisco Pires, Holger Ettinger, Miguel Rodriguez Paz, Paul Ledger, Prihambodo Hendro Saksono, Sava Slijepčević, Sivakumar Kulasegaram and Yolanda Vidal, with whom I had many interesting discussions and who made my stay in Swansea very enjoyable.

I am very grateful to my parents for their unconditional and constant support.

Finally, I would like to thank Sandra sincerely for her understanding, support and patience, and for all the memorable days, which we spent in the beautiful countries of Wales and England.



# Summary

This work is concerned with the modelling of fluid flows on moving domains. The physical problems considered are free surface flows, possibly in the presence of the surface tension phenomena, fluid-rigid body and fluid-structure interaction.

The fluid flow considered is governed by the incompressible Navier-Stokes equations. It is modelled by stabilised low order velocity-pressure finite elements. A detailed analysis of time integration strategies is performed leading to the choice of the discrete implicit generalised- $\alpha$  method for the temporal discretisation. The motion of the fluid domain is accounted for by an arbitrary Lagrangian-Eulerian (ALE) strategy. Different mesh update methods are considered. The free surfaces and the fluid-solid interfaces are modelled carefully, satisfying the necessary conservation properties.

These computational ingredients result in fully implicit and strongly coupled sets of nonlinear equations, which are rephrased in a common general framework by decomposing the problems into the fluid, the interface and possibly the solid domains. In order to obtain the exact solution variables, a partitioned Newton-Raphson procedure, based on the exact linearisation of the residuals, is developed. Thus, the strong coupling is resolved and optimal convergence can be expected.

Finally, a number of two dimensional or axisymmetric numerical examples is presented which demonstrate the robustness and the efficiency of the overall algorithm. The strategy is verified against various reference solutions. The numerical examples include the simulation of the filling of drops, the stretching of liquid bridges, the vortex induced oscillations and the galloping of solid bodies, and the fall of a model parachute. The effects of coarse and dense spatial and temporal discretisations are studied. The partitioned Newton-Raphson procedure allows the employment of large time steps and requires a relatively small number of iterations. For the problems considered, the computational costs associated with the developed solution strategy seem very competitive.



# Zusammenfassung

Die vorliegende Arbeit befaßt sich mit der Modellierung von Strömungen in bewegten Gebieten. Die betrachteten physikalischen Probleme umfassen Strömungen mit freien Oberflächen unter Berücksichtigung von Oberflächenspannung sowie die Interaktion von Strömungen mit starren und flexiblen Festkörpern.

Das Fluid wird durch die inkompressiblen Navier-Stokes Gleichungen beschrieben. Zur numerischen Modellierung der Strömung werden stabilisierte lineare finite Elemente mit gleichen Interpolationsansätzen für die Geschwindigkeit und den Druck eingesetzt. Eine detaillierte Untersuchung verschiedener Strategien zur Zeitintegration wird durchgeführt, in der sich die „generalised- $\alpha$ “ Methode als vorteilhaft für die zeitliche Diskretisierung der Strömung erweist. Die zeitliche Veränderung des Strömungsgebietes wird mit einer „arbitrary Lagrangian-Eulerian“ (ALE) Strategie beschrieben. Verschiedene Methoden zur Netzbewegung werden diskutiert. Unter Berücksichtigung der mechanischen Erhaltungssätze werden numerische Modelle für freie Oberflächen und Fluid-Festkörper Interfaces formuliert.

Dieses Vorgehen führt zu Systemen aus stark gekoppelten, nichtlinearen Gleichungen. Die konsequente Unterscheidung von Strömungsgleichungen, Kopplungsbedingungen und gegebenenfalls Festkörpergleichungen erlaubt eine einheitliche allgemeine Darstellung der unterschiedlichen Probleme. Zur Lösung des diskretisierten Gesamtsystems wird ein partitioniertes Newton Verfahren entwickelt, das auf exakter Linearisierung beruht. Auf diese Weise wird die starke Kopplung aufgelöst, und optimale Konvergenz des Verfahrens ist zu erwarten.

Schließlich werden zahlreiche zweidimensionale oder axisymmetrische Beispiele vorgestellt, die die Robustheit und Effizienz der gesamten Lösungsstrategie demonstrieren. Die Beispiele umfassen unter anderem verschiedene Untersuchungen des mechanischen Verhaltens von Tropfen sowie die Simulation wirbelerregter Schwingungen und des Galoppierens von starren und flexiblen Festkörpern. Auch der Fall eines Modelfallschirms wird berechnet. Vergleiche mit verschiedenen Referenzlösungen werden vorgenommen, und der Einfluß grober und feiner räumlicher und zeitlicher Diskretisierungen wird untersucht. Das partitionierte Newton Verfahren erlaubt die Verwendung großer Zeitinkremente und benötigt nur wenige Iterationsschritte. Im Hinblick auf den Rechenaufwand erscheint die in dieser Arbeit entwickelte Lösungsstrategie wettbewerbsfähig.



# Contents

<b>1</b>	<b>Introduction</b>	<b>1</b>
1.1	Numerical Strategies . . . . .	4
1.2	The Aim of the Thesis . . . . .	6
1.3	Layout of the Thesis . . . . .	6
<b>2</b>	<b>Mathematical Problem Description</b>	<b>9</b>
2.1	Fluid Flow on Moving Domains . . . . .	9
2.1.1	The Moving Reference Frame . . . . .	10
2.1.2	Conservation Laws . . . . .	12
2.1.3	Boundary Conditions, Free Surfaces and Interfaces . . . . .	14
2.1.4	On the Incompressible Navier-Stokes Equations . . . . .	17
2.2	Mechanics of Flexible Solids . . . . .	18
2.3	Rigid Body Dynamics . . . . .	20
2.4	Summary . . . . .	21
<b>3</b>	<b>The Basics of Finite Element Modelling</b>	<b>23</b>
3.1	The Weak Form and the Classical Galerkin Method . . . . .	24
3.2	Isoparametric Finite Elements . . . . .	27
3.3	Solution Procedure, Nonlinear Problems . . . . .	31
3.4	Problems with Constraints . . . . .	32
3.4.1	Mixed Methods . . . . .	34
3.4.2	Penalty Methods . . . . .	36
<b>4</b>	<b>Introduction to Stabilised Finite Elements for Fluid Flow</b>	<b>39</b>
4.1	The Galerkin Method and its Deficiencies . . . . .	40
4.1.1	Oscillatory Behaviour of the Velocity . . . . .	41
4.1.2	Spurious Pressure Modes . . . . .	44
4.2	Velocity Stabilisation . . . . .	46
4.2.1	Artificial Damping, SUPG and GLS Methods . . . . .	46
4.2.2	Stabilisation with Bubbles, Multiscale Method . . . . .	49
4.2.3	Summary, Equivalence of Methods . . . . .	53

4.3	Pressure Stabilisation . . . . .	58
4.3.1	PSPG and GLS Methods . . . . .	58
4.3.2	Stabilisation with Bubbles . . . . .	60
4.3.3	Summary, Equivalence of Methods . . . . .	62
4.4	SUPG/PSPG Formulation . . . . .	65
4.4.1	The Stabilisation Parameter . . . . .	66
4.4.2	Example: Lid Driven Cavity Flow . . . . .	69
<b>5</b>	<b>Time Integration Schemes for Unsteady Fluid Flow</b>	<b>73</b>
5.1	Scalar Model Problem . . . . .	75
5.1.1	Discrete Time Integration Schemes . . . . .	76
5.1.2	Time Finite Element Methods . . . . .	79
5.1.3	On the Algorithmic Treatment of the Schemes . . . . .	85
5.1.4	Discussion and Comparison of the Schemes . . . . .	87
5.1.5	Example . . . . .	90
5.2	One Dimensional Advection-Diffusion Problem . . . . .	90
5.2.1	Semi-Discrete Methods . . . . .	93
5.2.2	Space-Time Finite Element Methods . . . . .	97
5.2.3	Fourier Analysis . . . . .	101
5.2.4	Example . . . . .	114
5.3	Incompressible Navier-Stokes Equations . . . . .	122
5.3.1	Semi-Discrete Methods . . . . .	123
5.3.2	Space-Time Finite Element Methods . . . . .	125
5.3.3	Example I: Flow Around a Cylinder . . . . .	127
5.3.4	Example II: Flow Across a Backward Facing Step . . . . .	137
5.3.5	Conclusions . . . . .	141
<b>6</b>	<b>Arbitrary Lagrangian-Eulerian Description of Fluid Flow</b>	<b>145</b>
6.1	Fluid Finite Element Formulation on a Moving Domain . . . . .	147
6.2	Mesh Update Methods . . . . .	149
6.3	Fluid Flow with Prescribed Boundary Movement . . . . .	153
6.3.1	Example I: Flow Around a Cylinder . . . . .	153
6.3.2	Example II: Flow through a Narrowing Channel . . . . .	154
6.3.3	Example III: Channel with Wall Indentation . . . . .	157
<b>7</b>	<b>Surface Tension</b>	<b>161</b>
7.1	The Surface Tension Phenomena . . . . .	161
7.2	The Weak Form . . . . .	164
7.3	Two Dimensional Problems . . . . .	165
7.4	Axisymmetric Problems . . . . .	166

<b>8</b>	<b>Finite Elements in Solid Mechanics</b>	<b>169</b>
8.1	Continuum Element . . . . .	169
8.2	Membrane Element . . . . .	171
8.3	Beam Element . . . . .	173
8.4	Time Integration . . . . .	175
<b>9</b>	<b>Modelling of Interfaces</b>	<b>177</b>
9.1	Free Surface . . . . .	178
9.2	Fluid-Rigid Body Interface . . . . .	180
9.3	Fluid-Solid Interface . . . . .	183
<b>10</b>	<b>Solution Algorithm</b>	<b>187</b>
10.1	Domain Decomposition . . . . .	187
10.2	Partitioned Newton-Raphson Procedure . . . . .	191
10.3	Adaptive Time Stepping . . . . .	197
10.4	Alternative Solution Strategies . . . . .	197
	10.4.1 Weak Coupling – Staggered Solution Schemes . . . . .	199
	10.4.2 Strong Coupling . . . . .	200
<b>11</b>	<b>Examples I: Free Surface Flow</b>	<b>203</b>
11.1	Breaking Dam . . . . .	203
11.2	Small Amplitude Sloshing . . . . .	205
11.3	Large Amplitude Sloshing . . . . .	206
<b>12</b>	<b>Examples II: Free Surface Flow with Surface Tension</b>	<b>209</b>
12.1	Capillary Rise . . . . .	209
12.2	Large Sessile Drop . . . . .	212
12.3	Small Amplitude Oscillations of a Spherical Drop . . . . .	213
12.4	Large Amplitude Oscillations of a Liquid Cylinder . . . . .	215
12.5	Filling of a Drop . . . . .	217
12.6	Stretching of a Liquid Bridge . . . . .	222
<b>13</b>	<b>Examples III: Fluid - Rigid Body Interaction</b>	<b>229</b>
13.1	Vortex Induced Oscillations of a Cylinder . . . . .	229
13.2	Vortex Induced Oscillations and Galloping . . . . .	236
13.3	Rotational Galloping . . . . .	243
13.4	Flutter of a Bridge Deck . . . . .	250
13.5	Rotating Bar . . . . .	254

<b>14 Examples IV: Fluid - Solid Interaction</b>	<b>257</b>
14.1 Flow-Induced Oscillations of a Flexible Structure . . . . .	258
14.2 Flow through a Channel with a Flexible Wall . . . . .	271
14.3 Parachute at Low Reynolds Number . . . . .	276
14.4 A Pump with Two Valves . . . . .	280
<b>15 Conclusions</b>	<b>285</b>
15.1 Achievements and Conclusions . . . . .	285
15.2 Suggestions for Future Research . . . . .	287
<b>Bibliography</b>	<b>289</b>

# Chapter 1

## Introduction

The phenomena of fluid flows with moving free surfaces and interfaces is encountered not only in various areas of modern engineering, but also in nature and biology. In the following, some prominent examples are listed.

*Chemical engineering.* Many processes in chemical engineering and food processing involve free surface flows. Often, as for instance in sprays, these flows occur at very small scales and are governed by surface tension effects. Furthermore, various mixing processes represent fluid flows with moving interfaces.

*Mechanical engineering.* The flows through flexible hoses and pumps as well as the opening of an airbag or the rotation of a ship screw represent fluid flows with moving interfaces. Such flows also occur in combustion engines. The analysis of the stability and the dynamics of ships involves a moving free surface and a moving water-ship interface. In many printing techniques, the application of the ink to the paper is indeed a free surface fluid flow influenced substantially by the phenomena of surface tension.

*Aerospace engineering.* In this area of engineering, there are various evident examples of air flow with moving interfaces. The interaction of air flow with (elastic) structures is commonly referred to as *aeroelasticity*. Some of the most prominent examples are the flutter of airplane wings, propellers, rotors and the opening and the drag of parachutes.

*Civil engineering.* The exposure to wind represents a major factor in the appropriate design of many civil engineering structures. Especially, slender, wide or tall constructions, such as, for instance, bridges with wide spans, antennas, slim towers and transmission lines, may be excited to large deformations by the air flow. This can lead to structural failure. A prominent example of the fatal effect of wind flow on inappropriately designed construc-

tions is the Tacoma Narrows bridge, which was excited to large transverse and rotational oscillations and consequently collapsed, see Figure 1.1. Typically, the components of civil engineering structures are very stiff, and large displacements arise from the summation of small local deformations. Thus, the representation of the structures by flexibly supported rigid bodies is often sufficiently accurate to account for the wind-structure interaction.

*Biomechanical engineering and nature.* The blood flow through veins and arteries and the heart itself represents complex fluid flow with moving interfaces. Also the design of medical devices, such as micropumps, may require the understanding of such fluid flows. On a larger scale, tidal flows and the propagation of flood waves in rivers are examples of natural free surface fluid flows.

These examples suggest the following classification of fluid flows with moving free surfaces and interfaces:

1. *free surface flows* (possibly with surface tension),
2. *fluid-rigid body interaction* (fluid and flexibly supported rigid body),
3. *fluid-solid interaction* (fluid and flexible body or structure).

The interaction of fluid flow with rigid and flexible solid bodies belongs to the wide range of *coupled multifield problems*. The coupling arises from boundary conditions at the interface, which relate the boundary data of the adjacent fields <sup>1</sup>. In Zienkiewicz and Taylor [132], two criteria are given for the identification of coupled multifield systems:

- Neither domain can be solved while separated from the other.
- Neither set of dependent variables can be explicitly eliminated at the differential equation level.

Both criteria hold for fluid-rigid body and fluid-solid interaction. It shall become clear later in this work that the fluid flow itself may pose a coupled two field problem. This shall follow from the distinction between the physical fluid flow and the purely geometrical motion of the fluid domain, which are coupled at the moving free surface or interface. In this sense, one may regard free surface flows, fluid-rigid body and fluid-solid interaction problems, respectively, as coupled two and three field systems.

---

<sup>1</sup>Note that there exists a class of different physical multifield problems, where the spatial domains coincide and the coupling occurs through the governing differential equations. An example for such problems are fast metal forming processes, the simulation of which needs to account for the coupling of the deformation and the temperature.

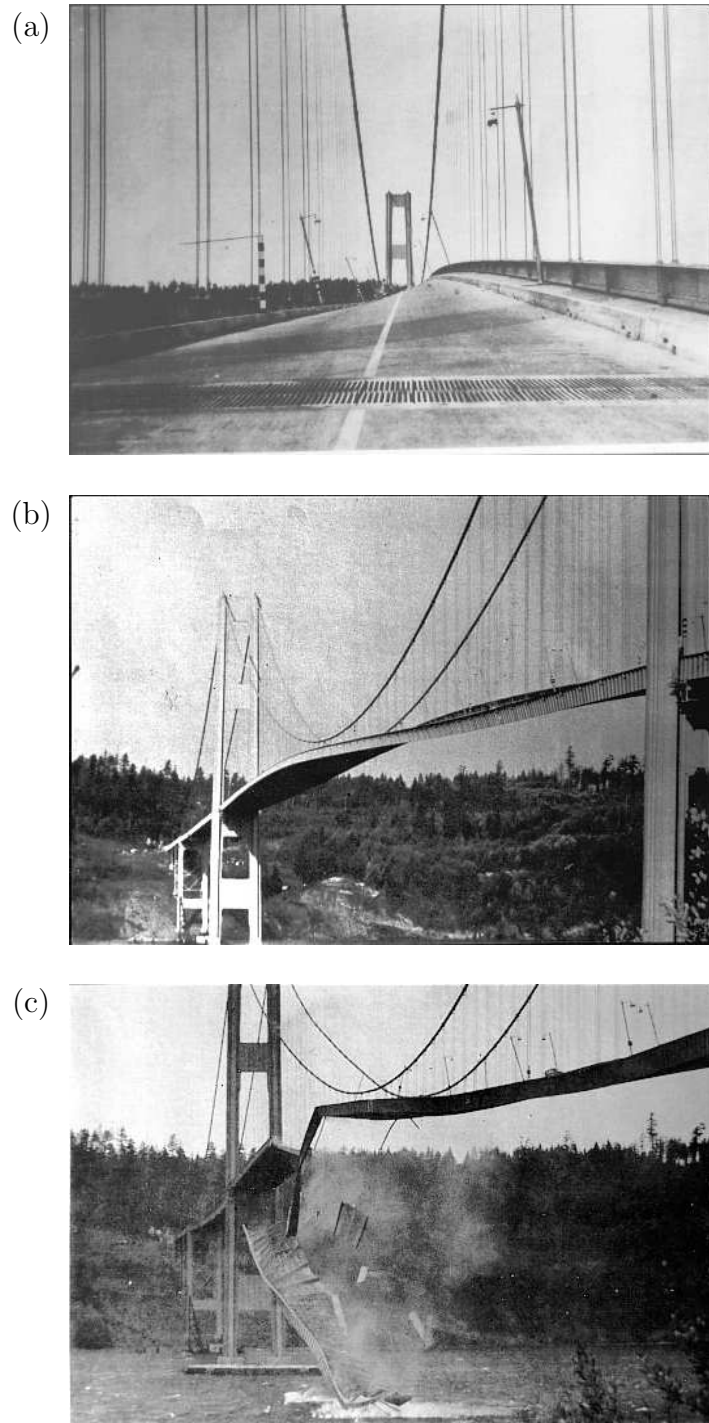


Figure 1.1: Collapse of the Tacoma Narrows suspension bridge, U.S.A., in 1940, large rotational oscillations of the bridge deck (a) and (b), collapse of the bridge (c).

The strong relevance and the widespread applicability of the problem classes 1. – 3. is clearly demonstrated by the given list of examples. Thus, the desire of the engineering industry to accurately analyse and predict free surface flows and problems of fluid-rigid body and fluid-solid interaction is evident. Due to the rapid development of computer hardware and computational methods during the last decades, the computer simulation of such problems can today be undertaken. The relevance attributed to the subject by the present day researchers is reflected in the considerable number of related scientific publications, few of which date back more than five years. It is, however, pointed out that the computational ingredients, which are part of the solution strategies, are much older.

In this context it may be said that no common agreement has yet been reached on the right choice of these ingredients and the question how they should be combined to achieve a robust, accurate and efficient computational tool. The work at hand aims to contribute to this area of research. Namely, a solution strategy for fluid flow with moving free surfaces and interfaces is outlined and detailed insight is provided into various aspects of the computational ingredients and of the overall strategy. All problem classes 1. – 3. are considered. For the brevity of this thesis, it is however essential to restrict the attention to a specific type of fluid flow. Thus, this work focusses on laminar incompressible Newtonian fluid flow. Certain stages of this research work have already been published by Dettmer and Perić in [29–35, 87].

The following sections briefly introduce the different approaches to the subject and provide a more detailed formulation of the task addressed by this work. The chapter concludes with a description of the layout of the thesis.

## 1.1 Numerical Strategies

*Modelling of the fluid flow.* Three methodologies are available for the numerical modelling of the fluid flow: *finite differences*, *finite volumes* and *finite elements*. Various techniques based on these strategies have been developed for different types of fluid flows, such as compressible or incompressible, laminar or turbulent fluid flow. All methods employ some kind of spatial mesh or grid of the fluid domain. Finite differences represent the oldest solution strategy, but nowadays they are seldom used due to the difficulties associated with their application to complex domain geometries. It may be said that for a long time finite volumes have been the unrivalled favourite in computational fluid dynamics simulations, but during recent years, finite element strategies have been developed which are equally attractive. Details of finite difference and finite volume methods are provided by Ferziger and Perić [47],

whereas several finite element strategies for fluid flow problems are discussed in the third volume of Zienkiewicz and Taylor [132] and references therein. In this work we shall employ a stabilised low equal order velocity/pressure finite element method. Details and references are given in Chapter 4.

*Modelling of the free surfaces and interfaces.* Two strategies exist for the modelling of moving fluid boundaries. The first is referred to as *interface tracking*. Here, the fluid mesh remains fixed in space throughout the simulation. Each cell or element of the mesh may be full or void of fluid. The motion of the interface is computed from the fluid velocity field. This strategy is applicable to moving free surfaces as well as interfaces. However, it often fails to accurately satisfy the mechanical conservation laws. Therefore, dense spatial meshes are usually required. A powerful computational tool has recently been developed by combining the so-called level set and the extended finite element strategies, see *e. g.* Sukumar *et al* [116] and references therein. The success of this methodology is based on the local enrichment of elements which contain the interface.

The second approach may be termed *interface capturing* and is followed in this work. It consists in the identification of the fluid mesh boundary with the free surface or the interface. Clearly, as the boundary nodes of the mesh follow the motion of the surface or interface, the internal nodes of the mesh have to adjust to the changes of the mesh geometry. The limits of this strategy are met when the displacement of the mesh boundary becomes so significant that it leads to extreme distortion of the cells or elements of the mesh. However, in this case, a single straightforward remeshing of the fluid domain allows the simulation to be continued. This strategy is usually referred to as the *Arbitrary Lagrangian-Eulerian* description of the fluid domain (ALE). The motion of the internal nodes of the fluid mesh is indeed arbitrary as long as the topology of the mesh is maintained. It is shown in this work that the strategy allows the accurate satisfaction of the conservation laws, and it minimises the necessity of remeshing. Details and references are given in Chapter 6.

*Time integration.* Two classes of finite element methods for transient fluid flow with moving free surfaces or interfaces may be distinguished: the so-called space-time finite element methods and semi-discrete methods. The space-time strategies are based on the finite element interpolation of the trial and test functions in both space and time, whereas semi-discrete methodologies rely on the finite element discretisation of space and the subsequent application of a discrete time integration scheme. References and details of both approaches are provided in Chapter 5. In this work, preference is given to the semi-discrete strategy.

*Solid structures.* The finite element method may today be regarded as the undisputed strategy for the numerical modelling of flexible solid structures. Depending on the problem under consideration, the appropriate discretisation of the structure may be achieved with continuum elements, truss, membrane, beam or shell elements. A small selection of standard finite elements shall be employed to demonstrate the generality of the solution strategy for fluid-solid interaction problems developed in this work.

*Surface tension.* Following Saksono [103], the surface tension boundary condition is rephrased such that its incorporation into the finite element framework is straightforward.

*Solution of the coupled nonlinear system.* The spatial and temporal discretisation of the problem under consideration leads to a strongly coupled set of highly nonlinear equations. In this work, a *partitioned Newton-Raphson procedure* is developed to solve for the unknown solution variables. The strategy is based on the analytical linearisation of the overall problem. Alternative solution algorithms comprise *partitioned* or *monolithic*, *weakly* or *strongly coupled* methodologies, which are discussed in some detail in Section 10.4.

## 1.2 The Aim of the Thesis

The aim of this thesis is the development of a robust, accurate and efficient numerical solution procedure for free surface fluid flows and the interaction of fluid flow with rigid or flexible solid bodies. The attention is restricted to laminar incompressible Newtonian fluid flow.

The solution strategy to be developed shall be based on finite element formulations of the fluid flow and the flexible solids. The free fluid surfaces or fluid-solid interfaces shall be captured by the motion of the fluid mesh or both the fluid and the solid mesh, respectively. Furthermore, for fluid-rigid body and fluid-solid interaction problems, the strategy is required to resolve the strong coupling of the fluid and solid phases exactly (up to machine precision).

## 1.3 Layout of the Thesis

*Chapter 2.* The governing equations of the laminar incompressible Newtonian fluid flow are derived in the ALE framework. The boundary conditions and the equations which govern the free surfaces and interfaces are presented. The solid mechanics equations used in this work are also given.

*Chapter 3.* This chapter presents a general introduction to the finite element method. It provides the preliminaries for the Chapters 4 and 8.

*Chapter 4.* Two numerical problems associated with the application of the standard Galerkin method to the incompressible Navier-Stokes equations are identified. Two representative model problems, *i. e.* the advection-diffusion equation and the Stokes flow, are employed to outline and compare several modified Galerkin strategies, which can overcome the numerical deficiencies of the standard formulation. Finally, the stabilised SUPG/PSPG finite element method for the steady state incompressible Navier-Stokes equations is presented. Its good performance is illustrated in the simulation of the lid driven cavity flow.

*Chapter 5.* Several time integration strategies including both discrete and time finite element methods are introduced by means of their application to a scalar model problem. The different numerical properties are established. The time integration schemes are then applied to a stabilised finite element formulation of the one dimensional advection-diffusion equation, which renders both semi-discrete and space-time finite element methods. The different properties of the overall schemes are studied in detail by means of a Fourier analysis. Finally, the time integration schemes are employed for the temporal discretisation of the SUPG/PSPG finite element formulation of the incompressible Navier-Stokes equations on fixed domains. The resulting semi-discrete and space-time strategies are employed to simulate the flow around a cylinder and the flow across a backward facing step. The numerical results are compared in detail and related to the conclusions drawn from the model problems. Preference is given to the semi-discrete strategy based on the generalised- $\alpha$  method.

*Chapter 6.* The finite element formulation of the incompressible Navier-Stokes equations of Chapter 5 is extended to moving domains by means of an ALE strategy. Several mesh update strategies are discussed. The issue of the geometrical conservation law is briefly addressed. Three numerical examples, including the flow through a channel with a moving wall indentation, are presented.

*Chapter 7.* The Laplace-Young equation, which describes the phenomena of surface tension, is derived and rephrased in a finite element framework. Detailed expressions are derived for the two dimensional and the axisymmetric situations.

*Chapter 8.* The solid mechanics finite element methods, which are employed in the numerical examples of Chapter 14, are presented.

*Chapter 9.* The numerical modelling of the free surfaces and the fluid-rigid body and fluid-solid interfaces is described.

*Chapter 10.* A general representation of the overall problems is achieved by the introduction of the interface domain. A partitioned solution strategy based on the Newton-Raphson method is developed to solve the coupled system of nonlinear equations. Alternative solution procedures are discussed.

*Chapter 11.* Numerical examples for free surface flow. The collapsing liquid column and sloshing in a rectangular tank are simulated.

*Chapter 12.* Numerical examples for free surface flow with surface tension. These examples include the rise of water in a capillary pipe, the oscillation of drops, the filling of a drop and the stretching of a liquid bridge under the influence of gravity. Different spatial and temporal discretisations are considered. The conservation of the fluid volume and the robustness of the solution strategy are studied. Reference solutions are employed to verify the numerical results.

*Chapter 13.* Numerical examples for fluid-rigid body interaction. The phenomena of vortex induced transverse oscillations, transverse and rotational galloping and flutter of rigid bodies in uniform flow are simulated. The last example concerns the damping of an oscillating rigid body by the surrounding fluid. Different levels of discretisation are studied. The numerical results are compared to reference solutions.

*Chapter 14.* Numerical examples for fluid-solid interaction. The vortex induced oscillations of a flexible beam in uniform fluid flow are simulated and compared to reference solutions. Three different solid mechanics finite element representations of the beam are considered. Next, the flow through a channel with a flexible wall section is studied in detail. Finally, the robustness of the methodology is illustrated by examples of a two dimensional model parachute and a pump with valves.

*Chapter 15.* The achievements of this work are summarised and conclusions are drawn. The thesis concludes with suggestions for future research.

# Chapter 2

## Mathematical Problem Description

In this chapter the equations are presented, which govern the behaviour of the mechanical systems under consideration. The physical components of the problems discussed in this work are the fluid and flexible or rigid solid bodies, which are, at least partly, submerged in the fluid.

Accordingly, the following three sections are concerned with the mechanics of the fluid flow, the solid structure and rigid body dynamics. The focus is clearly on the description of the fluid flow on moving domains. The presentation of the laws of solid mechanics is restricted to a brief discussion of the theory underlying the finite element formulations described in Chapter 8. It has been chosen to discuss the particulars of free fluid surfaces and fluid-solid interfaces in the framework of the boundary conditions for the fluid flow. The complete set of the governing equations, or in other words, the complete mathematical description of the problems considered in this thesis is summarised in Box 2.1 at the end of this chapter.

This work is restricted to incompressible Newtonian fluids and elastic solids. It should however be noted that, with no or little modification, the computational framework developed in the later chapters is applicable to a much wider range of constitutive behaviour.

### 2.1 Fluid Flow on Moving Domains

The mathematical description of the fluid flow is organised as follows: First, in Section 2.1.1, a frame of reference is introduced, which allows the formulation of the mechanical conservation laws on moving domains. Due to the focus on incompressible Newtonian fluids, it suffices to consider the conser-

vation of mass and momentum, which are presented in Section 2.1.2. For more information on fluid mechanics and its mathematical modelling one is referred to the various text books on the subject, *e. g.* Bird *et al* [8], Currie [26], Spurk [113], Chorin and Marsden [21]. In Section 2.1.3, the boundary conditions and interface equations relevant for the problems considered in this work are presented. Finally, Section 2.1.4 briefly comments on the range of applicability and the limitations of the mathematical fluid mechanics model adopted in this work.

### 2.1.1 The Moving Reference Frame

An essential common feature of the problems under consideration is the motion of the boundary of the fluid domain. The geometry of the fluid domain may change substantially during the time domain of interest. The fluid particles flow in or through a spatial domain, which is itself at motion. Therefore, a moving reference frame is introduced, in which the conservation laws are formulated.

Thus, we distinguish the *initial* configuration  $\mathcal{B}_0$  and the *current* configuration  $\mathcal{B}$  of the fluid body, and, similarly, we define the initial and the current configurations  $\Omega_0$  and  $\Omega$  of the reference domain. The coordinate systems associated with these domains are  $\mathbf{x}_0 \in \mathcal{B}_0$ ,  $\mathbf{x} \in \mathcal{B}$ ,  $\hat{\mathbf{x}}_0 \in \Omega_0$  and  $\hat{\mathbf{x}} \in \Omega$ . Commonly,  $\mathbf{x}_0$  and  $\mathbf{x}$  are denoted, respectively, as the *material* and *spatial* coordinates. The motion of the fluid body and the reference domain are such that there exist the unique maps

$$\mathbf{x} = \phi(\mathbf{x}_0, t), \quad \hat{\mathbf{x}} = \lambda(\hat{\mathbf{x}}_0, t). \quad (2.1)$$

Thus, each  $\mathbf{x} = \hat{\mathbf{x}} \in (\mathcal{B} \cap \Omega)$  is associated with a material point  $\mathbf{x}_0$  and a reference point  $\hat{\mathbf{x}}_0$ , as illustrated in Figure 2.1. Preliminary to the formulation of the conservation laws, an expression is now derived for the time derivative of the velocity  $\mathbf{u}$  of the specific material particle  $\mathbf{x}_0$ , which happens to pass through the position  $\hat{\mathbf{x}}$  at the time instant  $t$ . This derivative is commonly denoted as the *material* time derivative of  $\mathbf{u}$ .

Therefore, it is noted that, for  $\mathbf{x} = \hat{\mathbf{x}}$ , there exists a unique map  $\psi$  with

$$\hat{\mathbf{x}}_0 = \psi(\mathbf{x}_0, t) = \lambda^{-1}(\phi(\mathbf{x}_0, t), t). \quad (2.2)$$

It may then be written that

$$\mathbf{x} = \phi(\mathbf{x}_0, t) = \lambda(\hat{\mathbf{x}}_0, t) = \lambda(\psi(\mathbf{x}_0, t), t) = \hat{\mathbf{x}}. \quad (2.3)$$

Differentiating this expression with respect to time for a specific constant material point  $\mathbf{x}_0$  renders

$$\frac{\partial \phi(\mathbf{x}_0, t)}{\partial t} = \frac{\partial \lambda(\hat{\mathbf{x}}_0, t)}{\partial t} + \frac{\partial \lambda(\hat{\mathbf{x}}_0, t)}{\partial \hat{\mathbf{x}}_0} \frac{\partial \psi(\mathbf{x}_0, t)}{\partial t}. \quad (2.4)$$

The left hand side of this equation is identified as the current velocity  $\mathbf{u}$  of the material particle  $\mathbf{x}_0$ , whereas the first term on the right hand side represents the current velocity  $\hat{\mathbf{v}}$  of the reference point  $\hat{\mathbf{x}}_0$ . Hence,

$$\frac{\partial \lambda(\hat{\mathbf{x}}_0, t)}{\partial \hat{\mathbf{x}}_0} \frac{\partial \psi(\mathbf{x}_0, t)}{\partial t} = \mathbf{u} - \hat{\mathbf{v}}. \quad (2.5)$$

Keeping in mind that the velocity field  $\mathbf{u}$  may be given in terms of  $\hat{\mathbf{x}}_0$  or  $\hat{\mathbf{x}}$ , namely

$$\mathbf{u} = \hat{\mathbf{u}}(\hat{\mathbf{x}}_0, t) = \tilde{\mathbf{u}}(\hat{\mathbf{x}}, t), \quad (2.6)$$

it is now sought to determine the time derivative of  $\mathbf{u}$  for the material particle  $\mathbf{x}_0$  which passes through  $\hat{\mathbf{x}}$  at time instant  $t$ . One obtains

$$\frac{D \mathbf{u}}{D t} = \frac{\partial \hat{\mathbf{u}}(\hat{\mathbf{x}}_0, t)}{\partial \hat{\mathbf{x}}_0} \frac{\partial \psi(\mathbf{x}_0, t)}{\partial t} + \frac{\partial \hat{\mathbf{u}}(\hat{\mathbf{x}}_0, t)}{\partial t} \quad (2.7)$$

$$= \frac{\partial \tilde{\mathbf{u}}(\hat{\mathbf{x}}, t)}{\partial \hat{\mathbf{x}}} \frac{\partial \lambda(\hat{\mathbf{x}}_0, t)}{\partial \hat{\mathbf{x}}_0} \frac{\partial \psi(\mathbf{x}_0, t)}{\partial t} + \frac{\partial \hat{\mathbf{u}}(\hat{\mathbf{x}}_0, t)}{\partial t} \quad (2.8)$$

By using (2.5) and by defining  $\dot{\mathbf{u}} = \partial \hat{\mathbf{u}}(\hat{\mathbf{x}}_0, t) / \partial t$ , one arrives at

$$\frac{D \mathbf{u}}{D t} = \nabla_{\hat{\mathbf{x}}} \mathbf{u} (\mathbf{u} - \hat{\mathbf{v}}) + \dot{\mathbf{u}}. \quad (2.9)$$

The operator  $\nabla_{\hat{\mathbf{x}}}(\bullet)$  denotes the derivatives with respect to the current referential coordinates  $\hat{\mathbf{x}}$ . The expression  $\dot{\mathbf{u}}$  corresponds to the change of the

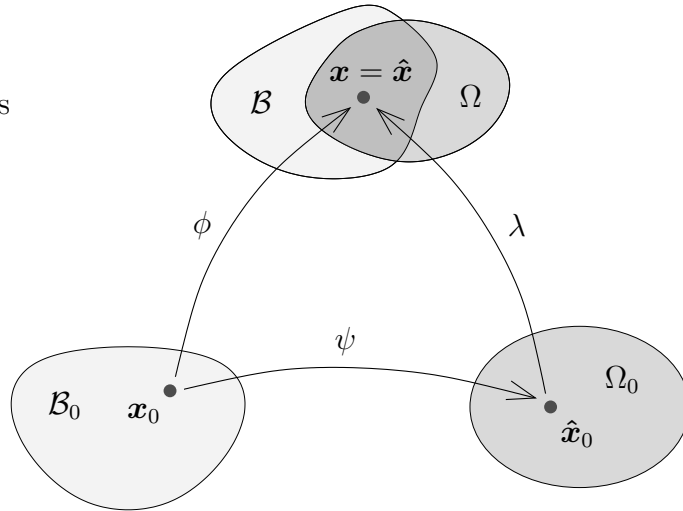


Figure 2.1: Mappings and configurations in ALE description.

material particle velocity, which is noted by an observer travelling with the referential coordinate  $\hat{\mathbf{x}}_0$ . The relation (2.9) is sometimes referred to as the *fundamental arbitrary Lagrangian-Eulerian equation* (ALE). The velocity difference  $\mathbf{u} - \hat{\mathbf{v}}$  is denoted as the *convective velocity*. Even though not relevant for this work, it is important to note that, analogously to (2.9), expressions can be derived for the material time derivatives of any scalar or vector-valued quantity associated with the fluid particles, such as for instance temperature. More information on the coordinate mappings and the derivation of (2.9) may be found in *e. g.* Wall and Ramm [128], Wall [127], Donea [36], Soulaimani *et al* [111], Braess and Wriggers [12], Belytschko *et al* [7]. In the framework of the finite element method, the moving reference frame is identified with the finite element mesh, which is moving and deforming over time and thereby adapts to the motion of the mesh boundaries.

The motivation for the terminology of the ‘‘ALE’’ description is readily shown by considering two special cases:

*Eulerian description.* In fluid flow problems with fixed boundaries, the reference frame may remain fixed in space. Consequently, the velocity field  $\hat{\mathbf{v}}$  disappears and the material derivative (2.9) reduces to

$$\frac{D\mathbf{u}}{Dt} = (\nabla_{\hat{\mathbf{x}}}\mathbf{u})\mathbf{u} + \dot{\mathbf{u}}, \quad (2.10)$$

which is the classical expression employed in standard *Eulerian* fluid flow analyses.

*Lagrangian description.* The other special case is obtained when the reference frame is attached to the fluid particles, *i. e.*  $\mathbf{u} = \hat{\mathbf{v}}$ . Then the relation (2.9) becomes

$$\frac{D\mathbf{u}}{Dt} = \dot{\mathbf{u}}. \quad (2.11)$$

Thus, the observer travels with the material particle itself, and the convective velocity completely vanishes. This approach is the basis of the classical *Lagrangian* description of solid mechanics.

*Notational agreement.* Throughout this work, the gradient operator  $\nabla(\bullet)$  without subscript denotes the derivatives with respect to the coordinates of the domain within which the expression is formulated. Subscripts may be used in some cases, where this is not clear from the context.

## 2.1.2 Conservation Laws

*Conservation of mass.* Let  $\Omega' \in \Omega$  denote a subregion of the current referential configuration, such that  $\Omega'$  contains a fixed set of referential points

and is always filled with fluid, but is otherwise arbitrary. For incompressible fluids, it follows that, per time unit, the amount of fluid particles leaving or entering  $\Omega'$  must be equalled by the change of the size of  $\Omega'$ . Thus, one may write

$$\int_{\Gamma'} (\mathbf{u} - \hat{\mathbf{v}}) \cdot \hat{\mathbf{n}} \, da = \int_{\Gamma'} -\hat{\mathbf{v}} \cdot \hat{\mathbf{n}} \, da, \quad (2.12)$$

where  $\Gamma'$  denotes the boundary of  $\Omega'$  and the vector  $\hat{\mathbf{n}}$  represents the outward unit normal vector of  $\Gamma'$ . The divergence theorem renders

$$\int_{\Omega'} \nabla \cdot \mathbf{u} \, dv = 0, \quad (2.13)$$

and, since this holds for any  $\Omega'$  at any time instant  $t \in I$ , the local form of the mass conservation law is obtained as

$$\nabla \cdot \mathbf{u} = 0 \quad \forall (\hat{\mathbf{x}}, t) \in \Omega \times I, \quad (2.14)$$

where  $I = [0, T_{\text{end}}]$  denotes the time interval of interest. The relation (2.14) is commonly referred to as the *continuity* equation.

*Conservation of momentum.* At any time instant  $t \in I$ , the fluid particles currently in  $\Omega'$  are subjected to the body forces, which may be associated with the fluid mass, and the surface forces, which act on  $\Gamma'$  and arise from the internal stress of the fluid. Following Newton's second law, these forces are balanced by the inertia of the fluid. Thus, one may write

$$\int_{\Omega'} \rho \mathbf{f} \, dv + \int_{\Gamma'} \boldsymbol{\sigma} \hat{\mathbf{n}} \, da = \int_{\Omega'} \rho (\nabla \mathbf{u} (\mathbf{u} - \hat{\mathbf{v}}) + \dot{\mathbf{u}}) \, dv, \quad (2.15)$$

where the tensor  $\boldsymbol{\sigma}$ , the vector  $\mathbf{f}$  and the scalar  $\rho$  denote, respectively, the *Cauchy* stress tensor, the body force associated with a unit mass and the fluid density. The application of the divergence theorem on the second integral renders

$$\int_{\Omega'} \rho (\dot{\mathbf{u}} + \nabla \mathbf{u} (\mathbf{u} - \hat{\mathbf{v}}) - \mathbf{f}) - \nabla \cdot \boldsymbol{\sigma} \, dv = \mathbf{0}, \quad (2.16)$$

which holds for any  $\Omega'$ . Thus, the local form of the momentum balance is obtained as

$$\rho (\dot{\mathbf{u}} + \nabla \mathbf{u} (\mathbf{u} - \hat{\mathbf{v}}) - \mathbf{f}) - \nabla \cdot \boldsymbol{\sigma} = \mathbf{0} \quad \forall (\hat{\mathbf{x}}, t) \in \Omega \times I. \quad (2.17)$$

*Constitutive law.* In this work, only Newtonian fluids are considered which are governed by

$$\boldsymbol{\sigma} = -p \mathbf{I} + 2\mu \nabla^s \mathbf{u}. \quad (2.18)$$

The quantities  $p$ ,  $\mathbf{I}$  and  $\mu$  denote, respectively, the pressure, the identity tensor and the fluid viscosity. The operator  $\nabla^s(\bullet)$  represents the symmetric part of the gradient, *e. g.*  $\nabla^s \mathbf{u} = \frac{1}{2}(\nabla \mathbf{u} + \nabla^T \mathbf{u})$ .

Together, the equations (2.14), (2.17) and (2.18) are commonly referred to as the *Navier-Stokes equations for incompressible fluid flow*.

### 2.1.3 Boundary Conditions, Free Surfaces and Interfaces

At this stage, the referential configuration  $\Omega$  is identified with the computational spatial domain  $\Omega_f$ , within which one seeks to compute the fluid flow for all times  $t \in I$ . Consequently, the velocity  $\hat{\mathbf{v}}$  of the referential coordinates  $\hat{\mathbf{x}}$  needs to be chosen appropriately, such that the domain  $\Omega_f$  may adapt to the changing configurations of free surfaces and fluid-solid interfaces.

Figure 2.2 illustrates that the problems treated in this work require the consideration of various types of boundary conditions for the domain  $\Omega_f$ . The boundary of  $\Omega_f$  may be decomposed into several complementary subsections which represent at least some of the boundary types listed below.

First, those sections are considered, the motion of which is known a priori. Along such boundaries, the velocity  $\hat{\mathbf{v}}$  (or at least its normal component  $\hat{\mathbf{v}} \cdot \hat{\mathbf{n}}$ ) is given at all times  $t \in I$ . Indeed, in most cases, one simply has  $\hat{\mathbf{v}} = \mathbf{0}$ .

- *in-flow boundary*  $\Gamma_{\text{in}}$ . Usually, all components of the fluid velocity  $\mathbf{u}$  are prescribed. The boundary traction forces (flux of momentum) are unknown. The boundary condition may be written as

$$\mathbf{u} - \mathbf{u}_{\text{in}} = \mathbf{0} \quad \forall (\hat{\mathbf{x}}, t) \in \Gamma_{\text{in}} \times I. \quad (2.19)$$

- *out-flow boundary*  $\Gamma_{\text{out}}$ . Usually, the fluid velocity vector is unknown, and the boundary traction forces are set to zero, *i. e.*

$$\boldsymbol{\sigma} \hat{\mathbf{n}} = \mathbf{0} \quad \forall (\hat{\mathbf{x}}, t) \in \Gamma_{\text{out}} \times I. \quad (2.20)$$

Note that it is useful to prescribe zero pressure in at least a point on the out-flow boundary.

- *slip boundary*  $\Gamma_{\text{slip}}$ . This type of boundary does not allow any non-zero fluid velocity components normal to the boundary, whereas the tangential flow is free. Hence, the slip boundary condition may be expressed as, *i. e.*

$$\mathbf{u} \cdot \hat{\mathbf{n}} = 0, \quad (\boldsymbol{\sigma} \hat{\mathbf{n}}) \cdot \hat{\mathbf{m}} = 0 \quad \forall (\hat{\mathbf{x}}, t) \in \Gamma_{\text{slip}} \times I, \quad (2.21)$$

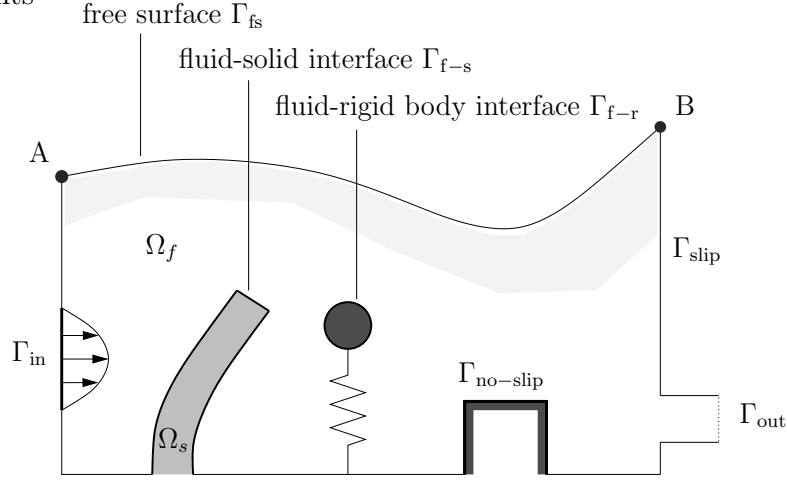


Figure 2.2: Fluid domain  $\Omega_f$  and different boundary types.

where  $\hat{\mathbf{n}}$  and  $\hat{\mathbf{m}}$  denote the normal and the tangential unit vectors of the boundary  $\Gamma_{\text{slip}}$ . Though not considered in this work, it is pointed out that for the realistic modelling of most physical problems with wall-slip, it is necessary to define a specific amount of wall friction, see *e. g.* Rippl [98] and Ettinger [42] and references therein.

- *no-slip boundary*  $\Gamma_{\text{no-slip}}$ . All velocity components are set to zero,

$$\mathbf{u} = \mathbf{0} \quad \forall (\hat{\mathbf{x}}, t) \in \Gamma_{\text{no-slip}} \times I. \quad (2.22)$$

The remaining types of boundary conditions have in common, that the motion of these boundary sections is not known a priori. In fact, the geometry changes arise from the simultaneous satisfaction of both the kinematic boundary conditions and the stress equilibrium equations given below.

- *free surface boundary*  $\Gamma_{\text{fs}}$ . On free surfaces the normal component of the velocity  $\hat{\mathbf{v}}$  of the referential frame must equal the normal component of the fluid velocity  $\mathbf{u}$ . Thus, by requiring

$$(\mathbf{u} - \hat{\mathbf{v}}) \cdot \hat{\mathbf{n}} = 0 \quad \forall (\hat{\mathbf{x}}, t) \in \Gamma_{\text{fs}} \times I, \quad (2.23)$$

it is ensured that the boundary  $\Gamma_{\text{fs}}$  accurately represents the free surface at all times  $t \in I$ . Equation (2.23) is often referred to as the *free surface consistency condition*. For free surface flows, where the surface tension phenomena may be neglected, zero traction forces and a zero pressure need to be prescribed, *i. e.*

$$\boldsymbol{\sigma} \hat{\mathbf{n}} = \mathbf{0}, \quad p = 0 \quad \forall (\hat{\mathbf{x}}, t) \in \Gamma_{\text{fs}} \times I. \quad (2.24)$$

For many small scale free surface flows, it is essential to take into account the surface tension effects. The boundary condition (2.24) then becomes

$$\boldsymbol{\sigma} \hat{\mathbf{n}} - (-p_{\text{ext}} \hat{\mathbf{n}} + 2\gamma_{\text{st}} H \hat{\mathbf{n}}) = \mathbf{0} \quad \forall (\hat{\mathbf{x}}, t) \in \Gamma_{\text{fs}} \times I, \quad (2.25)$$

where  $p_{\text{ext}}$ ,  $\gamma_{\text{st}}$  and  $H$  denote, respectively, the external pressure, the surface tension coefficient and the mean curvature of the surface. The relation (2.25) is known as the *Laplace-Young* equation. It is derived and discussed in more detail in Chapter 7. Note that the fluid pressure  $p$  at the boundary must not be set to zero, but can be computed from the equation (2.25).

As illustrated in Figure 2.2, free surfaces are usually bounded by solid walls, on which the slip boundary condition is specified. For two dimensional problems, the velocity  $\hat{\mathbf{v}}$  in the contact points A and B must equal the fluid velocity  $\mathbf{u}$ .

- *fluid-rigid body interface*  $\Gamma_{\text{f-r}}$ . Analogously to the boundary conditions discussed above, one may distinguish slip and no-slip fluid-solid interfaces. In this work, the focus is on no-slip interfaces, which account much more accurately for the physics of real fluid-structure interaction. The employment of the slip condition may be computationally advantageous in problems with very large Reynolds numbers (see Section 2.1.4), where the boundary layers are thin and the fluid-solid interaction is not driven by vortex shedding.

The no-slip condition is readily expressed as

$$\mathbf{u} = \dot{\mathbf{d}}_{\Gamma_{\text{f-r}}} \quad \forall (\hat{\mathbf{x}}, t) \in \Gamma_{\text{f-r}} \times I, \quad (2.26)$$

where  $\mathbf{d}_{\Gamma_{\text{f-r}}}$  denotes the displacement of the solid material particles at the surface of the rigid body. Note that any  $\mathbf{d}_{\Gamma_{\text{f-r}}}$  can be written exclusively in terms of the current translational or rotational degrees of freedom of the rigid body (see Section 9.2). Similar to the free surface, the velocity  $\hat{\mathbf{v}}$  of the reference frame needs to satisfy

$$(\mathbf{u} - \hat{\mathbf{v}}) \cdot \hat{\mathbf{n}} = 0 \quad \forall (\hat{\mathbf{x}}, t) \in \Gamma_{\text{f-r}} \times I. \quad (2.27)$$

Thus, one may allow the reference coordinates to “slide” along the surface of the submerged rigid body. However, in Section 9.2, the relation (2.27) is simply satisfied by setting  $\hat{\mathbf{v}} = \mathbf{u}$ .

The equilibrium of the stresses along the interface requires that

$$\int_{\Gamma_{\text{f-r}}} \boldsymbol{\sigma} \hat{\mathbf{n}} \, da = -\mathbf{F}, \quad \int_{\Gamma_{\text{f-r}}} \|(\boldsymbol{\sigma} \hat{\mathbf{n}}) \times \Delta \mathbf{x}\| \, da = -M \quad \forall t \in I, \quad (2.28)$$

where  $\Delta \mathbf{x}$  denotes the position of a reference material point of the rigid body, *e. g.* the centre of gravity, relative to the points on  $\Gamma_{f-r}$ . The quantities  $\mathbf{F}$  and  $M$  represent, respectively, the force vector and the moment exerted on the fluid by the rigid body. The relation (2.28)<sub>2</sub> describes the two dimensional situation with only one rotational degree of freedom.

- *fluid-solid interface*  $\Gamma_{f-s}$ . Corresponding to the no-slip fluid-rigid body interface discussed above, this work is concerned with “no-slip” fluid-solid interfaces. Thus, it follows that

$$\mathbf{u} = \dot{\mathbf{d}} \quad \forall (\hat{\mathbf{x}}, t) \in \Gamma_{f-s} \times I. \quad (2.29)$$

The vector  $\mathbf{d}$  denotes the displacements of the solid structure. Analogously to (2.23) and (2.27), the velocity  $\hat{\mathbf{v}}$  is required to satisfy

$$(\mathbf{u} - \hat{\mathbf{v}}) \cdot \hat{\mathbf{n}} = 0 \quad \forall (\hat{\mathbf{x}}, t) \in \Gamma_{f-s} \times I, \quad (2.30)$$

which is guaranteed in Section 9.3 by setting  $\hat{\mathbf{v}} = \mathbf{u}$ . The equilibrium of the stresses in the interface yields

$$(\boldsymbol{\sigma} \hat{\mathbf{n}})_f = -(\boldsymbol{\sigma} \mathbf{n})_s \quad \forall (\hat{\mathbf{x}}, t) \in \Gamma_{f-s} \times I, \quad (2.31)$$

where the expressions  $(\boldsymbol{\sigma} \hat{\mathbf{n}})_f$  and  $(\boldsymbol{\sigma} \mathbf{n})_s$  represent the traction forces exerted by the fluid and the solid on the interface.

## 2.1.4 On the Incompressible Navier-Stokes Equations

*Laminar and turbulent flows.* In any fluid flow, the ratio of the inertial forces and the viscous forces can be measured by the dimensionless *Reynolds* number, which is defined as

$$Re = \frac{U D \rho}{\mu}, \quad (2.32)$$

where  $U$  and  $D$  denote the characteristic velocity and a characteristic length scale of the fluid flow, respectively. The various types of flows occurring in nature and engineering are associated with Reynolds numbers which range from less than 0.2 (water flow around a paramecium) to more than  $2 \cdot 10^{+9}$  (air flow around a Boing 747).

The direct dependency of the fluid flow on the Reynolds number becomes evident by considering the non-dimensionalised form of the incompressible

Navier-Stokes equations. Therefore, by means of appropriate multiplication or division with the constants  $U$ ,  $D$  and  $\rho$ , non-dimensionalised velocities, pressure, spatial and temporal coordinates are defined. Using those in the balance of momentum (2.17), whereby  $\boldsymbol{\sigma}$  is substituted by the constitutive law (2.18), renders in fact a non-dimensionalised equation with the Reynolds number as the only parameter (see *e. g.* Spurk [113], Chorin and Marsden [21]).

Generally, it is observed from experiments that fluid flows at low Reynolds numbers are *laminar*, whereas, if a critical Reynolds number is exceeded, the flow becomes *turbulent*. This critical Reynolds number depends crucially on the problem under consideration. For example, it is generally accepted that the critical Reynolds number for fluid flow through a circular pipe is approximately 2300. Turbulent flows are always unsteady, three dimensional and rotational. Typically, they exhibit extensive vortex shedding on a small scale, such that the velocity of the fluid particles seems chaotic and random. The numerical modelling of turbulent flows requires the modification of the governing equations, such that the turbulence is accounted for in an average sense. The formulation of appropriate turbulence models is at present a focus of intense investigation. A detailed review of turbulence research is provided by Ferziger and Perić [47].

For the sake of brevity, the turbulence is not considered in this work. Hence, all the numerical examples presented in Chapters 11 – 14 involve fluid flows with the Reynolds number in the laminar range.

*Incompressibility.* Real fluids, especially gases, are compressible. A measure of the relevance of the compressibility for a specific problem is given by the *Mach* number, which is defined as the ratio  $Ma = U/c$  of the characteristic velocity and the speed of sound in the fluid. For  $Ma < 0.3$ , the fluid flow may be regarded as incompressible, see *e. g.* Ferziger and Perić [47]. Thus, almost all liquid fluid flows occurring in nature and engineering, but also many problems with gaseous fluids such as, for instance, air flows at the whole range of realistic wind speeds, can be modelled as incompressible.

## 2.2 Mechanics of Flexible Solids

The kinematics of flexible solids is commonly described in a Lagrangian manner. Thus, with respect to the general setting introduced in Section 2.1.1, the configurations  $\Omega_0$  and  $\mathcal{B}_0$  coincide and the map  $\lambda$  is identical to  $\phi$ . Hence, the current configuration of the solid material body serves as the computational domain  $\Omega_s$ . The displacements of the solid particles are represented by the vector field  $\boldsymbol{d}$ . The current position of the material points can then be

written as  $\mathbf{x} = \mathbf{x}_0 + \mathbf{d}$ , where  $\mathbf{x}_0$  are the particle coordinates at  $t = 0$ . With  $\mathbf{d} = \hat{\mathbf{d}}(\mathbf{x}_0, t)$ , the material velocity follows as  $\partial \hat{\mathbf{d}}(\mathbf{x}_0, t) / \partial t = \dot{\mathbf{d}}$ . The particle acceleration or material derivative of  $\dot{\mathbf{d}}$  is obtained as

$$\frac{D^2 \mathbf{d}}{Dt^2} = \frac{\partial^2 \hat{\mathbf{d}}(\mathbf{x}_0, t)}{\partial t^2} = \ddot{\mathbf{d}}, \quad (2.33)$$

which corresponds to (2.11).

*Momentum conservation law.* The balance of momentum may then be expressed as

$$\rho(\ddot{\mathbf{d}} - \mathbf{f}) - \nabla \cdot \boldsymbol{\sigma} = \mathbf{0} \quad \forall (\mathbf{x}, t) \in \Omega_s \times I. \quad (2.34)$$

Note that the material is assumed to be compressible. Thus, the densities  $\rho_0$  and  $\rho$  of an undeformed and a deformed volume element, respectively, need to be distinguished. By introducing an alternative representation of the stress and by replacing  $\rho$  with  $\rho_0$ , it is straightforward to rephrase (2.34) in the initial undeformed configuration  $\Omega_{s,0}$ , see *e. g.* Stein and Barthold [114], Wriggers [129], Bonet and Wood [10]. If the displacements  $\mathbf{d}$  are small, the configuration  $\Omega_s$  may be approximated by  $\Omega_{s,0}$  and one obtains the setting for classical small strain analysis.

*Constitutive law.* In this work, the solid structures are assumed to consist of a specific type of Neo-Hookean elastic material. Thus, the constitutive stress-strain relation employed reads

$$\boldsymbol{\sigma} = \mu J^{-\frac{5}{3}} (\mathbf{B} - \frac{1}{3} \text{tr}(\mathbf{B}) \mathbf{I}) + K \frac{J^2 - 1}{2J} \mathbf{I}. \quad (2.35)$$

The scalars  $\mu$  and  $K$  denote the shear and bulk moduli of the material, respectively. The *left Cauchy-Green tensor*  $\mathbf{B}$  and the scalar  $J$  are related to the deformation gradient  $\mathbf{F}$  by

$$\mathbf{B} = \mathbf{F} \mathbf{F}^T, \quad J = \det(\mathbf{F}), \quad (2.36)$$

where

$$\mathbf{F} = \frac{\partial \mathbf{x}}{\partial \mathbf{x}_0} = \mathbf{I} + \frac{\partial \mathbf{d}}{\partial \mathbf{x}_0}. \quad (2.37)$$

More information on (2.35) is provided by Wriggers [129]. For small strain elasticity, (2.35) reduces to

$$\boldsymbol{\sigma} = 2\mu \left( \nabla^s \mathbf{d} - \frac{1}{3} (\nabla \cdot \mathbf{d}) \mathbf{I} \right) + K (\nabla \cdot \mathbf{d}) \mathbf{I}. \quad (2.38)$$

*Boundary conditions.* The boundary of  $\Omega_s$  may consist of several complementary subsections, in each of which one of the following conditions holds:

- *fixed boundary*  $\Gamma_{\text{clamp}}$

$$\mathbf{d} = \mathbf{0} \quad \forall (\mathbf{x}, t) \in \Gamma_{\text{clamp}} \times I \quad (2.39)$$

- *free boundary*  $\Gamma_{\text{free}}$

$$\boldsymbol{\sigma} \mathbf{n} = \mathbf{0} \quad \forall (\mathbf{x}, t) \in \Gamma_{\text{free}} \times I \quad (2.40)$$

- *slip or symmetry boundary*  $\Gamma_{\text{sym}}$

$$(\boldsymbol{\sigma} \mathbf{n}) \cdot \mathbf{m} = 0, \quad \mathbf{d} \cdot \mathbf{n} = 0 \quad \forall (\mathbf{x}, t) \in \Gamma_{\text{sym}} \times I \quad (2.41)$$

- *fluid-solid interface*  $\Gamma_{\text{f-s}}$

$$\dot{\mathbf{d}} = \mathbf{u}, \quad (\boldsymbol{\sigma} \mathbf{n})_s = -(\boldsymbol{\sigma} \hat{\mathbf{n}})_f \quad \forall (\mathbf{x}, t) \in \Gamma_{\text{f-s}} \times I \quad (2.42)$$

The vectors  $\mathbf{n}$  and  $\mathbf{m}$  denote, respectively, the outward normal and the tangential vectors of the boundary. The relations in (2.42) clearly correspond to (2.29) and (2.31).

## 2.3 Rigid Body Dynamics

This work is also concerned with the interaction of fluid flow and submerged rigid bodies. In two dimensions, a rigid body may possess three degrees of freedom: the displacements  $d_x$  and  $d_y$ , and the angle of rotation  $\theta$ . Each degree of freedom may be associated with inertia, damping and stiffness. Thus, if the damping and the stiffness are assumed to be linear, the equilibrium of the rigid body can be written as

$$\begin{aligned} m_x \ddot{d}_x + c_x \dot{d}_x + k_x d_x &= F_x \\ m_y \ddot{d}_y + c_y \dot{d}_y + k_y d_y &= F_y \\ I_\theta \ddot{\theta} + c_\theta \dot{\theta} + k_\theta \theta &= M, \end{aligned} \quad (2.43)$$

where  $m_x$ ,  $m_y$ ,  $I_\theta$  represent, respectively, the relevant masses in the  $x$  and  $y$  directions and the rotational moment of inertia, which depends on the geometry and the density of the body. The damping coefficients are denoted as  $c_x$ ,  $c_y$  and  $c_\theta$ , while the stiffness moduli are given by  $k_x$ ,  $k_y$  and  $k_\theta$ . Depending on the problem under consideration, one or two of these degrees of freedom may be fixed or certain mass, damping or stiffness coefficients may be zero.

The boundary conditions, by means of which the rigid body interacts with the fluid flow, are given by (2.26) and (2.28), where forces  $F_x$  and  $F_y$  are represented by the vector  $\mathbf{F}$ .

## 2.4 Summary

For convenience the governing equations considered in this work are summarised in Box 2.1.

equations to be satisfied in the fluid domain  $\Omega_f$ :

$$\rho (\dot{\mathbf{u}} + \nabla \mathbf{u} (\mathbf{u} - \hat{\mathbf{v}}) - \mathbf{f}) - \nabla \cdot \boldsymbol{\sigma} = \mathbf{0} \quad \forall (\hat{\mathbf{x}}, t) \in \Omega_f \times I \quad (2.44)$$

$$\nabla \cdot \mathbf{u} = 0 \quad \forall (\hat{\mathbf{x}}, t) \in \Omega_f \times I \quad (2.45)$$

$$\boldsymbol{\sigma} = -p \mathbf{I} + 2\mu \nabla^s \mathbf{u} \quad (2.46)$$

two dimensional rigid body dynamics:

$$\begin{aligned} m_x \ddot{d}_x + c_x \dot{d}_x + k_x d_x &= F_x \\ m_y \ddot{d}_y + c_y \dot{d}_y + k_y d_y &= F_y \\ I_\theta \ddot{\theta} + c_\theta \dot{\theta} + k_\theta \theta &= M \end{aligned} \quad (2.47)$$

equations to be satisfied in the domain  $\Omega_s$  of the flexible solid:

$$\rho (\ddot{\mathbf{d}} - \mathbf{f}) - \nabla \cdot \boldsymbol{\sigma} = \mathbf{0} \quad \forall (\mathbf{x}, t) \in \Omega_s \times I \quad (2.48)$$

$$\boldsymbol{\sigma} = \mu J^{-\frac{5}{3}} (\mathbf{B} - \frac{1}{3} \text{tr}(\mathbf{B}) \mathbf{I}) + K \frac{J^2 - 1}{2J} \mathbf{I} \quad (2.49)$$

boundary conditions on free fluid surface  $\Gamma_{fs}$ :

$$(\mathbf{u} - \hat{\mathbf{v}}) \cdot \hat{\mathbf{n}} = 0 \quad \forall (\hat{\mathbf{x}}, t) \in \Gamma_{fs} \times I \quad (2.50)$$

$$\boldsymbol{\sigma} \hat{\mathbf{n}} = \mathbf{0} \quad \text{or} \quad \boldsymbol{\sigma} \hat{\mathbf{n}} - (-p_{\text{ext}} \hat{\mathbf{n}} + 2\gamma_{\text{st}} H \hat{\mathbf{n}}) = \mathbf{0} \quad \forall (\hat{\mathbf{x}}, t) \in \Gamma_{fs} \times I \quad (2.51)$$

boundary conditions on fluid-rigid body interface  $\Gamma_{f-r}$ :

$$\mathbf{u} = \dot{\mathbf{d}}_{\Gamma_{f-r}}, \quad (\mathbf{u} - \hat{\mathbf{v}}) \cdot \hat{\mathbf{n}} = 0 \quad \forall (\hat{\mathbf{x}}, t) \in \Gamma_{f-r} \times I \quad (2.52)$$

$$\int_{\Gamma_{f-r}} \boldsymbol{\sigma} \hat{\mathbf{n}} da = -\mathbf{F}, \quad \int_{\Gamma_{f-r}} \|(\boldsymbol{\sigma} \hat{\mathbf{n}}) \times \Delta \mathbf{x}\| da = -M \quad \forall t \in I \quad (2.53)$$

boundary conditions on fluid-solid interface  $\Gamma_{f-s}$ :

$$\mathbf{u} = \dot{\mathbf{d}}, \quad (\mathbf{u} - \hat{\mathbf{v}}) \cdot \hat{\mathbf{n}} = 0 \quad \forall (\hat{\mathbf{x}}, t) \in \Gamma_{f-s} \times I \quad (2.54)$$

$$(\boldsymbol{\sigma} \hat{\mathbf{n}})_f = -(\boldsymbol{\sigma} \mathbf{n})_s \quad \forall (\hat{\mathbf{x}}, t) \in \Gamma_{f-s} \times I \quad (2.55)$$

Standard fluid and solid boundary conditions are given by (2.19) – (2.22) and (2.39) – (2.41). Equation (2.49) may be replaced by its linear version (2.38). Initially, at  $t = 0$ , all data is known. The clear reference of the following chapters to either the fluid or the solid domain allows the omission of the subscripts f and s of  $\Omega_f$  and  $\Omega_s$  in the remainder of this work.

Box 2.1: Overview of governing equations considered in this work.

# Chapter 3

## The Basics of Finite Element Modelling

Many physical field problems can be described by partial differential equations and certain boundary conditions. The complexity of the problem may arise from the governing equation itself or from the complex geometry of the problem domain, or indeed from both. Thus, reliable numerical solution techniques are required.

The good performance on structured as well as unstructured meshes makes the finite element method a very suitable solution technique for complex domain geometries. Also, during the last decades, many different finite element formulations have been designed for various types of partial differential equations. Thus, the finite element method has emerged as one of the most powerful and most widely employed numerical solution techniques. Comprehensive introductions to the methodology of finite elements are provided, for example, in the text books by Hughes [64], Bathe [5], Zienkiewicz and Taylor [132], Cook *et al* [24], Wriggers [129].

This chapter provides a brief introduction to finite element solution procedures. The focus is on linear steady state problems on fixed domains with “nice” properties, where only one scalar or vectorial solution field is sought. In this chapter, the solution variables  $u$  or  $\mathbf{u}$  may represent any physical field variables. Section 3.4 addresses general problems that may arise in the presence of constraints like, for instance, the incompressibility constraint in solid or fluid mechanics. The specific difficulties and necessary modifications associated with the finite element modelling of the incompressible Navier-Stokes equations are the subject of Chapter 4. Similarly, Chapter 8 introduces some special finite elements for solid mechanics.

### 3.1 The Weak Form and the Classical Galerkin Method

Let  $\mathcal{L}(\bullet)$  be a linear differential operator, such that the governing equation can be written as

$$\mathcal{L}(u) = -f \quad \forall \mathbf{x} \in \Omega \quad (3.1)$$

$$u - g = 0 \quad \forall \mathbf{x} \in \Gamma_g \quad (3.2)$$

$$\mathbf{q}(u) \cdot \mathbf{n} - t = 0 \quad \forall \mathbf{x} \in \Gamma_t, \quad (3.3)$$

where  $\Omega$  is the domain of the problem and  $\Gamma_g$  and  $\Gamma_t$  are complementary subsets of the boundary  $\Gamma = \Gamma_g \cup \Gamma_t$ . The quantities  $g$  and  $t$  represent prescribed boundary values of the solution and prescribed fluxes across the boundary, respectively. The vector  $\mathbf{n}$  denotes the outward normal unit vector to the boundary  $\Gamma$ . The flux  $\mathbf{q}(u)$  is a linear function of the first derivatives of  $u$ . Boundary conditions of the type (3.2) are commonly referred to as *Dirichlet* boundary conditions, whereas (3.3) represents a *Neumann* boundary condition. The unknown function  $u$  may also be a vector field, in which case the boundary conditions change slightly.

*Example 1: Heat conduction.* The scalar function  $u$  represents the temperature distribution over the domain  $\Omega$ . The operator  $\mathcal{L}$  is defined as  $\mathcal{L}(\bullet) = \kappa \Delta(\bullet)$  such that the problem reads

$$\kappa \Delta u = -f \quad \forall \mathbf{x} \in \Omega, \quad (3.4)$$

where  $\Delta(\bullet) = \nabla \cdot (\nabla(\bullet))$  denotes the Laplace operator. The quantities  $f$  and  $\kappa$  represent, respectively, the distribution of heat sources in  $\Omega$  and the conductivity of the medium under consideration, which is assumed to be constant in  $\Omega$ . The temperature flux is defined as  $\mathbf{q} = \kappa \nabla u$ .

*Example 2: Linear elasticity.* The second order stress tensor  $\boldsymbol{\sigma}$  is introduced as a linear function of the displacement vector field  $\mathbf{u}$ . The problem may then be written as

$$\mathcal{L}(\mathbf{u}) = \nabla \cdot \boldsymbol{\sigma}(\mathbf{u}) = -\mathbf{f} \quad \forall \mathbf{x} \in \Omega \quad (3.5)$$

$$\boldsymbol{\sigma}(\mathbf{u}) = \Lambda (\nabla \cdot \mathbf{u}) \mathbf{I} + 2\mu \nabla^s \mathbf{u} \quad (3.6)$$

$$\mathbf{u} - \mathbf{g} = \mathbf{0} \quad \forall \mathbf{x} \in \Gamma_g \quad (3.7)$$

$$\boldsymbol{\sigma}(\mathbf{u}) \mathbf{n} - \mathbf{t} = \mathbf{0} \quad \forall \mathbf{x} \in \Gamma_t, \quad (3.8)$$

where the scalars  $\Lambda$  and  $\mu$  represent the Lamé constants. The quantities  $\mathbf{f}$  and  $\mathbf{t}$  now denote body forces and prescribed boundary traction vectors, respectively. Note that (3.5) and (3.6) correspond to (2.34) and (2.38).

A different representation of the problem may be obtained from the governing equation (3.1) by multiplication with an admissible virtual perturbation  $w$  and subsequent integration over the domain  $\Omega$ . The perturbations  $w$  are commonly referred to as *test* or *weighting* functions. It is known that  $u \in H^1(\Omega)$ , and thus all  $w \in \{w \in H^1(\Omega) \mid w = 0 \forall \mathbf{x} \in \Gamma_g\}$  are admissible. The resulting expression may be integrated by parts, such that the order of the highest derivatives is reduced in comparison to the original equation. Thus, by using the divergence theorem one obtains for the heat conduction problem

$$\int_{\Omega} w (\kappa \Delta u) \, dv = \int_{\Gamma} \kappa w (\nabla u \cdot \mathbf{n}) \, da - \int_{\Omega} \kappa \nabla w \cdot \nabla u \, dv \quad (3.9)$$

$$= \int_{\Gamma_t} w (\mathbf{q} \cdot \mathbf{n}) \, da - \int_{\Omega} \kappa \nabla w \cdot \nabla u \, dv = - \int_{\Omega} w f \, dv . \quad (3.10)$$

Employing the Neumann or flux boundary condition (3.3) renders

$$\int_{\Omega} \kappa \nabla w \cdot \nabla u \, dv = \int_{\Gamma_t} w t \, da + \int_{\Omega} w f \, dv . \quad (3.11)$$

A similar procedure may be applied to the elasticity problem (3.6) – (3.8), resulting in the following equation

$$\int_{\Omega} \nabla \mathbf{w} : \boldsymbol{\sigma}(\mathbf{u}) \, dv = \int_{\Gamma_t} \mathbf{w} \cdot \mathbf{t} \, da + \int_{\Omega} \mathbf{w} \cdot \mathbf{f} \, dv \quad (3.12)$$

with

$$\int_{\Omega} \nabla \mathbf{w} : \boldsymbol{\sigma}(\mathbf{u}) \, dv = \int_{\Omega} \Lambda (\nabla \cdot \mathbf{w})(\nabla \cdot \mathbf{u}) + 2 \mu \nabla \mathbf{w} : \nabla^s \mathbf{u} \, dv . \quad (3.13)$$

It is noted that both (3.11) and (3.12) can be cast in the format

$$a(w, u) = F(w) , \quad (3.14)$$

where  $a(w, u)$  and  $F(w)$  are, respectively, a bilinear and a linear form on  $\Omega$ . Obviously, the exact solution  $u$  of (3.1) satisfies (3.14) for every admissible test function  $w$ .

The equation given by (3.14) is commonly referred to as the *weak form* of the differential equation (3.1), which, in turn, may be denoted as the *strong*

form of the problem. For the examples of heat conduction and elasticity, the formulations (3.11) and (3.12) are also known as the *principles of virtual temperature* and *virtual work*, respectively.

In order to briefly point out the substantial difference of the original representation (3.1) and the weak form (3.14), it is assumed, for simplicity and without loss of generality, that  $g = 0 \ \forall \ \mathbf{x} \in \Gamma_g$ . Furthermore, let the space  $\mathcal{W}$  be defined as  $\mathcal{W} = \{w \in H^1(\Omega) \mid w|_{\Gamma_g} = 0\}$  and let  $\mathcal{W}^h \subset \mathcal{W}$  denote a finite dimensional subspace of  $\mathcal{W}$ .

The *Lax-Milgram Lemma* guarantees that, for every *continuous* and *elliptic* bilinear form  $a(\bullet, \bullet)$  and continuous linear functional  $F(\bullet)$ , there exists a unique  $u \in \mathcal{W}$  such that

$$a(w, u) = F(w) \quad \forall w \in \mathcal{W}. \quad (3.15)$$

A bilinear form  $a(\bullet, \bullet)$  is said to be continuous and elliptic if the following relations hold

$$|a(w_1, w_2)| \leq C_c \|w_1\|_1 \|w_2\|_1 \quad \forall w_1, w_2 \in \mathcal{W} \quad (\text{continuity}) \quad (3.16)$$

$$a(w, w) \geq C_e \|w\|_1^2 \quad \forall w \in \mathcal{W} \quad (\text{ellipticity}), \quad (3.17)$$

where  $C_c$  and  $C_e$  are positive constants. The operator  $\|\bullet\|_1 = \|\bullet\|_{H^1(\Omega)}$  represents the Sobolev norm of order one on  $\Omega$ . The bilinear forms associated with heat conduction and linear elasticity satisfy (3.16) and (3.17).

The crucial point is, that the Lax-Milgram Lemma also holds for functions  $u^h, w^h \in \mathcal{W}^h$ . Namely, there exists a unique  $u^h \in \mathcal{W}^h$ , such that

$$a(w^h, u^h) = F(w^h) \quad \forall w^h \in \mathcal{W}^h. \quad (3.18)$$

Thus, the weak form possesses solutions  $u^h$  in spaces  $\mathcal{W}^h \subset \mathcal{W}$  with  $u \notin \mathcal{W}^h$  (if indeed  $u \in \mathcal{W}^h$ , then  $u^h = u$ ), whereas the differential equation or strong form (3.1) can not be satisfied by any function other than the exact solution  $u$ .

The relaxed requirements on the smoothness of  $u^h$  are essential for the finite element method, which particularly exploits the fact that, with appropriately constructed  $\mathcal{W}^h$ , solutions  $u^h \in C^0(\Omega)$  with  $u^h \notin C^1(\Omega)$  can be computed, i. e.  $u^h$  may be piecewise smooth. Note also that usually, as shown for the two examples considered above, the order of the highest derivatives in the weak form is smaller than in the strong form. This allows to find solutions of (3.18) in very ‘‘coarse’’ spaces  $\mathcal{W}^h$ .

It remains to establish a link between the solutions  $u^h \in \mathcal{W}^h$  and  $u \in \mathcal{W}$ . Therefore, the following two relations are considered

$$a(u - u^h, w^h) = 0 \quad \forall w^h \in \mathcal{W}^h \quad (\text{orthogonality of the error}) \quad (3.19)$$

$$\|u - u^h\|_1 \leq \frac{C_c}{C_e} \|u - w^h\|_1 \quad \forall w^h \in \mathcal{W}^h \quad (\text{Céa's Lemma}) . \quad (3.20)$$

The relation (3.19) states that, with respect to the bilinear form  $a(\bullet, \bullet)$ , the difference  $u - u^h$  is orthogonal to every  $w^h \in \mathcal{W}^h$ . Thus,  $u^h$  can be regarded as the best possible approximation of  $u$  in the space  $\mathcal{W}^h$ . Neglecting the constants  $C_c$  and  $C_e$ , the following conclusion may be drawn from the inequality (3.20): There do not exist any  $w^h \in \mathcal{W}^h$ , such that the difference  $\|u - w^h\|_1$  is smaller than the error  $\|u - u^h\|_1$ . Consequently, the error decreases as “larger” spaces  $\mathcal{W}^h$  are considered. In other words, the accuracy of the approximation of  $u$  by  $u^h$  increases as  $\mathcal{W}^h$ , in some sense, approaches  $\mathcal{W}$ .

The *classical Galerkin* method or *Bubnov-Galerkin* method evolves naturally from this mathematical background: Obtain an approximate solution  $u^h \approx u$  in the following manner. Given an appropriately constructed  $\mathcal{W}^h$ , find  $u^h \in \mathcal{W}^h$  such that

$$a(w^h, u^h) = F(w^h) \quad \forall w^h \in \mathcal{W}^h . \quad (3.21)$$

Note that solutions  $u^h$  exactly satisfy the Dirichlet boundary conditions, while Neumann boundary conditions are satisfied in a “weak” sense.

The detailed mathematical foundation of the Galerkin method is provided in *e. g.* Reddy [96], Brenner and Scott [13], Ciarlet [23], Schwab [107]. In the next subsection particular choices of the space  $\mathcal{W}^h$  are introduced, thus leading to the finite element method.

In Chapter 4, modified Galerkin methods are discussed, which may be cast into the following format: Find  $u^h \in \mathcal{W}^h$  such that

$$a(\tilde{w}^h, u^h) = F(\tilde{w}^h) \quad \forall \tilde{w}^h \in \tilde{\mathcal{W}}^h , \quad (3.22)$$

where  $\tilde{\mathcal{W}}^h \neq \mathcal{W}^h$  is an appropriately constructed space of functions. Such formulations which employ different trial and test spaces are referred to as the *Petrov-Galerkin* methods.

## 3.2 Isoparametric Finite Elements

The previous section provides the basic mathematical background of the classical Galerkin method. Solutions  $u^h \in \mathcal{W}^h$  of the weak form (3.21) approximate, in some sense, the solution  $u$  of the strong differential equation (3.1). The *standard finite element method* is a classical Galerkin method employing certain finite dimensional spaces  $\mathcal{W}^h$ .

Such *finite element spaces*  $\mathcal{W}^h$  are commonly defined as spaces of continuous piecewise polynomials. Thus,  $\mathcal{W}^h$  may be written as

$$\mathcal{W}^h = \left\{ w^h \in H^1(\Omega) \mid w^h|_{\mathbf{x}^h \in \Omega^e} \in P_k(\Omega^e), w^h|_{\mathbf{x}^h \in \Gamma_g} = 0 \right\} , \quad (3.23)$$

where  $\Omega = \bigcup_{e=1}^{n_{el}} \Omega^e$  is a decomposition of the domain  $\Omega$  into  $n_{el}$  subdomains with  $\Omega^i \cap \Omega^j = \emptyset \forall i, j = 1, 2, \dots, n_{el}; i \neq j$ . The subdomains  $\Omega^e$  are denoted as *finite elements*. The decomposition of  $\Omega$  is required to have the following properties: For each element there exists a map between the domain  $\Omega^e$  and a parametric element domain denoted as  $\square$ . In two dimensions, the domain  $\square$  may be the unit triangle or the unit square (see Figure 3.1). The map from the parametric coordinates  $\boldsymbol{\xi} \in \square$  to the coordinates  $\boldsymbol{x}^h \in \Omega^e$  is defined as

$$\boldsymbol{x}^h = \bar{\boldsymbol{x}}^h(\boldsymbol{\xi}) = \bar{N}_A(\boldsymbol{\xi}) \boldsymbol{x}_A, \quad (3.24)$$

where the summation is performed for  $A = 1, 2, \dots, n_{ne}$ , and  $n_{ne}$  denotes the number of *nodes* of the element (see Figure 3.1). The vector  $\boldsymbol{x}_A$  represents the coordinates of node  $A$  in the configuration  $\Omega^e$ .

The *shape functions*  $N_A = \bar{N}_A(\boldsymbol{\xi})$  are polynomials in terms of the parametric coordinates  $\boldsymbol{\xi}$ . Each  $N_A$  is equal to one in node  $A$  and zero in all other nodes of the element, *i. e.*  $\bar{N}_A(\boldsymbol{\xi}_B) = 1$  for  $A = B$ , and  $\bar{N}_A(\boldsymbol{\xi}_B) = 0$  for  $A \neq B$ , with  $A, B = 1, 2, \dots, n_{ne}$ . The order  $k$  of the polynomials is related to  $n_{ne}$ . The functions  $\bar{N}_A(\boldsymbol{\xi})$  are linearly independent and represent a *nodal basis* of the space  $P_k(\square)$  of polynomials of order  $k$  on  $\square$ .

Over each element  $e$ , a function  $w^h \in \mathcal{W}^h$  may be expressed as

$$w^h = \bar{N}_A(\boldsymbol{\xi}) \boldsymbol{w}_A = \hat{N}_A(\bar{\boldsymbol{x}}^h(\boldsymbol{\xi})) \boldsymbol{w}_A, \quad \boldsymbol{\xi} \in \square \quad (3.25)$$

$$= \hat{N}_A(\boldsymbol{x}^h) \boldsymbol{w}_A, \quad \boldsymbol{x}^h \in \Omega^e, \quad (3.26)$$

where  $\boldsymbol{w}_A$  are the nodal values of  $w^h$ . The strategy of employing the same shape functions  $N_A$  in (3.24) and (3.25) is referred to as the *isoparametric concept*, and leads to a convenient framework for the computer implementation. The representation  $N_A = \hat{N}_A(\boldsymbol{x}^h)$  of the shape functions provides a nodal basis of the space  $P_k(\Omega^e)$ . Some standard two dimensional finite elements, which are used later in this work, are displayed in Figure 3.1. The associated shape functions are given later in (3.29).

By joining the finite elements together, such that the nodes are shared by the adjoint elements, one obtains the *finite element mesh*. The number of nodes of the finite element mesh is denoted as  $n_{nd}$ . For each node  $a$ ,  $a = 1, 2, \dots, n_{nd}$ , a *global* shape function  $N_a^g$  may then be constructed from the element shape functions defined on the adjoint elements and associated with node  $a$  (see Figure 3.2). The set of all global shape functions represents a nodal basis of  $\mathcal{W}^h$ , and thus, the dimension of  $\mathcal{W}^h$  corresponds to the number of nodes  $n_{nd}$  of the finite element mesh (in order to be precise the nodes on  $\Gamma_g$  should be excluded).

Any function  $w^h \in \mathcal{W}^h$  can thus be written in the following representations

$$w^h = \sum_{e=1}^{n_{\text{el}}} \hat{N}_A(\mathbf{x}^h) \mathbf{w}_A = \sum_{e=1}^{n_{\text{el}}} \bar{N}_A(\boldsymbol{\xi}) \mathbf{w}_A = \hat{N}_a^g(\mathbf{x}^h) \mathbf{w}_a. \quad (3.27)$$

where  $\mathbf{w}_A$  or  $\mathbf{w}_a$ , respectively, are the values of  $w^h$  at the nodes. Details on the construction of admissible finite element discretisations are presented in *e. g.* Bathe [5], Zienkiewicz and Taylor [132], Reddy [96], Brenner and Scott [13].

Using Céa's Lemma (3.20), it is then possible to prove the following a priori error estimate for the finite element solution  $u^h \in \mathcal{W}^h$ ,

$$\|u - u^h\|_1 \leq C h^k, \quad (3.28)$$

where  $h$  represents the characteristic element size of the mesh under consideration. The constant  $C$  is independent of  $h$ . Thus, it follows from the definition of the norm  $\|\bullet\|_1 = \|\bullet\|_{H^1(\Omega)}$  that, if piecewise linear finite element interpolation is employed, the approximation  $u^h$  of  $u$  is second order accurate. Detailed information on (3.28) is given, for instance, in the aforementioned references [5, 13, 96].

Using  $\boldsymbol{\xi} = \{\xi, \eta\}$ , the shape functions  $N_A$  associated with the finite elements displayed in Figure 3.1 read:

*3 noded linear triangle (P1)*

$$\begin{aligned} N_1 &= 1 - \xi - \eta \\ N_2 &= \xi \\ N_3 &= \eta \end{aligned}$$

*4 noded bilinear quadrilateral (Q1)*

$$\begin{aligned} N_1 &= \frac{1}{4}(1 - \xi)(1 - \eta) \\ N_2 &= \frac{1}{4}(1 + \xi)(1 - \eta) \\ N_3 &= \frac{1}{4}(1 + \xi)(1 + \eta) \\ N_4 &= \frac{1}{4}(1 - \xi)(1 + \eta) \end{aligned}$$

*9 noded quadratic quadrilateral (Q2)*

$$\begin{aligned} N_1 &= \frac{1}{4}((1 - \xi)(1 - \eta) + 2N_8 + 2N_5 - N_9) \\ N_2 &= \frac{1}{4}((1 + \xi)(1 - \eta) + 2N_5 + 2N_6 - N_9) \\ N_3 &= \frac{1}{4}((1 + \xi)(1 + \eta) + 2N_6 + 2N_7 - N_9) \\ N_4 &= \frac{1}{4}((1 - \xi)(1 + \eta) + 2N_7 + 2N_8 - N_9) \\ N_5 &= \frac{1}{2}(1 - \xi^2)(1 - \eta) \\ N_6 &= \frac{1}{2}(1 + \xi)(1 - \eta^2) \\ N_7 &= \frac{1}{2}(1 - \xi^2)(1 + \eta) \\ N_8 &= \frac{1}{2}(1 - \xi)(1 - \eta^2) \\ N_9 &= (1 - \xi^2)(1 - \eta^2) \end{aligned} \quad (3.29)$$

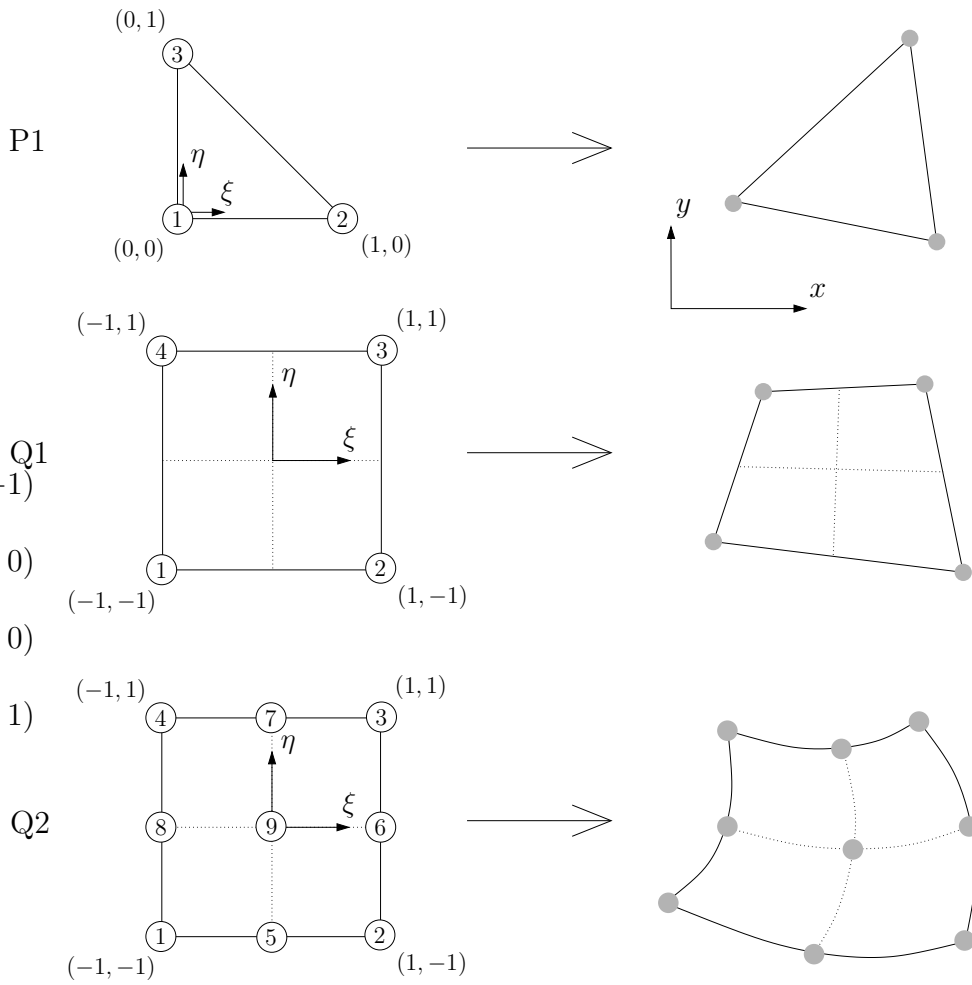


Figure 3.1: Some two dimensional finite elements.

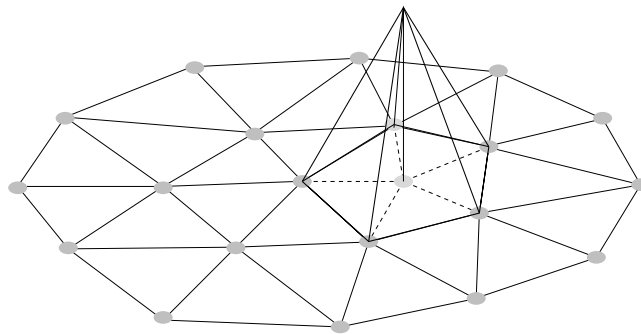


Figure 3.2: Discretisation of a two dimensional domain with P1 elements; schematic representation of a global shape function.

### 3.3 Solution Procedure, Nonlinear Problems

Using the representation (3.26) for both  $w^h$  and  $u^h$ , the Galerkin formulation (3.21) for linear problems can be rewritten as

$$\begin{aligned} a(w^h, u^h) &= \sum_{e=1}^{n_{\text{el}}} \mathbf{w}_A \mathbf{k}_{AB}^e \mathbf{u}_B = \mathbf{w} \cdot \mathbf{K} \mathbf{u} \\ &= \mathbf{w} \cdot \mathbf{P} = \sum_{e=1}^{n_{\text{el}}} \mathbf{w}_A \mathbf{p}_A^e = F(w^h), \end{aligned} \quad (3.30)$$

where  $\mathbf{w}$  and  $\mathbf{u}$  are the  $n_{\text{nd}}$ -dimensional vectors of the nodal values of the weighting function  $w^h$  and the trial solution  $u^h$ . The *stiffness* or *system matrix*  $\mathbf{K}$  and the *external force vector*  $\mathbf{P}$  are then obtained from the assembly of the element contributions as

$$\mathbf{K} = \mathbf{A} \mathbf{k}^e, \quad \mathbf{P} = \mathbf{A} \mathbf{p}^e. \quad (3.31)$$

For the examples of heat conduction and linear elasticity, the expressions (3.11) and (3.12), respectively, render

$$\mathbf{k}_{AB}^e = \int_{\Omega^e} \kappa \nabla N_A \cdot \nabla N_B \, dv \quad (3.32)$$

$$\mathbf{p}_A^e = \int_{\Gamma_t \cap \Gamma^e} N_A \mathbf{t} \, da + \int_{\Omega^e} N_A \mathbf{f} \, dv \quad (3.33)$$

and

$$\mathbf{k}_{AB}^e = \int_{\Omega^e} \Lambda \nabla N_A \otimes \nabla N_B + \mu (\nabla N_A \cdot \nabla N_B \mathbf{I} + \nabla N_B \otimes \nabla N_A) \, dv \quad (3.34)$$

$$\mathbf{p}_A^e = \int_{\Gamma_t \cap \Gamma^e} N_A \mathbf{t} \, da + \int_{\Omega^e} N_A \mathbf{f} \, dv. \quad (3.35)$$

The integration over the element domains  $\Omega^e$  is typically performed by means of Gauß quadrature. Since  $\mathbf{w}$  is arbitrary, equation (3.30) basically gives

$$\mathbf{K} \mathbf{u} = \mathbf{P}. \quad (3.36)$$

Thus, the original continuous field problem given by (3.1) has been transformed into an algebraic system of equations in terms of discrete unknowns.

For nonlinear problems the form  $a(w^h, u^h)$  is linear in  $w^h$ , but nonlinear in  $u^h$ . Thus, (3.21) may be written as

$$\begin{aligned} a(w^h, u^h) &= \sum_{e=1}^{n_{el}} \mathbf{w}_A \mathbf{r}_A^e(\mathbf{u}_1, \mathbf{u}_2, \dots, \mathbf{u}_{n_{ne}}) = \mathbf{w} \cdot \mathbf{R}(\mathbf{u}) \\ &= \mathbf{w} \cdot \mathbf{P} = \sum_{e=1}^{n_{el}} \mathbf{w}_A \mathbf{p}_A^e = F(w^h), \end{aligned} \quad (3.37)$$

where  $\mathbf{R}$  is assembled from the  $\mathbf{r}_A^e$ , similarly to (3.31)<sub>2</sub>. The numbering of the nodal values  $\mathbf{u}_1, \mathbf{u}_2, \dots, \mathbf{u}_{n_{ne}}$  refers to the local node numbering of the element  $e$ . The resulting nonlinear algebraic problem

$$\mathbf{R}(\mathbf{u}) = \mathbf{P} \quad (3.38)$$

may be solved iteratively by means of the Newton-Raphson procedure. The solution is then obtained by application of the following algorithm:

1. estimate solution  $\mathbf{u}$
2. compute  $\mathbf{R}(\mathbf{u}) - \mathbf{P}$
3. if  $\|\mathbf{R}(\mathbf{u}) - \mathbf{P}\| \leq tol$  goto 8.
4. compute  $\mathbf{K}(\mathbf{u}) = \frac{\partial \mathbf{R}(\mathbf{u})}{\partial \mathbf{u}}$
5. solve  $\mathbf{K}(\mathbf{u}) \Delta \mathbf{u} = \mathbf{P} - \mathbf{R}(\mathbf{u})$
6. update  $\mathbf{u} \leftarrow \mathbf{u} + \Delta \mathbf{u}$
7. goto 2.
8. exit

The system matrix  $\mathbf{K}(\mathbf{u})$  is computed as

$$\mathbf{K}(\mathbf{u}) = \frac{\partial \mathbf{R}(\mathbf{u})}{\partial \mathbf{u}} = \mathbf{A} \mathbf{k}^e(\mathbf{u}_1, \mathbf{u}_2, \dots, \mathbf{u}_{n_{ne}}) \quad (3.40)$$

with

$$\mathbf{k}_{AB}^e(\mathbf{u}_1, \mathbf{u}_2, \dots, \mathbf{u}_{n_{ne}}) = \frac{\partial \mathbf{r}_A^e(\mathbf{u}_1, \mathbf{u}_2, \dots, \mathbf{u}_{n_{ne}})}{\partial \mathbf{u}_B}. \quad (3.41)$$

### 3.4 Problems with Constraints

As a preliminary to the subject of this section, it should be noted that, for symmetric, continuous and elliptic bilinear forms  $a(\bullet, \bullet)$ , the weak form

(3.15) corresponds to the following variational problem: Find  $u \in \mathcal{W}$  such that

$$\Pi(u) = \frac{1}{2}a(u, u) - F(u) \Rightarrow MIN. \quad (3.42)$$

This can easily be established from the following argument: If a specific function  $u$  renders a minimum of the functional  $\Pi$ , then the derivative of  $\Pi$  in the direction of any  $w \in \mathcal{W}$  disappears. Thus, it follows

$$\begin{aligned} 0 &= \frac{d}{d\varepsilon} \Pi(u + \varepsilon w)|_{\varepsilon=0} & (3.43) \\ &= \frac{d}{d\varepsilon} \left( \frac{1}{2}a(u, u) + \varepsilon a(w, u) + \frac{1}{2}\varepsilon^2 a(w, w) - F(u) - \varepsilon F(w) \right) \Big|_{\varepsilon=0} \\ &= a(w, u) - F(w) \quad \forall w \in \mathcal{W}. \end{aligned}$$

The same argument can be applied to functions  $u^h, w^h \in \mathcal{W}^h$ . Hence, the Galerkin solution  $u^h$  of (3.21) renders the minimum of  $\Pi(u^h)$ . In linear elasticity,  $\Pi$  can be identified with the potential energy. Thus, the principle of virtual work for linear elasticity and the minimisation of the potential energy are equivalent.

Often one has to find the function  $u$ , which minimises a functional  $\Pi(u)$  subject to a specific constraint on  $u$ : Find  $u \in \mathcal{W}$  such that

$$\Pi(u) = \frac{1}{2}a(u, u) - F(u) \Rightarrow MIN \quad (3.44)$$

subject to the linear constraint

$$\bar{\mathcal{L}}(u) = -\bar{f} \quad \forall \mathbf{x} \in \bar{\Omega}, \quad (3.45)$$

where (3.45) applies to the domain  $\bar{\Omega} \subseteq \Omega$ . For convenience, the space  $\bar{\mathcal{W}} \subset \mathcal{W}$  of functions which satisfy (3.45) is introduced.

A prominent example of such a problem is the modelling of incompressible linear elasticity. The associated potential energy can be written as

$$\Pi(\mathbf{u}) = \frac{1}{2}a(\mathbf{u}, \mathbf{u}) - F(\mathbf{u}) \quad (3.46)$$

$$= \frac{1}{2} \int_{\Omega} 2\mu \nabla^s \mathbf{u} : \nabla^s \mathbf{u} \, dv - \left( \int_{\Gamma_t} \mathbf{u} \cdot \mathbf{t} \, da + \int_{\Omega} \mathbf{u} \cdot \mathbf{f} \, dv \right) \quad (3.47)$$

and the incompressibility constraint reads

$$\bar{\mathcal{L}}(\mathbf{u}) = \nabla \cdot \mathbf{u} = 0. \quad (3.48)$$

Using the equivalence of the weak form (3.21) and the variational problem (3.44), one could, theoretically, employ a classical Galerkin method based on a space  $\overline{\mathcal{W}}^h$ , every member of which satisfies the constraint a priori. In praxis, however, the construction of such spaces is usually too complicated.

More feasible approaches are discussed in the following two subsections.

### 3.4.1 Mixed Methods

An extended functional  $\mathcal{L}(u, p)$  may be introduced as

$$\mathcal{L}(u, p) = \Pi(u) + b(u, p) + G(p) \quad (3.49)$$

where

$$b(u, p) = \int_{\overline{\Omega}} \overline{\mathcal{L}}(u) p \, dv, \quad G(p) = \int_{\overline{\Omega}} \overline{f} p \, dv. \quad (3.50)$$

The function  $p \in \mathcal{P}$  is referred to as the *Lagrangian multiplier* and the space  $\mathcal{P}$  may be given as  $\mathcal{P} = L^2(\overline{\Omega})$ . Clearly, if the derivatives of  $\mathcal{L}(w, p)$  in the direction of any  $q \in \mathcal{P}$  disappear, then  $w \in \overline{\mathcal{W}}$ . Also, at the solution  $u$ , the derivatives of  $\mathcal{L}(u, p)$  in the direction of any  $w \in \overline{\mathcal{W}}$  are zero independently of  $p$ . It follows, that if one can find  $u$  and  $p$ , such that  $\mathcal{L}(u, p)$  is stationary, then  $u$  is a solution of the constrained minimisation problem (3.44) – (3.45). The associated  $p$  has adjusted such that also the derivatives of  $\mathcal{L}(u, p)$  in the direction of any  $w \in \mathcal{W}$  with  $w \notin \overline{\mathcal{W}}$  disappear. The existence and uniqueness of a solution  $u$  and  $p$  are subject to the properties of the forms  $a(\bullet, \bullet)$  and  $b(\bullet, \bullet)$  and are discussed in *e. g.* Schwab [107]. Note that in most practical cases, the Lagrangian multiplier  $p$  can be identified with a physical quantity.

The stationarity of  $\mathcal{L}(u, p)$  (*saddle point problem*) requires

$$0 = \frac{d}{d\varepsilon} \mathcal{L}(u + \varepsilon w, p)|_{\varepsilon=0} \quad \forall w \in \mathcal{W} \quad (3.51)$$

$$0 = \frac{d}{d\varepsilon} \mathcal{L}(u, p + \varepsilon q)|_{\varepsilon=0} \quad \forall q \in \mathcal{P} \quad (3.52)$$

Thus, the following representation of the problem is obtained: Find  $u \in \mathcal{W}$  and  $p \in \mathcal{P}$  such that

$$\begin{aligned} a(w, u) + b(w, p) &= F(w) \quad \forall w \in \mathcal{W} \\ b(u, q) &= G(q) \quad \forall q \in \mathcal{P}. \end{aligned} \quad (3.53)$$

For the example of incompressible linear elastic material the constraint (3.48) gives

$$b(\mathbf{u}, p) = \int_{\Omega} (\nabla \cdot \mathbf{u}) p \, dv, \quad (3.54)$$

where the Lagrangian multiplier  $p$  is identified with the physical pressure. Using (3.47) and (3.54), the problem (3.53) becomes: Find  $\mathbf{u} \in \mathcal{W}$  and  $p \in \mathcal{P}$  such that for all  $\mathbf{w} \in \mathcal{W}$  and  $q \in \mathcal{P}$

$$\int_{\Omega} 2\mu \nabla^s \mathbf{w} : \nabla^s \mathbf{u} + (\nabla \cdot \mathbf{w}) p + (\nabla \cdot \mathbf{u}) q \, dv = \int_{\Gamma_t} \mathbf{w} \cdot \mathbf{t} \, da + \int_{\Omega} \mathbf{w} \cdot \mathbf{f} \, dv . \quad (3.55)$$

The compact representation of (3.55) as one instead of two equations is possible due to the independence of  $\mathbf{w}$  and  $q$ . Interestingly, (3.55) can be obtained from the governing equations

$$\nabla \cdot \boldsymbol{\sigma}(\mathbf{u}, p) = -\mathbf{f} , \quad \nabla \cdot \mathbf{u} = 0 , \quad \boldsymbol{\sigma}(\mathbf{u}, p) = p \mathbf{I} + 2\mu \nabla^s \mathbf{u} \quad (3.56)$$

by the procedure outlined in Section 3.1, namely by multiplication with the virtual displacement  $\mathbf{w}$  and the virtual pressure  $q$ , subsequent integration over the domain  $\Omega$  and integration by parts. Note that, in this way, formulations (3.53) may be obtained for problems, which do not correspond to a constraint minimisation problem. In other words, (3.53) is more general than (3.44) – (3.45), (see *e. g.* Schwab [107]).

The representation (3.53) is a weak form of the general problem. Similar to (3.18), it can be proven that unique solutions  $(u^h, p^h) \in \mathcal{W}^h \times \mathcal{P}^h$  exist, if the spaces  $\mathcal{W}$  and  $\mathcal{P}$  are replaced by subspaces  $\mathcal{W}^h \subset \mathcal{W}$ ,  $\mathcal{P}^h \subset \mathcal{P}$ . This suggests the application of a Galerkin procedure with finite element spaces  $\mathcal{W}^h$ ,  $\mathcal{P}^h$  to obtain approximations  $u^h, p^h$  of  $u, p$ .

Namely, a *mixed Galerkin method* reads: Find  $u^h \in \mathcal{W}^h$  and  $p^h \in \mathcal{P}^h$  such that

$$\begin{aligned} a(w^h, u^h) + b(w^h, p^h) &= F(w^h) \quad \forall w^h \in \mathcal{W}^h \\ b(u^h, q^h) &= G(q^h) \quad \forall q^h \in \mathcal{P}^h . \end{aligned} \quad (3.57)$$

However, the spaces  $\mathcal{W}^h$  and  $\mathcal{P}^h$  to be employed in (3.57) can not be chosen independently. For a given  $\mathcal{W}^h$ , the wrong choice of  $\mathcal{P}^h$  renders badly conditioned system matrices and usually results in solutions obliterated by spurious modes. The numerical example provided in Section 4.1.2 illustrates the failure of a mixed Galerkin method based on inappropriate choices of  $\mathcal{W}^h$  and  $\mathcal{P}^h$ . The problem may be attributed to the absence of any terms involving both  $p^h$  and  $q^h$  in (3.57). The function  $p^h$  is not “tested” with  $q^h$ . Thus, the system matrix resulting from a finite element discretisation possesses a square submatrix of zeros centred on the diagonal. The dimension of the zero submatrix corresponds to the dimension of the space  $\mathcal{P}^h$ . This hints that, for a given  $\mathcal{W}^h$ , the maximum dimension of  $\mathcal{P}^h$  is restricted.

The detailed mathematical analysis of the problem led to the formulation of the so-called *inf-sup condition* by Babuška [3] and Brezzi [14]. This condition, which is also referred to as the *Babuška-Brezzi condition*, relates the

spaces  $\mathcal{W}^h$  and  $\mathcal{P}^h$ . It can be written as

$$0 < \beta \leq \inf_{q^h \in \mathcal{P}^h} \sup_{w^h \in \mathcal{W}^h} \frac{b(w^h, q^h)}{\|w^h\|_1 \|q^h\|_1}, \quad (3.58)$$

where the scalar  $\beta$  is independent of the finite element mesh. The restriction, which (3.58) imposes on the spaces  $\mathcal{W}^h$  and  $\mathcal{P}^h$ , may be expressed as follows: For each  $q^h \in \mathcal{P}^h$  there must exist a  $w^h \in \mathcal{W}^h$ , such that

$$b(w^h, q^h) \geq \beta \|w^h\|_1 \|q^h\|_1. \quad (3.59)$$

Thus, for a given  $\mathcal{P}^h$ , the space  $\mathcal{W}^h$  needs to be large enough to satisfy (3.59). If the Babuška-Brezzi condition is not satisfied, then the finite element procedure is not necessarily stable and the convergence of the solution  $u^h \rightarrow u$  as  $h \rightarrow 0$  can not be proven.

The mathematical derivation of (3.58) is provided in various publications, see *e. g.* Bathe [5], Brenner and Scott [13], Schwab [107], Brezzi and Fortin [16]. A compilation of various mixed finite elements for the simulation of incompressible materials is presented in *e. g.* Bathe [5]. Mathematical procedures, which may be used to establish the conformity or nonconformity of a particular finite element formulation with the Babuška-Brezzi condition, are discussed by Brezzi and Fortin [16]. Alternatively, a numerical test suggested by Bathe [5] can be performed. Namely, the inf-sup value may be computed for a sequence of finite element meshes. If these values asymptotically approach some  $\beta > 0$  as  $h \rightarrow 0$ , then the element formulation is likely to be consistent with the Babuška-Brezzi condition.

In Section 4.3, two strategies are discussed, which enable the formulation of successful mixed finite element methods for incompressible materials employing equal order interpolations for the displacement  $\mathbf{u}^h$  and the pressure  $p^h$ . One approach lies in the appropriate modification of the Galerkin method (3.57), such that the Babuška-Brezzi condition becomes irrelevant, and the other satisfies the condition by means of a trick applied on element level.

### 3.4.2 Penalty Methods

An alternative strategy to obtain approximative solutions of the constraint minimisation problem (3.44) – (3.45) lies in the extension of the functional  $\Pi(u)$  with a *penalty* term. Unlike the method based on Lagrangian multipliers, this strategy offers the incorporation of the constraint into the variational problem without the introduction of additional unknowns.

Consider the minimisation of the functional

$$\bar{\Pi}(u) = \Pi(u) + \frac{1}{2} \bar{b}(u, u) - \bar{G}(u) \Rightarrow MIN \quad (3.60)$$

with

$$\bar{b}(w, u) = K \int_{\bar{\Omega}} \bar{\mathcal{L}}(w) \bar{\mathcal{L}}(u) dv, \quad \bar{G}(u) = K \int_{\bar{\Omega}} u \bar{f} dv. \quad (3.61)$$

Clearly,  $\bar{b}(w, w) \geq 0 \forall w \in \mathcal{W}$ . The solution of (3.60) balances the minimisation of  $\Pi(u)$  with the satisfaction of the constraint. The larger the scalar penalty parameter  $K$  is chosen, the more emphasis is put on the constraint. Note, that the exact solution  $u$  of the constraint minimisation problem (3.44) – (3.45) is obtained only for  $K \rightarrow \infty$ .

Similar to (3.43), one can derive the associated weak form as

$$a(w, u) + \bar{b}(w, u) = F(w) + \bar{G}(w). \quad (3.62)$$

For incompressible linear elasticity (3.47) – (3.48) one obtains

$$\int_{\Omega} 2\mu \nabla^s \mathbf{w} : \nabla^s \mathbf{u} + K (\nabla \cdot \mathbf{w}) (\nabla \cdot \mathbf{u}) dv = \int_{\Gamma_t} \mathbf{w} \cdot \mathbf{t} da + \int_{\Omega} \mathbf{w} \cdot \mathbf{f} dv. \quad (3.63)$$

If the parameter  $K$  is redefined as  $K - \frac{2}{3}\mu$ , then (3.63) coincides with the standard weak form of linear elastic material described by the shear and bulk moduli. The left hand side of (3.63) becomes

$$\int_{\Omega} 2\mu \nabla \mathbf{w} : \left( \nabla^s \mathbf{u} - \frac{1}{3} (\nabla \cdot \mathbf{u}) \mathbf{I} \right) + K (\nabla \cdot \mathbf{w}) (\nabla \cdot \mathbf{u}) dv. \quad (3.64)$$

The penalty parameter  $K$  has thus been identified as the bulk modulus and the penalty formulation of incompressible material is, in fact, a standard formulation (3.15) of “nearly” incompressible material.

A classical Galerkin method may then be used to find an approximate solution  $u^h$  of (3.62). Namely, find  $u^h \in \mathcal{W}^h$  such that

$$a(w^h, u^h) + \bar{b}(w^h, u^h) = F(w^h) + \bar{G}(w^h) \quad \forall w^h \in \mathcal{W}^h. \quad (3.65)$$

However, a finite element method based on (3.65) may render very inaccurate results and may show a poor convergence behaviour as  $h \rightarrow 0$ . Generally, the numerical model is observed to be too stiff. The matrix form of a linear problem represented by (3.65) reads

$$\mathbf{K} \mathbf{u} + K \bar{\mathbf{K}} \mathbf{u} = \mathbf{P} + K \bar{\mathbf{P}}, \quad (3.66)$$

where

$$\mathbf{w} \cdot \bar{\mathbf{K}} \mathbf{u} = \frac{1}{K} \bar{b}(w^h, u^h), \quad \mathbf{w} \cdot \bar{\mathbf{P}} = \frac{1}{K} \bar{G}(w^h). \quad (3.67)$$

If  $\bar{\mathbf{K}}$  is regular, it follows for  $K \rightarrow \infty$ , that the vector of nodal unknowns  $\mathbf{u}$  is determined by

$$\bar{\mathbf{K}} \mathbf{u} = \bar{\mathbf{P}}. \quad (3.68)$$

Thus, for very large  $K$ , the satisfaction of the constraint may dominate the minimisation of  $\Pi(u^h)$ , which results in the artificial stiffness of the discrete model. This phenomena is referred to as *locking*.

Various techniques to avoid locking have been suggested in literature. Many of the strategies are based on *selective reduced integration*. The bilinear form  $\bar{b}(\bullet, \bullet)$  of the constraint is computed with a reduced number of Gauß points. Thereby, the singularity of  $\bar{\mathbf{K}}$  is ensured and a situation like (3.68) can not arise. On the other hand, reduced integration often introduces zero energy modes of the finite elements. The subject of locking and the stabilisation of zero energy modes is addressed at length in *e. g.* Bathe [5], Zienkiewicz and Taylor [132], Wriggers [129].

# Chapter 4

## Introduction to Stabilised Finite Elements for Fluid Flow

It has long been known that a standard equal order velocity-pressure Galerkin finite element formulation is not suitable for the solution of the incompressible Navier-Stokes equations. For most problems the velocity and the pressure fields exhibit spurious oscillations. In particular, the spurious pressure modes can not be reduced by refinement of the discretisation.

In Section 4.1 these instabilities are investigated and it is shown that their origin is twofold. Sections 4.2 and 4.3 demonstrate how the formulation can be improved without sacrificing the computationally convenient features of low, equal order approximations for the velocity and the pressure. It is also shown, that for linear finite element interpolations the stabilisation techniques based on *element bubble functions* are essentially identical to the *streamline-upwinding/* and the *pressure-stabilising/Petrov-Galerkin* methods (SUPG and PSPG). Finally, the complete stabilised finite element formulation for the incompressible Navier-Stokes equations, as it is used in the remainder of this work, is presented in Section 4.4.

For the sake of simplicity this chapter is restricted to steady state fluid flow on a fixed domain ( $\hat{\mathbf{v}} = \mathbf{0} \forall (\hat{\mathbf{x}}, t) \in \Omega \times I$ ) with standard Dirichlet and Neumann boundary conditions. The extension of the methodology to the unsteady flow on a moving domain is the subject of Chapters 5 and 6. Thus, the momentum conservation equation (2.44), the continuity equation (2.45) and the boundary conditions discussed in Chapter 2 reduce to

$$\rho((\nabla \mathbf{u}) \mathbf{u} - \mathbf{f}) - \nabla \cdot \boldsymbol{\sigma} = \mathbf{0} \quad \forall \hat{\mathbf{x}} \in \Omega \quad (4.1)$$

$$\nabla \cdot \mathbf{u} = 0 \quad \forall \hat{\mathbf{x}} \in \Omega \quad (4.2)$$

$$\mathbf{u} - \mathbf{g} = \mathbf{0} \quad \forall \hat{\mathbf{x}} \in \Gamma_g \quad (4.3)$$

$$\boldsymbol{\sigma} \mathbf{n} - \mathbf{t} = \mathbf{0} \quad \forall \hat{\mathbf{x}} \in \Gamma_t \quad (4.4)$$

with

$$\boldsymbol{\sigma} = -p\mathbf{I} + 2\mu\nabla^s\mathbf{u}. \quad (4.5)$$

By introducing the virtual velocity  $\mathbf{w}$  and the virtual pressure  $q$ , the weak form of the problem is obtained from (4.1) – (4.5) by means of the standard procedure, discussed at length in Chapter 3: Find  $\mathbf{u} \in \mathcal{U}$  and  $p \in \mathcal{P}$ , such that for all  $\mathbf{w} \in \mathcal{W}$  and  $q \in \mathcal{P}$

$$\begin{aligned} \int_{\Omega} \mathbf{w} \cdot \rho \left( (\nabla\mathbf{u})\mathbf{u} - \mathbf{f} \right) - (\nabla \cdot \mathbf{w})p + 2\mu\nabla\mathbf{w} : \nabla^s\mathbf{u} + q(\nabla \cdot \mathbf{u}) dv \\ - \int_{\Gamma_t} \mathbf{w} \cdot \mathbf{t} da = 0, \end{aligned} \quad (4.6)$$

where

$$\begin{aligned} \mathcal{U} &= \left\{ \mathbf{u} \in (H^1(\Omega))^{n_{sd}} \mid \mathbf{u}|_{\hat{\mathbf{x}} \in \Gamma_g} = \mathbf{g} \right\} \\ \mathcal{W} &= \left\{ \mathbf{w} \in (H^1(\Omega))^{n_{sd}} \mid \mathbf{w}|_{\hat{\mathbf{x}} \in \Gamma_g} = \mathbf{0} \right\} \\ \mathcal{P} &= \left\{ p \in L^2(\Omega) \right\}, \end{aligned} \quad (4.7)$$

and  $n_{sd} = 2$  or  $n_{sd} = 3$  is the dimension of space.

## 4.1 The Galerkin Method and its Deficiencies

A standard Galerkin formulation is obtained from (4.6) simply by replacing the spaces  $\mathcal{U}$ ,  $\mathcal{W}$  and  $\mathcal{P}$  with the finite element spaces. Thus, the problem reads: Find  $\mathbf{u}^h \in \mathcal{U}^h$  and  $p^h \in \mathcal{P}^h$  such that for all  $\mathbf{w}^h \in \mathcal{W}^h$  and  $q^h \in \mathcal{P}^h$

$$\begin{aligned} \int_{\Omega} \left[ \mathbf{w}^h \cdot \rho \left( (\nabla\mathbf{u}^h)\mathbf{u}^h - \mathbf{f} \right) - (\nabla \cdot \mathbf{w}^h)p^h \right. \\ \left. + 2\mu\nabla\mathbf{w}^h : \nabla^s\mathbf{u}^h + q^h(\nabla \cdot \mathbf{u}^h) \right] dv - \int_{\Gamma_t} \mathbf{w}^h \cdot \mathbf{t}^h da = 0. \end{aligned} \quad (4.8)$$

with

$$\begin{aligned} \mathcal{U}^h &= \left\{ \mathbf{u}^h \in (H^1(\Omega))^{n_{sd}} \mid \mathbf{u}^h|_{\hat{\mathbf{x}}^h \in \Omega^e} \in (P_k(\Omega^e))^{n_{sd}}, \mathbf{u}^h|_{\hat{\mathbf{x}}^h \in \Gamma_g} = \mathbf{g} \right\} \\ \mathcal{W}^h &= \left\{ \mathbf{w}^h \in (H^1(\Omega))^{n_{sd}} \mid \mathbf{w}^h|_{\hat{\mathbf{x}}^h \in \Omega^e} \in (P_k(\Omega^e))^{n_{sd}}, \mathbf{w}^h|_{\hat{\mathbf{x}}^h \in \Gamma_g} = \mathbf{0} \right\} \\ \mathcal{P}^h &= \left\{ p^h \in H^1(\Omega) \mid p^h|_{\hat{\mathbf{x}}^h \in \Omega^e} \in P_k(\Omega^e) \right\}, \end{aligned} \quad (4.9)$$

where  $\Omega = \cup_{e=1}^{n_{el}} \Omega^e$  is a standard subdivision of the domain into  $n_{el}$  finite elements  $\Omega^e$ . The space  $P_k(\Omega^e)$  consists of all the polynomials of order  $k$  on  $\Omega^e$ .

Solutions obtained with (4.8) usually suffer severely from the aforementioned spurious oscillations of the velocity and pressure fields. In the following it is shown, that the instabilities in the velocity field arise from the advection term  $(\nabla \mathbf{u}^h) \mathbf{u}^h$ , whereas the oscillations in the pressure field can be attributed to the equal order interpolation of the velocity and the pressure.

### 4.1.1 Oscillatory Behaviour of the Velocity

Consider the linear advection-diffusion problem given by

$$\mathbf{a} \cdot \nabla u - \mu \Delta u = 0 \quad \forall \mathbf{x} \in \Omega \quad (4.10)$$

$$u - g = 0 \quad \forall \mathbf{x} \in \Gamma, \quad (4.11)$$

where  $u$  is a scalar unknown and  $\mathbf{a}$  is a given divergence free velocity field defined over the fixed spatial domain  $\Omega$ , while  $\mu$  represents the diffusion coefficient. The term  $\Delta u = \nabla \cdot (\nabla u)$  is the Laplace operator applied to the unknown  $u$ . For simplicity, pure Dirichlet boundary conditions are considered. Clearly, this problem is a special case of the Navier-Stokes equations for a Newtonian fluid (4.1) – (4.4). The so-called Peclet number  $\alpha = |\mathbf{a}| L / (2\mu)$ , where  $L$  is a typical length scale of the problem, is introduced to distinguish diffusion dominated ( $\alpha < 1$ ) and advection dominated ( $\alpha > 1$ ) problems. Similar to (4.7), the spaces  $\mathcal{U}$  and  $\mathcal{W}$  are introduced.

The associated classical Galerkin formulation reads: Find  $u^h \in \mathcal{U}^h$ , such that for any  $w^h \in \mathcal{W}^h$

$$a(w^h, u^h) = 0, \quad (4.12)$$

where  $\mathcal{U}^h \subset \mathcal{U}$  and  $\mathcal{W}^h \subset \mathcal{W}$  are defined similarly to (4.9) and the bilinear form  $a$  is given as

$$a(w, u) = \int_{\Omega} w \mathbf{a} \cdot \nabla u + \mu \nabla w \cdot \nabla u \, dv. \quad (4.13)$$

In order to assess the suitability of (4.12) for the computation of approximate solutions  $u^h$ , the ellipticity property (3.17) and Céa's Lemma (3.20) are recalled

$$a(w, w) \geq C_e \|w\|_1^2 \quad \forall w \in \mathcal{W} \quad (4.14)$$

$$\|u - u^h\|_1 \leq \frac{C_c}{C_e} \|u - \tilde{g} - w^h\|_1 \quad \forall w^h \in \mathcal{W}^h, \quad (4.15)$$

where  $\tilde{g} \in \mathcal{U}$  is a fixed function on  $\Omega$ , which satisfies the Dirichlet boundary condition, but is otherwise arbitrary. Thus,  $(u - \tilde{g}) \in \mathcal{W}$ . It follows from

$\nabla \cdot \mathbf{a} = 0$  and from the disappearance of  $w$  on the boundary that

$$a(w, w) = \int_{\Omega} \mu \nabla w \cdot \nabla w \, dv = \mu \|\nabla w\|_{L_2(\Omega)}^2. \quad (4.16)$$

Furthermore, the *Poincaré inequality* states that

$$\|w\|_1^2 \leq C_p \|\nabla w\|_{L_2(\Omega)}^2, \quad (4.17)$$

where  $C_p$  denotes the positive Poincaré constant. It follows from the comparison of (4.14), (4.16) and (4.17) that the Poincaré constant  $C_p$  corresponds to the ratio  $\mu/C_e$ , and thus, Céa's Lemma (4.15) may be rewritten as

$$\|u - u^h\|_1 \leq \frac{C_c C_p}{\mu} \|u - \tilde{g} - w^h\|_1 \quad \forall w^h \in \mathcal{W}^h. \quad (4.18)$$

Hence, the Galerkin method renders accurate solutions for large  $\mu$  (small  $\alpha$ ), whereas for small  $\mu$  (large  $\alpha$ ) greater errors can be expected. The error estimate completely fails for the pure advection case.

In order to demonstrate this shortcoming of (4.12) with a numerical example, it is sufficient to consider the one dimensional situation. In one dimension the advection-diffusion problem (4.10) and (4.11) reduces to

$$a u_{,x} - \mu u_{,xx} = 0 \quad \forall x \in [0, L], \quad u(0) = u_0, \quad u(L) = u_L. \quad (4.19)$$

The discretised weak form reads

$$\int_{\Omega^h} a w^h u_{,x} + \mu w_{,x}^h u_{,x} \, dx = 0. \quad (4.20)$$

A continuous piecewise linear finite element interpolation renders

$$u^h = \sum_{i=0}^{n_{el}-1} \{N_i, N_{i+1}\} \cdot \left\{ \begin{array}{c} \mathbf{u}_i \\ \mathbf{u}_{i+1} \end{array} \right\}, \quad w^h = \sum_{i=0}^{n_{el}-1} \{N_i, N_{i+1}\} \cdot \left\{ \begin{array}{c} \mathbf{w}_i \\ \mathbf{w}_{i+1} \end{array} \right\} \quad (4.21)$$

$$N_i = \frac{\mathbf{x}_{i+1} - x}{\Delta x}, \quad N_{i+1} = \frac{x - \mathbf{x}_i}{\Delta x} \quad (4.22)$$

where  $\Delta x = \mathbf{x}_{i+1} - \mathbf{x}_i$ . Employing this in (4.20) yields

$$\sum_{i=0}^{n_{el}-1} \left\{ \begin{array}{c} \mathbf{w}_i \\ \mathbf{w}_{i+1} \end{array} \right\} \cdot \left( \frac{a}{2} \begin{bmatrix} -1 & 1 \\ -1 & 1 \end{bmatrix} + \frac{\mu}{\Delta x} \begin{bmatrix} 1 & -1 \\ -1 & 1 \end{bmatrix} \right) \left\{ \begin{array}{c} \mathbf{u}_i \\ \mathbf{u}_{i+1} \end{array} \right\} = 0. \quad (4.23)$$

The exact solution of (4.19) is easily obtained as

$$u = u_0 + (u_L - u_0) \frac{e^{\frac{a}{\mu}x} - 1}{e^{\frac{a}{\mu}L} - 1}. \quad (4.24)$$

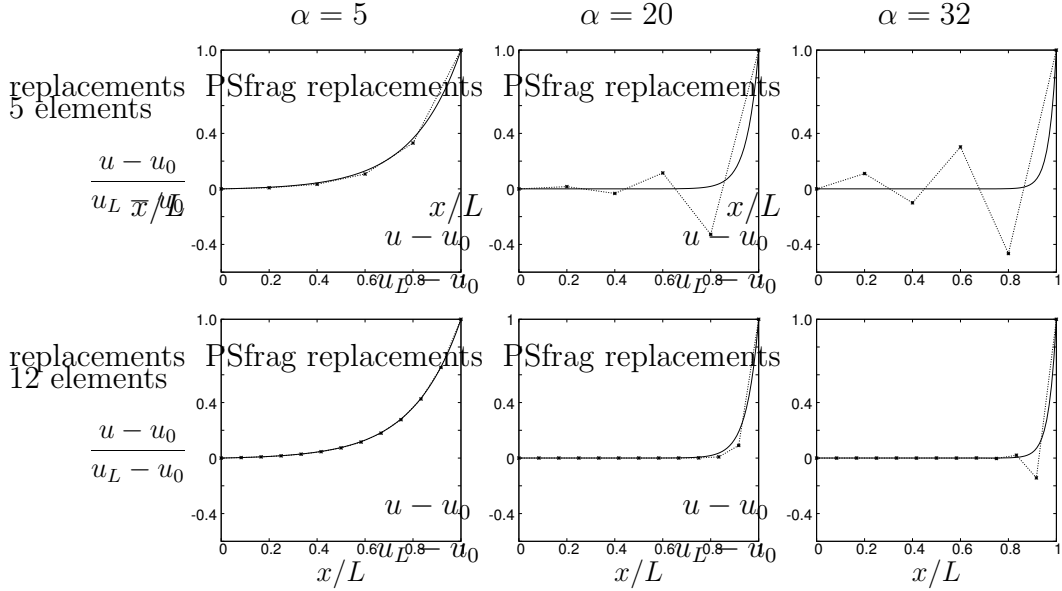


Figure 4.1: Galerkin solution and exact solution for the one dimensional advection diffusion equation.

Figure 4.1 shows the solution obtained from (4.23) and the exact solution for different Peclet numbers. The exact solution develops a strong boundary layer at the outflow boundary as the Peclet number increases. The numerical results show strong oscillatory behaviour, which originates in the unresolved boundary layer and spreads out into the whole domain. The figure also shows that the instabilities can be reduced by refining the discretisation. Thus, the likeliness of the unwanted oscillations may be measured by the element Peclet number  $\alpha^e = a \Delta x / (2\mu)$  rather than the global Peclet number  $\alpha$ .

In order to understand the origin of the problem, (4.23) is used to obtain an equation for  $\mathbf{u}_i$  in terms of  $\mathbf{u}_{i-1}$  and  $\mathbf{u}_{i+1}$ . This is achieved by assembling the nodal forces of two neighbouring elements, both of which are assumed to have the length  $\Delta x$ . It follows

$$0 = \frac{a}{2} (\mathbf{u}_{i+1} - \mathbf{u}_{i-1}) - \frac{\mu}{\Delta x} (\mathbf{u}_{i+1} - 2\mathbf{u}_i + \mathbf{u}_{i-1}), \quad (4.25)$$

which is, in fact, a central difference scheme of the governing equation (4.19). It has long been known that this scheme is unsuitable for modelling of advection dominated problems. To see this, simply rewrite (4.25) as

$$\mathbf{u}_i = \frac{1}{2} ((-\alpha^e + 1) \mathbf{u}_{i+1} + (\alpha^e + 1) \mathbf{u}_{i-1}) \quad (4.26)$$

and consider the situation  $\mathbf{u}_{i-1} = 0$  and  $\mathbf{u}_{i+1} = 10$ . It follows  $\mathbf{u}_i = 5(1 - \alpha^e)$ , which gives a negative value if  $\alpha^e > 1$ !

In Section 4.2, it is shown that the addition of appropriate stabilisation terms to the standard Galerkin formulation smoothes the solution without jeopardising the accuracy.

### 4.1.2 Spurious Pressure Modes

Consider the Stokes problem given by

$$\nabla \cdot \boldsymbol{\sigma} = \mathbf{0} \quad \forall \mathbf{x} \in \Omega \quad (4.27)$$

$$\nabla \cdot \mathbf{u} = 0 \quad \forall \mathbf{x} \in \Omega \quad (4.28)$$

$$\mathbf{u} - \mathbf{g} = \mathbf{0} \quad \forall \mathbf{x} \in \Gamma \quad (4.29)$$

with  $\boldsymbol{\sigma} = -p\mathbf{I} + 2\mu\nabla^s\mathbf{u}$ . Again, for the sake of simplicity, pure Dirichlet boundary conditions are considered. This problem is obtained from the Navier-Stokes equations (4.1) – (4.4) simply by neglecting the inertia terms. Note that the equations in (3.56), which describe the behaviour of a linear elastic incompressible continuum, are identical to (4.27) and (4.28), if the vectors  $\mathbf{u}$  are regarded as displacements and if the different sign of the pressure is accounted for.

Similar to (3.55), the corresponding mixed velocity-pressure Galerkin formulation can be obtained by the application of the procedures discussed in Section 3.4.1: Find  $\mathbf{u}^h \in \mathcal{U}^h$  and  $p^h \in \mathcal{P}^h$ , such that for any  $\mathbf{w}^h \in \mathcal{W}^h$  and  $q^h \in \mathcal{P}^h$

$$\int_{\Omega} \left( -(\nabla \cdot \mathbf{w}^h) p^h + 2\mu \nabla \mathbf{w}^h : \nabla^s \mathbf{u}^h + q^h (\nabla \cdot \mathbf{u}^h) \right) dv = 0. \quad (4.30)$$

If the spaces  $\mathcal{U}^h$ ,  $\mathcal{P}^h$  and  $\mathcal{W}^h$  are chosen as defined in (4.9), namely, if computationally convenient equal order piecewise polynomials are employed for the approximation of the pressure and the velocity, then the formulation (4.30) renders useless solutions for the pressure field.

In order to demonstrate these shortcomings, the lid driven cavity flow is simulated with equal order piecewise linear velocity-pressure elements. The geometry, the boundary conditions and the finite element discretisation of the problem are displayed in Figure 4.2. Note that the velocity is set to zero on the complete boundary except at the lid, where the horizontal velocity, including nodes A and B (“leaky cavity”), is prescribed as  $u_{\text{lid}}$ . Figures 4.3 (a) and (b) show the pressure distribution and the velocity vectors obtained with the Galerkin method (4.30) and, alternatively, with an appropriately

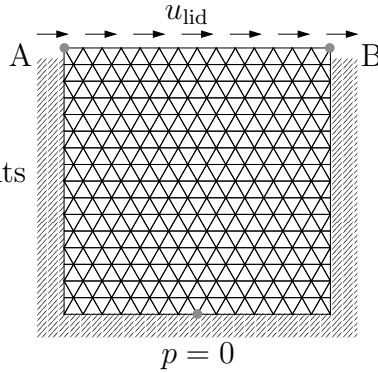


Figure 4.2: Stokes flow, driven cavity problem; width and height of cavity  $b = h = 1$ ,  $u_{\text{lid}} = 1$ ,  $\mu = 0.01$ ; mesh with 464 elements and problem set up.

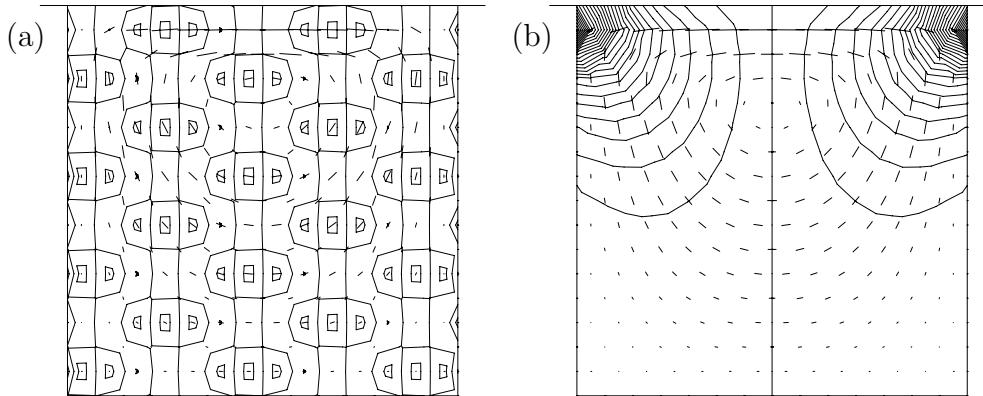


Figure 4.3: Stokes flow, driven cavity problem; pressure isolines and velocity vectors obtained with (4.30) (a), and with stabilised formulation (4.67) (b).

stabilised finite element formulation (see Section 4.3). Clearly, the pressure field computed with (4.30) is rendered useless by spurious pressure modes. These modes do not disappear as the discretisation is refined.

The failure of a finite element method based on the velocity-pressure formulation (4.30) and the spaces given in (4.9) follows from the violation of the Babuška-Brezzi condition (3.58). In Section 3.4.1, the Babuška-Brezzi condition has been introduced as a requirement, which needs to be satisfied by the velocity and pressure finite element spaces in order to guarantee the stability and convergence of the Galerkin formulation (4.30). Detailed information on the derivation of the condition, its different representations and its significance as a verification tool for mixed finite element formulations are provided in *e. g.* Bathe [5], Brezzi and Fortin [16], Brenner and Scott [13], Schwab [107].

In Section 4.3, two alternative strategies are introduced, which offer the formulation of stable equal order velocity-pressure finite element methods.

## 4.2 Velocity Stabilisation

In Section 4.1.1 the standard Galerkin method for the advection-diffusion problem has been shown to give poor results, which are rendered useless by oscillatory behaviour, unless the element Peclet number is very small. Small element Peclet numbers may be achieved by refining the finite element mesh. In most cases however, this strategy leads to excessive computational cost. This section provides a brief introduction to finite element stabilisation techniques for advection dominated problems. Two main approaches, which have been developed independently, are outlined in the following two subsections. Subsequently, it is shown that, for linear finite element interpolation, the stabilisation techniques are equivalent.

### 4.2.1 Artificial Damping, SUPG and GLS Methods

The simplest stabilisation technique, which was developed originally for finite difference schemes, consists in adding *artificial diffusion* to the physical diffusion given by  $\mu$ . The optimal amount of artificial diffusion is likely to vary within the domain  $\Omega$ . It depends on the local values of the properties  $|\mathbf{a}|$ ,  $\mu$ ,  $h$  of the discretised problem. For simplicity, a vector of the local properties is defined as  $\boldsymbol{\alpha}^e = \{|\mathbf{a}^e|, \mu, h^e\}$ . The approach maintains the framework of the standard Galerkin method. An improved finite element formulation of the advection-diffusion problem (4.10) – (4.11) can then be written as

$$\sum_{e=1}^{n_{\text{el}}} \int_{\Omega^e} w^h \mathbf{a} \cdot \nabla u^h + (\mu + \mu_{\text{art}}(\boldsymbol{\alpha}^e)) \nabla w^h \cdot \nabla u^h \, dv = 0. \quad (4.31)$$

The summation over the elements accounts for the discontinuities of the integrand across the inter element edges, which arise from the expression  $\mu_{\text{art}}(\boldsymbol{\alpha}^e)$ . Obviously, the performance of (4.31) depends very much on the choice of  $\mu_{\text{art}}(\boldsymbol{\alpha}^e)$ . Note that, for consistency with the original equation (4.10),  $\mu_{\text{art}}(\boldsymbol{\alpha}^e)$  is required to approach zero as  $h^e \rightarrow 0$ . More information on artificial diffusion methods can be found in *e. g.* Roache [99], Hirsch [58], Johnson [73] and references therein.

The accuracy of the formulation (4.31) can be improved significantly by restricting the artificial diffusion to the direction  $\mathbf{a}$  of the flow. The finite element formulation then becomes

$$\sum_{e=1}^{n_{\text{el}}} \int_{\Omega^e} w^h \mathbf{a} \cdot \nabla u^h + \mu \nabla w^h \cdot \nabla u^h + \tau(\boldsymbol{\alpha}^e) (\mathbf{a} \cdot \nabla w^h) (\mathbf{a} \cdot \nabla u^h) \, dv = 0. \quad (4.32)$$

The formulation (4.32) does not exhibit the undesirable diffusion perpendicular to the streamlines (*crosswind diffusion*), which is a major drawback

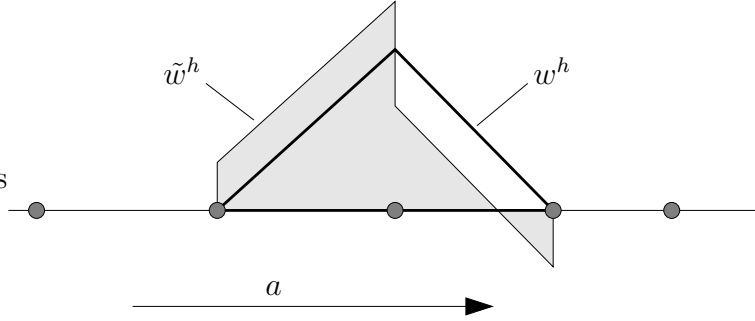


Figure 4.4: Streamline-upwinding/Petrov-Galerkin method, modified weighting function  $\tilde{w}$  in one dimension.

of (4.31). The strategy is therefore referred to as the *streamline diffusion method*. Unlike the artificial diffusion  $\mu_{\text{art}}$ , the quantity  $\tau$  has the dimension of time. Similar to  $\mu_{\text{art}}(\boldsymbol{\alpha}^e)$ , for consistency,  $\tau(\boldsymbol{\alpha}^e)$  is required to approach zero as the discretisation is refined.

A further improvement of the strategy is obtained by noting that, if linear finite element interpolations are employed, the formulation (4.32) is a special case of

$$\int_{\Omega} w^h \mathbf{a} \cdot \nabla u^h + \mu \nabla w^h \cdot \nabla u^h \, dv + \sum_{e=1}^{n_{\text{el}}} \int_{\Omega^e} \tau(\boldsymbol{\alpha}^e) (\mathbf{a} \cdot \nabla w^h) (\mathbf{a} \cdot \nabla u^h - \mu \Delta u^h) \, dv = 0, \quad (4.33)$$

which, in turn, can be rewritten as

$$\sum_{e=1}^{n_{\text{el}}} \int_{\Omega^e} \tilde{w}^h (\mathbf{a} \cdot \nabla u^h - \mu \Delta u^h) \, dv = 0, \quad (4.34)$$

where the modified weighting function  $\tilde{w}^h$  is defined as

$$\tilde{w}^h = w^h + \tau(\boldsymbol{\alpha}^e) (\mathbf{a} \cdot \nabla w^h). \quad (4.35)$$

Clearly, (4.34) is a Petrov-Galerkin formulation (compare (3.22)). The weighting functions are defined such that, with respect to a finite element node, the adjoint upstream elements are weighted more heavily than the downstream elements. This is demonstrated in Figure 4.4. Thus, the formulation is referred to as the *streamline-upwinding/Petrov-Galerkin* (SUPG) method.

Usually, the SUPG formulation is given in the format of (4.33). Namely, it is presented as the sum of the standard Galerkin expression given in (4.12) and a stabilisation term, which is evaluated for each element.

Very importantly, (4.34) shows that the formulation is consistent with the strong form of the problem (4.10) independently of the choice of  $\tau$ , provided the element interpolation is at least quadratic. If piecewise linear finite element spaces are chosen, the method coincides with the streamline diffusion formulation (4.32) and, for the sake of consistency, the expression  $\tau(\boldsymbol{\alpha}^e)$  is required to disappear as  $h^e \rightarrow 0$ . Thus, for piecewise linear finite element interpolation, the SUPG method may be said to be *weakly consistent*.

The first researchers to cast the streamline diffusion method strictly into the general format of a Petrov-Galerkin formulation were Brooks and Hughes [20]. The good convergence properties of the scheme and its superiority over the standard Galerkin and artificial diffusion methods were mathematically proven by Johnson *et al* [73, 74].

The formulation was further generalised by Hughes *et al* [68], when they introduced the following weak form:

$$\int_{\Omega} w^h \mathbf{a} \cdot \nabla u^h + \mu \nabla w^h \cdot \nabla u^h \, dv + \sum_{e=1}^{n_{el}} \int_{\Omega^e} \tau(\boldsymbol{\alpha}^e) (\mathbf{a} \cdot \nabla w^h - \mu \Delta w^h) (\mathbf{a} \cdot \nabla u^h - \mu \Delta u^h) \, dv = 0. \quad (4.36)$$

This new formulation consists of the standard Galerkin term, to which a least squares term of the residual of the original equation has been added. The expression  $\tau(\boldsymbol{\alpha}^e)$  can now be regarded as a weighting parameter of the least squares term. For linear shape functions, the diffusion terms in the least squares part of (4.36) disappear and the formulation coincides with the SUPG and the streamline diffusion methods. In Hughes *et al* [68], a mathematical a priori error estimate is given for (4.36). It is shown, that the *Galerkin/least-squares* (GLS) method is conceptually simpler and more general than the SUPG method.

For the mathematical proofs of the consistency, stability and improved convergence of the methods we again refer to the aforementioned references [20, 68, 73, 74]. It should, however, be noted here, that the concepts of SUPG and GLS provide a sound mathematical basis for the stabilised methods. Thus, the stabilisation terms do not jeopardise the accuracy or consistency of the standard Galerkin scheme, as had been argued in some publications *e. g.* Gresho and Lee [52], Gresho and Sani [53].

A summary of the stabilisation techniques introduced in this and the next section is given in Table 4.2 of Section 4.2.3.

## 4.2.2 Stabilisation with Bubbles, Multiscale Method

Independently of the numerical techniques described in the previous section, another approach to the stabilisation of advection dominated problems may be taken, which was originally developed for the pressure stabilisation of the Stokes flow. For that purpose, Arnold *et al* [2] suggested the introduction of additional velocity degrees of freedom inside the finite elements. The shape functions associated with the additional degrees of freedom are usually required to be zero on the element boundaries. Thus, they are commonly referred to as “*bubbles*”. The stabilisation of equal order velocity-pressure interpolations for incompressible flow problems is discussed in Section 4.3. Here, the relevance of bubble functions is considered with respect to the advection-diffusion problem.

Additional “bubble” degrees of freedom inside each element can be used to augment the finite element interpolation spaces. In the framework of a standard Galerkin method, these degrees of freedom can be eliminated locally. Thus, the benefit of the augmented spaces is achieved without significant increase in the overall computational effort.

A finite element formulation of the advection-diffusion problem (4.10) – (4.11) can then be written as

$$\int_{\Omega} \tilde{w}^h \mathbf{a} \cdot \nabla \tilde{u}^h + \mu \nabla \tilde{w}^h \cdot \nabla \tilde{u}^h \, dv = 0, \quad (4.37)$$

where

$$\tilde{u}^h = u^h + u^b, \quad \tilde{w}^h = w^h + w^b. \quad (4.38)$$

The bubble functions  $u^b, w^b \in \mathcal{W}^b$  may belong to the following mathematical space

$$\mathcal{W}^b = \{w^b \in P_k(\Omega^e) \mid w^b|_{\Gamma^e} = 0, \, e = 1, 2, \dots, n_{\text{el}}\}. \quad (4.39)$$

Clearly, (4.37) can be expected to render better results than the standard Galerkin formulation. Further improvement can be achieved, if the exact solution of the local boundary value problem posed by each finite element is contained in the space  $\mathcal{W}^b$ . In other words, the bubble should be capable of satisfying the strong form of the governing equation inside each finite element. The space  $\mathcal{W}^b$  of such bubble functions, which are referred to as *residual free bubbles* (RFB), is, however, very difficult to construct. Approximation techniques have, for example, been suggested by Franca *et al* [49] and Brezzi *et al* [18].

Equation (4.37) can be rewritten as

$$\begin{aligned} & \int_{\Omega} w^h \mathbf{a} \cdot \nabla(u^h + u^b) + \mu \nabla w^h \cdot \nabla(u^h + u^b) \, dv \\ & + \sum_{e=1}^{n_{\text{el}}} \int_{\Omega^e} w^b \mathbf{a} \cdot \nabla(u^h + u^b) + \mu \nabla w^b \cdot \nabla(u^h + u^b) \, dv = 0, \end{aligned} \quad (4.40)$$

where all integrals, including every integral in the sum, need to be zero, since  $w^h$  and  $w^b$  are independent. Thus, one global and  $n_{\text{el}}$  local equations are obtained

$$\int_{\Omega} w^h \mathbf{a} \cdot \nabla(u^h + u^b) + \mu \nabla w^h \cdot \nabla(u^h + u^b) \, dv = 0 \quad (4.41)$$

$$\int_{\Omega^e} w^b \mathbf{a} \cdot \nabla(u^h + u^b) + \mu \nabla w^b \cdot \nabla(u^h + u^b) \, dv = 0, \quad e = 1, 2, \dots, n_{\text{el}}. \quad (4.42)$$

If the bubble functions are expressed as

$$u^b = \mathbf{u}^b N^b, \quad w^b = \mathbf{w}^b N^b, \quad (4.43)$$

where  $\mathbf{u}^b$  and  $\mathbf{w}^b$  are the nodal values associated with the bubble shape function  $N^b$ , then, the unknown  $\mathbf{u}^b$  is obtained from (4.42) as

$$\mathbf{u}^b = - \frac{1}{\mu \|\nabla N^b\|_{0,\Omega^e}^2} \int_{\Omega^e} N^b \mathbf{a} \cdot \nabla u^h + \mu \nabla N^b \cdot \nabla u^h \, dv. \quad (4.44)$$

Note that  $\|\bullet\|_{0,\Omega^e}^2 = \int_{\Omega^e} (\bullet) \cdot (\bullet) \, dv$ . In the derivation of (4.44) the following relation has been used

$$\int_{\Omega^e} N^b \mathbf{a} \cdot \nabla N^b \, dv = 0, \quad (4.45)$$

which follows from  $\nabla \cdot \mathbf{a} = 0$  and from the disappearance of  $N^b$  on the element boundary. Note that, if  $u^h$  is chosen to be piecewise linear, the diffusion term in the integral of (4.44) vanishes. The expression (4.44) can now be employed in (4.41) to solve for the nodal values of  $u^h$ .

The concept of the bubbles may be regarded as belonging to the wider framework of the *variational multiscale* method, which was introduced by Hughes *et al* [65, 66]. It is based on the additive split of the solution into two components associated with the resolvable and unresolvable scales,  $u^r$  and  $u^u$ , respectively. The resolvable scales  $u^r$  can be identified with the finite element solution  $u^r = u^h$ ,

$$\tilde{u}^h = u^r + u^u = u^h + u^u. \quad (4.46)$$

The numerical analyst is not interested in the unresolvable scales  $u^u$ , but their effect on the resolvable scales needs to be accounted for. Thus, it is desired to solve for the unresolved scales locally, and then accurately consider their impact on the larger scales within the global solution for the resolvable scales  $u^h$ .

For the formulation of a standard Galerkin method within these settings, the following trial and weighting functions are introduced

$$\begin{aligned}\tilde{u}^h &= u^h + u^u \in \mathcal{U}^h \oplus \mathcal{W}^u \\ \tilde{w}^h &= w^h + w^u \in \mathcal{W}^h \oplus \mathcal{W}^u,\end{aligned}\tag{4.47}$$

where the space of the unresolved functions  $\mathcal{W}^u$  has to be defined such that the decomposition of the trial and weighting functions (4.47) into resolved and unresolved components is unique.

If, within this framework,  $\mathcal{W}^u$  could be chosen so large that

$$\mathcal{U}^h \oplus \mathcal{W}^u = \{\tilde{u}^h \in H^1(\Omega) \mid \tilde{u}^h|_{\mathbf{x}^h \in \Gamma} = g\},\tag{4.48}$$

then the  $\tilde{u}^h$  would be obtained equal to the exact solution  $u$  and the finite element solution  $u^h$  would be an interpolant of  $u$ . However, it is desired to eliminate the unresolved scales on element level. This is only possible, if the functions  $u^u$  and  $w^u$  disappear on the element boundaries. Thus, the largest possible space  $\mathcal{W}^u$  is obtained as

$$\mathcal{W}^u = \bigoplus_{e=1}^{n_{el}} H_0^1(\Omega^e).\tag{4.49}$$

In other words, only the unresolved scales that vanish on the element boundaries are taken into account, hoping that their effect on  $u^h$  is representative enough of all unresolved scales. According to Brezzi *et al* [17], “this assumption is quite strong, and up to now its validity can only be justified

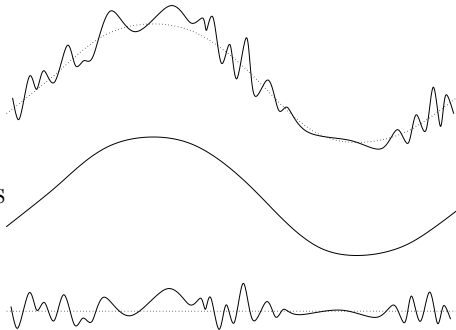


Figure 4.5: Resolved and unresolved scales of the solution.

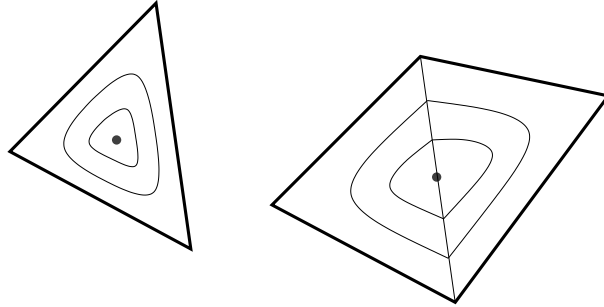


Figure 4.6: Isolines of a bubble and an edge function in two dimensions.

a posteriori by seeing that in many cases it is general enough to give good approximation schemes”.

This is also the crucial point for the equivalence of the concept of residual free bubbles and the multiscale approach (see *e. g.* Hughes *et al* [65, 66], Brezzi *et al* [17]), since, by this assumption, in the best case, the unresolved scales  $u^u$  will take the shape of a residual free bubble.

However, in [66], in order to weaken this restriction, the so-called edge functions are introduced. In a finite element discretisation of a two dimensional domain, edge functions are defined on every pair of elements that have one element edge in common (see Figure 4.6). They may be regarded as bubbles on the joined domains of two neighbouring elements. In three dimensions, the situation is more complex, since also face functions are required. Obviously, in one dimension, (4.49) implies (4.48), and the residual free bubble method renders the exact nodal solutions for  $u^h$ . The concept of edge and face functions can be used to keep the space  $\mathcal{W}^u$  large and generic. On the other hand, however, it introduces unresolved scales, which can only be eliminated on pairs or groups of neighbouring elements. Hence, the response of each element depends on information from the neighbouring elements. Clearly, this is not consistent with the usual implementational finite element framework.

The improved performance of the Galerkin method, when enriched with bubbles, is shown for the example of the one dimensional advection-diffusion problem given by (4.19). Therefore, the continuous piecewise linear finite element interpolation space, which, in Section 4.1.1, has been shown to render undesirable strong oscillations of the solution, is augmented with bubble functions. Different bubble functions are considered resulting in different approximation schemes. In order to assess the accuracy, difference stencils of the following format are derived for each scheme

$$u_i = \zeta_1 u_{i+1} + \zeta_2 u_{i-1}, \quad (4.50)$$

where equal nodal spacing is assumed. It follows from the analytical solution (4.24), that exact nodal values are obtained for

$$\zeta_1^{\text{ex}} = \frac{e^{2\alpha^e} - 1}{e^{4\alpha^e} - 1} = \frac{1}{2} - \frac{1}{2}\alpha^e + \frac{1}{6}(\alpha^e)^3 - \frac{1}{15}(\alpha^e)^5 + O((\alpha^e)^7) \quad (4.51)$$

and  $\zeta_2^{\text{ex}} = 1 - \zeta_1^{\text{ex}}$ . For the standard Galerkin method without bubble enrichment it has already been derived in (4.26) that

$$\zeta_1^{\text{Gal}} = \frac{1}{2} - \frac{1}{2}\alpha^e \quad \text{and} \quad \zeta_2^{\text{Gal}} = 1 - \zeta_1^{\text{Gal}}, \quad (4.52)$$

which, in comparison with (4.51), reflects the well known fact that the Galerkin method is second order accurate. For the Galerkin method with bubble functions, the coefficients  $\zeta_1$  and  $\zeta_2$  are obtained by evaluating (4.44) and employing the result in (4.41). Analogously to the procedure in Section 4.1.1, the forces at node  $i$  of the two neighbouring finite elements are added together. The sum is required to vanish and thus, an equation in terms of  $\mathbf{u}_{i-1}$ ,  $\mathbf{u}_i$  and  $\mathbf{u}_{i+1}$  is obtained. Table 4.1 provides a summary of the expressions  $\zeta_1$  and  $\zeta_2$  obtained for different types of bubbles. As expected, every bubble method exceeds the accuracy of the standard Galerkin method. The primitive piecewise linear bubble renders a less accurate method than the smooth quadratic bubble function. Note, that the results obtained with piecewise linear bubbles coincide with a standard Galerkin solution based on twice as many finite elements. The shape of the residual free bubble has been constructed from the exact solution of the local boundary value problem. In accordance with the aforementioned special property of the one dimensional situation, the residual free bubbles render exact nodal values  $\mathbf{u}_i$ .

### 4.2.3 Summary, Equivalence of Methods

In Sections 4.2.1 and 4.2.2 two different approaches to the stabilisation of the Galerkin method for advection dominated problems have been outlined. The starting point of the first are the artificial diffusion methods originally introduced in the framework of finite differences. The second approach is based on local enrichment of the finite element space and has been developed initially for mixed finite element problems.

In this subsection it is shown, that within the framework of continuous piecewise linear finite element interpolations the two approaches render identical finite element schemes. This was first recognised by Brezzi *et al* [15]. The equivalence of the concepts of the stabilisation methods may also be proven for the general case, as shown in *e. g.* Hughes *et al* [65, 66], Brezzi *et al* [17].

The formal equivalence of the strategies is obtained simply by rewriting (4.41) as

$$\begin{aligned} & \int_{\Omega} w^h \mathbf{a} \cdot \nabla u^h + \mu \nabla w^h \cdot \nabla u^h \, dv \\ & + \int_{\Omega} w^h \mathbf{a} \cdot \nabla u^b + \mu \nabla w^h \cdot \nabla u^b \, dv = 0, \end{aligned} \quad (4.53)$$

where the first integral is observed to coincide with the standard Galerkin formulation (4.12). Thus, similarly to the artificial diffusion, SUPG or GLS methods, the formulation stabilised with bubble functions can be written as the sum of a Galerkin term and a stabilisation term. By recalling the inclusion of the bubble techniques in the general multiscale method (Section 4.2.2), the stabilisation term can thus be identified as representing the effect of the small unresolved scales on the large resolved scales.

It remains to show that, for piecewise linear finite element interpolation, the second integral in (4.53) is identical to the stabilisation terms of the

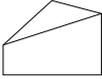
	$N^b$	$\zeta_1$	$\zeta_1 - \zeta_1^{\text{ex}}$
exact solution	—	$\frac{1}{2} - \frac{1}{2}\alpha^e + \frac{1}{6}(\alpha^e)^3 - \frac{1}{15}(\alpha^e)^5 + O((\alpha^e)^7)$	—
 standard Galerkin method	—	$\frac{1}{2} - \frac{1}{2}\alpha^e$	$O((\alpha^e)^3)$
 piecewise linear bubbles	$\begin{cases} 2 \frac{x - x_i}{\Delta x}, & x \leq \frac{x_i + x_{i+1}}{2} \\ 2 \frac{x_{i+1} - x}{\Delta x}, & x > \frac{x_i + x_{i+1}}{2} \end{cases}$	$\frac{1}{2} - \frac{1}{2}\alpha^e + \frac{1}{8}(\alpha^e)^3 - \frac{1}{32}(\alpha^e)^5 + O((\alpha^e)^7)$	$O((\alpha^e)^3)$
 quadratic bubbles	$4 \left( \frac{x - x_i}{\Delta x} - \left( \frac{x - x_i}{\Delta x} \right)^2 \right)$	$\frac{1}{2} - \frac{1}{2}\alpha^e + \frac{1}{6}(\alpha^e)^3 - \frac{1}{18}(\alpha^e)^5 + O((\alpha^e)^7)$	$O((\alpha^e)^5)$
 residual free bubbles	$\frac{x - x_i}{\Delta x} - \frac{e^{2\alpha^e \frac{x - x_i}{\Delta x}} - 1}{e^{2\alpha^e} - 1}$	$\frac{1}{2} - \frac{1}{2}\alpha^e + \frac{1}{6}(\alpha^e)^3 - \frac{1}{15}(\alpha^e)^5 + O((\alpha^e)^7)$	0

Table 4.1: Bubble stabilisation of the one dimensional advection-diffusion equation;  $u_i = \zeta_1 u_{i+1} + \zeta_2 u_{i-1}$ ; for every scheme  $\zeta_2 = 1 - \zeta_1$ .

SUPG or GLS methods given in (4.33) or (4.36), respectively. Restricting the finite element interpolations  $u^h$  and  $w^h$  to the piecewise linear functions  $u^l$  and  $w^l$  and recalling (4.43) and (4.44), the second integral in (4.53) can be rewritten as

$$\int_{\Omega} w^l \mathbf{a} \cdot \nabla u^b + \mu \nabla w^l \cdot \nabla u^b \, dv \quad (4.54)$$

$$= \sum_{e=1}^{n_{el}} \int_{\Omega^e} w^l \mathbf{a} \cdot \nabla N^b \, dv \quad \mathbf{u}^b \quad (4.55)$$

$$= \sum_{e=1}^{n_{el}} \left( - \int_{\Omega^e} \mathbf{a} \cdot \nabla w^l N^b \, dv \right) \left( - \frac{1}{\mu \|\nabla N^b\|_{0,\Omega^e}^2} \int_{\Omega^e} N^b \mathbf{a} \cdot \nabla u^l \, dv \right) \quad (4.56)$$

$$= \sum_{e=1}^{n_{el}} \frac{1}{\mu \|\nabla N^b\|_{0,\Omega^e}^2 V^e} V^e (\mathbf{a} \cdot \nabla w^l) (\mathbf{a} \cdot \nabla u^l) \left( \int_{\Omega^e} N^b \, dv \right)^2 \quad (4.57)$$

$$= \sum_{e=1}^{n_{el}} \int_{\Omega^e} \underbrace{\frac{\left( \int_{\Omega^e} N^b \, dv \right)^2}{\mu \|\nabla N^b\|_{0,\Omega^e}^2 V^e}}_{\tau} (\mathbf{a} \cdot \nabla w^l) (\mathbf{a} \cdot \nabla u^l) \, dv \quad (4.58)$$

$$= \sum_{e=1}^{n_{el}} \int_{\Omega^e} \tau (\mathbf{a} \cdot \nabla w^l) (\mathbf{a} \cdot \nabla u^l) \, dv, \quad (4.59)$$

where  $\mathbf{a}$  is assumed to be constant within each element. The diffusion term in (4.54) vanishes due to the linearity of  $w^l$  and the disappearance of  $N^b$  on the element boundaries. The derivation of (4.56) from (4.55) is based on  $\nabla \cdot \mathbf{a} = 0$ . The quantity  $V^e$  denotes the volume of element  $e$ . Clearly, (4.59) is identical to the stabilisation terms in (4.33) and (4.36) without the diffusive parts, which disappear for piecewise linear  $u^h$  and  $w^h$ .

At this stage the following conclusions may be drawn:

- The SUPG and GLS stabilisation techniques for finite element solutions of advection dominated problems are conceptually similar to the enrichment of the finite element space with bubbles functions. For linear finite element interpolation, the strategies render identical numerical schemes.
- The challenge in the framework of SUPG and GLS lies in the choice of the optimal parameter  $\tau$ , whereas the stabilisation with bubbles requires the non-trivial construction of the optimal bubble function (therefore, the expression for the stabilisation parameter  $\tau$  derived in (4.59) helps to understand the nature of  $\tau$ , but does not solve the problem of finding the optimal  $\tau$ ).

It may thus be said, that the choice of the one technique or the other seems a matter of taste, and the decision may very well be based on computational convenience. A summary of the different stabilisation techniques is given in Table 4.2. In this work, it is chosen to employ the SUPG method for the stabilisation of the velocity field of the Navier-Stokes equations. The detailed formulation, used in the remainder of this work, is provided in Section 4.4.

Finally, the expression for the stabilisation parameter  $\tau$ , which has been derived in (4.59), is investigated more closely. Therefore, it is evaluated for the three different types of bubbles presented in Table 4.1 for the stabilisation of the one dimensional advection-diffusion equation. For the piecewise linear

standard Galerkin	$a(w^h, u^h) = 0$
artificial diffusion	$a(w^h, u^h) + [\mu_{\text{art}}(\boldsymbol{\alpha}^e), \nabla w^h \cdot \nabla u^h]_{\Sigma\Omega^e} = 0$
streamline diffusion	$a(w^h, u^h) + [\tau(\boldsymbol{\alpha}^e) (\mathbf{a} \cdot \nabla w^h), (\mathbf{a} \cdot \nabla u^h)]_{\Sigma\Omega^e} = 0$
SUPG	$a(w^h, u^h) + [\tau(\boldsymbol{\alpha}^e) (\mathbf{a} \cdot \nabla w^h), \mathcal{L}(u^h)]_{\Sigma\Omega^e} = 0$
GLS	$a(w^h, u^h) + [\tau(\boldsymbol{\alpha}^e) \mathcal{L}(w^h), \mathcal{L}(u^h)]_{\Sigma\Omega^e} = 0$
bubbles	$a(w^h, u^h) + a(w^h, u^b) = 0$ $u^b = N^b \mathbf{u}^b, \quad \mathbf{u}^b = -\frac{a(N^b, u^h)}{\mu \ \nabla N^b\ _{0, \Omega^e}^2}$
$\mathcal{L}(u) = \mathbf{a} \cdot \nabla u - \mu \Delta u$ $a(w, u) = \int_{\Omega} w \mathbf{a} \cdot \nabla u + \mu \nabla w \cdot \nabla u \, dv$ $[w, u]_{\Sigma\Omega^e} = \sum_{e=1}^{n_{\text{el}}} \int_{\Omega^e} w u \, dv$	

Table 4.2: Summary of finite element stabilisation techniques for the advection-diffusion problem (4.10) – (4.11); general representation, valid for any continuous finite element interpolation.

bubble function one obtains

$$\tau_{\text{pl}} = \frac{\Delta x^2}{16\mu} = \frac{\Delta x}{2a} \xi_{\text{pl}}(\alpha^e) \quad \text{with} \quad \xi_{\text{pl}}(\alpha^e) = \frac{\alpha^e}{4}. \quad (4.60)$$

The quadratic bubble function yields

$$\tau_{\text{q}} = \frac{\Delta x^2}{12\mu} = \frac{\Delta x}{2a} \xi_{\text{q}}(\alpha^e) \quad \text{with} \quad \xi_{\text{q}}(\alpha^e) = \frac{\alpha^e}{3}, \quad (4.61)$$

and finally the residual free bubble renders

$$\tau_{\text{ex}} = \frac{\Delta x}{2a} \xi_{\text{ex}}(\alpha^e) \quad \text{with} \quad \xi_{\text{ex}}(\alpha^e) = \coth(\alpha^e) - \frac{1}{\alpha^e}. \quad (4.62)$$

A critical  $\tau_{\text{crit}}$  may be derived as follows. Obtain  $\zeta_1$  and  $\zeta_2$  for the SUPG method from a derivation along the lines of Section 4.2.2, (4.50),

$$\zeta_1 = \frac{1}{2} \left( 1 - \frac{\alpha^e}{1 + \alpha^e \frac{2a}{\Delta x} \tau} \right), \quad \zeta_2 = 1 - \zeta_1. \quad (4.63)$$

The case  $\mathbf{u}_i = \mathbf{u}_{i-1}$  is regarded as critical. It corresponds to the limit where  $\mathbf{u}_i$  is completely independent of the downstream situation. From (4.50) it follows that  $\zeta_1(\tau_{\text{crit}}) = 0$  and thus

$$\tau_{\text{crit}} = \frac{\Delta x}{2a} \xi_{\text{crit}}(\alpha^e) \quad \text{with} \quad \xi_{\text{crit}}(\alpha^e) = \frac{\alpha^e - 1}{\alpha^e}. \quad (4.64)$$

The coefficients  $\xi(\alpha^e)$  are displayed in Figure 4.7. It is observed that the quadratic bubble renders the nodally exact solution in the viscous limit  $\alpha \rightarrow 0$ , since  $\xi_{\text{q}}(\alpha^e)$  describes basically the tangent to  $\xi_{\text{ex}}(\alpha^e)$  at  $\alpha^e = 0$ . The piecewise linear bubble yields a very rough approximation of  $\xi_{\text{ex}}(\alpha^e)$ , in fact,  $\xi_{\text{pl}}(\alpha^e)$  is a tangent to  $\xi_{\text{crit}}(\alpha^e)$  at  $\alpha^e = 2$ . As  $\alpha^e \rightarrow \infty$  both  $\xi_{\text{crit}}(\alpha^e)$  and  $\xi_{\text{ex}}(\alpha^e)$  tend to 1. This follows from the fact that, in the advective limit, the exact solution for any  $\mathbf{u}_i$ , like the critical one, depends only on upstream values. Based on these findings, it has been suggested by Simo *et al* [109] to improve the performance of bubble methods by appropriately scaling the bubbles. It should, however, be recalled from Section 4.2.2, that for real problems in two or three dimensions an expression like  $\xi_{\text{ex}}(\alpha^e)$  can not be derived in this way and may not exist.

Note that the expressions for  $\zeta_1$  and  $\zeta_2$ , given in (4.63), also demonstrate that, for piecewise linear finite element interpolation the consistency of the stabilised methods may be said to be “weak”. From the comparison of (4.63) with (4.51) it follows that the appropriate choice of  $\tau$  is essential for the success of the scheme.

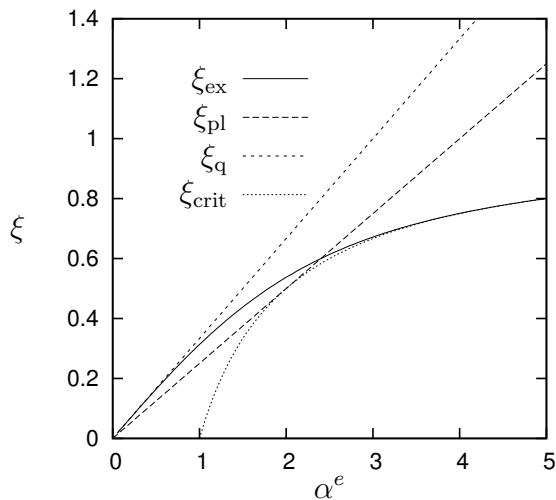


Figure 4.7: Coefficients  $\xi(\alpha^e)$  of the stabilisation parameter  $\tau$  for the one dimensional advection-diffusion equation.

### 4.3 Pressure Stabilisation

In Section 4.1.2, the equal order velocity-pressure Galerkin method has been shown to be inappropriate for the simulation of Stokes flow. The resulting pressure fields are rendered useless by persistent spurious pressure modes, which do not disappear as the mesh is refined. This has been attributed to the violation of the Babuška-Brezzi condition. Thus, a different computational strategy is indispensable. This section provides a brief introduction to finite element stabilisation techniques for incompressible flow problems. Two main approaches, which have been developed independently during recent decades and which may be characterised by *circumventing* or *satisfying* the Babuška-Brezzi condition, are outlined in the following two subsections. Subsequently, it is shown that, for linear finite element interpolation, the stabilisation techniques are equivalent. Many similarities with the stabilisation of advection dominated problems, as described in Section 4.2, may be observed. In fact, these similarities enable the straightforward formulation of both velocity and pressure stabilised finite element methods for the Navier-Stokes equations without further complications. This is addressed in Section 4.4.

#### 4.3.1 PSPG and GLS Methods

An elegant stabilisation technique for computationally convenient equal order velocity-pressure finite element methods was introduced by Hughes *et al* [67].

It has become well known as the *pressure-stabilising/Petrov-Galerkin* (PSPG) method. Based on the work by Brezzi and Pitkäranta [19] and Johnson and Saranen [75], Hughes *et al* suggested the following finite element formulation: Find  $\mathbf{u}^h \in \mathcal{U}^h$  and  $p^h \in \mathcal{P}^h$ , such that for all  $\mathbf{w}^h \in \mathcal{W}^h$  and  $q^h \in \mathcal{P}^h$

$$\sum_{e=1}^{n_{el}} \int_{\Omega^e} \tilde{\mathbf{w}}^h \cdot (\nabla p^h - 2\mu \nabla \cdot \nabla^s \mathbf{u}^h) + q^h (\nabla \cdot \mathbf{u}^h) \, dv = 0, \quad (4.65)$$

where the weighting function  $\tilde{\mathbf{w}}^h$  is defined as

$$\tilde{\mathbf{w}}^h = \mathbf{w}^h + \tau(h^e, \mu) \nabla q^h. \quad (4.66)$$

Clearly, the formulation is a consistent Petrov-Galerkin method since the terms in the integrals, which are weighted with  $\tilde{\mathbf{w}}^h$  and  $q^h$ , respectively, are the residuals of the governing equations (4.27) and (4.28). Using integration by parts, (4.65) can be rewritten as

$$\begin{aligned} & \int_{\Omega} -(\nabla \cdot \mathbf{w}^h) p^h + 2\mu \nabla \mathbf{w}^h : \nabla^s \mathbf{u}^h + q^h (\nabla \cdot \mathbf{u}^h) \, dv \\ & + \sum_{e=1}^{n_{el}} \int_{\Omega^e} \tau(h^e, \mu) \nabla q^h \cdot (\nabla p^h - 2\mu \nabla \cdot \nabla^s \mathbf{u}^h) \, dv = 0. \end{aligned} \quad (4.67)$$

Thus, similar to the stabilised methods for the advection diffusion problem, the improved formulation consists of the standard Galerkin term to which a stabilisation term has been added. Note, that the diffusion part of the stabilisation term in (4.67) disappears, if piecewise linear finite element interpolation is employed. The consistency with the strong form of the problem then requires that the parameter  $\tau$  tends to zero as the mesh is refined. Similar to the SUPG and GLS methods for the advection diffusion equation, the formulation based on linear interpolation spaces may be said to be only *weakly consistent*. In [67], Hughes *et al* present an a priori error estimate, showing that the method is stable and that optimal convergence is achieved if  $\tau(h, \mu)$  is of  $O(h^2)$ .

The good performance of the stabilised scheme (4.67) may briefly be explained as follows: In the standard Galerkin method (4.30) the pressure is tested only by means of the expression  $(\nabla \cdot \mathbf{w}^h) p^h$ . For equal order velocity and pressure interpolations this is not sufficient to damp out the spurious modes of the pressure. In this sense, the Babuška-Brezzi condition (3.58) may be regarded as formulating the minimum requirements to the velocity test space, such that  $(\nabla \cdot \mathbf{w}^h) p^h$  suffices to suppress spurious pressure modes. The success of the method (4.67) can then be attributed to the fact that

the pressure is indeed more severely tested now by means of  $(\nabla \cdot \mathbf{w}^h) p^h$  and  $\nabla q^h \cdot \nabla p^h$ . Hence, the Babuška-Brezzi condition is circumvented by the introduction of the term  $\nabla q^h \cdot \nabla p^h$ .

An example of the good performance of the method has already been given in Section 4.1.2, where the driven cavity flow is simulated. The pressure distribution shown in Figure 4.3 (b) has been obtained with (4.67), employing piecewise linear equal order interpolation spaces. The stabilisation parameter has been set to

$$\tau(h^e, \mu) = \frac{(h^e)^2}{12\mu}. \quad (4.68)$$

Similar to the stabilisation techniques for the advection diffusion equation, the PSPG scheme may be viewed as a *Galerkin/least-squares* (GLS) method. In fact, the stabilisation term in (4.67) consists of a least squares term of the momentum equation formulated with respect to the pressure and weighted with the parameter  $\tau(h^e, \mu)$ .

Finally, it is pointed out, that the employment of equal order piecewise linear velocity and pressure interpolations may lead to inaccurate pressure boundary layers. Due to the disappearance of every second order derivative, the stabilisation term can be rewritten as

$$\sum_{e=1}^{n_{el}} \int_{\Omega^e} \tau(h^e, \mu) (\nabla q^1 \cdot \nabla p^1) \, dv = \sum_{e=1}^{n_{el}} \int_{\Gamma^e} \tau(h^e, \mu) q^1 (\nabla p^1 \cdot \mathbf{n}) \, da, \quad (4.69)$$

where  $\mathbf{n}$  is the outward normal to the element boundary  $\Gamma^e$  and the superscript 1 denotes piecewise linear finite element interpolation. At the boundaries  $\Gamma^e \cap \Gamma$ , the expression (4.69) weakly enforces an artificial pressure boundary condition,  $\nabla p \cdot \mathbf{n} = 0$ . Namely, the pressure isolines tend to align themselves perpendicular to the boundary  $\Gamma$ . On inter element boundaries this effect is neutralised by the neighbouring elements. Droux and Hughes [38] introduce an additional consistent boundary term, which removes this drawback.

### 4.3.2 Stabilisation with Bubbles

An obvious strategy to construct stable velocity-pressure elements lies in the careful choice of different interpolations for the velocity and the pressure, such that the Babuška-Brezzi condition is satisfied. Since the formulation of the Babuška-Brezzi condition various such elements have been suggested. A summary is, for example, given in Bathe [5]. Proofs of the conformity of specific finite elements with the Babuška-Brezzi condition are presented by Brezzi and Fortin [16].

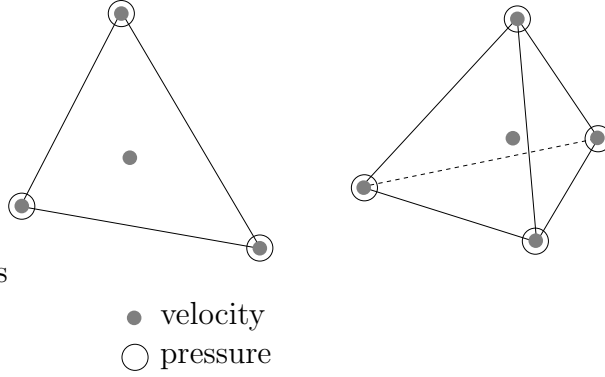


Figure 4.8: MINI element in two and three dimensions.

However, in this work, the focus is on computationally convenient low equal order velocity-pressure interpolations. Thus, there remains only the piecewise linear so-called *MINI element*, which passes the Babuška-Brezzi test by means of velocity space enrichment with element bubble functions (see Figure 4.8). The velocity degrees of freedom, which are associated with the bubble, can be eliminated at element level. Hence, within the global finite element framework, the MINI element can be treated as a linear equal order velocity-pressure element. The MINI element was originally developed by Arnold *et al* [2].

The finite element formulation may then be written as

$$\int_{\Omega} -(\nabla \cdot \tilde{\mathbf{w}}^1) p^1 + 2\mu \nabla \tilde{\mathbf{w}}^1 : \nabla^s \tilde{\mathbf{u}}^1 + q^1 (\nabla \cdot \tilde{\mathbf{u}}^1) dv = 0, \quad (4.70)$$

with

$$\tilde{\mathbf{u}}^1 = \mathbf{u}^1 + \mathbf{u}^b, \quad \tilde{\mathbf{w}}^1 = \mathbf{w}^1 + \mathbf{w}^b, \quad (4.71)$$

where the superscript 1 denotes piecewise linear finite element interpolation. The bubble functions  $\mathbf{u}^b, \mathbf{w}^b \in \mathcal{W}^b$  may belong to the following mathematical space

$$\mathcal{W}^b = \left\{ \mathbf{w}^b \in (H^1(\Omega))^{n_{\text{sd}}} \mid \mathbf{w}^b|_{\mathbf{x}^h \in \Omega^e} \in (P_k(\Omega^e))^{n_{\text{sd}}}, \mathbf{w}^b|_{\mathbf{x}^h \in \Gamma^e} = \mathbf{0} \right\}. \quad (4.72)$$

Usually, the bubble shape function  $N^b$  of the MINI element is taken as

$$N^b = 3^{n_{\text{ne}}} \prod_{A=1}^{n_{\text{ne}}} N_A^1, \quad (4.73)$$

where the number of nodes per element  $n_{\text{ne}}$  is 3 or 4 in two or three dimensions, respectively, and the functions  $N_A^1$  represent the standard linear shape functions of the triangle or tetrahedron.

It remains to outline the local elimination procedure for the bubble, which follows the strategy already described in Section 4.2.2, (4.37) – (4.44), for the stabilisation of the advection-diffusion equation with bubbles.

First, (4.70) is rewritten as

$$\int_{\Omega} -(\nabla \cdot \mathbf{w}^l) p^l + 2\mu \nabla \mathbf{w}^l : \nabla^s(\mathbf{u}^l + \mathbf{u}^b) + q^l (\nabla \cdot (\mathbf{u}^l + \mathbf{u}^b)) \, dv = 0 \quad (4.74)$$

and

$$\int_{\Omega^e} -(\nabla \cdot \mathbf{w}^b) p^l + 2\mu \nabla \mathbf{w}^b : \nabla^s(\mathbf{u}^l + \mathbf{u}^b) \, dv = 0 \quad (4.75)$$

for  $e = 1, 2, \dots, n_{\text{el}}$ . Recalling  $\mathbf{u}^b = N^b \mathbf{u}^b$ , the local problems (4.75) can be solved for the velocities  $\mathbf{u}^b$ . By using

$$\int_{\Omega^e} \nabla \mathbf{w}^b : \nabla^s \mathbf{u}^l \, dv = 0, \quad (4.76)$$

which follows from the linearity of  $\mathbf{u}^l$  and from the disappearance of  $N^b$  on the element boundaries, one obtains

$$\mathbf{u}^b = \frac{1}{\mu} (\mathbf{A}^{b,e})^{-1} \int_{\Omega_e} p^l \nabla N^b \, dv \quad (4.77)$$

with

$$\mathbf{A}^{b,e} = \int_{\Omega_e} (\nabla N^b \cdot \nabla N^b) \mathbf{I} + \nabla N^b \otimes \nabla N^b \, dv. \quad (4.78)$$

The expression (4.77) may then be employed in (4.74), such that the global system can be solved for the nodal unknowns of  $\mathbf{u}^l$  and  $p^l$ .

### 4.3.3 Summary, Equivalence of Methods

In the previous subsections two different stabilisation techniques of the mixed Galerkin method for incompressible Stokes flow have been outlined. With respect to the central importance of the Babuška-Brezzi condition (3.58), the PSPG method (Section 4.3.1) may be said to circumvent the condition, whereas the MINI element (Section 4.3.2) satisfies it.

In this subsection it is shown, that the PSPG method with continuous piecewise linear finite element interpolations is identical to the MINI element. Thus, this subsection closely follows the procedure in Section 4.2.3, where similar stabilisation techniques of the advection diffusion problem have been compared.

Therefore, (4.74) is rewritten as

$$\begin{aligned} \int_{\Omega} -(\nabla \cdot \mathbf{w}^l) p^l + 2\mu \nabla \mathbf{w}^l : \nabla^s \mathbf{u}^l + q^l (\nabla \cdot \mathbf{u}^l) dv \\ + \int_{\Omega} 2\mu \nabla \mathbf{w}^l : \nabla^s \mathbf{u}^b + q^l (\nabla \cdot \mathbf{u}^b) dv = 0, \end{aligned} \quad (4.79)$$

where the first integral is observed to coincide with the standard Galerkin term (4.30). Thus, similarly to the PSPG method, the MINI element formulation can be written as the sum of a Galerkin and a stabilisation term.

It remains to show that the particular stabilisation given by the second integral in (4.79) is identical to the one associated with the PSPG method in (4.67). Using  $\mathbf{u}^b = N^b \mathbf{u}^b$  and (4.77), and recalling that the superscript  $l$  denotes piecewise linear finite element interpolation, the second integral in (4.79) can be rewritten as

$$\int_{\Omega} 2\mu \nabla \mathbf{w}^l : \nabla^s \mathbf{u}^b + q^l (\nabla \cdot \mathbf{u}^b) dv \quad (4.80)$$

$$= \sum_{e=1}^{n_{el}} \int_{\Omega^e} q^l \nabla N^b dv \cdot \mathbf{u}^b \quad (4.81)$$

$$= \sum_{e=1}^{n_{el}} \left( - \int_{\Omega^e} \nabla q^l N^b dv \right) \cdot \left( - \frac{1}{\mu} (\mathbf{A}^{b,e})^{-1} \int_{\Omega^e} \nabla p^l N^b dv \right) \quad (4.82)$$

$$= \sum_{e=1}^{n_{el}} \int_{\Omega^e} \nabla q^l \cdot \underbrace{\left( \frac{(\int_{\Omega^e} N^b dv)^2}{\mu V^e} (\mathbf{A}^{b,e})^{-1} \right)}_{\boldsymbol{\tau}} \nabla p^l dv \quad (4.83)$$

$$= \sum_{e=1}^{n_{el}} \int_{\Omega^e} \nabla q^l \cdot \boldsymbol{\tau} \nabla p^l dv, \quad (4.84)$$

where the quantity  $V^e$  denotes the volume of element  $e$ . Clearly, (4.84) is identical to the stabilisation term in (4.67). Note, that the diffusive part of the stabilisation term in (4.67) disappears for piecewise linear  $\mathbf{u}^l$ . Interestingly, the stabilisation parameter, which was introduced as a scalar quantity  $\tau$  in Section 4.3.1, has now been obtained as a matrix  $\boldsymbol{\tau}$ . Note, that the expression  $\boldsymbol{\tau}$  given in (4.84) may not be optimal. It merely makes the PSPG method equivalent to the MINI element formulation. However, better choices for the stabilisation parameter may exist. Alternatively, it can be said, that better bubbles than the one given by (4.73) may exist.

Thus, similar to Section 4.2.3, the following conclusions may be drawn:

- The PSPG method stabilises the pressure field in essentially the same way as the MINI element, which is based on the enrichment of the velocity finite element space with bubbles.
- The challenge in the framework of PSPG lies in the choice of the optimal parameter  $\tau$ , whereas the MINI element requires the choice of the optimal bubble function.

Again, similar to Section 4.2.3, the choice of the one technique or the other seems a matter of taste, and the decision may be based on computational convenience. A summary of the stabilisation techniques is given in Table 4.3. In this work, we choose to employ the PSPG method for the stabilisation of the pressure field of the Navier-Stokes equations. The detailed formulation is provided in Section 4.4.

standard Galerkin	$g(\mathbf{w}^h, q^h; \mathbf{u}^h, p^h) = 0$
SUPG	$g(\mathbf{w}^h, q^h; \mathbf{u}^h, p^h) + [\tau(h^e, \mu) \nabla q^h, \mathcal{L}(\mathbf{u}^h, p^h)]_{\Sigma\Omega^e} = 0$
GLS	$g(\mathbf{w}^h, q^h; \mathbf{u}^h, p^h) + [\tau(h^e, \mu) \mathcal{L}(\mathbf{w}^h, q^h), \mathcal{L}(\mathbf{u}^h, p^h)]_{\Sigma\Omega^e} = 0$
bubbles	$g(\mathbf{w}^1, q^1; \mathbf{u}^1, p^1) + a(\mathbf{w}^1, \mathbf{u}^b) + b(\mathbf{u}^b, q^1) = 0$ $\mathbf{u}^b = N^b \mathbf{u}^b, \quad \mathbf{u}^b = \frac{1}{\mu} (\mathbf{A}^{b,e})^{-1} \int_{\Omega_e} p^1 \nabla N^b dv$
$g(\mathbf{w}, q; \mathbf{u}, p) = a(\mathbf{w}, \mathbf{u}) - b(\mathbf{w}, p) + b(\mathbf{u}, q)$ $a(\mathbf{w}, \mathbf{u}) = \int_{\Omega} \mu \nabla \mathbf{w} : \nabla^s \mathbf{u} dv, \quad b(\mathbf{w}, p) = \int_{\Omega} (\nabla \cdot \mathbf{w}) p dv$ $\mathcal{L}(\mathbf{u}, p) = -\nabla p + 2\mu \nabla \cdot \nabla^s \mathbf{u}$ $[\mathbf{w}, \mathbf{u}]_{\Sigma\Omega^e} = \sum_{e=1}^{n_{el}} \int_{\Omega^e} \mathbf{w} \cdot \mathbf{u} dv$	

Table 4.3: Summary of finite element stabilisation techniques for the Stokes flow (4.27) – (4.29); see (4.78) for definition of  $\mathbf{A}^{b,e}$ .

## 4.4 SUPG/PSPG Formulation

In Section 4.2, the SUPG method has been introduced for the finite element modelling of the advection-diffusion equation. It efficiently suppresses the oscillatory behaviour of the solution, which is an inherent, undesirable characteristic of the classical Galerkin method when applied to advection dominated problems. Subsequently, in Section 4.3, the PSPG method has been presented as a stable equal order velocity-pressure finite element technique for the modelling of incompressible flow.

Thus, the SUPG and PSPG strategies are combined in order to obtain a stable finite element method for the modelling of the incompressible steady state Navier-Stokes equations (4.1) – (4.4). The formulation allows the employment of piecewise linear equal order velocity and pressure interpolations. It reads: Find  $\mathbf{u}^h \in \mathcal{U}^h$  and  $p^h \in \mathcal{P}^h$  such that for any  $\mathbf{w}^h \in \mathcal{W}^h$  and  $q^h \in \mathcal{P}^h$

$$\begin{aligned} & \int_{\Omega} \left[ \mathbf{w}^h \cdot \rho \left( (\nabla \mathbf{u}^h) \mathbf{u}^h - \mathbf{f} \right) - \left( \nabla \cdot \mathbf{w}^h \right) p^h \right. \\ & \quad \left. + 2 \mu \nabla \mathbf{w}^h : \nabla^s \mathbf{u}^h + \left( \nabla \cdot \mathbf{u}^h \right) q^h \right] dv - \int_{\Gamma_t} \mathbf{w}^h \cdot \mathbf{t}^h da \quad (4.85) \\ + \sum_{e=1}^{n_{el}} \int_{\Omega^e} & \left[ \tau_u \rho (\nabla \mathbf{w}^h) \mathbf{u}^h + \tau_p \nabla q^h \right] \cdot \left[ \rho \left( (\nabla \mathbf{u}^h) \mathbf{u}^h - \mathbf{f} \right) + \nabla p^h \right] dv = 0, \end{aligned}$$

where the spaces  $\mathcal{U}^h$ ,  $\mathcal{W}^h$  and  $\mathcal{P}^h$  are defined by (4.9) with  $k = 1$

$$\begin{aligned} \mathcal{U}^h &= \left\{ \mathbf{u}^h \in (H^1(\Omega))^{n_{sd}} \mid \mathbf{u}^h|_{\mathbf{x}^h \in \Omega^e} \in (P_1(\Omega^e))^{n_{sd}}, \mathbf{u}^h|_{\mathbf{x}^h \in \Gamma_g} = \mathbf{g} \right\} \\ \mathcal{W}^h &= \left\{ \mathbf{w}^h \in (H^1(\Omega))^{n_{sd}} \mid \mathbf{w}^h|_{\mathbf{x}^h \in \Omega^e} \in (P_1(\Omega^e))^{n_{sd}}, \mathbf{w}^h|_{\mathbf{x}^h \in \Gamma_g} = \mathbf{0} \right\} \quad (4.86) \\ \mathcal{P}^h &= \left\{ p^h \in H^1(\Omega) \mid p^h|_{\mathbf{x}^h \in \Omega^e} \in P_1(\Omega^e) \right\}. \end{aligned}$$

Higher order methods based on  $k > 1$ , which use the formulation (4.85) or slightly modified versions of (4.85), are possible, but not necessarily more efficient, and are not discussed in this work.

The formulation (4.85) consists of the standard Galerkin terms (4.8), to which a stabilisation term has been added. If the incompressibility condition is disregarded and the velocity  $\mathbf{u}^h$  is replaced by a scalar  $u^h$  and a fixed divergence free velocity field  $\mathbf{a}$ , then the formulation coincides with the SUPG method for the advection-diffusion problem (4.33). Also, by omitting the advection terms, the formulation clearly becomes identical to the PSPG method for the Stokes flow (4.67). The diffusive parts of the stabilisation term have disappeared due to the employment of piecewise linear finite element interpolation.

Two stabilisation parameters  $\tau_{\mathbf{u}}$  and  $\tau_p$  are employed, thus enabling independent control of the velocity and pressure stabilisations, SUPG and PSPG, respectively. The combined formulation (4.85) has been suggested by Tezduyar *et al* [123]. It is often referred to as the *SUPG/PSPG* method for the modelling of the incompressible Navier-Stokes equations.

Note that, for  $\tau_{\mathbf{u}} = \tau_p$ , the formulation (4.85) can be obtained from the governing equations by a straightforward GLS stabilisation strategy.

Due to the convection term (and the dependency of the stabilisation parameters on the velocity  $\mathbf{u}^h$ , see Section 4.4.1) the formulation (4.85) is non-linear. Thus, a Newton-Rahpson procedure as described in (3.39) is employed to compute the nodal values of the velocity and the pressure.

During the last decade, various numerical methods have been developed on the basis of the formulation (4.85) for the solution of different, mostly unsteady, incompressible flow problems, see *e. g.* Dettmer and Perić [31,32], Dettmer *et al* [35], Tezduyar *et al* [121,122], Behr and Tezduyar [6], Perić and Slijepčević [88,110], Wall [127] and references therein. Note that some researchers include a stabilisation term for the continuity equation. To the knowledge of the author, the beneficial effect of such an extension of (4.85) has, however, not yet been proven. In the course of this work, it has been experimented with several modifications of the formulation, none of which was superior to (4.85).

#### 4.4.1 The Stabilisation Parameter

Both stabilisation parameters  $\tau_{\mathbf{u}}$  and  $\tau_p$  are defined as

$$\tau = \frac{h^e}{2 \|\mathbf{u}^e\| \rho} \xi, \quad \xi = \frac{\beta_1}{\sqrt{1 + \left(\frac{\beta_1}{\beta_2 Re^e}\right)^2}}, \quad Re^e = \frac{\|\mathbf{u}^e\| h^e \rho}{2 \mu}, \quad (4.87)$$

but they have different scaling parameters  $\beta_1$  and  $\beta_2$ , which may be set independently. The characteristic element size, the fluid velocity in the element centroid and the element Reynolds number are represented by  $h^e$ ,  $\mathbf{u}^e$ , and  $Re^e$ , respectively. The parameters  $\beta_1$  and  $\beta_2$  control the limit behaviour of  $\xi$ , *i. e.*

$$\lim_{Re^e \rightarrow \infty} \xi = \beta_1 \quad (4.88)$$

$$\lim_{Re^e \rightarrow 0} \xi = \beta_2 Re^e. \quad (4.89)$$

In two dimensions the element size  $h^e$  is defined as the diameter of the circle, which corresponds to the area  $A^e$  of the triangular finite element

$$h^e = \sqrt{\frac{4 A^e}{\pi}} . \quad (4.90)$$

This choice of the stabilisation parameters is motivated as follows:

- In the diffusive limit,  $\tau_{\mathbf{u}}$  and  $\tau_p$  recover the expressions derived from the stabilisation with bubbles. It follows from (4.87)<sub>1</sub> and (4.89) that

$$\lim_{Re^e \rightarrow 0} \tau = \frac{\beta_2}{4} \frac{(h^e)^2}{\mu} . \quad (4.91)$$

In Section 4.2.3, equation (4.59), it has been shown that the stabilisation of advection dominated problems with bubbles coincides with the SUPG method if

$$\tau = \tau_{\text{bubble}} = \frac{\left( \int_{\Omega^e} N^b \, dv \right)^2}{\mu \|\nabla N^b\|_{0,\Omega^e}^2 V^e} . \quad (4.92)$$

For a two dimensional linear triangular finite element one obtains

$$\tau_{\text{bubble}} = \frac{(A^e)^2}{5 (s_1^2 + s_2^2 + s_3^2) \mu} , \quad (4.93)$$

where  $s_1$ ,  $s_2$  and  $s_3$  denote the lengths of the edges of element  $e$  and the bubble function  $N^b$  has been chosen as in (4.73). Using (4.90), it follows for an equilateral triangle

$$\tau_{\text{bubble}} = \frac{\pi}{80 \sqrt{3}} \frac{(h^e)^2}{\mu} , \quad (4.94)$$

which coincides with (4.91), if  $\beta_2 = \pi/(20 \sqrt{3}) \approx 0.091$ .

For the modelling of incompressible flow with linear equal order elements, it has been derived in Section 4.3.3, equation (4.84), that the PSPG method is identical to the stabilisation with bubbles, if a matrix  $\boldsymbol{\tau}_{\text{bubble}}$  is employed with

$$\boldsymbol{\tau}_{\text{bubble}} = \frac{\left( \int_{\Omega^e} N^b \, dv \right)^2}{\mu V^e} \left( \mathbf{A}^{b,e} \right)^{-1} , \quad (4.95)$$

where  $\mathbf{A}^{b,e}$  is given by (4.78). If the orientation of the element in the global coordinate system is neglected,  $\boldsymbol{\tau}_{\text{bubble}}$  of a two dimensional equilateral triangular finite element is obtained as the identity matrix multiplied with a scalar parameter  $\tau_{\text{bubble}}$  similar to (4.94).

- Johnson and Saranen [75] and Hughes *et al* [67] have proven that optimal convergence of the method is achieved if, in the diffusive and advective limits, the order of  $\tau_{\mathbf{u}}$  and  $\tau_p$  is, respectively,  $O((h^e)^2)$  and  $O(h^e)$ . Using (4.88) and (4.89), it is easily shown that (4.87) possesses the correct limit behaviour:

$$\begin{aligned}\tau &= \frac{\beta_2}{4} \frac{(h^e)^2}{\mu} = O((h^e)^2), & \text{if } Re^e \text{ small} \\ \tau &= \frac{\beta_1}{2} \frac{h^e}{\|\mathbf{u}^e\| \rho} = O(h^e), & \text{if } Re^e \text{ large.}\end{aligned}\tag{4.96}$$

- The choice  $\beta_1 = 1$  and  $\beta_2 = \frac{1}{3}$  gives

$$\xi = \frac{1}{\sqrt{1 + \left(\frac{3}{Re^e}\right)^2}} = \coth(Re^e) - \frac{1}{Re^e} + O((Re^e)^3). \tag{4.97}$$

which is an accurate approximation of the coefficient  $\xi_{\text{ex}}$ , which has been shown in Section 4.2.3, equation (4.62), to render nodally exact solutions of the one dimensional advection-diffusion equation.

Different formulae for the evaluation of the stabilisation parameters have been introduced by *e. g.* Tezduyar and Osawa [124], Oñate [85]. More information may be found in the references given in Wall [127]. In Tezduyar [119] and references therein, the characteristic local length scale  $h^e$  is related to the element diameter in the direction of the flow  $\mathbf{u}^h$  through the element. This strategy is said to improve the accuracy of the method on distorted meshes. Throughout this work, the expressions given in (4.87) are employed. Also throughout this work, in all numerical examples, the following values are employed for the parameters  $\beta_1$  and  $\beta_2$  unless otherwise stated

$$\begin{aligned}\tau_{\mathbf{u}} : \beta_1 &= 1, & \beta_2 &= \frac{1}{3} \\ \tau_p : \beta_1 &= 30, & \beta_2 &= \frac{1}{10}.\end{aligned}\tag{4.98}$$

The relatively large value  $\beta_1 = 30$  for  $\tau_p$  has in a few cases been thought to be beneficial for very coarse meshes. It has then been kept without further consideration. Generally, unless very small or large values are chosen, the influence of the parameters  $\beta_1$  and  $\beta_2$  is found to be small.

*REMARK 4.1: Stabilisation of unsteady problems.* In anticipation of Chapter 5, where the extension of the formulation (4.85) to unsteady problems is discussed at length, it should be noted that many publications suggest

expressions for the stabilisation parameters  $\tau_{\mathbf{u}}$  and  $\tau_p$ , which depend on the time increment  $\Delta t$ , such that  $\tau_{\mathbf{u}}$  and  $\tau_p$  vanish as  $\Delta t \rightarrow 0$ . Thus, the stabilisation is basically “switched off”, when the time discretisation is refined. Such a mechanism is clearly not desirable, since the instabilities addressed in this chapter are associated with the modelling of space. In the opinion of the author the independence of the parameters  $\tau_{\mathbf{u}}$  and  $\tau_p$  from the time increment  $\Delta t$  is essential for the method to be robust and to allow independent refinement of the discretisations of space and time (see also Section 5.2.3).

#### 4.4.2 Example: Lid Driven Cavity Flow

In order to demonstrate the accuracy and robustness of the SUPG/PSPG formulation (4.85), the lid driven cavity flow is simulated. The width and the height of the cavity are  $b = h = 1$ , the velocity at the lid and the density of the fluid are set to  $u_{\text{lid}} = 1$  and  $\rho = 1$ , respectively. Three different fluid viscosities are considered,  $\mu = 0.01$ ,  $\mu = 0.001$  and  $\mu = 0.0001$ , resulting in the global Reynolds numbers  $Re = b u_{\text{lid}} \rho / \mu = 100$ ,  $Re = 1000$  and  $Re = 10,000$ , respectively. Four different meshes with 1192 (4248) {8983} [17,832] elements and 665 (2241) {4659} [9153] nodes are used. The mesh with 1192 finite elements and the boundary conditions are displayed in Figure 4.9. Note that at the corner nodes A and B the velocity is set to zero (“non-leaky” cavity). For both stabilisation parameters,  $\beta_1$  and  $\beta_2$  are set to  $\beta_1 = 1$  and  $\beta_2 = 1/3$ , such that  $\tau_{\mathbf{u}} = \tau_p$ .

Some characteristic results are displayed in Figures 4.10 – 4.15. The diagrams in Figures 4.10 – 4.12 also show the solution obtained by Ghia *et al* [50] by means of a finite difference method on very dense grids. The agreement of the finite element results with the solution by Ghia *et al* is excellent. For  $Re \leq 1000$  the solutions of the different meshes almost coincide, which proves the accuracy of the method (4.85). For  $Re = 10,000$ , the local Reynolds numbers  $Re^e$  become very large, and a dense mesh is required to obtain an accurate solution. The streamlines and pressure isolines displayed in Figures 4.13 – 4.15 are free from spurious oscillations.

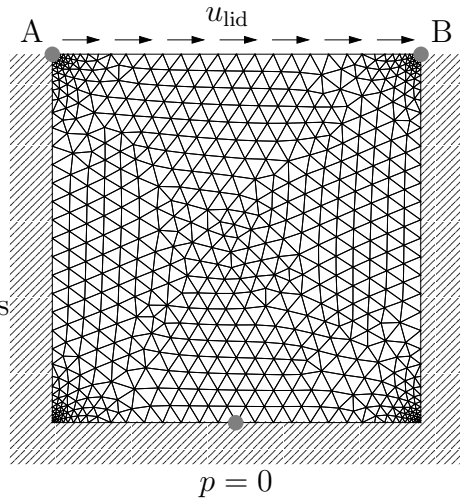


Figure 4.9: Driven cavity flow, mesh with 1192 elements, problem set-up.

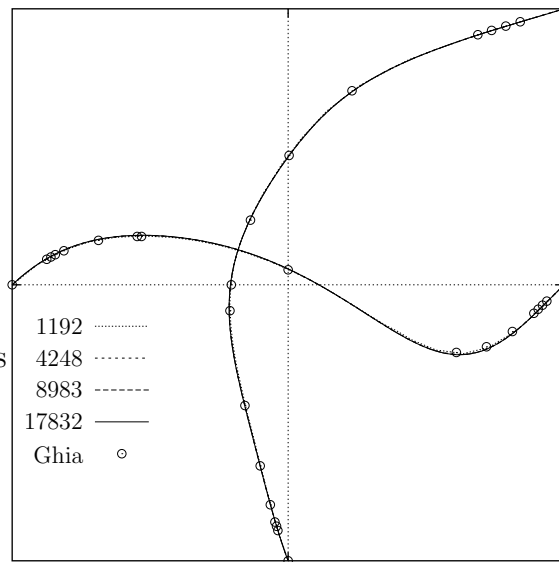


Figure 4.10: Driven cavity flow,  $Re = 100$ ,  $x$ - and  $y$ -velocity profiles along vertical and horizontal lines through the geometric centre of the cavity; different meshes and results by Ghia *et al* [50].

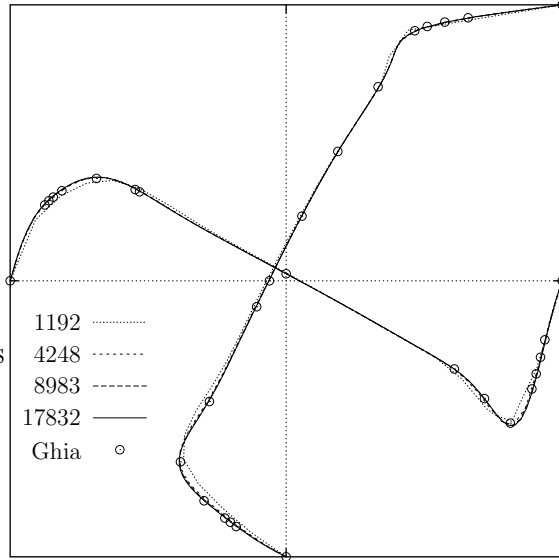


Figure 4.11: Driven cavity flow,  $Re = 1000$ ,  $x$ - and  $y$ -velocity profiles along vertical and horizontal lines through the geometric centre of the cavity; different meshes and results by Ghia *et al* [50].

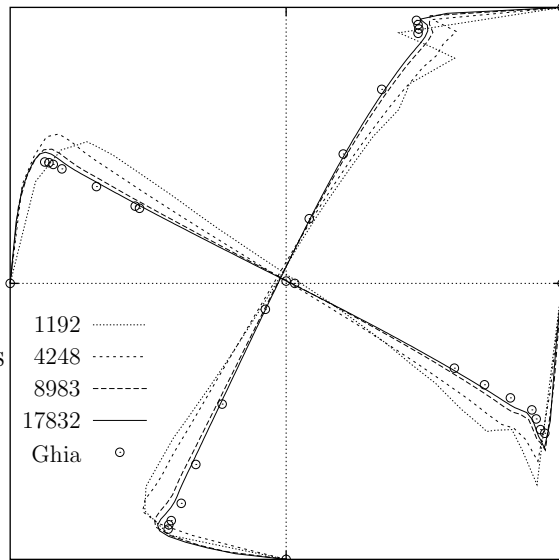


Figure 4.12: Driven cavity flow,  $Re = 10,000$ ,  $x$ - and  $y$ -velocity profiles along vertical and horizontal lines through the geometric centre of the cavity; different meshes and results by Ghia *et al* [50].

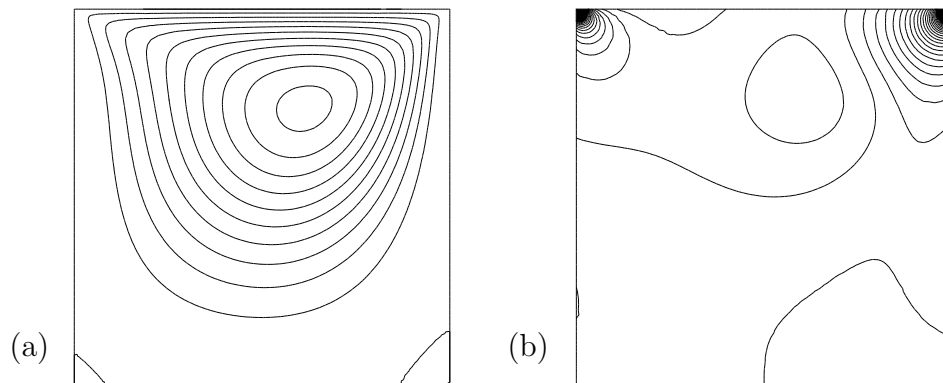


Figure 4.13: Driven cavity flow,  $Re = 100$ , 8983 elements; streamlines (a) and pressure isolines (b).

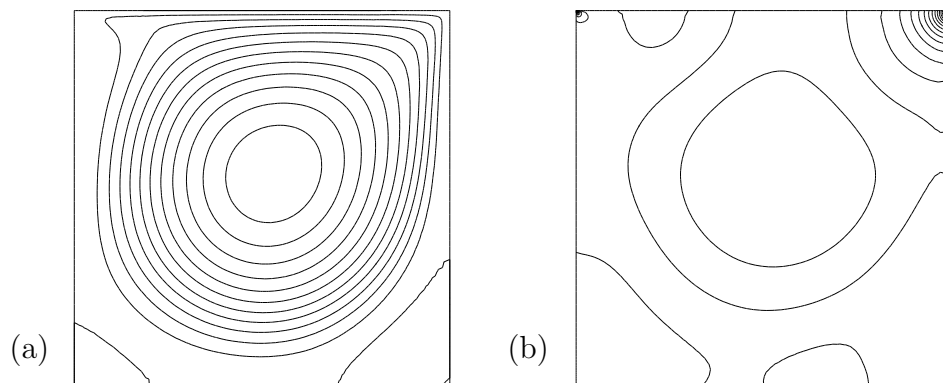


Figure 4.14: Driven cavity flow,  $Re = 1000$ , 8983 elements; streamlines (a) and pressure isolines (b).

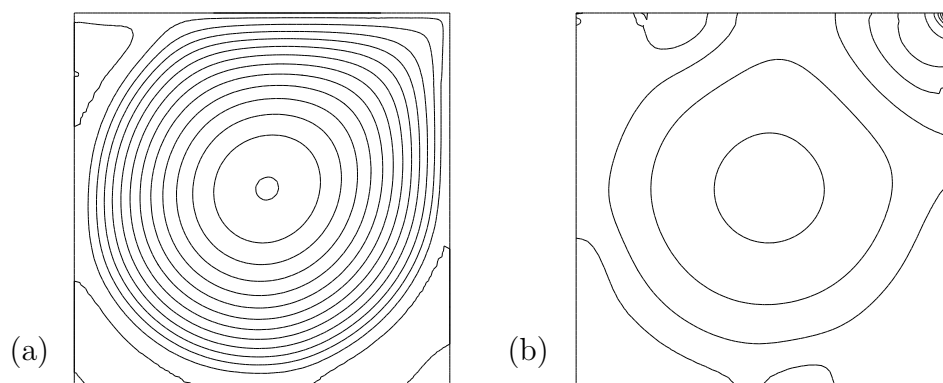


Figure 4.15: Driven cavity flow,  $Re = 10,000$ , 8983 elements; streamlines (a) and pressure isolines (b).

# Chapter 5

## Time Integration Schemes for Unsteady Fluid Flow

The extension of the stabilised finite element formulation for steady incompressible Newtonian fluid flow, discussed in Chapter 4, equation (4.85), to unsteady flows requires the application of an appropriate time integration scheme. First, a choice needs to be made between the *discrete* time integration schemes and the so-called *time finite element methods*. Both strategies then offer a variety of schemes with substantially varying properties. Therefore, it is the objective of this chapter to assess the suitability of a selection of different numerical procedures for the time integration of the stabilised finite element formulation of the unsteady incompressible Navier-Stokes equations. An important aspect is the coupling between spatial and temporal discretisation.

The algorithms which are obtained by combining the discrete time integration schemes and the spatial finite element method are referred to as *semi-discrete* solution procedures, whereas the employment of finite element interpolations in space and time domain results in the so-called *space-time finite element methods*.

The discrete time integration schemes considered are the well-known *generalised midpoint rule* and the more recent *generalised- $\alpha$  method*, which has been shown, in the context of structural dynamics problems, to possess a good accuracy combined with user controlled high frequency damping (see Chung and Hulbert [22] and Jansen *et al* [72]). The finite element time integration schemes discussed in this work are the *constant* and *linear discontinuous* in time formulations as well as the *linear continuous* in time finite element method (see *e. g.* Johnson [73], Eriksson *et al* [41], Thomée [126], or Zienkiewicz and Taylor [132], Dettmer and Perić [31]). The latter method is usually considered to offer no substantial advantages in comparison to other

more standard schemes. However, it has been included in this work in order to illustrate some basic features of time finite element methods. Note that only *implicit single step* integration procedures are considered.

In order to analyse the main features of the different integration schemes, regarding their accuracy, stability properties and long term behaviour, they are applied to two model problems before the incompressible Navier-Stokes equations are considered. Thus, this chapter consists of three main sections:

- *scalar model problem.* The purpose of the simple model problem is to briefly introduce the different time integration schemes considered and to establish their basic properties.
- *one dimensional unsteady advection-diffusion equation.* This is a well-known model problem for fluid dynamics in the one dimensional space and time domain. The stabilised finite element formulation is combined with the time integration schemes. The resulting fully discretised formulations of the problem are analysed in detail by employing a Fourier analysis. For the discontinuous in time space-time finite element method a similar analysis has been performed by Shakib and Hughes [108]. However, some additional insights are provided in this work.
- *incompressible Navier-Stokes equations.* These equations are so complex that the properties of the discretised formulations can in general not be established by an analytical procedure. Thus, Section 5.3 is restricted to the description of the fully discretised formulation and aspects of the solution algorithm. Two classical numerical examples are discussed in detail: the unsteady flow around a cylinder and the flow across a backward facing step. An attempt is made to relate the results to the conclusions drawn from the Fourier analysis of the advection-diffusion model problem.

For the sake of brevity, the following notation is employed throughout this chapter:

- BE – backward Euler scheme,
- TR – trapezoidal rule,
- GM – generalised midpoint rule,
- AM – generalised- $\alpha$  method,
- LC – linear continuous time finite element method,
- CD – constant discontinuous time finite element method,
- MC – modified continuous time finite element method,
- LD – linear discontinuous time finite element method.

## 5.1 Scalar Model Problem

*Governing equation.* The problem considered is defined by a first order ordinary differential equation and an initial condition, given respectively as

$$\dot{u}(t) - \lambda u(t) = 0 \quad \forall t \in I \quad (5.1)$$

$$u(0) = u_0, \quad (5.2)$$

where  $u(t)$  is the scalar valued solution variable and  $\lambda$  is a specified parameter. The time domain of interest is denoted as  $I = [0, T_{\text{end}}]$ . The exact solution of this problem reads

$$u(t) = u_0 e^{\lambda t}. \quad (5.3)$$

The parameter  $\lambda$  is assumed to be complex and given by

$$\lambda = -\xi + i\omega. \quad (5.4)$$

Thus, the solution  $u(t)$  is an exponentially damped oscillation with the frequency  $2\pi\omega$  and the damping factor  $\xi$ . The choice of this model problem is motivated by the fact that the system matrix of the discretised Navier-Stokes equations is often characterised by complex eigenvalues.

*Numerical solution.* Let  $0 = t_0 < t_1 < \dots < t_N = T_{\text{end}}$  be a partition of  $I$  and let  $I_n = [t_{n-1}, t_n]$  be the  $n$ -th time interval. In what follows, equation (5.1) will be discretised by employing different implicit numerical time integration schemes. The following analysis will be performed in order to assess the performance of the schemes:

By employing the standard arguments (see *e. g.* Hughes [64], Gustafsson [55]), for each method the amplification factor  $\zeta^h$  will be evaluated, which is defined as

$$\zeta^h = \frac{\mathbf{u}_{n+1}}{\mathbf{u}_n}, \quad (5.5)$$

where  $\mathbf{u}_n$  and  $\mathbf{u}_{n+1}$  are the approximations of  $u(t_n)$  and  $u(t_{n+1})$ , at the time instants  $t_n$  and  $t_{n+1}$ , respectively. The spectral radius  $\rho^h$  is then defined as

$$\rho^h = |\zeta^h| = \sqrt{(\text{Re}(\zeta^h))^2 + (\text{Im}(\zeta^h))^2}. \quad (5.6)$$

By employing the standard argument  $\rho^h \leq 1$  for any  $\Delta t = t_{n+1} - t_n \geq 0$ , the unconditional stability of the methods will be proven. From (5.3) it follows that the exact amplification factor  $\zeta$  is

$$\zeta = e^{\lambda \Delta t}. \quad (5.7)$$

It shall be shown that the complex parameter  $\lambda$  renders a complex numerical amplification factor  $\zeta^h$ . Thus, the approximation of the solution is also an exponentially damped oscillation with a constant frequency. The numerical counterparts  $\lambda^h$ ,  $\zeta^h$ ,  $\xi^h$  and  $\omega^h$  of  $\lambda$ ,  $\zeta$ ,  $\xi$  and  $\omega$ , respectively, are introduced as

$$\zeta^h = e^{\lambda^h \Delta t}, \quad \lambda^h = -\xi^h + i\omega^h. \quad (5.8)$$

It follows that

$$\xi^h = -\frac{1}{\Delta t} \ln(|\zeta^h|) \quad \text{and} \quad \omega^h = \frac{1}{\Delta t} \arg(\zeta^h). \quad (5.9)$$

Using  $\zeta^h$  given by (5.5) in (5.9) yields expressions for  $\xi^h$  and  $\omega^h$  in terms of  $\xi$ ,  $\omega$  and  $\Delta t$ . These can be expanded as power series of  $\Delta t$  and thus enable an assessment of the accuracy of the method. The comparisons of  $\xi^h$  with  $\xi$  and  $\omega^h$  with  $\omega$  indicate the amount of *numerical damping* and *numerical dispersion*, respectively.

## 5.1.1 Discrete Time Integration Schemes

### 5.1.1.1 Generalised Midpoint Rule (GM)

Within the generalised midpoint rule the solution  $y$  and the time derivative of  $y$  at the time instant  $t_{n+\gamma}$  are approximated as

$$\mathbf{u}_{n+\gamma} = \gamma \mathbf{u}_{n+1} + (1-\gamma) \mathbf{u}_n, \quad \dot{\mathbf{u}}_{n+\gamma} = \frac{\mathbf{u}_{n+1} - \mathbf{u}_n}{\Delta t}, \quad (5.10)$$

where  $0 \leq \gamma \leq 1$ . Evaluating equation (5.1) at  $t_{n+\gamma}$  gives

$$\mathbf{u}_{n+1} - \mathbf{u}_n - \lambda \Delta t (\gamma \mathbf{u}_{n+1} + (1-\gamma) \mathbf{u}_n) = \mathbf{0}.$$

By using (5.5), (5.6) and (5.4) the amplification factor and the spectral radius are obtained as

$$\zeta^h = \frac{1 + (1-\gamma)\lambda\Delta t}{1 - \gamma\lambda\Delta t}, \quad (5.11)$$

$$\rho^h = \sqrt{\frac{(1 - (1-\gamma)\xi\Delta t)^2 + ((1-\gamma)\omega\Delta t)^2}{(1 + \gamma\xi\Delta t)^2 + (\gamma\omega\Delta t)^2}}. \quad (5.12)$$

For unconditional stability the spectral radius must satisfy  $\rho^h \leq 1$  for any  $\Delta t \geq 0$ . This requirement yields

$$\gamma \geq \frac{1}{2}. \quad (5.13)$$

The limit of  $\rho^h$  for  $\Delta t \rightarrow \infty$  is obtained as

$$\rho_\infty^h = \lim_{\Delta t \rightarrow \infty} \rho^h = \frac{1 - \gamma}{\gamma}. \quad (5.14)$$

By using (5.11) in (5.9),  $\xi^h$  and  $\omega^h$  can be written as

$$\begin{aligned} \xi^h &= \xi + \frac{2\gamma - 1}{2}(\omega^2 - \xi^2) \Delta t \\ &\quad + \frac{1 - 3\gamma + 3\gamma^2}{3} \xi (\xi^2 - 3\omega^2) \Delta t^2 + O(\Delta t^3), \end{aligned} \quad (5.15)$$

$$\begin{aligned} \omega^h &= \omega - (2\gamma - 1) \xi \omega \Delta t \\ &\quad + \frac{1 - 3\gamma + 3\gamma^2}{3} \omega (3\xi^2 - \omega^2) \Delta t^2 + O(\Delta t^3). \end{aligned} \quad (5.16)$$

For  $\gamma = 1/2$  the integration scheme becomes second order accurate. Otherwise the scheme is first order accurate. It follows from (5.14) that the parameter  $\gamma$  can be expressed in terms of the limit of the spectral radius as  $\gamma = 1/(1 + \rho_\infty^h)$ . Using  $0 \leq \rho_\infty^h \leq 1$  as the free parameter will prove convenient in what follows.

By choosing  $\rho_\infty^h = 1$  one obtains the *trapezoidal* rule or *Crank-Nicolson* method, whereas  $\rho_\infty^h = 0$  yields the *backward Euler* scheme. Note that, for the situation  $\xi = 0$ , the frequency  $\omega^h$  is second order accurate, independently of  $\gamma$ . An important characteristic of the trapezoidal rule is that for  $\xi = 0$  the numerical damping disappears.

### 5.1.1.2 Generalised- $\alpha$ Method (AM)

The generalised- $\alpha$  method for the problem (5.1) reads

$$\dot{\mathbf{u}}_{n+\alpha_m} - \lambda \mathbf{u}_{n+\alpha_f} = 0, \quad (5.17)$$

with

$$\mathbf{u}_{n+1} = \mathbf{u}_n + \Delta t \left( (1 - \gamma) \dot{\mathbf{u}}_n + \gamma \dot{\mathbf{u}}_{n+1} \right), \quad (5.18)$$

$$\mathbf{u}_{n+\alpha_f} = (1 - \alpha_f) \mathbf{u}_n + \alpha_f \mathbf{u}_{n+1}, \quad (5.19)$$

$$\dot{\mathbf{u}}_{n+\alpha_m} = (1 - \alpha_m) \dot{\mathbf{u}}_n + \alpha_m \dot{\mathbf{u}}_{n+1}. \quad (5.20)$$

In the following it is briefly shown that the parameters  $\alpha_m$ ,  $\alpha_f$  and  $\gamma$  reduce to one free integration parameter if the requirements for the second order accuracy and user controlled high frequency damping are satisfied. Details are given in Jansen *et al* [72].

The system of equations (5.17) – (5.20) is rewritten in matrix form as

$$\begin{Bmatrix} \mathbf{u}_{n+1} \\ \Delta t \dot{\mathbf{u}}_{n+1} \end{Bmatrix} = \frac{1}{d} \begin{bmatrix} \alpha_m - (\alpha_f - 1)\gamma\lambda\Delta t & \alpha_m - \gamma \\ \lambda \Delta t & \alpha_m - 1 + \alpha_f\lambda\Delta t(1 - \gamma) \end{bmatrix} \begin{Bmatrix} \mathbf{u}_n \\ \Delta t \dot{\mathbf{u}}_n \end{Bmatrix},$$

or briefly

$$\mathbf{u}_{n+1} = \mathbf{A} \mathbf{u}_n, \quad (5.21)$$

where  $d = \alpha_m - \alpha_f \gamma \lambda \Delta t$ . By using (5.21) and  $\mathbf{u}_n = \mathbf{A} \mathbf{u}_{n-1}$  the rate terms  $\dot{\mathbf{u}}_{n-1}$ ,  $\dot{\mathbf{u}}_n$  and  $\dot{\mathbf{u}}_{n+1}$  can be eliminated and it follows that

$$\mathbf{u}_{n+1} - \text{tr}(\mathbf{A}) \mathbf{u}_n + \det(\mathbf{A}) \mathbf{u}_{n-1} = 0. \quad (5.22)$$

According to (5.5),  $\mathbf{u}_n$  and  $\mathbf{u}_{n+1}$  can be related to  $\mathbf{u}_{n-1}$  with the amplification factor  $\zeta^h$ . Thus, equation (5.22) may be written as

$$(\zeta^h)^2 - \text{tr}(\mathbf{A}) \zeta^h + \det(\mathbf{A}) = 0. \quad (5.23)$$

Using the exact amplification factor  $\zeta$  from (5.7) instead of  $\zeta^h$  renders an expression the order of which corresponds to the order of accuracy of  $\zeta^h$  with respect to  $\Delta t$ . One obtains

$$\zeta^2 - \text{tr}(\mathbf{A}) \zeta + \det(\mathbf{A}) = \frac{1 - 2\alpha_f + 2\alpha_m - 2\gamma}{2\alpha_m} (\lambda \Delta t)^2 + O(\Delta t^3). \quad (5.24)$$

Thus, the condition for second order accuracy reads

$$\gamma = \frac{1}{2} + \alpha_m - \alpha_f. \quad (5.25)$$

For the method to be unconditionally stable it is required that the moduli of the eigenvalues  $\zeta_{1,2}^h$  of the matrix  $\mathbf{A}$  are smaller than or equal to one. Since the expressions for  $\zeta_{1,2}^h$  are rather complicated, a limit analysis is performed and it follows that

$$\begin{aligned} \lim_{\Delta t \rightarrow 0} \{\zeta_1^h, \zeta_2^h\} &= \left\{1, 1 - \frac{1}{\alpha_m}\right\} \Rightarrow \alpha_m \geq \frac{1}{2} \\ \lim_{\Delta t \rightarrow \infty} \{\zeta_1^h, \zeta_2^h\} &= \left\{1 - \frac{1}{\alpha_f}, \frac{2(\alpha_m - \alpha_f) - 1}{2(\alpha_m - \alpha_f) + 1}\right\} \Rightarrow \alpha_m \geq \alpha_f \geq \frac{1}{2}. \end{aligned} \quad (5.26)$$

In order to control high frequency damping the parameters  $\alpha_m$  and  $\alpha_f$  are chosen such that the moduli of both eigenvalues tend to the same prescribed limit as  $\Delta t \rightarrow \infty$ . Since the spectral radius is defined as

$$\rho^h = \max(|\zeta_1^h|, |\zeta_2^h|), \quad (5.27)$$

this limit coincides with  $\rho_\infty^h = \lim_{\Delta t \rightarrow \infty} \rho^h$ . It can then be derived from (5.26)<sub>2</sub> that  $|\zeta_1^h|$  and  $|\zeta_2^h|$  tend to  $\rho_\infty^h$  as  $\Delta t \rightarrow 0$ , if  $\alpha_m$  and  $\alpha_f$  are chosen as

$$\alpha_m = \frac{1}{2} \frac{3 - \rho_\infty^h}{1 + \rho_\infty^h}, \quad \alpha_f = \frac{1}{1 + \rho_\infty^h}, \quad (5.28)$$

where  $0 \leq \rho_\infty^h \leq 1$ .

Next, the eigenvalues  $\zeta_{1,2}^h$  can be written in terms of  $\xi$ ,  $\omega$ ,  $\Delta t$  and the only remaining integration parameter  $\rho_\infty^h$ . Since the resulting expressions are rather long they are not given here.

Using equation (5.9), the series expansions of  $\xi^h$  and  $\omega^h$  are obtained as

$$\xi^h = \xi + \frac{1 - \rho_\infty^h + \rho_\infty^{h^2}}{3(1 + \rho_\infty^h)^2} \xi (\xi^2 - 3\omega^2) \Delta t^2 + O(\Delta t^3), \quad (5.29)$$

$$\omega^h = \omega + \frac{1 - \rho_\infty^h + \rho_\infty^{h^2}}{3(1 + \rho_\infty^h)^2} \omega (3\xi^2 - \omega^2) \Delta t^2 + O(\Delta t^3). \quad (5.30)$$

Clearly the method is second order accurate in terms of the damping and frequency errors. For pure advection with  $\xi = 0$  the numerical damping reduces to the third order terms in  $\Delta t$ . Finally it should be noted that, similarly to the generalised midpoint rule, the generalised- $\alpha$  method becomes identical to the trapezoidal rule, if  $\rho_\infty^h = 1$ .

## 5.1.2 Time Finite Element Methods

### 5.1.2.1 Linear Continuous Finite Elements (LC)

Let  $\mathcal{W}^h$  denote the appropriate space of trial and test functions with standard properties. Consider continuous piecewise linear finite element interpolation in time. On the  $n$ -th time interval the shape functions may be written as

$$N_n = \hat{N}_n(t) = \frac{\mathbf{t}_{n+1} - t}{\Delta t}, \quad N_{n+1} = \hat{N}_{n+1}(t) = \frac{t - \mathbf{t}_n}{\Delta t}. \quad (5.31)$$

By introducing

$$u^h(t) = \hat{N}_n(t) \mathbf{u}_n + \hat{N}_{n+1}(t) \mathbf{u}_{n+1} \quad \text{for } \mathbf{t}_n < t \leq \mathbf{t}_{n+1} \quad (5.32)$$

as a trial function and

$$w^h(t) = \hat{N}_{n+1}(t) \mathbf{w}_{n+1} \quad \text{for } \mathbf{t}_n < t \leq \mathbf{t}_{n+1} \quad (5.33)$$

as a test function, the weak form of the model problem can be stated as follows: Find  $u^h \in \mathcal{W}^h$  such that  $\forall w^h \in \mathcal{W}^h$

$$\begin{aligned} 0 &= \int_{\mathbf{t}_n}^{\mathbf{t}_{n+1}} (w^h \dot{u}^h - \lambda w^h u^h) dt \\ &= \mathbf{w}_{n+1} \left( \left[ \int_{\mathbf{t}_n}^{\mathbf{t}_{n+1}} (N_{n+1} \dot{N}_n - \lambda N_{n+1} N_n) dt \right] \mathbf{u}_n \right. \\ &\quad \left. + \left[ \int_{\mathbf{t}_n}^{\mathbf{t}_{n+1}} (N_{n+1} \dot{N}_{n+1} - \lambda N_{n+1}^2) dt \right] \mathbf{u}_{n+1} \right). \end{aligned} \quad (5.34)$$

By evaluating the integrals and recalling the fact that  $\mathbf{w}_{n+1}$  is arbitrary, the amplification factor  $\zeta^h$  is obtained as

$$\zeta^h = \frac{3 + \lambda \Delta t}{3 - 2 \lambda \Delta t}. \quad (5.35)$$

The spectral radius is obtained from (5.6) and (5.4) as

$$\rho^h = \sqrt{\frac{(\xi \Delta t - 3)^2 + (\omega \Delta t)^2}{(2 \xi \Delta t + 3)^2 + (2 \omega \Delta t)^2}}. \quad (5.36)$$

Since  $\rho^h \leq 1$ , the scheme is unconditionally stable. Using (5.35) in (5.9),  $\xi^h$  and  $\omega^h$  are obtained as

$$\xi^h = \xi + \frac{\omega^2 - \xi^2}{6} \Delta t + \frac{\xi(\xi^2 - 3\omega^2)}{9} \Delta t^2 + O(\Delta t^3), \quad (5.37)$$

$$\omega^h = \omega - \frac{\xi \omega}{3} \Delta t + \frac{\omega(3\xi^2 - \omega^2)}{9} \Delta t^2 + O(\Delta t^3). \quad (5.38)$$

Thus, the continuous linear time finite element method is first order accurate in terms of damping and frequency errors. By comparison with (5.11) it follows that the method becomes identical to the generalised midpoint rule discussed in Section 5.1.1.1 for the choice of  $\rho_\infty^h = 1/2$  or  $\gamma = 2/3$ . Note that the first and second order terms in  $\Delta t$  are three times smaller for the linear continuous finite element method than for the backward Euler time integration scheme.

### 5.1.2.2 Constant Discontinuous Finite Elements (CD)

In discontinuous time finite element schemes the approximation of the solution  $u^h$  is allowed to be discontinuous at the inter element boundaries  $\mathbf{t}_n$

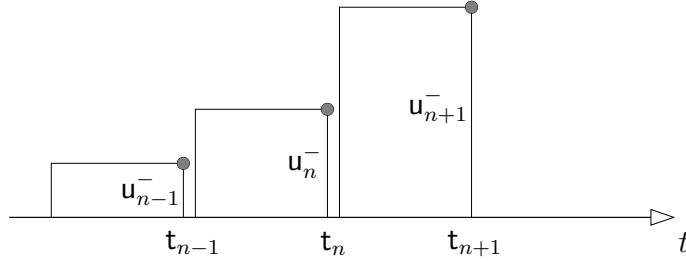


Figure 5.1: Constant discontinuous finite elements in time.

and  $t_{n+1}$ . The variational form for these methods is obtained from equation (5.34) by the addition of the so-called jump term. For the model problem considered here, the weak form can then be written: Find  $u^h \in \mathcal{W}^h$  such that  $\forall w^h \in \mathcal{W}^h$

$$0 = \int_{t_n}^{t_{n+1}} (w^h \dot{u}^h - \lambda w^h u^h) dt + \beta \mathbf{w}_n^+ (u_n^+ - u_n^-), \quad (5.39)$$

where  $u_n^+$  and  $u_n^-$  are defined by

$$u_n^- = \lim_{\Delta t \rightarrow 0} u^h(t_n - \Delta t), \quad u_n^+ = \lim_{\Delta t \rightarrow 0} u^h(t_n + \Delta t), \quad (5.40)$$

and similarly for  $\mathbf{w}_n^+$ . The dimensionless parameter  $\beta > 0$  controls how strongly continuity of  $u^h$  is enforced at the element boundary  $t_n$ .

In this section a formulation based on the constant shape functions is considered (see Figure 5.1), which gives

$$u^h(t) = u_{n+1}^- = u_n^+ \quad \text{for } t_n < t < t_{n+1}, \quad (5.41)$$

$$w^h(t) = \mathbf{w}_{n+1}^- = \mathbf{w}_n^+ \quad \text{for } t_n < t < t_{n+1}. \quad (5.42)$$

Thus equation (5.39) becomes

$$0 = -\lambda \Delta t u_{n+1}^- + \beta (u_{n+1}^- - u_n^-), \quad (5.43)$$

where the fact that  $\mathbf{w}_{n+1}^-$  is arbitrary has been used. Note that the time derivative  $\dot{u}^h$  in (5.39) vanishes. The amplification factor  $\zeta^h$  and the spectral radius  $\rho^h$  are obtained as

$$\zeta^h = \frac{\beta}{\beta - \lambda \Delta t}, \quad (5.44)$$

$$\rho^h = \frac{\beta}{\sqrt{(\beta + \xi \Delta t)^2 + (\omega \Delta t)^2}}. \quad (5.45)$$

Clearly  $\rho^h \leq 1$  holds for any  $\Delta t \geq 0$  and the method is unconditionally stable.

By using (5.44) in (5.9),  $\xi^h$  and  $\omega^h$  are obtained as

$$\xi^h = \frac{\xi}{\beta} + \frac{\omega^2 - \xi^2}{2\beta^2} \Delta t + \frac{\xi(\xi^2 - 3\omega^2)}{3\beta^3} \Delta t^2 + O(\Delta t^3), \quad (5.46)$$

$$\omega^h = \frac{\omega}{\beta} - \frac{\xi\omega}{\beta^2} \Delta t + \frac{\omega(3\xi^2 - \omega^2)}{3\beta^3} \Delta t^2 + O(\Delta t^3). \quad (5.47)$$

Thus, only for  $\beta = 1$  the method is first order accurate. It then becomes identical with the backward Euler scheme. It is observed that the method is not consistent for any other choice of  $\beta$ .

### 5.1.2.3 Modified Continuous Finite Elements (MC)

In this formulation the trial function  $u^h$  and the test function  $w^h$  are chosen to be defined by (5.32) and (5.42), respectively. Thus,  $u^h$  is linear continuous, whereas  $w^h$  is constant discontinuous in time. The resulting approximation algorithm is a Petrov-Galerkin method. By using (5.32) and (5.42) in the weak form (5.34) the amplification factor and the spectral radius are obtained as

$$\zeta^h = \frac{2 + \lambda \Delta t}{2 - \lambda \Delta t}, \quad (5.48)$$

$$\rho^h = \sqrt{\frac{(2 - \xi \Delta t)^2 + (\omega \Delta t)^2}{(2 + \xi \Delta t)^2 + (\omega \Delta t)^2}}. \quad (5.49)$$

Since  $\rho^h \leq 1$ , the scheme is unconditionally stable. Using (5.48) in (5.9),  $\xi^h$  and  $\omega^h$  are obtained as

$$\xi^h = \xi + \frac{\xi(\xi^2 - 3\omega^2)}{12} \Delta t^2 + O(\Delta t^3), \quad (5.50)$$

$$\omega^h = \omega + \frac{\omega(3\xi^2 - \omega^2)}{12} \Delta t^2 + O(\Delta t^3). \quad (5.51)$$

The comparison of (5.48) with (5.11) shows that, for the model problem considered, the modified continuous time finite element method is identical to the generalised midpoint rule for  $\gamma = 1/2$  or, respectively, the second order accurate trapezoidal rule.

### 5.1.2.4 Linear Discontinuous Finite Elements (LD)

For this method the approximate solution  $u^h$  and the test function  $w^h$  are linear within the time element and discontinuous at the boundaries (see Figure 5.2). Thus,  $u^h$  and  $w^h$  may be written as

$$u^h(t) = \left\{ \hat{N}_n(t), \hat{N}_{n+1}(t) \right\} \cdot \begin{Bmatrix} \mathbf{u}_n^+ \\ \mathbf{u}_{n+1}^- \end{Bmatrix} \quad (5.52)$$

$$w^h(t) = \left\{ \hat{N}_n(t), \hat{N}_{n+1}(t) \right\} \cdot \begin{Bmatrix} \mathbf{w}_n^+ \\ \mathbf{w}_{n+1}^- \end{Bmatrix} \quad (5.53)$$

for  $\mathbf{t}_n < t < \mathbf{t}_{n+1}$ . The shape functions  $N_n$  and  $N_{n+1}$  are defined by (5.31). The weak form (5.39) then renders:

$$\left( \frac{1}{2} \begin{bmatrix} -1 & 1 \\ -1 & 1 \end{bmatrix} - \frac{\lambda \Delta t}{6} \begin{bmatrix} 2 & 1 \\ 1 & 2 \end{bmatrix} + \begin{bmatrix} \beta & 0 \\ 0 & 0 \end{bmatrix} \right) \begin{Bmatrix} \mathbf{u}_n^+ \\ \mathbf{u}_{n+1}^- \end{Bmatrix} = \begin{Bmatrix} \beta \mathbf{u}_n^- \\ 0 \end{Bmatrix}. \quad (5.54)$$

Thus, the following amplification factors are obtained

$$\zeta_n^{h+} = \frac{\beta(6 - 4\lambda\Delta t)}{\beta(6 - 4\lambda\Delta t) + (\lambda\Delta t)^2}, \quad (5.55)$$

$$\zeta_{n+1}^{h-} = \frac{\beta(6 + 2\lambda\Delta t)}{\beta(6 - 4\lambda\Delta t) + (\lambda\Delta t)^2}. \quad (5.56)$$

The factors  $\zeta_n^{h+}$  and  $\zeta_{n+1}^{h-}$  relate  $\mathbf{u}_n^+$  and  $\mathbf{u}_{n+1}^-$  to  $\mathbf{u}_n^-$ . Note that  $\mathbf{u}_{n-1}^+$  does not influence the approximate solution for  $t > \mathbf{t}_n$ . It can be shown that

$$\lim_{\beta \rightarrow \infty} \zeta_n^{h+} = 1, \quad (5.57)$$

and

$$\lim_{\beta \rightarrow \infty} \zeta_{n+1}^{h-} = \frac{3 + \lambda\Delta t}{3 - 2\lambda\Delta t}. \quad (5.58)$$

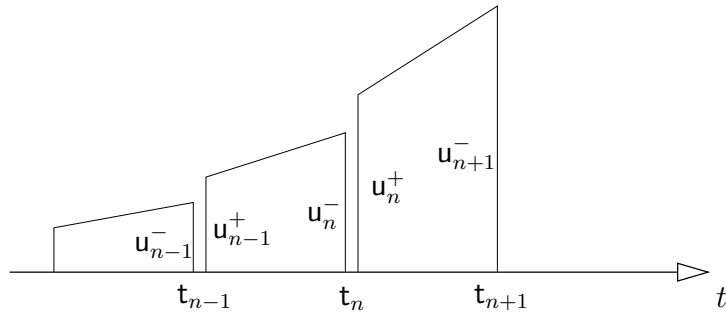


Figure 5.2: Linear discontinuous finite elements in time.

Since (5.58) is identical to (5.35), the method clearly recovers the previously discussed linear continuous time finite element method as expected. Using  $\lambda = -\xi + i\omega$  in (5.55) and (5.56) renders lengthy expressions for the amplification factors and the spectral radii, which are not given here. It follows, however, that

$$\rho_n^{h+} \leq 1 \quad \text{only if} \quad \beta \rightarrow \infty, \quad (5.59)$$

$$\rho_{n+1}^{h-} \leq 1 \quad \text{only if} \quad \beta \geq 1, \quad (5.60)$$

for any  $\Delta t \geq 0$ . The requirement for stability is given by expression (5.60), since  $u_n^+$  does not propagate in time. Thus, the method is unconditionally stable for any  $\beta \geq 1$ . In Figure 5.3 the spectral radii  $\rho_n^{h+}$  and  $\rho_{n+1}^{h-}$  are displayed for different values of  $\beta$ .

The series expansion of (5.9) applied to the amplification factor  $\zeta_{n+1}^{h-}$  yields

$$\begin{aligned} \xi^h = & \xi + \frac{(1-\beta)(\xi^2 - \omega^2)}{6\beta} \Delta t + \frac{(1-\beta)\xi(3\omega^2 - \xi^2)}{9\beta} \Delta t^2 \\ & - \frac{(3-16\beta+10\beta^2)(\xi^4 - 6\xi^2\omega^2 + \omega^4)}{216\beta^2} \Delta t^3 + O(\Delta t^4), \end{aligned} \quad (5.61)$$

$$\begin{aligned} \omega^h = & \omega + \frac{(1-\beta)\xi\omega}{3\beta} \Delta t + \frac{(1-\beta)\omega(\omega^2 - 3\xi^2)}{9\beta} \Delta t^2 \\ & + \frac{(3-16\beta+10\beta^2)\xi\omega(\omega^2 - \xi^2)}{54\beta^2} \Delta t^3 + O(\Delta t^4). \end{aligned} \quad (5.62)$$

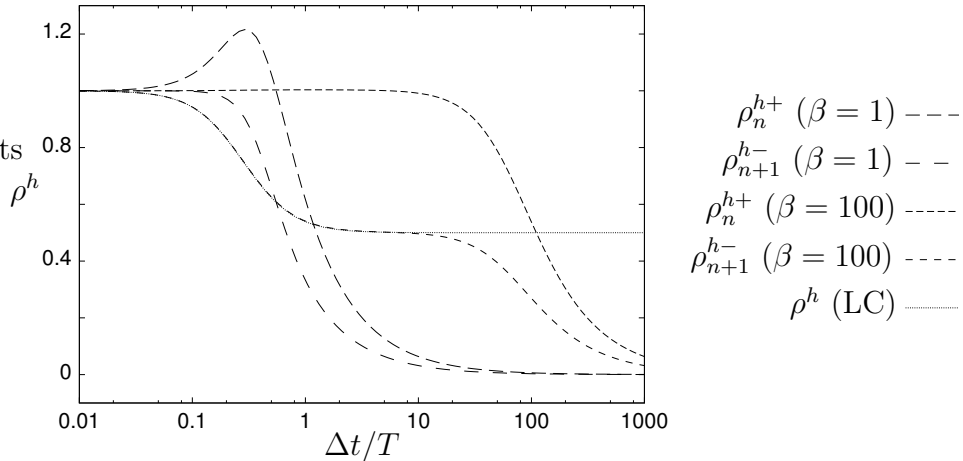


Figure 5.3: Linear discontinuous finite elements in time; spectral radii for  $\omega = 2\pi/T$  and  $\xi = 0$ ; showing also linear continuous scheme (LC).

For  $\beta = 1$  the second and the third terms disappear and the method is third order accurate, while any choice  $\beta > 1$  renders only first order accuracy. For  $\beta \rightarrow \infty$ , the method coincides with the linear continuous scheme discussed in Section 5.1.2.1.

### 5.1.3 On the Algorithmic Treatment of the Schemes

The time integration methods described in Sections 5.1.1 and 5.1.2 lead to incremental time stepping algorithms. In the following, the solution procedures are briefly described for the situation in which the factor  $\lambda$  depends on the unknown  $u$ , *i. e.*

$$\dot{u} - \lambda(u) u = 0. \quad (5.63)$$

This type of nonlinearity is normally encountered in fluid dynamics problems.

Note that the stability and accuracy analysis performed in the preceding subsections is restricted to the linear problem (5.1). However, if the nonlinearity in (5.63) is not dominant, or if the time step size  $\Delta t$  is chosen sufficiently small, the results of Sections 5.1.1 and 5.1.2 also hold for the approximate solutions of (5.63).

Furthermore, it should be noted that the nonlinearity in (5.63) may make the exact integration over a time finite element impossible. Thus, the time finite element methods usually require the application of a numerical integration formula for each time step, which results in additional computational effort. Importantly, it follows from the integration of the nonlinear expression, that the time finite element methods (LC, CD, MC) cease to represent special cases of the generalised midpoint rule.

- (i) *generalised midpoint rule* (GM), *finite element methods* (LC, CD, MC). In the case of the nonlinearity (5.63) the amplification factor depends on the unknown, and the equation for the solution  $\mathbf{u}_{n+1}$  becomes implicit

$$\mathbf{u}_{n+1} = \zeta^h(\mathbf{u}_{n+1}, \mathbf{u}_n) \mathbf{u}_n. \quad (5.64)$$

This equation can easily be solved by employing the Newton-Raphson procedure. Problems in space and time, where space is discretised with an appropriate finite element scheme, require the solution of a matrix equation for each time step.

- (ii) *linear discontinuous time finite element method* (LD). This method yields a system of two nonlinear implicit equations

$$\begin{aligned} \mathbf{u}_n^+ &= \zeta_n^{h+}(\mathbf{u}_n^+, \mathbf{u}_{n+1}^-) \mathbf{u}_n^- \\ \mathbf{u}_{n+1}^- &= \zeta_{n+1}^{h-}(\mathbf{u}_n^+, \mathbf{u}_{n+1}^-) \mathbf{u}_n^-. \end{aligned} \quad (5.65)$$

Thus, for problems in space and time the dimension of the system matrix is doubled in comparison to schemes in (i). It is noted, however, that the number of solution variables, which are needed as initial conditions for the subsequent time step, remains the same, since only  $\mathbf{u}_n^-$  is required.

- (iii) *generalised- $\alpha$  method* (AM). This scheme is the only one to involve the rate of the solution. Thus, its algorithmic treatment requires some clarification: For the nonlinear model problem (5.63), the equations (5.17) – (5.20) represent a system of one nonlinear and three linear equations with the unknowns  $\mathbf{u}_{n+1}$ ,  $\dot{\mathbf{u}}_{n+1}$ ,  $\mathbf{u}_{n+\alpha_f}$  and  $\dot{\mathbf{u}}_{n+\alpha_m}$ . Note that in (5.17)  $\lambda$  is replaced by  $\lambda(\mathbf{u}_{n+\alpha_f})$ . Equation (5.18) can be rewritten as

$$\dot{\mathbf{u}}_{n+1} = \frac{1}{\gamma \Delta t} (\mathbf{u}_{n+1} - \mathbf{u}_n) - \frac{1-\gamma}{\gamma} \dot{\mathbf{u}}_n . \quad (5.66)$$

This expression is used in (5.20) to obtain

$$\dot{\mathbf{u}}_{n+\alpha_m} = \left(1 - \frac{\alpha_m}{\gamma}\right) \dot{\mathbf{u}}_n + \frac{\alpha_m}{\gamma \Delta t} (\mathbf{u}_{n+1} - \mathbf{u}_n) . \quad (5.67)$$

Inserting (5.19) and (5.67) into (5.17) gives an equation in terms of  $\mathbf{u}_{n+1}$  as the only unknown

$$r(\mathbf{u}_{n+1}, \mathbf{u}_n, \dot{\mathbf{u}}_n) = 0 . \quad (5.68)$$

For computer implementation the solution procedure can be summarised as follows:

1. Solve (5.68) for  $\mathbf{u}_{n+1}$
  2. Compute  $\dot{\mathbf{u}}_{n+1}$  from (5.66)
  3.  $(\mathbf{u}_n, \dot{\mathbf{u}}_n) \leftarrow (\mathbf{u}_{n+1}, \dot{\mathbf{u}}_{n+1})$
  4. Goto 1.
- (5.69)

Thus, the nonlinear equation (5.68) has the same dimension as for the methods in (i). However, the generalised- $\alpha$  method requires twice as much memory for the storage of previous solution variables since  $\mathbf{u}_{n+1}$  and  $\dot{\mathbf{u}}_{n+1}$  are needed for the subsequent time step.

### 5.1.4 Discussion and Comparison of the Schemes

The main conclusions and results of the previous subsections are summarised in Table 5.1. The number of unknowns per time step and the requirements of computer memory are also given, since they characterise the computational costs of the integration methods. However, it is not a straightforward task to establish the overall efficiency of a particular method. Often this depends on the problem under consideration.

In the diagrams in Figure 5.4 the spectral radii of the methods are displayed against  $\Delta t/T$ , where  $T = 2\pi/\omega$ . In the low frequency range  $\Delta t/T \rightarrow 0$  the spectral radius  $\rho^h$  of an optimal method should be close to the exact  $\rho = e^{-\xi \Delta t}$ , and for  $\Delta t/T \approx O(1)$  it should be smaller than one in order to damp out oscillations which are not resolved by the chosen time step size  $\Delta t$ . The optimal amount of such high frequency damping is difficult to define precisely. Solutions of complex fluid dynamics problems are often characterised by a wide range of frequencies, where the high frequencies trigger oscillations in the low frequency range. In such cases too much numerical high frequency damping may not be beneficial.

It is observed in Figure 5.4 that the limit  $\rho_\infty^h$  depends only on the integration method employed. For  $\xi > 0$  the exact spectral radius  $\rho$  tends to zero, but its numerical counterpart  $\rho^h$  recovers the same value as for  $\xi = 0$ . In this situation the numerical damping is smaller than the exact damping.

For the generalised midpoint rule and the generalised- $\alpha$  method, the free parameter  $\rho_\infty^h$  clearly determines the high frequency damping limit. The generalised- $\alpha$  method exhibits much less numerical damping in the low frequency range than the generalised midpoint rule. The diagram associated with the linear discontinuous in time finite element scheme indicates a favourable numerical damping behaviour of the method.

The effects of unwanted numerical low frequency damping and dispersion are illustrated in Table 5.2. The ratio of the numerical and the exact amplitude and the relative phase error are given for certain values  $\xi$  and  $\omega$  at time  $t = 20 T$ . The time step size  $\Delta t$  has been chosen 30 times smaller than the wave length  $T$ . For the backward Euler method the solution has almost vanished due to excessive numerical damping. The linear discontinuous in time finite element scheme performs very well for both the situations with and without physical damping. The table also shows that the numerical phase error is generally less dominant than the error of the amplitude following from numerical damping.

integration method	stability	order of accuracy	$\rho_{\infty}^h$	number of unknowns	memory requirements
BE, CD	uncond. stable	1.	0	1	1 ( $u_n$ )
GM	uncond. stable	1. – 2.	user defined	1	1 ( $u_n$ )
AM	uncond. stable	2.	user defined	1	2 ( $u_n, \dot{u}_n$ )
TR, MC	uncond. stable	2.	1	1	1 ( $u_n$ )
LC	uncond. stable	1.	$\frac{1}{2}$	1	1 ( $u_n$ )
LD	uncond. stable	3.	0	2	1 ( $u_n^-$ )

Table 5.1: Comparison of the time integration schemes.

integration method	$\xi = 0$		$\xi = 1.5$	
	$e^{-(\xi^h - \xi) \cdot 20}$	$\frac{T^h - T}{T} \cdot 20$	$e^{-(\xi^h - \xi) \cdot 20}$	$\frac{T^h - T}{T} \cdot 20$
GM 0.0*, BE, CD	$2.6 \cdot 10^{-6}$	0.289	$1.7 \cdot 10^{-5}$	1.276
AM 0.0*	0.771	0.281	2.729	0.275
GM 0.5, LC	0.013	0.097	0.025	0.415
AM 0.5	0.990	0.097	1.518	0.082
GM 1.0, TR, MC, AM 1.0	1.000	0.073	1.377	0.061
LD	0.984	$1.4 \cdot 10^{-4}$	0.990	0.002

\* The number represents the integration parameter  $\rho_{\infty}^h$ .

Table 5.2: Comparison of low frequency damping and dispersion, ratio of numerical and exact amplitude and relative phase error at  $t = 20$ ;  $T = 1$ ,  $\Delta t = 1/30$ .

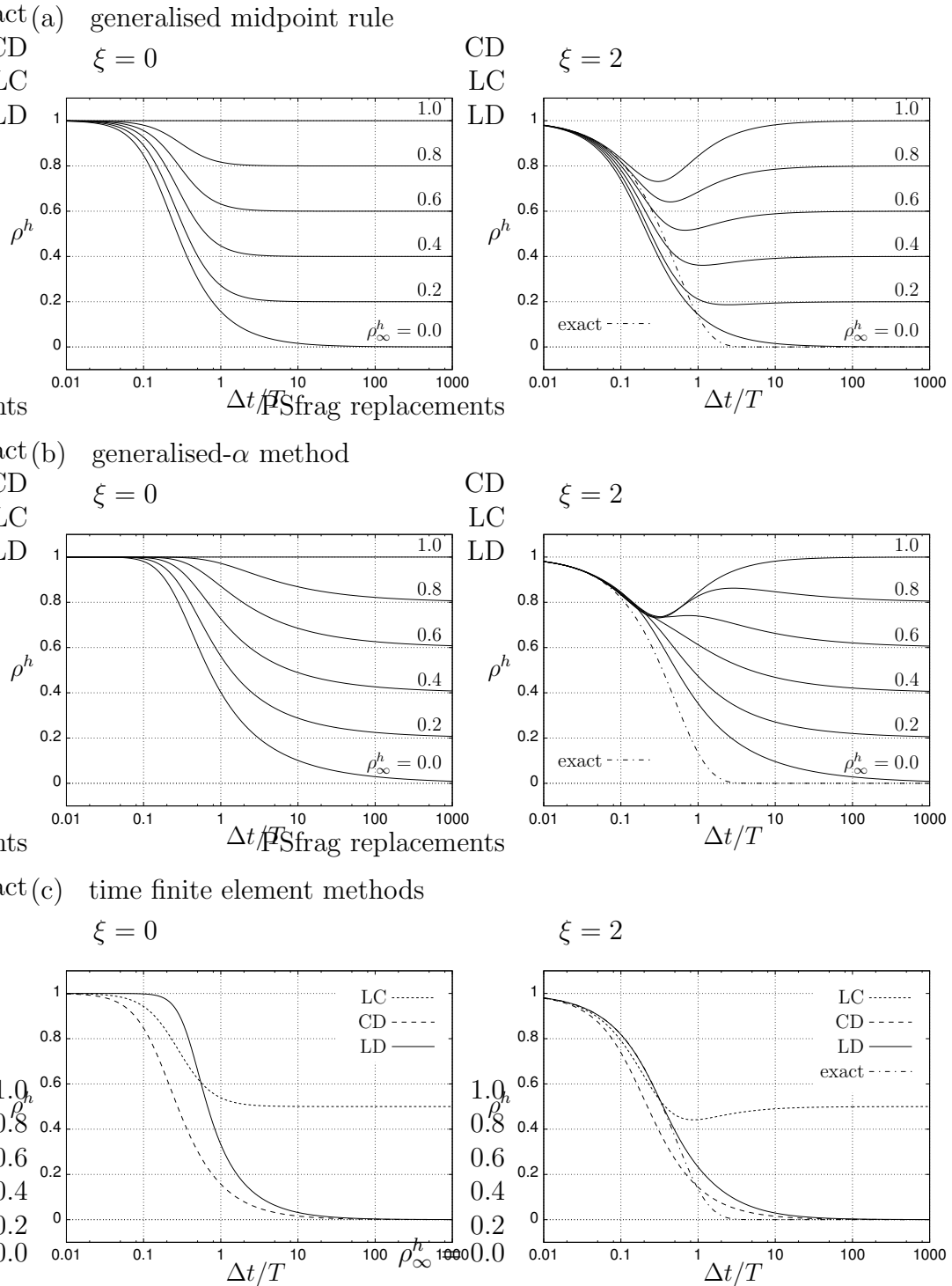


Figure 5.4: Spectral radii displayed against  $\Delta t/T$ ,  $T = 1$ ,  $\xi = 0$  (left) and  $\xi = 2$  (right).

### 5.1.5 Example

In order to demonstrate the damping behaviour of the integration methods a model problem with four degrees of freedom is considered

$$\begin{Bmatrix} \dot{u}_1 \\ \dot{u}_2 \\ \dot{u}_3 \\ \dot{u}_4 \end{Bmatrix} - \begin{bmatrix} 0 & 0 & 1 & 0 \\ 0 & 0 & 0 & 1 \\ -201 & +200 & 0 & 0 \\ +200 & -200 & 0 & 0 \end{bmatrix} \begin{Bmatrix} u_1 \\ u_2 \\ u_3 \\ u_4 \end{Bmatrix} = \begin{Bmatrix} 0 \\ 0 \\ 0 \\ 0 \end{Bmatrix}, \quad \begin{Bmatrix} u_1(0) \\ u_2(0) \\ u_3(0) \\ u_4(0) \end{Bmatrix} = \begin{Bmatrix} 2 \\ 10 \\ 0 \\ 0 \end{Bmatrix}. \quad (5.70)$$

The exact solution for  $u_1$  is the superposition of two oscillations with the wave lengths

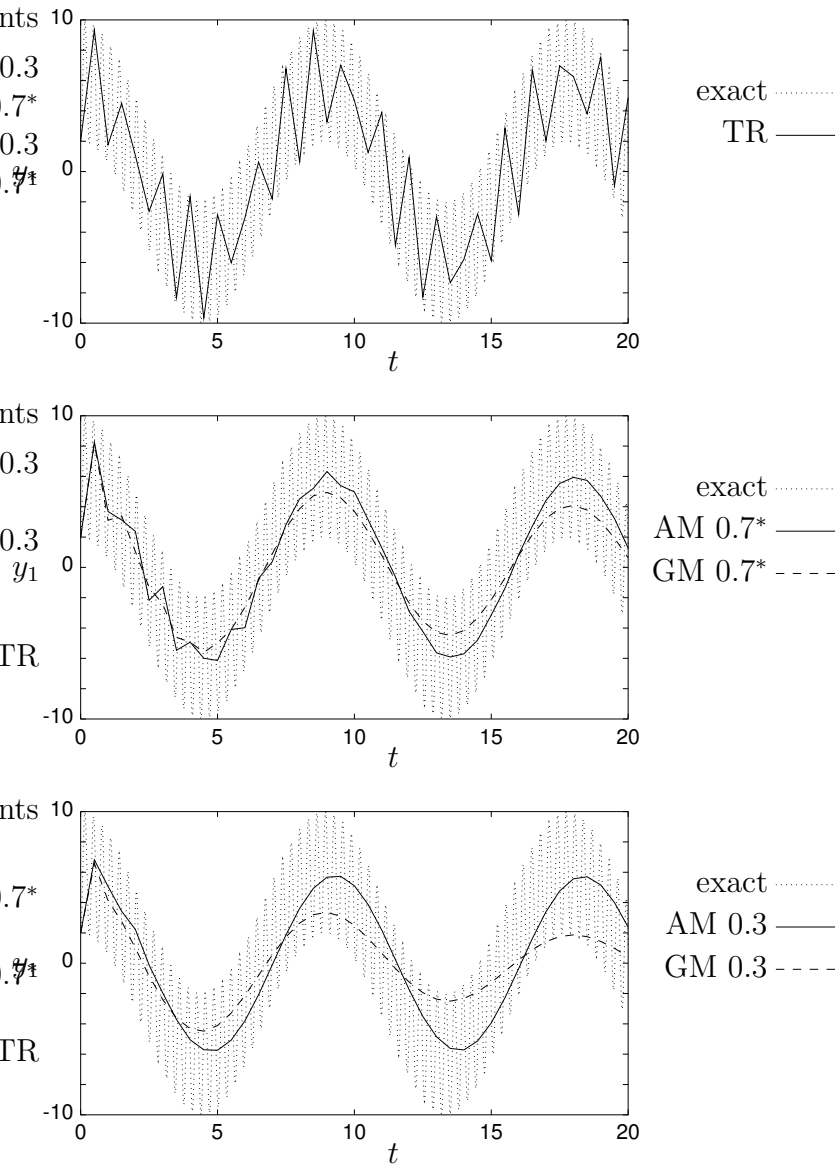
$$T_1 = 8.891, \quad T_2 = 0.314.$$

Figure 5.5 shows the exact solution and the results obtained by applying the generalised- $\alpha$  method (AM) and the generalised midpoint rule (GM) for different values of  $\rho_\infty^h$  and a time step size  $\Delta t = 0.5 > T_2$ . Naturally, for small time steps  $\Delta t \rightarrow 0$ , both methods tend to the exact solution. Here, however, the numerical analyst is assumed to be interested only in the long wave response. Thus, an optimal integration scheme should accurately account for the long wave and damp out the unresolved high frequency.

It is observed that  $\rho_\infty^h = 1$  ( $\rightarrow$  trapezoidal rule (TR)) is a very problematic choice since the unresolved frequency causes strong numerical oscillations due to the lack of numerical damping. These oscillations can be damped out by setting  $\rho_\infty^h < 1$ . Generally, it is noted that, for  $\rho_\infty^h < 1$ , the generalised midpoint rule suppresses the effects of the unresolved frequency after a smaller number of time steps than the generalised- $\alpha$  method. However, the long wave response of the generalised midpoint rule is subjected to significantly more unwanted low frequency damping.

## 5.2 One Dimensional Advection-Diffusion Problem

A more complex model problem to be considered is the one dimensional unsteady advection-diffusion equation. Fully discretised formulations are obtained by the combination of the SUPG stabilisation technique discussed in Section 4.2.1 with the different time integration schemes described in Section 5.1. In order to understand their performance and properties, a Fourier analysis is performed for each of the resulting numerical schemes. A similar analysis has previously been provided by Shakib and Hughes [108] with attention restricted to the backward Euler and the discontinuous time finite element schemes.



\* The number represents the integration parameter  $\rho_\infty^h$ .

Figure 5.5: Numerical example, effect of unresolved frequency.

*Governing equation.* Let the spatial and temporal domains be given as  $\Omega = [0, L]$  and  $I = [0, T_{\text{end}}]$ , respectively. Then, the one dimensional unsteady advection-diffusion problem with periodic boundary conditions reads

$$\dot{u} + a u_{,x} - \mu u_{,xx} = 0 \quad \forall (x, t) \in \Omega \times I \quad (5.71)$$

$$u(x, 0) = u_0(x) \quad \forall x \in \Omega \quad (5.72)$$

$$\dot{u}(x, 0) = \dot{u}_0(x) \quad \forall x \in \Omega \quad (5.73)$$

$$u(0, t) = u(L, t) \quad \forall t \in I \quad (5.74)$$

$$u_{,x}(0, t) = u_{,x}(L, t) \quad \forall t \in I, \quad (5.75)$$

where  $a$  is the advective speed and  $\mu$  is the diffusion coefficient (compare to the steady problem (4.19)).

*Analytical solution.* It is assumed that the function  $u_0(x)$  can be written as a series

$$u_0(x) = \sum_{m=0}^{\infty} b_m e^{i K_m x}, \quad (5.76)$$

where

$$K_m = \frac{2\pi}{L} m \quad (5.77)$$

is denoted as the spatial wave number. The solution of the problem (5.71) – (5.75) then becomes

$$u(x, t) = \sum_{m=0}^{\infty} b_m e^{(-\xi_m + i \omega_m) t + i K_m x}, \quad (5.78)$$

with

$$\omega_m = -a K_m \quad \text{and} \quad \xi_m = \mu K_m^2. \quad (5.79)$$

Since the equation (5.71) is linear, the imaginary parts of (5.76) and (5.78) can also be taken as real numbers. By adding together the values of the real and imaginary parts (5.76) becomes a complete Fourier series and the solution can be obtained for any  $u_0(x)$ , provided that there are no infinite jumps in  $u_0(x)$ . The notation using complex numbers will provide a more convenient setting for the analysis in Section 5.2.3.

*Stabilised formulation.* Based on the standard finite element discretisation of the domain, i. e.  $\Omega = \cup_{e=1}^{n_{el}} \Omega^e$  with  $\Omega^j = [x_{j-1}, x_j]$ , the trial and test spaces may be defined as

$$\begin{aligned} \mathcal{U}^h &= \left\{ u^h(\bullet, t) \in H^1(\Omega) \mid t \in I, u^h|_{x \in \Omega^e} \in P_1(\Omega^e), u^h(0, t) = u^h(L, t) \right\} \\ \mathcal{W}^h &= \left\{ w^h \in H^1(\Omega) \mid w^h|_{x \in \Omega^e} \in P_1(\Omega^e), w^h(0) = w^h(L) \right\}. \end{aligned} \quad (5.80)$$

The stabilised finite element formulation of (5.71) is obtained from the standard Galerkin expression by adding a SUPG stabilisation term (see (4.33) and Table 4.2). For linear finite element interpolation second derivatives vanish and the SUPG formulation may be expressed as: For each time instant  $t \in I$ , find  $u^h \in \mathcal{U}^h$  such that for all  $w^h \in \mathcal{W}^h$

$$\int_0^L w^h (\dot{u}^h + a u_{,x}^h) + \mu w_{,x}^h u_{,x}^h \, dx + \sum_{j=1}^{n_{\text{el}}} \int_{x_{j-1}}^{x_j} \tau^j a w_{,x}^h (\dot{u}^h + a u_{,x}^h) \, dx = 0. \quad (5.81)$$

Note that, throughout this chapter, the superscript  $h$  relates to the piecewise linear finite element interpolation. Higher order methods are possible, but computationally less convenient and not necessarily more efficient for the problem considered. Note also, that (5.81) has not yet been discretised in time. With  $\Delta x^j = x_j - x_{j-1}$  the stabilisation parameter is evaluated as

$$\tau^j = \frac{\Delta x^j}{2a} \xi^j, \quad \xi^j = \frac{1}{\sqrt{1 + \left(\frac{3}{\alpha^j}\right)^2}}, \quad \alpha^j = \frac{a \Delta x^j}{2\mu}. \quad (5.82)$$

The relations (5.82) are motivated in Sections 4.2.3 and 4.4.1.

For the clarity of the notation used in the following sections, recall from Section 5.1 that  $0 = t_0 < t_1 < \dots < t_N = T_{\text{end}}$  is a sequence of discrete time instants in  $I$ , and  $I = \cup_{n=1}^N I_n$  with  $I_n = [t_{n-1}, t_n]$  is a partition of the time interval of interest. The subscript  $n$  denotes the approximative value of the quantity under consideration at time instant  $t_n$ .

In the following sections, the formulation (5.81) is subjected to the different time integration schemes, and space-time difference stencils are derived for the special case of uniform discretisation in both space and time. The properties of the difference equations are then elucidated from a Fourier analysis. Particular attention is paid to the influence of the stabilisation parameter. Finally, some numerical results are presented to demonstrate the varying properties of the schemes.

### 5.2.1 Semi-Discrete Methods

The discrete time integration schemes GM and AM are based on the substitution of  $u^h$  and  $\dot{u}^h$  in (5.81) by quantities which may be denoted as  $u_\alpha^h$  and  $\dot{u}_\beta^h$  and which can be expressed as linear combinations of  $u_n^h$ ,  $u_{n+1}^h$ ,  $\dot{u}_n^h$  and  $\dot{u}_{n+1}^h$ . In fact, the schemes GM and AM render

$$\begin{aligned} u_\alpha^h &= c_1 u_{n+1}^h + c_2 u_n^h + c_3 \dot{u}_n^h \\ \dot{u}_\beta^h &= c_4 u_{n+1}^h + c_5 u_n^h + c_6 \dot{u}_n^h, \end{aligned} \quad (5.83)$$

where the coefficients  $c_i$  are determined by the time step size  $\Delta t$  and the particular discrete time integration scheme chosen. For example the backward Euler scheme (GM,  $\rho_\infty^h = 0$ ) gives

$$c_1 = 1, \quad c_4 = -c_5 = \frac{1}{\Delta t}, \quad c_2 = c_3 = c_6 = 0. \quad (5.84)$$

The trial and test function spaces are defined as

$$\begin{aligned} \mathcal{U}_n^h &= \left\{ u_n^h \in H^1(\Omega) \mid u_n^h|_{x \in \Omega^e} \in P_1(\Omega^e), u_n^h(L) = u_n^h(0) \right\} \\ \mathcal{W}^h &= \left\{ w^h \in H^1(\Omega) \mid w^h|_{x \in \Omega^e} \in P_1(\Omega^e), w^h(L) = w^h(0) \right\}. \end{aligned} \quad (5.85)$$

Note that effectively  $\mathcal{U}_n^h = \mathcal{U}_{n+1}^h$  and, due to the periodic boundary conditions, also  $\mathcal{U}_n^h = \mathcal{W}^h$ . The fully discretised problem then reads: Given the solution  $u_n^h$  and possibly  $\dot{u}_n^h$ , find  $u_{n+1}^h \in \mathcal{U}_{n+1}^h$  such that for all  $w^h \in \mathcal{W}^h$

$$\int_0^L w^h \left( \dot{u}_\beta^h + a u_{\alpha,x}^h \right) + \mu w_{,x}^h u_{\alpha,x}^h \, dx + \sum_{j=1}^{n_{el}} \int_{x_{j-1}}^{x_j} \tau^j a w_{,x}^h \left( \dot{u}_\beta^h + a u_{\alpha,x}^h \right) \, dx = 0. \quad (5.86)$$

In the following subsections space-time difference stencils are derived for the generalised midpoint rule and the generalised- $\alpha$  method. It is assumed that the spatial and temporal discretisations are uniform, *i. e.*  $\Delta x$  and  $\Delta t$  do not vary.

### 5.2.1.1 Generalised Midpoint Rule (GM)

The linear shape functions in space are defined as

$$N_j = \hat{N}_j(x) = \frac{x_{j+1} - x}{\Delta x}, \quad N_{j+1} = \hat{N}_{j+1}(x) = \frac{x - x_j}{\Delta x} \quad (5.87)$$

for  $x_j \leq x \leq x_{j+1}$ . The approximate solution at the time instant  $t_n$  is

$$u_n^h(x) = \sum_{j=0}^{n_{el}-1} \left\{ N_j, N_{j+1} \right\} \cdot \left\{ \mathbf{u}_{j,n}, \mathbf{u}_{j+1,n} \right\}. \quad (5.88)$$

The solution  $u_{n+1}^h$  and the test function  $w^h$  are defined similarly. According to the generalised midpoint rule described in Section 5.1.1.1 the quantities  $u_\alpha^h$  and  $\dot{u}_\beta^h$  may be written in the format of (5.83) as

$$u_\alpha^h = \gamma u_{n+1}^h + (1 - \gamma) u_n^h, \quad \dot{u}_\beta^h = \frac{u_{n+1}^h - u_n^h}{\Delta t}. \quad (5.89)$$

Using the above discretisation of time and space domains in the variational formulation (5.86) yields

$$\sum_{j=0}^{n_{\text{el}}-1} \begin{Bmatrix} \mathbf{w}_j \\ \mathbf{w}_{j+1} \end{Bmatrix} \cdot \left( \mathbf{A} \begin{Bmatrix} \mathbf{u}_{j,n+1} \\ \mathbf{u}_{j+1,n+1} \end{Bmatrix} + \mathbf{B} \begin{Bmatrix} \mathbf{u}_{j,n} \\ \mathbf{u}_{j+1,n} \end{Bmatrix} \right) = 0, \quad (5.90)$$

or by recalling that the nodal values of the test function  $w^h$  are arbitrary

$$\sum_{j=0}^{n_{\text{el}}-1} \left( \mathbf{A} \begin{Bmatrix} \mathbf{u}_{j,n+1} \\ \mathbf{u}_{j+1,n+1} \end{Bmatrix} + \mathbf{B} \begin{Bmatrix} \mathbf{u}_{j,n} \\ \mathbf{u}_{j+1,n} \end{Bmatrix} \right) = \mathbf{0}. \quad (5.91)$$

The  $2 \times 2$  matrices  $\mathbf{A}$  and  $\mathbf{B}$  are obtained as

$$\begin{aligned} \mathbf{A} &= \frac{1}{6} \begin{bmatrix} 2 & 1 \\ 1 & 2 \end{bmatrix} + \frac{\tau a}{2 \Delta x} \begin{bmatrix} -1 & -1 \\ 1 & 1 \end{bmatrix} + \frac{\gamma a \Delta t}{2 \Delta x} \begin{bmatrix} -1 & 1 \\ -1 & 1 \end{bmatrix} \\ &\quad + \frac{\gamma \Delta t (\mu + \tau a^2)}{\Delta x^2} \begin{bmatrix} 1 & -1 \\ -1 & 1 \end{bmatrix} \end{aligned} \quad (5.92)$$

$$\begin{aligned} \mathbf{B} &= -\frac{1}{6} \begin{bmatrix} 2 & 1 \\ 1 & 2 \end{bmatrix} - \frac{\tau a}{2 \Delta x} \begin{bmatrix} -1 & -1 \\ 1 & 1 \end{bmatrix} + \frac{(1-\gamma) a \Delta t}{2 \Delta x} \begin{bmatrix} -1 & 1 \\ -1 & 1 \end{bmatrix} \\ &\quad + \frac{(1-\gamma) \Delta t (\mu + \tau a^2)}{\Delta x^2} \begin{bmatrix} 1 & -1 \\ -1 & 1 \end{bmatrix}. \end{aligned} \quad (5.93)$$

The expressions (5.91) – (5.93) represent a system of  $n_{\text{el}}$  equations for the unknowns  $\mathbf{u}_{j,n+1}$ ,  $j = 1, 2, \dots, n_{\text{el}}$ . By performing the assembly for two neighbouring elements these equations can be written as the following  $3 \times 2$  difference stencil in space and time

$$\begin{aligned} &\left( \frac{1}{6} \begin{Bmatrix} 1 \\ 4 \\ 1 \end{Bmatrix} + C_1 \begin{Bmatrix} 1 \\ 0 \\ -1 \end{Bmatrix} + C_2 \begin{Bmatrix} -1 \\ 2 \\ -1 \end{Bmatrix} \right) \cdot \begin{Bmatrix} \mathbf{u}_{j-1,n+1} \\ \mathbf{u}_{j,n+1} \\ \mathbf{u}_{j+1,n+1} \end{Bmatrix} \\ &= \left( \frac{1}{6} \begin{Bmatrix} 1 \\ 4 \\ 1 \end{Bmatrix} + C_3 \begin{Bmatrix} 1 \\ 0 \\ -1 \end{Bmatrix} + C_4 \begin{Bmatrix} -1 \\ 2 \\ -1 \end{Bmatrix} \right) \cdot \begin{Bmatrix} \mathbf{u}_{j-1,n} \\ \mathbf{u}_{j,n} \\ \mathbf{u}_{j+1,n} \end{Bmatrix} \end{aligned} \quad (5.94)$$

with

$$\begin{aligned} C_1 &= \frac{(\tau - \gamma \Delta t) a}{2 \Delta x}, & C_2 &= \frac{\gamma \Delta t (\mu + \tau a^2)}{\Delta x^2} \\ C_3 &= \frac{(\tau + (1-\gamma) \Delta t) a}{2 \Delta x}, & C_4 &= -\frac{(1-\gamma) \Delta t (\mu + \tau a^2)}{\Delta x^2}. \end{aligned} \quad (5.95)$$

### 5.2.1.2 Generalised- $\alpha$ Method (AM)

For the terms  $w^h$ ,  $u_{n+1}^h$ ,  $u_n^h$  and  $\dot{u}_n^h$ , a linear in space approximation similar to equation (5.87) and (5.88) is employed. It follows from (5.17) – (5.20) that the expressions  $u_\alpha^h$  and  $\dot{u}_\beta^h$  in the variational equation (5.86) can be written in the format of (5.83) as

$$\begin{aligned} u_\alpha^h &= u_{n+\alpha_f}^h = \beta_1 u_{n+1}^h + \beta_2 u_n^h, \\ \dot{u}_\beta^h &= \dot{u}_{n+\alpha_m}^h = \frac{1}{\Delta t} \beta_3 u_{n+1}^h + \frac{1}{\Delta t} \beta_4 u_n^h + \beta_5 \dot{u}_n^h, \end{aligned} \quad (5.96)$$

where

$$\begin{aligned} \beta_1 &= \alpha_f, & \beta_2 &= 1 - \alpha_f, \\ \beta_3 &= \frac{\alpha_m}{\gamma}, & \beta_4 &= -\frac{\alpha_m}{\gamma}, & \beta_5 &= 1 - \frac{\alpha_m}{\gamma}. \end{aligned} \quad (5.97)$$

The variational formulation (5.86) can then be rewritten as

$$\sum_{j=1}^{n_{el}} \left( \mathbf{A} \begin{Bmatrix} \mathbf{u}_{j,n+1} \\ \mathbf{u}_{j+1,n+1} \end{Bmatrix} + \mathbf{B} \begin{Bmatrix} \mathbf{u}_{j,n} \\ \mathbf{u}_{j+1,n} \end{Bmatrix} + \mathbf{C} \begin{Bmatrix} \dot{\mathbf{u}}_{j,n} \Delta t \\ \dot{\mathbf{u}}_{j+1,n} \Delta t \end{Bmatrix} \right) = \mathbf{0}. \quad (5.98)$$

The matrices  $\mathbf{A}$ ,  $\mathbf{B}$  and  $\mathbf{C}$  read

$$\begin{aligned} \mathbf{A} &= \frac{\beta_3}{6} \begin{bmatrix} 2 & 1 \\ 1 & 2 \end{bmatrix} + \frac{\beta_3 \tau a}{2 \Delta x} \begin{bmatrix} -1 & -1 \\ 1 & 1 \end{bmatrix} + \frac{\beta_1 a \Delta t}{2 \Delta x} \begin{bmatrix} -1 & 1 \\ -1 & 1 \end{bmatrix} \\ &\quad + \frac{\beta_1 \Delta t (\mu + \tau a^2)}{\Delta x^2} \begin{bmatrix} 1 & -1 \\ -1 & 1 \end{bmatrix} \end{aligned} \quad (5.99)$$

$$\begin{aligned} \mathbf{B} &= \frac{\beta_4}{6} \begin{bmatrix} 2 & 1 \\ 1 & 2 \end{bmatrix} + \frac{\beta_4 \tau a}{2 \Delta x} \begin{bmatrix} -1 & -1 \\ 1 & 1 \end{bmatrix} + \frac{\beta_2 a \Delta t}{2 \Delta x} \begin{bmatrix} -1 & 1 \\ -1 & 1 \end{bmatrix} \\ &\quad + \frac{\beta_2 \Delta t (\mu + \tau a^2)}{\Delta x^2} \begin{bmatrix} 1 & -1 \\ -1 & 1 \end{bmatrix} \end{aligned} \quad (5.100)$$

$$\mathbf{C} = \frac{\beta_5}{6} \begin{bmatrix} 2 & 1 \\ 1 & 2 \end{bmatrix} + \frac{\beta_5 \tau a}{2 \Delta x} \begin{bmatrix} -1 & -1 \\ 1 & 1 \end{bmatrix}. \quad (5.101)$$

Furthermore, from equation (5.66) it is known that

$$\begin{Bmatrix} \dot{\mathbf{u}}_{j-1,n+1} \Delta t \\ \dot{\mathbf{u}}_{j,n+1} \Delta t \\ \dot{\mathbf{u}}_{j+1,n+1} \Delta t \end{Bmatrix} = \frac{1}{\gamma} \begin{Bmatrix} \mathbf{u}_{j-1,n+1} \\ \mathbf{u}_{j,n+1} \\ \mathbf{u}_{j+1,n+1} \end{Bmatrix} - \frac{1}{\gamma} \begin{Bmatrix} \mathbf{u}_{j-1,n} \\ \mathbf{u}_{j,n} \\ \mathbf{u}_{j+1,n} \end{Bmatrix} - \frac{1-\gamma}{\gamma} \begin{Bmatrix} \dot{\mathbf{u}}_{j-1,n} \Delta t \\ \dot{\mathbf{u}}_{j,n} \Delta t \\ \dot{\mathbf{u}}_{j+1,n} \Delta t \end{Bmatrix}. \quad (5.102)$$

By performing the assembly for two neighbouring elements and after a series of straightforward but tedious algebraic manipulations based on the equations (5.98) and (5.102), a difference stencil in space and time may be obtained. The final expression is an equation in terms of  $3 \times 3 = 9$  nodal values of  $u^h$ . It is rather complicated and is not given here.

## 5.2.2 Space-Time Finite Element Methods

In order to proceed with the space-time formulations notions of a space-time slab and a space-time finite element domain are introduced as  $Q_n = \Omega \times I_n$  and  $Q_n^e = \Omega^e \times I_n$ , respectively. Then, the trial and test function spaces for the space-time formulations can be, respectively, defined as

$$\begin{aligned} \mathcal{U}_n^h &= \left\{ u^h \in H^1(Q_n) \mid u^h|_{(x,t) \in Q_n^e} \in P_1(Q_n^e), u^h(L, t) = u^h(0, t) \right\} \\ \mathcal{W}_n^h &= \left\{ w^h \in H^1(Q_n) \mid w^h|_{(x,t) \in Q_n^e} \in P_1(Q_n^e), w^h(L, t) = w^h(0, t) \right\}, \end{aligned} \quad (5.103)$$

where  $P_1(Q_n^e)$  denotes the space of linear polynomials on the  $n$ -th space-time slab. In the following, linear interpolation shall be employed in space, whereas the interpolation in time may be piecewise linear or piecewise constant. Note that, due to the periodic boundary conditions,  $\mathcal{U}_n^h = \mathcal{W}_n^h$ .

The space-time finite element formulation is obtained from (5.81) by employing  $u^h \in \mathcal{U}_{n+1}^h$  and  $w^h \in \mathcal{W}_{n+1}^h$ , by integration over the time interval  $I_{n+1}$  and by adding the jump term in order to weakly enforce continuity at the space-time slab boundaries. Thus, the fully discretised space-time formulation reads: For each space-time slab  $Q_n, n = 1, 2, \dots, N$ , find  $u^h \in \mathcal{U}_{n+1}^h$  such that for any  $w^h \in \mathcal{W}_{n+1}^h$

$$\begin{aligned} \int_{t_n}^{t_{n+1}} \left( \int_0^L w^h \left( \dot{u}^h + a u_{,x}^h \right) + \mu w_{,x}^h u_{,x}^h \, dx + \sum_{j=1}^{n_{el}} \int_{x_{j-1}}^{x_j} \tau^j a w_{,x}^h \left( \dot{u}^h + a u_{,x}^h \right) \, dx \right) dt \\ + \int_0^L w_n^{h+} \left( u_n^{h+} - u_n^{h-} \right) \, dx = 0, \end{aligned} \quad (5.104)$$

where the weighting factor  $\beta$  for the jump term is omitted since it has been shown in Sections 5.1.2.2 and 5.1.2.4 that the optimal accuracy is obtained for  $\beta = 1$ . For continuous in time formulations the jump term, of course, disappears. The stabilisation factor  $\tau$  is evaluated according to (5.82).

*REMARK 5.1: The time derivative  $\dot{w}^h$ .* Unlike the semi-discrete schemes in Section 5.2.1, the space-time methods allow the evaluation of the expression  $\dot{w}^h$ . Thus, if the stabilised finite element formulation is obtained by

following the Galerkin/least-squares (GLS) strategy (see Section 4.2.1), then the integrand in the stabilisation term will read

$$\tau^j \left( \dot{w}^h + a w_{,x}^h \right) \left( \dot{w}^h + a u_{,x}^h \right) . \quad (5.105)$$

As before, the diffusion terms have disappeared due to the linear interpolation in space. Using (5.105) in (5.104) has, however, been observed to be problematic. For the methods employing piecewise linear interpolation in time, the expression  $\tau^j(\dot{w}^h + a w_{,x}^h)$ , with which the residual in the stabilisation term is weighted, becomes very large as  $\Delta t$  is refined. Numerical experiments with a piecewise linear continuous space-time method including  $\dot{w}^h$  have shown, that the scheme converges only for  $\mu = 0$ , when the residual in the stabilisation term is evaluated accurately. It seems that, within the framework of linear interpolation in space, the term  $\dot{w}^h$  should be omitted, or, alternatively, the parameter  $\tau$  has to be chosen such that it approaches zero as  $\Delta t \rightarrow 0$  (compare Remark 4.1). In some publications concerned with this method the latter approach has been taken, see *e. g.* Tezduyar *et al* [121, 122], Shakib and Hughes [108], Hughes *et al* [69].

### 5.2.2.1 Linear Continuous Finite Elements (LC)

The shape functions are linear in time and space and can be written as

$$\begin{aligned} N_{j,n} &= \hat{N}_{j,n}(x, t) = \frac{x_{j+1} - x}{\Delta x} \frac{t_{n+1} - t}{\Delta t} \\ N_{j+1,n} &= \hat{N}_{j+1,n}(x, t) = \frac{x - x_j}{\Delta x} \frac{t_{n+1} - t}{\Delta t} \\ N_{j,n+1} &= \hat{N}_{j,n+1}(x, t) = \frac{x_{j+1} - x}{\Delta x} \frac{t - t_n}{\Delta t} \\ N_{j+1,n+1} &= \hat{N}_{j+1,n+1}(x, t) = \frac{x - x_j}{\Delta x} \frac{t - t_n}{\Delta t} \end{aligned} \quad (5.106)$$

for  $(x, t) \in Q_{n+1}^{j+1}$ . The approximate solution for the space-time slab  $Q_{n+1}$  can then be written as

$$u^h(x, t) = \sum_{j=0}^{n_{el}-1} \left\{ N_{j,n}, N_{j,n+1}, N_{j+1,n}, N_{j+1,n+1} \right\} \cdot \left\{ \begin{array}{c} \mathbf{u}_{j,n} \\ \mathbf{u}_{j,n+1} \\ \mathbf{u}_{j+1,n} \\ \mathbf{u}_{j+1,n+1} \end{array} \right\} . \quad (5.107)$$

The test function is expressed as

$$w^h(x, t) = \sum_{j=0}^{n_{el}-1} \left\{ N_{j,n+1}, N_{j+1,n+1} \right\} \cdot \left\{ \begin{array}{c} \mathbf{w}_{j,n+1} \\ \mathbf{w}_{j+1,n+1} \end{array} \right\} . \quad (5.108)$$

Recalling that for the continuous in time finite element method the jump term vanishes, the variational formulation (5.104) yields

$$\sum_{j=1}^{n_{el}} \left( \mathbf{A} \begin{Bmatrix} \mathbf{u}_{j,n+1} \\ \mathbf{u}_{j+1,n+1} \end{Bmatrix} + \mathbf{B} \begin{Bmatrix} \mathbf{u}_{j,n} \\ \mathbf{u}_{j+1,n} \end{Bmatrix} \right) = \mathbf{0}, \quad (5.109)$$

where the matrices  $\mathbf{A}$  and  $\mathbf{B}$  coincide with those in (5.92) and (5.93) of the generalised midpoint rule, if the parameter  $\gamma$  is set to  $2/3$ . Consequently, the  $3 \times 2$  space-time difference stencil which may be obtained from the assembly of two neighbouring finite elements in the space-time slab  $Q_{n+1}$  is a special case of (5.94).

### 5.2.2.2 Constant Discontinuous Finite Elements (CD)

The shape functions are linear in space and constant in time allowing discontinuities at the space-time slab boundaries. Recalling from Section 5.1.2.2 that  $\mathbf{u}_{j,n}^{h+} = \mathbf{u}_{j,n+1}^{h-}$ , the approximate solution  $\mathbf{u}_{j,n}^{h+}$  at  $\mathbf{t}_n^+$  can be eliminated. It follows that

$$\begin{aligned} N_{j,n+1}^- &= \hat{N}_{j,n+1}^-(x, t) = \frac{\mathbf{x}_{j+1} - x}{\Delta x} \\ N_{j+1,n+1}^- &= \hat{N}_{j+1,n+1}^-(x, t) = \frac{x - \mathbf{x}_j}{\Delta x}, \end{aligned} \quad (5.110)$$

for  $(x, t) \in Q_{n+1}^{j+1}$ . The derivative of the shape functions with respect to time obviously vanishes. The approximate solution for the space-time slab  $Q_{n+1}$  can then be written as

$$u^h(x, t) = \sum_{j=0}^{n_{el}-1} \left\{ N_{j,n+1}^-, N_{j+1,n+1}^- \right\} \cdot \begin{Bmatrix} \mathbf{u}_{j,n+1}^- \\ \mathbf{u}_{j+1,n+1}^- \end{Bmatrix}. \quad (5.111)$$

The test function  $w^h(x)$  is defined similarly. Using these expressions in the variational equation (5.104) yields

$$\sum_{j=0}^{n_{el}-1} \left( \mathbf{A} \begin{Bmatrix} \mathbf{u}_{j,n+1}^- \\ \mathbf{u}_{j+1,n+1}^- \end{Bmatrix} + \mathbf{B} \begin{Bmatrix} \mathbf{u}_{j,n}^- \\ \mathbf{u}_{j+1,n}^- \end{Bmatrix} \right) = \mathbf{0}. \quad (5.112)$$

The  $2 \times 2$  matrices  $\mathbf{A}$  and  $\mathbf{B}$  are obtained as

$$\mathbf{A} = \frac{1}{6} \begin{bmatrix} 2 & 1 \\ 1 & 2 \end{bmatrix} + \frac{a \Delta t}{2 \Delta x} \begin{bmatrix} -1 & 1 \\ -1 & 1 \end{bmatrix} + \frac{\Delta t (\mu + \tau a^2)}{\Delta x^2} \begin{bmatrix} 1 & -1 \\ -1 & 1 \end{bmatrix} \quad (5.113)$$

$$\mathbf{B} = -\frac{1}{6} \begin{bmatrix} 2 & 1 \\ 1 & 2 \end{bmatrix}. \quad (5.114)$$

By assembling the matrices of two neighbouring elements a difference stencil with  $3 \times 2 = 6$  points in the space-time domain is easily obtained. Note that the expressions (5.92) and (5.93) of the generalised midpoint rule for  $\gamma = 1$  (backward Euler) differ from (5.113) and (5.114) only by an additional stabilisation term in  $\mathbf{B}$ .

### 5.2.2.3 Modified Continuous Finite Elements (MC)

For the modified continuous scheme introduced in Section 5.1.2.3, a derivation along the lines of Sections 5.2.2.1 and 5.2.2.2 renders a  $3 \times 2$  space-time difference stencil, which coincides with the stencil (5.94) for  $\gamma = 1/2$  ( $\rightarrow$  trapezoidal rule).

### 5.2.2.4 Linear Discontinuous Finite Elements (LD)

The shape functions are linear in time and space and identical to the ones introduced in (5.106) for the linear continuous space-time finite element scheme. The approximate solution for the space-time slab  $Q_{n+1}$  can be written as

$$u^h(x, t) = \sum_{j=0}^{n_{\text{el}}-1} \{N_{j,n}, N_{j,n+1}, N_{j+1,n}, N_{j+1,n+1}\} \cdot \begin{Bmatrix} \mathbf{u}_{j,n}^+ \\ \mathbf{u}_{j,n+1}^- \\ \mathbf{u}_{j+1,n}^+ \\ \mathbf{u}_{j+1,n+1}^- \end{Bmatrix}. \quad (5.115)$$

The test function  $w^h$  is discretised similarly. The variational formulation (5.104) yields

$$\sum_{j=0}^{n_{\text{el}}-1} \left( \mathbf{A} \begin{Bmatrix} \mathbf{u}_{j,n}^+ \\ \mathbf{u}_{j,n+1}^- \\ \mathbf{u}_{j+1,n}^+ \\ \mathbf{u}_{j+1,n+1}^- \end{Bmatrix} + \mathbf{B} \begin{Bmatrix} \mathbf{u}_{j,n-1}^+ \\ \mathbf{u}_{j,n}^- \\ \mathbf{u}_{j+1,n-1}^+ \\ \mathbf{u}_{j+1,n}^- \end{Bmatrix} \right) = \mathbf{0}, \quad (5.116)$$

where the  $4 \times 4$  matrices  $\mathbf{A}$  and  $\mathbf{B}$  are obtained as

$$\begin{aligned} \mathbf{A} &= \frac{1}{12} \begin{bmatrix} 2 & 2 & 1 & 1 \\ -2 & 2 & -1 & 1 \\ 1 & 1 & 2 & 2 \\ -1 & 1 & -2 & 2 \end{bmatrix} + \frac{\tau a}{4 \Delta x} \begin{bmatrix} 1 & -1 & 1 & -1 \\ 1 & -1 & 1 & -1 \\ -1 & 1 & -1 & 1 \\ -1 & 1 & -1 & 1 \end{bmatrix} \\ &+ \frac{a \Delta t}{12 \Delta x} \begin{bmatrix} -2 & -1 & 2 & 1 \\ -1 & -2 & 1 & 2 \\ -2 & -1 & 2 & 1 \\ -1 & -2 & 1 & 2 \end{bmatrix} + \frac{\Delta t (\mu + \tau a^2)}{6 \Delta x^2} \begin{bmatrix} 2 & 1 & -2 & -1 \\ 1 & 2 & -1 & -2 \\ -2 & -1 & 2 & 1 \\ -1 & -2 & 1 & 2 \end{bmatrix} \quad (5.117) \end{aligned}$$

$$\mathbf{B} = -\frac{1}{6} \begin{bmatrix} 0 & 2 & 0 & 1 \\ 0 & 0 & 0 & 0 \\ 0 & 1 & 0 & 2 \\ 0 & 0 & 0 & 0 \end{bmatrix}. \quad (5.118)$$

After the assembly of four neighbouring elements and the tedious elimination of the nodal unknowns at  $t_n^+$ , a difference stencil in terms of  $5 \times 2 = 10$  nodal solution variables at  $t_n^-$  and  $t_{n+1}^-$  may be obtained.

### 5.2.3 Fourier Analysis

The difference stencils derived in Section 5.2.2 are now used to establish the properties of the different time integration schemes when combined with the stabilised finite element method. For this purpose, a Fourier analysis is performed.

Motivated by the exact solution (5.78), the approximation  $u^h$  may be written as

$$\mathbf{u}_{j,n}^h = b (\zeta^h)^n (e^{iK\Delta x})^j \quad (5.119)$$

with the numerical amplification factor  $\zeta^h$  defined as

$$\zeta^h = e^{(-\xi^h + i\omega^h)\Delta t}. \quad (5.120)$$

Due to the linear character of the problem the solution is considered for only one of the Fourier terms of (5.76). Thus, the subscript  $m$  is omitted henceforth. The expressions for  $\xi^h$  and  $\omega^h$ , which need to be determined from the time integration scheme under consideration, are the numerical counterparts of the exact damping factor and the exact frequency, respectively, given by (5.79).

By employing (5.119) in the difference stencils the resulting equations can be solved for  $\zeta^h$ . Similarly to Section 5.1, the numerical damping factor  $\xi^h$ , the numerical frequency  $\omega^h$  and the spectral radius  $\rho^h$  can be obtained from the equations (5.9) and (5.6) or (5.27), respectively. The resulting expressions depend on the constants  $\mu$  and  $a$ , on the stabilisation parameter  $\tau$ , the spatial wave number  $K$  and the space and time increments  $\Delta x$  and  $\Delta t$ . It can be shown that for every method the spectral radius satisfies  $\rho^h \leq 1$  for any  $\Delta x \geq 0$ ,  $\Delta t \geq 0$  and  $\tau \geq 0$ . Thus, all the schemes are unconditionally stable in time as it is expected from the analysis in Section 5.1. The numerical damping factor  $\xi^h$  and the numerical frequency  $\omega^h$  can be expanded as power series of  $\Delta x$ ,  $\Delta t$  and  $\tau$ . The results are described in the following.

### 5.2.3.1 Power Series Expansions of $\xi^h$ and $\omega^h$

Table 5.3 shows the lowest order terms of  $\Delta x$ ,  $\Delta t$  and  $\tau$  and the lowest order mixed terms of the errors of  $\xi^h$  and  $\omega^h$  for the case of mixed advection-diffusion ( $\mu > 0$ ). The dominant terms of the discretisation errors of the pure advection problem ( $\mu = 0$ ) are given in Table 5.4. In comparison to Table 5.3 some expressions have vanished or have been replaced by higher order or mixed terms.

The following observations are made on the basis of the series expansions of  $\xi^h$  and  $\omega^h$ :

1. *consistency.* For every method considered, the constant terms in the power series expansions of  $\xi^h$  and  $\omega^h$  are identical to the exact expressions  $\xi = \mu K^2$  and  $\omega = -a K$ . Thus, convergence is ensured for each case as  $\Delta x \rightarrow 0$ ,  $\Delta t \rightarrow 0$  and  $\tau \rightarrow 0$ .
2. *accuracy with respect to  $\Delta x$ .* The methods considered are equally accurate in terms of the spatial discretisation  $\Delta x$ . For the errors of both the damping factor  $\xi^h$  and the frequency  $\omega^h$  the lowest order terms of  $\Delta x$  are  $\Delta x^2$  or mixed terms involving  $\Delta x^2$ . It is observed that for the pure advection problem ( $\mu = 0$ ) the error of the damping factor  $\xi^h$  includes  $\Delta x$  only in mixed terms with the stabilisation parameter  $\tau$ . In this case, the discretisation in space affects numerical damping only for  $\tau > 0$ . This holds for all the integration schemes considered.
3. *accuracy with respect to  $\Delta t$ .* The errors of the damping factor and the frequency in Tables 5.3 and 5.4 show that for both the advection-diffusion and pure advection case, the power terms of  $\Delta t$  are consistent with the order of accuracy of the time integration schemes as established in Section 5.1. Apart from one exception, there are no mixed terms which involve lower powers of  $\Delta t$ .

This exception is the linear discontinuous in time finite element method. In Section 5.1.2.4 the method has been shown to be third order accurate for the model problem considered. However, in the case of the stabilised formulation for the advection-diffusion problem, the errors of the damping factor and the frequency contain the term  $\Delta t \tau$ . Hence, if the spatial mesh is coarse, such that a significant amount of stabilisation is required, then the accuracy in time of the method decreases. For the pure advection problem this undesirable phenomena is weaker since the term  $\Delta t \tau$  in the error of the damping factor is replaced by  $\Delta t^2 \tau$ .

integration method	$\xi^h$	$\omega^h$
BE, LC, GM < 1.0*	$O(\Delta x^2, \Delta t, \tau^2, \Delta x^2 \tau, \Delta t \tau)$	$O(\Delta x^4, \Delta t, \tau, \Delta x^2 \Delta t, \Delta x^2 \tau)$
AM < 1.0*	$O(\Delta x^2, \Delta t^2, \tau^2, \Delta x^2 \tau, \Delta t^2 \tau)$	$O(\Delta x^4, \Delta t^2, \tau, \Delta x^2 \Delta t^2, \Delta x^2 \tau)$
TR, GM 1.0, MC, AM 1.0	$O(\Delta x^2, \Delta t^2, \tau^2, \Delta x^2 \tau, \Delta t^2 \tau)$	$O(\Delta x^4, \Delta t^2, \tau, \Delta x^2 \Delta t^2, \Delta x^2 \tau)$
CD	$O(\Delta x^2, \Delta t, \tau)$	$O(\Delta x^4, \Delta t, \Delta x^2 \Delta t, \Delta t \tau)$
LD	$O(\Delta x^2, \Delta t^3, \tau^2, \Delta x^2 \tau, \Delta t \tau)$	$O(\Delta x^4, \Delta t^3, \tau, \Delta x^2 \Delta t^3, \Delta x^2 \tau, \Delta t \tau)$

\* The number represents the integration parameter  $\rho_\infty^h$ .

Table 5.3: Accuracy of the time integration schemes for the advection-diffusion problem ( $\mu > 0$ ); lowest order terms of  $\Delta x$ ,  $\Delta t$  and  $\tau$  and the lowest order mixed terms.

integration method	$\xi^h$	$\omega^h$
BE, LC, GM < 1.0*	$O(\Delta t, \Delta x^2 \tau)$	$O(\Delta x^4, \Delta t^2, \Delta x^2 \Delta t \tau, \Delta x^2 \tau^2)$
AM < 1.0*	$O(\Delta t^3, \Delta x^2 \Delta t^2 \tau, \Delta x^2 \tau)$	$O(\Delta x^4, \Delta t^2, \Delta x^2 \tau^2)$
TR, GM 1.0, MC, AM 1.0	$O(\Delta x^2 \Delta t^2 \tau, \Delta x^2 \tau)$	$O(\Delta x^4, \Delta t^2, \Delta x^2 \tau^2)$
CD	$O(\Delta t, \tau, \Delta x^2 \tau)$	$O(\Delta x^4, \Delta t^2, \Delta x^2 \Delta t \tau, \Delta t \tau)$
LD	$O(\Delta t^3, \Delta x^2 \tau, \Delta t^2 \tau)$	$O(\Delta x^4, \Delta t^4, \Delta x^2 \tau^2, \Delta t \tau)$

\* The number represents the integration parameter  $\rho_\infty^h$ .

Table 5.4: Accuracy of the time integration schemes for the pure advection problem ( $\mu = 0$ ); lowest order terms of  $\Delta x$ ,  $\Delta t$  and  $\tau$  and the lowest order mixed terms.

Importantly, it should also be noted that for  $\mu = 0$  the damping factor  $\xi^h$  of the generalised- $\alpha$  method is almost third order accurate due to the error term  $\Delta t^3$  and the negligible mixed term  $\Delta x^2 \Delta t^2 \tau$ . In this case the damping behaviour of the scheme AM is, in fact, superior to the damping properties of the method LD.

Finally it is observed that, for pure advection, the numerical dissipation of the trapezoidal rule disappears if  $\tau = 0$ , which is consistent with the results of Section 5.1.1.1. If  $\tau > 0$ , however, the stabilisation technique introduces numerical dissipation and thus, it may make the trapezoidal rule a viable integration method for advection dominated problems.

4. *influence of the stabilisation technique on accuracy.* For the advection-diffusion problem, the stabilisation parameter  $\tau$  or the term  $\tau^2$  appear in almost every series expansion of  $\xi^h$  and  $\omega^h$ . Thus, an inappropriate choice of  $\tau$  may affect considerably the accuracy of the method.

In the case of pure advection, the terms  $\tau$  and  $\tau^2$  vanish for all schemes apart from the constant discontinuous finite element method. The stabilisation parameter then only appears in mixed terms with  $\Delta x$  or  $\Delta t$ . This is due to the fact that for  $\mu = 0$  the residual expression in the stabilised variational formulation (5.104) is recovered exactly by the linear in space finite elements and the method converges for any value of  $\tau$ . For  $\mu > 0$ , it is important that  $\tau \rightarrow 0$  as  $\Delta x \rightarrow 0$  (see also Section 4.2).

By considering that (5.82) renders

$$\tau = \frac{\Delta x^2}{12\mu} - \frac{a^4 \Delta x^4}{864\mu^3} + O(\Delta x^6) \quad (\text{advection-diffusion}) \quad (5.121)$$

$$\tau = \frac{\Delta x}{2a} \quad (\text{pure advection}), \quad (5.122)$$

it becomes evident that the formula (5.82) for the stabilisation parameter does not jeopardise the accuracy in space or time.

### 5.2.3.2 Diagrams for Relative Numerical Damping and Dispersion

The following definitions are recalled or introduced

$$\begin{aligned}
 \lambda &= \frac{L}{m} && \text{(spatial wave length)} \\
 \bar{K} &= \frac{2\pi}{\lambda} \Delta x = K \Delta x && \text{(non-dimensionalised wave number)} \\
 \alpha &= \frac{a \lambda}{2\mu} = \alpha^h \frac{2\pi}{\bar{K}} && \text{(global Peclet number)} \\
 C^h &= \frac{\Delta t}{\Delta x} a && \text{(element Courant number)}.
 \end{aligned} \tag{5.123}$$

The non-dimensionalised spatial wave number  $\bar{K}$  indicates the density of the spatial finite element mesh with respect to the wave length  $\lambda$ . In the following the terminology of short or long waves will be used for  $\bar{K} \rightarrow \pi$  or  $\bar{K} \rightarrow 0$ , respectively. The element Courant number  $C^h$  is a non-dimensionalised measure for the discretisation of time for a fixed  $\Delta x$ . Thus, for  $C^h \rightarrow 0$  the response of a fully discretised method depends only on the spatial mesh.

In Figures 5.6 – 5.12, the relative dispersion  $\omega^h/\omega$  and the relative numerical damping  $\xi^h/\xi$  or  $\xi^h/\omega$ , respectively, are displayed against  $\bar{K}$  for different values of  $C^h$ . The figures provide diagrams for the advection-diffusion ( $\alpha = 10$ ) and the pure advection case. Both the stabilised and the non-stabilised methods are considered, *i. e.* using (5.82) or  $\tau = 0$ , respectively. In this way, the effect of the stabilisation becomes transparent. Similar diagrams have been provided by Shakib and Hughes [108].

The optimal damping behaviour requires  $\xi^h$  to be identical to  $\xi$  in the range of long waves and to be significantly larger for short waves, which are not resolved properly by the spatial finite element mesh. In order to minimise dispersion, it is desirable that  $\omega^h/\omega \rightarrow 1$  in the long wave response, which is not damped out by numerical dissipation.

The detailed discussion of the Figures 5.6 – 5.12 follows on page 113.

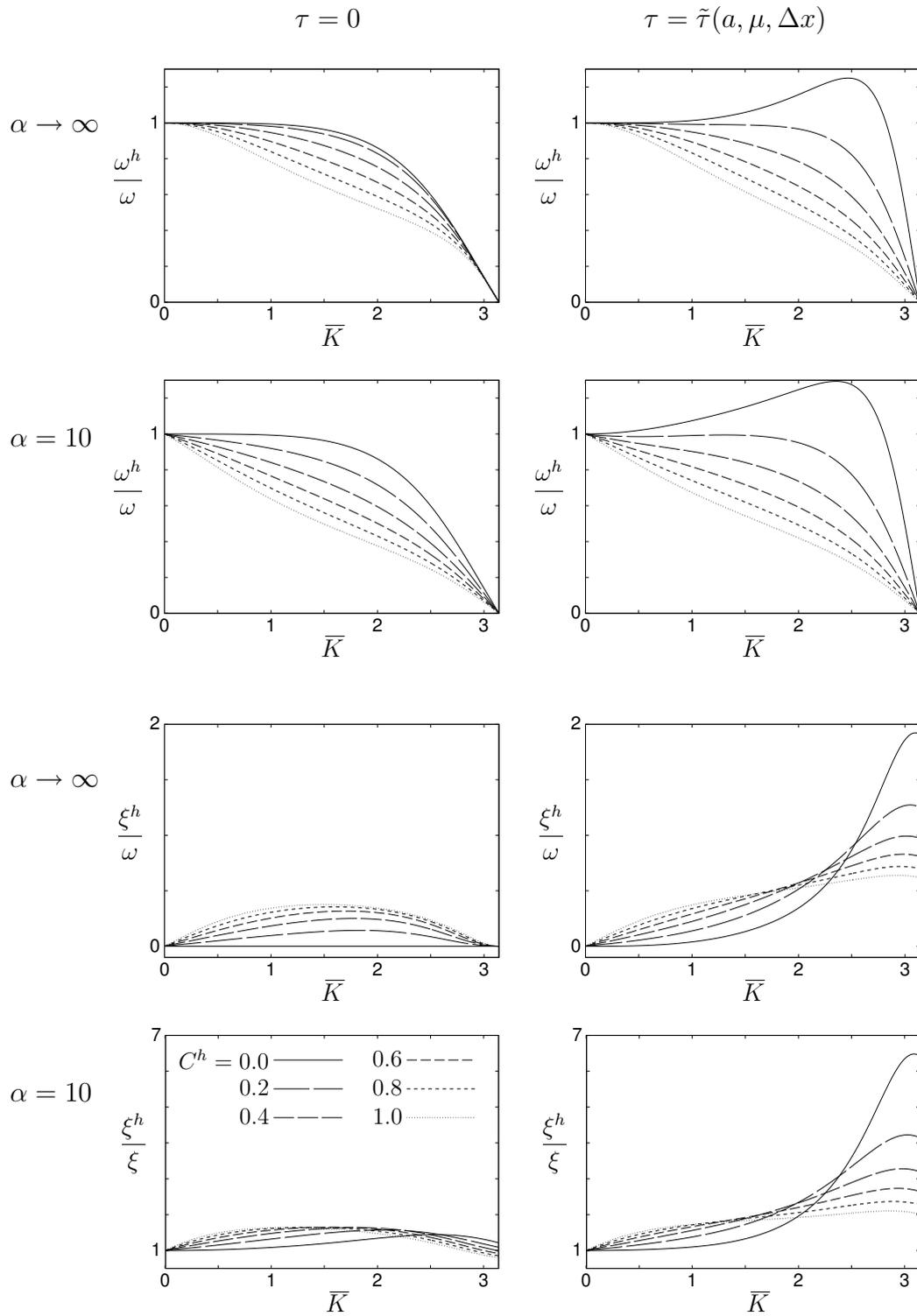


Figure 5.6: Numerical damping and dispersion; BE, GM  $\rho_\infty^h = 0.0$ ;  $\tilde{\tau}(a, \mu, \Delta x)$  according to (5.82).

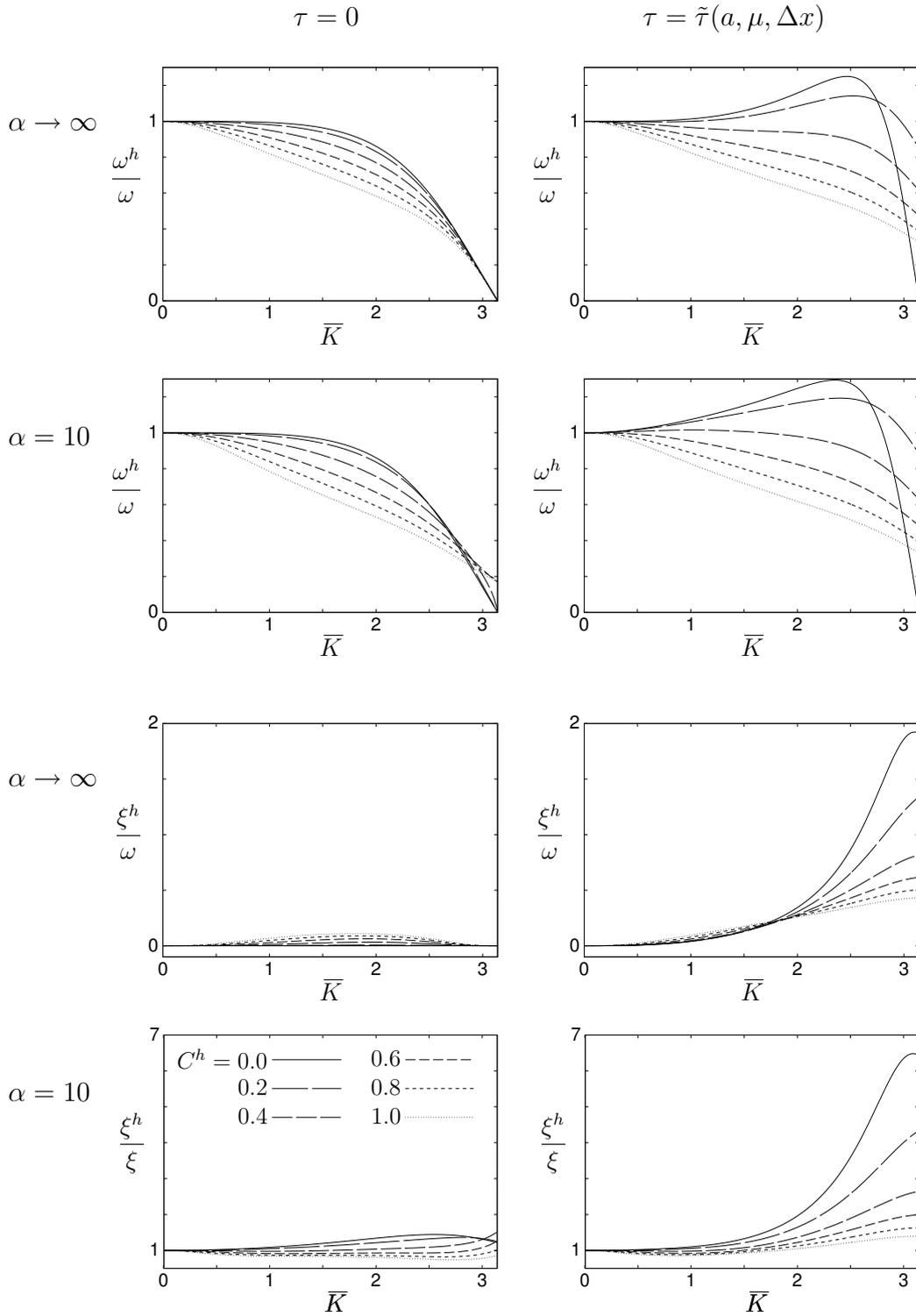


Figure 5.7: Numerical damping and dispersion; AM  $\rho_\infty^h = 0.0$ ;  $\tilde{\tau}(a, \mu, \Delta x)$  according to (5.82).

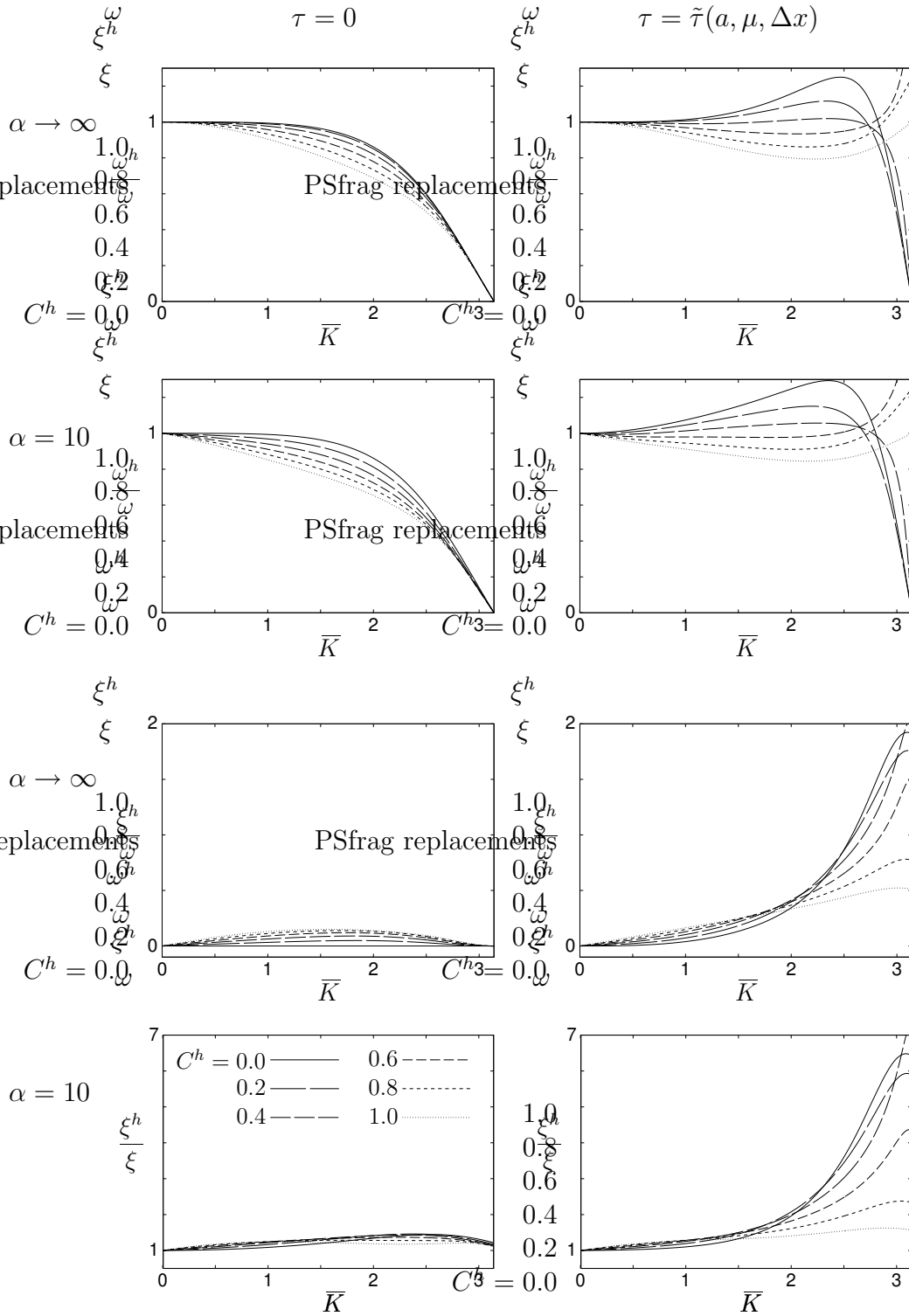


Figure 5.8: Numerical damping and dispersion; LC, GM  $\rho_\infty^h = 0.5$ ;  $\tilde{\tau}(a, \mu, \Delta x)$  according to (5.82).

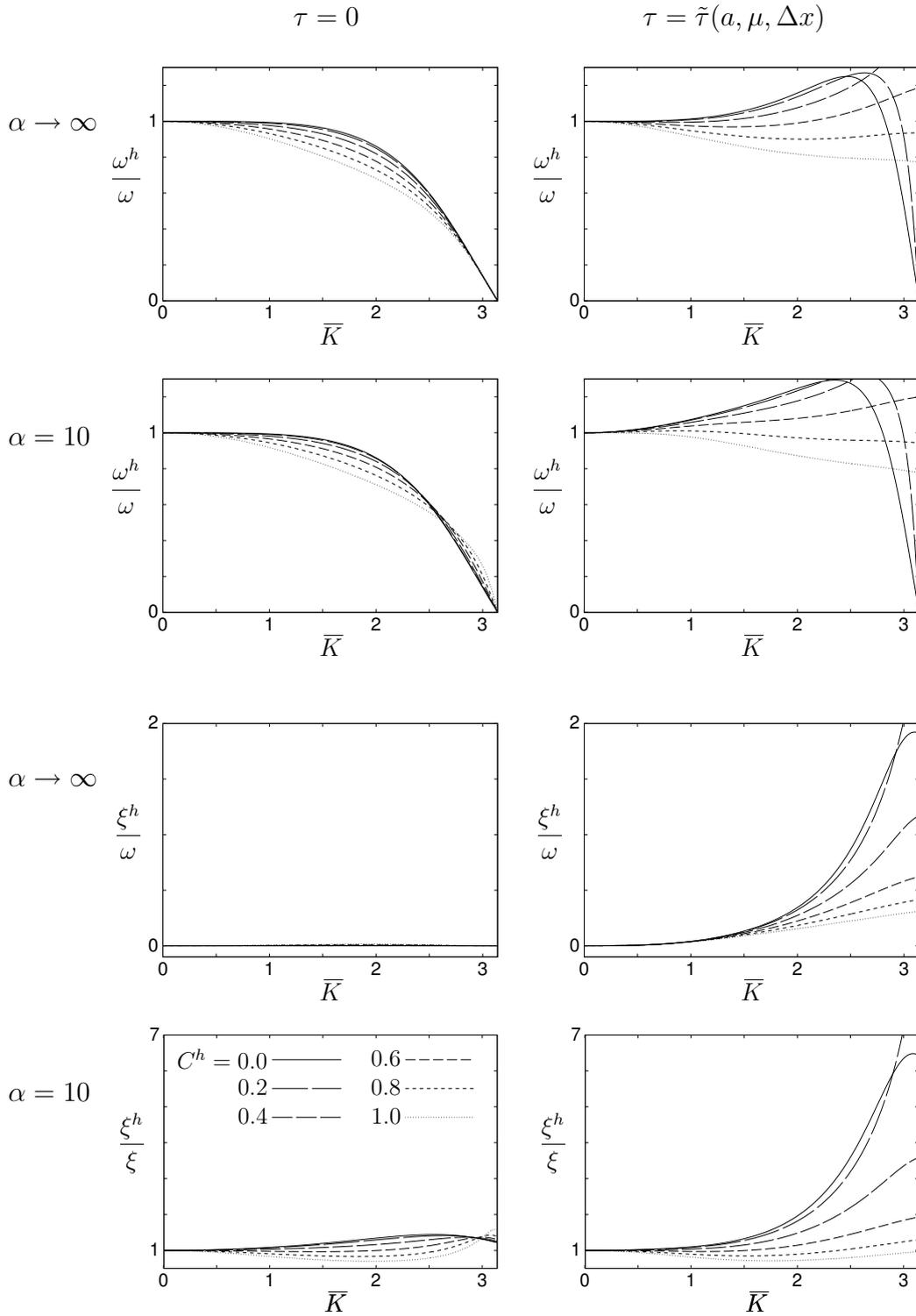


Figure 5.9: Numerical damping and dispersion; AM  $\rho_\infty^h = 0.5$ ;  $\tilde{\tau}(a, \mu, \Delta x)$  according to (5.82).

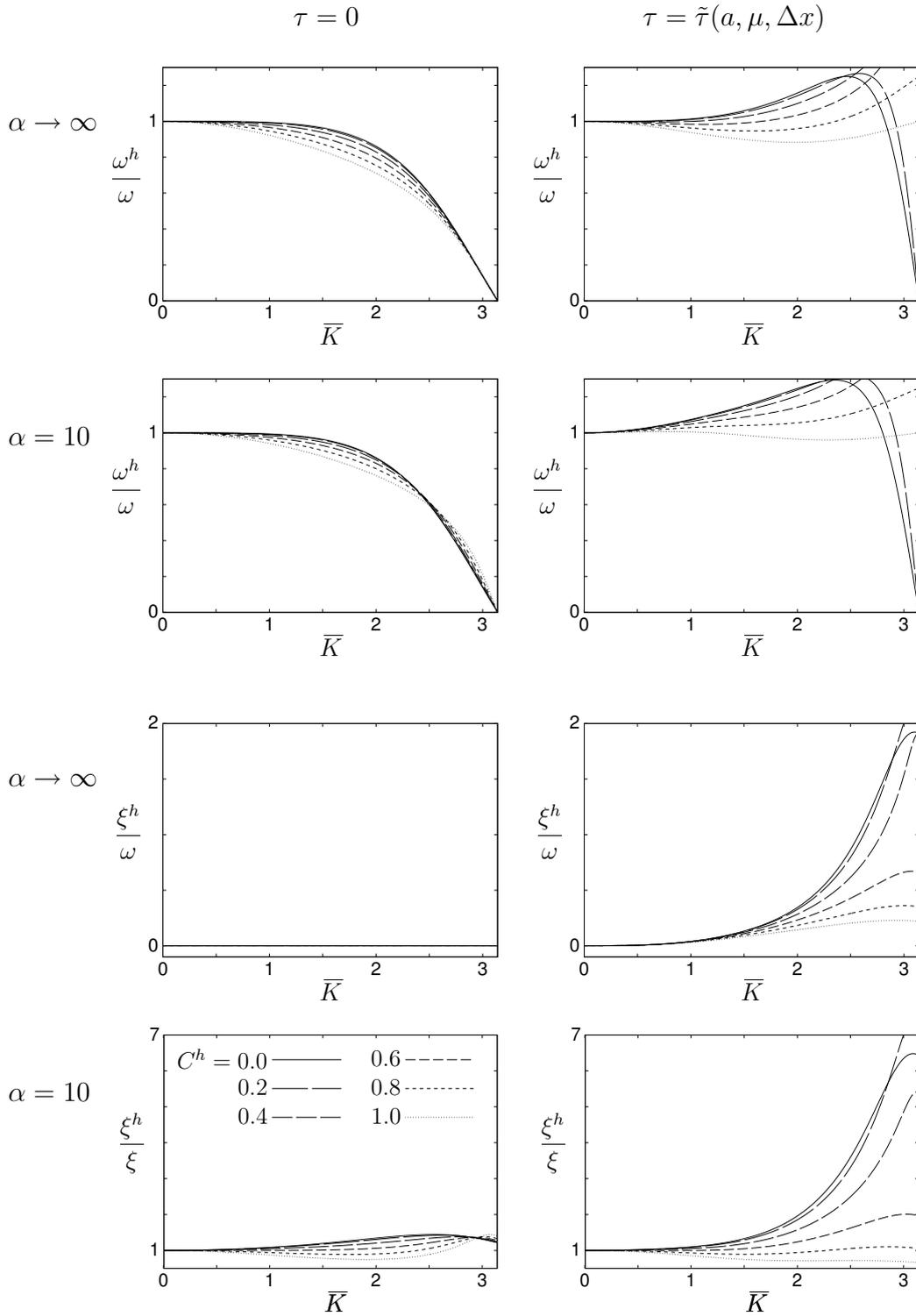


Figure 5.10: Numerical damping and dispersion; TR, MC, GM  $\rho_\infty^h = 1.0$ , AM  $\rho_\infty^h = 1.0$ ;  $\tilde{\tau}(a, \mu, \Delta x)$  according to (5.82).

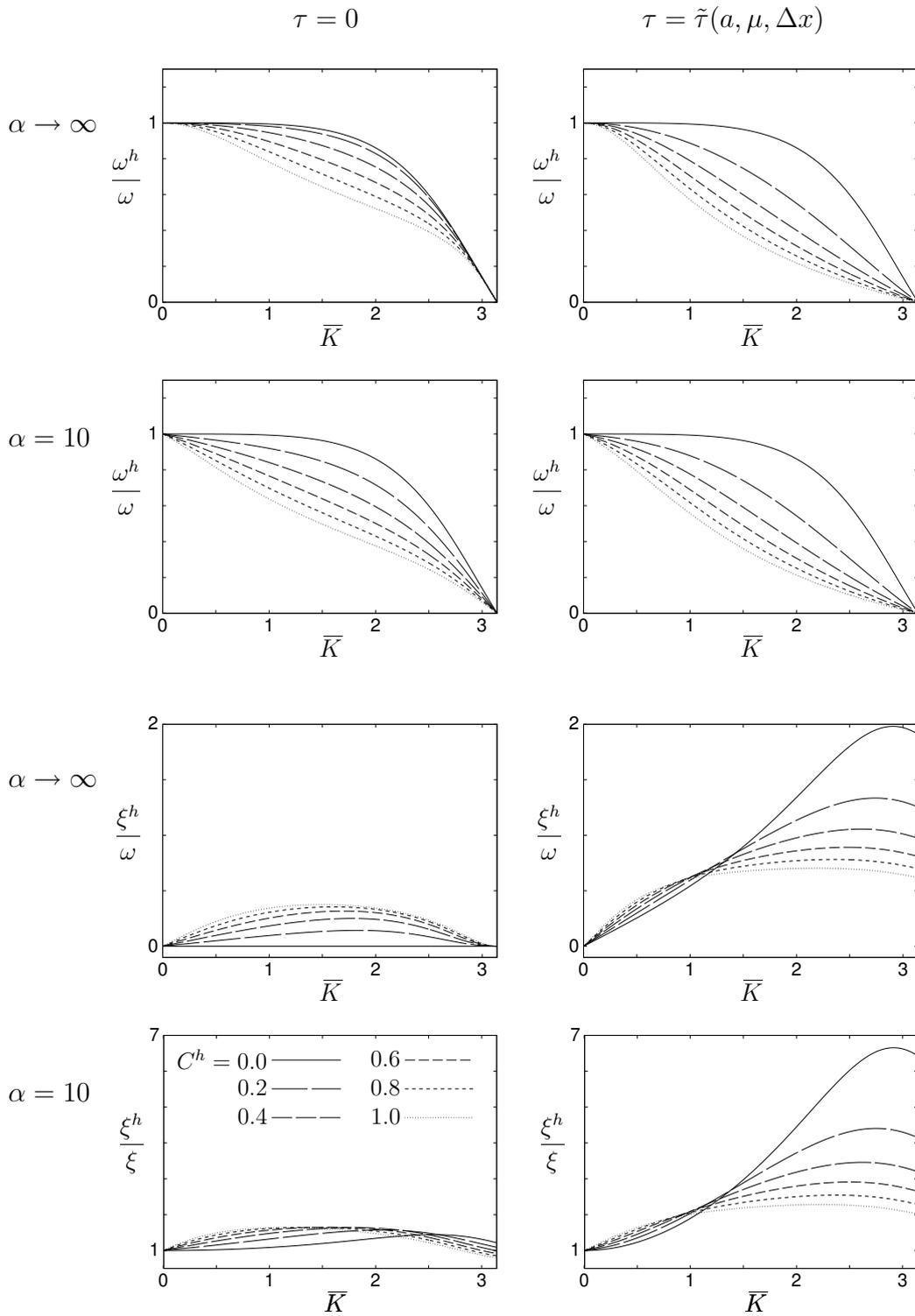


Figure 5.11: Numerical damping and dispersion; CD;  $\tilde{\tau}(a, \mu, \Delta x)$  according to (5.82).

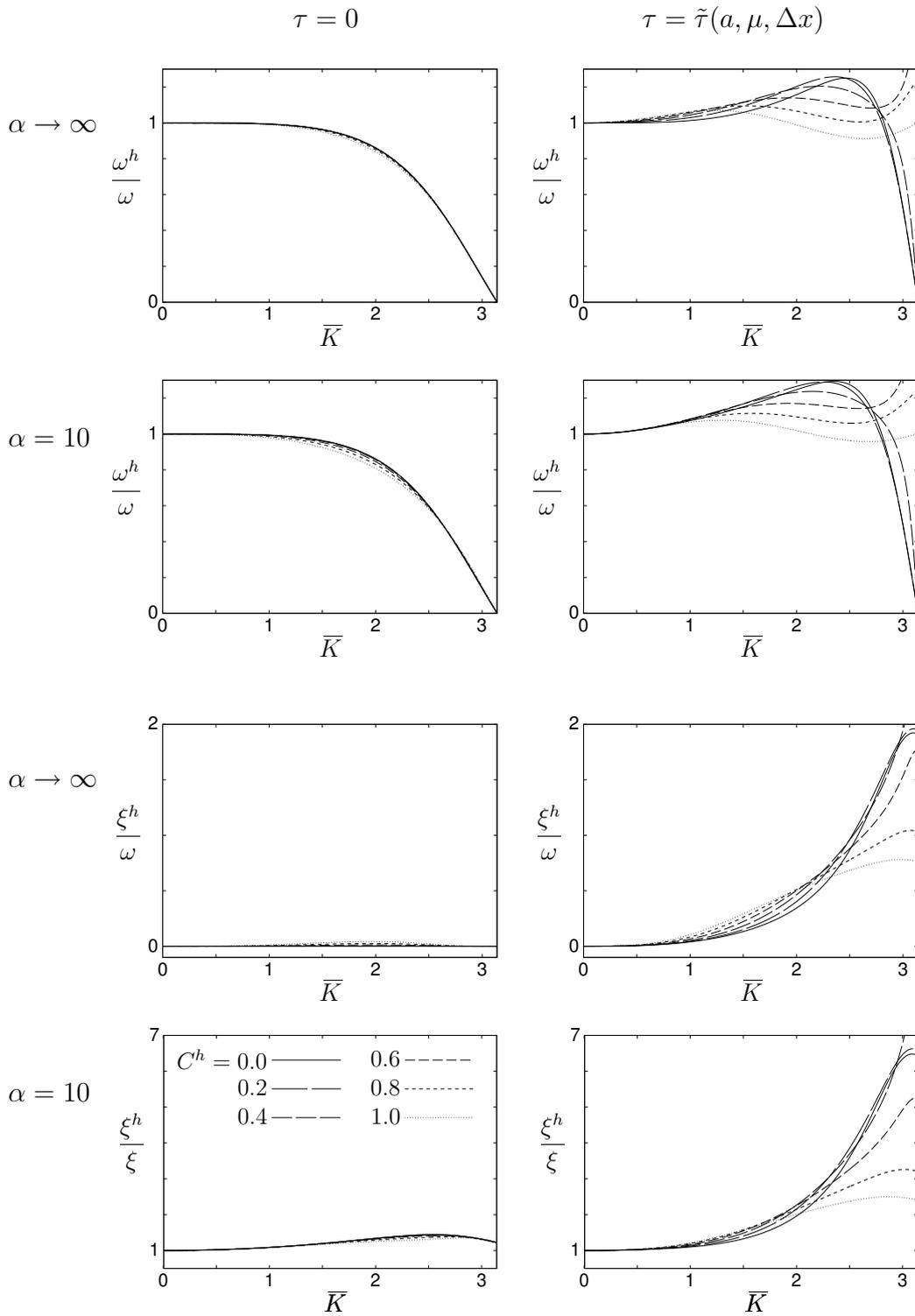


Figure 5.12: Numerical damping and dispersion; LD;  $\tilde{\tau}(a, \mu, \Delta x)$  according to (5.82).

The following observations can be made from the Figures 5.6 – 5.12:

1. *influence of the stabilisation on damping and frequency characteristics.* In the long wave range ( $\bar{K} \rightarrow 0$ ) the difference between the characteristics of the stabilised methods and the standard Galerkin schemes is negligible. This is due to the fact that, the parameter  $\tau$  as defined by (5.82) is proportional to  $\bar{K}$  (if  $\alpha$  is large) or  $\bar{K}^2$  (if  $\alpha$  is small) and thus,  $\tau$  vanishes as  $\bar{K} \rightarrow 0$ . In the short wave range the stabilised formulation introduces a significant amount of additional numerical dissipation for each of the methods considered. This is clearly welcome, especially for advection dominated problems, for which the numerical damping associated with the standard Galerkin methods ( $\tau = 0$ ) disappears as  $C^h \rightarrow 0$ .
2. *limit behaviour as  $\Delta t \rightarrow 0$ .* It can be observed that, apart from one exception, the diagrams for damping and dispersion become identical for all the methods considered as  $C^h \rightarrow 0$ . Thus, every time integration scheme converges to the same mesh dependent solution, if the time step size  $\Delta t$  is reduced. The only exception is the constant discontinuous space-time finite element method. This is due to the fact that the time derivative  $\dot{u}^h$  in the stabilisation term vanishes.

The qualitative and quantitative deviation of the diagrams associated with different Courant numbers from the mesh dependent limit solution depends on the method under consideration. Thus, a large Courant number may render different magnitudes of the temporal discretisation error as well as qualitatively different behaviour of the approximate solution, *e. g.* numerical oscillations, excessive numerical damping, too fast or too slow propagation of waves (see 3. and 4.).

3. *generalised midpoint rule and generalised- $\alpha$  method.* For  $\rho_\infty^h = 1$  these two schemes coincide with the trapezoidal rule, but for  $\rho_\infty^h < 1$ , the following observations can be made on the basis of the Figures 5.6 – 5.10.

For the generalised- $\alpha$  method the long wave range where the diagrams associated with different values of  $C^h$  almost coincide is wider than for the generalised midpoint rule. Thus, on the same spatial mesh the generalised- $\alpha$  method can be expected to render significantly more accurate results. This is due to the second order accuracy with respect to  $\Delta t$ .

It is also possible to predict the different qualitative behaviour of the methods. As  $C^h \rightarrow 0$ , the generalised midpoint rule approaches the mesh dependent limit of the long wave damping from above. Thus, for

$C^h > 0$ , there is more damping of the long waves than for  $C^h = 0$ . However, the generalised- $\alpha$  method, if  $\rho_\infty^h > \epsilon \approx 0.35$ , exhibits less numerical dissipation for  $C^h > 0$  than for the mesh dependent limit  $C^h = 0$ . In other words, for high Peclet numbers  $\alpha$ , the solutions obtained with the generalised midpoint rule can be expected to be smoother for  $C^h > 0$  than for  $C^h = 0$ , whereas the generalised- $\alpha$  method may yield solutions which exhibit more numerical oscillations for  $C^h > 0$  than for  $C^h = 0$ .

4. *space-time finite element methods.* As known from the comparison of the difference stencils, the space-time methods LC and MC are identical to the generalised midpoint schemes based on  $\rho_\infty^h = 0.5$  and  $\rho_\infty^h = 1.0$ , respectively. It has also been shown that the non-stabilised version of the method CD coincides with the non-stabilised generalised midpoint scheme for  $\rho_\infty^h = 0$  ( $\rightarrow$  backward Euler). Interestingly, the Figures 5.6 and 5.11 show, that the stabilised method CD exhibits substantially more numerical dissipation, even in the long wave range, than the corresponding stabilised version of GM with  $\rho_\infty^h = 0$ .

The diagrams associated with the non-stabilised linear discontinuous in time space-time finite element method clearly show the superior convergence behaviour of  $\xi^h$  and  $\omega^h$  as  $C^h \rightarrow 0$ , due to the third order accuracy in time of the method. The diagrams for  $C^h > 0$  and  $C^h = 0$  almost coincide. However, the corresponding stabilised formulation does not appear to be generally superior to the generalised- $\alpha$  method. Especially for the case of pure advection, the diagrams associated with the stabilised method LD suggest a less favourable damping behaviour than the scheme AM. This confirms the observation made in Section 5.2.3.1, that the stabilisation technique has reduced the accuracy in time of the linear discontinuous finite element method.

## 5.2.4 Example

The finite element methods for the one dimensional unsteady advection-diffusion problem described in Sections 5.2.1 and 5.2.2 can be easily implemented. The example considered here represents the standard problem of the propagation of an initially rectangular wave, which is often used as a validation test for the time integration of advection-diffusion equations. Both pure advection and advection-diffusion cases are considered. Some characteristic results obtained from the different methods are displayed in Figures 5.13 – 5.19. They confirm the conclusions drawn from the Fourier analysis in Section 5.2.3. A discussion of the results is therefore deemed unnecessary.

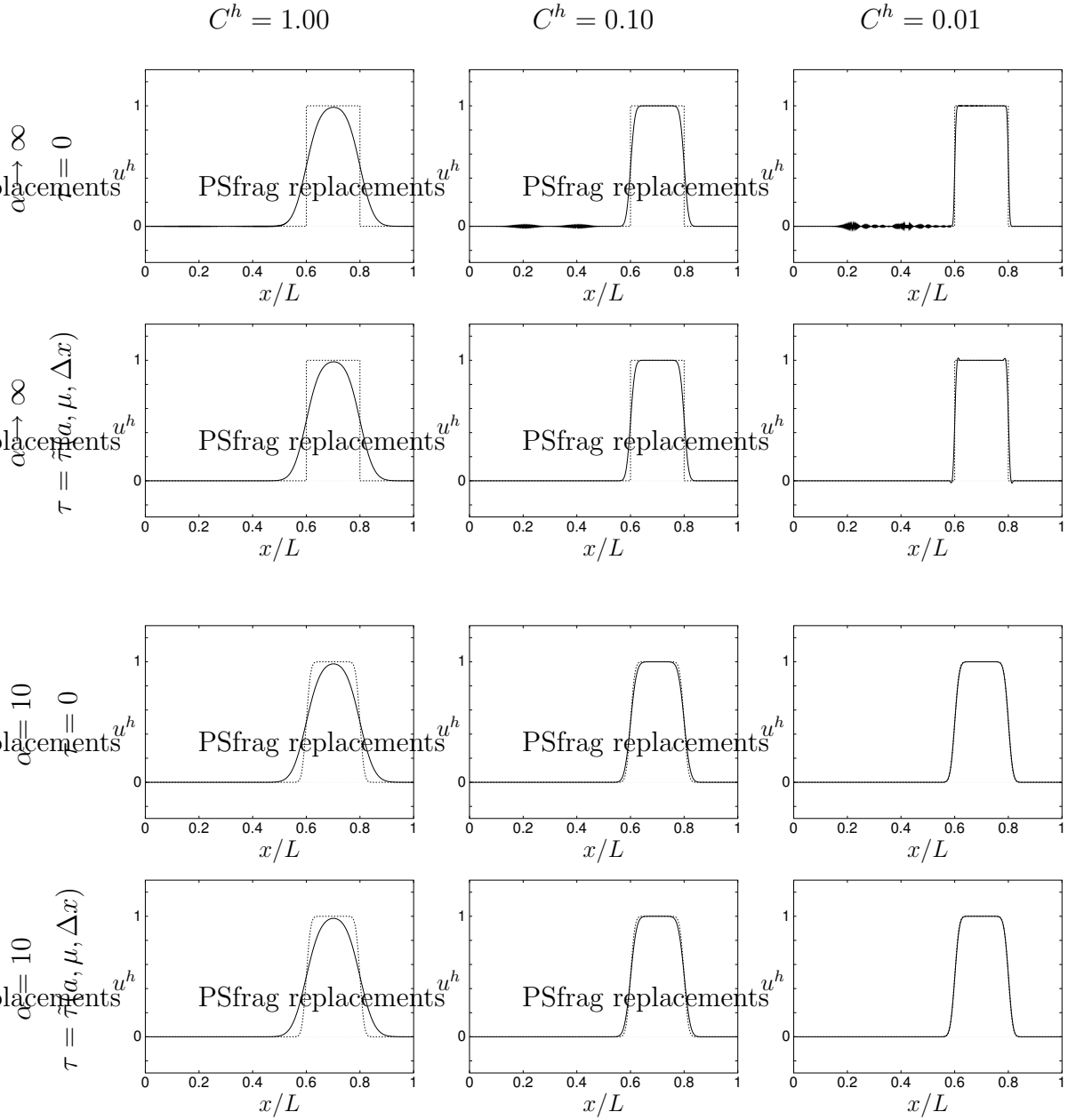


Figure 5.13: One dimensional advection-diffusion, solution  $u^h(x, t = 1.6 L/a)$  obtained with 1000 spatial elements, BE, GM  $\rho_\infty^h = 0$ ;  $\tilde{\tau}(a, \mu, \Delta x)$  according to (5.82); the exact solution is given by the dotted line.

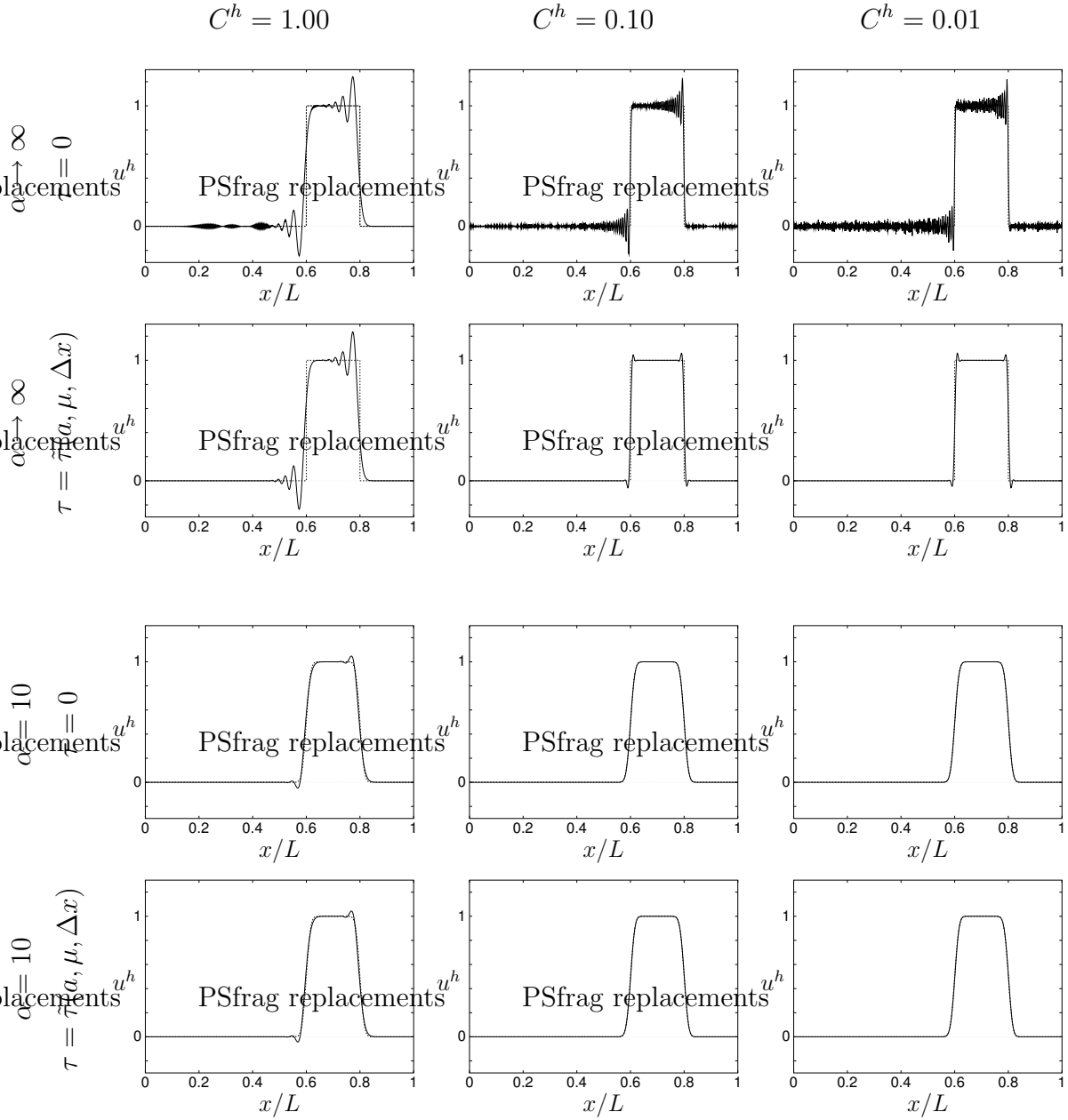


Figure 5.14: One dimensional advection-diffusion, solution  $u^h(x, t = 1.6 L/a)$  obtained with 1000 spatial elements, AM  $\rho_\infty^h = 0$ ;  $\tilde{\tau}(a, \mu, \Delta x)$  according to (5.82); the exact solution is given by the dotted line.

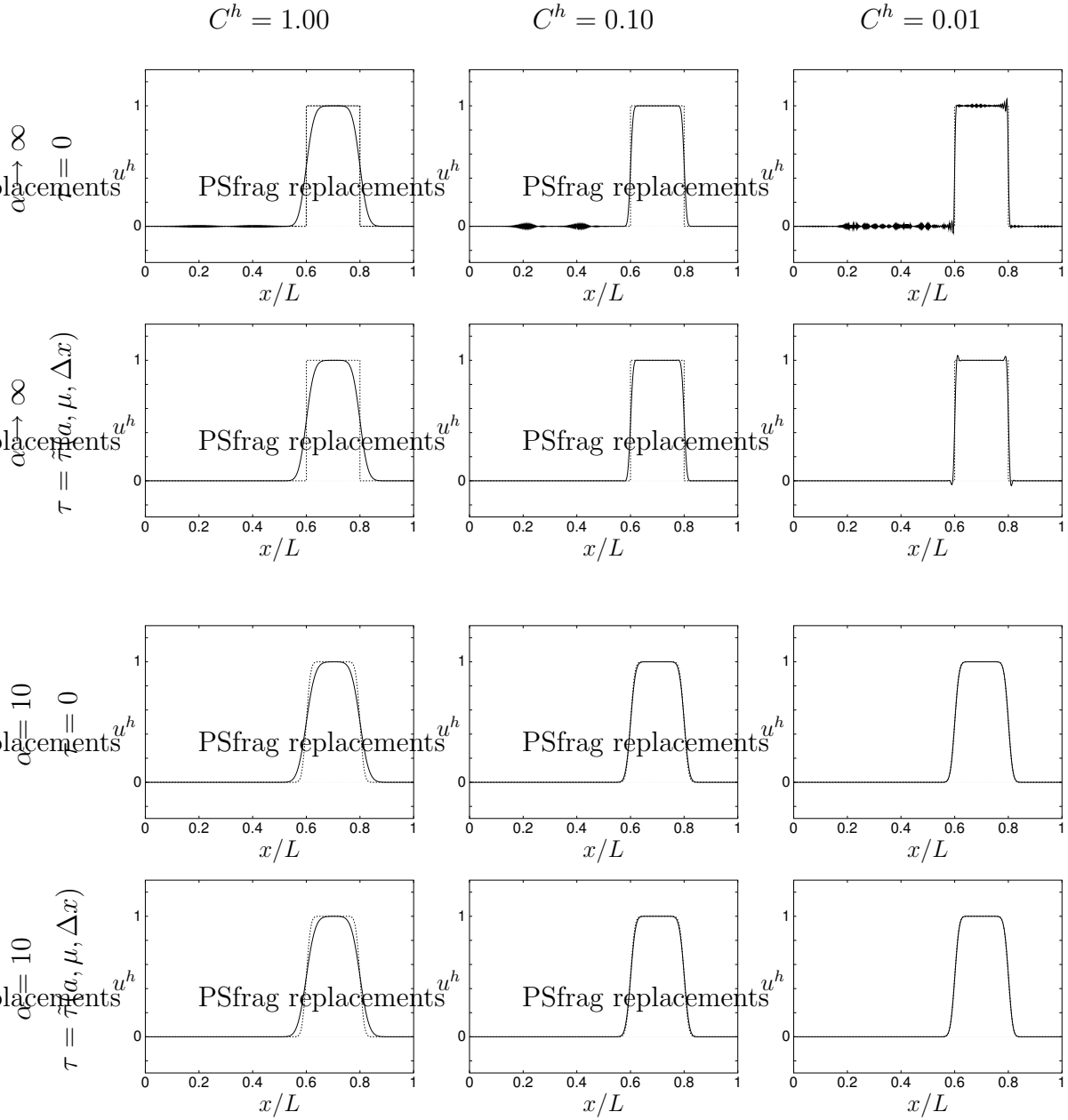


Figure 5.15: One dimensional advection-diffusion, solution  $u^h(x, t = 1.6 L/a)$  obtained with 1000 spatial elements, LC, GM  $\rho_\infty^h = 0.5$ ;  $\tilde{\tau}(a, \mu, \Delta x)$  according to (5.82); the exact solution is given by the dotted line.

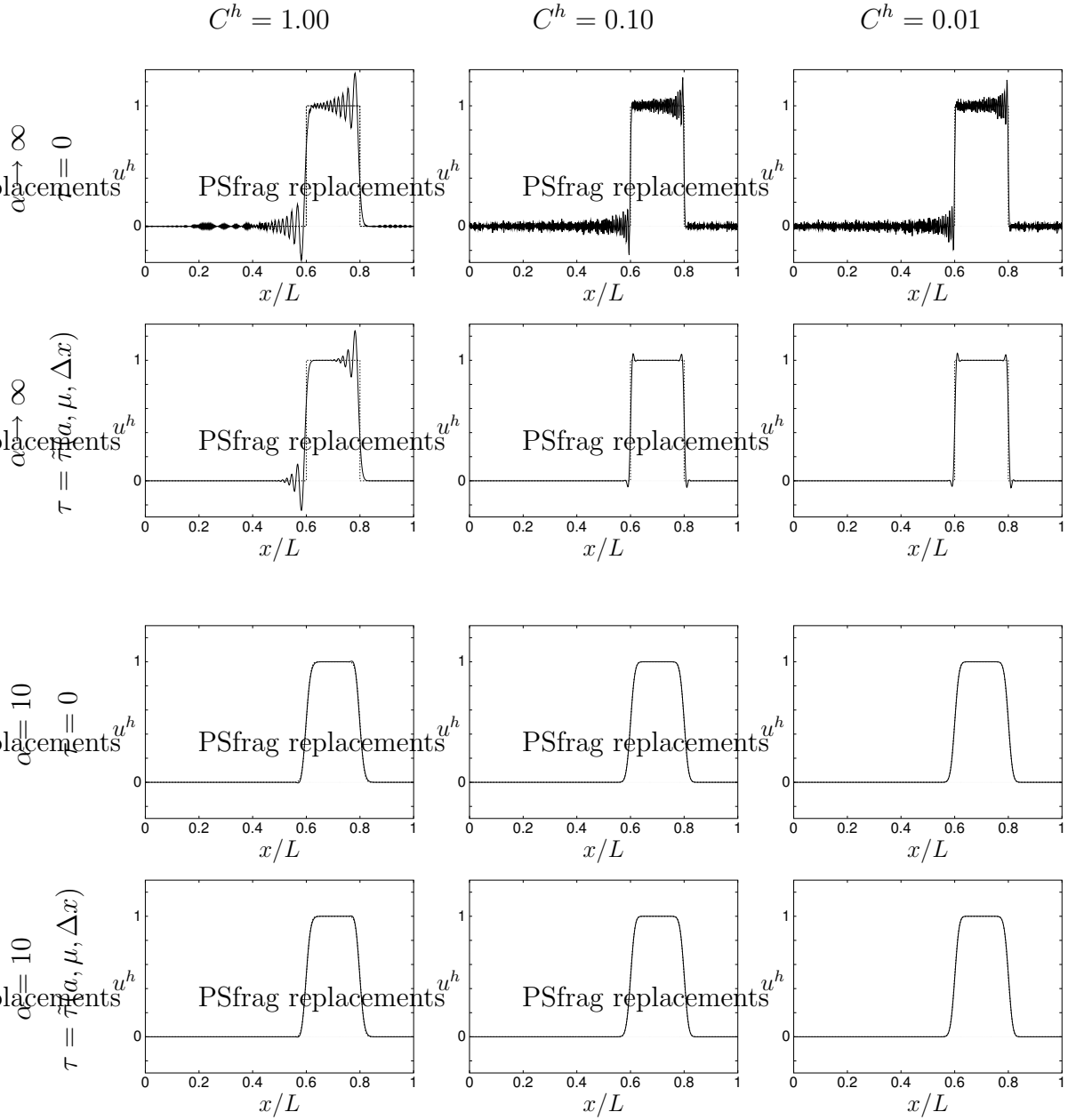


Figure 5.16: One dimensional advection-diffusion, solution  $u^h(x, t = 1.6 L/a)$  obtained with 1000 spatial elements, AM  $\rho_\infty^h = 0.5$ ;  $\tilde{\tau}(a, \mu, \Delta x)$  according to (5.82); the exact solution is given by the dotted line.

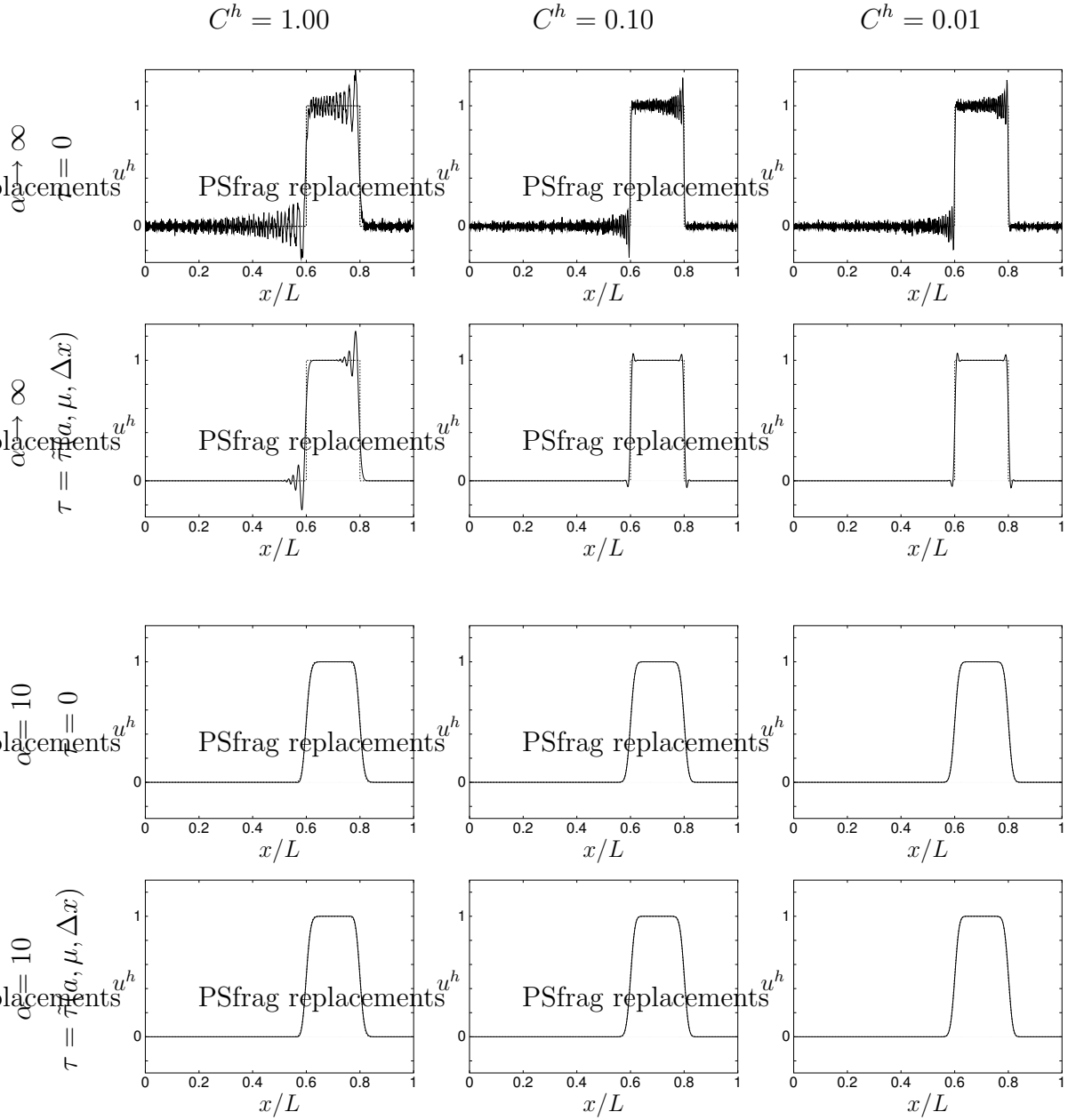


Figure 5.17: One dimensional advection-diffusion, solution  $u^h(x, t = 1.6 L/a)$  obtained with 1000 spatial elements, TR, MC, GM  $\rho_\infty^h = 1$ , AM  $\rho_\infty^h = 1$ ;  $\tilde{\tau}(a, \mu, \Delta x)$  according to (5.82); the exact solution is given by the dotted line.

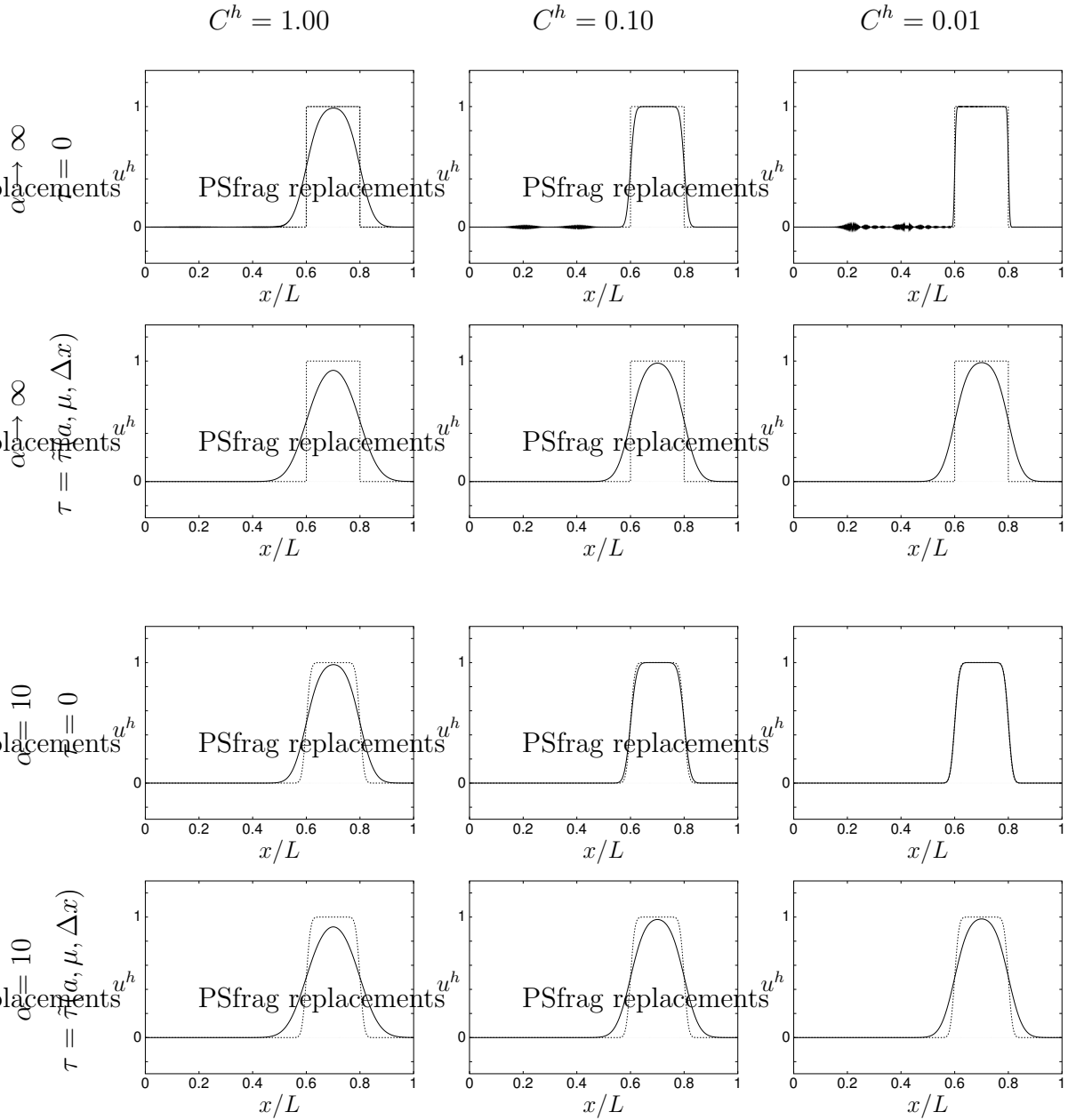


Figure 5.18: One dimensional advection-diffusion, solution  $u^h(x, t = 1.6 L/a)$  obtained with 1000 spatial elements, CD;  $\tilde{\tau}(a, \mu, \Delta x)$  according to (5.82); the exact solution is given by the dotted line.

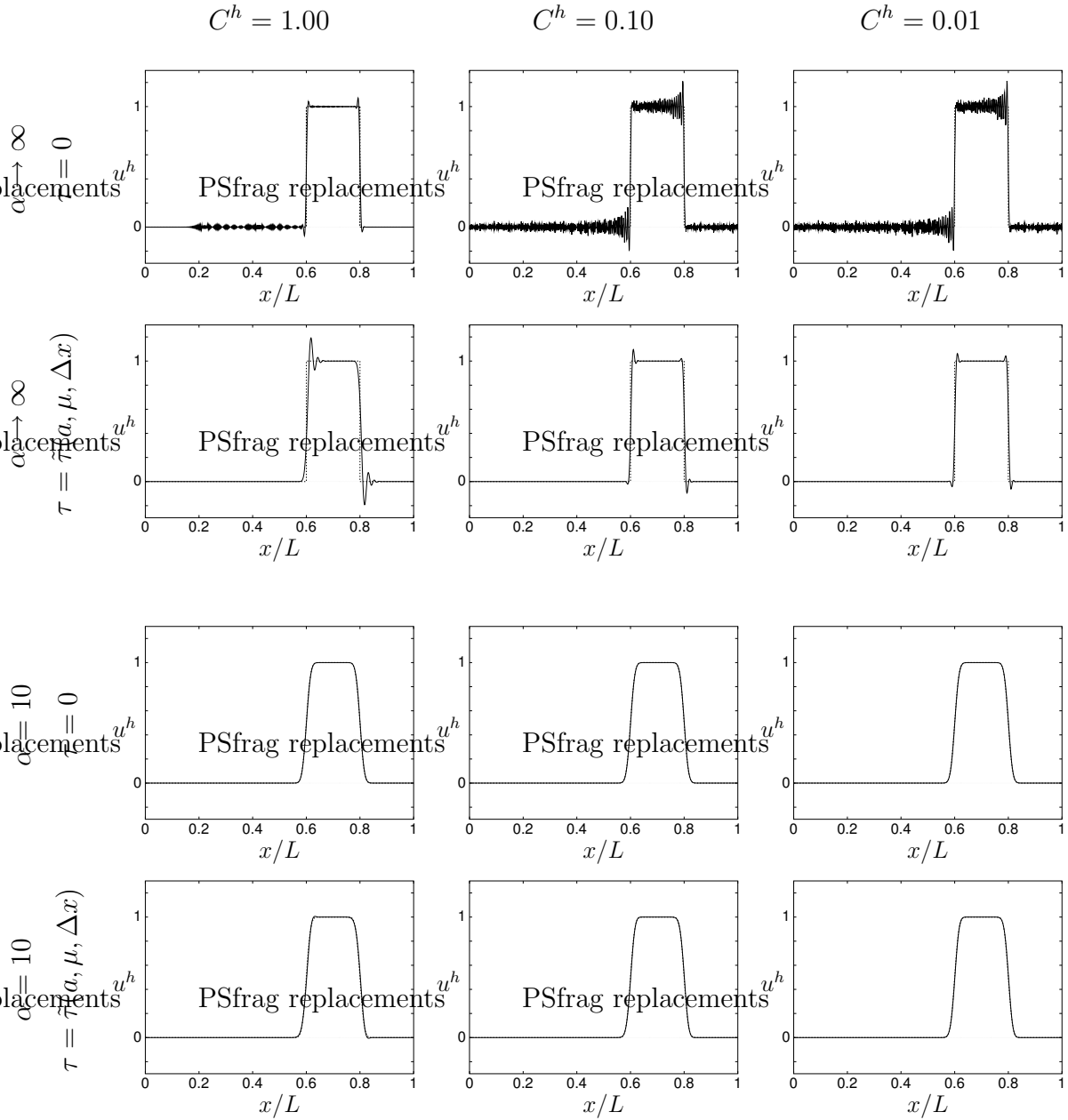


Figure 5.19: One dimensional advection-diffusion, solution  $u^h(x, t = 1.6 L/a)$  obtained with 1000 spatial elements, LD;  $\tilde{\tau}(a, \mu, \Delta x)$  according to (5.82); the exact solution is given by the dotted line.

### 5.3 Incompressible Navier-Stokes Equations

In the following, the stabilised finite element method of the steady state incompressible Navier-Stokes equations (4.85) is extended to account for transient effects by means of the different time integration schemes described earlier in this chapter. The conclusions reached in the Sections 5.1 and 5.2 are employed in understanding and judging the performance and efficiency of the resulting numerical methods.

The governing equations and boundary conditions of the unsteady flow of an incompressible Newtonian fluid on a fixed spatial domain are given by (2.44) – (2.46) and (2.19) – (2.22), respectively, with  $\hat{\mathbf{v}} = \mathbf{0} \forall (\hat{\mathbf{x}}, t) \in \Omega \times I$ . For simplicity and without loss of generality, the boundary of  $\Omega$  is assumed to be decomposed into pure Dirichlet and Neumann boundary subsections  $\Gamma_{\mathbf{g}}$  and  $\Gamma_{\mathbf{t}}$ , respectively. Preliminary to the presentation of the finite element formulation, the following spaces are defined on the basis of a standard linear finite element decomposition of the spatial domain  $\Omega = \cup_{e=1}^{n_{\text{el}}} \Omega^e$

$$\begin{aligned} \mathcal{U}^h &= \left\{ \mathbf{u}^h(\bullet, t) \in (H^1(\Omega))^{n_{\text{sd}}} \mid t \in I, \mathbf{u}^h|_{\hat{\mathbf{x}}^h \in \Omega^e} \in (P_1(\Omega^e))^{n_{\text{sd}}}, \mathbf{u}^h|_{\hat{\mathbf{x}}^h \in \Gamma_{\mathbf{g}}} = \mathbf{g} \right\} \\ \mathcal{W}^h &= \left\{ \mathbf{w}^h \in (H^1(\Omega))^{n_{\text{sd}}} \mid \mathbf{w}^h|_{\hat{\mathbf{x}}^h \in \Omega^e} \in (P_1(\Omega^e))^{n_{\text{sd}}}, \mathbf{w}^h|_{\hat{\mathbf{x}}^h \in \Gamma_{\mathbf{g}}} = \mathbf{0} \right\} \quad (5.124) \\ \mathcal{P}^h &= \left\{ p^h \in H^1(\Omega) \mid p^h|_{\hat{\mathbf{x}}^h \in \Omega^e} \in P_1(\Omega^e) \right\}. \end{aligned}$$

The SUPG/PSPG stabilised formulation may then be written as: For every time instant  $t \in I$ , find  $\mathbf{u}^h \in \mathcal{U}^h$  and  $p^h \in \mathcal{P}^h$  such that for any  $\mathbf{w}^h \in \mathcal{W}^h$  and  $q^h \in \mathcal{P}^h$

$$\begin{aligned} &\int_{\Omega} \left[ \mathbf{w}^h \cdot \rho \left( \dot{\mathbf{u}}^h + (\nabla \mathbf{u}^h) \mathbf{u}^h - \mathbf{f} \right) - (\nabla \cdot \mathbf{w}^h) p^h \right. \\ &\quad \left. + 2\mu \nabla \mathbf{w}^h : \nabla^s \mathbf{u}^h + (\nabla \cdot \mathbf{u}^h) q^h \right] dv - \int_{\Gamma_{\mathbf{t}}} \mathbf{w}^h \cdot \mathbf{t}^h da \quad (5.125) \\ &+ \sum_{e=1}^{n_{\text{el}}} \int_{\Omega^e} \left[ \tau_{\mathbf{u}} \rho (\nabla \mathbf{w}^h) \mathbf{u}^h + \tau_p \nabla q^h \right] \cdot \left[ \rho \left( \dot{\mathbf{u}}^h + (\nabla \mathbf{u}^h) \mathbf{u}^h - \mathbf{f} \right) + \nabla p^h \right] dv = 0, \end{aligned}$$

where the stabilisation parameters  $\tau_{\mathbf{u}}$  and  $\tau_p$  are given by (4.87). The derivation of the formulation (5.125) follows the same procedure as the one leading to (4.85) in Section 4.4. The resulting expressions deviate from (4.85) only by the appearance of the time derivative  $\dot{\mathbf{u}}^h$  in both the standard Galerkin and the stabilisation term. The time domain has not yet been discretised.

For the clarity of the notation used in the following sections, recall from Sections 5.1 and 5.2 that  $0 = t_0 < t_1 < \dots < t_N = T_{\text{end}}$  is a sequence of

discrete time instants in  $I$ , and  $I = \cup_{n=1}^N I_n$  with  $I_n = [t_{n-1}, t_n]$  is a partition of the time interval of interest. The subscript  $n$  denotes the approximative value of the quantity under consideration at time instant  $t_n$ .

Subsequent to the brief descriptions of the fully discretised numerical models, a detailed computational study is performed of two standard examples in order to establish the accuracy and efficiency of the time integration schemes. The two numerical examples to be considered are the well-known unsteady flow around a cylinder and the flow across a backward facing step.

### 5.3.1 Semi-Discrete Methods

In this section, the discretisation of (5.125) in time is achieved by means of the discrete time integration schemes GM or AM. Therefore, the strategy of Section 5.2.1 is employed and the quantities  $\mathbf{u}_\alpha^h$  and  $\dot{\mathbf{u}}_\beta^h$  are introduced as

$$\begin{aligned}\mathbf{u}_\alpha^h &= c_1 \mathbf{u}_{n+1}^h + c_2 \mathbf{u}_n^h + c_3 \dot{\mathbf{u}}_n^h \\ \dot{\mathbf{u}}_\beta^h &= c_4 \mathbf{u}_{n+1}^h + c_5 \mathbf{u}_n^h + c_6 \dot{\mathbf{u}}_n^h.\end{aligned}\tag{5.126}$$

Furthermore, the boundary traction vector  $\mathbf{t}_\alpha^h$  is defined as

$$\mathbf{t}_\alpha^h = c_7 \mathbf{t}_{n+1}^h + c_8 \mathbf{t}_n^h,\tag{5.127}$$

where  $\mathbf{t}_n^h$  and  $\mathbf{t}_{n+1}^h$  are the traction vectors at time instants  $t_n$  and  $t_{n+1}$ , respectively. The coefficients  $c_j$ ,  $j = 1, 2, \dots, 8$  depend on the particular time integration scheme employed and on the time step size  $\Delta t = t_{n+1} - t_n$ .

The pressure, which serves as a Lagrangian multiplier ensuring incompressibility (see Section 3.4.1), does not need to be subjected to a time integration scheme. In order to indicate that the pressure in the formulation is associated with the same time instant as  $\mathbf{u}_\alpha^h$  and  $\dot{\mathbf{u}}_\beta^h$  the notation  $p_\alpha^h$  is introduced.

The finite element spaces are defined as

$$\begin{aligned}\mathcal{U}_n^h &= \left\{ \mathbf{u}_n^h \in (H^1(\Omega))^{n_{\text{sd}}} \mid \mathbf{u}_n^h|_{\hat{\mathbf{x}}^h \in \Omega^e} \in (P_1(\Omega^e))^{n_{\text{sd}}}, \mathbf{u}_n^h|_{\hat{\mathbf{x}}^h \in \Gamma_g} = \mathbf{g}_n \right\} \\ \mathcal{W}^h &= \left\{ \mathbf{w}^h \in (H^1(\Omega))^{n_{\text{sd}}} \mid \mathbf{w}^h|_{\hat{\mathbf{x}}^h \in \Omega^e} \in (P_1(\Omega^e))^{n_{\text{sd}}}, \mathbf{w}^h|_{\hat{\mathbf{x}}^h \in \Gamma_g} = \mathbf{0} \right\} \\ \mathcal{P}^h &= \left\{ q^h \in H^1(\Omega) \mid q^h|_{\hat{\mathbf{x}}^h \in \Omega^e} \in P_1(\Omega^e) \right\},\end{aligned}\tag{5.128}$$

where the quantity  $\mathbf{g}_n$  denotes the prescribed velocity at the boundary  $\Gamma_g$  at time instant  $t_n$ . The fully discretised problem may then be written as: For a given  $\mathbf{u}_n^h$  and  $\dot{\mathbf{u}}_n^h$ , find  $\mathbf{u}_{n+1}^h \in \mathcal{U}_{n+1}^h$  and  $p_\alpha^h \in \mathcal{P}^h$  such that for any  $\mathbf{w}^h \in \mathcal{W}^h$  and  $q^h \in \mathcal{P}^h$

$$\begin{aligned}
& \int_{\Omega} \left[ \mathbf{w}^h \cdot \rho \left( \dot{\mathbf{u}}_{\beta}^h + (\nabla \mathbf{u}_{\alpha}^h) \mathbf{u}_{\alpha}^h - \mathbf{f} \right) - (\nabla \cdot \mathbf{w}^h) p_{\alpha}^h \right. \\
& \quad \left. + 2 \mu \nabla \mathbf{w}^h : \nabla^s \mathbf{u}_{\alpha}^h + (\nabla \cdot \mathbf{u}_{\alpha}^h) q^h \right] dv - \int_{\Gamma_t} \mathbf{w}^h \cdot \mathbf{t}_{\alpha}^h da \quad (5.129) \\
& + \sum_{e=1}^{n_{el}} \int_{\Omega^e} \left[ \tau_u \rho (\nabla \mathbf{w}^h) \mathbf{u}_{\alpha}^h + \tau_p \nabla q^h \right] \cdot \left[ \rho \left( \dot{\mathbf{u}}_{\beta}^h + (\nabla \mathbf{u}_{\alpha}^h) \mathbf{u}_{\alpha}^h - \mathbf{f} \right) + \nabla p_{\alpha}^h \right] dv = 0.
\end{aligned}$$

The formula (4.87) for the stabilisation parameters  $\tau_u$  and  $\tau_p$  is evaluated on the basis of  $\mathbf{u}_{\alpha}^h$ .

### 5.3.1.1 Generalised Midpoint Rule (GM)

Similarly to the procedure described in Section 5.2.1.1, the relations (5.126) and (5.127) are obtained as

$$\begin{aligned}
\mathbf{u}_{\alpha}^h &= \gamma \mathbf{u}_{n+1}^h + (1 - \gamma) \mathbf{u}_n^h, & \dot{\mathbf{u}}_{\beta}^h &= \frac{1}{\Delta t} \left( \mathbf{u}_{n+1}^h - \mathbf{u}_n^h \right) \\
\mathbf{t}_{\alpha}^h &= \gamma \mathbf{t}_{n+1}^h + (1 - \gamma) \mathbf{t}_n^h.
\end{aligned} \quad (5.130)$$

Using these expressions in equation (5.129) yields a set of nonlinear equations in terms of the only unknowns  $\mathbf{u}_{n+1}^h$  and  $p_{\alpha}^h$ . The solution can be obtained by employing a standard Newton-Raphson procedure.

### 5.3.1.2 Generalised- $\alpha$ Method (AM)

For the generalised- $\alpha$  method the relations (5.19), (5.66) and (5.67) render (see also Section 5.2.1.2)

$$\begin{aligned}
\mathbf{u}_{\alpha}^h &= \alpha_f \mathbf{u}_{n+1}^h + (1 - \alpha_f) \mathbf{u}_n^h \\
\dot{\mathbf{u}}_{\beta}^h &= \frac{\alpha_m}{\gamma \Delta t} \mathbf{u}_{n+1}^h - \frac{\alpha_m}{\gamma \Delta t} \mathbf{u}_n^h + \left( 1 - \frac{\alpha_m}{\gamma} \right) \dot{\mathbf{u}}_n^h \\
\mathbf{t}_{\alpha}^h &= \alpha_f \mathbf{t}_{n+1}^h + (1 - \alpha_f) \mathbf{t}_n^h
\end{aligned} \quad (5.131)$$

and

$$\dot{\mathbf{u}}_{n+1}^h = \frac{1}{\gamma \Delta t} \mathbf{u}_{n+1}^h - \frac{1}{\gamma \Delta t} \mathbf{u}_n^h - \frac{1 - \gamma}{\gamma} \dot{\mathbf{u}}_n^h. \quad (5.132)$$

Using these expressions in the formulation (5.129) gives a nonlinear equation in terms of the only unknowns  $\mathbf{u}_{n+1}^h$  and  $p_{\alpha}^h$ . Given the known solution

of the previous time step  $\mathbf{u}_n^h$  and  $\dot{\mathbf{u}}_n^h$ , a Newton-Raphson procedure may be employed to solve for  $\mathbf{u}_{n+1}^h$  and  $p_\alpha^h$ . Subsequently, the quantity  $\dot{\mathbf{u}}_{n+1}^h$  is evaluated from (5.132). The procedure is then to be repeated for the next time step.

### 5.3.2 Space-Time Finite Element Methods

Similar to Section 5.2.2, the notions of a space-time slab  $Q_n = \Omega \times I_n$  and a space-time finite element  $Q_n^e = \Omega^e \times I_n$  are introduced. The finite element spaces are then defined as

$$\begin{aligned}\mathcal{U}_n^h &= \left\{ \mathbf{u}^h \in (H^1(Q_n))^{n_{\text{sd}}} \mid \mathbf{u}^h|_{(\hat{\mathbf{x}}^h, t) \in Q_n^e} \in (P_1(Q_n^e))^{n_{\text{sd}}}, \mathbf{u}^h|_{(\hat{\mathbf{x}}^h, t) \in (\Gamma_g \times I_n)} = \mathbf{g} \right\} \\ \mathcal{W}_n^h &= \left\{ \mathbf{w}^h \in (H^1(Q_n))^{n_{\text{sd}}} \mid \mathbf{w}^h|_{(\hat{\mathbf{x}}^h, t) \in Q_n^e} \in (P_1(Q_n^e))^{n_{\text{sd}}}, \mathbf{w}^h|_{(\hat{\mathbf{x}}^h, t) \in (\Gamma_g \times I_n)} = \mathbf{0} \right\} \\ \mathcal{P}_n^h &= \left\{ p^h \in H^1(Q_n) \mid p^h|_{(\hat{\mathbf{x}}^h, t) \in Q_n^e} \in P_1(Q_n^e) \right\} .\end{aligned}\quad (5.133)$$

Similar to Section 5.2.2, the space-time finite element formulation is obtained from (5.125) by employing  $u^h \in \mathcal{U}_{n+1}^h$ ,  $w^h \in \mathcal{W}_{n+1}^h$  and  $p^h, q^h \in \mathcal{P}_{n+1}^h$ , by integration over the time interval  $I_{n+1}$  and by adding the jump term in order to weakly enforce continuity at the space-time slab boundaries. Thus, the fully discretised space-time formulation reads: For each space-time slab  $Q_n, n = 1, 2, \dots, N$ , find  $\mathbf{u}^h \in \mathcal{U}_{n+1}^h$  and  $p^h \in \mathcal{P}_{n+1}^h$  such that for any  $w^h \in \mathcal{W}_{n+1}^h$  and  $q^h \in \mathcal{P}_{n+1}^h$

$$\begin{aligned}\int_{t_n}^{t_{n+1}} \left( \int_{\Omega} \left[ \mathbf{w}^h \cdot \rho \left( \dot{\mathbf{u}}^h + (\nabla \mathbf{u}^h) \mathbf{u}^h - \mathbf{f} \right) - (\nabla \cdot \mathbf{w}^h) p^h \right. \right. \\ \left. \left. + 2\mu \nabla \mathbf{w}^h : \nabla^s \mathbf{u}^h + (\nabla \cdot \mathbf{u}^h) q^h \right] dv - \int_{\Gamma_t} \mathbf{w}^h \cdot \mathbf{t}^h da \right. \\ \left. + \sum_{e=1}^{n_{\text{el}}} \int_{\Omega^e} \left[ \tau_u \rho (\nabla \mathbf{w}^h) \mathbf{u}^h + \tau_p \nabla q^h \right] \cdot \left[ \rho \left( \dot{\mathbf{u}}^h + (\nabla \mathbf{u}^h) \mathbf{u}^h - \mathbf{f} \right) + \nabla p^h \right] dv \right) dt \\ \left. + \int_{\Omega} \rho \mathbf{w}_n^{h+} \cdot (\mathbf{u}_n^{h+} - \mathbf{u}_n^{h-}) dv = 0 .\end{aligned}\quad (5.134)$$

For continuous in time formulations the jump term, of course, disappears. The stabilisation parameters  $\tau_u$  and  $\tau_p$  are evaluated according to (4.87). Similarly to Section 5.2.2, a formulation derived from the GLS rather than the SUPG/PSPG strategy contains the expression  $\dot{\mathbf{w}}^h$  in the stabilisation term. Note that such a formulation may, however, be problematic and may require

a different choice for the stabilisation parameters  $\tau_{\mathbf{u}}$  and  $\tau_p$ , as discussed in Remark 5.1.

Some details on the linear continuous and linear discontinuous in time space-time methods (LC,LD) are given below. For both methods, the integration over time is approximated with second order Gauß quadrature. Thus, the integrand has to be evaluated at the time instants  $\mathbf{t}_n + (3 \pm \sqrt{3})\Delta t/6$ . Note that the computational cost on element level is thus twice as high as for the semi-discrete methods.

### 5.3.2.1 Linear Continuous Finite Elements (LC)

The linear continuous in time space-time interpolation is defined by

$$\begin{aligned}
\mathbf{u}^h(\hat{\mathbf{x}}^h, t) &= \hat{N}_n(t) \hat{N}_a(\hat{\mathbf{x}}^h) \mathbf{u}_{a,n} + \hat{N}_{n+1}(t) \hat{N}_a(\hat{\mathbf{x}}^h) \mathbf{u}_{a,n+1} \\
p^h(\hat{\mathbf{x}}^h, t) &= \hat{N}_n(t) \hat{N}_a(\hat{\mathbf{x}}^h) p_{a,n} + \hat{N}_{n+1}(t) \hat{N}_a(\hat{\mathbf{x}}^h) p_{a,n+1} \\
\dot{\mathbf{u}}^h(\hat{\mathbf{x}}^h, t) &= \dot{N}_n \hat{N}_a(\hat{\mathbf{x}}^h) \mathbf{u}_{a,n} + \dot{N}_{n+1} \hat{N}_a(\hat{\mathbf{x}}^h) \mathbf{u}_{a,n+1} \\
\mathbf{w}^h(\hat{\mathbf{x}}^h, t) &= \hat{N}_{n+1}(t) \hat{N}_a(\hat{\mathbf{x}}^h) \mathbf{w}_{a,n+1} \\
q^h(\hat{\mathbf{x}}^h, t) &= \hat{N}_{n+1}(t) \hat{N}_a(\hat{\mathbf{x}}^h) \mathbf{q}_{a,n+1},
\end{aligned} \tag{5.135}$$

where  $N_n$  and  $N_{n+1}$  are given by (5.31) and  $N_a = \hat{N}_a(\hat{\mathbf{x}}^h)$  denotes the standard spatial shape function for node  $a$  of the space-time finite element.

By using (5.135) in (5.134), whereby the jump term is omitted, one obtains a set of nonlinear equations in terms of the unknown nodal values of  $\mathbf{u}_{n+1}^h$  and  $p_{n+1}^h$ . As for the semi-discrete schemes the linearisation of the problem and the application of a Newton-Raphson procedure are straightforward.

### 5.3.2.2 Linear Discontinuous Finite Elements (LD)

For the linear discontinuous in time space-time method, the trial and test functions in the space-time element  $Q_n^e$  are defined as

$$\begin{aligned}
\mathbf{u}^h(\hat{\mathbf{x}}^h, t) &= \hat{N}_n(t) \underbrace{\hat{N}_a(\hat{\mathbf{x}}^h) \mathbf{u}_{a,n}^+}_{\mathbf{u}_n^{h+}} + \hat{N}_{n+1}(t) \underbrace{\hat{N}_a(\hat{\mathbf{x}}^h) \mathbf{u}_{a,n+1}^-}_{\mathbf{u}_{n+1}^{h-}} \\
p^h(\hat{\mathbf{x}}^h, t) &= \hat{N}_n(t) \hat{N}_a(\hat{\mathbf{x}}^h) p_{a,n}^+ + \hat{N}_{n+1}(t) \hat{N}_a(\hat{\mathbf{x}}^h) p_{a,n+1}^- \\
\dot{\mathbf{u}}^h(\hat{\mathbf{x}}^h, t) &= \dot{N}_n \hat{N}_a(\hat{\mathbf{x}}^h) \mathbf{u}_{a,n}^+ + \dot{N}_{n+1} \hat{N}_a(\hat{\mathbf{x}}^h) \mathbf{u}_{a,n+1}^- \\
\mathbf{w}^h(\hat{\mathbf{x}}^h, t) &= \hat{N}_n(t) \underbrace{\hat{N}_a(\hat{\mathbf{x}}^h) \mathbf{w}_{a,n}^+}_{\mathbf{w}_n^{h+}} + \hat{N}_{n+1}(t) \hat{N}_a(\hat{\mathbf{x}}^h) \mathbf{w}_{a,n+1}^- \\
q^h(\hat{\mathbf{x}}^h, t) &= \hat{N}_n(t) \hat{N}_a(\hat{\mathbf{x}}^h) \mathbf{q}_{a,n}^+ + \hat{N}_{n+1}(t) \hat{N}_a(\hat{\mathbf{x}}^h) \mathbf{q}_{a,n+1}^-.
\end{aligned} \tag{5.136}$$

For clarity the expressions which enter the jump term have been identified. Note that we have decided not to employ a jump term for the pressure.

Using (5.136) in (5.134) gives a set of nonlinear equations in terms of the unknown nodal values of the velocity and the pressure at  $\mathbf{t}_n^+$  and  $\mathbf{t}_{n+1}^-$ . Thus, the number of unknowns has doubled in comparison to the other methods considered in this work. Consequently, the dimension of the linear system of equations which needs to be solved within each step of the Newton-Raphson iteration has also doubled.

### 5.3.3 Example I: Flow Around a Cylinder

In this example the two dimensional flow of a viscous incompressible fluid around a cylinder is considered. This problem has often been used to establish the accuracy of numerical solution algorithms.

The spatial domain is assumed to be infinite and the flow far away from the cylinder is uniform with the velocity  $u_\infty$ . The long term behaviour of the flow is a periodic vortex shedding behind the cylinder, also denoted as the *von Kármán* vortex street, which subjects the cylinder to oscillating drag and lift forces  $F_D$  and  $F_L$  perpendicular and parallel to the direction of the flow. The frequency  $f$  of the lift force is known from experiments. It depends mainly on the Reynolds number  $Re = u_\infty D \rho / \mu$ , where  $D$  is the diameter of the cylinder. The non-dimensional lift and drag coefficients  $C_L$  and  $C_D$  and the Strouhal number  $Sr$  are introduced as follows

$$C_L = \frac{2 F_L}{\rho u_\infty^2 D}, \quad C_D = \frac{2 F_D}{\rho u_\infty^2 D}, \quad Sr = \frac{f D}{u_\infty}. \quad (5.137)$$

The geometry and the boundary conditions used in the numerical simulation are given in Figure 5.20, in which  $u$ ,  $v$  and  $p$  denote the velocity components in  $x$  and  $y$  direction and the pressure, respectively. A slight imperfection is applied to the geometry in Figure 5.20 in order to trigger the unsteady flow. This is achieved by shifting the lower boundary downwards by 0.1% of the width of the domain. However, with hindsight, it is likely that the imperfections arising from the unstructured mesh and the computer round-off suffice to trigger the vortex shedding.

The simulations are performed for three different Reynolds numbers  $Re = 100$ ,  $400$  and  $1000$  with  $\rho = 1$ ,  $\mu = 0.01$  and  $u_\infty = 1$ ,  $u_\infty = 4$  and  $u_\infty = 10$ , respectively. At the inflow boundary the velocity component  $u$  is smoothly increased from zero to  $u_\infty$  within the time intervals  $[0, 2]$ ,  $[0, 0.4]$  or  $[0, 0.16]$  for, respectively, the Reynolds numbers  $100$ ,  $400$ ,  $1000$  by employing a section of a sine curve. Note that the long term periodic flow can also be simulated with less smooth initial conditions. Different meshes (see Figure 5.21) and

varying time step sizes are used. Four different formulations (GM, AM, LC, LD) are tested.

The diagrams in Figure 5.22 show the time evolution of the drag and lift coefficients for different Reynolds numbers. A typical velocity field vector plot for  $Re = 100$  is given in Figure 5.23 and the evolution of the pressure isolines is displayed in Figure 5.24.

Figures 5.25 – 5.27 show the convergence of the Strouhal number and the lift coefficient for the different methods as the time step size  $\Delta t$  is reduced. Clearly, all the methods converge to the same solution. Note that for the high Reynolds number flow with  $Re = 1000$  the solution can not be obtained on a coarse mesh since the Newton-Raphson algorithm fails.

The effect of refinement of the spatial mesh on the limit solution obtained for  $\Delta t \rightarrow 0$  is displayed in Figure 5.28. The diagrams show the Strouhal number and the amplitude of the lift coefficient against the number of degrees of freedom of the spatial finite element mesh. The values displayed are the converged solutions from Figures 5.25 – 5.27, and thus they are independent of the time integration scheme used. The convergence behaviour with spatial refinement is clearly illustrated. Table 5.5 shows the Strouhal numbers denoted as  $Sr_9$ , which have been obtained for  $\Delta t \rightarrow 0$ ,  $h \rightarrow 0$ . They can be regarded as the “exact” solutions to the model problem defined by Figure 5.20 for the different Reynolds numbers.

However, these values differ from the Strouhal numbers established from experiments, see *e. g.* Roshko [101]. One suspects, that the size of the spatial domain chosen for the model problem may be too small to represent the larger physical domain. Therefore, the upper, lower and left boundary of the domain in Figure 5.20 are shifted by 5 unit lengths, thus obtaining a domain of  $25 \times 19$  unit lengths. In order to make the results comparable, the inner part of this domain is discretised with mesh E used in Figure 5.28. The large finite element mesh is displayed in Figure 5.29. The simulation is repeated and, clearly, the resulting Strouhal numbers are much closer to the experimental values. For large Reynolds numbers, due to the smaller amount of physical damping, the enlarged domain may still be considered “small” and, consequently, the improvement of the Strouhal numbers is less significant than for smaller Reynolds numbers.

A discussion of the performance of the different methods (GM, AM, LC, LD) is provided in Section 5.3.5.

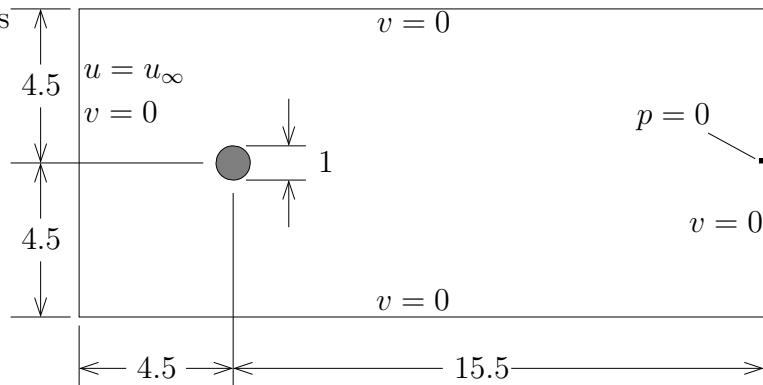


Figure 5.20: Flow around a cylinder, geometry and boundary conditions.

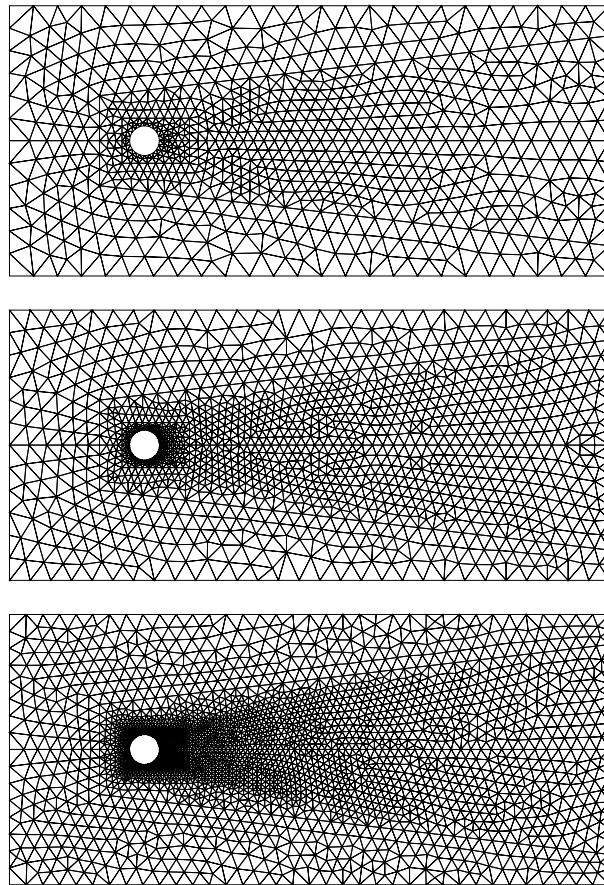


Figure 5.21: Flow around a cylinder, finite element meshes with 1576 (2600) [5276] elements, 835 (1363) [2724] nodes, 2388 (3928) [7937] degrees of freedom and 20 (38) [64] nodes describing the cylinder.

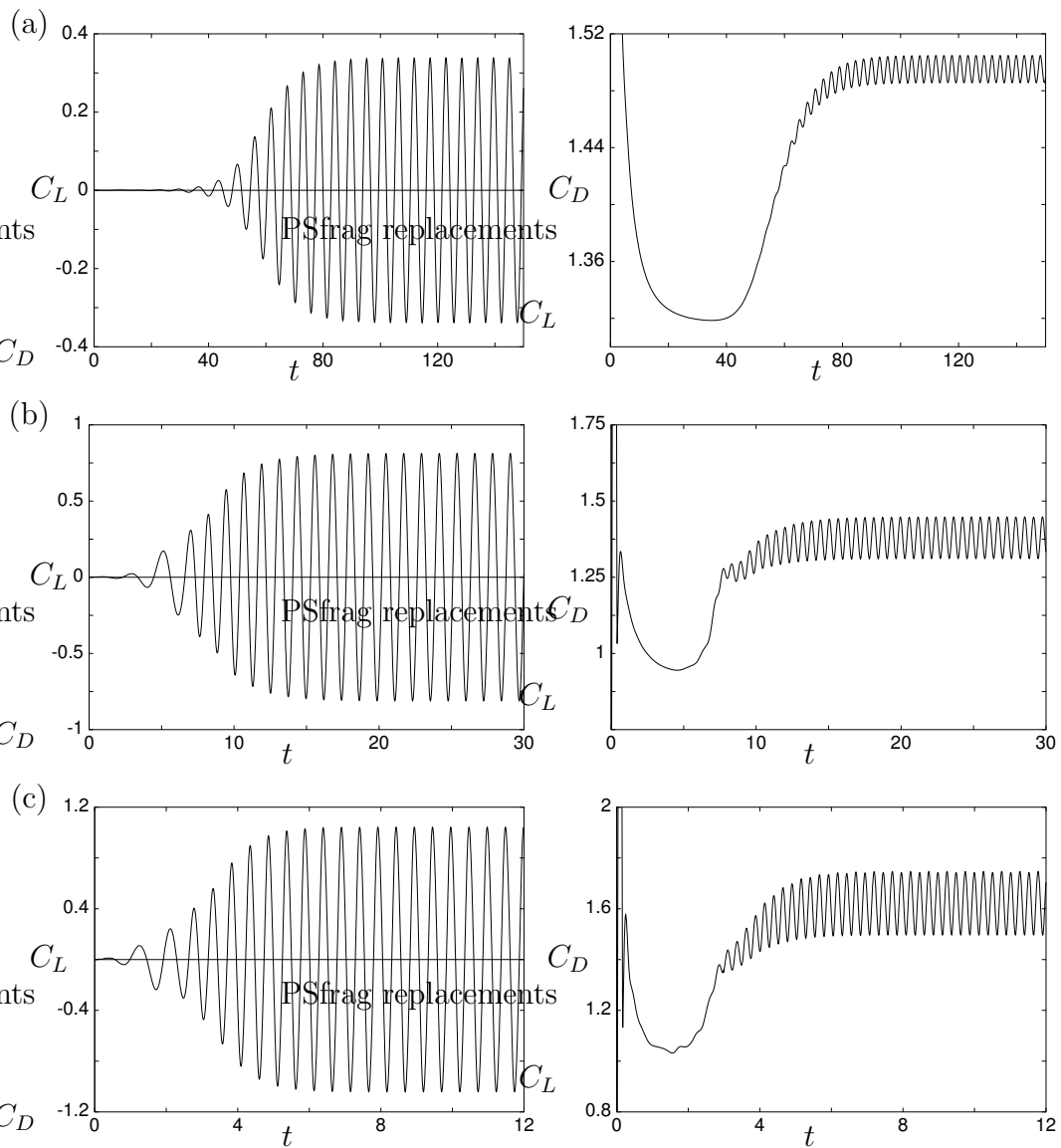


Figure 5.22: Flow around a cylinder, evolution of lift and drag coefficients;  
(a)  $Re = 100$ , 5276 elements,  $AM \rho_\infty^h = 0.9$ ,  $\Delta t = 0.1$ ;  
(b)  $Re = 400$ , 2600 elements,  $AM \rho_\infty^h = 0.9$ ,  $\Delta t = 0.01$ ;  
(c)  $Re = 1000$ , 2600 elements,  $AM \rho_\infty^h = 0.9$ ,  $\Delta t = 0.006$ .

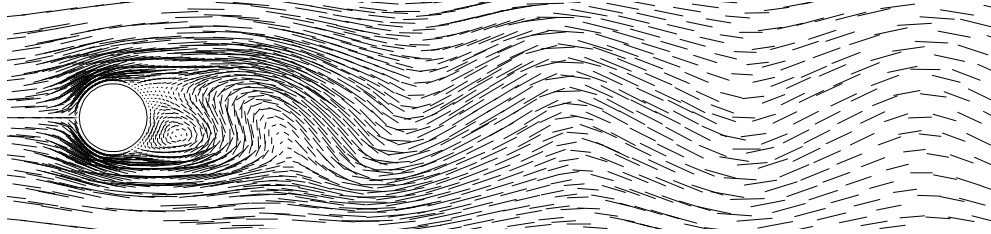


Figure 5.23: Flow around a cylinder, velocity vector plot at  $t=120$ ,  $Re = 100$ , 5276 elements, AM  $\rho_{\infty}^h = 0.9$ ,  $\Delta t = 0.1$ .

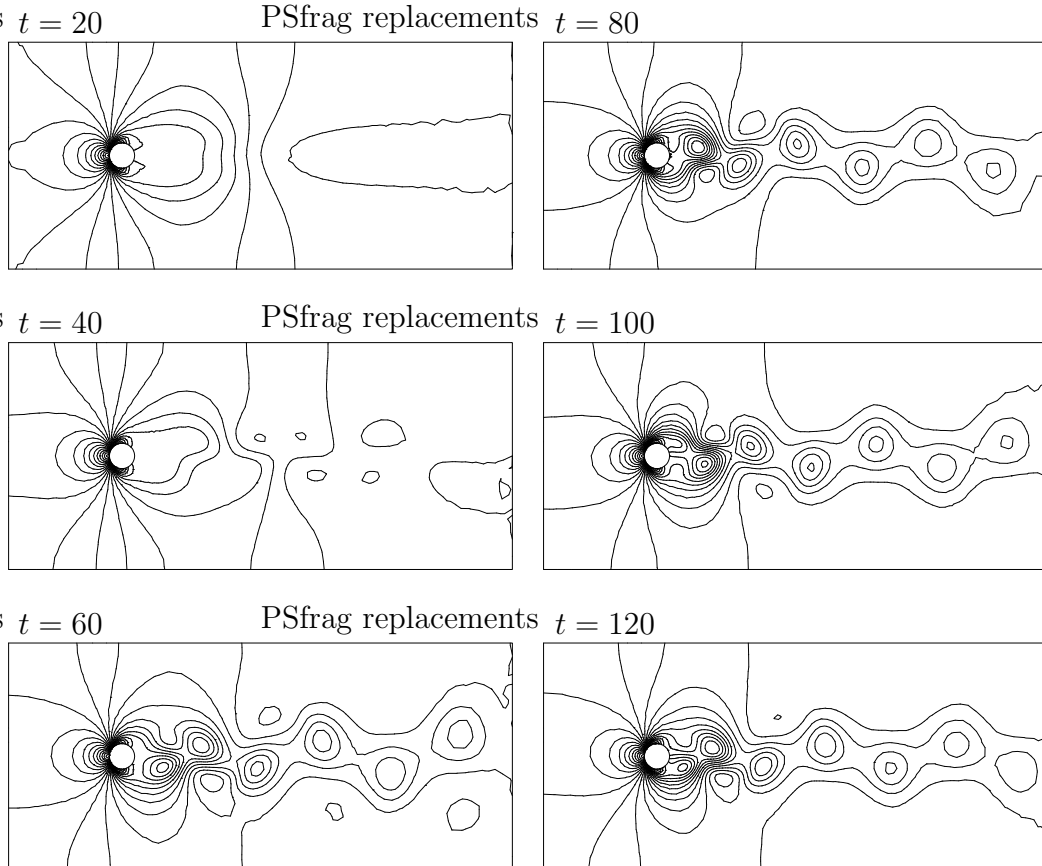


Figure 5.24: Flow around a cylinder, pressure contours,  $Re = 100$ , 5276 elements, AM  $\rho_{\infty}^h = 0.9$ ,  $\Delta t = 0.1$ .

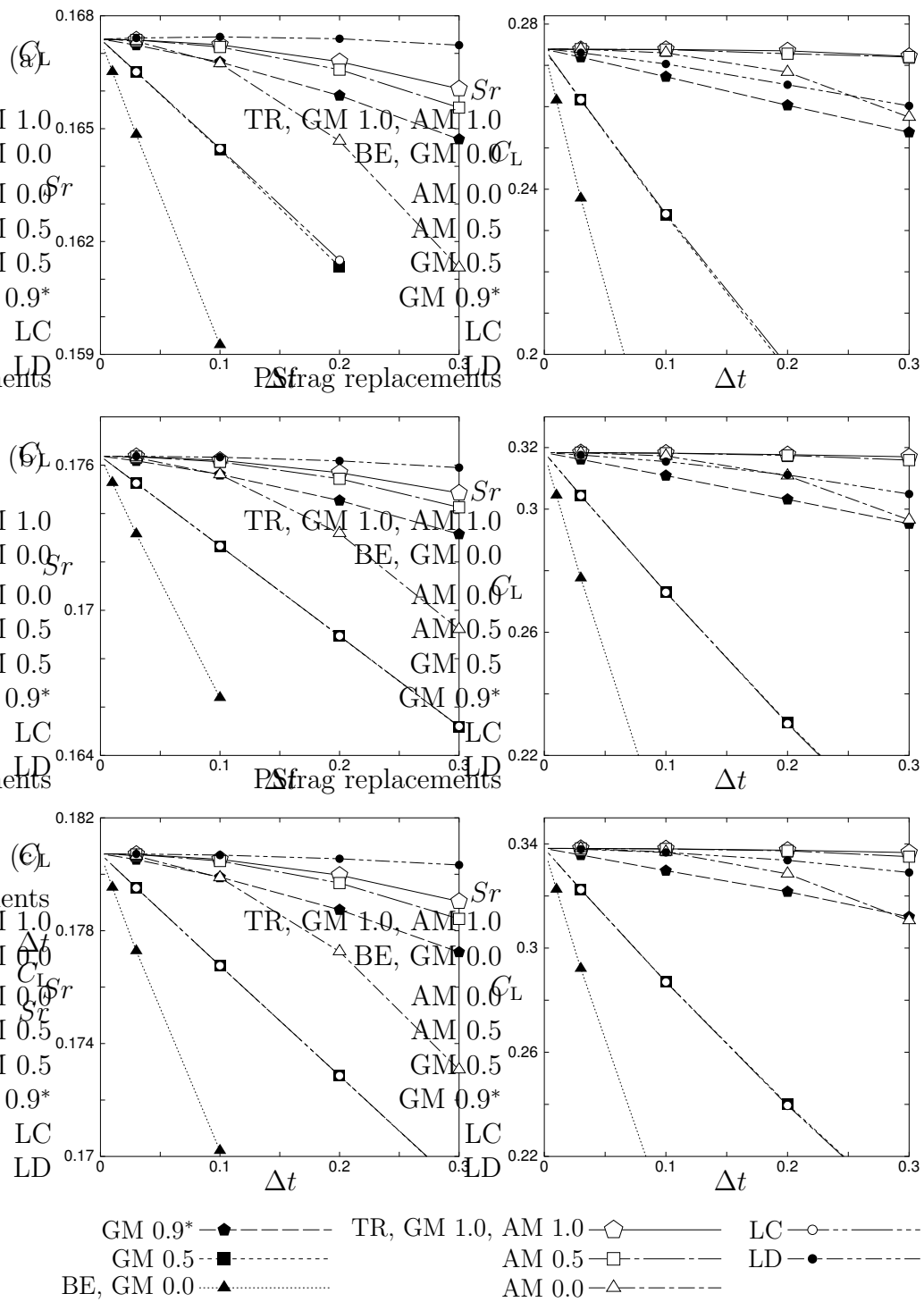


Figure 5.25: Flow around a cylinder, convergence of  $Sr$  and  $\max(C_L)$  as  $\Delta t \rightarrow 0$ ,  $Re = 100, 1576$  (a),  $2600$  (b) and  $5276$  elements (c).

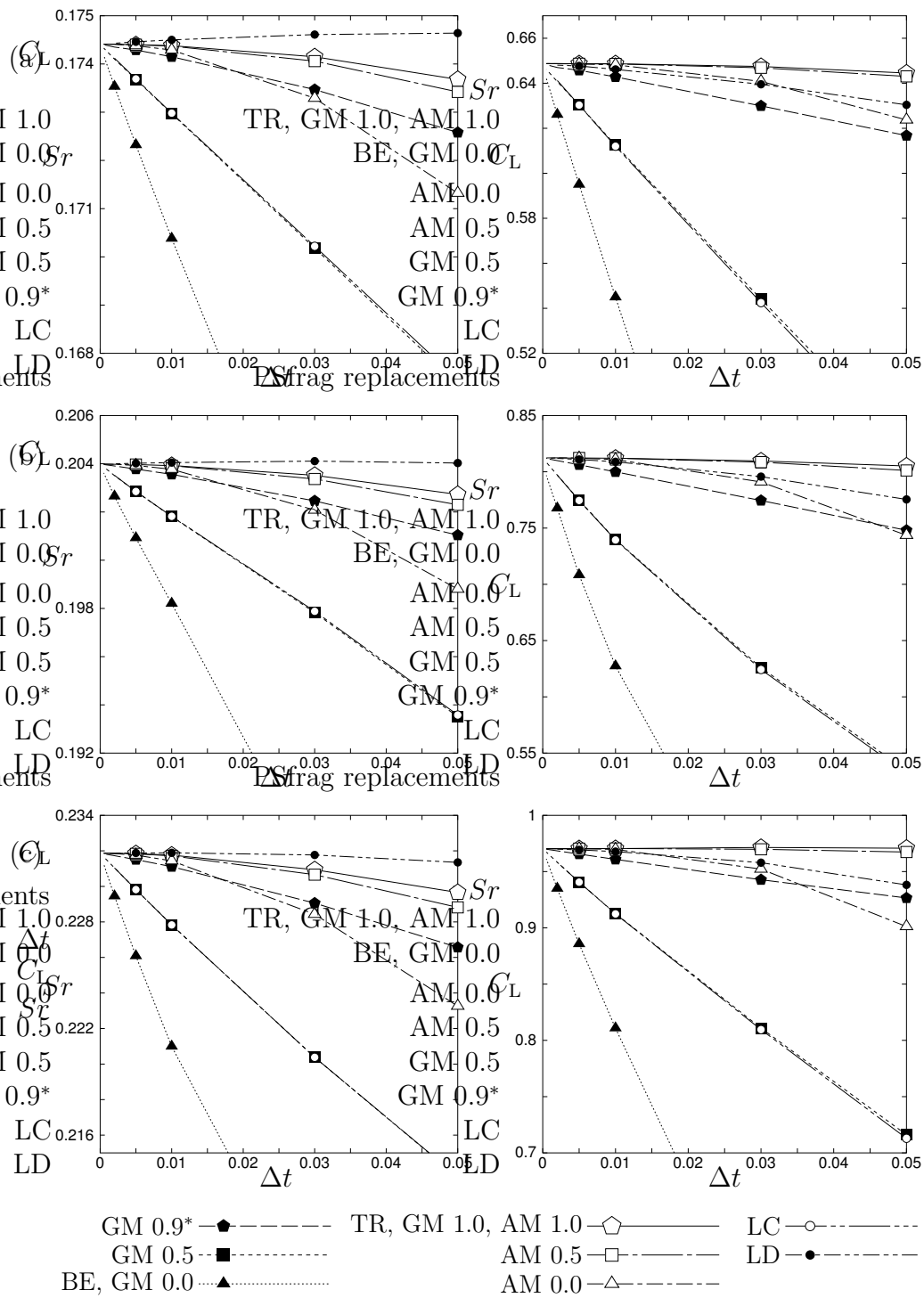


Figure 5.26: Flow around a cylinder, convergence of  $Sr$  and  $\max(C_L)$  as  $\Delta t \rightarrow 0$ ,  $Re = 400, 1576$  (a),  $2600$  (b) and  $5276$  elements (c).

(a) Newton-Raphson procedure fails.

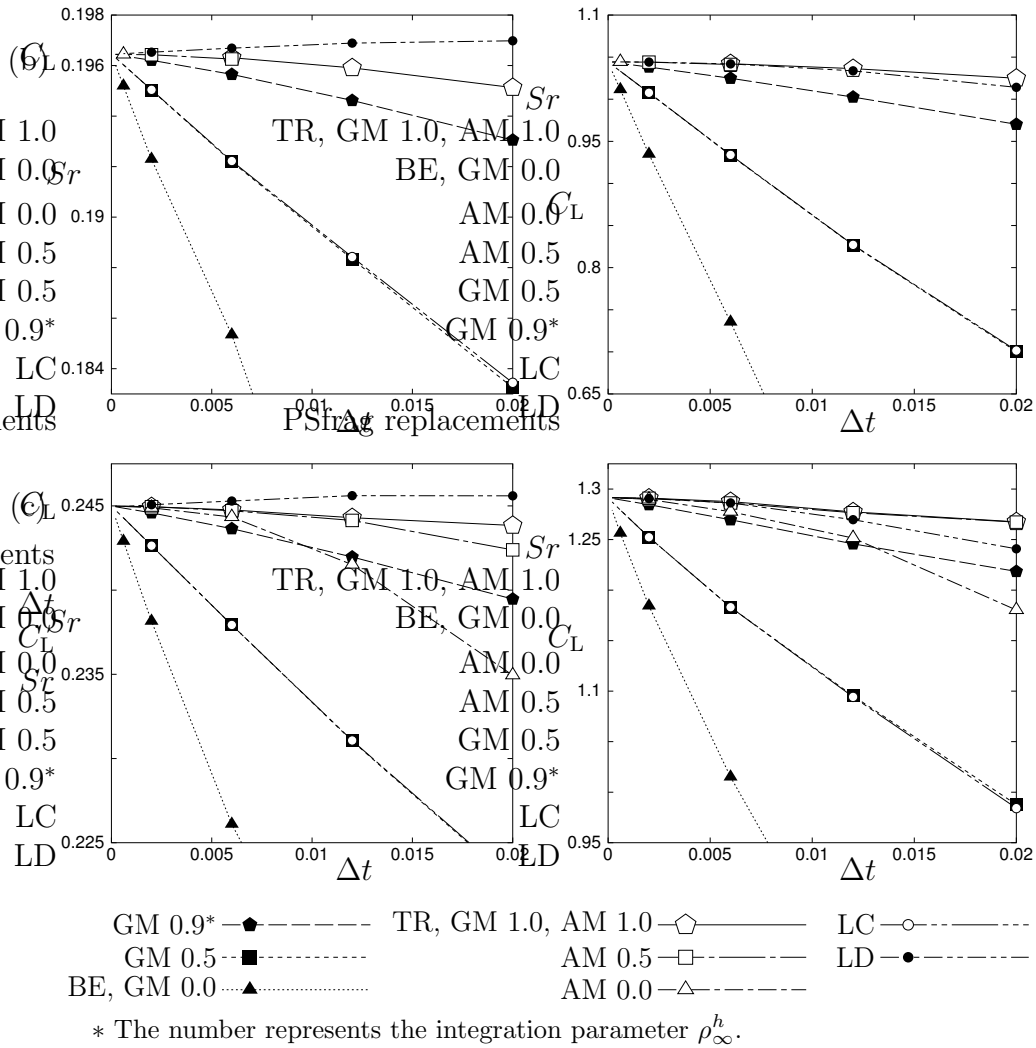


Figure 5.27: Flow around a cylinder, convergence of  $Sr$  and  $\max(C_L)$  as  $\Delta t \rightarrow 0$ ,  $Re = 1000, 1576$  (a),  $2600$  (b) and  $5276$  elements (c).

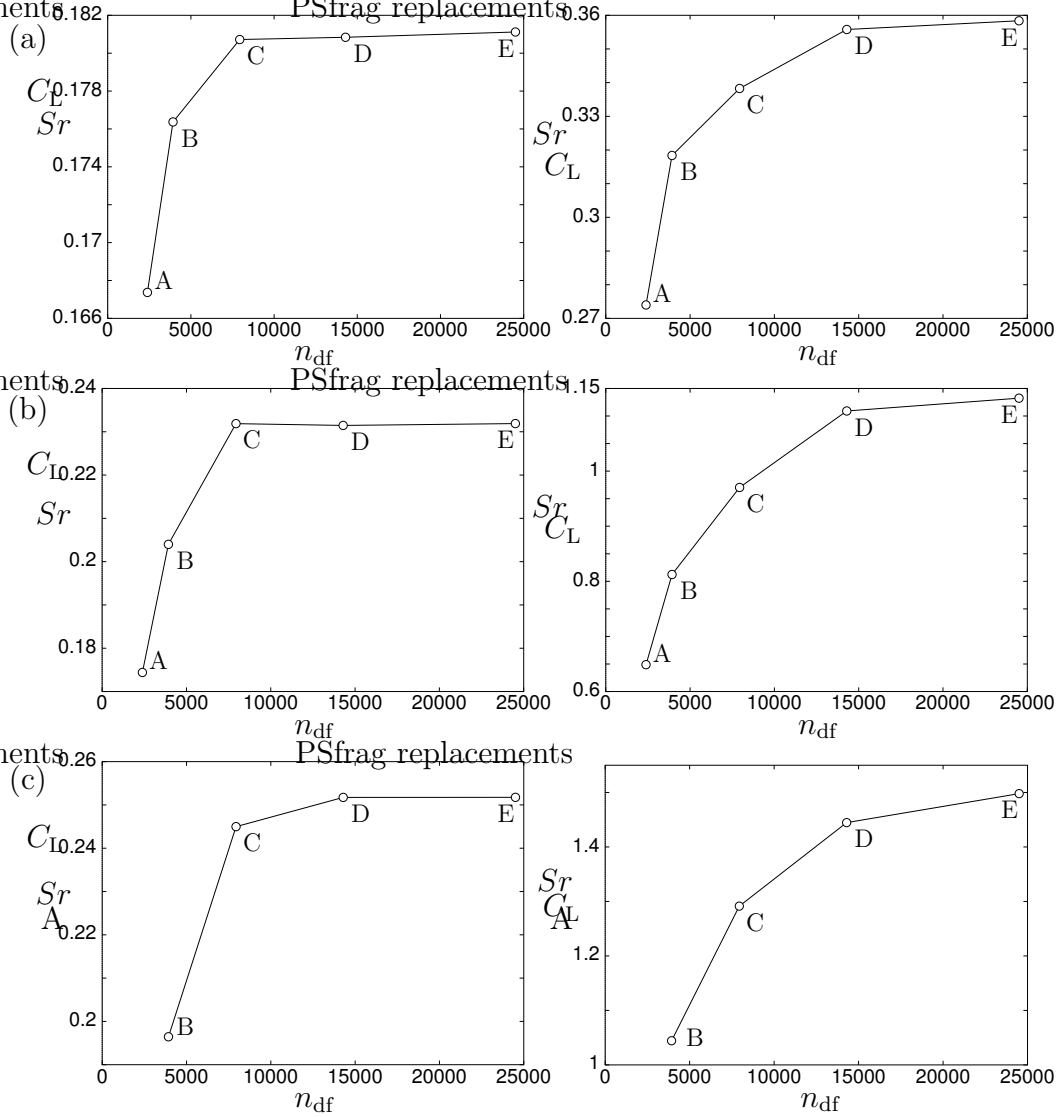


Figure 5.28: Flow around a cylinder, convergence of  $Sr$  and  $\max(C_L)$  as  $h \rightarrow 0$ , (a)  $Re = 100$ , (b) 400, (c) 1000;  $n_{df}$  = number of degrees of freedom (mesh A – E: 1576, 2600, 5276, 9510, 16310 elements); the values displayed have been obtained with very small time steps  $\Delta t$  and can be considered as the limits  $\Delta t \rightarrow 0$  (see Figures 5.25 – 5.27).

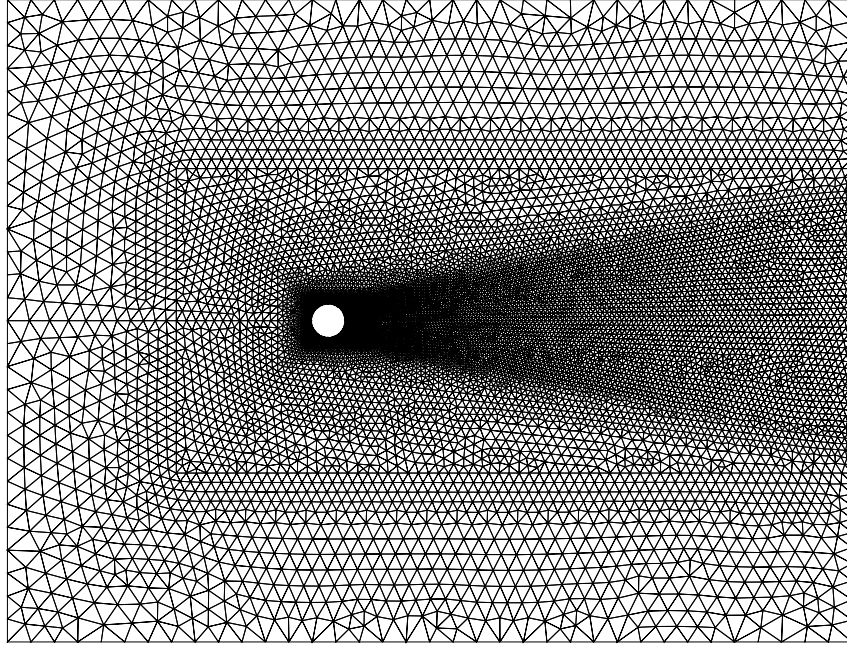


Figure 5.29: Flow around a cylinder, mesh for enlarged domain with 19,800 elements, 10,054 nodes, 29,743 degrees of freedom and 144 element edges describing the cylinder.

$Re$	$Str_{exp.}$	$Str_9$ (relative error)	$Str_{19}$ (relative error)
100	0.167	0.181 (8 %)	0.171 (2 %)
400	$\approx 0.205$	0.232 (13 %)	0.223 (9 %)
1000	$\approx 0.210$	0.252 (20 %)	0.243 (16 %)

Table 5.5: Flow around a cylinder, Strouhal numbers; experimental values and converged solution of model problem with small and large domain (width = 9 or 19 unit lengths).

### 5.3.4 Example II: Flow Across a Backward Facing Step

In this example the two dimensional incompressible flow in a channel with a backward facing step is considered. The fluid is initially at rest. The upstream height of the channel is  $h$ , while the downstream height is  $H = h + s$ , where  $s$  is the height of the step (see Figure 5.30). Upstream, far away from the step, the average velocity of the fluid is  $\bar{u}_{in}$  and the velocity profile is parabolic according to undisturbed viscous flow in a channel.

The long term solution for this problem varies with the Reynolds number  $Re = \bar{u}_{in} h \rho / \mu$ . To the knowledge of the author neither the exact nor the experimental solution to this problem is available. The long term solutions obtained by Yee *et al* [130] with several different numerical methods vary from chaotic unsteady flow to steady flow. In the following it is shown, that all the methods discussed in this chapter converge to the same steady state long term solution, which agrees well with the results obtained by Gresho *et al* [51].

The geometry and the boundary conditions for the numerical model of the problem are given in Figure 5.30, in which  $u$ ,  $v$  and  $p$  denote the velocity components in  $x$  and  $y$  direction and the pressure, respectively. The prescribed velocity profile at the inflow boundary is parabolic. The average velocity is raised smoothly from zero to  $\bar{u}_{in}$ , employing a section of the sine function. The length and height of the model are  $h = 1$ ,  $s = 0.94231$ ,  $l = 1$  and  $L = 34$ . The density and the viscosity are set to  $\rho = 1$  and  $\mu = 0.01$ . Simulations are performed for  $\bar{u}_{in} = 2.5$  and  $\bar{u}_{in} = 4$ , corresponding to  $Re = 500$  and  $Re = 800$ , respectively. Two different meshes (see Figure 5.31) and different time step sizes are employed. The problem is simulated with the different schemes GM, AM, LC, LD.

The most important characteristic of the numerical results is that all the methods considered give the same steady state solution, which depends only on the spatial mesh and the Reynolds number. The limit solution is independent of the time step size  $\Delta t$  with which it is approached. Figure 5.32 shows the pressure isolines for  $Re = 800$  at various time instants. The Figures 5.33 – 5.35 show the evolution of the velocity in  $y$ -direction at point A in the middle of the channel at distance  $\Delta l = 5$  from the outflow boundary. Similar to the flow around the cylinder, it is found that for a given Reynolds number and mesh the methods converge to essentially the same transient solution as  $\Delta t \rightarrow 0$ . For  $\Delta t = 0.02$  the diagrams are almost identical. The curves obtained with larger time steps give an idea of the different damping and convergence characteristics of the various time integration methods.

A discussion of the performance of the different methods (GM, AM, LC, LD) is provided in Section 5.3.5.

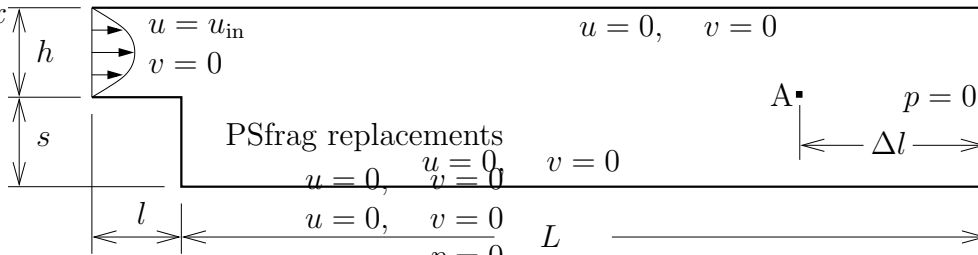


Figure 5.30: Flow across a backward facing step, geometry and boundary conditions.

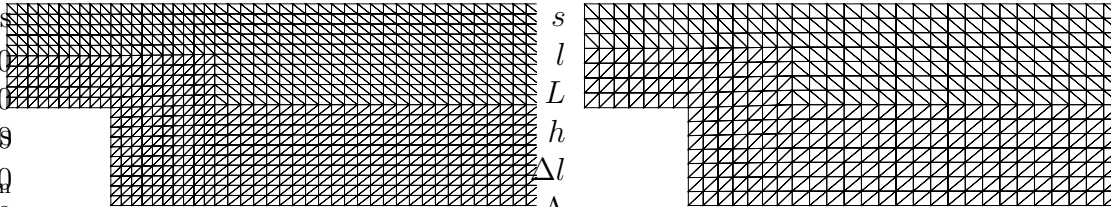


Figure 5.31: Flow across a backward facing step, details of the finite element meshes with 11160 (5838) elements, 6215 (3392) nodes and 16476 (8559) degrees of freedom.

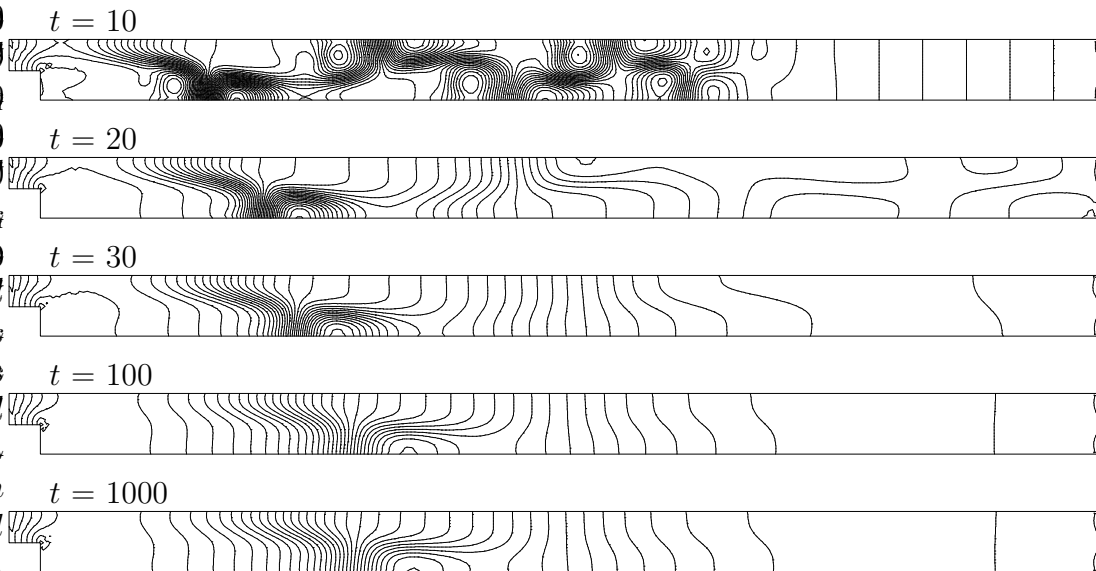


Figure 5.32: Flow across a backward facing step, evolution of pressure isolines for  $Re = 800$ , 11160 elements, AM  $\rho_{\infty}^h = 0.9$ ,  $\Delta t = 0.1$ .

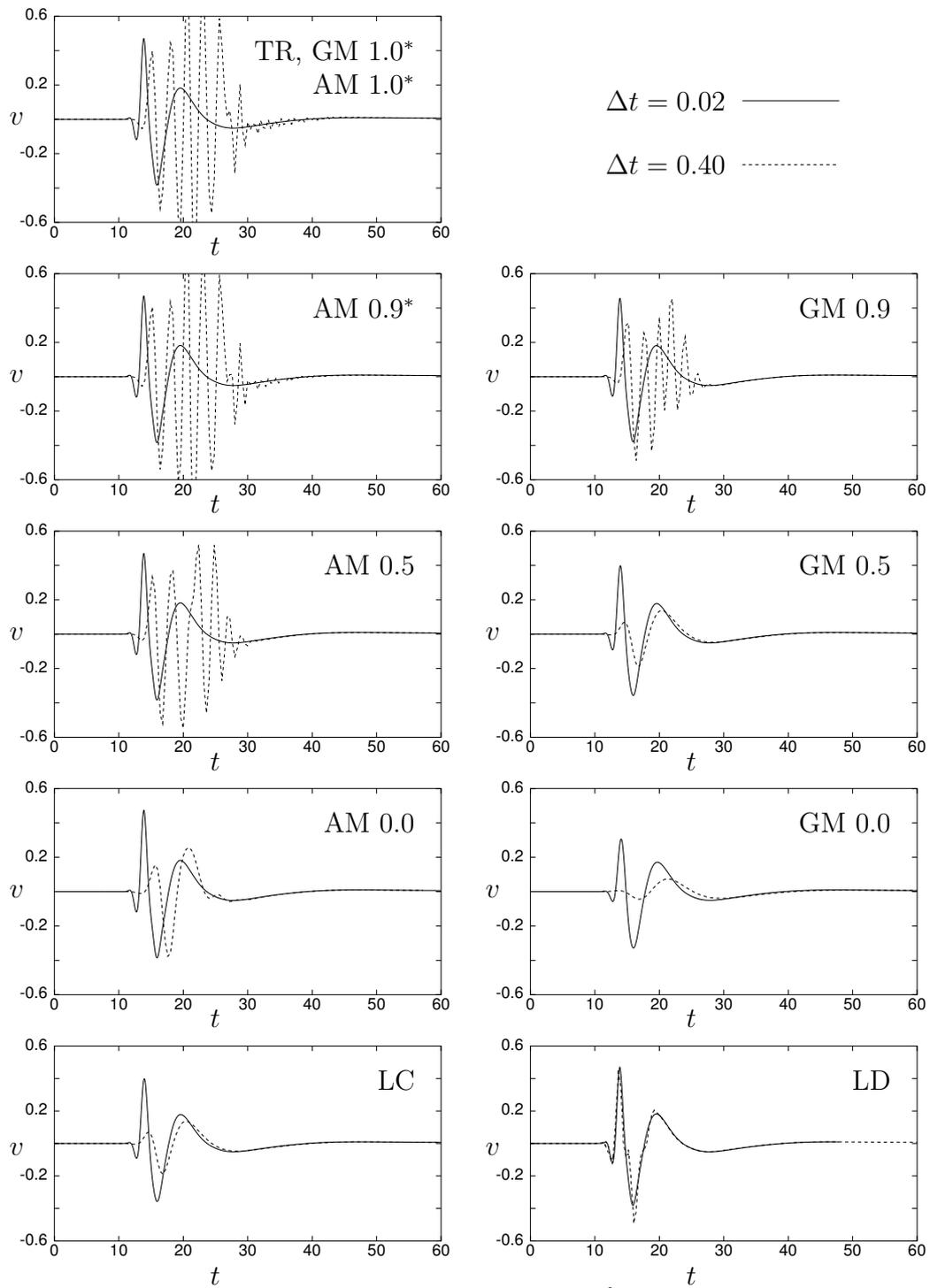


Figure 5.33: Flow across a backward facing step, evolution of the velocity in  $y$ -direction at point A,  $Re = 800$ , 11160 elements.

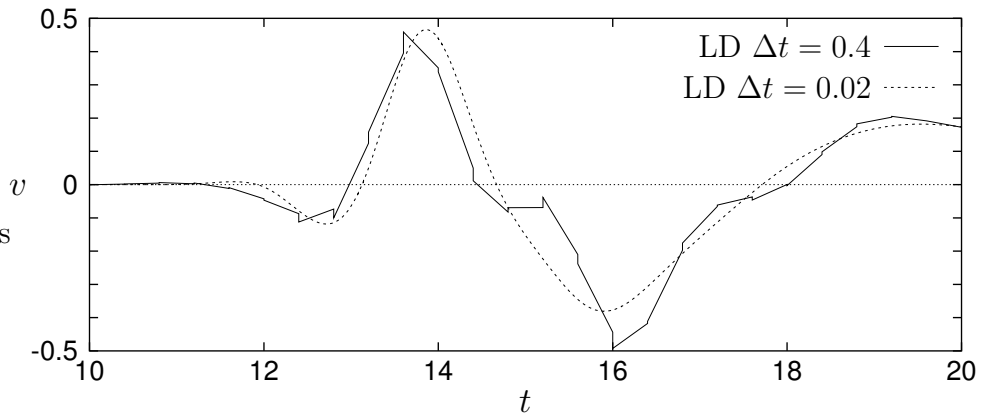


Figure 5.34: Flow across a backward facing step, detail of the evolution of the velocity in  $y$ -direction at point A,  $Re = 800$ , 11160 elements, linear discontinuous in time space time method (LD).

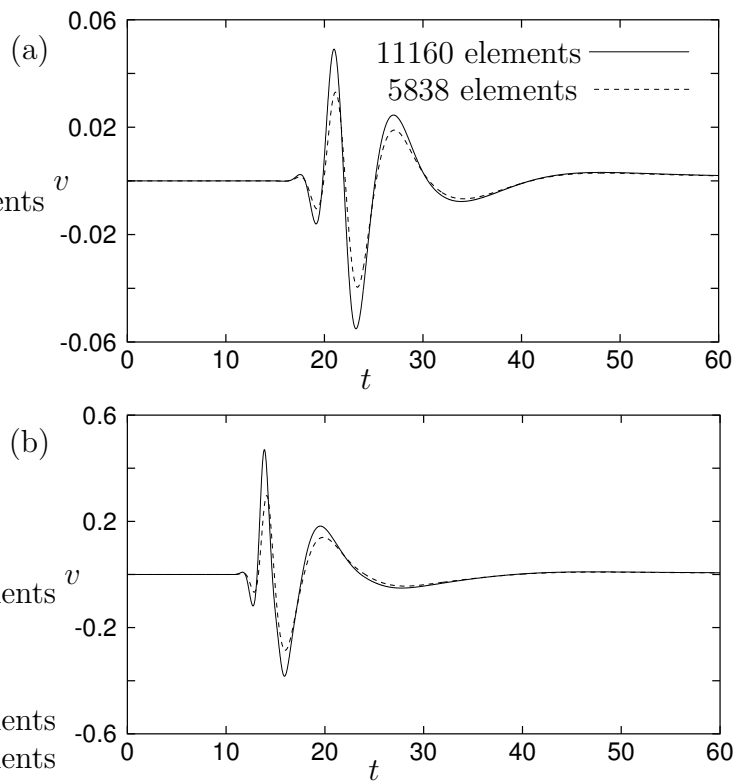


Figure 5.35: Flow across a backward facing step, evolution of the velocity in  $y$ -direction at point A, solution for different meshes, (a)  $Re = 500$ , (b)  $Re = 800$ ; AM  $\rho_\infty^h = 0.9$ ,  $\Delta t = 0.02$ .

### 5.3.5 Conclusions

In general, it may be said that many of the properties of the solution procedures of the scalar model problem (Section 5.1) and the one dimensional advection-diffusion problem (Section 5.2) are also characteristic for the incompressible Navier-Stokes equations. Summarising, the following observations are made from the numerical examples in Sections 5.3.3 and 5.3.4:

1. *limit behaviour as  $\Delta t \rightarrow 0$ .* Clearly, all the time integration schemes considered converge to the same solution as  $\Delta t \rightarrow 0$ . This solution depends only on the spatial mesh.
2. *convergence as  $\Delta t \rightarrow 0$ .* It can be observed from the simulations of the flow around the cylinder (see Figures 5.25 – 5.27) that, for  $\rho_\infty^h < 1$ , the errors associated with the discretisation in time are significantly smaller for the generalised- $\alpha$  method AM than for the generalised midpoint rule GM. It can be perceived, especially for small values  $\rho_\infty^h$ , that the qualitative convergence of the method AM as  $\Delta t \rightarrow 0$  is quadratic rather than linear, whereas GM converges linearly. Naturally, both methods AM and GM coincide with the trapezoidal rule if  $\rho_\infty^h = 1$ . Notably, the trapezoidal rule renders very good results for the flow around the cylinder. The example of the backward facing step clearly demonstrates the strong numerical damping associated with the method GM and the tendency of the scheme AM to oscillatory behaviour (see Figure 5.33).

The linear continuous in time space-time finite element method renders results, which are almost identical to the generalised midpoint rule for  $\rho_\infty^h = 0.5$  (see Figures 5.25 – 5.27, 5.33). Note, however, that the methods are identical only for linear problems.

Figures 5.25 – 5.27 show that, for both the linear discontinuous in time space-time finite element method LD and the generalised- $\alpha$  method AM, the time discretisation errors of the Strouhal number and the lift coefficient are small, even for a relatively coarse mesh and moderate time step. In particular, the method LD renders highly accurate Strouhal numbers, whereas the scheme AM with  $\rho_\infty^h > 0$  gives better approximations of the lift coefficient. These observations agree with the conclusions drawn from the Fourier analysis of the advection-diffusion problem in Section 5.2.3.2, if the Strouhal number and the lift coefficient are regarded as corresponding to the frequency  $\omega^h$  and the damping coefficient  $\xi^h$ , respectively. For the flow across the backward facing step the method LD performs remarkably well (see Figures 5.33 and 5.34). It gives an acceptable approximation of the solution

for a time step size, which causes oscillatory behaviour or excessive numerical damping when used with any of the other methods considered. However, it should be recalled that this good performance has been achieved at a computational cost more than twice as high as for the semi-discrete schemes.

3. *pressure distribution and velocity field.* For any time step size  $\Delta t$  the pressure field is free of spurious modes. Numerical oscillations of the velocity field have not been observed.
4. *performance of the Newton-Raphson procedure.* The Newton-Raphson procedure has proved to be very robust and stable. The convergence of the residual is quadratic. For reasonable time step sizes the number of necessary iterations is usually smaller than or equal to three or four.
5. *limits of the methods.* The Newton-Raphson procedure fails only in situations where the time step size is chosen unreasonably large or the spatial finite element mesh is so coarse that the local Reynolds numbers become very large. In both cases the nonlinearities of the problem are very strong and they affect the convergence of the Newton-Raphson procedure. In order to avoid large local Reynolds numbers the spatial mesh is required to be refined as the global Reynolds number increases.

In some cases it has been observed that, for a given spatial mesh, the temporal discretisation could not be refined beyond a critical small time step size, due to the occurrence of spurious oscillations in time. Thus, the numerical damping associated with the spatial discretisation is not always sufficient to damp out high frequency waves, which are not resolved by the spatial mesh. The problem is easily overcome by employing a more dissipative time integration scheme (damp out high frequency effects) or by refining the spatial mesh (resolve high frequency effects). However, this restriction of the independence of the spatial and temporal discretisations may sometimes be encountered, especially with very complex fluid flows.

Generally, it seems that accurate solutions can be obtained with reasonable computational cost for the whole range of Reynolds numbers occurring in laminar flow problems, to which this work is restricted.

Thus, the major conclusions to be drawn from the investigation of the time integration schemes in this chapter may be summarised as follows:

1. Many phenomena exhibited by the solution procedures for the Navier-Stokes equations can be explained from the analysis of the scalar model problem and the one dimensional advection-diffusion equation.

2. For the numerical strategies considered, the discretisation of space and time can, at least to a high degree, be refined independently. Taking into account the good performance of the Newton-Raphson procedure, it may be said that the solution methodologies are very robust.
3. In the numerical test problems, the generalised- $\alpha$  method AM, including the trapezoidal rule as its limit case, has proved very efficient. For large time steps the linear discontinuous in time space-time finite element method LD neither suffers from excessive numerical damping, nor does the solution exhibit unwanted oscillations. However, the numerical damping behaviour is not always superior to the generalised- $\alpha$  method (see Sections 5.2.3.2 and 5.3.3) and, once the time step is reasonably small with respect to the time scales which ought to be resolved, the method LD appears not to be more accurate than the generalised- $\alpha$  method. Most importantly, for the same time step size, its computational cost are twice as high as for the method AM.

Thus, we here decide to employ the generalised- $\alpha$  method for the extension of the numerical model to moving domains and fluid-solid interaction problems in the following chapters. It may be argued that the investigation of the time integration schemes has to account for the motion of the fluid domain, before this decision can be made. However, for the sake of brevity, such an extended investigation is not performed in this thesis.



## Chapter 6

# Arbitrary Lagrangian-Eulerian Description of Fluid Flow

The semi-discrete and space-time stabilised finite element formulations as described in Section 5.3 are restricted to fluid flow problems on fixed domains. The *Eulerian* methods are, however, incapable of accounting for any change in the geometry of the domain during the time interval of interest.

Some fluid flows in moving domains at low Reynolds numbers may be modelled in a *Lagrangian* framework, possibly employing adaptive remeshing (see e. g. Ramaswamy and Kawahara [95], Saksono and Perić [104,105] or Radovitzky and Ortiz [92]). The more elegant and certainly more efficient solution lies, however, in the use of the so-called *arbitrary Lagrangian-Eulerian* (ALE) description of the flow. Therefore, the reference frame, which is otherwise fixed in space (Euler) or coincides with the fluid particle positions (Lagrange), is allowed to move independently of the fluid flow (see Section 2.1.1). Practically, this means, that the boundary of the finite element mesh may follow the motion of eventual interfaces of the fluid phase with other liquid or solid phases. Thus, the ALE formulation makes a wide range of fluid flow problems accessible to the finite element method without requiring excessive remeshing. Such problems include free surface flows and fluid-solid interaction, both of which are treated in detail in the following chapters.

Some of the first researchers to demonstrate the potential of the ALE strategy are, among others, Hirt *et al* [59], Hughes *et al* [70], Donea [36], Ramaswamy and Kawahara [93,94], Huerta and Liu [63], Soulaimani *et al* [111], Tezduyar *et al* [121,122], Nomura and Hughes [84]. More recent publications are e. g. Sackinger *et al* [102], Masud and Hughes [80], Soulaimani and Saad [112], Behr and Tezduyar [6], Braess and Wriggers [12], Belytschko *et al* [7], Wall [127], Hübner *et al* [61], Sarrate *et al* [106].

The ALE strategy may be based on either semi-discrete or space-time

finite element formulations <sup>1</sup>. In Chapter 5 a comparative study of semi-discrete and space-time stabilised finite element methods in an Eulerian framework has been performed. The semi-discrete scheme based on the generalised- $\alpha$  method has been shown to achieve a high degree of accuracy at relatively low computational cost. Thus, it is the objective of this chapter to adapt the semi-discrete formulation given by (5.129) to the ALE framework. There are, however, many researchers, who consider the space-time formulation as more appropriate for the treatment of moving domains. Amongst the references given above the publications [6, 61, 80, 121, 122], are based on space-time methods, whereas the others employ semi-discrete formulations.

Generally, it is the changing geometry of the boundary, or, more precisely, the motion of the boundary nodes, which drives the deformation of the mesh. For a wide range of fluid flow problems, each section of the boundary of the finite element mesh may either be fixed in space (i), or its motion may be known a priori (ii), it may represent a free surface (iii), or it may coincide with a fluid-solid or fluid-fluid interface, the motion of which follows from the mechanical interaction of the two phases (iv). The motion of the internal nodes of the finite element mesh is constrained by the deformed boundary and required to maintain the admissibility of the mesh, but otherwise it is arbitrary. Hence, the internal nodes should be moved such that, at all times, the quality of the finite element mesh is as good as possible. For this purpose, many different mesh update algorithms have been developed. The techniques used in this work are presented in Section 6.2.

It should be noted that certain parts of the mesh, which are far away from the moving boundary sections, may remain fixed in space throughout the time interval of interest  $I = [0, T_{\text{end}}]$ . In such areas of the domain, the finite element formulation is purely Eulerian. The computational efficiency may thus be increased significantly.

In the following sections, the finite element formulation for the moving mesh is presented and, subsequently, the mesh update techniques are discussed. In Section 6.3, two numerical examples are presented, for which the boundary movement is known a priori and independent of the fluid flow. The more interesting and computationally challenging cases, where parts of the boundary coincide with a free surface or a fluid-solid interface, are discussed in the subsequent chapters of this work.

---

<sup>1</sup>Often, the terminology of “ALE” is restricted to semi-discrete methodologies and space-time methods are presented as an alternative to ALE strategies. However, in both cases the crucial point is to allow arbitrary motion of the finite element mesh. The only motivation for this differentiation is that, in space-time methods, the mesh velocity does not appear explicitly in the convection term.

## 6.1 Fluid Finite Element Formulation on a Moving Domain

In order to extend the formulation (5.129) to moving meshes, the fixed spatial reference frame, on which equation (5.129) is based, needs to be replaced by the ALE framework, which has been introduced in Section 2.1.1. Thus, the mesh coordinates  $\hat{\mathbf{x}}^h$  are no longer fixed in space, but describe the current configuration of the mesh, and the velocity field  $\hat{\mathbf{v}}^h$  represents the current mesh motion. Both  $\hat{\mathbf{x}}^h$  and  $\hat{\mathbf{v}}^h$  may change significantly during the time interval of interest. In this work, the same piecewise linear spatial finite element interpolation is employed for the primary unknowns  $\mathbf{u}^h$  and  $p^h$  and for the mesh related quantities  $\hat{\mathbf{x}}^h$  and  $\hat{\mathbf{v}}^h$ . Therefore, the nodal basis vectors  $\hat{\mathbf{x}}_a$  and  $\hat{\mathbf{v}}_a$ ,  $a = 1, 2, \dots, n_{\text{nd}}$  are introduced. The discretisation in time requires the definition of the vector fields  $\hat{\mathbf{x}}_n^h$  and  $\hat{\mathbf{v}}_n^h$ , which describe the configuration of the mesh and the mesh velocity field, respectively, at time instant  $t_n$ .

Two modifications of the formulation (5.129) are necessary. First, the convective velocity  $\mathbf{u}_\alpha^h$  has to be replaced by  $\mathbf{u}_\alpha^h - \hat{\mathbf{v}}_{\hat{\alpha}}^h$ . This follows directly from the representation of the governing equations in a moving reference frame (2.44). Second, the integration has to be performed over the deformed spatial domain  $\Omega_{\hat{\alpha}}$  given by  $\hat{\mathbf{x}}_{\hat{\alpha}}^h$ . Similar to  $\alpha$ , the subscripts  $\hat{\alpha}$  and  $\tilde{\alpha}$  denote time instants in the interval  $[t_n, t_{n+1}]$  and remain to be specified precisely.

The stabilised finite element formulation for a moving mesh may then be written as: Given the previous solution  $\mathbf{u}_n^h$ , find  $\mathbf{u}_{n+1}^h \in \mathcal{U}_{n+1}$  and  $p_\alpha^h \in \mathcal{P}^h$ , such that for all  $\mathbf{w}^h \in \mathcal{W}^h$  and  $q^h \in \mathcal{P}^h$

$$\begin{aligned} & \int_{\Omega_{\hat{\alpha}}} \left[ \mathbf{w}^h \cdot \rho \left( \dot{\mathbf{u}}_\beta^h + (\nabla \mathbf{u}_\alpha^h) (\mathbf{u}_\alpha^h - \hat{\mathbf{v}}_{\hat{\alpha}}^h) - \mathbf{f} \right) - (\nabla \cdot \mathbf{w}^h) p_\alpha^h \right. \\ & \quad \left. + 2\mu \nabla \mathbf{w}^h : \nabla^s \mathbf{u}_\alpha^h + (\nabla \cdot \mathbf{u}_\alpha^h) q^h \right] dv - \int_{\Gamma_t} \mathbf{w}^h \cdot \mathbf{t}_\alpha^h da \\ & + \sum_{e=1}^{n_{\text{el}}} \int_{\Omega_{\hat{\alpha}}^e} \left[ \tau_u \rho (\nabla \mathbf{w}^h) (\mathbf{u}_\alpha^h - \hat{\mathbf{v}}_{\hat{\alpha}}^h) + \tau_p \nabla q^h \right] \\ & \quad \cdot \left[ \rho \left( \dot{\mathbf{u}}_\beta^h + (\nabla \mathbf{u}_\alpha^h) (\mathbf{u}_\alpha^h - \hat{\mathbf{v}}_{\hat{\alpha}}^h) - \mathbf{f} \right) + \nabla p_\alpha^h \right] dv = 0, \end{aligned} \quad (6.1)$$

where, similarly to (5.128), the finite element spaces are defined as

$$\begin{aligned} \mathcal{U}_{n+1}^h &= \left\{ \mathbf{u}_{n+1}^h \in (H^1(\Omega_{\hat{\alpha}}))^{n_{\text{sd}}} \mid \mathbf{u}_{n+1}^h|_{\hat{\mathbf{x}}^h \in \Omega_{\hat{\alpha}}^e} \in (P_1(\Omega_{\hat{\alpha}}^e))^{n_{\text{sd}}}, \mathbf{u}_{n+1}^h|_{\hat{\mathbf{x}}^h \in \Gamma_{\mathbf{g}, \hat{\alpha}}} = \mathbf{g}_n \right\} \\ \mathcal{W}^h &= \left\{ \mathbf{w}^h \in (H^1(\Omega_{\hat{\alpha}}))^{n_{\text{sd}}} \mid \mathbf{w}^h|_{\hat{\mathbf{x}}^h \in \Omega_{\hat{\alpha}}^e} \in (P_1(\Omega_{\hat{\alpha}}^e))^{n_{\text{sd}}}, \mathbf{w}^h|_{\hat{\mathbf{x}}^h \in \Gamma_{\mathbf{g}, \hat{\alpha}}} = \mathbf{0} \right\} \\ \mathcal{P}^h &= \left\{ q^h \in H^1(\Omega_{\hat{\alpha}}) \mid q^h|_{\hat{\mathbf{x}}^h \in \Omega_{\hat{\alpha}}^e} \in P_1(\Omega_{\hat{\alpha}}^e) \right\}. \end{aligned} \quad (6.2)$$

Note that the convective velocity also has to be changed in the formula for the stabilisation parameters, which results in the relations

$$\begin{aligned}\tau &= \frac{h^e}{2 \|\mathbf{u}_\alpha^e - \hat{\mathbf{v}}_\alpha^e\| \rho} \xi \\ \xi &= \frac{\beta_1}{\sqrt{1 + \left(\frac{\beta_1}{\beta_2 Re^e}\right)^2}}, \quad Re^e = \frac{\|\mathbf{u}_\alpha^e - \hat{\mathbf{v}}_\alpha^e\| h^e \rho}{2 \mu}.\end{aligned}\quad (6.3)$$

As before,  $\beta_1$  and  $\beta_2$  may be set differently for  $\tau_u$  and  $\tau_p$ . From Section 5.3.1.2 it is recalled that for the generalised- $\alpha$  method

$$\begin{aligned}\mathbf{u}_\alpha^h &= \alpha_f \mathbf{u}_{n+1}^h + (1 - \alpha_f) \mathbf{u}_n^h \\ \dot{\mathbf{u}}_\beta^h &= \frac{\alpha_m}{\gamma \Delta t} \mathbf{u}_{n+1}^h - \frac{\alpha_m}{\gamma \Delta t} \mathbf{u}_n^h + \left(1 - \frac{\alpha_m}{\gamma}\right) \dot{\mathbf{u}}_n^h \\ \mathbf{t}_\alpha^h &= \alpha_f \mathbf{t}_{n+1}^h + (1 - \alpha_f) \mathbf{t}_n^h\end{aligned}\quad (6.4)$$

and

$$\dot{\mathbf{u}}_{n+1}^h = \frac{1}{\gamma \Delta t} \mathbf{u}_{n+1}^h - \frac{1}{\gamma \Delta t} \mathbf{u}_n^h - \frac{1 - \gamma}{\gamma} \dot{\mathbf{u}}_n^h, \quad (6.5)$$

where the integration parameters depend on the user defined limit of the spectral radius  $\rho_\infty^h$ ,

$$\gamma = \frac{1}{2} + \alpha_m - \alpha_f, \quad \alpha_m = \frac{1}{2} \frac{3 - \rho_\infty^h}{1 + \rho_\infty^h}, \quad \alpha_f = \frac{1}{1 + \rho_\infty^h}. \quad (6.6)$$

It remains to clarify the temporal discretisation of the mesh motion. In this work,  $\hat{\mathbf{x}}_n^h$  and  $\hat{\mathbf{v}}_n^h$  are related by a simple generalised midpoint scheme

$$\hat{\mathbf{v}}_{n+1}^h = \frac{1}{\hat{\gamma} \Delta t} \hat{\mathbf{x}}_{n+1}^h - \frac{1}{\hat{\gamma} \Delta t} \hat{\mathbf{x}}_n^h - \frac{1 - \hat{\gamma}}{\hat{\gamma}} \hat{\mathbf{v}}_n^h, \quad (6.7)$$

where  $\hat{\gamma}$  is an integration parameter to be defined such that  $\frac{1}{2} \leq \hat{\gamma} \leq 1$ . We set  $\hat{\gamma} = \gamma$  (see (6.6)<sub>1</sub>), and thus  $\hat{\gamma}$  follows from the choice of  $\rho_\infty^h$ . Similar to (6.4)<sub>1</sub>, the quantities  $\hat{\mathbf{x}}_\alpha^h$  and  $\hat{\mathbf{v}}_\alpha^h$  are then defined as

$$\hat{\mathbf{x}}_\alpha^h = \alpha_f \hat{\mathbf{x}}_{n+1}^h + (1 - \alpha_f) \hat{\mathbf{x}}_n^h \quad (6.8)$$

$$\hat{\mathbf{v}}_\alpha^h = \alpha_f \hat{\mathbf{v}}_{n+1}^h + (1 - \alpha_f) \hat{\mathbf{v}}_n^h. \quad (6.9)$$

The vector field  $\hat{\mathbf{x}}_\alpha^h$  describes the configuration of the domain  $\Omega_{\hat{\alpha}}$ , over which the integrals in (6.1) are computed. The employment of  $\alpha_f$  in the relations

(6.8) and (6.9) is motivated from the generalised- $\alpha$  method for second order problems (see Section 8.4).

Assuming that the mesh configuration or, in other words, the nodal positions  $\hat{\mathbf{x}}_{a,n}$  at each discrete time instant  $t_n$  are known, the equations (6.1) – (6.9) provide all the necessary relations to solve for the unknowns  $\mathbf{u}_{n+1}^h$  and  $p_\alpha^h$ , by means of a Newton-Raphson procedure.

*REMARK 6.1: Geometrical Conservation Law (GCL).* It has very early been observed that finite volume, finite difference and also some finite element methods perform well on fixed grids, but very poorly on moving meshes unless certain precautions are taken. In particular, the conservation of mass was often violated significantly. The investigation of this effect led to the formulation of the so-called *geometrical conservation laws* (GCL), which are necessary (but not necessarily sufficient) conditions to ensure that the numerical scheme is equally accurate on a moving mesh and a fixed mesh. The GCL of a particular formulation is derived from the requirement that uniform flow must be recovered exactly. Usually, this leads to a specific time integration scheme for the mesh movement, which is given here by the relations (6.7) – (6.9). Recent publications on the GCL are *e. g.* Lesoinne and Farhat [78], Guillard and Farhat [54], Le Tallec and Mouro [117]. It should also be noted that the significance of the GCL is still being discussed, since many numerical schemes, which do not satisfy the GCL exactly, render good results.

In this work, the issue of the GCL does not seem relevant since the formulation (6.1) recovers uniform flow exactly and independently of the relations (6.7) – (6.9), as can be easily verified. In this context it is also referred to Sections 6.3.1 and 6.3.2, where two numerical examples are presented, which allow the comparison of Eulerian and ALE solutions. The results obtained are identical, *i. e.* the errors are of the same order of magnitude.

## 6.2 Mesh Update Methods

In order to adjust the positions of the internal nodes to the changing configuration of the mesh boundary, an appropriate mesh update algorithm is required. It should possess the following properties:

- (i) It should be computationally inexpensive,
- (ii) It should render optimal mesh quality, *i. e.* avoid extreme element distortion,
- (iii) It should work on unstructured as well as structured meshes,

- (iv) It should be robust, *i. e.* capable of adapting the finite element mesh to very distorted geometries,
- (v) In this work, we also require the mesh update algorithm to allow the computation of its linearisation, *e. g.* the derivative of the positions of the internal nodes with respect to those of the boundary nodes,  $d\hat{\mathbf{x}}^{\text{internal}}/d\hat{\mathbf{x}}^{\text{boundary}}$ .

Many different mesh update techniques have been suggested in recent publications. A basic classification distinguishes three main strategies:

- *interpolation techniques.* Such strategies range from very simple interpolation of the nodal positions in structured meshes to rather sophisticated algorithms, which are also applicable to unstructured meshes. These methods require relatively little computational effort and have been reported to work well for small and moderate distortion of the geometry. However, they fail or render poorly shaped elements when applied to problems with more significant deformation of the finite element mesh. Also, they require the assignment of certain boundary nodes to each moving internal node of the mesh, such that the position of the internal node can be obtained from the interpolation between the appropriate boundary nodes. More information on interpolation strategies is provided in Wall [127] and references therein.
- *pseudo-elastic technique.* In this approach, the mesh is simply assumed to represent an elastic solid body. A standard Lagrangian finite element technique typically employed in solid mechanics can then be used to adapt the mesh to the new geometry of the domain. Note that some numerical aspects of the finite element modelling of elasticity, for example volumetric locking, are entirely irrelevant in this context.

For small distortions of the geometry the linear elastic model is sufficient. In the presence of large deformations of the fluid domain a hyperelastic model may be more suitable. For problems with periodically repeated deformation of the domain, *e. g.* free surface waves or flow around oscillating solid structures, the “stress free” reference configuration should be kept unchanged throughout the simulation, whereas severe non-periodic deformation of the fluid domain seems to be more successfully treated, if, for each mesh update, the previous finite element mesh is assumed to be “stress free”.

The mesh does not necessarily need to represent an elastic continuum. In literature, alternative methodologies have been suggested in which the mesh is, for example, assumed to be a network of elastic springs

(see *e. g.* Degand and Farhat [28] and references therein). Nonlinear models require the application of a Newton-Raphson procedure.

- *optimisation of mesh quality.* The mesh can be moved in such a way that its quality, with respect to a certain criteria, is optimal.

A popular strategy consists in iterative smoothing, whereby, sequentially, each node is positioned in the centre of the patch of the adjacent elements. After four or five iterations, each node usually lies in the centre of the associated patch of elements, which corresponds to a smooth mesh. However, this procedure lacks robustness, since it often fails at sharp concave corners of the boundary, where it creates elements with negative volumes. Furthermore, it cannot be linearised.

More sophisticated optimisation strategies for different element types are presented in Bar-Yoseph *et al* [4]. The quality criteria are mostly based on the aspect ratio of the elements. In particular, for the three noded two dimensional triangular or the four noded three dimensional tetrahedron elements, it is suggested to update the finite element mesh such that it satisfies the condition

$$W = \sum_{e=1}^{n_{el}} \left( \frac{r_{out}^e}{r_{in}^e} \right) \Rightarrow MIN, \quad (6.10)$$

where the quantities  $r_{in}^e$  and  $r_{out}^e$  denote the radii of the inner and the outer circle or sphere of the triangular or tetrahedron finite element, respectively. This methodology renders acceptable meshes even for very distorted geometries. Note that also the initial mesh should be optimal with respect to the chosen criteria. In Braess and Wriggers [12] an expression very similar to (6.10) is employed.

The optimisation strategies often require the solution of a highly nonlinear system of equations for each mesh update by means of a Newton-Raphson procedure. Thus, they may involve considerable computational effort, but, in fact, they possess all the other desirable properties (ii) – (v) listed above.

For the two dimensional meshes of linear triangular finite elements employed in the numerical examples of this work, two closely related pseudo-elastic strategies and one optimisation method are considered. In the following chapters, they are referred to as the mesh update methods of type A, B and C. Note that all of them are nonlinear and require the employment of a Newton-Raphson procedure. The strategies are described as follows:

- (A) *Neo-Hookean elasticity*. The mesh is treated as a simple hyperelastic Neo-Hookean continuum under plane strain conditions, with two material parameters  $\mu_{\text{mesh}}$  and  $K_{\text{mesh}}$ , representing the shear and bulk modulus, respectively. A straightforward linear finite element formulation is employed, whereby only one Gauß point is needed for the integration over each element. The strong locking effects associated with the low order triangular elements are irrelevant. Details of the standard finite element formulation for a Neo-Hookean elastic continuum are given in the Section 8.1.
- (B) *Neo-Hookean elasticity with updated reference configuration*. This technique is identical to type A, apart from the choice of the “stress free” reference configuration. Type A employs a fixed reference configuration, which usually coincides with the configuration of the mesh at time instant  $t_0$ , whereas here, each updated mesh serves as the “stress free” reference configuration for the next time step. This strategy allows the overall algorithm to cope with extremely distorted geometries, but is not recommended for problems with oscillating mesh boundaries, since the mesh quality degenerates with each cycle.
- (C) *optimisation of aspect ratio*. For each mesh update the expression  $W$  in (6.10) is minimised. For an arbitrary triangle, it can be shown that

$$\frac{r_{\text{out}}}{r_{\text{in}}} = \frac{a b c s}{4 A^2}, \quad s = \frac{a + b + c}{2}, \quad A^2 = s(s - a)(s - b)(s - c), \quad (6.11)$$

where the terminology is taken from Figure 6.1. The expression  $W$  assumes a minimum, if all the derivatives  $\partial W / \partial \mathbf{x}_{a,i}$ ,  $a = 1, 2, \dots, n_{\text{nd}}^{\text{ALE}}$ ,  $i = 1, \dots, n_{\text{sd}}$ , disappear. The number of nodes, the position of which needs to be updated, is denoted as  $n_{\text{nd}}^{\text{ALE}}$ . Thus, one obtains a system of nonlinear equations, which can be solved by means of a Newton-Raphson procedure.

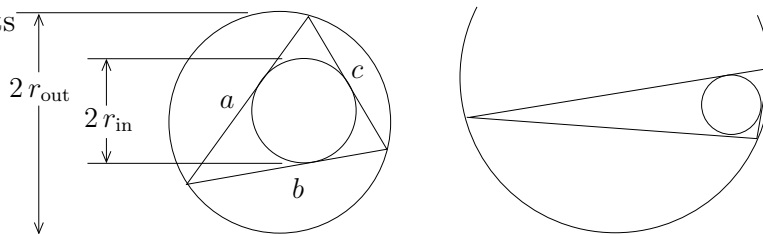


Figure 6.1: A well shaped and a distorted triangular element.

The employment of large time steps in problems involving severe deformations of the domain often requires the adaptation of the mesh to substantial changes of the geometry within one time step. In such cases the Newton-Raphson procedure may fail to converge. In this work, this problem is overcome by increment cutting within the mesh update procedure, *i. e.* the new displacement of the boundary is applied in increments if necessary.

Finally, it should be noted that the mesh update procedure is always applied to the nodal positions at the discrete time instants  $t_n$ . Consequently, the mesh configuration  $\Omega_{\tilde{\alpha}}$ , over which the integration in (6.1) is performed, represents an interpolation between two “optimal” mesh configurations.

## 6.3 Fluid Flow with Prescribed Boundary Movement

In this section three numerical examples are provided which belong to the class of problems, for which the movement of the boundary is known a priori. Thus, the motion of the mesh is entirely independent of the fluid flow. Consequently, the convergence of the Newton-Raphson procedure, employed to solve (6.1) for the unknowns  $\mathbf{u}_{n+1}^h$  and  $p_{\alpha}^h$ , is not affected by the movement of the mesh.

The first two examples test the accuracy of the formulation in comparison with fixed mesh solutions. In both cases, the ALE formulation on the moving mesh is as accurate as the Eulerian reference solution.

### 6.3.1 Example I: Flow Around a Cylinder

The steady movement of a rigid cylinder through a fluid at rest is modelled. The finite element mesh is attached to the cylinder and performs a translational rigid body motion through the physical fluid domain. Consequently, there is no need for a mesh update procedure as described in Section 6.2. The mesh velocity field  $\hat{\mathbf{v}}_n$  is uniform and identical for all time instants  $t_n$ .

The geometry of the domain and also the mesh with 1576 finite elements are taken from Section 5.3.3, Figures 5.20 and 5.21. The problem parameters are set to  $\mu = 0.01$ ,  $\rho = 1$  and  $u_{\infty} = 1$ , which corresponds to  $Re = u_{\infty} D \rho / \mu = 100$ . Note that  $u_{\infty}$  now denotes the velocity of the cylinder and the mesh. The time step size is chosen as  $\Delta t = 0.2$  and the time integration parameter is set to  $\rho_{\infty}^h = 0.5$ . The velocity and pressure boundary conditions are identical to Figure 5.20, apart from the inflow boundary, where the fluid velocity in  $x$ -direction is set to zero.

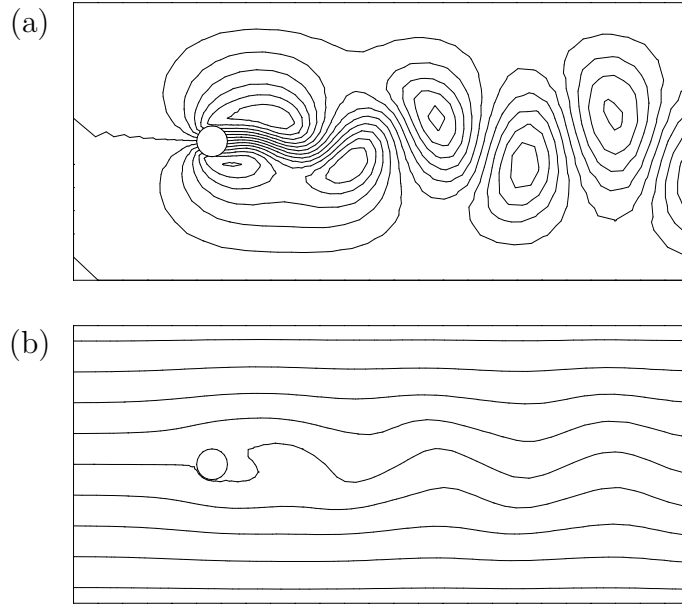


Figure 6.2: Streamlines for a cylinder moving through a fluid at rest (a) and for the flow around a cylinder (b);  $Re = 100$ ,  $t = 200.2$ , 1576 elements,  $\Delta t = 0.2$ .

After approximately 80 time units, stable periodic vortex shedding is observed in the wake of the cylinder. Figure 6.2 (a) shows typical streamlines. Using (5.137), the lift coefficient  $C_L$  and the Strouhal number  $Sr$  are evaluated from the fluid reaction force on the cylinder. The results read

$$\max(C_L) = 0.2731 \quad \text{and} \quad Sr = 0.1666, \quad (6.12)$$

which agrees exactly with the values obtained from the corresponding Eulerian simulation in Section 5.3.3 and displayed in the diagrams of Figure 5.25 (a).

### 6.3.2 Example II: Flow through a Narrowing Channel

In this example, the two dimensional flow through a narrowing channel is simulated. The geometry of the problem is displayed in Figure 6.3. Advantage is taken of the symmetry of the domain. The fluid parameters are set to  $\rho = 1$ ,  $\mu = 0.01$  and the average inflow velocity is chosen as  $\bar{u}_{\text{in}} = 2/3$ . The quadratic distribution of the velocity over the inflow orifice corresponds to undisturbed Poiseuille flow. Thus, the Reynolds number of the problem is obtained as  $Re = \bar{u}_{\text{in}} D \rho / \mu \approx 53$ , where  $D = 0.8$  denotes the diameter of the

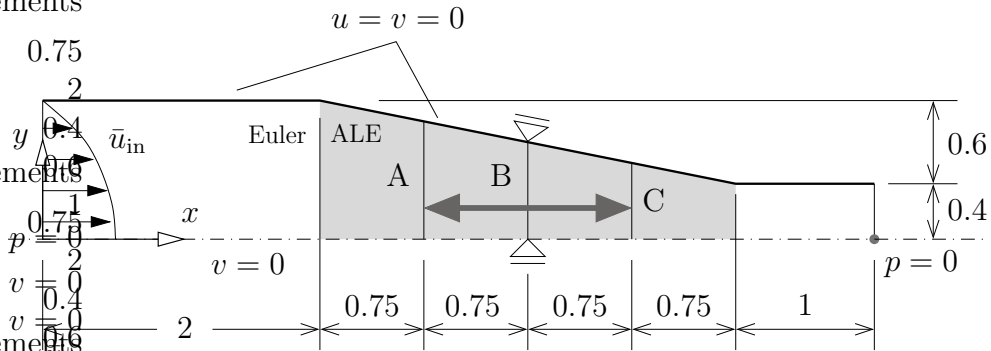


Figure 6.3: Narrowing channel, geometry of the problem.

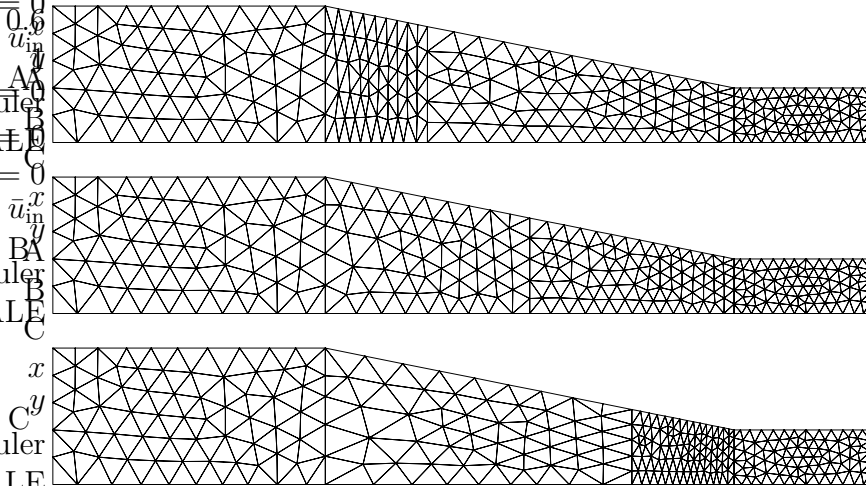


Figure 6.4: Narrowing channel, mesh configurations A, B and C, 531 elements.

outflow cross section. The channel wall is modelled as a no-slip boundary. A finite element mesh with 531 elements is employed.

Clearly, the flow can be modelled in an Eulerian framework. However, for testing purposes, the mesh in the funnel shaped part of the domain is being deformed as follows: The finite element nodes on B are subjected to a sinusoidal motion with  $T_{\text{mesh}} = 1$ , such that they oscillate between positions on A and C. The letters A, B and C refer to the vertical lines displayed in Figure 6.3. Thus, the mesh configurations A, B and C are defined as displayed in Figure 6.4. Apart from the prescribed horizontal motion of the driving nodes and the constraint given by the fixed geometry of the domain, the motion of the finite element nodes in the ALE region is subject to the mesh update technique defined as type C in Section 6.2.

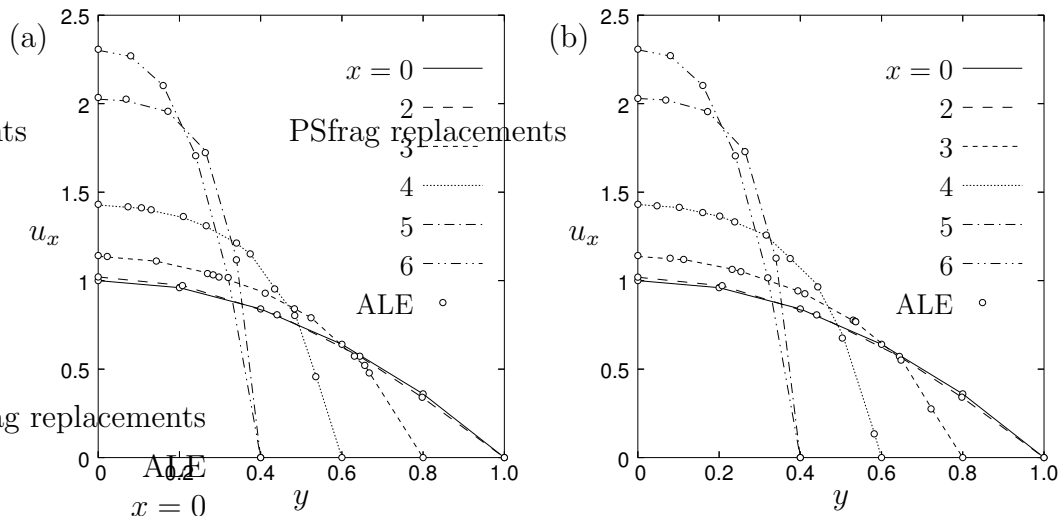


Figure 6.5: Narrowing channel, velocities in  $x$ -direction at different cross sections; Eulerian (lines) and ALE (points) solutions, mesh in configurations A (a) and B (b),  $\rho_\infty^h = 0.5$ .

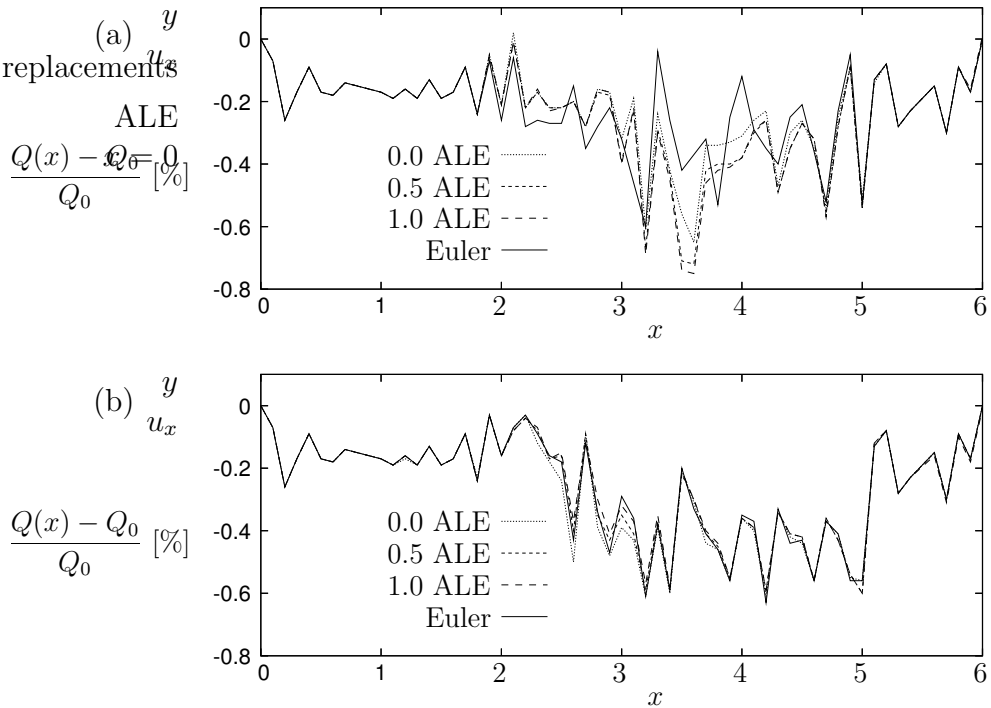


Figure 6.6: Narrowing channel, relative error of the flow rate along  $x$ -axis; mesh in configurations A (a) and B (b), different integration parameters  $\rho_\infty^h = 0.0, 0.5, 1.0$ .

Simulations are performed for  $\rho_\infty^h = 0.0, 0.5, 1.0$ . The time step size is chosen as  $\Delta t = T_{\text{mesh}}/20 = 0.05$ . In order to eliminate the unsteady effects of the initial sudden start of the flow, the simulations are run for a sufficient number of time periods  $T_{\text{mesh}}$ , which varies between five and ten. Also purely Eulerian simulations are performed employing both a fixed mesh in configuration A and a fixed mesh in configuration B. The steady state Eulerian solutions, which are obtained after a few time steps, are independent of the time integration parameter  $\rho_\infty^h$  (compare Section 5.3.4).

Figure 6.5 shows the velocity in  $x$ -direction across different cross sections of the channel. The Eulerian and ALE solutions are represented by the lines and the points, respectively. The agreement is excellent. The diagrams in Figure 6.6, which display the relative error of the flow rate  $Q = \int u_x dy$  along the axis of the channel, show this agreement in more detail. Clearly, the order of magnitude of the error is the same for the moving mesh as for the fixed mesh. Note in particular, the small deviation of the flow rate errors in Figure 6.5 (b), which represents the situation, when the mesh velocities are maximal.

### 6.3.3 Example III: Channel with Wall Indentation

This example considers the two dimensional flow through a channel with an oscillating wall indentation. The problem has been investigated both experimentally and numerically by several researchers, see *e. g.* Pedley and Stephanoff [86], Wall [127] and references therein. The original motivation is to understand incompressible fluid flow through collapsible tubes such as arteries and veins. The geometry as displayed in Figure 6.7 and the problem parameters are taken from Wall [127]. The fluid properties are set to  $\rho = 1$ ,  $\mu = 0.00197$  and the average inflow velocity is chosen as  $\bar{u}_{\text{in}} = 1$ , which leads to the Reynolds number  $Re = \bar{u}_{\text{in}} b \rho / \mu = 507$ , where  $b = 1$  is the width of the channel. Again, the quadratic distribution of the prescribed velocity over the inflow orifice corresponds to undisturbed Poiseuille flow. The time dependency of the indentation is described by

$$h(t) = \frac{1}{2} \epsilon \left( 1 - \cos \left( 2\pi \frac{t}{T} \right) \right), \quad (6.13)$$

where the time period and the amplitude are chosen as  $T = 27.027$  and  $\epsilon = 0.38$ . The smooth transitions between the fixed parts of the wall and the indentation follow sections of sine curves. Note that, at the indentation, the vertical fluid velocity of the boundary nodes must be set to the time derivative of the corresponding nodal positions in order to represent the physical problem correctly.

For the numerical simulation of the problem, a mesh with 6672 finite elements is employed. The ALE region is restricted to the section of the channel with the indentation. The mesh update method type A is used with  $\mu_{\text{mesh}} = 1$  and  $K_{\text{mesh}} = 2$ . The time integration parameter is set to  $\rho_{\infty}^h = 0.8$  and the time step size is chosen as  $\Delta t = 0.5$ . Figure 6.8 shows a detail of the finite element mesh.

The solution obtained from the simulation features the periodical separation of vortices shortly after the maximum indentation of the wall. Whenever the indentation has disappeared, the flow almost returns into steady state Poiseuille flow.

The diagrams in Figure 6.9 show the vorticity distribution in the downstream region of the indentation. They agree accurately with the figures given in Wall [127].

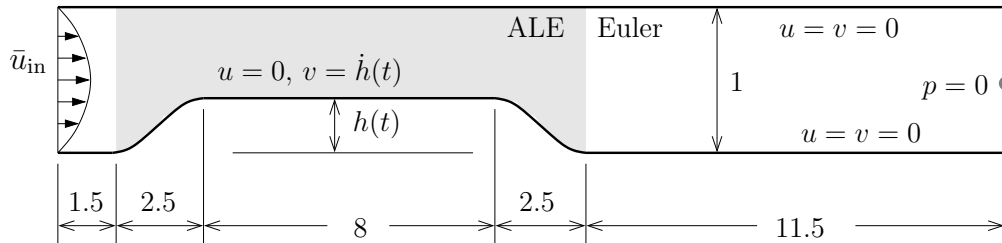


Figure 6.7: Channel with wall indentation, geometry of the problem.

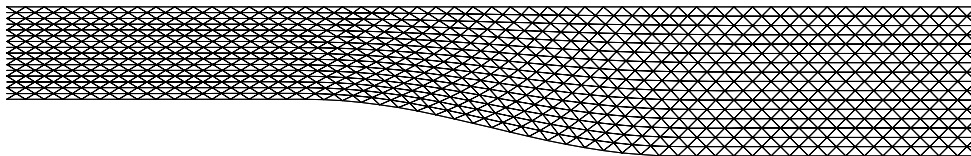


Figure 6.8: Channel with wall indentation, detail of the mesh with 6672 elements at  $t = 13.5 \approx T/2$ .

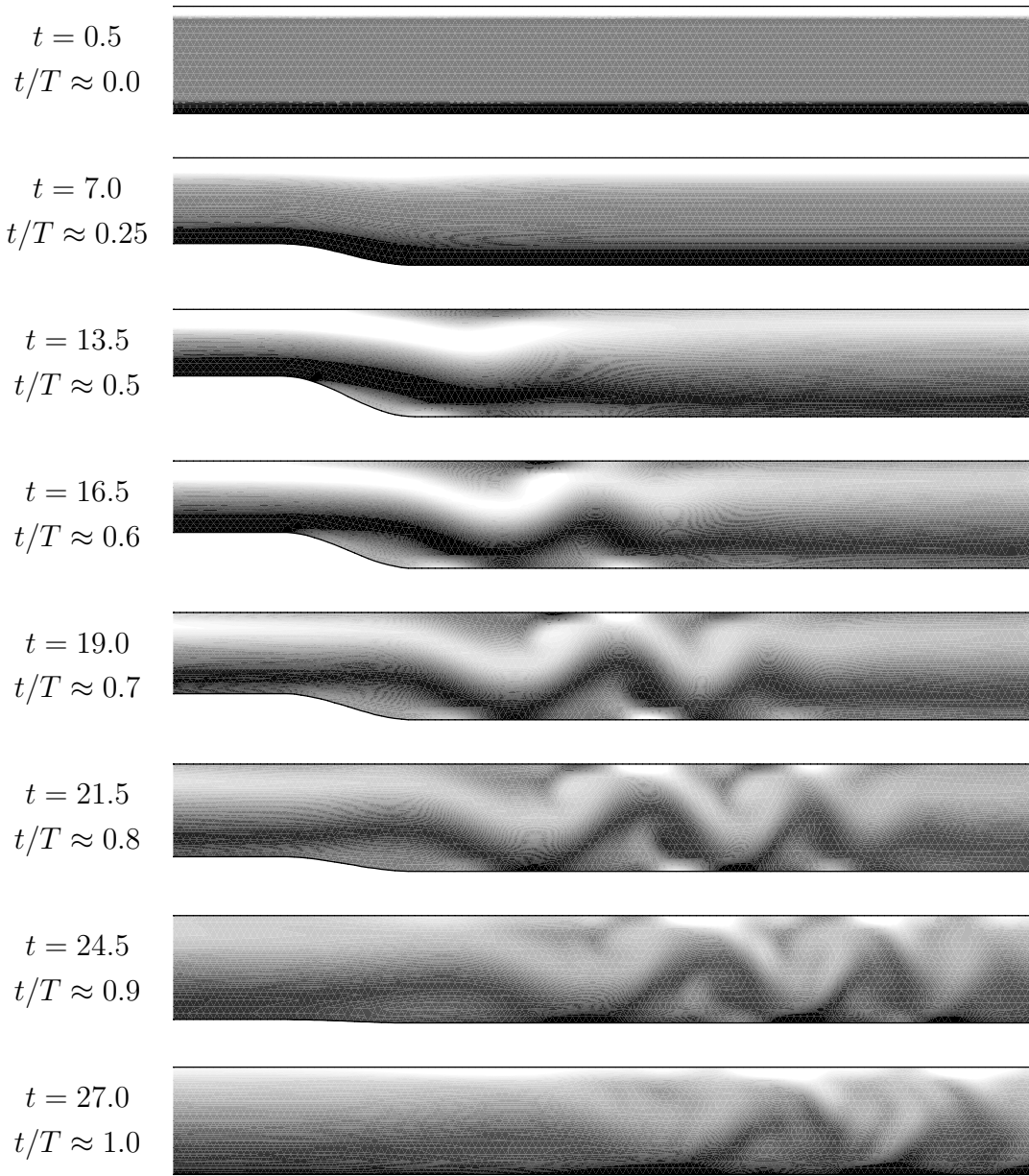


Figure 6.9: Channel with wall indentation, vorticity (width scaled with factor 2);  $\text{vort}(\mathbf{u}^h) \leq -6 \rightarrow \text{black}$ ,  $\text{vort}(\mathbf{u}^h) \geq +6 \rightarrow \text{white}$ .



# Chapter 7

## Surface Tension

This chapter provides a brief introduction to the physics of the surface tension phenomena and shows, how the surface tension boundary condition  $(2.51)_2$  can be rephrased in the framework of linear fluid finite elements. In Sections 7.3 and 7.4, nodal force vectors are derived for the two dimensional and the axisymmetric situations, which represent the surface tension and which can easily be added as surface loads to the fluid finite element formulation given by (6.1). More details on the subject are provided in the work by Saksono [103], on which most of the following sections are based.

### 7.1 The Surface Tension Phenomena

From a microscopic point of view, the phenomena of surface tension is due to the fact that molecules on the free surface are in a different environment than those molecules within the fluid. Each molecule in the interior of the fluid is surrounded by others on every side. Therefore, it is subject to equal molecular attraction forces in all directions. Figure 7.1 clearly shows, that, for a molecule on the free surface, the resultant of the attraction forces does not vanish, but acts in the direction of the inward normal of the surface. Its absolute value depends on the fluid under consideration. Hence, the molecules at the free surface are pulled towards the interior of the fluid, which causes the free surface to contract and gives the impression that the fluid body is surrounded by an elastic membrane in the state of tension. It follows, that the pressure is discontinuous across interfaces with surface tension. If the molecular attraction forces in the medium on the other side of the interface are not negligible, then the difference of the forces is relevant for the surface tension effect.

At the *contact line* of three different phases the equilibrium of the molec-

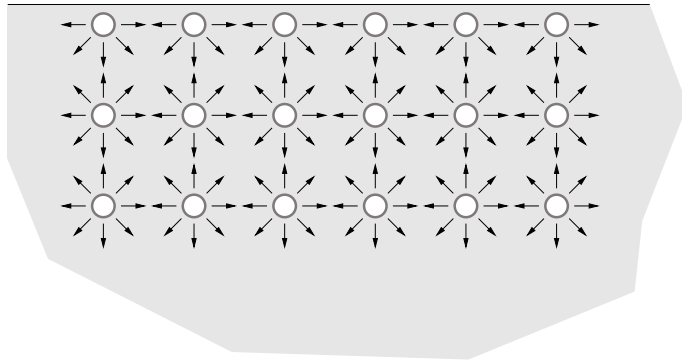


Figure 7.1: Surface tension, molecular attractions.

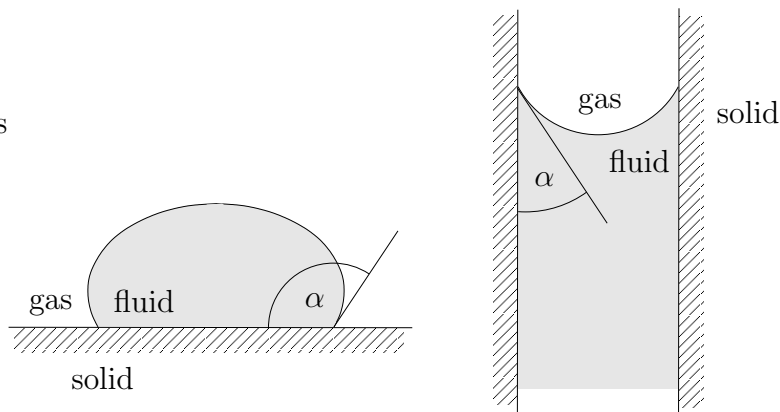


Figure 7.2: Surface tension, contact angle  $\alpha$ .

ular forces is satisfied only if the angles between the tangential planes of the interface surfaces take certain values. These *contact angles*  $\alpha$  depend on the three different materials. The common phenomena of sitting drops or capillary rise involve contact lines between a rigid solid, a fluid and a gas. They are schematically depicted in Figure 7.2.

For the derivation of the surface tension boundary condition (2.51)<sub>2</sub>, an infinitesimal rectangular area element  $da$  of a free surface in equilibrium is considered. If the surface element  $da$  is subjected to a virtual displacement  $\delta h$  as shown in Figure 7.3, then the virtual work  $\delta dW_p$  done by the pressure difference  $p - p_{\text{ext}}$  along  $\delta h$  must equal the virtual work  $\delta dW_{\text{st}}$  of the surface tension forces. The work  $\delta dW_p$  may be written as

$$\delta dW_p = (p - p_{\text{ext}}) \delta h da . \quad (7.1)$$

The work of the surface tension forces is proportional to the change  $\delta da$  of  $da$  associated with the virtual displacement  $\delta h$ . If  $\delta da$  is positive, more fluid

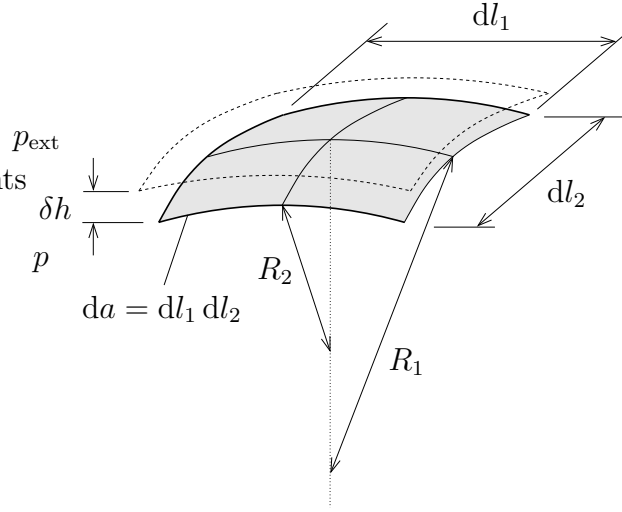


Figure 7.3: Surface tension, infinitesimal surface element.

particles need to be pulled to the surface against the molecular forces which attract them to the interior of the fluid body. Hence, it follows that

$$\delta dW_{\text{st}} = \gamma_{\text{st}} \delta da , \quad (7.2)$$

where the constant  $\gamma_{\text{st}}$  is denoted as the *surface tension coefficient*. From Figure 7.3 it can be deduced that

$$\delta da = \left(1 + \frac{\delta h}{R_1}\right) \left(1 + \frac{\delta h}{R_2}\right) dl_1 dl_2 - dl_1 dl_2 , \quad (7.3)$$

where  $R_1$  and  $R_2$  represent the principal radii of curvature of the surface element  $da$ . By omitting second order terms one obtains

$$\delta da = \left(\frac{1}{R_1} + \frac{1}{R_2}\right) \delta h da . \quad (7.4)$$

Equating  $\delta dW_p$  and  $\delta dW_{\text{st}}$  renders the *Laplace-Young* equation as

$$p - p_{\text{ext}} = \gamma_{\text{st}} \left(\frac{1}{R_1} + \frac{1}{R_2}\right) . \quad (7.5)$$

By using the mean curvature  $H = \frac{1}{2} \left(\frac{1}{R_1} + \frac{1}{R_2}\right)$  one obtains

$$p - p_{\text{ext}} = 2 \gamma_{\text{st}} H . \quad (7.6)$$

If, furthermore, the viscous stresses  $\boldsymbol{\sigma}^{\text{visc}}$  of the fluid are taken into account, the equation may be written as

$$\boldsymbol{\sigma} \hat{\mathbf{n}} - (-p_{\text{ext}} \hat{\mathbf{n}} + 2 \gamma_{\text{st}} H \hat{\mathbf{n}}) = \mathbf{0} , \quad (7.7)$$

where the fluid stress decomposition  $\boldsymbol{\sigma} = -p \mathbf{I} + \boldsymbol{\sigma}^{\text{visc}}$  has been used and  $\hat{\mathbf{n}}$  represents the outward normal unit vector of the free surface. Equation (7.7) is, in fact, identical to the boundary condition given by (2.51)<sub>2</sub>.

More details on the physics of the surface tension phenomena are provided in *e. g.* Lamb [77], Isenberg [71], Davies [27], Pozrikidis [90, 91], Saksono [103].

## 7.2 The Weak Form

The surface tension equation (2.51)<sub>2</sub> may be regarded as a special Neumann boundary condition on a moving boundary with a traction vector  $\mathbf{t} = -p_{\text{ext}} \hat{\mathbf{n}} + 2 \gamma_{\text{st}} H \hat{\mathbf{n}}$ , which depends on the current configuration of the boundary. Therefore, the incorporation of the surface tension term into the weak form of the fluid flow is straightforward. Let  $G(\mathbf{u}, p, \mathbf{w}, q) = 0$  represent the weak form of the incompressible Navier-Stokes equations, corresponding, for instance, to equation (6.1). In the presence of a free surface boundary  $\Gamma_{\text{fs}}$ , surface tension effects are then accounted for by requiring

$$G(\mathbf{u}, p, \mathbf{w}, q) - \int_{\Gamma_{\text{fs}}} \mathbf{w} \cdot (-p_{\text{ext}} \hat{\mathbf{n}} + 2 \gamma_{\text{st}} H \hat{\mathbf{n}}) da = 0. \quad (7.8)$$

For linear finite element interpolation, it is, however, not possible to evaluate the mean curvature  $H$ . Thus, the divergence theorem for curved surfaces

$$\int_{\Gamma_{\text{fs}}} \nabla_{\text{s}} \cdot \mathbf{w} da = \int_C \mathbf{w} \cdot \hat{\mathbf{m}} ds - \int_{\Gamma_{\text{fs}}} 2 H \mathbf{w} \cdot \hat{\mathbf{n}} da \quad (7.9)$$

is employed to reduce the degree of the highest derivatives. The boundary line of the surface  $\Gamma_{\text{fs}}$  is denoted as  $C$  and, in any point on  $C$ , the quantity  $\hat{\mathbf{m}}$  denotes the unit vector normal to  $C$ , but tangential to  $\Gamma_{\text{fs}}$ . The divergence  $\nabla_{\text{s}} \cdot \mathbf{w}$  on the curved surface  $\Gamma_{\text{fs}}$  is related to the gradient  $\nabla \mathbf{w}$  by

$$\nabla_{\text{s}} \cdot \mathbf{w} = (\mathbf{I} - \hat{\mathbf{n}} \otimes \hat{\mathbf{n}}) : (\nabla \mathbf{w}). \quad (7.10)$$

Hence, equation (7.8) becomes

$$G(\mathbf{u}, p, \mathbf{w}, q) + \int_{\Gamma_{\text{fs}}} (p_{\text{ext}} \mathbf{w} \cdot \hat{\mathbf{n}} + \gamma_{\text{st}} \nabla_{\text{s}} \cdot \mathbf{w}) da - \int_C \gamma_{\text{st}} \mathbf{w} \cdot \hat{\mathbf{m}} ds = 0. \quad (7.11)$$

The boundary line  $C$  of  $\Gamma_{\text{fs}}$  can be identified as the three phase contact line discussed in Section 7.1. Thus, the vector  $\hat{\mathbf{m}}$  is determined by the contact

angle  $\alpha$ . The introduction of isoparametric finite element interpolations allows to rewrite the surface tension expressions on element level in terms of external nodal forces:

$$\begin{aligned} \int_{\Gamma_{fs}} \gamma_{st} \nabla_s \cdot \mathbf{w} \, da &\rightarrow \sum_{e=1}^{n_{el}} \int_{\Gamma^e \cap \Gamma_{fs}} \gamma_{st} \nabla_s \cdot \mathbf{w}^h \, da = \sum_{e=1}^{n_{el}} \mathbf{F}_{stA} \cdot \mathbf{w}_A \\ \int_C \gamma_{st} \mathbf{w} \cdot \hat{\mathbf{m}} \, ds &\rightarrow \sum_{e=1}^{n_{el}} \int_{C^e \cap C} \gamma_{st} \mathbf{w}^h \cdot \hat{\mathbf{m}}^h \, ds = \sum_{e=1}^{n_{el}} \mathbf{F}_{\alpha A} \cdot \mathbf{w}_A . \end{aligned} \quad (7.12)$$

The external pressure is usually set to zero, and thus vanishes. In the following two sections, detailed expressions, which correspond to the force vectors  $\mathbf{F}_{st}$  and  $\mathbf{F}_{\alpha}$ , are evaluated for the special case of linear finite element interpolation in the two dimensional and the axisymmetric situations.

### 7.3 Two Dimensional Problems

For two dimensional linear finite elements the following relations can be derived (see Figure 7.4)

$$\begin{aligned} \Delta x &= x_2 - x_1 , & \Delta y &= y_2 - y_1 , & l &= \sqrt{\Delta x^2 + \Delta y^2} , \\ \hat{\mathbf{n}}^h &= \frac{1}{l} \begin{Bmatrix} \Delta y \\ -\Delta x \end{Bmatrix} , & \mathbf{I} - \hat{\mathbf{n}}^h \otimes \hat{\mathbf{n}}^h &= \frac{1}{l^2} \begin{bmatrix} \Delta x^2 & \Delta x \Delta y \\ \Delta x \Delta y & \Delta y^2 \end{bmatrix} . \end{aligned} \quad (7.13)$$

Thus, the expression  $\nabla_s \cdot \mathbf{w}^h$  may be written as

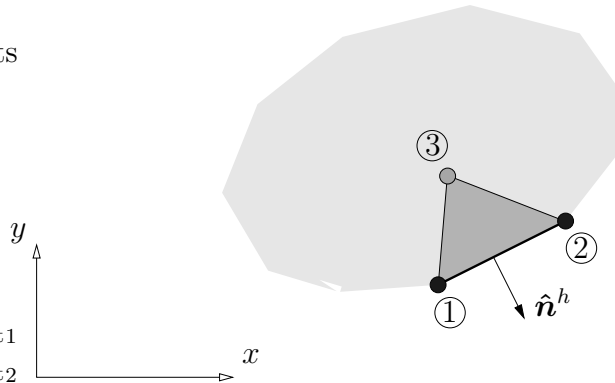


Figure 7.4: Surface tension, two dimensional linear elements.

$$\begin{aligned}
\nabla_s \cdot \mathbf{w}^h &= (\mathbf{I} - \hat{\mathbf{n}}^h \otimes \hat{\mathbf{n}}^h) : (\nabla \mathbf{w}^h) \\
&= \frac{1}{l^2} \left( \Delta x^2 w_{x,x}^h + \Delta x \Delta y (w_{x,y}^h + w_{y,x}^h) + \Delta y^2 w_{y,y}^h \right). \quad (7.14)
\end{aligned}$$

Furthermore, for a linear three noded triangular finite element, it can be shown that the derivatives of the shape functions may be expressed as

$$\begin{aligned}
N_{1,x} &= \frac{y_2 - y_3}{2A}, & N_{2,x} &= \frac{-y_1 + y_3}{2A}, \\
N_{1,y} &= \frac{-x_2 + x_3}{2A}, & N_{2,y} &= \frac{x_1 - x_3}{2A},
\end{aligned} \quad (7.15)$$

where  $A = ((x_1 - x_3)(y_2 - y_3) - (x_2 - x_3)(y_1 - y_3))/2$  is the area of the triangle. By using (7.15) and the finite element interpolation  $\mathbf{w}^h = N_A(x, y) \mathbf{w}_A$  the gradient  $\nabla \mathbf{w}^h$  can be evaluated. After some mathematical manipulation, the equation (7.14) can then be rewritten as

$$\nabla_s \cdot \mathbf{w}^h = -\frac{\Delta x}{l^2} \mathbf{w}_{x1} - \frac{\Delta y}{l^2} \mathbf{w}_{y1} + \frac{\Delta x}{l^2} \mathbf{w}_{x2} + \frac{\Delta y}{l^2} \mathbf{w}_{y2}. \quad (7.16)$$

Importantly, the result is independent of the position of node 3. Thus, the integral in (7.12)<sub>1</sub> becomes

$$\int_{\Gamma^e \cap \Gamma_{fs}} \gamma_{st} \nabla_s \cdot \mathbf{w}^h da = \frac{\gamma_{st}}{l} \left( -\Delta x \mathbf{w}_{x1} - \Delta y \mathbf{w}_{y1} + \Delta x \mathbf{w}_{x2} + \Delta y \mathbf{w}_{y2} \right), \quad (7.17)$$

which can be rewritten as the product of a force vector with the nodal virtual velocities

$$\int_{\Gamma^e \cap \Gamma_{fs}} \gamma_{st} \nabla_s \cdot \mathbf{w}^h da = \frac{\gamma_{st}}{l} \begin{Bmatrix} -\Delta x \\ -\Delta y \\ +\Delta x \\ +\Delta y \end{Bmatrix} \cdot \begin{Bmatrix} \mathbf{w}_{x1} \\ \mathbf{w}_{y1} \\ \mathbf{w}_{x2} \\ \mathbf{w}_{y2} \end{Bmatrix}. \quad (7.18)$$

In the two dimensional case the contact line  $C$  reduces to a point and the unit vector  $\hat{\mathbf{m}}^h$  can be expressed in terms of the contact angle  $\alpha$ , such that one obtains

$$\int_{C^e \cap C} \gamma_{st} \mathbf{w}^h \cdot \hat{\mathbf{m}}^h ds = \gamma_{st} \begin{Bmatrix} -\cos \alpha \\ \sin \alpha \end{Bmatrix} \cdot \begin{Bmatrix} \mathbf{w}_{xC} \\ \mathbf{w}_{yC} \end{Bmatrix}. \quad (7.19)$$

## 7.4 Axisymmetric Problems

In the axisymmetric case, the following definitions are used

$$\Delta r = r_2 - r_1, \quad \Delta z = z_2 - z_1, \quad l = \sqrt{\Delta r^2 + \Delta z^2}. \quad (7.20)$$

Furthermore, some relations are established on the basis of Figure 7.5 for later use

$$\begin{aligned}
r &= \sqrt{x^2 + y^2}, & \cos \varphi &= \frac{x}{r}, & \sin \varphi &= \frac{y}{r}, \\
\frac{\partial r}{\partial x} &= \cos \varphi, & \frac{\partial r}{\partial y} &= \sin \varphi, \\
\frac{\partial \sin \varphi}{\partial x} &= -\frac{\sin \varphi \cos \varphi}{r}, & \frac{\partial \sin \varphi}{\partial y} &= \frac{\cos^2 \varphi}{r}, \\
\frac{\partial \cos \varphi}{\partial x} &= \frac{\sin^2 \varphi}{r}, & \frac{\partial \cos \varphi}{\partial y} &= -\frac{\sin \varphi \cos \varphi}{r}.
\end{aligned} \tag{7.21}$$

The normal unit vector  $\hat{\mathbf{n}}^h$  to the element edge may be written as

$$\hat{\mathbf{n}}^h = \begin{Bmatrix} \hat{n}_x^h \\ \hat{n}_y^h \\ \hat{n}_z^h \end{Bmatrix} = \frac{1}{l} \begin{Bmatrix} \Delta z \cos \varphi \\ \Delta z \sin \varphi \\ -\Delta r \end{Bmatrix}. \tag{7.22}$$

It then follows that

$$\begin{aligned}
&\mathbf{I} - \hat{\mathbf{n}}^h \otimes \hat{\mathbf{n}}^h \\
&= \frac{1}{l^2} \begin{bmatrix} l^2 - \Delta z^2 \cos^2 \varphi & -\Delta z^2 \sin \varphi \cos \varphi & \Delta r \Delta z \cos \varphi \\ -\Delta z^2 \sin \varphi \cos \varphi & l^2 - \Delta z^2 \sin^2 \varphi & \Delta r \Delta z \sin \varphi \\ \Delta r \Delta z \cos \varphi & \Delta r \Delta z \sin \varphi & \Delta z^2 \end{bmatrix}
\end{aligned} \tag{7.23}$$

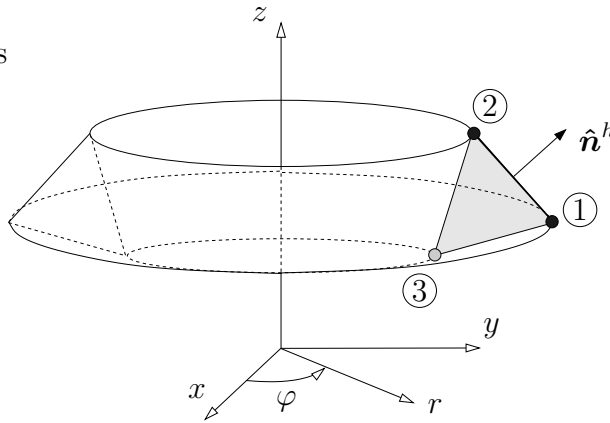


Figure 7.5: Axisymmetric linear finite element at the surface boundary.

Recalling that  $w_\varphi^h = 0$ , the vector  $\mathbf{w}^h$  may be written as

$$\hat{\mathbf{w}}^h = \begin{Bmatrix} w_x^h \\ w_y^h \\ w_z^h \end{Bmatrix} = \begin{Bmatrix} w_r^h \cos \varphi \\ w_r^h \sin \varphi \\ w_z^h \end{Bmatrix}. \quad (7.24)$$

Using the relations (7.21), the gradient  $\nabla \mathbf{w}^h$  is then obtained as

$$\nabla \mathbf{w}^h = \begin{bmatrix} w_{x,x}^h & w_{x,y}^h & w_{x,z}^h \\ w_{y,x}^h & w_{y,y}^h & w_{y,z}^h \\ w_{z,x}^h & w_{z,y}^h & w_{z,z}^h \end{bmatrix} = \begin{bmatrix} w_{r,r}^h c^2 + w_r^h \frac{s^2}{r} & (w_{r,r}^h - w_r^h \frac{1}{r}) s c & w_{r,z}^h c \\ (w_{r,r}^h - w_r^h \frac{1}{r}) s c & w_{r,r}^h s^2 + w_r^h \frac{c^2}{r} & w_{r,z}^h s \\ w_{z,r}^h c & w_{z,r}^h s & w_{z,z}^h \end{bmatrix}, \quad (7.25)$$

where  $s$  and  $c$  denote  $\sin \varphi$  and  $\cos \varphi$ , respectively. Thus, using (7.23) and (7.25), it follows that

$$\begin{aligned} \nabla_s \cdot \mathbf{w}^h &= (\mathbf{I} - \hat{\mathbf{n}}^h \otimes \hat{\mathbf{n}}^h) : (\nabla \mathbf{w}^h) \\ &= \frac{w_r^h}{r} + \frac{1}{l^2} \left( \Delta r^2 w_{r,r}^h + \Delta r \Delta z (w_{r,z}^h + w_{z,r}^h) + \Delta z^2 w_{z,z}^h \right), \end{aligned} \quad (7.26)$$

which is identical to the corresponding expression (7.14) in two dimensions, except for the additional term  $w_r^h/r$ . Thus, similar to (7.16), one obtains

$$\nabla_s \cdot \mathbf{w}^h = \frac{w_r^h}{r} - \frac{\Delta r}{l^2} \mathbf{w}_{r1} - \frac{\Delta z}{l^2} \mathbf{w}_{z1} + \frac{\Delta r}{l^2} \mathbf{w}_{r2} + \frac{\Delta z}{l^2} \mathbf{w}_{z2}. \quad (7.27)$$

It is convenient for the integration over the element edge, which represents the free surface, to express  $w_r^h$  and  $r$  in terms of an edge coordinate  $0 \leq s \leq l$

$$r = \frac{1}{l} \left( (l-s) \mathbf{r}_1 + s \mathbf{r}_2 \right), \quad w_r^h = \frac{1}{l} \left( (l-s) \mathbf{w}_{r1} + s \mathbf{w}_{r2} \right). \quad (7.28)$$

Thus, the nodal surface tension forces are finally obtained as

$$\begin{aligned} \int_{\Gamma^e \cap \Gamma_{fs}} \gamma_{st} \nabla_s \cdot \mathbf{w}^h da &= \int_0^l \gamma_{st} \nabla_s \cdot \mathbf{w}^h 2\pi r ds \\ &= \left( \pi \gamma_{st} \frac{\mathbf{r}_1 + \mathbf{r}_2}{l} \begin{Bmatrix} -\Delta r \\ -\Delta z \\ \Delta r \\ \Delta z \end{Bmatrix} + \pi \gamma_{st} l \begin{Bmatrix} 1 \\ 0 \\ 1 \\ 0 \end{Bmatrix} \right) \cdot \begin{Bmatrix} \mathbf{w}_{r1} \\ \mathbf{w}_{z1} \\ \mathbf{w}_{r2} \\ \mathbf{w}_{z2} \end{Bmatrix}. \end{aligned} \quad (7.29)$$

The forces in the contact lines can readily be expressed as

$$\int_{C^e \cap C} \gamma_{st} \mathbf{w}^h \cdot \hat{\mathbf{m}}^h ds = 2\pi r_C \gamma_{st} \begin{Bmatrix} -\cos \alpha \\ \sin \alpha \end{Bmatrix} \cdot \begin{Bmatrix} \mathbf{w}_{xC} \\ \mathbf{w}_{yC} \end{Bmatrix}. \quad (7.30)$$

# Chapter 8

## Finite Elements in Solid Mechanics

This chapter provides a brief introduction to the finite element formulations for solid structures employed in the numerical examples of Chapter 14. Generally, the computational framework for fluid-solid interaction described in the remainder of this work does not impose any restrictions to specific types of structural finite elements. Here, however, only standard elastic two dimensional continuum, membrane and beam elements are considered. The chapter concludes with some remarks on the time integration.

Following Section 2.2, the displacement field of solid bodies is denoted by the vector field  $\mathbf{d}$ . The current position of a specific solid particle is given by  $\mathbf{x} = \mathbf{x}_0 + \mathbf{d}$ , where  $\mathbf{x}_0$  is the position at  $t = 0$ . In this chapter, the vector  $\mathbf{w}$  denotes the virtual displacements of the solid structure.

### 8.1 Continuum Element

In this work, solid continua are modelled with standard two dimensional nine noded fully integrated finite elements. Such elements exhibit volumetric locking near the incompressibility limit (see Section 3.4). However, they are suitable for the modelling of bending of relatively thin structures.

If body forces are neglected, the local form of equilibrium (2.48) requires

$$\rho \ddot{\mathbf{d}} - \nabla \cdot \boldsymbol{\sigma} = 0 \quad \forall (\mathbf{x}, t) \in \Omega \times I, \quad (8.1)$$

where the domain  $\Omega$  denotes the current configuration of the solid. For simplicity, pure Dirichlet and Neumann boundary conditions are assumed. By the application of the standard arguments discussed in Section 3.1, the

weak form is obtained as

$$\int_{\Omega} \rho \ddot{\mathbf{d}} \cdot \mathbf{w} \, dv + \int_{\Omega} \boldsymbol{\sigma} : \nabla \mathbf{w} \, dv = \int_{\Gamma_t} \mathbf{t} \cdot \mathbf{w} \, da . \quad (8.2)$$

*Small strain regime.* If the strains and deformations are small, it is admissible to perform the integrals in (8.2) over the initial configuration of the solid domain and to assume the standard stress-strain relation

$$\boldsymbol{\sigma} = 2\mu \left( \nabla^s \mathbf{d} - \frac{1}{3} (\nabla \cdot \mathbf{d}) \mathbf{I} \right) + K (\nabla \cdot \mathbf{d}) \mathbf{I} . \quad (8.3)$$

where  $\mu$  and  $K$  denote the shear and the bulk moduli. After the discretisation along the lines of Section 3.2, based on nine noded isoparametric finite elements, the vector fields  $\mathbf{d}$  and  $\mathbf{w}$  may be written, in each element, as

$$\mathbf{d}^h = N_A \mathbf{d}_A , \quad \mathbf{w}^h = N_B \mathbf{w}_B , \quad A, B = 1, 2, \dots, 9 , \quad (8.4)$$

where the shape functions  $N_A, N_B$  are given in (3.29). By using (8.4) in the weak form (8.2), and by recalling that the nodal virtual displacements are arbitrary, one obtains the matrix equation

$$\mathbf{M} \ddot{\mathbf{d}} + \mathbf{K} \mathbf{d} = \mathbf{P} . \quad (8.5)$$

The stiffness matrix  $\mathbf{K}$  and the external force vector  $\mathbf{P}$  are given by (3.31) in Section 3.3. The matrix  $\mathbf{M}$  is referred to as *mass matrix*. It is obtained as

$$\mathbf{M} = \mathbf{A} \mathbf{m}^e , \quad \mathbf{m}_{AB}^e = \int_{\Omega^e} \rho N_A N_B \mathbf{I} \, dv . \quad (8.6)$$

*Large strain regime.* If the strains are expected to be large, it is necessary to employ a hyperelastic material model and to take into account the deformation of the geometry when evaluating (8.2). For Neo-Hooke elastic materials, to which this work is restricted, the Cauchy stress tensor is given by (2.49) as

$$\boldsymbol{\sigma} = \mu J^{-\frac{5}{3}} \left( \mathbf{B} - \frac{1}{3} \text{tr}(\mathbf{B}) \mathbf{I} \right) + K \frac{J^2 - 1}{2J} \mathbf{I} . \quad (8.7)$$

The integrals in (8.2) are performed over the current deformed configuration of  $\Omega$  and the gradient operator  $\nabla(\bullet)$  represents the derivatives with respect to the spatial coordinates  $\mathbf{x}$  rather than the material coordinates  $\mathbf{x}_0$ . Analogously to the small strain situation, isoparametric nine noded finite elements are employed for the spatial discretisation of the weak form. One obtains a nodal internal force vector, denoted here as  $\mathbf{F}(\mathbf{d})$ , which is nonlinear in terms

of the displacements  $\mathbf{d}$ . The mass matrix follows similarly to (8.6). Thus, the complete matrix equation reads

$$\mathbf{M}\ddot{\mathbf{d}} + \mathbf{F}(\mathbf{d}) = \mathbf{P} . \quad (8.8)$$

Note that the weak form may alternatively be formulated in terms of the initial configuration. The finite element discretisation then leads to exactly the same matrix equation (8.8). After the application of an appropriate time integration scheme (see Section 8.4), the matrix equation may be solved by means of a Newton-Raphson procedure. The linearisation of  $\mathbf{F}(\mathbf{d})$  is often decomposed into a *material* and a *geometrical* part, the latter of which arises from the exact consideration of the geometry changes.

Note that the finite element strategy employed in the pseudo-elastic mesh update methods A and B (see Section 6.2) differs from the formulation discussed here only in terms of the interpolation order. For the mesh update, the poor convergence behaviour of linear triangular elements is irrelevant, since the motion of the fluid mesh does not represent any physics. Taking into account the absence of inertia and the pure Dirichlet boundary conditions, the mesh update methods A and B therefore require the solution of a matrix equation of the form  $\mathbf{F}(\mathbf{d}) = \mathbf{0}$ .

Detailed information on the finite element modelling of elastic continua at small and finite strains is provided in various text books, such as Zienkiewicz and Taylor [132], Cook *et al* [24], Hughes [64], Bathe [5], Wriggers [129], Crisfield [25], Bonet and Wood [10].

## 8.2 Membrane Element

In two dimensions, a geometrically exact linear membrane finite element coincides with a truss element under plane strain conditions. Thus, the derivation of the formulation is straightforward. It is briefly outlined in the following.

The deformation of each material point may be described in terms of the the principal stretch  $\lambda$  in the plane tangential to the membrane. The only relevant stress  $\sigma$  is directed parallel to  $\lambda$ . For incompressible Neo-Hooke elastic membranes, an expression for the Cauchy stress  $\sigma$  can be obtained from equation (8.7), if the second term on the right hand side is replaced by  $p\mathbf{I}$ . The membrane stress state formulated in principal directions then allows the elimination of the pressure  $p$ . For two dimensional problems the stress  $\sigma$  is obtained as

$$\sigma = \mu \frac{\lambda^4 - 1}{\lambda^2} . \quad (8.9)$$

The principle of virtual work may be written as

$$\int_0^L \frac{\rho H}{\lambda} \ddot{\mathbf{d}} \cdot \mathbf{w} \, ds + \int_0^L \frac{H}{\lambda} \sigma \frac{d\mathbf{w}}{ds} \cdot \mathbf{m} \, ds = \int_0^L \mathbf{t} \cdot \mathbf{w} \, ds + \int_0^L p \mathbf{n} \cdot \mathbf{w} \, ds, \quad (8.10)$$

where  $s$  denotes a coordinate in the membrane surface ranging from 0 to the current length  $L$  of the membrane. The vectors  $\mathbf{m}$  and  $\mathbf{n}$  represent, respectively, the current tangential and normal unit vectors of the membrane surface. The quantities  $H$  and  $\rho$  denote the initial membrane thickness and the density, respectively. The last integral in (8.10) corresponds to a loading of the membrane with the external pressure  $p$ .

The membrane is decomposed into two noded linear isoparametric finite elements, *i. e.* in each element  $\mathbf{d}$  and  $\mathbf{w}$  are replaced by

$$\mathbf{d}^h = N_1 \mathbf{d}_1 + N_2 \mathbf{d}_2, \quad \mathbf{w}^h = N_1 \mathbf{w}_1 + N_2 \mathbf{w}_2 \quad (8.11)$$

with  $N_1 = (l - s)/l$  and  $N_2 = s/l$ , where  $s$  is now a local coordinate ranging from 0 to the current element length  $l$ . The discretisation of (8.10) on the basis of (8.11) is straightforward. Similarly to (8.8), one obtains a matrix equation of the form

$$\mathbf{M} \ddot{\mathbf{d}} + \mathbf{F}(\mathbf{d}) = \mathbf{P} + \mathbf{Q}(\mathbf{d}). \quad (8.12)$$

The four integrals in (8.10) render the following expressions:

$$\sum_{e=1}^{n_{\text{el}}} \int_0^{l^e} \frac{\rho H}{\lambda^e} \ddot{\mathbf{d}}^h \cdot \mathbf{w}^h \, ds = \sum_{e=1}^{n_{\text{el}}} \begin{Bmatrix} \mathbf{w}_{1x} \\ \mathbf{w}_{1y} \\ \mathbf{w}_{2x} \\ \mathbf{w}_{2y} \end{Bmatrix} \cdot \frac{H \rho l_0^e}{6} \begin{bmatrix} 2 & 0 & 1 & 0 \\ 0 & 2 & 0 & 1 \\ 1 & 0 & 2 & 0 \\ 0 & 1 & 0 & 2 \end{bmatrix} \begin{Bmatrix} \ddot{\mathbf{d}}_{1x} \\ \ddot{\mathbf{d}}_{1y} \\ \ddot{\mathbf{d}}_{2x} \\ \ddot{\mathbf{d}}_{2y} \end{Bmatrix} = \mathbf{w} \cdot \mathbf{M} \ddot{\mathbf{d}} \quad (8.13)$$

$$\sum_{e=1}^{n_{\text{el}}} \int_0^{l^e} \frac{H \sigma(\lambda^e)}{\lambda^e} \frac{d\mathbf{w}^h}{ds} \cdot \mathbf{m}^h \, ds = \sum_{e=1}^{n_{\text{el}}} \begin{Bmatrix} \mathbf{w}_{1x} \\ \mathbf{w}_{1y} \\ \mathbf{w}_{2x} \\ \mathbf{w}_{2y} \end{Bmatrix} \cdot \frac{H \sigma(\lambda^e)}{\lambda^e l^e} \begin{Bmatrix} -\Delta x \\ -\Delta y \\ \Delta x \\ \Delta y \end{Bmatrix} = \mathbf{w} \cdot \mathbf{F}(\mathbf{d}) \quad (8.14)$$

$$\sum_{e=1}^{n_{\text{el}}} \int_0^{l^e} \mathbf{t}^h \cdot \mathbf{w}^h \, ds = \sum_{e=1}^{n_{\text{el}}} \begin{Bmatrix} \mathbf{w}_{1x} \\ \mathbf{w}_{1y} \\ \mathbf{w}_{2x} \\ \mathbf{w}_{2y} \end{Bmatrix} \cdot \frac{l^e}{6} \begin{Bmatrix} 2 \mathbf{t}_{1x} + \mathbf{t}_{2x} \\ 2 \mathbf{t}_{1y} + \mathbf{t}_{2y} \\ \mathbf{t}_{1x} + 2 \mathbf{t}_{2x} \\ \mathbf{t}_{1y} + 2 \mathbf{t}_{2y} \end{Bmatrix} = \mathbf{w} \cdot \mathbf{P} \quad (8.15)$$

$$\sum_{e=1}^{n_{\text{el}}} \int_0^{l^e} p \mathbf{n}^h \cdot \mathbf{w}^h \, ds = \sum_{e=1}^{n_{\text{el}}} \begin{Bmatrix} \mathbf{w}_{1x} \\ \mathbf{w}_{1y} \\ \mathbf{w}_{2x} \\ \mathbf{w}_{2y} \end{Bmatrix} \cdot \frac{p}{2} \begin{Bmatrix} -\Delta y \\ \Delta x \\ -\Delta y \\ \Delta x \end{Bmatrix} = \mathbf{w} \cdot \mathbf{Q}(\mathbf{d}) \quad (8.16)$$

with

$$\begin{aligned}
\Delta x_0 &= x_{02} - x_{01}, & \Delta y_0 &= y_{02} - y_{01}, \\
\Delta x &= \Delta x_0 + \mathbf{d}_{2x} - \mathbf{d}_{1x}, & \Delta y &= \Delta y_0 + \mathbf{d}_{2y} - \mathbf{d}_{1y}, \\
l_0 &= \sqrt{\Delta x_0^2 + \Delta y_0^2}, & l &= \sqrt{\Delta x^2 + \Delta y^2}, & \lambda &= \frac{l}{l_0},
\end{aligned} \tag{8.17}$$

where the superscript  $e$  has been omitted.

### 8.3 Beam Element

In two dimensions, shell structures reduce to beams. The geometrically exact linear beam element employed in this work is described in detail in the text book by Zienkiewicz and Taylor [132]. More information on the modelling of beam structures with finite elements can be found in *e. g.* Crisfield [25] and Wriggers [129]. This section is restricted to the presentation of the essential simplifying assumptions of the beam kinematics and to the brief outline of the derivation of the finite element formulation.

Similarly to (8.10), the weak form or principle of virtual work for the two dimensional beam may be written as

$$\int_0^{L_0} \rho H \ddot{\mathbf{d}} \cdot \mathbf{w} \, ds_0 + \int_0^{L_0} \int_{-H/2}^{H/2} \mathbf{S} : \delta \mathbf{E} \, dt_0 \, ds_0 = \int_0^L \mathbf{t} \cdot \mathbf{w} \, ds + \int_0^L p \mathbf{n} \cdot \mathbf{w} \, ds, \tag{8.18}$$

where, for convenience, the inertia and the internal virtual work terms are expressed in the initial undeformed configuration. The coordinate  $s_0$  ranges from 0 to the initial length  $L_0$  of the beam, while  $t_0$  is a thickness coordinate. The tensors  $\mathbf{S}$  and  $\delta \mathbf{E}$  denote, respectively, the Second Piola-Kirchhoff stress and the virtual Green-Lagrange strain tensors, which remain to be specified exactly. The discretisation of the load and inertia terms with linear two noded elements is analogous to Section 8.2.

Following the theory developed by Reissner [97], the cross-sections of the beam remain plane as the beam deforms. Note that, in contrast to the Bernoulli theory, they are not assumed to remain normal to the beam axis. As illustrated in Figure 8.1, the deformed configuration of the beam can then be described by

$$\begin{aligned}
x &= x_0 + d_x + y_0 \sin \beta \\
y &= d_y + y_0 \cos \beta,
\end{aligned} \tag{8.19}$$

where, for simplicity, the axis of the beam in the initial configuration is assumed to coincide with  $y = 0$ . This leads to the deformation gradient

$$\mathbf{F} = \frac{\partial \mathbf{x}}{\partial \mathbf{x}_0} = \begin{bmatrix} 1 + d_{x,x_0} + y_0 \beta_{,x_0} \cos \beta & \sin \beta \\ d_{y,x_0} - y_0 \beta_{,x_0} \sin \beta & \cos \beta \end{bmatrix}. \quad (8.20)$$

It follows, that the Green-Lagrange strain tensor  $\mathbf{E} = (\mathbf{F}^T \mathbf{F} - \mathbf{I})/2$  has two non-zero coefficients. Using the notation of Zienkiewicz and Taylor [132], one obtains

$$E_{xx} = E^0 + y_0 K^b, \quad 2 E_{xy} = \Gamma, \quad (8.21)$$

where the quantities  $E^0$ ,  $K^b$  and  $\Gamma$  are identified as the average axial strain, the axial strain due to the beam curvature, and the shear strain

$$\begin{aligned} E^0 &= d_{x,x_0} + \frac{1}{2} (d_{x,x_0}^2 + d_{y,x_0}^2) \\ K^b &= ((1 + d_{x,x_0}) \cos \beta + d_{y,x_0} \sin \beta) \beta_{,x_0} \\ \Gamma &= (1 + d_{x,x_0}) \sin \beta + d_{y,x_0} \cos \beta. \end{aligned} \quad (8.22)$$

Quadratic terms of  $y_0$  have been neglected, since the thickness  $H$  of the beam is assumed to be small. It follows that the internal virtual work can be rewritten as

$$\int_0^{L_0} \int_{-H/2}^{H/2} S_{xx} \delta E_{xx} + 2 S_{xy} \delta E_{xy} dy_0 dx_0 = \int_0^{L_0} T \delta E^0 + S \delta \Gamma + M \delta K^b dx_0 \quad (8.23)$$

where  $\delta$  indicates the variation of the strains with respect to  $d_x$ ,  $d_y$  and  $\beta$ . The quantities  $T$ ,  $S$  and  $M$  represent, respectively, the axial and the shear forces and the bending moment, namely

$$T = \int_{-H/2}^{H/2} S_{xx} dy_0, \quad S = \int_{-H/2}^{H/2} S_{xy} dy_0, \quad M = \int_{-H/2}^{H/2} S_{xx} y_0 dy_0. \quad (8.24)$$

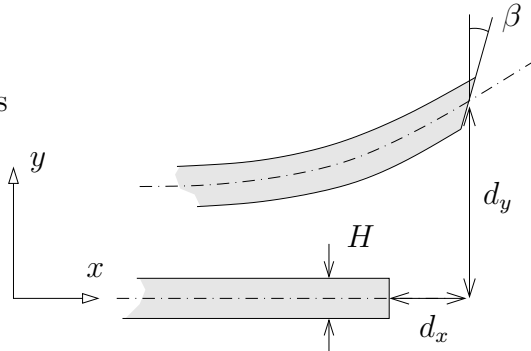


Figure 8.1: Kinematics of the geometrically exact beam, Reissner [97].

The right hand side of (8.23) may now be discretised with isoparametric linear finite elements. Importantly, each finite element node possesses three degrees of freedom,  $\mathbf{d}_x$ ,  $\mathbf{d}_y$  and  $\beta$ . The generalisation of the resulting expression to beam elements which are not aligned with the coordinate system requires the rotation of the displacements and of the element residual vector and is straightforward. For elastic materials it is common to assume linear relations between the Second Piola-Kirchoff stresses and the Green-Lagrange strains, which leads to

$$T = E A E^0, \quad S = \kappa \mu A \Gamma, \quad M = E I K^b. \quad (8.25)$$

The scalar quantities  $E$ ,  $\mu$ ,  $A$ ,  $I$  and  $\kappa = 5/6$  denote, respectively, the Young's modulus, the shear modulus, the cross-section area, the second moment of inertia and the shear correction factor. For beams with rectangular cross-sections, the relations  $A = H$  and  $I = H^3/12$  hold, whereby the beam thickness in the out of plane direction is assumed to be one unit length. An efficient measure to avoid shear locking is the employment of a single Gauß point for the integration over the element length.

Finally, one arrives at a matrix equation with the same format as (8.12), namely

$$\mathbf{M} \ddot{\mathbf{d}} + \mathbf{F}(\mathbf{d}) = \mathbf{P} + \mathbf{Q}(\mathbf{d}). \quad (8.26)$$

Note that the first integral in (8.18) renders a singular mass matrix  $\mathbf{M}$ , which does not possess any non-zero coefficients in the rows and columns associated with the nodal rotations  $\beta$ .

## 8.4 Time Integration

The matrix formulations of the structural finite element methods considered in Sections 8.1 – 8.3 all resemble the the general form

$$\mathbf{M} \ddot{\mathbf{d}} + \mathbf{C} \dot{\mathbf{d}} + \mathbf{F}(\mathbf{d}) = \mathbf{P} + \mathbf{Q}(\mathbf{d}), \quad (8.27)$$

where, for the sake of completeness, a linear damping term has been added. The relation (8.27) is a vector valued second order differential equation in the time domain of interest  $t \in [0, T]$ . In this work, the incremental integration of (8.27) in time is achieved by means of the discrete implicit generalised- $\alpha$  method developed by Chung and Hulbert [22]. The adaptation of the scheme to first order differential problems by Jansen *et al* [72] has been discussed at length in Chapter 5. The direct application of the integration scheme to (8.27) renders

$$\mathbf{M} \ddot{\mathbf{d}}_{n+\alpha_m} + \mathbf{C} \dot{\mathbf{d}}_{n+\alpha_f} + \mathbf{F}(\mathbf{d}_{n+\alpha_f}) = \mathbf{P}_{n+\alpha_f} + \mathbf{Q}(\mathbf{d}_{n+\alpha_f}) \quad (8.28)$$

$$\mathbf{d}_{n+1} = \mathbf{d}_n + \Delta t \dot{\mathbf{d}}_n + \Delta t^2 \left( \left( \frac{1}{2} - \beta \right) \ddot{\mathbf{d}}_n + \beta \ddot{\mathbf{d}}_{n+1} \right) \quad (8.29)$$

$$\dot{\mathbf{d}}_{n+1} = \dot{\mathbf{d}}_n + \Delta t \left( (1 - \gamma) \ddot{\mathbf{d}}_n + \gamma \ddot{\mathbf{d}}_{n+1} \right) \quad (8.30)$$

$$\mathbf{d}_{n+\alpha_f} = (1 - \alpha_f) \mathbf{d}_n + \alpha_f \mathbf{d}_{n+1} \quad (8.31)$$

$$\dot{\mathbf{d}}_{n+\alpha_f} = (1 - \alpha_f) \dot{\mathbf{d}}_n + \alpha_f \dot{\mathbf{d}}_{n+1} \quad (8.32)$$

$$\ddot{\mathbf{d}}_{n+\alpha_m} = (1 - \alpha_m) \ddot{\mathbf{d}}_n + \alpha_m \ddot{\mathbf{d}}_{n+1} \quad (8.33)$$

$$\beta = \frac{1}{4} (1 + \alpha_m - \alpha_f)^2, \quad \gamma = \frac{1}{2} + \alpha_m - \alpha_f \quad (8.34)$$

$$\alpha_f = \frac{1}{1 + \rho_\infty^h}, \quad \alpha_m = \frac{2 - \rho_\infty^h}{1 + \rho_\infty^h}. \quad (8.35)$$

For linear problems, the scheme can be proven to be second order accurate and unconditionally stable for  $0 \leq \rho_\infty^h \leq 1$ . Similarly to the discussion in Chapter 5, the free parameter  $\rho_\infty^h$  prescribes the limit of the spectral radius as  $\Delta t \rightarrow \infty$ . Thus,  $\rho_\infty^h = 0$  corresponds to very strong high frequency damping, whereas  $\rho_\infty^h = 1$  conserves the energy of all frequencies. In fact, for  $\rho_\infty^h = 1$ , the scheme coincides with the trapezoidal rule. The detailed analysis of the accuracy, stability and damping properties of the method is provided by Chung and Hulbert [22].

The superiority of the generalised- $\alpha$  method over other implicit schemes such as the generalised midpoint rule or the well-known *Newmark* method is readily shown by means of analyses along the lines of Section 5.1. In contrast to fluid mechanics, the generalised- $\alpha$  method is widely used in the simulation of solid mechanics problems.

Due to the linearity of the relations (8.29) – (8.33), the quantities  $\ddot{\mathbf{d}}_{n+\alpha_m}$ ,  $\dot{\mathbf{d}}_{n+\alpha_f}$  and  $\mathbf{d}_{n+\alpha_f}$  can be expressed in terms of the displacement  $\mathbf{d}_{n+1}$ . Thus, the system (8.28) can easily be rewritten in terms of  $\mathbf{d}_{n+1}$  as the only unknown. Similar strategies have been discussed at length in Chapter 5 for the time integration of the fluid flow.

Finally, it should be noted that the generalised- $\alpha$  method employed for the first order problem in Chapter 5 is a special case of the scheme (8.28) – (8.35). By cancelling the terms  $\mathbf{F}$  and  $\mathbf{Q}$  in (8.28), by disregarding (8.29) and by employing (5.28) for the definition of the time integration parameters one obtains the scheme presented by Jansen *et al* [72].

# Chapter 9

## Modelling of Interfaces

In Chapter 6, a finite element formulation for incompressible fluid flow on moving domains has been presented. Several algorithms have been discussed for the continuous adjustment of the positions of the internal finite element nodes to the changing configuration of the mesh boundary. In Section 6.3, some fluid flow problems have then been simulated successfully, for which the motion of the boundary nodes and the velocity boundary conditions on the moving parts of the boundary are known a priori.

This chapter is concerned with the further generalisation of the numerical model to problems involving moving interfaces between the fluid and an adjacent phase. In particular, the following cases are considered:

- The mesh boundary represents a *free surface*. The scale of the problem may be sufficiently small to require the modelling of the surface tension phenomena.
- The mesh boundary represents the interface between the fluid and a *rigid body* which is free to move.
- The mesh boundary represents the interface between the fluid and a *flexible solid*.

With respect to the finite element model of the fluid phase, these different situations lead to different, interacting boundary conditions for the mesh motion, the fluid velocity field and the boundary traction vector field.

The three sections of this chapter describe in detail the modelling of the physical problems enumerated above.

## 9.1 Free Surface

It is known from Section 2.1.3 that, on the free surface boundary, the fluid velocity  $\mathbf{u}$  and the motion of the reference domain  $\hat{\mathbf{v}}$  are required to satisfy the consistency condition (2.50), *i. e.*

$$(\mathbf{u} - \hat{\mathbf{v}}) \cdot \hat{\mathbf{n}} = 0 \quad \forall (\hat{\mathbf{x}}, t) \in \Gamma_{\text{fs}} \times I. \quad (9.1)$$

The normal unit vector  $\hat{\mathbf{n}}$  can be computed from the current positions  $\hat{\mathbf{x}}$  of the boundary.

In the finite element framework the mesh is required to move such that the vector fields  $\mathbf{u}^h$ ,  $\hat{\mathbf{x}}^h$  and  $\hat{\mathbf{v}}^h$  satisfy (9.1). It is recalled from Section 6.1, equation (6.7), that the boundary configuration and the boundary velocity are related by

$$\hat{\mathbf{v}}_{n+1}^h = \frac{1}{\hat{\gamma} \Delta t} \hat{\mathbf{x}}_{n+1}^h - \frac{1}{\hat{\gamma} \Delta t} \hat{\mathbf{x}}_n^h - \frac{1 - \hat{\gamma}}{\hat{\gamma}} \hat{\mathbf{v}}_n^h, \quad (9.2)$$

Thus, an appropriate strategy for the computation of  $\hat{\mathbf{x}}_{n+1}^h$  or  $\hat{\mathbf{v}}_{n+1}^h$  on the mesh boundary has to be developed. Generally, there exist the following three approaches:

- *Lagrangian description.* The most straightforward strategy is the purely Lagrangian description of the free surface, based on  $\hat{\mathbf{v}}^h = \mathbf{u}^h \forall (\hat{\mathbf{x}}^h, t) \in \Gamma_{\text{fs}} \times I$ . However, this often very quickly leads to distortion of the surface mesh. Even in the two dimensional or the axisymmetric situation some boundary edges tend to become substantially distorted, and thus create badly shaped elements near the free surface, which often forces the simulation to crash (see also Braess and Wriggers [12]).
- *optimisation of surface mesh quality.* This is the approach adopted in this work. Similar to the methodology for the internal nodes described in Section 6.2, the surface mesh may be moved such that certain quality criteria are met. For the three dimensional situation this can be the minimisation of  $W$  from (6.10) applied to the triangles that constitute the free surface. For the two dimensional and the axisymmetric situation, one can enforce equal spacing of the nodes on the free boundary (see *e. g.* Braess and Wriggers [12]). In both cases, the optimisation criteria combined with (9.1) fully determines the motion of the finite element nodes on  $\Gamma_{\text{fs}}^h$ .

Note that, for the piecewise linear discretisation of the boundary, the condition (9.1) is too strong to allow sufficient flexibility of the free

surface. Thus, the condition is weighted with a scalar test function  $\lambda^h$  defined on  $\Gamma_{\text{fs}}$  and then satisfied weakly.

For the two dimensional or axisymmetric linear finite elements, the equal spacing condition reads

$$\|\hat{\mathbf{x}}_i - \hat{\mathbf{x}}_{i-1}\| - \|\hat{\mathbf{x}}_i - \hat{\mathbf{x}}_{i+1}\| = 0. \quad (9.3)$$

By employing a continuous and piecewise linear test function  $\lambda^h$ , the consistency condition (9.1) requires for all admissible  $\lambda^h$

$$\int_{\Gamma_{\text{fs}}} \lambda^h (\mathbf{u}^h - \hat{\mathbf{v}}^h) \cdot \hat{\mathbf{n}}^h \, ds = 0, \quad (9.4)$$

which renders

$$\sum_e \{\lambda_1, \lambda_2\} \cdot \frac{l^e}{6} \begin{bmatrix} 2 & 1 \\ 1 & 2 \end{bmatrix} \begin{Bmatrix} (\mathbf{u}_1 - \hat{\mathbf{v}}_1) \cdot \hat{\mathbf{n}}^e \\ (\mathbf{u}_2 - \hat{\mathbf{v}}_2) \cdot \hat{\mathbf{n}}^e \end{Bmatrix} = 0, \quad (9.5)$$

where the sum includes all element edges on the free surface. The assembly of the contributions to node  $i$  of the two adjacent element edges results in the difference stencil

$$l^i \hat{\mathbf{n}}^i \cdot (2(\mathbf{u}_i - \hat{\mathbf{v}}_i) + (\mathbf{u}_{i-1} - \hat{\mathbf{v}}_{i-1})) + l^{i+1} \hat{\mathbf{n}}^{i+1} \cdot (2(\mathbf{u}_i - \hat{\mathbf{v}}_i) + (\mathbf{u}_{i+1} - \hat{\mathbf{v}}_{i+1})) = 0. \quad (9.6)$$

The terminology is taken from Figure 9.1. Note that the weak enforcement of (9.1) by means of (9.4) guarantees that the integral of the flow across each boundary edge disappears.

With respect to the discrete time stepping employed in this work, we have chosen to satisfy equation (9.3) at the time instants  $t_{n+1}$ , consistently with the positioning of the internal nodes of the mesh, whereas the relation (9.4) is enforced in the mesh configuration employed for the integration over the fluid domain (see Section 6.1). Using the terminology of Chapter 6,  $\hat{\mathbf{x}}_{n+1}$  is subjected to equation (9.3), whereas  $\hat{\mathbf{x}}_{\hat{\alpha}}^h$ ,  $\hat{\mathbf{v}}_{\hat{\alpha}}^h$  and  $\mathbf{u}_{\alpha}^h$  are employed in equation (9.4).

- *combination with internal node algorithm.* The third option to determine the motion of the boundary nodes consists in treating (9.1), or (9.4), respectively, as a boundary condition for the update algorithm of the internal nodes. However, it does not guarantee optimal quality of the surface mesh and requires a tedious elimination procedure in the mesh solver of the surface degrees of freedom. Therefore, this strategy has not been further investigated in this work.

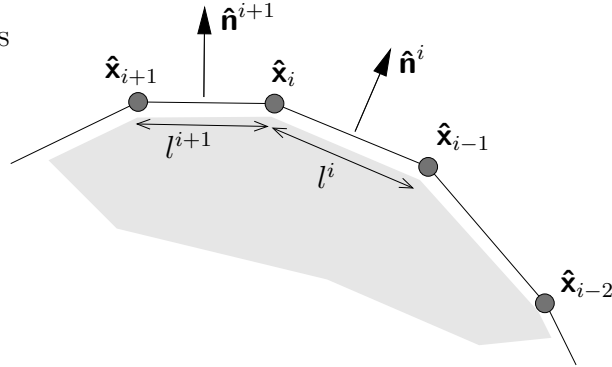


Figure 9.1: Equal spacing of boundary nodes on  $\Gamma_{\text{fs}}$ .

At the free surface, the boundary traction vectors are given by (2.51)<sub>1</sub> or (2.51)<sub>2</sub>, depending on whether the surface tension phenomena is neglected or accounted for. Both cases can easily be modelled with each of the free surface formulations outlined above. In the presence of surface tension, the numerical model developed in Chapter 7 may be used to compute nodal traction vectors on the basis of the current mesh configuration given by  $\hat{\mathbf{x}}_{\alpha}^h$ , which are then added as time dependent force loads to the fluid finite element formulation (6.1).

## 9.2 Fluid-Rigid Body Interface

This section is concerned with the numerical modelling of no-slip interfaces between the fluid and a fully submerged rigid body. In three dimensions a rigid body possesses six degrees of freedom consisting of translations and rotations. Each degree of freedom may be associated with inertia, with damping and with an elastic stiffness. In the following the focus is on the two dimensional situation, where the rigid body motion consists of translation in  $x$ - and  $y$ -direction or rotation. The degrees of freedom are denoted as  $d_x$ ,  $d_y$  and  $\theta$ , respectively. The extension of the strategy to three dimensions is tedious but straightforward.

*Kinematic consistency.* The approach taken in this work is based on a rigid body motion of the interface boundary of the fluid mesh. In other words, the finite element nodes on the interface boundary are assumed to “stick” to the surface of the rigid body. It follows that the configuration of the interface boundary is uniquely defined by the current values of  $d_x$ ,  $d_y$  and  $\theta$ . For the adjustment of the internal nodes of the fluid mesh any of the strategies presented in Section 6.2 may be employed. Due to the no-slip condition

(2.52)<sub>1</sub>, the fluid particles adjacent to the interface also stick to the surface of the rigid body. Therefore, the fluid velocity on the interface coincides with the mesh velocity.

Let  $\mathbf{x}_0$  denote the position of a reference material point S of the rigid body, *e. g.* the centre of gravity, at time instant  $t = 0$ , while  $\mathbf{d} = \{d_x, d_y\}$  and  $\Delta\mathbf{x} = \{\Delta x, \Delta y\}$  represent, respectively, the current displacement of S and the relative position of a point on the rigid body surface with respect to S, as depicted in Figure 9.2. It then follows that, at the interface, the quantities  $\hat{\mathbf{x}}^h$ ,  $\hat{\mathbf{v}}^h$ ,  $\mathbf{u}^h$  and  $\dot{\mathbf{u}}^h$  can be expressed as

$$\hat{\mathbf{x}}^h = \mathbf{x}_0 + \mathbf{d} + \Delta\mathbf{x} \quad (9.7)$$

$$\mathbf{u}^h = \hat{\mathbf{v}}^h = \dot{\mathbf{d}} + \Delta\dot{\mathbf{x}} \quad (9.8)$$

$$\dot{\mathbf{u}}^h = \ddot{\mathbf{d}} + \Delta\ddot{\mathbf{x}} \quad (9.9)$$

The vector  $\Delta\mathbf{x}$  is obtained from Figure 9.2 as

$$\Delta x = \cos\theta \Delta x_0 - \sin\theta \Delta y_0 \quad (9.10)$$

$$\Delta y = \sin\theta \Delta x_0 + \cos\theta \Delta y_0. \quad (9.11)$$

Its time derivatives follow as

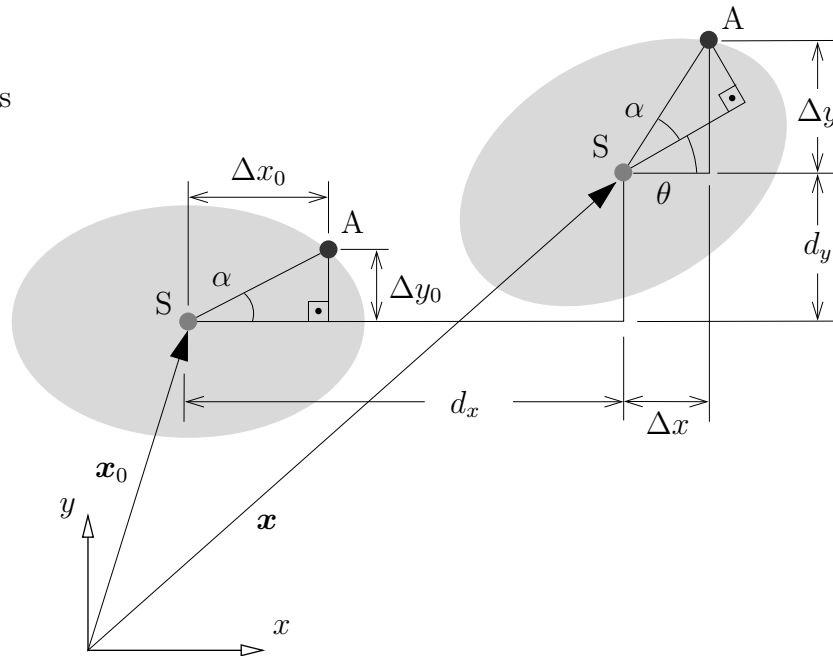


Figure 9.2: Motion of a rigid body in two dimensions.

$$\begin{aligned}
\Delta \dot{x} &= (-\sin \theta \Delta x_0 - \cos \theta \Delta y_0) \dot{\theta} \\
\Delta \dot{y} &= (+\cos \theta \Delta x_0 - \sin \theta \Delta y_0) \dot{\theta} \\
\Delta \ddot{x} &= (-\sin \theta \Delta x_0 - \cos \theta \Delta y_0) \ddot{\theta} \\
&\quad + (-\cos \theta \Delta x_0 + \sin \theta \Delta y_0) \dot{\theta}^2 \\
\Delta \ddot{y} &= (+\cos \theta \Delta x_0 - \sin \theta \Delta y_0) \ddot{\theta} \\
&\quad + (-\sin \theta \Delta x_0 - \cos \theta \Delta y_0) \dot{\theta}^2 .
\end{aligned} \tag{9.12}$$

*Equilibrium of the forces.* In two dimensions, the integration of the traction vector field exerted by the fluid on the surface of the rigid body renders a force vector  $\mathbf{F}^f$  acting on the reference point S and a moment  $M^f$  with respect to S. In Chapter 2,  $\mathbf{F}^f$  and  $M^f$  are given by the left hand sides of the equations in (2.53). In the context of the finite element model,  $\mathbf{F}^f$  and  $M^f$  are obtained naturally from the summation of, respectively, the nodal residual forces at the interface boundary of the fluid mesh and the moments of these residual forces with respect to S. The force  $\mathbf{F}^r$  and moment  $M^r$  exerted by the rigid body on the fluid interface follow from the summation of the inertia, the damping and the elastic stiffness associated with the rigid body degrees of freedom (see Section 2.3).

Equilibrium requires that

$$\mathbf{F}^f + \mathbf{F}^r = \mathbf{0} \quad \text{and} \quad M^f + M^r = 0 , \tag{9.13}$$

or in detail

$$\sum_{a=1}^{n_{\text{nd}}^{\text{f-r}}} \mathbf{g}_a^f + \begin{bmatrix} m_x & 0 \\ 0 & m_y \end{bmatrix} \ddot{\mathbf{d}} + \begin{bmatrix} c_x & 0 \\ 0 & c_y \end{bmatrix} \dot{\mathbf{d}} + \begin{bmatrix} k_x & 0 \\ 0 & k_y \end{bmatrix} \mathbf{d} = \mathbf{0} \tag{9.14}$$

$$\sum_{a=1}^{n_{\text{nd}}^{\text{f-r}}} (\Delta x_a \mathbf{g}_{a,y}^f - \Delta y_a \mathbf{g}_{a,x}^f) + m_\theta \ddot{\theta} + c_\theta \dot{\theta} + k_\theta \theta = 0 , \tag{9.15}$$

where  $n_{\text{nd}}^{\text{f-r}}$  denotes the number of finite element nodes on the interface boundary of the fluid mesh and  $\mathbf{g}_a^f = \{\mathbf{g}_{a,x}^f, \mathbf{g}_{a,y}^f\}$  represent the nodal residual forces of the fluid.

*Conservation of momentum and energy.* It follows clearly from the exact transfer of the kinematical data and the interface loads that the momentum and the energy released by the fluid are equal to the momentum and energy absorbed by the rigid body and vice versa. Note that this statement refers to the time continuous model and may need to be revised after the temporal discretisation.

The kinematic consistency conditions (9.7) – (9.9) are enforced at the discrete time instants  $t_n, t_{n+1}, \dots$ . This strategy allows the employment of different discrete time integration schemes for the fluid and the rigid body. In this work, the generalised- $\alpha$  method is employed for both the fluid and the rigid body. However, the formula for the coefficients  $\alpha_m$  and  $\alpha_f$  is chosen differently (fluid: (6.6), optimal for the first order problem; rigid body: (8.35), optimal for the second order problem) and the free integration parameters  $\rho_\infty^h$  are set independently. Note that this may lead to a slight deviation of the configurations for which equilibrium is enforced. In other words, the relations (9.14) and (9.15) may be associated with a small time discretisation error.

### 9.3 Fluid-Solid Interface

A typical detail of a discretised fluid-solid interaction problem is displayed in Figure 9.3. In most situations, the fluid requires a significantly denser spatial discretisation than the structure. In order to avoid unnecessarily fine structural meshes, it is essential to design the interface model for *non-matching* fluid and solid meshes, *i. e.* the boundary nodes of the fluid and the solid are not required to coincide.

*Kinematic consistency.* It follows from the Lagrangian modelling of the solid structure that, even for large structural deformations, the boundary nodes of the solid represent a good discretisation of the current interface configuration at all times of the simulation. Thus, it is suggestive to “stick” the fluid interface nodes to the surface of the solid. The position of the internal nodes of the fluid mesh can then be adjusted to the current interface configuration

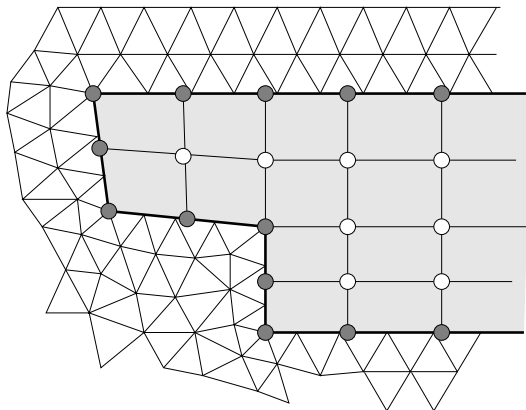


Figure 9.3: Typical fluid-solid interface, non-matching meshes.

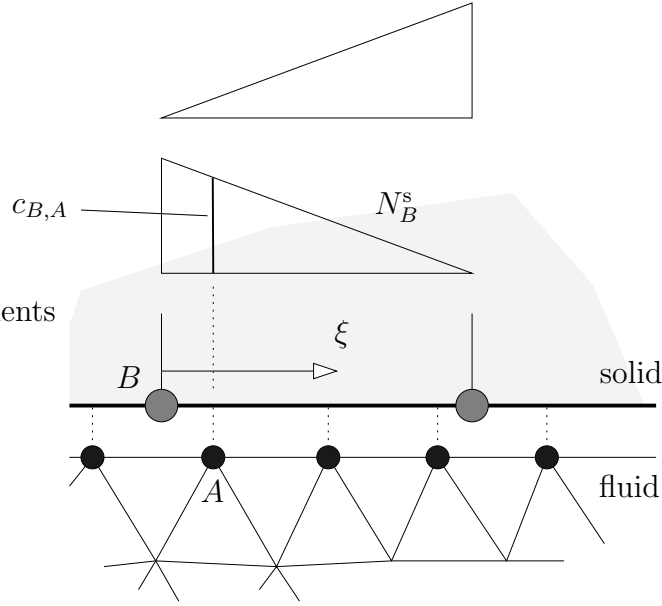


Figure 9.4: Fluid-solid interface, transfer of data based on the finite element interpolation of the solid structure.

by means of one of the strategies described in Section 6.2. Similarly to the model of the fluid-rigid body interface described in the previous section, it follows from the “no-slip” and the “sticky meshes” conditions that the displacements and the velocities of the of the fluid and solid particles in the interface coincide with the motion of the fluid and solid mesh boundaries. The kinematical data of the fluid may then be expressed in terms of the structural data by means of the finite element interpolation of the solid. This strategy is illustrated in Figure 9.4. The fluid data can then be expressed as

$$\hat{\mathbf{x}}_A = c_{B,A} (\mathbf{x}_{B,0} + \mathbf{d}_B) \quad (9.16)$$

$$\mathbf{u}_A = \hat{\mathbf{v}}_A = c_{B,A} \dot{\mathbf{d}}_B \quad (9.17)$$

$$\dot{\mathbf{u}}_A = c_{B,A} \ddot{\mathbf{d}}_B, \quad (9.18)$$

where the vectors  $\hat{\mathbf{x}}_A$ ,  $\mathbf{u}_A$ ,  $\hat{\mathbf{v}}_A$  and  $\dot{\mathbf{u}}_A$  represent, respectively, the nodal values of  $\hat{\mathbf{x}}^h$ ,  $\mathbf{u}^h$ ,  $\hat{\mathbf{v}}^h$  and  $\dot{\mathbf{u}}^h$  at the interface boundary of the fluid mesh. Similarly,  $\mathbf{d}_B$ ,  $\dot{\mathbf{d}}_B$  and  $\ddot{\mathbf{d}}_B$  are the displacement, velocity and acceleration of the solid finite element nodes at the interface. The coefficient  $c_{B,A} = N_B^s(\xi_A)$  denotes the value of the structural shape function associated with node  $B$  and evaluated at the position of the fluid node  $A$ , see Figure 9.4. Thus, the kinematics of the interface is determined by the finite element interpolation of the solid.

*Equilibrium of the forces.* The equilibrium of the stresses in the interface is satisfied by balancing the nodal residual forces of the fluid and the solid by means of the principle of virtual work. Following the interface kinematics described above, a virtual displacement of the interface may be expressed as

$$\delta \mathbf{d} = N_B^s \delta \mathbf{d}_B . \quad (9.19)$$

The sum of the work of the fluid and the solid nodal forces, done along the virtual displacement  $\delta \mathbf{d}$ , can then be written as

$$\delta W = \mathbf{g}_A^f N_B^s(\xi_A) \delta \mathbf{d}_B + \mathbf{g}_B^s \delta \mathbf{d}_B = 0 , \quad (9.20)$$

where the vectors  $\mathbf{g}_A^f$  and  $\mathbf{g}_B^s$  denote, respectively, the fluid residual force in the fluid node  $A$  and the solid residual force in the solid node  $B$ . Note that summation is performed over all nodes  $A$  and  $B$  along the interface. Thus, one obtains

$$\mathbf{g}_A^f c_{B,A} + \mathbf{g}_B^s = \mathbf{0} . \quad (9.21)$$

*Conservation of momentum and energy.* It follows from the virtual work equation (9.20), which is formulated consistently with the interface kinematics given by (9.16) – (9.18), that the momentum and energy released by the fluid is identical to the momentum and energy absorbed by the solid and vice versa. However, similarly to the fluid-rigid body interaction model of Section 9.2, the exact conservation may be jeopardised slightly by the time discretisation.

For the implementation in a computer program it is important to note that the coefficients  $c_{B,A}$  are constant throughout the simulation. The computational effort associated with the transfer of the forces and the kinematical data is negligible.

Some structural elements, *e. g.* beam or shell elements, typically possess rotational degrees of freedom besides the nodal translational displacements. Similarly to the fluid pressure, these degrees of freedom do not need to be transferred across the interface. Despite their association with nodes on the interface boundary, they are treated like those degrees of freedom belonging to the internal nodes of the solid structure. It should also be noted that the strategy outlined above is readily applicable to structural elements which are “wet” on more than one face. In such cases, the kinematical data of beam, membrane or plate elements, which are submerged in the fluid, is transferred to the adjacent fluid nodes on both sides.

Following Section 9.2, the kinematic consistency conditions (9.16) – (9.18) are enforced at the discrete time instants  $t_n, t_{n+1}, \dots$ . This strategy allows the

employment of different discrete time integration schemes for the fluid and the solid. Again, the generalised- $\alpha$  method is employed for both the fluid and solid phases, deviating only in terms of the formula for the coefficients  $\alpha_m$  and  $\alpha_f$  and the user controlled free integration parameters  $\rho_\infty^h$ . This strategy may introduce a small time discretisation error to equation (9.21).

*REMARK 9.1: Alternative methods.* The most rigorous strategy to model fluid-solid interfaces certainly is the employment of matching meshes. It eliminates any overlapping of the meshes or the opening of any gaps. It is also readily implemented in a computer program. On the other hand, it requires the refinement of the coarser finite element mesh, usually the solid, towards the interface to match the nodes of the denser mesh, usually the fluid. This not only increases the computational cost to determine the response of the solid structure, but, more importantly, it leads to an unnecessarily large number of degrees of freedom of the interface kinematics. It is shown in the following chapters, that the majority of the computational time is spent to resolve the coupling of the fluid and the solid. Thus, it is generally advantageous to keep the number of degrees of freedom of the interface as small as possible. A further disadvantage lies in the tedious generation of matching meshes itself.

The strategy described by (9.16) – (9.18) and (9.21) is based on the finite element interpolation of one of the adjacent phases and allows the employment of non-matching meshes. For extreme deformation of the solid structure, small areas of overlapping or small gaps may occur. However, this hints that the discretisation of the structure is indeed too coarse.

Alternatively, one may decide to employ Lagrangian multipliers to enforce kinematic consistency at the mesh boundaries. Such methods, which have been introduced in the context of non-matching meshes, are known as “*mortar* methods”. They may help to further reduce the number of degrees of freedom of the interface kinematics. However, their conservation properties need to be investigated carefully. Similarly, one has to ensure the accurate modelling of sharp edges of the interface, which is often crucial to capture the flow characteristics.

More information on the modelling of fluid-solid interfaces is provided in Farhat *et al* [44] and references therein.

# Chapter 10

## Solution Algorithm

At this stage, a complete description of the numerical models for free surface flow, fluid-rigid body and fluid-solid interaction problems has been given. In Section 10.1, a general discrete representation of fluid flow on moving domains is introduced, which incorporates the different types of interfaces associated with the problems enumerated above. This generalisation is achieved by means of decomposing the problem into three domains: the fluid domain, the interface and the adjacent phase. Following this strategy, one obtains three strongly coupled sets of highly nonlinear equations. In this work, it is sought to resolve the coupling exactly (up to machine precision). Thus, the solution of the system of equations poses a major difficulty. Therefore, a partitioned Newton-Raphson procedure based on exact linearisation has been developed. It is described in Section 10.2. The chapter concludes with a brief review of alternative solution strategies in Section 10.4.

### 10.1 Domain Decomposition

The formulation of a general discrete model of fluid flows on moving domains, which incorporates free surface flows as well as fluid-rigid body and fluid-solid interaction, is essentially based on the introduction of the *interface domain*. Similarly to the fluid or the solid phases, the interface domain possesses degrees of freedom, which describe the current interface configuration and possibly other data which is exchanged between the two phases, such as, for instance, temperature. In this work, an isoparametric linear finite element type interpolation based on nodes and shape functions is employed to define the kinematics of the interface and the distribution of any other relevant data. For fluid-rigid body interaction, the degrees of freedom of the interface coincide with those of the rigid body and thus, no such interpolation

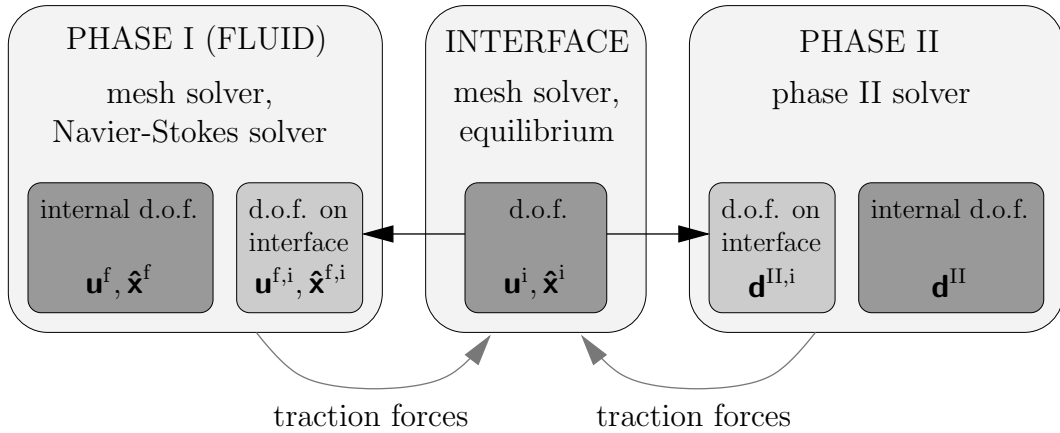


Figure 10.1: Domain decomposition; the black arrows represent appropriate transfer operators; the independent degrees of freedom are given in the dark gray boxes.

is needed.

Figure 10.1 illustrates the decomposition of the problem into the three subdomains of phase I, phase II and the interface. The degrees of freedom on the interface boundaries of phases I and II are related to the degrees of freedom of the interface domain by means of appropriate transfer operators. The transfer operators need to be designed such that the kinematic consistency conditions associated with the physical problem under consideration are satisfied. In Figure 10.1, the independent unknowns of the overall problem are represented by the dark gray boxes. For the sake of notational convenience, all degrees of freedom of phases I and II, which are not exchanged across the interface, *e. g.* the fluid pressure or eventual structural rotations, are included in the vectors  $\mathbf{u}^f$  and  $\mathbf{d}^{II}$ , respectively. Figure 10.1 also identifies the systems of equations associated with each domain. The equilibrium of the stresses in the interface is enforced by the equations denoted as “equilibrium”, which relate the traction forces exerted on the interface by the adjacent phases.

For the numerical examples presented in Chapters 11 – 14, the interface kinematics, the transfer operators and the “equilibrium” equations are chosen such that the resulting decomposed problem is merely a different representation of what has been described in detail in Chapter 9 for the modelling of free surface flows, fluid-rigid body and fluid-solid interaction. In other words, for free surface flows, the interface nodes and shape functions coincide with the surface mesh of the fluid domain. For fluid-rigid body interaction, the degrees of freedom of the interface and the rigid body are identical and, for fluid-solid interaction, the interface mesh coincides with the discretisation of

the surface of the structure. This is also indicated in Figure 10.3. The interface model for two adjacent finite element meshes, which has actually been implemented in the course of this work, is schematically depicted in Figure 10.2. Hence, the interpolation strategy described in Section 9.3 between the solid and the fluid is applied separately between the interface and phase I and the interface and phase II. This choice has been made in order to enhance the flexibility and modularity of the computer program. It is expected to be particularly advantageous for mesh adaptivity in one or both phases.

The advantages of the domain decomposition as illustrated in Figure 10.1 may be summarised as follows:

- It allows the employment of the same implementational framework for the different physical problems under consideration.
- It significantly enhances the modularity and readability of the computer program.
- It facilitates future extensions of the program (*e. g.* remeshing of all or of selected domains, employment of mortar methods for the interface modelling, simulation of fluid-fluid interaction).

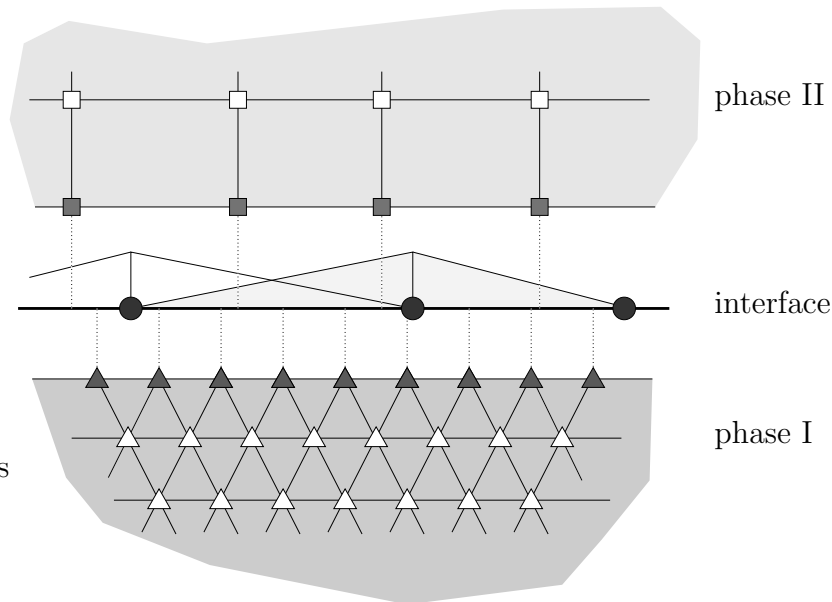
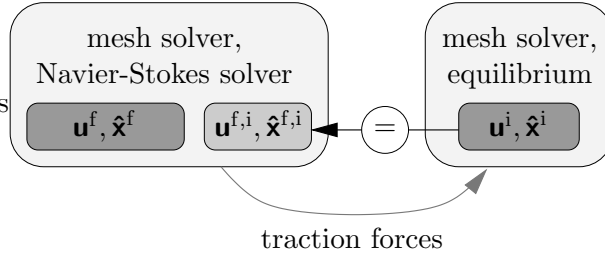


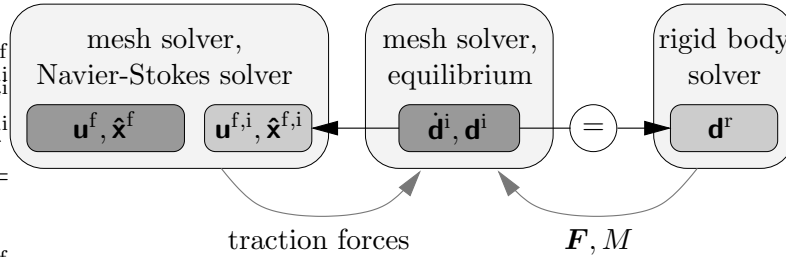
Figure 10.2: General interface modelling, transfer based on finite element type interpolation of the interface domain.

(a) free surface flow:



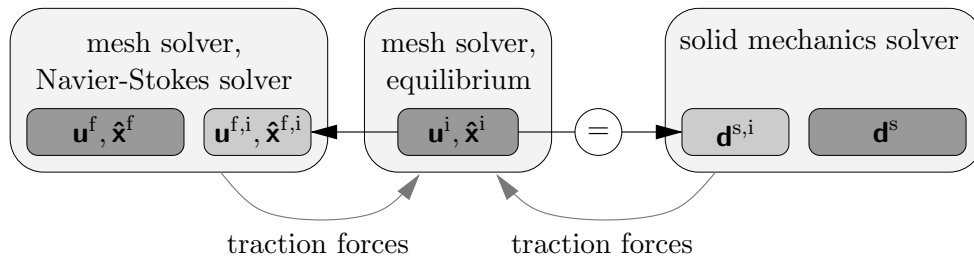
interface mesh solver: enforce equal nodal spacing  
 interface equilibrium: enforce zero fluid traction forces,  
 or balance them with surface tension forces

(b) fluid-rigid body interaction:



interface mesh solver: relate  $\mathbf{d}^i$  and  $\dot{\mathbf{d}}^i$  by means of time integration scheme  
 interface equilibrium: balance fluid traction forces with  $\mathbf{F}$ ,  $M$ ; see (9.14), (9.15)  
 data transfer to fluid: see (9.7) – (9.9)

(c) fluid-solid interaction:



interface mesh solver: relate  $\mathbf{u}^i$  and  $\dot{\mathbf{x}}^i$  by means of time integration scheme  
 interface equilibrium: balance fluid and solid traction forces, see (9.21)  
 data transfer to fluid: see (9.16) – (9.18)

Figure 10.3: Domain decomposition, accommodation of different problems in the framework of Figure 10.1; in (b),  $\mathbf{d}^i$  and  $\mathbf{d}^f$  include translational and rotational degrees of freedom.

## 10.2 Partitioned Newton-Raphson Procedure

*Strongly coupled set of discrete equations.* After the domain decomposition described in the previous section, the overall problem may be represented by the following set of equations

$$\begin{array}{l}
 \text{fluid} \quad [\mathbf{u}^f, \hat{\mathbf{x}}^f] \quad \left\{ \begin{array}{l} \text{mesh solver} \quad \mathbf{m}^f(\hat{\mathbf{x}}^f, \hat{\mathbf{x}}^i) = \mathbf{0} \\ \text{Navier-Stokes solver} \quad \mathbf{g}^f(\mathbf{u}^f, \mathbf{u}^i, \hat{\mathbf{x}}^f, \hat{\mathbf{x}}^i) = \mathbf{0} \end{array} \right. \\
 \\
 \text{interface} \quad [\mathbf{u}^i, \hat{\mathbf{x}}^i] \quad \left\{ \begin{array}{l} \text{mesh solver} \quad \mathbf{m}^i(\mathbf{u}^i, \hat{\mathbf{x}}^i) = \mathbf{0} \\ \text{equilibrium} \quad \mathbf{g}^i(\mathbf{u}^f, \mathbf{u}^i, \mathbf{d}^{\text{II}}, \hat{\mathbf{x}}^f, \hat{\mathbf{x}}^i) = \mathbf{0} \end{array} \right. \quad (10.1) \\
 \\
 \text{phase II} \quad [\mathbf{d}^{\text{II}}] \quad : \text{ phase II solver} \quad \mathbf{g}^{\text{II}}(\mathbf{d}^{\text{II}}, \hat{\mathbf{x}}^i) = \mathbf{0},
 \end{array}$$

where the terminology is taken from Figure 10.1 and, for clarity, the independent unknowns associated with each domain are given in the brackets. The interface equilibrium equation may be written as

$$\mathbf{g}^i(\mathbf{u}^f, \mathbf{u}^i, \mathbf{d}^{\text{II}}, \hat{\mathbf{x}}^f, \hat{\mathbf{x}}^i) = \mathbf{g}^{i,f}(\mathbf{u}^f, \mathbf{u}^i, \hat{\mathbf{x}}^f, \hat{\mathbf{x}}^i) + \mathbf{g}^{i,\text{II}}(\mathbf{d}^{\text{II}}, \hat{\mathbf{x}}^i) = \mathbf{0}. \quad (10.2)$$

Note that the dependency of  $\mathbf{g}^i$  on  $\mathbf{u}^f$ ,  $\hat{\mathbf{x}}^f$  and  $\mathbf{d}^{\text{II}}$  is restricted to the finite element nodes of the element layers adjacent to the interface boundaries of the fluid and phase II, respectively.

For the simplicity of what follows, the phase II solver is presented as dependent only on  $\hat{\mathbf{x}}^i$ , but not on  $\mathbf{u}^i$ . Naturally, the response of a solid structure with dissipative material behaviour and inertia also depends on the velocities and the accelerations. However, for the no-slip, Lagrangian type interfaces considered in this work, the displacement, the velocity and the acceleration are related linearly by scalar factors determined by the time integration scheme. Thus, all kinematic quantities can be recovered from  $\hat{\mathbf{x}}^i$  inside the phase II solver.

*Solution strategy.* The system (10.1) consists of strongly coupled sets of nonlinear equations. Given the solution of the previous time instant  $t_n$ , the system has to be solved for  $\mathbf{u}^f$ ,  $\hat{\mathbf{x}}^f$ ,  $\mathbf{u}^i$ ,  $\hat{\mathbf{x}}^i$ , and  $\mathbf{d}^{\text{II}}$  at the next time instant  $t_{n+1}$ . The solution strategy developed in the course of this work is based on the Newton-Raphson method. In the following, the solution vectors  $\mathbf{u}^f$  and  $\mathbf{u}^i$  are referred to as *primary* unknowns.

The methodology can be described as follows: On the basis of the solution at  $t_n$  an initial guess is made for the primary unknowns  $\mathbf{u}^f$  and  $\mathbf{u}^i$  at  $t_{n+1}$ .

The new configuration of the interface mesh  $\hat{\mathbf{x}}^i$  and the derivative  $\partial\hat{\mathbf{x}}^i/\partial\mathbf{u}^i$  are computed (interface mesh solver). Subsequently, the nodal positions  $\hat{\mathbf{x}}^f$  are adapted to the new geometry given by  $\hat{\mathbf{x}}^i$ , and the derivative  $\partial\hat{\mathbf{x}}^f/\partial\hat{\mathbf{x}}^i$  is evaluated (fluid mesh solver). Next, the response of phase II,  $\mathbf{d}^{II}$ , to the new interface configuration  $\hat{\mathbf{x}}^i$  is determined (phase II solver). The derivatives of  $\mathbf{d}^{II}$  with respect to  $\hat{\mathbf{x}}^i$  are computed. At this stage, all necessary data is available and the residuals  $\mathbf{g}^f$  and  $\mathbf{g}^i$  are evaluated. If the tolerances are met, then the procedure can be aborted to proceed with the next time step. Otherwise, the linearisations of  $\mathbf{g}^f$  and  $\mathbf{g}^i$  with respect to the primary unknowns  $\mathbf{u}^f$  and  $\mathbf{u}^i$  are computed. To this end, all partial derivatives of  $\mathbf{g}^f$  and  $\mathbf{g}^i$  are calculated and then, according to the chain rule, combined with the derivatives obtained above. The linearised versions of  $\mathbf{g}^f$  and  $\mathbf{g}^i$  can then be solved for the increments of the primary unknowns  $\mathbf{u}^f$  and  $\mathbf{u}^i$  (*combined fluid + interface solver*). The primary unknowns are updated, and the complete procedure is repeated for the improved values of  $\mathbf{u}^f$  and  $\mathbf{u}^i$ .

A summary of the algorithm is given in Box 10.1. Henceforth, the execution of steps 1. – 7. is referred to as one “overall Newton step”.

*Obtaining derivatives from implicit equations.* The following formula is extensively used for the computation of derivatives: Consider the equation  $f(x, y) = 0$ , which is assumed to be highly nonlinear such that no explicit expressions for  $x$  or  $y$  can be derived. Suppose  $y$  has been computed, for a given  $x$ , by means of a Newton-Raphson procedure such that  $f(x, y) = 0$  is satisfied. For very small  $dx$  and  $dy$ , it may then be written

$$\frac{\partial f(x, y)}{\partial x} dx + \frac{\partial f(x, y)}{\partial y} dy = 0, \quad (10.3)$$

and the derivative  $dy/dx$  is obtained as

$$\frac{dy}{dx} = - \left[ \frac{\partial f(x, y)}{\partial y} \right]^{-1} \frac{\partial f(x, y)}{\partial x}. \quad (10.4)$$

For vector valued problems  $\mathbf{f}(\mathbf{x}, \mathbf{y}) = \mathbf{0}$ , it may be more convenient to write

$$\frac{\partial \mathbf{f}(\mathbf{x}, \mathbf{y})}{\partial \mathbf{y}} \frac{\partial \mathbf{y}}{\partial \mathbf{x}} = - \frac{\partial \mathbf{f}(\mathbf{x}, \mathbf{y})}{\partial \mathbf{x}}, \quad (10.5)$$

where all the derivatives are matrices. The  $i$ th column of the wanted derivative  $\partial\mathbf{y}/\partial\mathbf{x}$  can then be obtained from a system of linear equations, where the  $i$ th column of  $-\partial\mathbf{f}(\mathbf{x}, \mathbf{y})/\partial\mathbf{x}$  is used as the right hand side vector. Note that the matrix  $\partial\mathbf{f}(\mathbf{x}, \mathbf{y})/\partial\mathbf{y}$  in (10.5) coincides with the linearisation matrix from the last step of the Newton procedure used to determine  $\mathbf{y}$  for the

given  $\mathbf{x}$ . Thus, conveniently, the LU-decomposition of  $\partial \mathbf{f}(\mathbf{x}, \mathbf{y})/\partial \mathbf{y}$  is still available, provided a direct solver has been employed. The wanted derivative can then be obtained from repeated backward and forward substitutions for different right hand sides. Importantly, by applying this strategy, no inverse matrices need to be assembled and costly matrix multiplication can be avoided. Formula (10.5) is used in the steps 2. – 4. in Box 10.1.

*Implementational details.* In the following, some implementational details of the algorithm are discussed. The numbering of the comments refers to the steps given in Box 10.1.

1. At the beginning of each time step, the solution of the previous time instant can be employed as the initial guess for  $\mathbf{u}^f$  and  $\mathbf{u}^i$ . A better guess may be obtained from more sophisticated extrapolation in time based on the previous solutions. Note, however, that, in the examples presented in Chapters 11 – 14, such strategies have rarely led to a smaller number of overall Newton steps. This proves the high degree of non-linearity of the problems considered, and also suggests the restriction of explicit solution techniques to small time steps (see Section 10.4).
2. The interface mesh solver renders the updated interface configuration  $\hat{\mathbf{x}}^i$  on the basis of the current values  $\mathbf{u}^i$ . For two dimensional free surface flow problems, this requires the solution of the equal nodal spacing and the free surface consistency conditions (see Section 9.1). Due to the equations being nonlinear and implicit, a Newton-Raphson procedure is employed. Once  $\hat{\mathbf{x}}^i$  has been obtained with sufficient accuracy, the derivative  $\partial \hat{\mathbf{x}}^i/\partial \mathbf{u}^i$  is, analogously to (10.5), computed from

$$\frac{\partial \mathbf{m}^i}{\partial \hat{\mathbf{x}}^i} \frac{\partial \hat{\mathbf{x}}^i}{\partial \mathbf{u}^i} = - \frac{\partial \mathbf{m}^i}{\partial \mathbf{u}^i} . \quad (10.6)$$

In case of fluid-rigid body or fluid-solid interaction, the vectors  $\mathbf{u}^i$  and  $\hat{\mathbf{x}}^i$  are related linearly by the time integration scheme and, thus, no equations need to be solved. The derivative  $\partial \hat{\mathbf{x}}^i/\partial \mathbf{u}^i$  reduces to a scalar factor.

3. The application of the fluid mesh solver renders new positions  $\hat{\mathbf{x}}^f$  of the internal nodes of the fluid mesh, which are adapted to the interface configuration  $\hat{\mathbf{x}}^i$ . The mesh update strategies considered in this work are nonlinear and thus, a Newton-Raphson procedure is employed (see Section 6.2). The derivative  $\partial \hat{\mathbf{x}}^f/\partial \hat{\mathbf{x}}^i$  is obtained along the lines of (10.5) from

$$\frac{\partial \mathbf{m}^f}{\partial \hat{\mathbf{x}}^f} \frac{\partial \hat{\mathbf{x}}^f}{\partial \hat{\mathbf{x}}^i} = - \frac{\partial \mathbf{m}^f}{\partial \hat{\mathbf{x}}^i} . \quad (10.7)$$

1. estimate  $\mathbf{u}^f, \mathbf{u}^i$
2. interface mesh solver  $\mathbf{m}^i(\mathbf{u}^i, \hat{\mathbf{x}}^i) = \mathbf{0}$ 
  - (a) compute  $\hat{\mathbf{x}}^i$  on the basis of  $\mathbf{u}^i$
  - (b) compute  $\frac{\partial \hat{\mathbf{x}}^i}{\partial \mathbf{u}^i}$  from  $\frac{\partial \mathbf{m}^i}{\partial \hat{\mathbf{x}}^i} \frac{\partial \hat{\mathbf{x}}^i}{\partial \mathbf{u}^i} = -\frac{\partial \mathbf{m}^i}{\partial \mathbf{u}^i}$
3. fluid mesh solver  $\mathbf{m}^f(\hat{\mathbf{x}}^f, \hat{\mathbf{x}}^i) = \mathbf{0}$ 
  - (a) compute  $\hat{\mathbf{x}}^f$  on the basis of  $\hat{\mathbf{x}}^i$
  - (b) compute  $\frac{\partial \hat{\mathbf{x}}^f}{\partial \hat{\mathbf{x}}^i}$  from  $\frac{\partial \mathbf{m}^f}{\partial \hat{\mathbf{x}}^f} \frac{\partial \hat{\mathbf{x}}^f}{\partial \hat{\mathbf{x}}^i} = -\frac{\partial \mathbf{m}^f}{\partial \hat{\mathbf{x}}^i}$
4. phase II solver  $\mathbf{g}^{\text{II}}(\mathbf{d}^{\text{II}}, \hat{\mathbf{x}}^i) = \mathbf{0}$ 
  - (a) compute  $\mathbf{d}^{\text{II}}$  on the basis of  $\hat{\mathbf{x}}^i$
  - (b) compute  $\frac{\partial \mathbf{d}^{\text{II}}}{\partial \hat{\mathbf{x}}^i}$  from  $\frac{\partial \mathbf{g}^{\text{II}}}{\partial \mathbf{d}^{\text{II}}} \frac{\partial \mathbf{d}^{\text{II}}}{\partial \hat{\mathbf{x}}^i} = -\frac{\partial \mathbf{g}^{\text{II}}}{\partial \hat{\mathbf{x}}^i}$
5. compute residuals  $\mathbf{g}^f(\mathbf{u}^f, \mathbf{u}^i, \hat{\mathbf{x}}^f, \hat{\mathbf{x}}^i), \mathbf{g}^i(\mathbf{u}^f, \mathbf{u}^i, \mathbf{d}^{\text{II}}, \hat{\mathbf{x}}^f, \hat{\mathbf{x}}^i)$ ,  
if  $\mathbf{g}^f, \mathbf{g}^i < \text{tol}$ , then exit

6. compute derivatives

$$A = \frac{\partial \mathbf{g}^f}{\partial \mathbf{u}^f}, \quad B = \frac{\partial \mathbf{g}^f}{\partial \mathbf{u}^i} + \left( \frac{\partial \mathbf{g}^f}{\partial \hat{\mathbf{x}}^f} \frac{\partial \hat{\mathbf{x}}^f}{\partial \hat{\mathbf{x}}^i} + \frac{\partial \mathbf{g}^f}{\partial \hat{\mathbf{x}}^i} \right) \frac{\partial \hat{\mathbf{x}}^i}{\partial \mathbf{u}^i}, \quad C = \frac{\partial \mathbf{g}^i}{\partial \mathbf{u}^f},$$

$$D = \frac{\partial \mathbf{g}^i}{\partial \mathbf{u}^i} + \frac{\partial \mathbf{g}^i}{\partial \mathbf{d}^{\text{II}}} \left( \frac{\partial \mathbf{d}^{\text{II}}}{\partial \mathbf{u}^i} + \frac{\partial \mathbf{d}^{\text{II}}}{\partial \hat{\mathbf{x}}^i} \frac{\partial \hat{\mathbf{x}}^i}{\partial \mathbf{u}^i} \right) + \left( \frac{\partial \mathbf{g}^i}{\partial \hat{\mathbf{x}}^f} \frac{\partial \hat{\mathbf{x}}^f}{\partial \hat{\mathbf{x}}^i} + \frac{\partial \mathbf{g}^i}{\partial \hat{\mathbf{x}}^i} \right) \frac{\partial \hat{\mathbf{x}}^i}{\partial \mathbf{u}^i}$$

7. solve *combined fluid + interface solver*

$$\begin{bmatrix} A & B \\ C & D \end{bmatrix} \begin{Bmatrix} \Delta \mathbf{u}^f \\ \Delta \mathbf{u}^i \end{Bmatrix} = - \begin{Bmatrix} \mathbf{g}^f \\ \mathbf{g}^i \end{Bmatrix}, \quad \begin{Bmatrix} \mathbf{u}^f \\ \mathbf{u}^i \end{Bmatrix} \leftarrow \begin{Bmatrix} \mathbf{u}^f \\ \mathbf{u}^i \end{Bmatrix} + \begin{Bmatrix} \Delta \mathbf{u}^f \\ \Delta \mathbf{u}^i \end{Bmatrix}$$

8. goto 2.

Box 10.1: Partitioned Newton-Raphson procedure to solve the system (10.1).

Note that the computational cost may be reduced by taking advantage of the sparseness of the right hand side matrix. The derivative  $\partial \mathbf{m}^f / \partial \hat{\mathbf{x}}^i$  possesses non-zero entries only in those rows, which are associated with the element layer adjacent to the interface.

4. The phase II solver computes the response  $\mathbf{d}^{\text{II}}$  of phase II to the new interface configuration  $\hat{\mathbf{x}}^i$ . It then determines the derivative  $\partial \mathbf{d}^{\text{II}} / \partial \hat{\mathbf{x}}^i$  from

$$\frac{\partial \mathbf{g}^{\text{II}}}{\partial \mathbf{d}^{\text{II}}} \frac{\partial \mathbf{d}^{\text{II}}}{\partial \hat{\mathbf{x}}^i} = - \frac{\partial \mathbf{g}^{\text{II}}}{\partial \hat{\mathbf{x}}^i} . \quad (10.8)$$

Similar to the situation in the fluid mesh solver, computational advantage may be taken from the sparseness of the right hand side matrix. Note that the derivative  $\partial \mathbf{g}^{\text{II}} / \partial \mathbf{d}^{\text{II}}$  represents the combined stiffness, damping and mass matrices of phase II

$$\frac{\partial \mathbf{g}^{\text{II}}}{\partial \mathbf{d}^{\text{II}}} = \frac{\partial \tilde{\mathbf{g}}^{\text{II}}}{\partial \mathbf{d}^{\text{II}}} + \frac{\partial \tilde{\mathbf{g}}^{\text{II}}}{\partial \dot{\mathbf{d}}^{\text{II}}} c_1 + \frac{\partial \tilde{\mathbf{g}}^{\text{II}}}{\partial \ddot{\mathbf{d}}^{\text{II}}} c_2 , \quad (10.9)$$

where  $\mathbf{d}^{\text{II}}$ ,  $\dot{\mathbf{d}}^{\text{II}}$  and  $\ddot{\mathbf{d}}^{\text{II}}$  are linearly dependent with factors  $c_1$ ,  $c_2$  determined by the time stepping scheme.

5. At this stage all the data is available to evaluate the residuals  $\mathbf{g}^f$  and  $\mathbf{g}^i$ . If the tolerances are met, then solution at time instant  $t_{n+1}$  is given by the current values of  $\mathbf{u}^f$ ,  $\mathbf{u}^i$ ,  $\hat{\mathbf{x}}^f$ ,  $\hat{\mathbf{x}}^i$ , and  $\mathbf{d}^{\text{II}}$ . One can proceed with the next time step.
6. A large percentage of the overall computational time is spent on the matrix multiplications required in this step, typically 20 – 40 %. Note however, that this depends on the efficiency of the computer implementation and on the ratios of  $N^f$ ,  $N^i$  and  $N^{\text{II}}$  of the problem under consideration, where  $N^f$ ,  $N^i$  and  $N^{\text{II}}$  denote the numbers of degrees of freedom of the fluid, the interface and phase II, respectively. For most problems,  $N^i$  and  $N^{\text{II}}$  are small in comparison to  $N^f$ . Thus, the effort associated with the multiplication of  $\partial \mathbf{g}^f / \partial \hat{\mathbf{x}}^f$  and  $\partial \hat{\mathbf{x}}^f / \partial \hat{\mathbf{x}}^i$ , which involves  $N^f \times N^f \times N^i$  scalar operations, exceeds the cost of the other matrix multiplications. Therefore, this part of the algorithm should be implemented carefully, taking all possible advantage of the sparseness of  $\partial \mathbf{g}^f / \partial \hat{\mathbf{x}}^f$ .
7. The pattern of non-zero entries of a typical system matrix of the combined fluid + interface solver is displayed in Figure 10.4. Clearly, for a small number of interface degrees of freedom, the pattern is almost

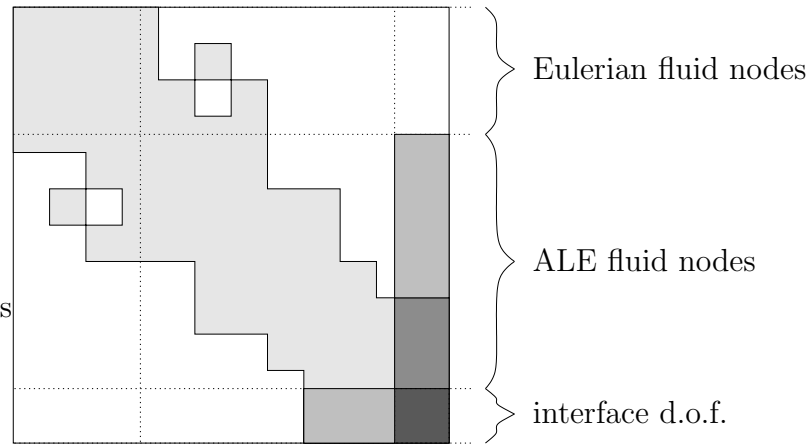


Figure 10.4: Typical system matrix of the combined fluid + interface solver.

symmetric. Therefore, a direct sparse solver for unsymmetric matrices is employed in this work, which performs most efficiently for matrices with symmetric patterns.

The interaction of fluid flow with a very stiff solid structure may lead to an ill-conditioned system matrix. In such cases, a standard preconditioning technique may be employed. For the choice of the optimal strategy it should be noted that any ill-conditioning arises from the structural contribution to part  $D$  of the matrix, which is usually relatively small. The matrix is regular even without the contribution of the structure. It is also pointed out, that the interaction of fluid flow with very stiff structures can be solved by means of basic iterative schemes (*e. g.* block Gauß-Seidel, see Section 10.4.2). However, such strategies fail or converge very poorly when applied to the interaction of fluid flow and relatively flexible structures, which is indeed the focus of this work. The solutions of the examples presented in the Chapters 11 – 14 are obtained without any preconditioning.

Finally, it is pointed out that the memory requirements for storing the various derivative matrices are smaller than the workspace typically required by the combined fluid + interface solver. Substantial amounts of computer memory may be saved by reusing the same physical memory for different purposes in the course of steps 1. to 8. Thus, the strategy outlined in Box 10.1 can not be said to require excessive amounts of computer memory.

For the steps 2. – 4. and 6., various element derivative matrices need to be implemented. The derivative  $\partial \mathbf{g}^f / \partial \hat{\mathbf{x}}^f$  is particularly tedious due to the formulation of (6.1) in the current mesh configuration. Thus, the element

area and all shape function derivatives need to be linearised. However, all derivatives are straightforward exercises and, therefore, are not addressed any further in this work. Analytical expressions for  $\partial \mathbf{g}^f / \partial \mathbf{u}^f$ , which are the only derivatives needed in Eulerian fluid flow simulations, are given in Slijepčević [110].

It is possible to think of different “partitioned Newton-Raphson” procedures to solve (10.1). Instead of using the combined fluid + interface solver, the fluid could be treated on the same level as phase II, which would lead to a pure “interface solver” in step 7. The strategy results in much more calls of the fluid solver and the requirement of computing the derivative  $\partial \mathbf{u}^f / \partial \mathbf{u}^i$ . This is very inefficient, since the number of unknowns associated with the fluid clearly dominates the problems considered in this work. The strategy outlined in Box 10.1 is particularly suitable for problems with large Eulerian parts of the fluid mesh.

### 10.3 Adaptive Time Stepping

Some of the numerical examples presented in the Chapters 11 – 14 involve significant changes in the values of solution variables throughout the simulation. Thus, it is convenient to introduce adaptive time stepping. In this work, the following simple criteria for the choice of the time step size is employed

$$\Delta t = t_{n+1} - t_n = (t_n - t_{n-1}) \left( \frac{1}{2} \right)^{(n_{\text{iter}} - n_{\text{opt}})}, \quad (10.10)$$

where  $n_{\text{iter}}$  is the number of overall Newton steps, needed in the previous time step to achieve the desired accuracy, and  $n_{\text{opt}}$  is the predefined desired number of iterations. If, despite this precaution, either the interface or fluid mesh solvers, the phase II solver or the combined fluid + interface solver fail to converge and no solution for  $t_{n+1}$  can be obtained, the time step size is halved and the algorithm is restarted at  $t_n$ .

### 10.4 Alternative Solution Strategies

In order to clarify the relation of the partitioned Newton-Raphson procedure described in Section 10.2 to alternative strategies, a brief overview of solution algorithms for coupled nonlinear systems of equations is provided. A rough classification of solution strategies is displayed in Figure 10.5. In Section 10.4.2 it is pointed out, that the partitioned Newton-Raphson procedure may be regarded as a specific type of the “exact block Newton methods”, which are highlighted in Figure 10.5.

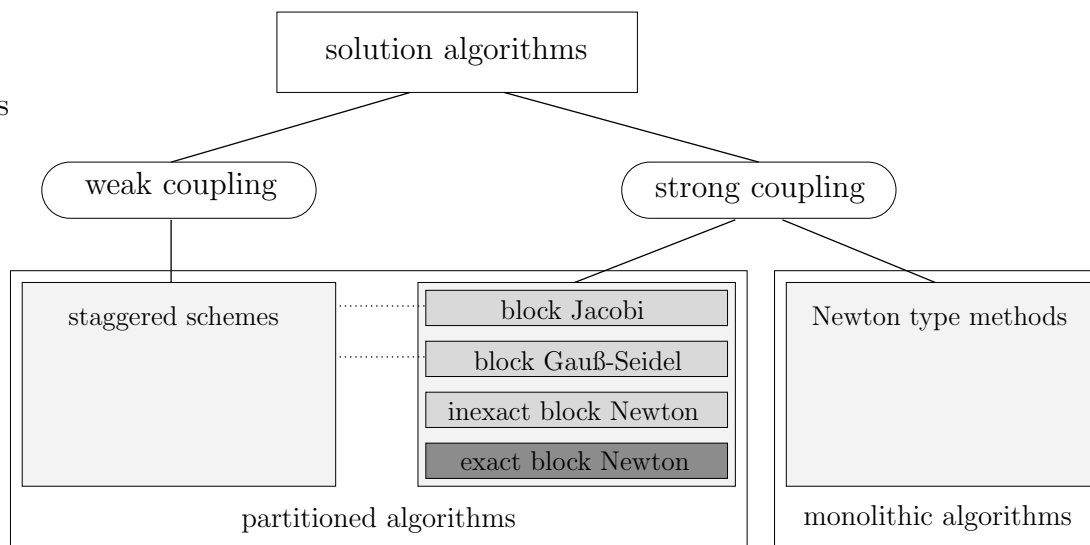


Figure 10.5: Classification of solution algorithms; the strategy described in Section 10.2 belongs to the “exact block Newton” methods.

The following criteria may help to evaluate the aptitude of particular solution strategies:

- *accuracy and stability.* Numerical instabilities may arise from the inaccurate resolution of the coupling.
- *robustness.* A solution algorithm may be called robust, if it converges for any time step sizes, which are reasonable with regard to the physical time scales and the temporal discretisation technique of the problem under consideration.
- *computational time and computer memory requirements.* Clearly, the desired accuracy should be achieved with as little computational time and requirements on the computer hardware as possible.
- *suitability for parallelisation.* With respect to large scale computations, the option to implement the solution strategy on a parallel computer platform may be regarded as a substantial advantage.
- *complexity of computer implementation.* This also relates to the question whether the solution strategy allows the combination of existing implementations of single phase solvers or requires the development of a new (large!) computer program, which incorporates all the phase solvers.

The numerical examples presented in the Chapters 11 – 14 show, that the strategy adopted in this work and described in Section 10.2 features excellent accuracy, stability and robustness and the computational costs seem reasonable. The implementation is, however, very complex.

It should be noted, that the comparison of different solution algorithms is extremely difficult since the information provided in literature on the computational details of the strategies is sparse and numerical examples tend to be poorly documented. In cases where results are reproducible it may not be possible to evaluate the difference in the computational costs.

The first choice to be made when trying to solve a coupled system of equations like, for instance, (10.1) is whether to resolve the coupling exactly (up to machine precision) or not. For some problems, sufficiently accurate results may be obtained by the approximate solution of (10.1) at each time instant. In such cases, one usually allows small errors in the residual of those equations, which account for the interaction of the different phases, *e. g.* (10.1)<sub>4</sub>. Thus, one distinguishes *strongly* and *weakly coupled* solution strategies.

#### 10.4.1 Weak Coupling – Staggered Solution Schemes

Typically, weakly coupled solution algorithms coincide with the so-called *staggered* schemes. They are based on the separate application of the phase I and phase II solvers and on the repeated communication of data between them. Thus, for each time step, a prescribed sequence of solution steps is performed, resulting in an approximation of the solution at time instant  $t_{n+1}$ . The quality of the results depends on the problem under consideration, the time step size and the sophistication of the staggered scheme. Staggered schemes involve combinations of predictor steps, substitution, interfield iteration, full step or midpoint corrections, subcycling, *etc.* More details are given in Felippa *et al* [45]. Staggered schemes belong to the class of *partitioned* strategies. They originate from the attempt to model interaction problems with two or more existing computer programs designed for the simulation of one of the interacting phases.

The disadvantages of such methodologies clearly lie in the inaccuracy and the resulting restriction to usually very small time steps. The resolution of the interaction is indeed similar to explicit time stepping and, thus, the simulations often suffer from numerical instabilities. On the other hand, staggered schemes are readily implemented and allow the relatively straightforward employment of existing computer codes. Most importantly, the smaller requirements on the computer hardware make them applicable to large scale

problems, the solution of which may not yet be possible with strongly coupled strategies.

Staggered solution schemes are employed by *e. g.* Löhner *et al* [79], Wall [127], Farhat and Lesoinne [43], Piperno and Farhat [89], Steindorf [115].

## 10.4.2 Strong Coupling

In order to solve the coupled systems of equations exactly, one may employ a *monolithic* or a *partitioned* strategy. Monolithic methodologies are based on the simultaneous solution of the complete set of variables, whereas partitioned schemes decompose the system of equations into subsystems which are then solved separately. Partitioned strongly coupled schemes require the appropriate iterative application of the subsystem solvers, such that the exact solution is obtained. A brief overview of some methods is given in the following paragraphs.

### Monolithic Algorithms

Usually, a Newton-Raphson type technique is employed in monolithic algorithms. Thus, a system matrix is assembled which includes all subsolvers. The resulting matrices are very large and tend to be ill conditioned due to the different characteristic lengths and time scales of the interacting phases. The employment of preconditioners is usually indispensable.

It is possible to obtain the exact monolithic system matrix by computing all partial derivatives analytically. However, to the knowledge of the author, this strategy has not been pursued yet. Notably, the computation of the derivatives required is also part of the strategy presented in Section 10.2. The implementation is tedious, but not associated with significant computational cost. Alternatively, *quasi Newton methods* may be employed to solve the monolithic system.

A substantial simplification of the problem, which is employed by Hübner *et al* [60, 62], consists in the decoupling of the fluid mesh solver from the Navier-Stokes solver. This is achieved by repositioning the nodes of the fluid mesh *after* each call of the combined monolithic fluid + solid solver. In this solver the motion of the fluid domain is treated as known. The increment of the interface deformation is then computed from the structural displacements and the fluid mesh nodes are repositioned. In our opinion, this simplification may adversely affect the convergence, especially for problems with large interface deformations, and may thus impose an undesirable restriction on the size of the time step.

## Partitioned Algorithms

An investigation of strongly coupled partitioned solution schemes has been provided by Matthies and Steindorf [81,82,115]. In [82], three general strategies are discussed, which allow to resolve the strong coupling by combining existing computer implementations of the subsolvers. For a brief introduction of the different methodologies, consider the interaction of two phases with the unknowns  $\mathbf{x}$  and  $\mathbf{y}$  and assume the availability of the single phase solvers

$$\mathbf{x}^{(i+1)} = \mathbf{F}(\mathbf{x}^{(i)}, \mathbf{y}) , \quad \mathbf{y}^{(i+1)} = \mathbf{G}(\mathbf{x}, \mathbf{y}^{(i)}) , \quad (10.11)$$

which converge for reasonable values of  $\mathbf{x}$  and  $\mathbf{y}$ . In the framework of fluid-solid interaction  $\mathbf{x}$  may represent the nodal fluid velocities and pressures, including those which determine the traction force on the solid, whereas  $\mathbf{y}$  may denote the displacements of the solid structure, which also define the current configuration of the interface. Hence, the motion of the fluid mesh depends only on  $\mathbf{y}$  and thus, the fluid mesh solver is easily included in (10.11)<sub>1</sub>.

*Block Jacobi method.* The conceptually simplest iteration strategy is

$$\mathbf{x}^{(i+1)} = \mathbf{F}^{[n]}(\mathbf{x}^{(i)}, \mathbf{y}^{(i)}) , \quad \mathbf{y}^{(i+1)} = \mathbf{G}^{[m]}(\mathbf{x}^{(i)}, \mathbf{y}^{(i)}) , \quad (10.12)$$

where the convergence may be improved by repeating the subsolvers  $n$  or  $m$  times with fixed  $\mathbf{y}^{(i)}$  or  $\mathbf{x}^{(i)}$ , respectively.

*Block Gauß-Seidel method.* Further improvement is achieved by modifying (10.12) to

$$\mathbf{x}^{(i+1)} = \mathbf{F}^{[n]}(\mathbf{x}^{(i)}, \mathbf{y}^{(i)}) , \quad \mathbf{y}^{(i+1)} = \mathbf{G}^{[m]}(\mathbf{x}^{(i+1)}, \mathbf{y}^{(i)}) . \quad (10.13)$$

Note, that the convergence now depends on the order of the subsolvers.

*Inexact block Newton method.* A monolithic Newton-Raphson procedure may be written as

$$\begin{bmatrix} D_{\mathbf{x}}\mathbf{F} - \mathbf{I} & D_{\mathbf{y}}\mathbf{F} \\ D_{\mathbf{x}}\mathbf{G} & D_{\mathbf{y}}\mathbf{G} - \mathbf{I} \end{bmatrix}_{\mathbf{x}^{(i)}, \mathbf{y}^{(i)}} \begin{Bmatrix} \mathbf{x}^{(i+1)} - \mathbf{x}^{(i)} \\ \mathbf{y}^{(i+1)} - \mathbf{y}^{(i)} \end{Bmatrix} = \begin{Bmatrix} \mathbf{x} - \mathbf{F} \\ \mathbf{y} - \mathbf{G} \end{Bmatrix}_{\mathbf{x}^{(i)}, \mathbf{y}^{(i)}} , \quad (10.14)$$

where  $D_{\mathbf{x}}$  and  $D_{\mathbf{y}}$  denote derivatives with respect to  $\mathbf{x}$  and  $\mathbf{y}$ , respectively. The difficulty with the system (10.14) is its size and the unavailability of the off-diagonal terms  $D_{\mathbf{y}}\mathbf{F}$  and  $D_{\mathbf{x}}\mathbf{G}$ . However, by splitting (10.14) into two separate equations and subsequent extensive use of

$$D_{\mathbf{y}}\mathbf{F}(\mathbf{x}, \mathbf{y}) \mathbf{z} = \frac{1}{\varepsilon} \left( \mathbf{F}(\mathbf{x}, \mathbf{y} + \varepsilon\mathbf{z}) - \mathbf{F}(\mathbf{x}, \mathbf{y}) \right) , \quad (10.15)$$

which, for small  $\varepsilon$ , allows the approximation of directional derivatives, the authors of [82] succeed in the development of an algorithm, consisting of several steps, which involves only standard calls of the subsolvers **F** and **G**. If **F** and **G** feature asymptotically quadratic convergence, then, in fact, this property is transferred to the overall algorithm.

It is shown by Matthies and Steindorf [82,115], that the inexact Block Newton method requires less calls of the fluid and solid solvers than Gauß-Seidel type strategies. The strategy developed in this work may be termed an *exact block Newton method*, since it also represents the decomposition of a monolithic Newton-Raphson step into several subsolvers. Some comments on the efficiency of the “exact” and “inexact” methodologies are given in Section 14.1.

Extensive use of strongly coupled partitioned solution schemes has also been made by Tezduyar, Stein, Kalro and other co-workers [76,118,120,125]. They successfully employ enhanced Gauß-Seidel type methods for the simulation of large scale three dimensional problems. They have also introduced a “mixed analytical/numerical element-vector-based” computation technique to recover expressions similar to the off-diagonal terms in (10.14). Le Tallec and Mouro [117] employ a block Gauß-Seidel technique, the convergence of which is accelerated by means of relaxation.

Finally, one should note that the block Jacobi and block Gauß-Seidel methods can be regarded as improved staggered schemes, which resolve the strong coupling by means of repeated interfield iterations. This relation of the solution strategies is illustrated in Figure 10.5 by the dotted lines.

# Chapter 11

## Examples I: Free Surface Flow

In this chapter, three examples of free surface flow are presented: the breaking dam problem, small and large amplitude sloshing. The phenomena of surface tension is not taken into account in this chapter. Thus, the pressure is set to zero along the free surface boundary of the fluid mesh. Particular attention is paid to the accuracy of the conservation of the fluid volume by the solution strategy developed in the previous chapters. Generally, the convergence of the residuals is observed to be asymptotically quadratic.

### 11.1 Breaking Dam

A rectangular column of fluid in hydrostatic equilibrium is confined between two vertical walls. The width and the height of the fluid column are  $b = 3.5$  and  $h = 7$  unit lengths, respectively. The viscosity, the density and the gravity acceleration are set to  $\mu = 0.01$ ,  $\rho = 1$  and  $g = -1$ , respectively. At  $t = 0$  one of the walls is removed instantaneously, and the liquid falls under the influence of gravity. This is one of the few problems which can also be simulated in a Lagrangian manner without requiring extensive remeshing (see *e. g.* Ramaswamy and Kawahara [95], Feng and Perić [46]).

The simulation is performed with 930 finite elements and 45 element edges on the free surface. The three corner nodes marked in Figure 11.1 (a) are treated as Lagrangian nodes. The other nodes on the free surface are subjected to the equal spacing condition. The pseudo-elastic technique (type B) with  $\mu_{\text{mesh}} = 1$  and  $K_{\text{mesh}} = 1$  is used to determine the position of the internal nodes. The time integration parameter is set to  $\rho_{\infty}^h = 0.85$ , and the time step size is chosen as  $\Delta t = 0.04$ .

Figure 11.1 (b) shows the progress of the tip of the fluid body in time. The diagram agrees closely with the experimental results taken from Ra-

maswamy and Kawahara [95]. Some configurations of the mesh at different time instants are displayed in Figure 11.2. The relative volume error at  $t = 2.4$  is obtained as  $(V_n - V_0)/V_0 \approx 0.17\%$ , where  $V_0$  and  $V_n$  correspond to the fluid volume at time instants  $t = 0$  and  $t = 2.4$ , respectively.

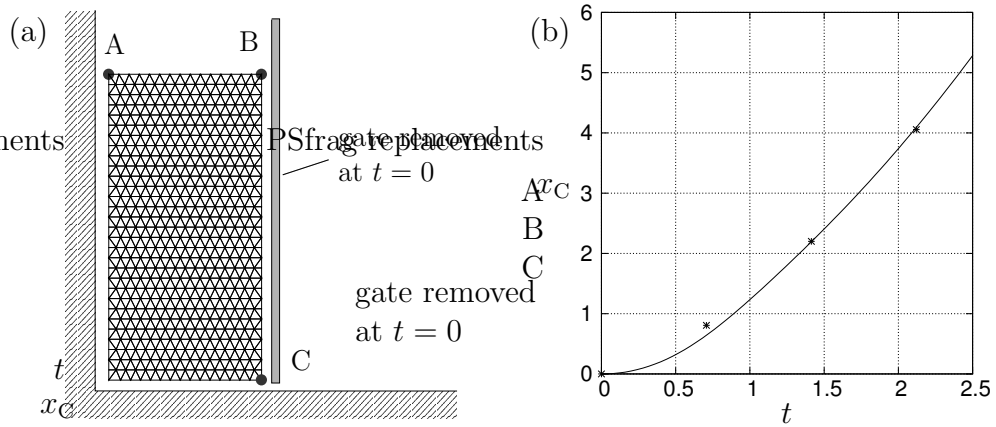


Figure 11.1: Breaking dam problem, initial mesh (a), evolution of the leading edge coordinate  $x_C$  in time, experiment (points) and simulation (line) (b).

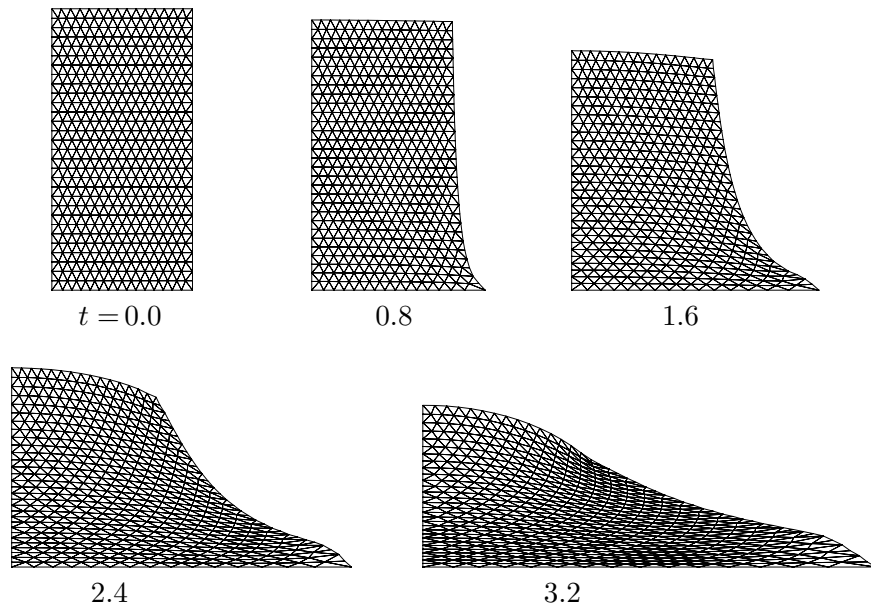


Figure 11.2: Breaking dam problem, mesh configurations at different time instants.

## 11.2 Small Amplitude Sloshing

This example considers two dimensional small amplitude sloshing of a fluid in a rectangular tank. The width  $b$ , the height  $h$  of the fluid in equilibrium, the viscosity  $\mu$ , the fluid density  $\rho$  and the gravity acceleration  $g$  are taken from Ramaswamy [93] and Braess and Wriggers [12] as  $b = h = 1$ ,  $\mu = 0.01$ ,  $\rho = 1$  and  $g = -1$ , respectively. Initially, the fluid is at rest, but the free surface is perturbed with  $\Delta h = A \cos(x \pi/b)$ , where  $A$  is chosen as 0.01. The fluid is then left free to oscillate.

The finite element model employed consists of 528 elements and 16 element edges on the free surface. The slip boundary condition is specified on the solid boundary of the tank. The motion of the mesh may be determined by any of the techniques discussed in Chapter 6. The time integration parameter and the time step are chosen as  $\rho_\infty^h = 0.85$  and  $\Delta t = 0.1$ , respectively.

Figure 11.3 (b) shows the evolution of the free surface level for  $x = 0$  and  $x = b$ . The diagram coincides with the results given in the aforementioned references [12,93]. The relative volume error at  $t = 25$  is obtained as  $(V_n - V_0)/V_0 \approx 2 \cdot 10^{-6}$ .

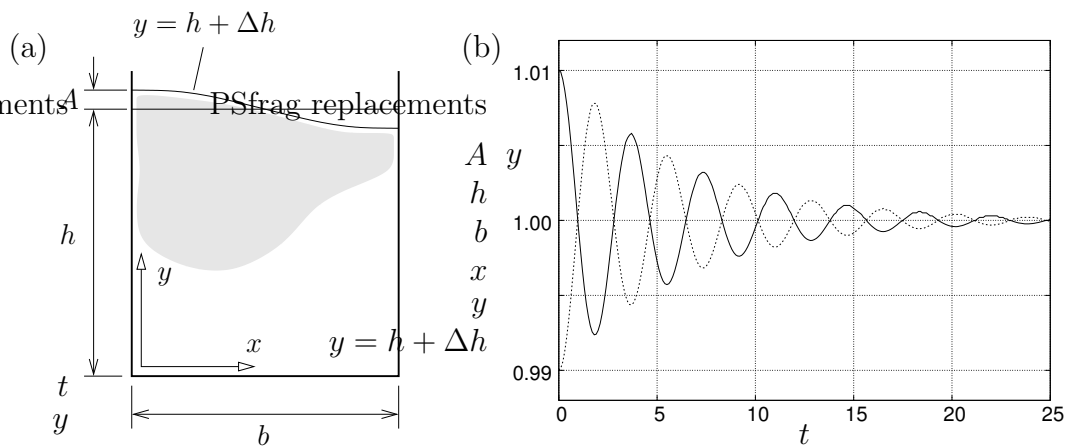


Figure 11.3: Small amplitude sloshing, geometry and initial surface displacement (a), amplitudes at both sides of the container (b).

### 11.3 Large Amplitude Sloshing

Again, the rectangular container from Section 11.2 is considered. It is subjected to a periodic displacement in  $x$ -direction. This is achieved by treating the horizontal motion of the finite element nodes at the vertical boundaries of the container in a Lagrangian manner. The  $x$ -velocity of these nodes is prescribed as  $u = A\omega \sin(\omega t)$ . Thus, the horizontal position of the container oscillates with the amplitude  $A$  and the frequency  $f = \omega/(2\pi)$  (see Figure 11.4). Initially, the fluid is at rest and in equilibrium.

The material parameters and the finite element discretisation are chosen identical to Section 11.2. The motion of the mesh is based on the pseudo-elastic methodology (type A) with  $\mu_{\text{mesh}} = 1$  and  $K_{\text{mesh}} = 15$ . Simulations are performed for  $A = 0.075$  and  $\omega = 1.0, 1.1, \dots, 2.2$ . Different time step sizes are used:  $\Delta t = T/50, T/100, T/200$  with  $T = 1/f$ .

Figure 11.5 (a) – (c) show the configuration of the mesh, velocity vectors and pressure isolines at different time instants for  $\omega = 1.5$ . The diagram in Figure 11.6 displays the amplitudes of the bubble and the spike for the different excitation frequencies  $\omega$ . A lock-in phenomena is clearly captured at  $\omega \approx 1.5$ . It can be observed that the deviation of the solutions obtained from the different time step sizes is small. The diagram also displays the results obtained from a denser mesh with 902 finite elements and  $\Delta t = T/200$ . They agree very closely with the solution on the coarser mesh. Figure 11.7 shows the oscillation of the fluid surface level at the container boundary for  $\omega = 1.5$ . Some relative volume errors at time instant  $t = 10T$  are displayed in Table 11.1.

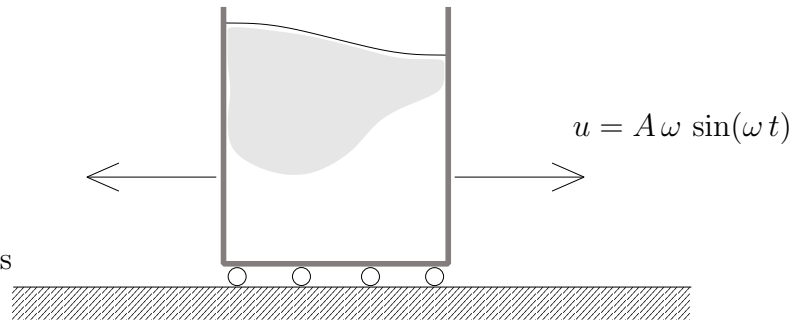


Figure 11.4: Large amplitude sloshing, problem definition.

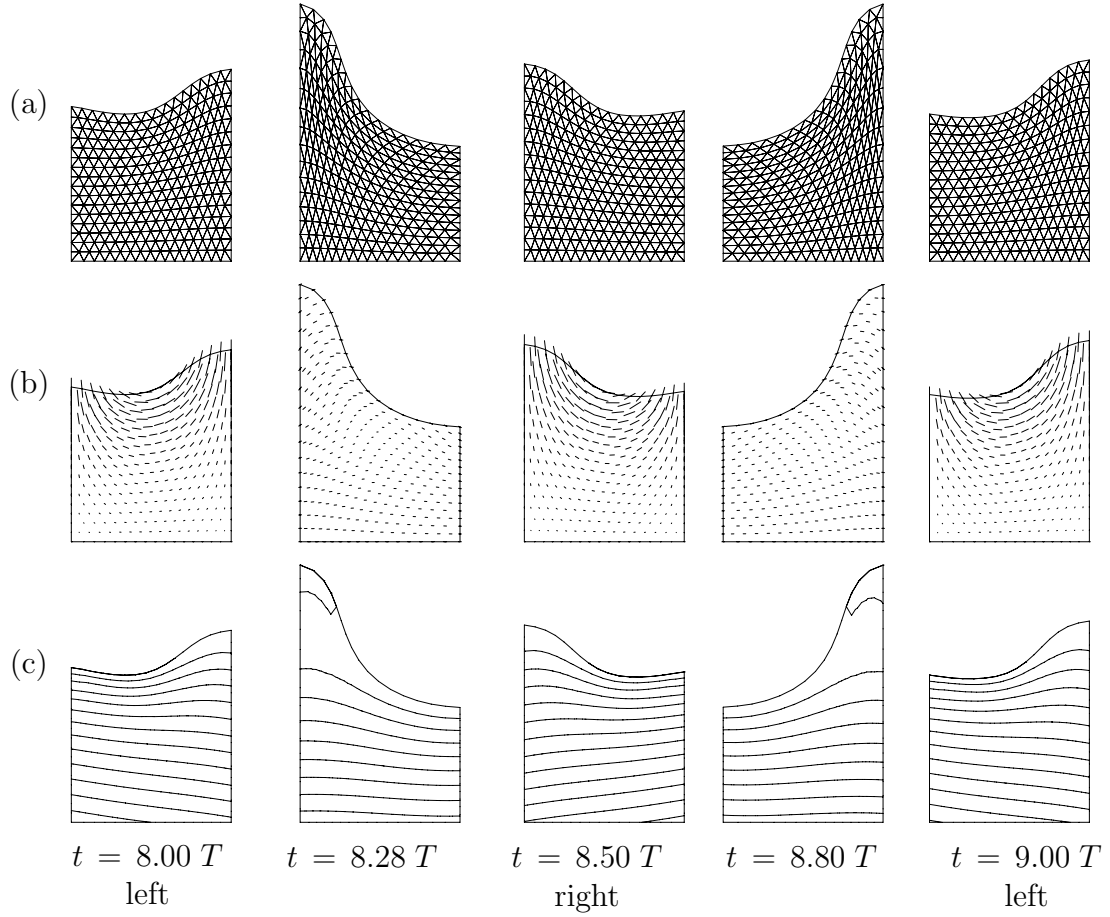


Figure 11.5: Large amplitude sloshing, mesh (a), velocity vectors (b) and pressure isolines (c) at different time instants;  $\omega = 1.5$ ,  $\Delta t = T/50$ ; time instants and position of container are given.

$\omega$	$\Delta t = T/50$	$\Delta t = T/100$	$\Delta t = T/200$
1.2	0.18	0.07	0.02
1.5	1.82	1.10	0.72

Table 11.1: Large amplitude sloshing, relative volume error  $(V_n - V_0)/V_0$  [%] at time instant  $t = 10 T$ ; 528 elements.

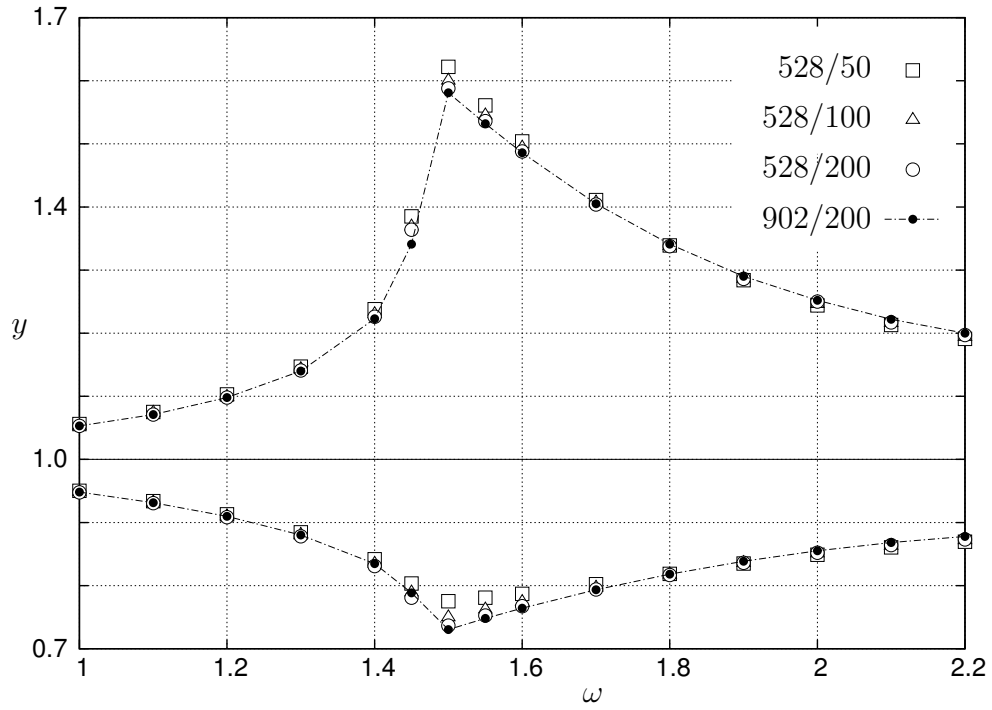


Figure 11.6: Large amplitude sloshing, amplitudes of spike and bubble for different  $\omega$ ; 528 (902) elements;  $\Delta t = T/50, T/100, T/200$ .

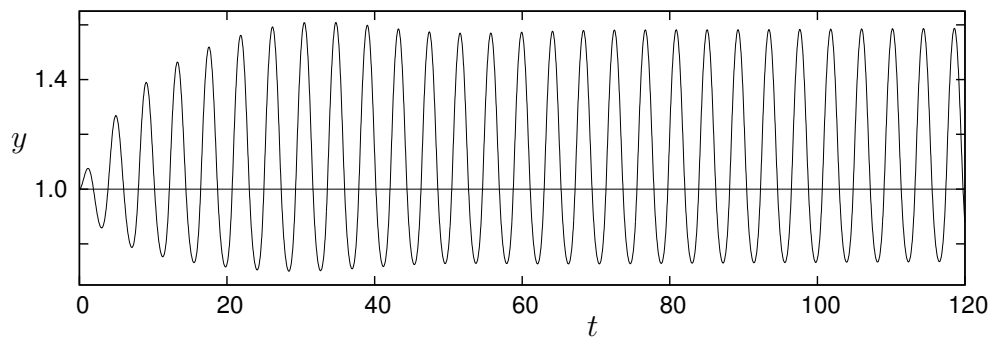


Figure 11.7: Large amplitude sloshing, evolution of amplitude for  $\omega = 1.5$ ; 528 elements;  $\Delta t = T/200$ .

# Chapter 12

## Examples II: Free Surface Flow with Surface Tension

In this chapter, the numerical solutions of a selection of free surface flow problems are presented, which are governed by the phenomena of surface tension. In some cases, analytical solutions or experimental data are available and are used to validate the numerical results. In order to assess the efficiency and robustness of the methodology, particular attention is paid to the convergence of the results as the spatial or temporal discretisation is refined, the conservation of the fluid volume and the robustness of the computational model with respect to large deformation of the fluid domain.

The simulations are performed in a two dimensional or axisymmetric setting. It is recalled from Section 2.1.3 that no pressure boundary conditions need to be set, since the surface tension formulations derived in Sections 7.3 and 7.4 imply  $p_{\text{ext}} = 0$ . Unless otherwise stated, all examples use the following parameters:

$$\begin{aligned} \text{time integration} & : \quad \rho_{\infty}^h = 0.85 \\ \text{gravity} & : \quad g = 9.80 \text{ m s}^{-2} \\ \text{water} & : \quad \mu_w = 0.0101 \text{ g (cm s)}^{-1} \\ & \quad \rho_w = 0.998 \text{ g cm}^{-3} \\ & \quad \gamma_{\text{st,w}} = 73.0 \text{ g s}^{-2} \end{aligned} \tag{12.1}$$

### 12.1 Capillary Rise

In order to verify the surface tension formulation employed in this work, we consider a vertical tube with the lower end immersed in a circular water tank. The inner radius of the tube is  $R = 0.1$  cm. Hence, there is one free surface inside and another free surface outside the tube (see Figure 12.1). Since the

purpose of the simulation is the prediction of the capillary rise in the tube, the surface tension effects are neglected for the free surface outside the tube. The external air pressure is assumed to be zero. Different contact angles at the water-air-tube interface are considered.

A mesh with 778 axisymmetric finite elements is employed in the numerical simulation. The free surface in the pipe consists of 17 element edges. The major part of the mesh is fixed ( $\rightarrow$  Eulerian formulation) and in the two ALE parts the mesh update is performed on the basis of the pseudo-elastic methodology (type A) with  $\mu_{\text{mesh}} = 1$  and  $K_{\text{mesh}} = 1$  (see Figure 12.1). Since the focus is exclusively on obtaining the equilibrium configuration, dynamic effects may be damped out and therefore, the viscosity of the fluid is set to  $\mu = 100 \mu_w$ . The surfaces of the pipe and the container are modelled as slip boundaries.

After the fluid is released, it quickly takes the equilibrium configurations displayed in Figure 12.2. The difference of the fluid surface levels inside and outside the tube can be compared to  $\Delta h = 2 \gamma_{\text{st}} \cos \alpha / (R \rho g)$ . This expression is readily derived from the Laplace-Young equation (7.5) on the basis of the simplifying assumption that the shape of the free surface inside the tube is spherical. Table 12.1 shows that the agreement with the results of the finite element model is excellent.

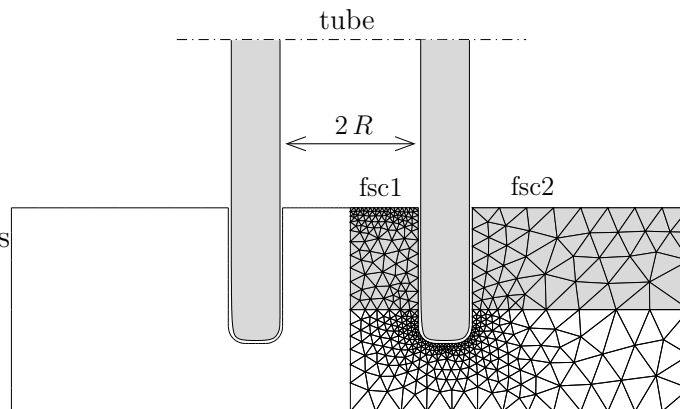


Figure 12.1: Capillary rise, problem set-up; 778 elements; free surface fsc1 with and free surface fsc2 without surface tension; ALE only in the grey parts of the mesh.

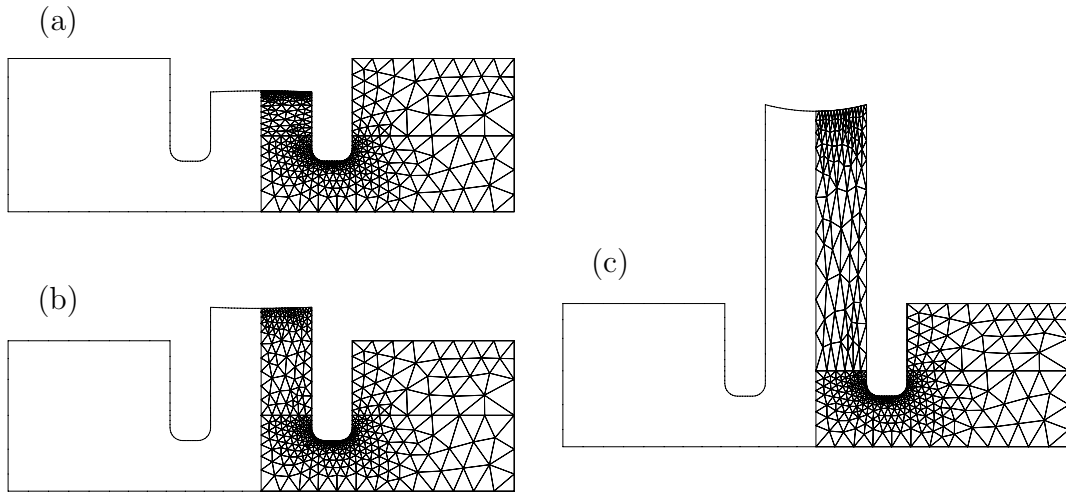


Figure 12.2: Capillary rise, equilibrium configurations for contact angles  $\alpha = 92.5^\circ$  (a),  $87.5^\circ$  (b) and  $75.0^\circ$  (c).

$\alpha$ [ $^\circ$ ]	$\frac{1}{2} (\Delta h(R) + \Delta h(0))$ [cm]	$\Delta h = \frac{2\gamma_{st} \cos \alpha}{R\rho g}$ [cm]
92.5	$\frac{1}{2} (-0.0662 - 0.0640) = -0.0651$	-0.0651
87.5	$\frac{1}{2} (0.0662 + 0.0640) = 0.0651$	0.0651
75.0	$\frac{1}{2} (0.3929 + 0.3798) = 0.3864$	0.3864

Table 12.1: Capillary rise, difference of water levels.

## 12.2 Large Sessile Drop

The exact static equilibrium configuration of a drop sitting on a rigid surface can be obtained as the solution of a nonlinear scalar differential equation by employing a simple numerical scheme (see Pozrikidis [90]). In the following, this solution is used to verify the finite element results. Thus, the objective is the computation of the equilibrium configuration of a large drop of water (volume  $V = 0.3203 \text{ cm}^3$ ), which sits on a rigid surface and is subjected to gravity, for different contact angles  $\alpha = 30^\circ, 60^\circ, 90^\circ, 120^\circ$ .

A half sphere is chosen as the initial configuration of the finite element mesh. It consists of 96 axisymmetric elements and the surface tension boundary is represented by 12 edges. Since dynamic effects are not being investigated, the viscosity  $\mu = 1000 \mu_w$  is employed to damp out oscillations quickly<sup>1</sup>. The mesh update is based on the pseudo-elastic methodology (type A) with  $\mu_{\text{mesh}} = 1$  and  $K_{\text{mesh}} = 1$ . The water is allowed to slip freely on the rigid surface.

Released and subjected to the surface tension forces and gravity, the drop assumes its equilibrium configuration, which is displayed in Figure 12.3. The diagrams are overlaid with the pseudo-analytical solution mentioned above, which, however, is so well matched by the finite element mesh, that the difference is not noticeable.

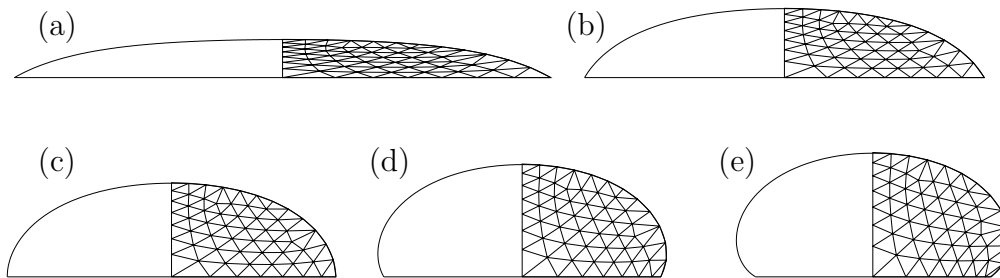


Figure 12.3: Large sessile drop, equilibrium configurations for contact angles  $\alpha = 30^\circ$  (a),  $60^\circ$  (b),  $90^\circ$  (c),  $120^\circ$  (d),  $150^\circ$  (e).

---

<sup>1</sup>A detailed study of the dynamics of sessile drops requires a more sophisticated mathematical model accounting for the so-called *contact angle hysteresis*, which denotes the common phenomena of different contact angles for advancing or receding contact lines (see e. g. Dussan [39]). An everyday example for this phenomena is found in the appearance of a raindrop moving down a windowpane.

## 12.3 Small Amplitude Oscillations of a Spherical Drop

A small spherical drop of water with radius  $R = 0.0125$  cm is considered. The axisymmetric  $n$ th eigenform of the spherical drop and the associated frequency and damping factor may be expressed as

$$r_n(\theta) = R + A P_n(\cos \theta) \quad (12.2)$$

$$\omega_n^2 = n(n-1)(n+2) \frac{\gamma_{st}}{\rho R^3} \quad (12.3)$$

$$\xi_n = (n-1)(2n+1) \frac{\mu}{\rho R^2}, \quad (12.4)$$

where  $P_n$  denotes the Legendre polynomial of order  $n$  and  $A$  is a scaling parameter (see Lamb [77], Foote [48]).

The drop of water is discretised with 384 axisymmetric finite elements, whereby the free surface boundary is modelled with 36 element edges, see Figure 12.4. For  $n = 2, 3, 4$ , the finite element model of the drop is subjected to an initial deformation defined by  $r_n$  with the amplitude  $A = 0.025 R$ , which is still in the range of small deformations. The drop is then left free to oscillate. The time integration parameter is set to  $\rho_\infty^h = 1.0$ , such that the time integration scheme coincides with the trapezoidal rule. The time step size is chosen as approximately  $\Delta t \approx T_n/30$ , where  $T_n = 2\pi/\omega_n$  is known from the analytical solution.

In the diagrams in Figure 12.5 (a) – (c), the  $z$ -coordinate of the top centre of the drop is displayed against time for  $n = 2, 3, 4$ . The agreement with the exact damping curve is excellent. The exact and numerical time periods  $T_n$  are also given in Figure 12.5 (a) – (c), and the deviations are clearly insignificant.

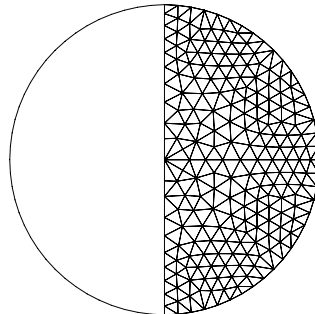


Figure 12.4: Small amplitude oscillation of a spherical drop, finite element mesh with 384 elements.

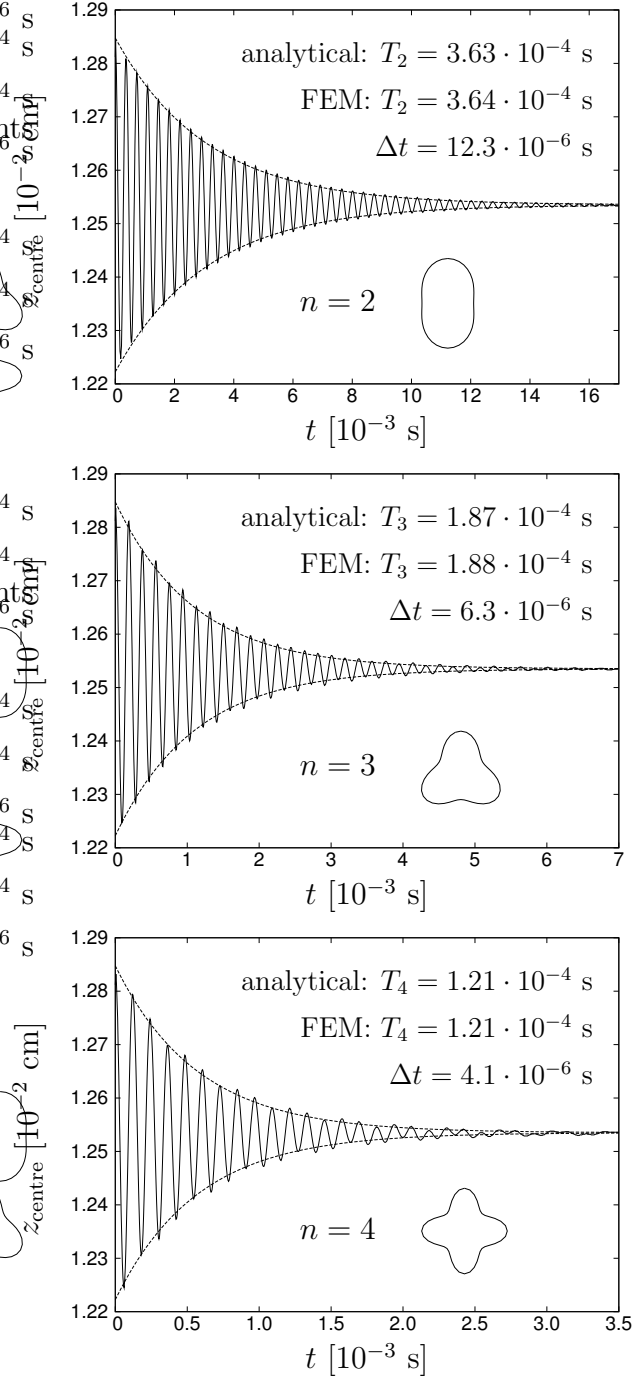


Figure 12.5: Small amplitude oscillation of a spherical drop, evolution of the  $z$ -coordinate of the top centre of the drop for  $n = 2, 3, 4$ ; the dotted line represents the exact damping  $\beta_n(t) = z_{\text{centre}}(t \rightarrow \infty) \pm 0.025 R \exp(-\xi_n t)$ .

## 12.4 Large Amplitude Oscillations of a Liquid Cylinder

A water cylinder is subjected to three different initial configurations defined by  $r_n(\theta) = R(1 + 0.5 \cos(n\theta))$  with  $R = 0.2$  cm,  $n = 2, 3, 4$ , and then released to oscillate. The cross section of the liquid cylinder is modelled with 612 two dimensional finite elements and 48 element edges on the free surface. The motion of the mesh is chosen to be governed by the strategy type C. The time integration parameter is set to  $\rho_\infty = 1.0$  ( $\rightarrow$  trapezoidal rule). The time step size is kept constant within each simulation,  $\Delta t = 0.001$  s, 0.0005 s, 0.00035 s for  $n = 2, 3, 4$ , respectively.

Figure 12.7 shows the configuration of the cross section at different time instants. Despite the severe deformations, the mesh quality is good.

For  $n = 4$ , which is the most complex of the situations considered, a study with different time step sizes is performed. The diagrams in Figure 12.6 display the evolution of the  $y$ -coordinate of point A and of the relative volume error  $\epsilon(t_n) = (V_n - V_0)/V_0$ . The integration in time is observed to be accurate since both quantities do not vary significantly as the time step size

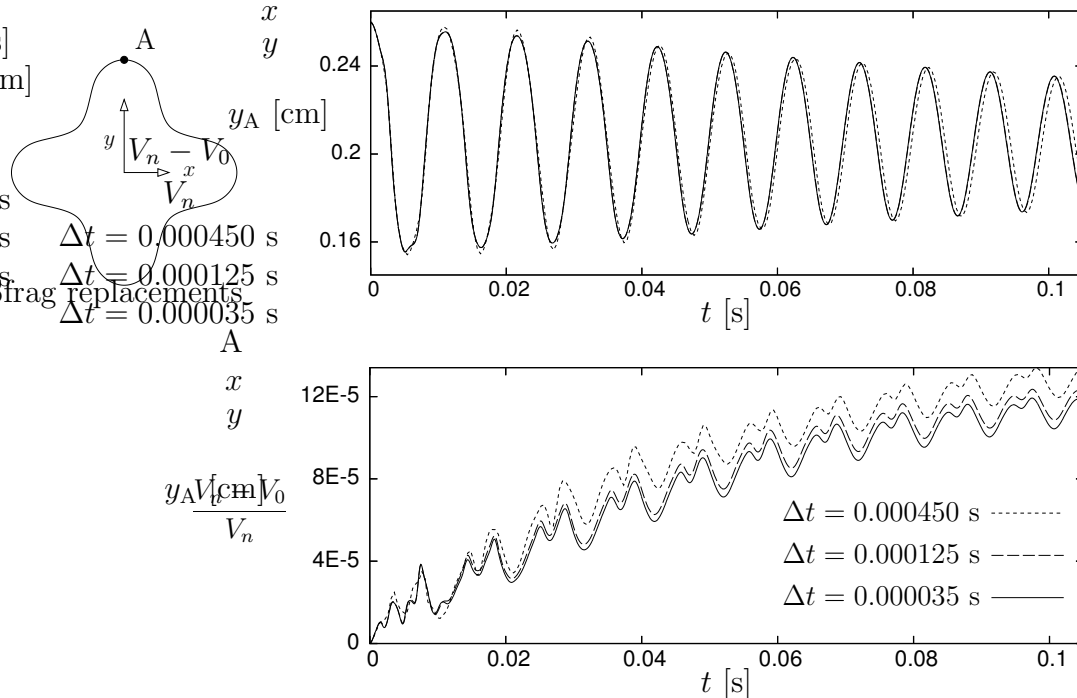


Figure 12.6: Large amplitude oscillation of a liquid cylinder,  $n = 4$ ; evolution of  $y_A$  and the relative volume error.

is changed. The volume is also conserved accurately with  $\epsilon < 0.014\%$  at all times of the simulation. The convergence of the partitioned Newton-Raphson procedure is asymptotically quadratic.

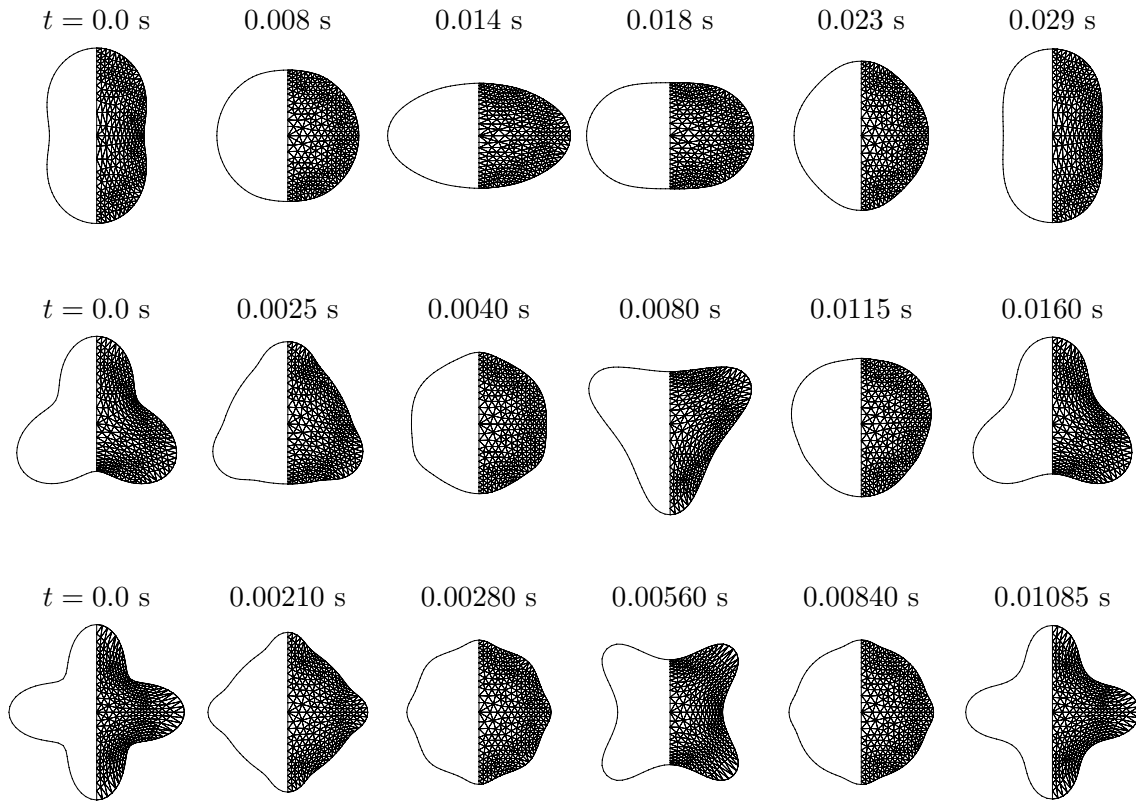


Figure 12.7: Large amplitude oscillation of a liquid cylinder,  $n = 2, 3, 4$ ; configuration of the cross section at different time instants.

## 12.5 Filling of a Drop

In this example the filling of a drop from a thin tube is considered. The inner radius of the tube is  $d = 0.26$  cm and the fluid under consideration is water. The distribution of the filling velocity over the orifice is constant. The velocity in  $r$ -direction in the orifice is prescribed as zero. Simulations have been performed for three different filling velocities  $u_{\text{fill}} = 0.33546$  cm s<sup>-1</sup>,  $u_{\text{fill}} = 10.0$  cm s<sup>-1</sup> and  $u_{\text{fill}} = 20.0$  cm s<sup>-1</sup>. A coarse mesh with 516 axisymmetric finite elements and 32 element edges on the free surface and a dense mesh with 1000 elements and 48 edges on the free surface are employed. In order to allow severe deformation of the domain the mesh is treated as a pseudo-elastic continuum (type B) with  $\mu_{\text{mesh}} = 1$  and  $K_{\text{mesh}} = 0$ . According to (10.10), adaptive time stepping with either  $n_{\text{opt}} = 4$  or  $n_{\text{opt}} = 3$  is employed to overcome the difficulties arising from the varying rate of deformation of the drop. The filling of the drop starts at  $t = 0$ . The initial configuration of the drop is identical to the static equilibrium shape of the pendent drop with the volume  $V_0 = 0.019894$  cm<sup>3</sup>. The initial velocity distribution is uniform with  $\mathbf{u}^h = \{0, u_{\text{fill}}\} \forall \hat{\mathbf{x}}^h \in \Omega$  at  $t = 0$ .

These rather non-physical initial conditions and also the uniform distribution of the filling velocity over the orifice of the tube are chosen in order to make the results comparable to the solution obtained with a one dimensional model of the problem. This simplified mathematical model can be derived from the axisymmetric incompressible Navier-Stokes equations and the Laplace-Young equation by means of Taylor series expansions (see *e. g.* Eggers and Dupont [40]). A finite element formulation of the one dimensional model is used to verify the results obtained with the computational strategy presented in this work.

The configurations of the drop at different time instants are displayed in the Figures 12.8 – 12.10. Figure 12.12 shows the evolution of the necking ratio  $r_{\text{min}}/d$  and the  $z$ -coordinate of the tip of the drop in time. In Figure 12.11 the time step sizes are displayed for  $u_{\text{fill}} = 0.33546$  cm s<sup>-1</sup>.

The following observations are made on the basis of the numerical results:

- As the drop is being filled the tip of the water jet develops into a sphere and the diameter of the fluid body at the onset of the sphere reduces to extremely small values. The ALE strategy seems to allow the modelling of the process until shortly before the break-up of the drop. It is observed that faster filling velocities lead to the formation of longer and wider water jets before the break-up.
- The diagrams in Figure 12.12 show that the agreement of the solutions obtained from the different discretisations of space and time is excel-

lent. Remarkably, the solutions agree accurately even when the finite element mesh has become very distorted. The agreement with the one dimensional model is also good, which can be regarded as a successful validation of the numerical algorithm.

- In Figure 12.11 it is observed that the time increments become very small towards the end of the simulation shortly before the break-up of the drop, when the rate of deformation is very large and the mesh is extremely distorted. Note however that, for  $n_{\text{opt}} = 4$ , the final configurations of the drop as displayed in Figures 12.8 – 12.10 are essentially reached after only 100 to 150 time steps, depending on the filling velocity. The choice of  $n_{\text{opt}} = 3$  clearly results in a larger number of time steps than  $n_{\text{opt}} = 4$ .
- At the end of each simulation the volume of the drop deviates from the exact value by 0.7 – 1.2 %. This is, however, not primarily due to the severe deformation of the domain. A careful analysis of the simulation results reveals that the loss of fluid mass occurs principally in the element at the edge of the orifice, as a consequence of the unrealistic uniform distribution of the filling velocity across the orifice.

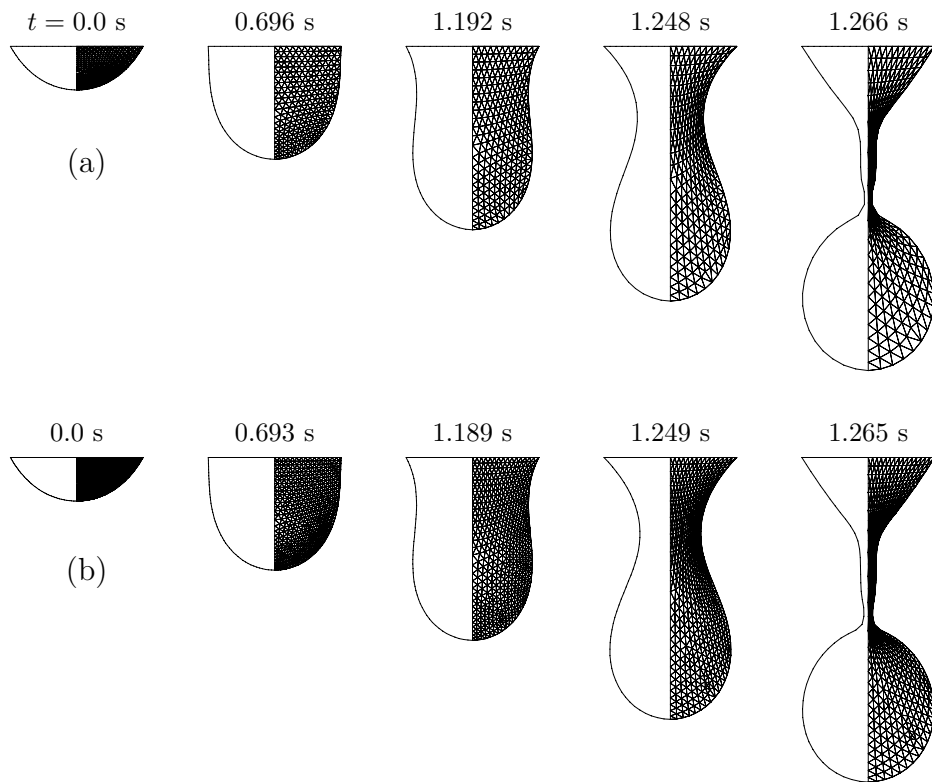


Figure 12.8: Filling of a drop, configurations at different time instants, coarse (a) and dense (b) mesh,  $u_{\text{fill}} = 0.33546 \text{ cm s}^{-1}$ .

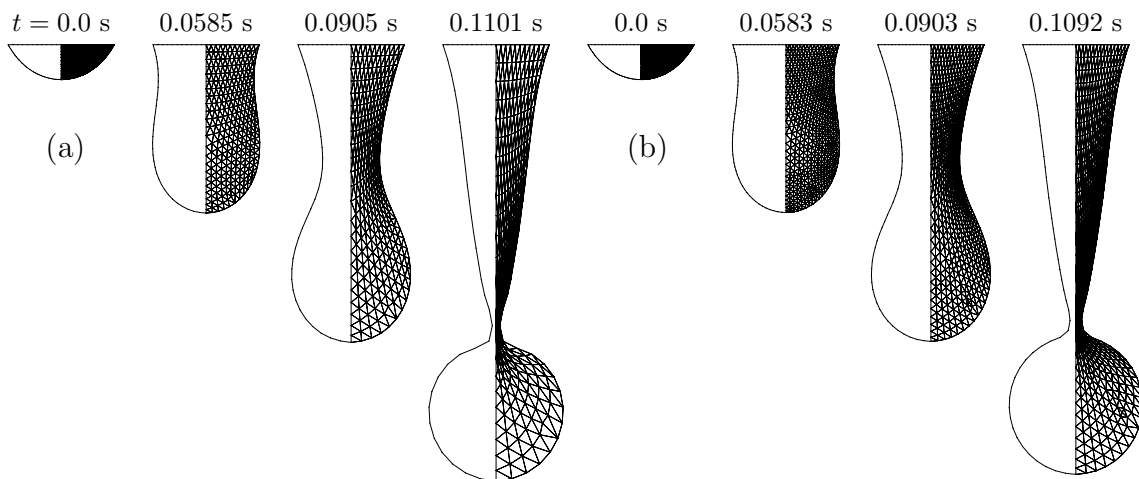


Figure 12.9: Filling of a drop, configurations at different time instants, coarse (a) and dense (b) mesh,  $u_{\text{fill}} = 10.0 \text{ cm s}^{-1}$ .

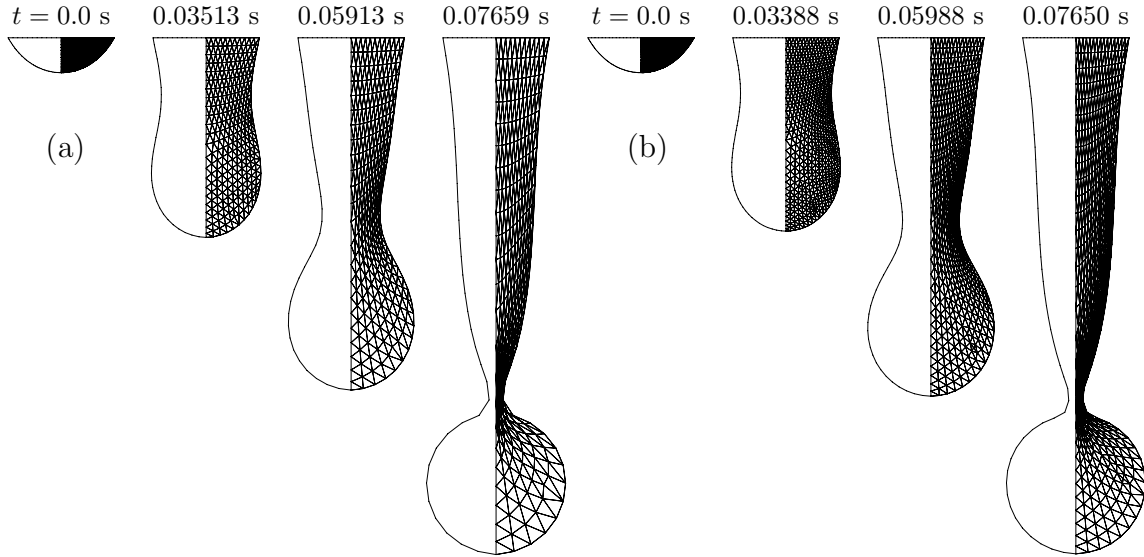


Figure 12.10: Filling of a drop, configurations at different time instants, coarse (a) and dense (b) mesh,  $u_{\text{fill}} = 20.0 \text{ cm s}^{-1}$ .

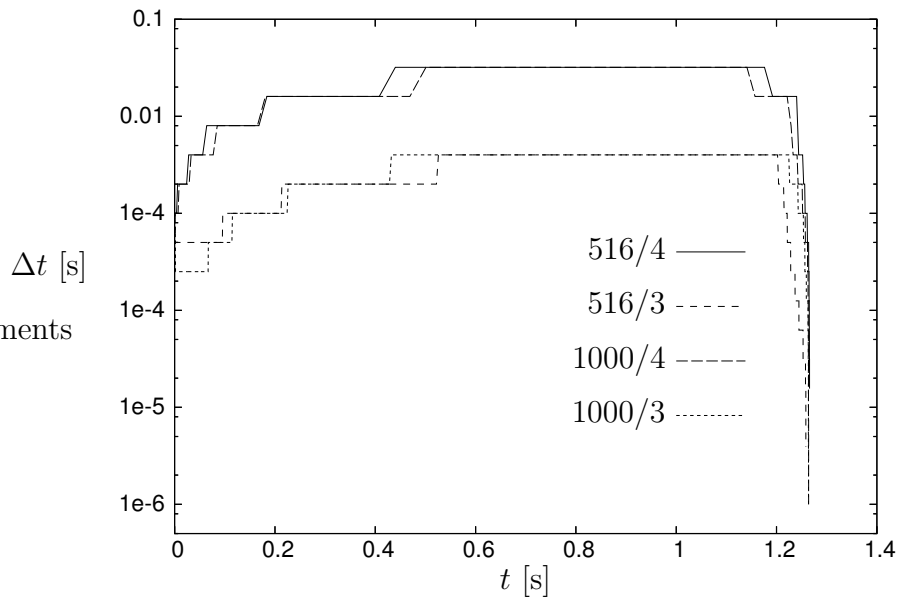


Figure 12.11: Filling of a drop, evolution of the time step size for adaptive time stepping,  $u_{\text{fill}} = 0.33546 \text{ m s}^{-1}$ ; 516 or 1000 finite elements,  $n_{\text{opt}} = 4$  or  $n_{\text{opt}} = 3$ .

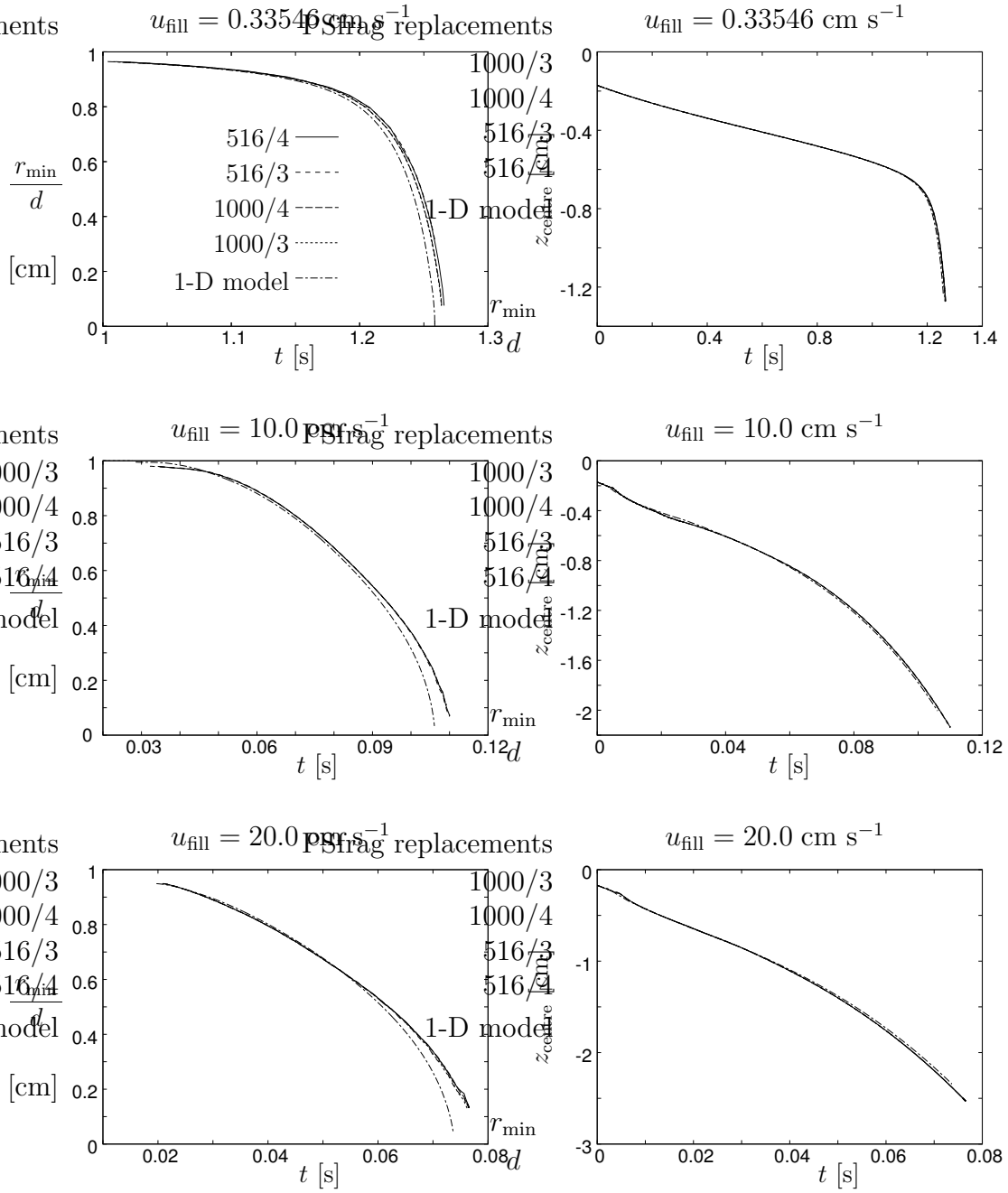


Figure 12.12: Filling of a drop, evolution of the necking ratio and the  $z$ -coordinate of the tip of the drop in time; 516 or 1000 elements,  $n_{\text{opt}} = 4$  or  $n_{\text{opt}} = 3$ , the results for the one dimensional model are also shown.

## 12.6 Stretching of a Liquid Bridge

In this example a liquid bridge is stretched between two rigid circular plates. The upper plate moves upwards with the constant velocity  $u_{\text{stretch}}$ . The geometry of the problem is given in Figure 12.13. The fluid under consideration is water. The radius of the plates, the initial height of the liquid bridge and the fluid volume are given as  $R = 0.16$  cm,  $h_0 = 0.32$  cm and  $V = 0.04$  cm<sup>3</sup>, respectively. The surfaces of the plates are no-slip boundaries. Initially, the fluid is at rest and in equilibrium. The stretching velocities considered are  $u_{\text{stretch}} = 0.6$  cm s<sup>-1</sup>, 10.0 cm s<sup>-1</sup>, 20.0 cm s<sup>-1</sup> and 25.0 cm s<sup>-1</sup>. Experimental data is available for  $u_{\text{stretch}} = 0.6$  cm s<sup>-1</sup> (see Zhang *et al* [131]).

The simulations are performed with three different meshes of 208 (510) {1350} axisymmetric finite elements and 16 (30) {50} element edges on the free surface, respectively. The initial equilibrium configurations for the meshes have been obtained by performing calculations similar to those described in Sections 12.1 and 12.2. The mesh update is based on the pseudo-elastic continuum (type B) with  $\mu_{\text{mesh}} = 1$  and  $K_{\text{mesh}} = 0$ . Adaptive time stepping is employed with either  $n_{\text{opt}} = 4$  or  $n_{\text{opt}} = 5$ .

The Figures 12.14 – 12.16 are associated with  $u_{\text{stretch}} = 0.6$  cm s<sup>-1</sup>. Figure 12.14 shows the configuration of the liquid bridge at different time instants for different meshes, and the diagrams in Figures 12.15 and 12.16 display the evolution of the necking ratio  $r_{\text{min}}/R$  and the relative volume error against time. Figure 12.17 shows the final configurations of the liquid bridge obtained

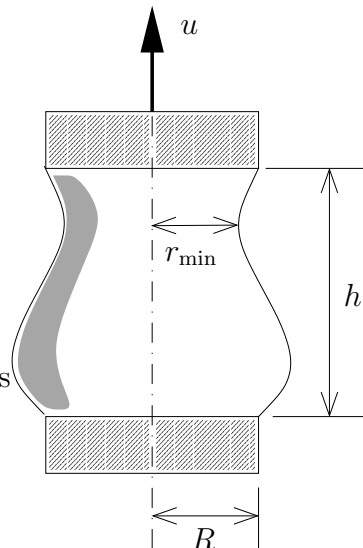


Figure 12.13: Stretching of a liquid bridge, geometry of the problem.

for  $u_{\text{stretch}} > 0.6 \text{ cm s}^{-1}$  with the mesh of 510 elements. Table 12.2 provides the number of time steps and the volume error at the end of the various computations performed here.

The following observations are made on the basis of the numerical results:

- When stretched, the liquid bridge develops two fluid domains which remain attached to the upper and lower rigid plates. In between, the radius of the liquid bridge decreases rapidly to very small values. At a certain stage, the simulation has to be aborted, since it can not account for the break-up of the the drop. Interestingly, it can be observed in Figure 12.17 that, for small stretching velocities, the point of separation develops near the lower bulk of fluid, whereas faster stretching leads to break-up near the upper plate. The figure suggests that certain stretching velocities with  $20 \text{ cm s}^{-1} < u_{\text{stretch}} < 25 \text{ cm s}^{-1}$  result in the development of a free satellite drop.
- For the different meshes and time step sizes, the deviation of the corresponding solutions is hardly noticeable. The agreement with the experimental data in Figure 12.15 is good.
- It is shown in Figure 12.16 and Table 12.2 that, for all simulations with moderately dense finite element meshes, the relative volume error is less than 0.2 % despite the severe deformation of the fluid domain. The error clearly reduces by increasing the mesh density.
- The Tables 12.3 and 12.4 show typical convergence behaviour of the algorithm. The rate of convergence is asymptotically quadratic for the interface and fluid mesh solvers as well as for the combined fluid + interface solver. Note that the tables are associated with the situation shortly before break-up. Thus, the mesh update procedure requires several increment cuts due to the large change of deformation within one time step.

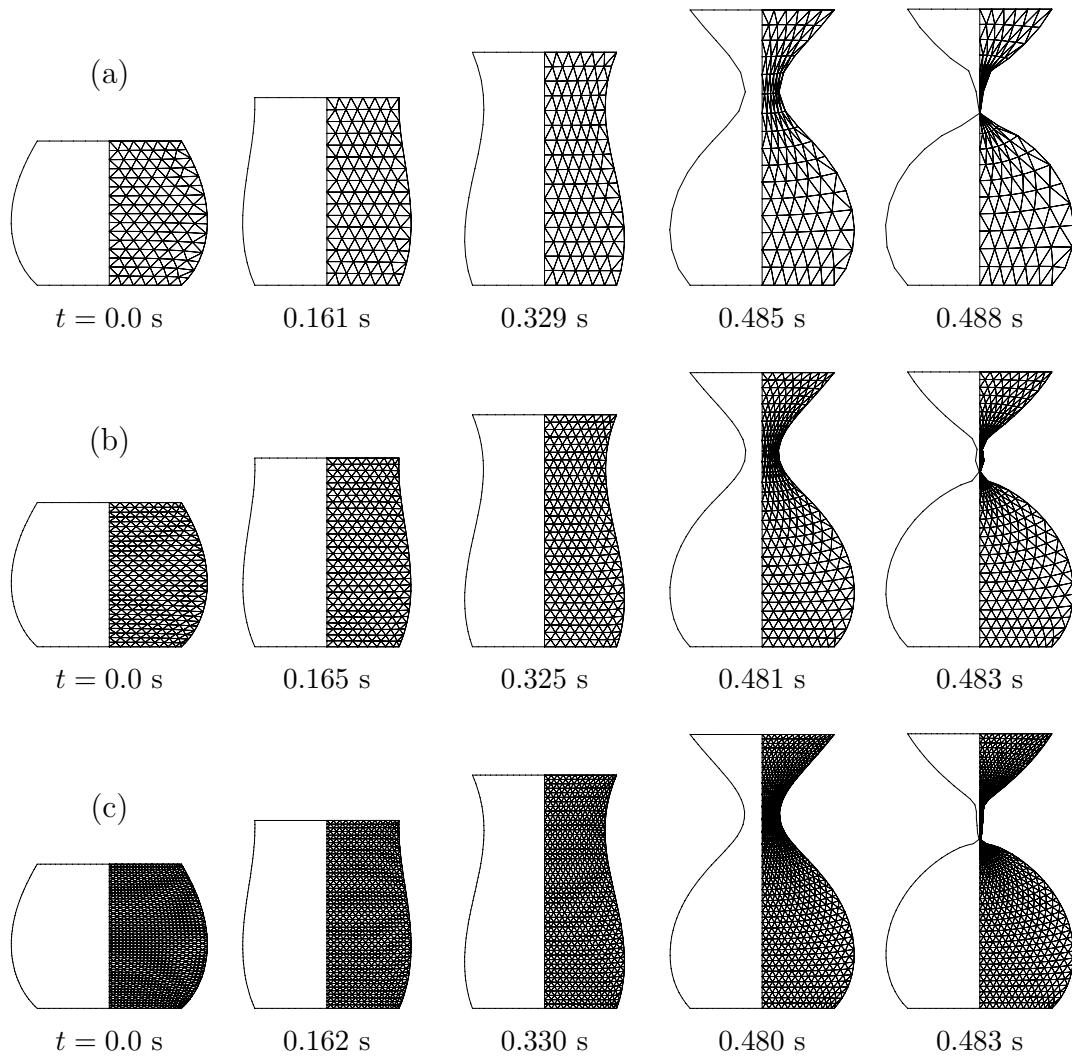


Figure 12.14: Stretching of a liquid bridge, configurations at different time instants, 208 (a), 510 (b), 1350 (c) finite elements;  $u_{\text{fill}} = 0.6 \text{ cm s}^{-1}$ ;  $n_{\text{opt}} = 4$ .

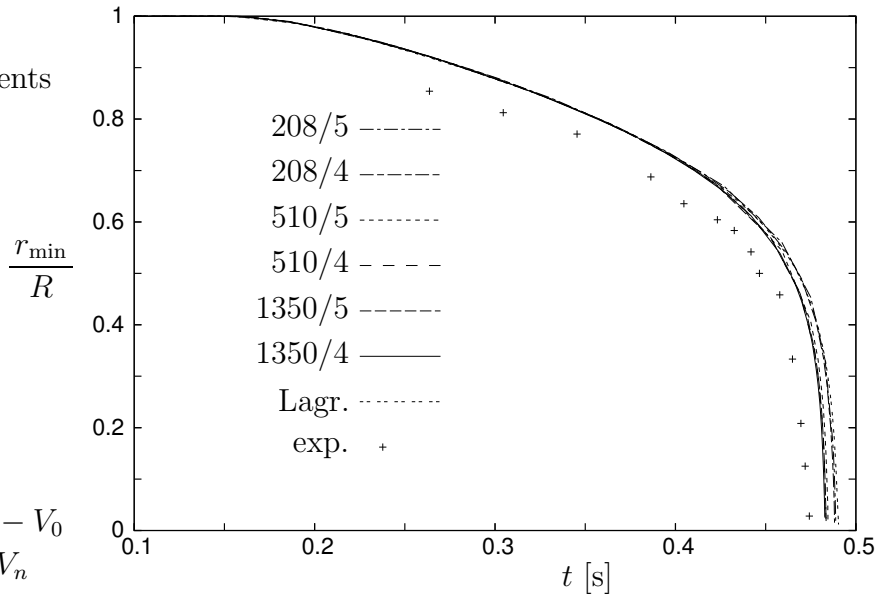


Figure 12.15: Stretching of a liquid bridge, evolution of necking ratio,  $u_{\text{stretch}} = 0.6 \text{ m s}^{-1}$ ; 208, 510, 1350 finite elements,  $n_{\text{opt}} = 5$  or  $n_{\text{opt}} = 4$ , adaptive Lagrangian finite element method (Saksono [103]), experiment.

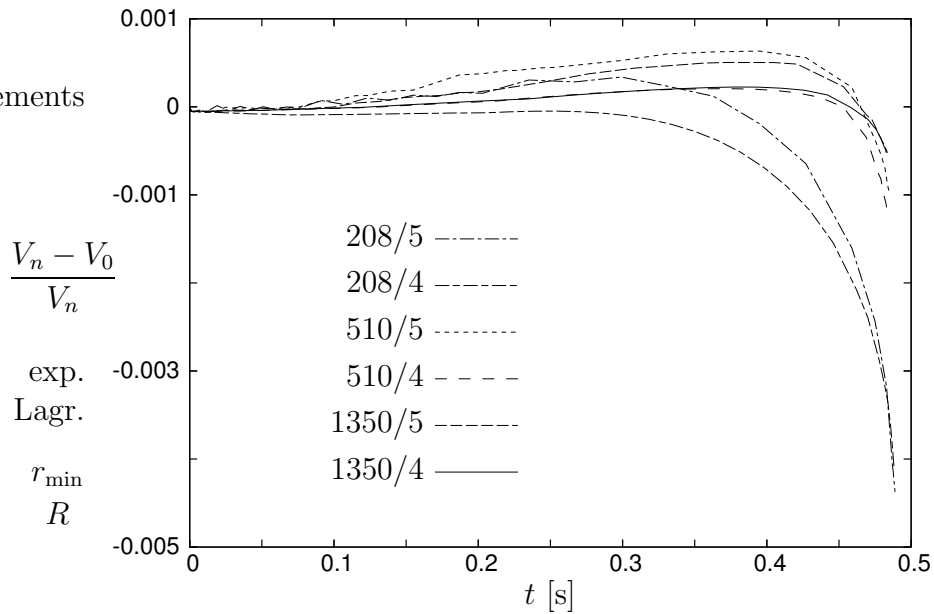


Figure 12.16: Stretching of a liquid bridge, evolution of relative volume error,  $u_{\text{stretch}} = 0.6 \text{ m s}^{-1}$ ; 208, 510, 1350 finite elements,  $n_{\text{opt}} = 5$  or  $n_{\text{opt}} = 4$ .

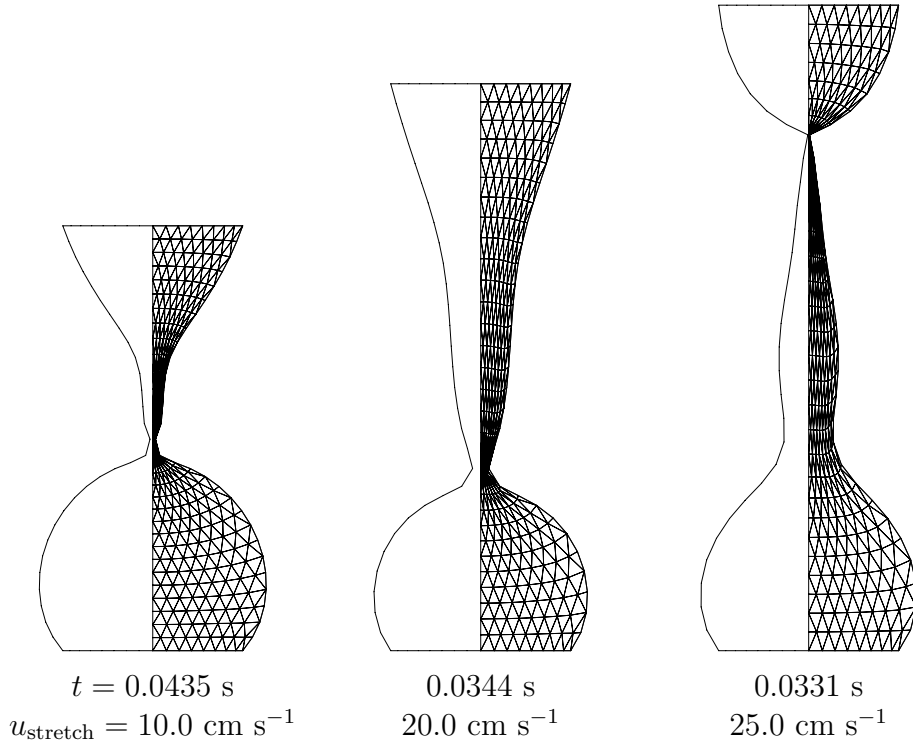


Figure 12.17: Stretching of a liquid bridge, configurations shortly before break-up, different stretching velocities; 510 elements;  $n_{\text{opt}} = 4$ .

elements	$n_{\text{opt}}$	$u_{\text{stretch}} [\text{cm s}^{-1}]$	$n$	$t_n [\text{s}]$	$\frac{V_n - V_0}{V_n} [\%]$
208	5	0.6	58	0.489	-0.44
208	4	0.6	93	0.488	-0.41
510	5	0.6	69	0.485	-0.09
510	4	0.6	110	0.483	-0.12
1350	5	0.6	98	0.483	-0.05
1350	4	0.6	120	0.483	-0.05
510	5	10.0	66	0.0430	-0.02
510	4	10.0	559	0.0435	-0.09
510	5	20.0	84	0.0347	+0.03
510	4	20.0	990	0.0344	-0.05
510	5	25.0	117	0.0333	+0.07
510	4	25.0	1299	0.0331	-0.06

Table 12.2: Stretching of a liquid bridge, shortly before break-up, number  $n$  of required time steps, volume conservation.

A	B	C	D							
2.			1.2E-1	2.1E-4	2.3E-7	6.1E-15				
3.		1.00	no conv.							
		0.50	no conv.							
		0.25	8.2E-2	3.2E-2	6.7E-3	3.1E-4	6.2E-7	2.5E-12		
		0.75	no conv.							
		0.50	1.0E-1	4.4E-2	1.3E-2	1.2E-3	9.6E-6	6.5E-10		
		1.00	no conv.							
		0.75	1.5E-1	6.8E-2	2.6E-2	5.0E-3	1.9E-4	2.7E-7	5.4E-13	
		1.00	2.9E-1	1.4E-1	6.8E-2	2.6E-2	5.0E-3	2.0E-4	3.3E-7	9.1E-13
5.	8.4E-1									
2.			7.4E-1	5.1E-3	3.1E-6	9.5E-13				
3.		1.00	no conv.							
		0.50	1.3E-1	5.8E-2	2.0E-2	3.2E-3	8.7E-5	6.5E-8	3.6E-14	
		1.00	2.1E-1	9.8E-2	4.2E-2	1.2E-2	1.3E-3	1.4E-5	1.8E-9	
5.	4.1E-2									
2.			6.2E-2	4.6E-5	2.4E-10	6.9E-16				
3.		1.00	8.1E-3	4.4E-4	1.7E-6	2.4E-11				
5.	4.5E-4									
2.			1.0E-3	1.2E-8	8.2E-16					
3.		1.00	1.8E-4	2.8E-7	7.1E-13					
5.	9.9E-8									
2.			2.2E-7	6.0E-16						
3.		1.00	4.4E-8	1.6E-14						
5.	4.4E-14									

column A: identifies step in Box 10.1, interface mesh solver (2.), fluid mesh solver (3.), residual of combined fluid + interface solver (5.),  
column B: combined fluid + interface residual,  
column C: increment cutting in the fluid mesh solver,  
column D: residuals of interface and fluid mesh solvers

Table 12.3: Stretching of a liquid bridge,  $u_{\text{stretch}} = 0.6 \text{ cm s}^{-1}$ , convergence of solution procedure; 208 elements, current time step  $\Delta t = 0.002 \text{ s}$ ,  $t = 0.485 \text{ s}$ .

A	B	C	D							
2.			5.8E-2	1.0E-4	8.5E-9	5.5E-16				
3.		1.00	no conv.							
		0.50	no conv.							
		0.25	7.1E-2	2.9E-2	9.0E-3	1.1E-3	1.9E-5	5.4E-9		
		0.75	no conv.							
		0.50	7.9E-2	3.4E-2	1.2E-2	2.0E-3	5.6E-5	4.8E-8	3.6E-14	
		1.00	no conv.							
		0.75	9.1E-2	4.0E-2	1.5E-2	3.3E-3	1.7E-4	4.5E-7	3.3E-12	
		1.00	1.1E-1	5.0E-2	2.0E-2	5.6E-3	5.1E-4	4.5E-6	3.6E-10	
5.	3.4E-1									
2.			1.9E-1	1.2E-3	1.4E-6	5.8E-13				
3.		1.00	no conv.							
		0.50	2.8E-1	1.4E-1	6.8E-2	.....	3.7E-3	3.1E-4	2.3E-6	1.2E-10
		1.00	no conv.							
		0.75	2.4E-2	5.8E-3	5.6E-4	6.6E-6	1.0E-9			
		1.00	2.4E-2	6.2E-3	6.5E-4	9.1E-6	2.0E-9			
5.	2.6E-2									
2.			7.3E-3	6.2E-6	9.0E-11					
3.		1.00	2.9E-3	9.6E-5	1.5E-7	4.6E-13				
5.	1.9E-3									
2.			4.3E-4	1.5E-8	1.9E-15					
3.		1.00	1.9E-4	5.8E-7	6.0E-12					
5.	3.3E-6									
2.			1.8E-7	5.0E-15						
3.		1.00	6.2E-8	4.3E-14						
5.	7.9E-12									

column A: identifies step in Box 10.1, interface mesh solver (2.), fluid mesh solver (3.), residual of combined fluid + interface solver (5.),  
column B: combined fluid + interface residual,  
column C: increment cutting in the fluid mesh solver,  
column D: residuals of interface and fluid mesh solvers

Table 12.4: Stretching of a liquid bridge,  $u_{\text{stretch}} = 0.6 \text{ cm s}^{-1}$ , convergence of solution procedure; 1350 elements, current time step  $\Delta t = 0.004 \text{ s}$ ,  $t = 0.475 \text{ s}$ .

# Chapter 13

## Examples III: Fluid - Rigid Body Interaction

In this chapter, five examples of fluid-rigid body interaction are presented. The focus is on the modelling of rigid body oscillations excited by perpendicular flow. This physical phenomena is very relevant for the appropriate design of many civil engineering structures, as pointed out in Chapter 1. The examples presented in Sections 13.1 – 13.4 show that the three types of flow excited oscillations, *i. e.* vortex induced oscillations, galloping and flutter, are captured accurately by the numerical strategy presented in this work. Section 13.5 provides an example of the damping of rigid body oscillations by the surrounding fluid.

### 13.1 Vortex Induced Oscillations of a Cylinder

This problem has been addressed both experimentally and numerically by a number of researchers, see *e. g.* Anagnostopoulos and Bearman [1], Nomura and Hughes [83,84], Blevins [9] and references therein. A circular cylinder is immersed in a uniform flow field. It is supported by a spring, such that it can perform oscillations perpendicular to the direction of the far field fluid flow. The channel or tank is large enough to be regarded as infinite. Different flow velocities are considered.

The characteristic behaviour of this system is the “lock-in” phenomena: It is observed that there is an interval of far field flow velocities  $u_\infty$ , for which the vortex shedding frequency  $f_v$  coincides with the natural frequency  $f_n$  of the cylinder-spring system. If the velocity  $u_\infty$  lies within this interval, then the cylinder performs stable oscillations, the amplitude of which has the order

of magnitude of the diameter of the cylinder. Otherwise, no oscillations occur or the relative amplitude is negligible. The significant width of the “lock-in region”, which is usually expressed in terms of the Reynolds number, is evidence for the two way coupling of the fluid and the solid systems. The fluid flow excites the oscillations of the cylinder, whereas the motion of the cylinder causes the lock-in effect by changing the vortex shedding frequency  $f_v$  to the frequency  $f_n$ . Detailed investigations of vortex induced oscillations have been provided by *e. g.* Den Hartog [56] and Blevins [9].

In the following the objective is to reproduce the results obtained experimentally by Anagnostopoulos and Bearman [1]. The geometry of the problem and the boundary conditions employed in the simulation are displayed in Figure 13.1. The spring is linear with the stiffness  $k = 5.79 \text{ N m}^{-1}$  and damping factor  $c = 0.325 \text{ g s}^{-1}$ . The mass and the diameter of the cylinder are given as  $m = 2.979 \text{ g}$  and  $D = 0.16 \text{ cm}$ , respectively. Thus, the natural frequency of the cylinder follows as  $f_n = 7.016 \text{ s}^{-1}$ . The fluid under consideration is water with  $\mu = 0.01 \text{ g (cm s)}^{-1}$  and  $\rho = 1.0 \text{ g cm}^{-3}$ . Different far field fluid velocities  $u_\infty$  are considered, such that the Reynolds number  $Re = u_\infty D \rho / \mu$  varies between 90 and 130. Every numerical experiment is started from rest.

Simulations are performed with three different meshes consisting of 1878 (3598) {5374} finite elements. The associated number of edges on the cylinder boundary is 34 (50) {100}. Figure 13.2 shows the coarse mesh. The ALE formulation is restricted to a square area of the domain as shown in Figure 13.1. For both the fluid and the rigid cylinder, the time integration parameter  $\rho_\infty^h$  is set to 0.9. The time step size is linked to the Reynolds number and varies between  $\Delta t = 0.0025$  and  $\Delta t = 0.003$ , such that each period of the lift force oscillation is modelled with 45 – 60 time increments. It is known from the numerical simulation of the flow around the fixed cylinder in Section 5.3.3, that this temporal discretisation is sufficiently fine to rule out significant deviation from the mesh dependent limit solution. The algorithm type C is employed for the update of the nodal positions in the ALE region.

The results of the simulations are displayed in the Figures 13.3 and 13.4. Figure 13.3 shows the relative amplitude  $Y/D$  of the cylinder oscillations and the vortex shedding frequency  $f_v$  displayed against the Reynolds number. The frequency  $f_v$  is evaluated from the evolution of the lift coefficient. The diagram also shows the experimental data obtained by Anagnostopoulos and Bearman [1] and the vortex shedding frequencies associated with the stationary cylinder as suggested by Roshko [101], namely  $Sr_{\text{Roshko}} = f_{v,\text{Roshko}} D / u_\infty = 0.212 (1 - 21.2 Re)$ . Figure 13.4 shows the evolution of the amplitudes of the cylinder oscillation obtained with the dense mesh for different Reynolds numbers.

The following observations are made:

- The “lock-in” phenomena is captured with each of the three meshes employed. The frequencies  $f_v$  and  $f_n$  coincide within the whole lock-in regions, which are clearly marked by the significant amplitudes of the cylinder oscillations. The resonance effect leads to forces in the mass-spring system of the cylinder, which are up to 250 times larger than the associated lift forces; for example, the simulation of the flow at  $Re = 100$  with the mesh of 3598 elements renders  $\max(F_L) = 1.506 \cdot 10^{-5}$  N and  $\max(F_{el}) = 375.2 \cdot 10^{-5}$  N. Outside the lock-in region, the oscillations are negligible or disappear and the frequency  $f_v$  recovers the values associated with the stationary cylinder. For the dense mesh, they accurately agree with the formula by Roshko [101].
- The deviation of the responses of the coarse and the medium mesh is significant, whereas the results obtained with the medium mesh agree well with those of the dense mesh. In other words, the numerical results display convergent behaviour with mesh refinement. Note that the medium mesh with 3598 elements is still rather coarse. Note also that the maximum amplitudes obtained with the different meshes are identical.
- The response of the dense mesh agrees roughly with the experimental data taken from Anagnostopoulos and Bearman [1]. The maximum amplitudes obtained numerically differ from the experimental values by 24 % and the lock-in region is narrower and shifted towards smaller Reynolds numbers.

This may, however, be due to some significant differences between the numerical and the experimental model: In the experiment, the submerged length of the cylinder and the depth of the water channel were 12 cm and 70 cm, respectively. No horizontal end plate had been fixed at the tip of the cylinder. Thus, the vortex shedding at the lower end of the cylinder was in fact three dimensional. Furthermore, the flow involved a free surface. In this context, it should also be noted that, outside the lock-in region, the flow in the experiment differs slightly from the generally accepted formula by Roshko, which, in turn, is recovered accurately by the dense mesh response.

The numerical study of the same problem by Nomura [83] is not sufficiently comprehensive to allow a comparison with this work. However, it is pointed out that the maximum amplitude of the oscillations obtained by Nomura amounts to roughly 50 % of the corresponding experimental value.

- At the low Reynolds number end of the lock-in region, the oscillations start with a sudden jump. As the Reynolds number increases, the amplitude of the oscillations smoothly decreases such that the jump at the upper end of the lock-in region is less significant. This qualitative behaviour is exhibited by the experimental solution as well as by the responses of the different finite element meshes. It is shown in Figure 13.4 that it takes more than one minute to trigger the stable oscillations near the lower end of the lock-in region.
- The numerical model and the solution algorithm have proved robust and efficient. The convergence of the residuals is observed to be asymptotically quadratic.

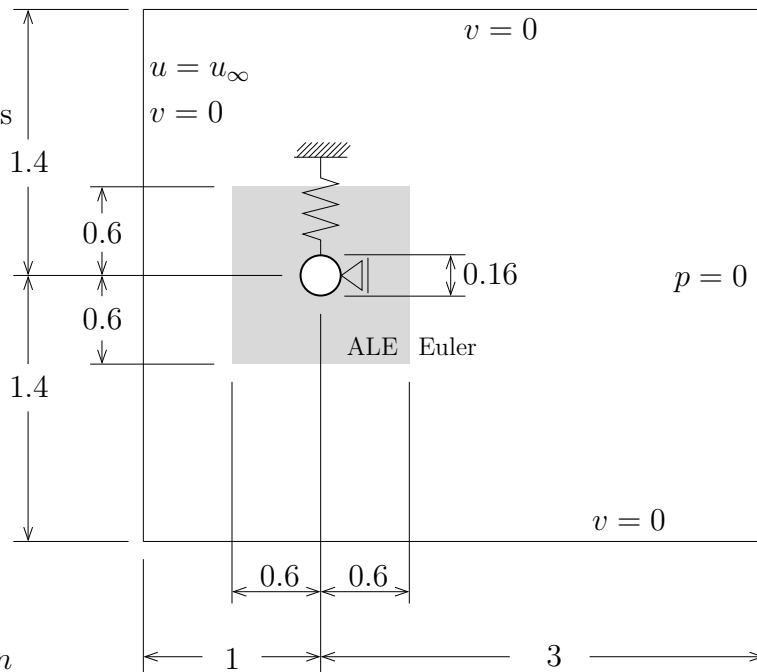


Figure 13.1: Oscillating cylinder, geometry and boundary conditions of the problem; 1 unit length corresponds to 1 cm.

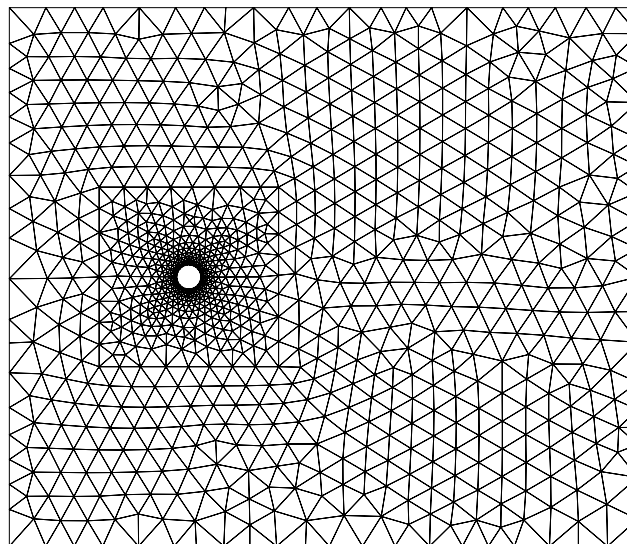


Figure 13.2: Oscillating cylinder, finite element mesh with 1878 elements.

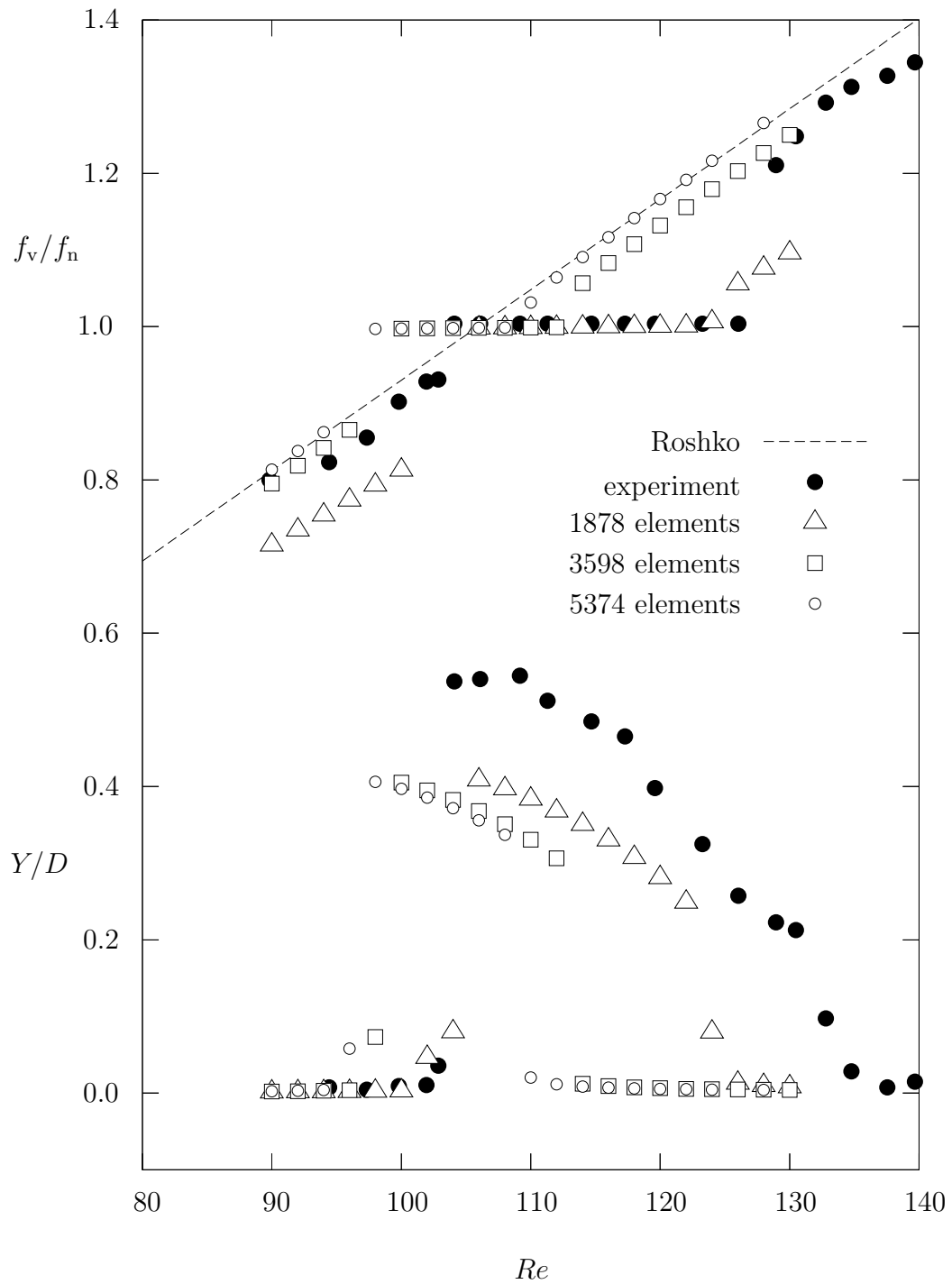


Figure 13.3: Oscillating cylinder, amplitudes and frequencies.

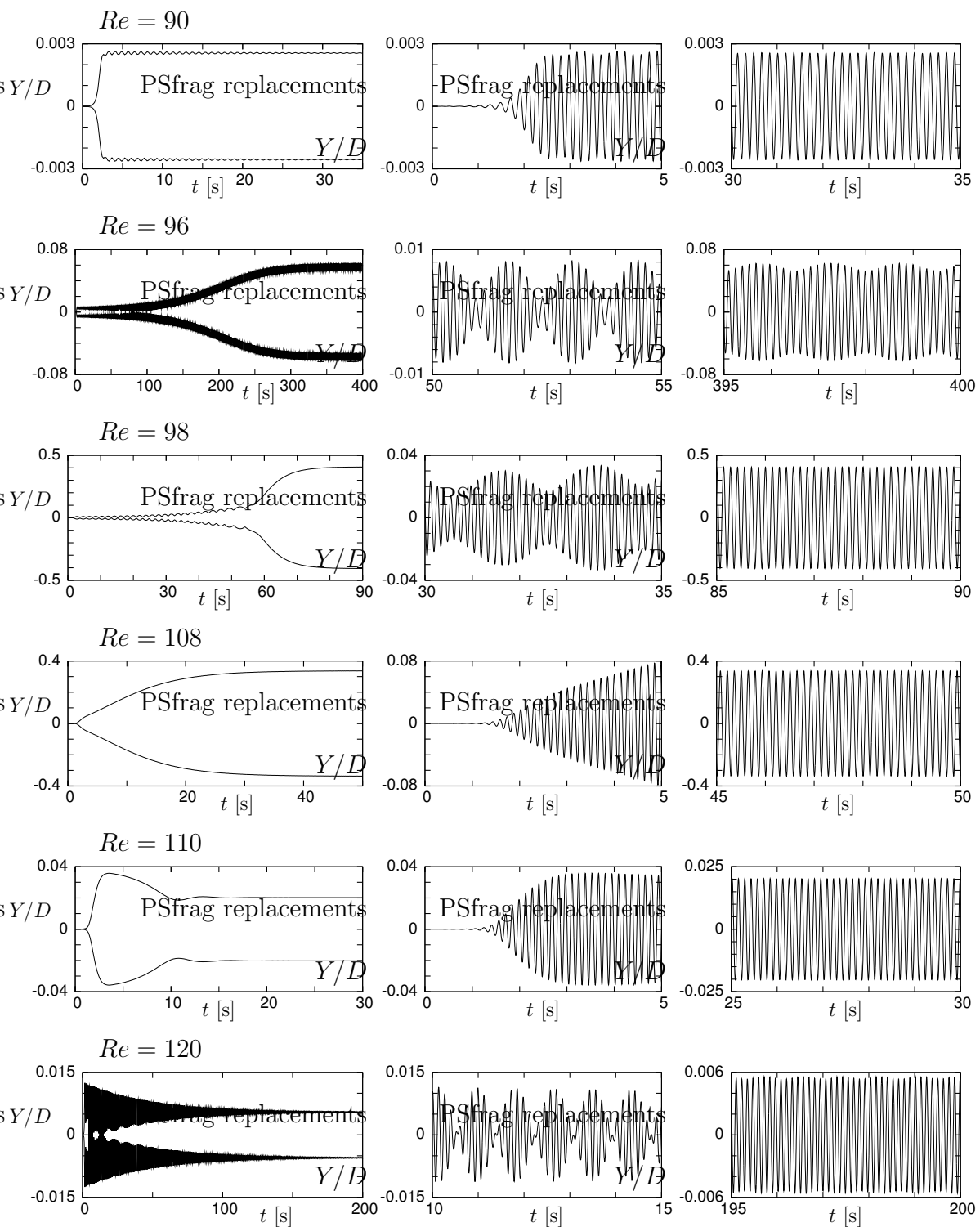


Figure 13.4: Oscillating cylinder, evolution of the amplitude  $Y/D$ ; different Reynolds numbers, mesh with 5374 elements.

## 13.2 Vortex Induced Oscillations and Galloping

In Section 13.1, the vortex induced oscillations of a circular cylinder have been investigated. The terminology of the “lock-in” region has been introduced for the interval of Reynolds numbers, where the vortex shedding frequency adjusts to the natural frequency of the cylinder and large amplitude oscillations are observed.

However, many flow induced vibrations happen at frequencies, which are much smaller than the vortex shedding frequencies of the flow. The associated flow velocities  $u_\infty$  are usually large. In the case of mechanical systems with only one degree of freedom, this phenomena is commonly denoted as *galloping*.

For a brief description of the physical background of galloping, a rigid body is considered, which is exposed to horizontal fluid flow with the velocity  $u_\infty$  and, for some reason, moves downward with velocity  $\dot{d}$ . As shown in Figure 13.5, the body is then, in fact, exposed to a relative fluid flow of velocity  $u_\alpha$  at an angle  $\alpha$ . The associated drag and lift forces  $F_D$  and  $F_L$  result in forces  $F_x$  and  $F_y$  parallel and perpendicular to the velocity  $u_\infty$ . Depending on the geometry of the body, the force  $F_y$  may have the same direction as the velocity  $\dot{d}$ , in which case the motion of the body is further accelerated. The same argument applies to an upward motion of the body. Larger velocities  $\dot{d}$  lead to greater angles  $\alpha$  and may finally change the sign of  $F_y$ , such that the rigid body motion decelerates. If the body is elastically supported, this mechanism may lead to oscillations, the amplitudes of which are usually significantly larger than the ones associated with vortex induced oscillations. The liability of a body to galloping depends on its geometry. If the geometry is such that  $F_y$  acts in the opposite direction of  $\dot{d}$ , then the body is said to be *aerodynamically stable*, otherwise it is *unstable*. An example of a stable cross section is the circular cylinder. For aerodynamically

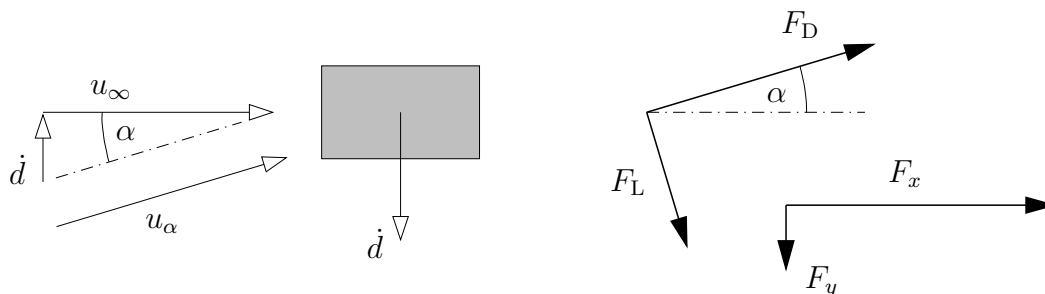


Figure 13.5: Galloping phenomena, velocities and forces.

unstable mechanical systems, the critical velocity  $u_\infty^{\text{crit}}$  can be derived from the equation of the positive structural and the negative aerodynamical damping. The mathematical analysis is, however, restricted to a linear behaviour of the fluid flow, which rarely occurs in practical problems. More information on the phenomena of galloping is provided in the publications by *e. g.* Den Hartog [56], Blevins [9] and Robertson *et al* [100].

In the following, a rigid body with a square cross section is exposed to fluid flow of different velocities  $u_\infty$ . The body is supported by an elastic spring with a small amount of structural damping such that it is free to oscillate perpendicularly to the direction of the flow. The properties of the body and its support are set to  $k = 3.08425$ ,  $c = 0.0581195$  and  $m = 20.0$ . The length of the sides of the square body is  $D = 1.0$ . The fluid density and viscosity read  $\rho = 1.0$  and  $\mu = 0.01$ , respectively. The maximum inflow velocity considered here is  $u_\infty = 2.5$ , which corresponds to the Reynolds number  $Re = u_\infty D \rho / \mu = 250$ . With the above material parameters the set-up of the problem, at  $Re = 250$ , corresponds to one of the numerical simulations performed by Robertson *et al* [100]. The geometry and the boundary conditions employed here are displayed in Figure 13.6.

The finite element mesh, which is used for the simulations, consists of 8718 elements, and the surface of the rigid body is modelled with 80 fluid element edges. Figure 13.7 shows a detail of the mesh. In order to avoid convergence studies similar to Section 13.1, the mesh has been chosen rather dense. For the rigid body the time integration parameter is set to  $\rho_\infty^h = 0.9$ . The parameter  $\rho_\infty^h$  for the time integration of the fluid and the time step size  $\Delta t$  are roughly adapted to the different inflow velocities  $u_\infty$  as is evident from Figure 13.8. The algorithm type C is employed for the update of the nodal positions in the ALE region.

In Figure 13.8 the frequency  $f_o$  and the amplitude  $Y/D$  of the rigid body oscillations as well as the frequency  $f_v$  of the vortex shedding are displayed against the Reynolds number. The diagrams in Figure 13.9 show the evolution of the amplitude  $Y/D$  in time for different Reynolds numbers. In Figure 13.10, typical oscillations of the displacement  $Y/D$  and the lift force  $F_y$ , obtained from two different time step sizes, are displayed for  $Re = 250$ . A typical flow pattern during galloping is shown in Figure 13.11.

On the basis of the numerical results, the following observations are made:

- The effects of vortex induced oscillations and galloping can clearly be distinguished: In Figure 13.8, the lock-in region is observed to coincide with the interval of Reynolds numbers  $Re \approx 50$  to  $55$ . The maximum amplitude of the vortex induced oscillations is  $\max(Y/D) = 0.186$ . In the lock-in region, the frequencies  $f_o$ ,  $f_v$  and  $f_n$  are almost iden-

tical. For  $Re \approx 55$  to 150, the rigid body oscillations are negligible. At  $Re \approx 150$ , the rigid body suddenly starts large amplitude oscillations. At  $Re = 250$ , the amplitude has risen to  $\max(Y/D) = 1.117$ . The frequency  $f_o$  coincides with the natural frequency  $f_n$ , whereas the frequency of the vortex shedding  $f_v$  is 3.6 to 6.3 times larger than  $f_n$ .

- At  $Re = 250$ , the rigid body oscillations ( $\max(Y/D) = 1.117$  and  $f_o \approx 0.943 f_n$ ) agree very well with the solution presented by Robertson *et al* [100] ( $\max(Y/D) \approx 1.15$  and  $f_o \approx 0.938 f_n$ ).
- The independence of the rigid body oscillations at high Reynolds numbers from the vortex shedding is illustrated in Figure 13.10. It is shown that the galloping effect is captured rather accurately for very large time step sizes ( $\Delta t \approx T_o/20$ ,  $T_o = 1/f_o$ ), which do not resolve the vortex shedding properly.
- The numerical model and the solution algorithm prove robust and efficient. The convergence of the residuals is observed to be asymptotically quadratic.

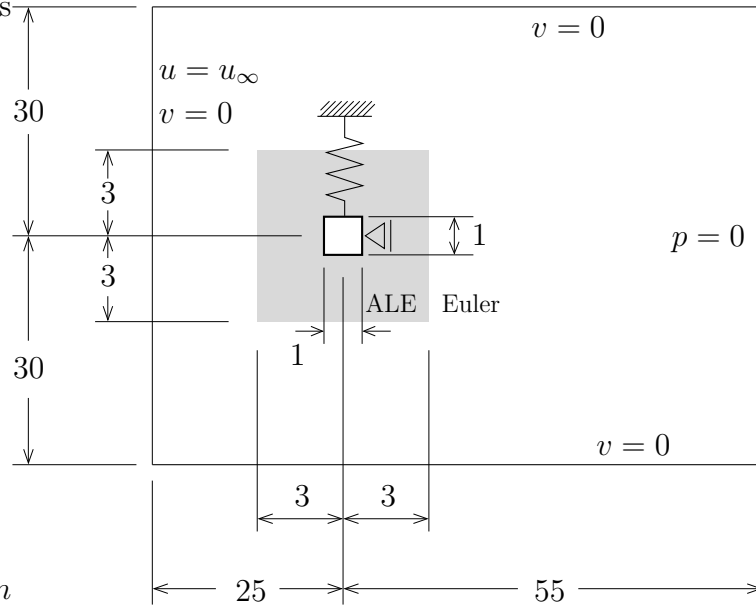


Figure 13.6: Oscillating square, geometry and boundary conditions of the problem.

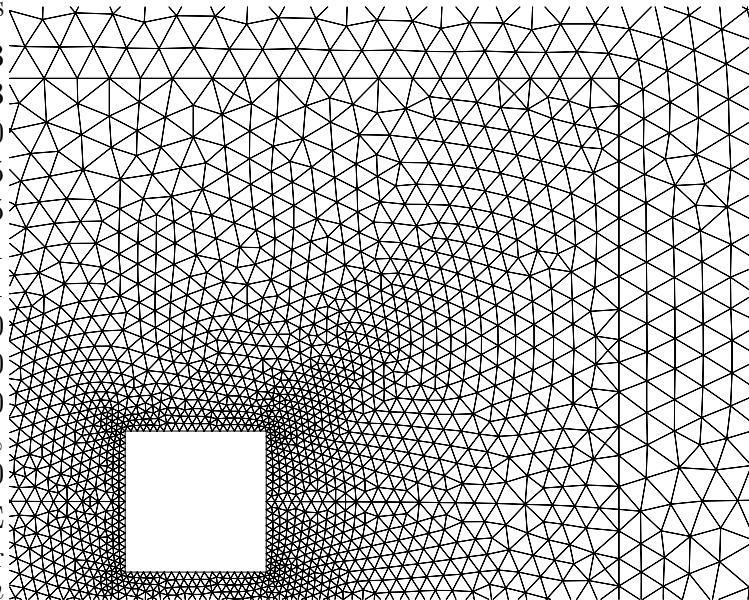


Figure 13.7: Oscillating square, detail of the mesh with 8718 finite elements.

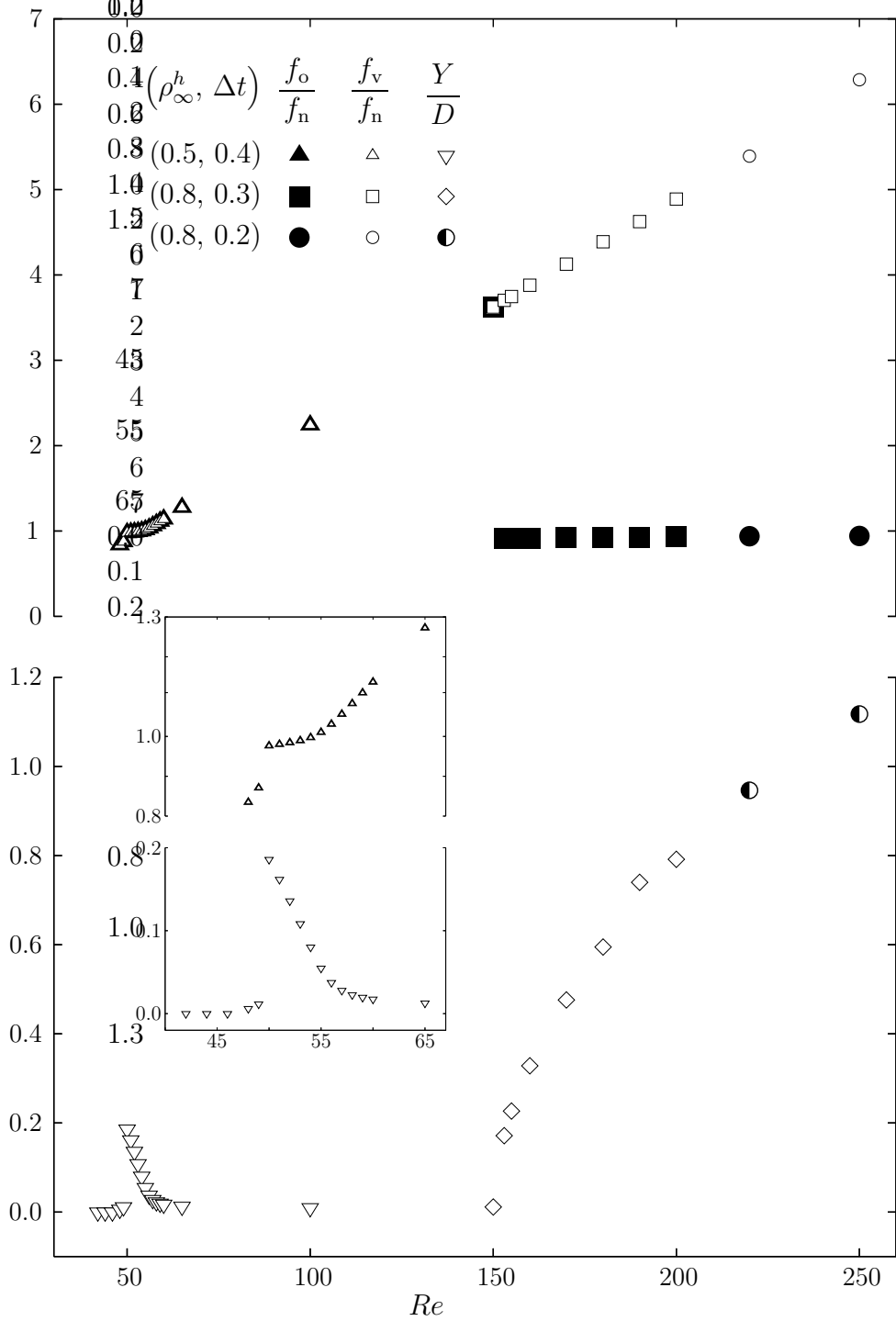


Figure 13.8: Oscillating square, amplitudes and frequencies; also showing a zoom of the lock-in region; different time integration parameters  $(\rho_\infty^h, \Delta t)$ .

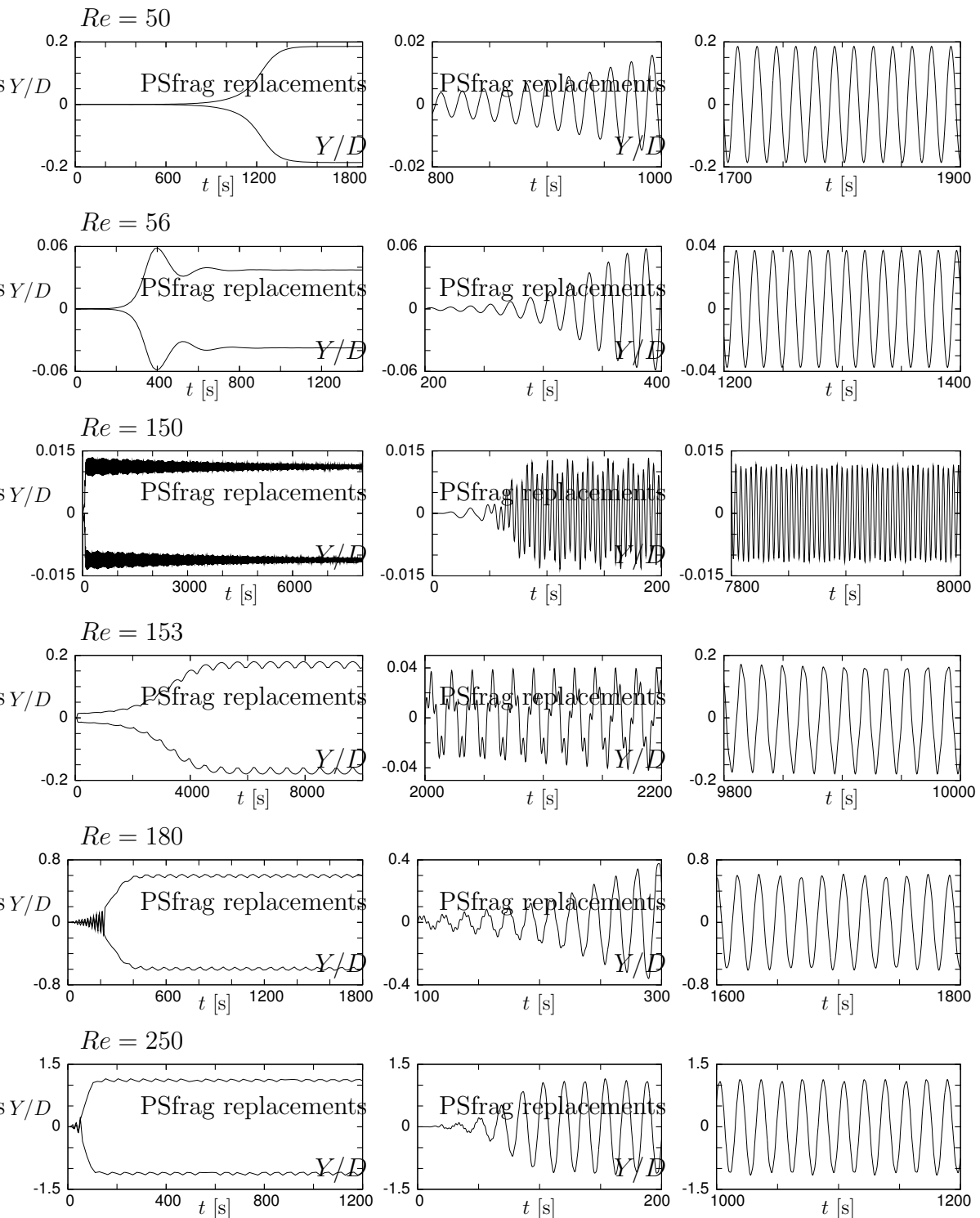


Figure 13.9: Oscillating square, evolution of the amplitude  $Y/D$ ;  $Re = 50, 56$  with  $\rho_\infty^h = 0.5$ ,  $\Delta t = 0.4$ ;  $Re = 150, 153, 180$  with  $\rho_\infty^h = 0.8$ ,  $\Delta t = 0.3$ ;  $Re = 250$  with  $\rho_\infty^h = 0.5$ ,  $\Delta t = 0.2$ .

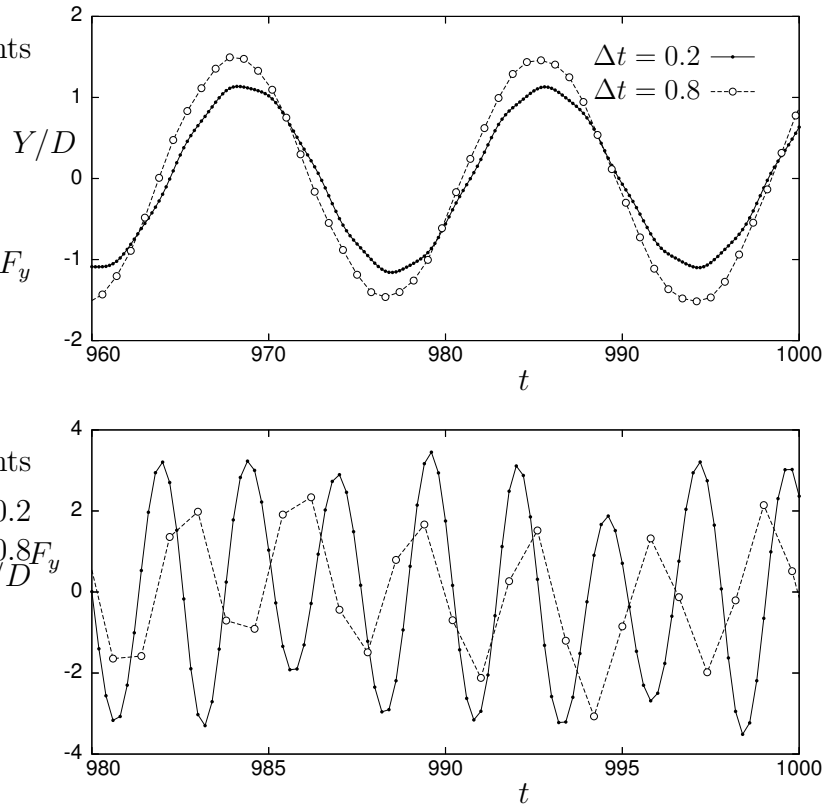


Figure 13.10: Oscillating square, oscillation of rigid body  $Y/D$  and lift force  $F_y$ ;  $Re = 250$ ,  $\rho_\infty^h = 0.8$ , two different time step sizes  $\Delta t$ .

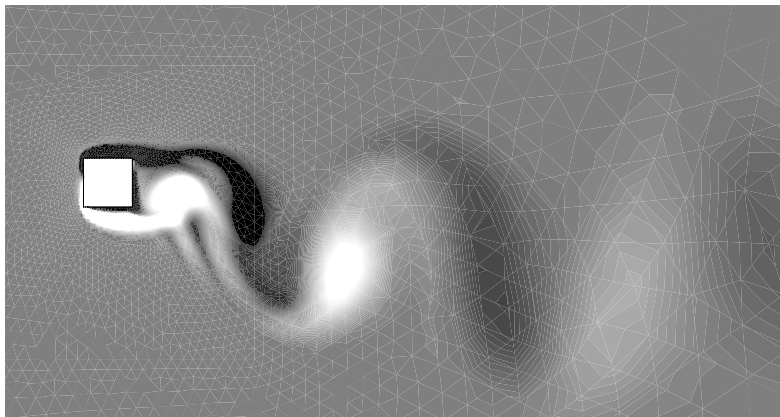


Figure 13.11: Oscillating square, typical vorticity distribution during galloping,  $Re = 250$ ,  $\text{vort}(\mathbf{u}^h) \leq -5 \rightarrow \text{black}$ ,  $\text{vort}(\mathbf{u}^h) \geq +5 \rightarrow \text{white}$ .

### 13.3 Rotational Galloping

In this example the objective is to simulate the phenomena of rotational galloping. The set-up of the problem is almost identical to Section 13.2, however, the length of the rigid body under consideration in the direction of the flow is now four times longer than its thickness, and the rigid body is free to rotate, but fixed in  $x$ - and  $y$ -direction. The rotational degree of freedom is associated with an elastic spring and a certain amount of linear damping. The physical background of rotational galloping is similar to transverse galloping as discussed in the first paragraphs of Section 13.2. The geometry and the boundary conditions of the problem, which are displayed in Figure 13.12, correspond to the work by Robertson *et al* [100].

The properties of the rigid body-spring system are set to  $I_\theta = 400$ ,  $c_\theta = 78.540$  and  $k_\theta = 61.685$ , thus  $f_n = \sqrt{k_\theta/I_\theta}/(2\pi) = 0.0625$ . The inflow velocity, the diameter of the rectangular body and the fluid density and viscosity are chosen as  $u_\infty = 2.5$ ,  $D = 1$ ,  $\rho = 1$  and  $\mu = 0.01$ , respectively, such that the global Reynolds number becomes  $Re = u_\infty D \rho/\mu = 250$ .

Two different finite element meshes are considered with 3454 (11696) elements and 84 (164) element edges on the boundary of the rigid body. The time integration parameters  $\rho_\infty^h$  are set to 0.9 and 0.8 for the rigid body and the fluid, respectively. The mesh update in the circular ALE region around the rigid body is performed on the basis of the strategy denoted as type C. Different time step sizes  $\Delta t$  are used. The sudden application of the inflow velocity at  $t = 0$  is overcome by the employment of one large initial time step with  $\Delta t = 3.0$ .

Figure 13.14 illustrates the typical evolution of the rigid body rotation  $\theta$  in time. The diagrams in Figure 13.15 show the convergence behaviour of the maximum amplitude  $\max(\theta)$  and the frequency  $f_o$  of the rigid body oscillation as the time step size is decreased. Typical flow patterns are displayed in Figure 13.16. Typical convergence behaviour of the partitioned Newton-Raphson procedure is displayed in the Tables 13.1 and 13.2.

The following observations are made on the basis of the numerical results:

- For the Reynolds number under consideration ( $Re = 250$ ), the rigid bar is galloping. It is observed that the vortex shedding frequency  $f_v$  is significantly larger than the frequency  $f_o$  of the oscillation. A rough estimate of the frequency  $f_v$ , obtained by observing the vortex shedding over a sufficiently long time interval before the onset of galloping, renders  $f_v \approx 5.2 f_n$ , whereas  $f_o \approx 0.8 f_n$ .
- The amplitude and frequency of the rigid body oscillations as displayed in Figure 13.15 (11696 elements,  $\Delta t = 0.05$ :  $\max(\theta) \approx 0.267$  and

$f_o \approx 0.780 f_n$ ) agree very well with the solution presented by Robertson *et al* [100] ( $\max(\theta) \approx 0.262$  and  $f_o \approx 0.762 f_n$ ).

- The diagrams in Figure 13.15 display a highly nonlinear convergence behaviour of the response characteristics  $\theta$  and  $f_o$ . This may be due to the complex and coupled nature of the problem considered. Coarse spatial and temporal discretisations may completely switch off certain wave lengths, which, for denser meshes and smaller time step sizes, introduce more noise to the solution and thus, require even further refinement of the discretisation.

Note that, for small time step sizes, the response of the very coarse mesh deviates from the solution obtained from the dense mesh only by 6 % of the amplitude and by 3 % of the frequency.

- The numerical model and the solution algorithm prove robust and efficient. As illustrated in the Tables 13.1 and 13.2, the convergence of the residuals is observed to be asymptotically quadratic.

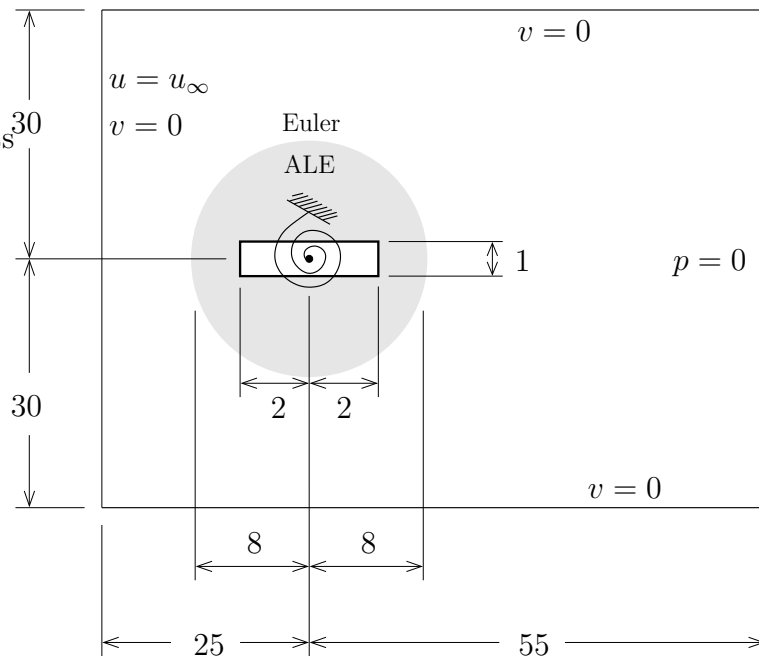


Figure 13.12: Rotational galloping, geometry and boundary conditions.

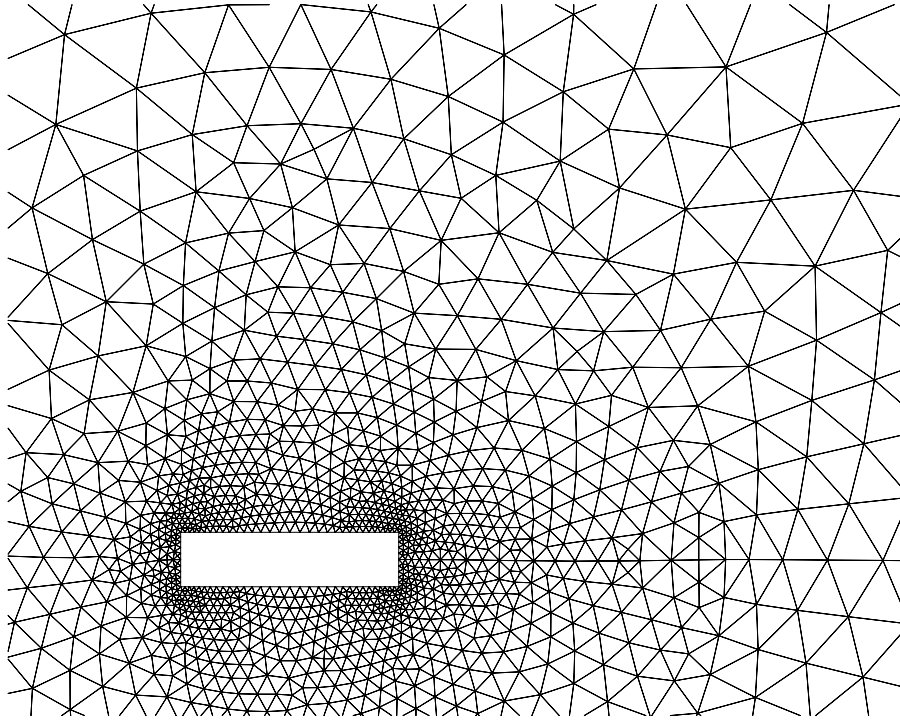


Figure 13.13: Rotational galloping, detail of the mesh with 3454 finite elements.

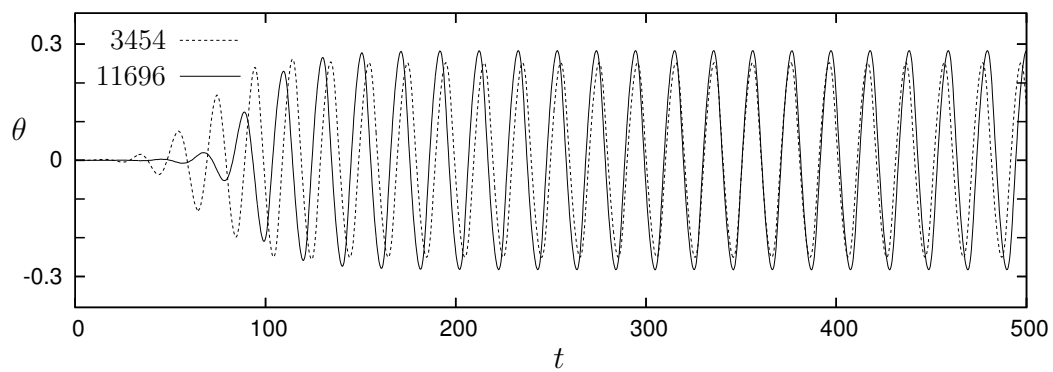


Figure 13.14: Rotational galloping, evolution of rotation  $\theta$  for  $\Delta t = 0.3$ , meshes with 3454 and 11696 elements.

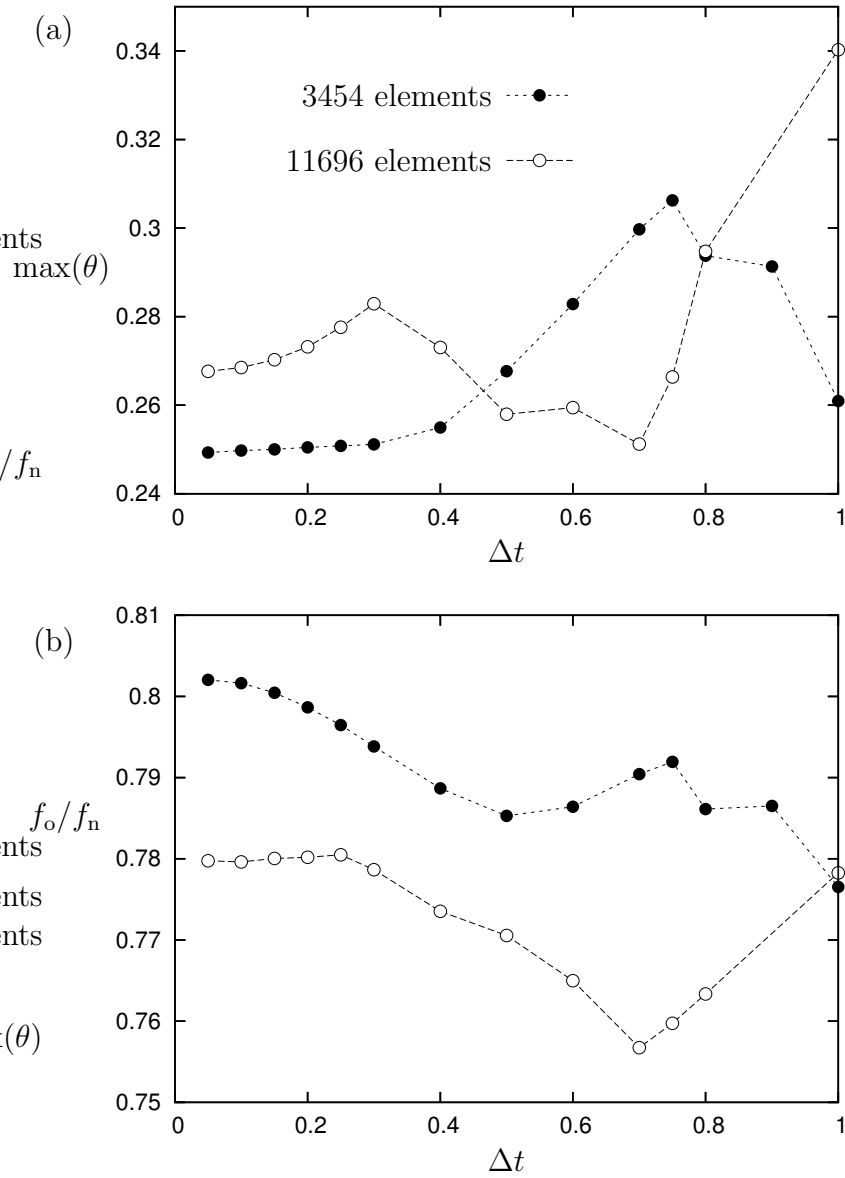


Figure 13.15: Rotational galloping, convergence of amplitude  $\max(\theta)$  (a) and frequency  $f_o$  (b) as  $\Delta t \rightarrow 0$ .

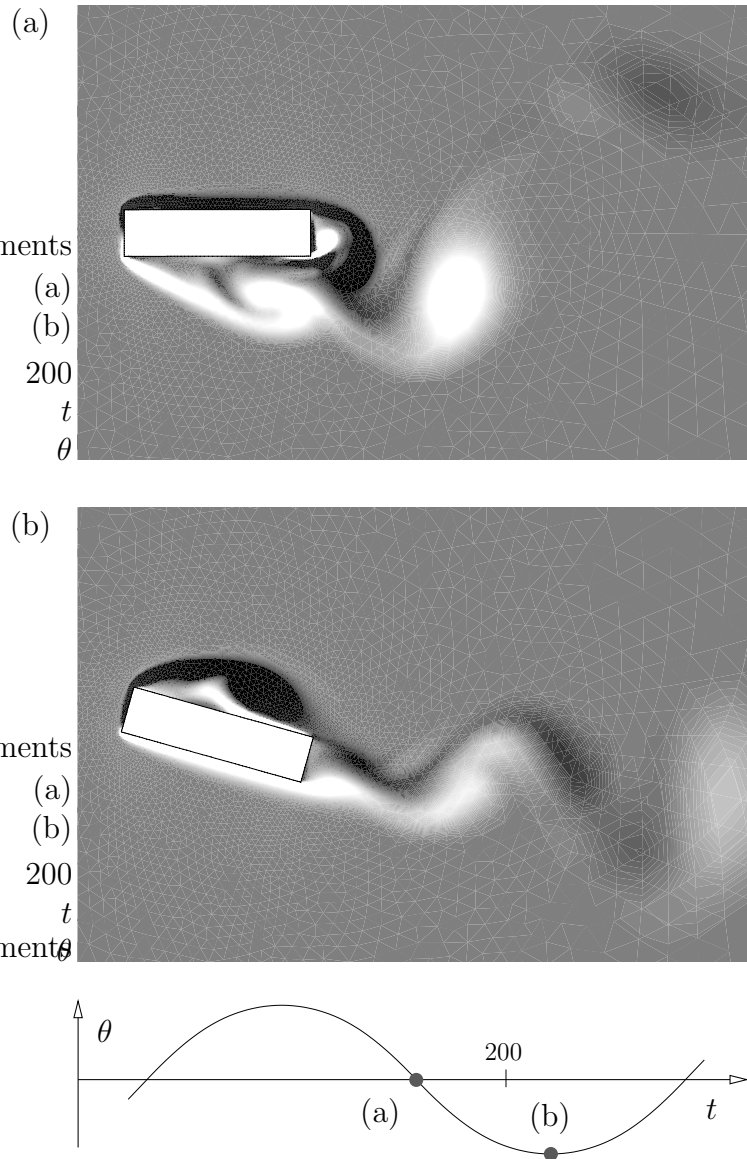


Figure 13.16: Rotational galloping, typical vorticity distribution, 11696 elements,  $\Delta t = 0.2$ ,  $\text{vort}(\mathbf{u}^h) \leq -5 \rightarrow \text{black}$ ,  $\text{vort}(\mathbf{u}^h) \geq +5 \rightarrow \text{white}$ .

A	B	C	D						
3.		1.00	no conv.						
		0.50	no conv.						
		0.25	2.5E+2	1.2E+2	3.1E+1	3.8E+0	8.3E-2	4.6E-5	1.5E-11
		0.50	2.5E+2	1.2E+2	3.1E+1	3.7E+0	7.8E-2	4.0E-5	1.1E-11
		0.75	2.6E+2	1.2E+2	3.0E+1	3.6E+0	7.2E-2	3.4E-5	8.9E-12
		1.00	2.6E+2	1.2E+2	3.0E+1	3.5E+0	6.7E-2	2.9E-5	7.1E-12
5.	4.7E+1								
3.		1.0	1.0E+1	3.1E-1	4.4E-4	9.9E-10			
5.	4.0E+0								
3.		1.0	1.9E+0	1.1E-2	6.0E-7	5.1E-12			
5.	3.3E-1								
3.		1.0	4.3E-2	5.8E-6	4.7E-12				
5.	9.6E-3								
3.		1.0	1.2E-2	4.7E-7	4.5E-12				
5.	2.0E-5								
3.		1.0	2.8E-6	4.9E-12					
5.	3.4E-10								

column A: identifies step in Box 10.1, fluid mesh solver (3.), residual of combined fluid + interface solver (5.),

column B: combined fluid + interface residual,

column C: increment cutting in the fluid mesh solver,

column D: residuals of fluid mesh solver

Table 13.1: Rotational galloping, convergence of solution procedure; 3454 elements,  $\Delta t = 0.7$  s,  $t = 146.5$  s.

A	B	C	D						
3.		1.000	no conv.						
		0.500	no conv.						
		0.250	no conv.						
		0.125	5.1E+2	2.3E+2	4.8E+1	4.0E+0	3.9E-2	4.2E-6	3.3E-11
		0.250	5.1E+2	2.3E+2	4.8E+1	4.1E+0	4.3E-2	5.2E-6	3.3E-11
		0.375	5.2E+2	2.3E+2	4.9E+1	4.3E+0	4.8E-2	7.1E-6	3.6E-11
		0.500	5.2E+2	2.3E+2	5.0E+1	4.6E+0	5.6E-2	1.0E-5	3.5E-11
		0.625	5.2E+2	2.3E+2	5.1E+1	4.9E+0	6.6E-2	1.5E-5	3.4E-11
		0.750	5.3E+2	2.4E+2	5.3E+1	5.2E+0	8.0E-2	2.3E-5	3.4E-11
		0.875	5.3E+2	2.4E+2	5.4E+1	5.7E+0	9.8E-2	3.6E-5	3.7E-11
		1.000	5.4E+2	2.5E+2	5.6E+1	6.2E+0	1.2E-1	5.5E-5	3.5E-11
5.	3.5E+1								
3.	4.4E+0	1.0	5.3E+1	3.8E+0	2.9E-2	1.9E-6	3.3E-11		
5.									
3.	2.0E-1	1.0	8.7E+0	1.0E-1	2.0E-5	3.5E-11			
5.									
3.	4.9E-3	1.0	5.8E-1	4.5E-4	4.1E-10				
5.									
3.	2.2E-5	1.0	6.1E-2	4.9E-6	3.4E-11				
5.									
3.	3.2E-9	1.0	4.1E-4	2.3E-10					
5.									

column A: identifies step in Box 10.1, fluid mesh solver (3.), residual of combined fluid + interface solver (5.),  
 column B: combined fluid + interface residual,  
 column C: increment cutting in the fluid mesh solver,  
 column D: residuals of fluid mesh solver

Table 13.2: Rotational galloping, convergence of solution procedure; 11696 elements,  $\Delta t = 0.7$  s,  $t = 146.5$  s.

## 13.4 Flutter of a Bridge Deck

In this example a rigid H-profile is considered. It is supported with a rotational and a vertical translational linear elastic spring. The horizontal motion is fixed to zero. The rigid body is exposed to uniform fluid flow in the horizontal direction. If the parameters of the supports are chosen such that they represent the torsional stiffness of the roadway and the stiffness of the vertical suspension, this model problem may be used to analyse the response of a suspension bridge to wind. The relevance of such investigations has been pointed out in Chapter 1, Figure 1.1. Similarly to the example in Section 13.2, oscillations of the bridge deck may occur, which are excited either by vortex shedding or by galloping. Coupled galloping of two or more degrees of freedom is commonly known as *flutter*, see *e. g.* den Hartog [56] or Blevins [9].

The geometry of the problem and the material parameters employed here are taken from Hübner *et al* [61]. The geometry and the boundary conditions are displayed in Figure 13.17. Thus, the fluid properties are set to  $\mu = 0.1 \text{ N s m}^{-2}$  and  $\rho = 1.25 \text{ kg m}^{-3}$ , the inflow velocity is chosen as  $u_\infty = 10 \text{ m s}^{-1}$  and the rigid body properties read  $k_y = 2000 \text{ N m}^{-1}$ ,  $m_y = 3000 \text{ kg}$ ,  $k_\theta = 40,000 \text{ N m}$  and  $I_\theta = 25,300 \text{ kg m}^2$ . The natural frequencies are thus obtained as  $f_{y,n} = 0.130 \text{ s}^{-1}$  and  $f_{\theta,n} = 0.200 \text{ s}^{-1}$ . Structural damping is ignored. If the Reynolds number is related to the width of the bridge deck  $b = 12 \text{ m}$ , it follows that  $Re = u_\infty b \rho / \mu = 1500$ .

For the numerical simulation, two finite element meshes with 4740 and 11432 elements are employed. The bridge deck is modelled with 156 or 312 element edges, respectively. Details of the coarse mesh are displayed in Figure 13.18. The mesh update is based on technique type C. The time integration parameter are set to  $\rho_\infty^h = 0.8$  for the fluid and  $\rho_\infty^h = 0.9$  for the rigid body. Different time step sizes  $\Delta t = 0.15 \text{ s}$ ,  $0.10 \text{ s}$ ,  $0.075 \text{ s}$  and  $0.05 \text{ s}$  are employed.

The evolution of the rigid body degrees of freedom  $Y$  and  $\theta$  is displayed in Figure 13.19. Figure 13.20 shows typical flow patterns.

The following observations can be made:

- After roughly 70 s, the bridge deck begins to oscillate with large amplitudes. At  $t \approx 200 \text{ s}$  the oscillations take a stable pattern. The amplitude of the rotation is  $\max(\theta) \approx 57^\circ$  and the maximum vertical displacement is obtained as  $0.75 \text{ m} \leq \max(Y) \leq 0.85 \text{ m}$ . The frequencies of the rotation and the translation coincide with  $f_o \approx 0.186 \text{ s}^{-1}$ . It is noted that this is close to the natural rotational frequency. In fact, the rotation is clearly the dominant motion.
- If the solution based on 11432 elements and  $\Delta t = 0.05 \text{ s}$  is taken as the



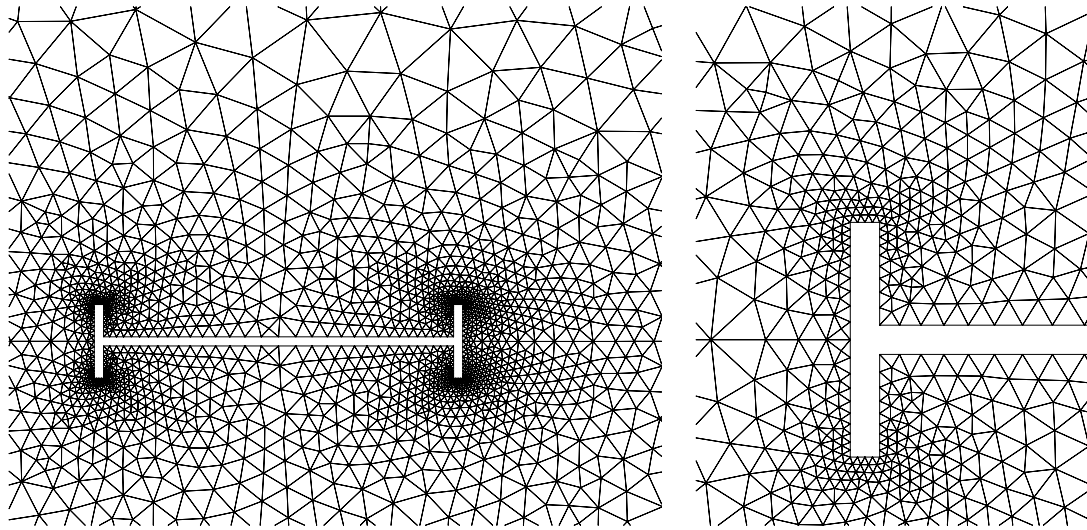


Figure 13.18: Flutter of bridge deck, details of the mesh with 4740 finite elements.

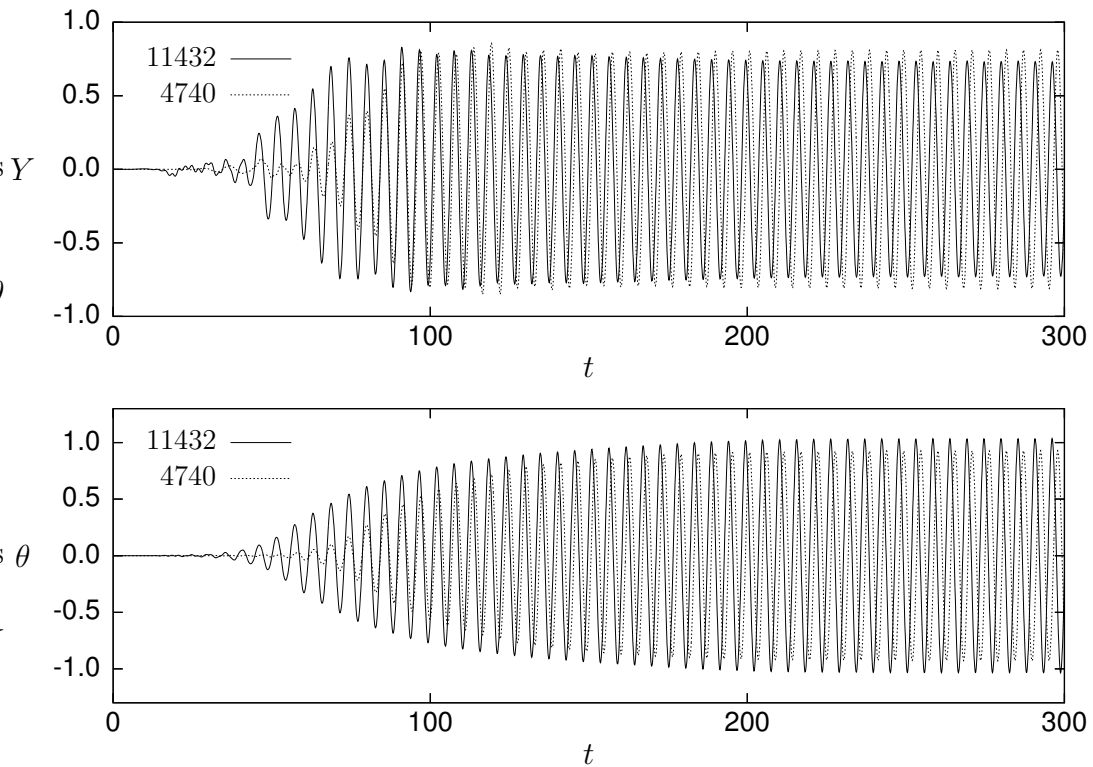


Figure 13.19: Flutter of bridge deck, translational and rotational oscillations;  $\Delta t = 0.10$  s, two different meshes.

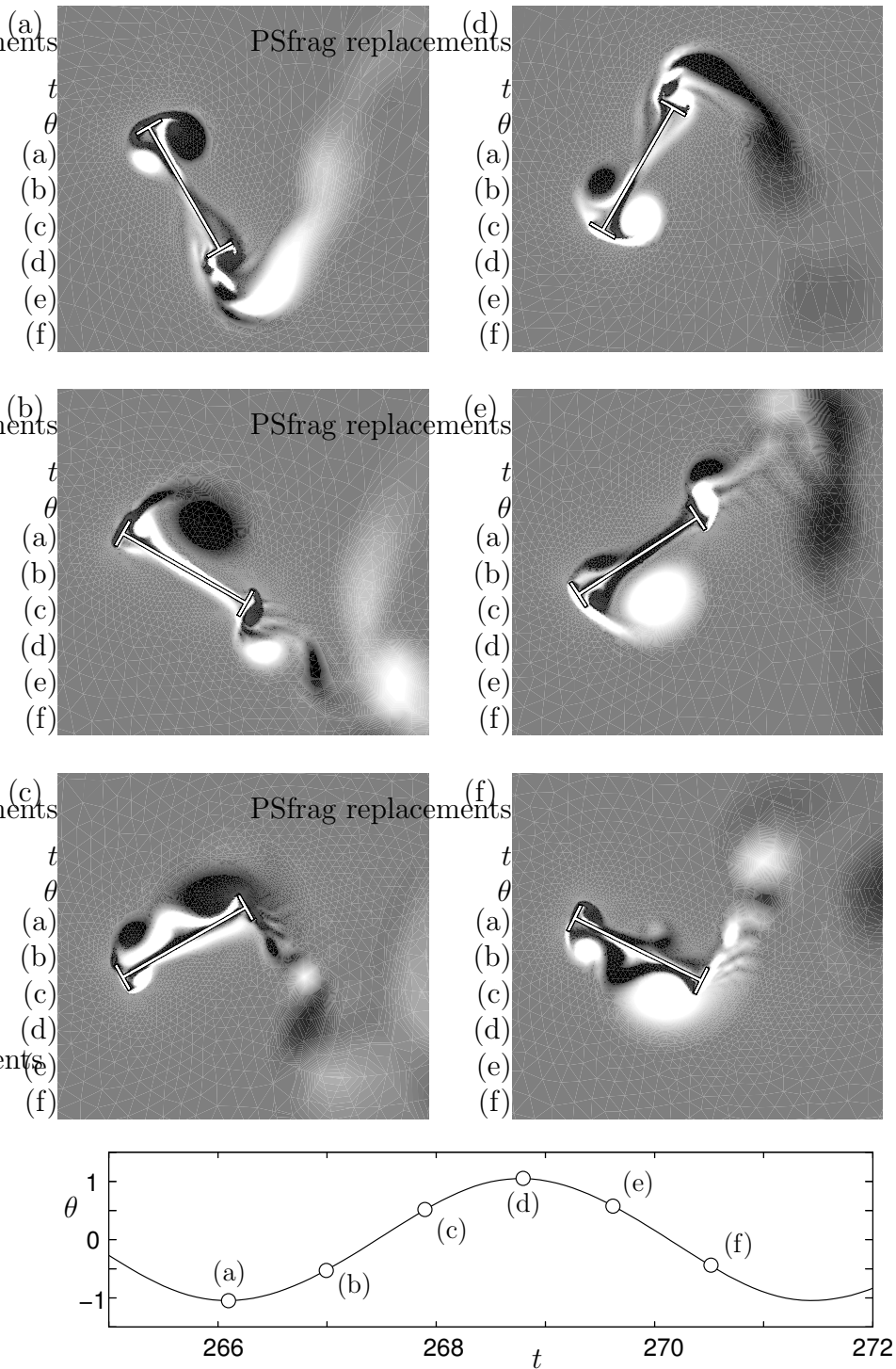


Figure 13.20: Flutter of bridge deck, typical vorticity distribution, 11432 elements,  $\Delta t = 0.075$ ,  $\text{vort}(\mathbf{u}^h) \leq -10 \rightarrow \text{black}$ ,  $\text{vort}(\mathbf{u}^h) \geq +10 \rightarrow \text{white}$ .

## 13.5 Rotating Bar

In this example the damping of the rotational oscillation of a rigid bar, which is submerged in a viscous fluid, is considered. The bar is supported by an elastic torsional spring without damping. Initially, the angle of rotation is  $\theta_0 = 0.5236 = 30^\circ$  and the fluid is at rest. The bar is then released to oscillate. The fluid gradually absorbs the energy of the bar through two mechanisms: The motion of the bar repeatedly accelerates and decelerates the fluid particles, and the resulting fluid flow dissipates energy due to the fluid viscosity. This problem has also been investigated by Sarrate *et al* [106].

The geometry and the boundary conditions are displayed in Figure 13.21. The properties of the rigid body-spring system are set to  $k_\theta = 7.056$  and  $I_\theta = 100$ . The natural frequency then follows as  $f_{\theta,n} = \sqrt{k_\theta/I_\theta}/(2\pi) = 0.0423$ . The fluid density is  $\rho = 1$ . Two different fluid viscosities  $\mu = 0.1$  and  $\mu = 0.001$  are considered. One half of the length of the bar  $d = L/2 = 1.25$  and the maximum velocity of point A associated with a free oscillation  $u_A = 2\pi f_{\theta,n} \theta_0 \sin(\pi) L/2 = 0.174$  may be used as the length scale and the characteristic velocity of the problem, respectively. Thus, the Reynolds numbers  $Re = u_A d \rho/\mu$  for the two viscosities considered are  $Re = 2.17$  and  $Re = 217$ .

The finite element mesh employed for the numerical simulation consists of 5008 finite elements. The rigid bar is modelled with 120 element edges. The mesh update is performed according to strategy type C. The time integration parameters are set to  $\rho_\infty^h = 0.8$  for the fluid and  $\rho_\infty^h = 0.9$  for the solid. The time step size is set to  $\Delta t = 0.5$ . For the sake of brevity, convergence studies are omitted.

Figure 13.22 shows a detail of the initial mesh with  $\theta_0 = 30^\circ$ . The evolution of the angle  $\theta$  for the two different viscosities is given in the diagram in Figure 13.23. Typical flow patterns are displayed in Figure 13.24.

The following observations can be made:

- After the rigid bar has been released, it performs oscillations at a frequency, which agrees closely to its natural frequency. The rigid body rotation causes a fluid flow, which propagates into the fluid domain. The fluid absorbs the energy of the rigid body. For  $\mu = 0.1$ , the flow is highly viscous and the oscillation has reduced to less than half of its initial amplitude after four cycles, whereas, for  $\mu = 0.001$ , the damping is much less significant (see Figure 13.23).
- The diagrams in Figure 13.24 show that, for  $\mu = 0.001$ , the fluid flow exhibits strong boundary layers and separating vortices at the surface

of the rigid bar, which do not occur in the low Reynolds number flow associated with  $\mu = 0.1$ .

- Again, the solution procedure renders asymptotically quadratic convergence of the residuals.

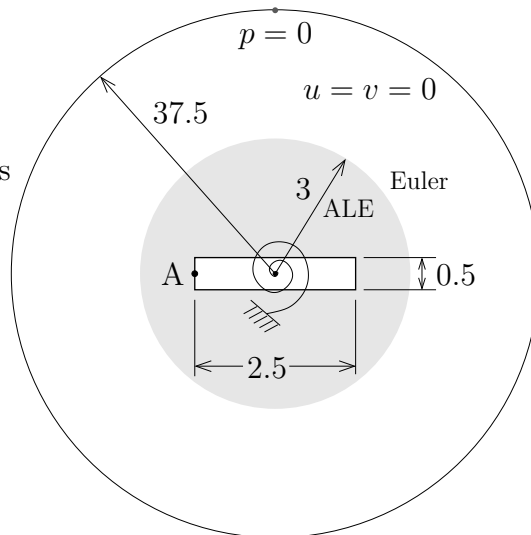


Figure 13.21: Rotating rigid bar, geometry and boundary conditions.

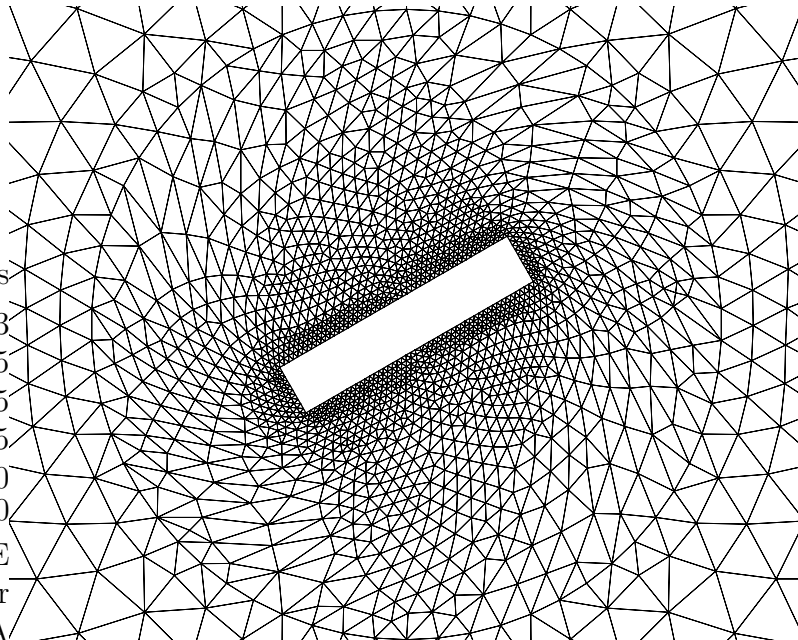


Figure 13.22: Rotating rigid bar, detail of initial mesh,  $\theta_0 = 30^\circ$ .

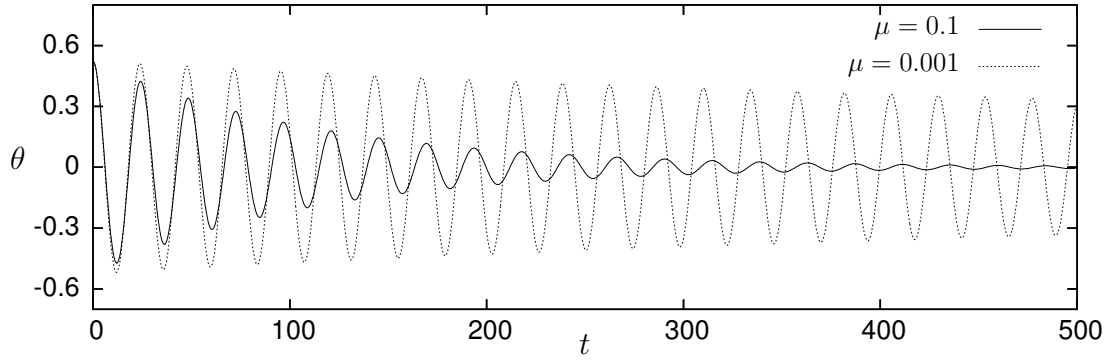


Figure 13.23: Rotating rigid bar, evolution of  $\theta$  for different fluid viscosities.

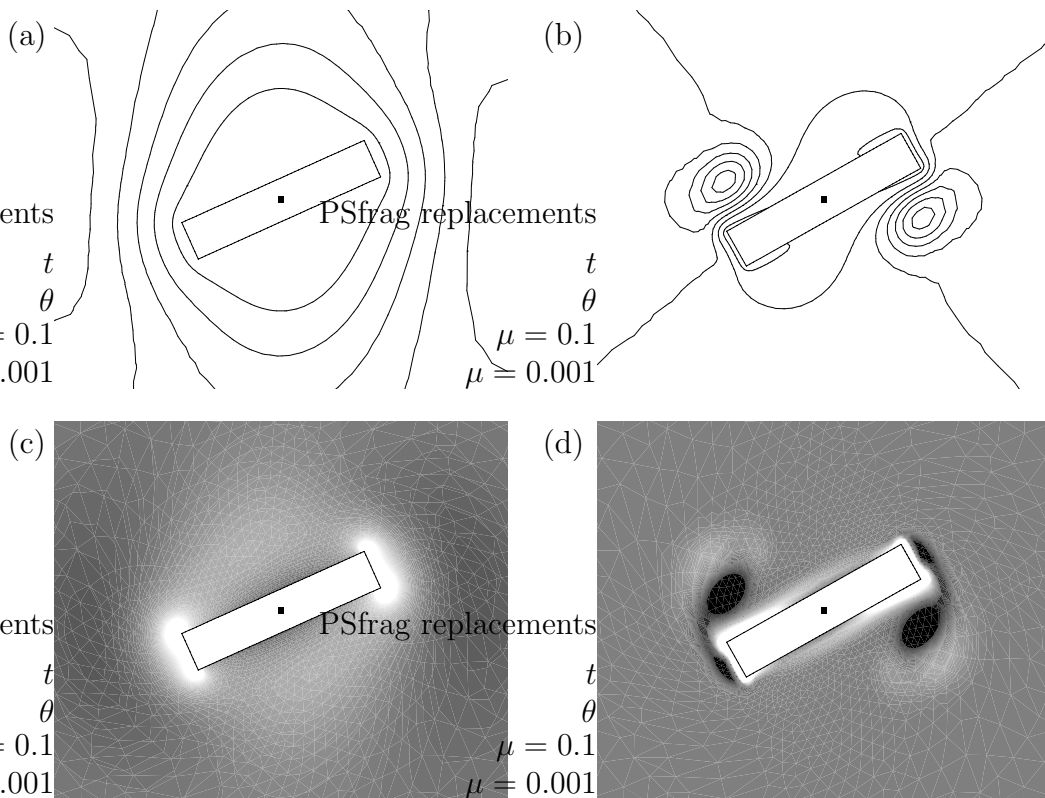


Figure 13.24: Rotating rigid bar, streamlines and vorticity distribution at  $t = 24.0 \approx 1T_\theta = 1/f_{\theta,n}$ ,  $\Delta t = 0.5$ ;  $\mu = 0.1$  (a),(c);  $\mu = 0.001$  (b),(d);  $\text{vort}(\mathbf{u}^h) \leq -0.1 \rightarrow \text{black}$ ,  $\text{vort}(\mathbf{u}^h) \geq +0.1 \rightarrow \text{white}$  (c);  $\text{vort}(\mathbf{u}^h) \leq -0.5 \rightarrow \text{black}$ ,  $\text{vort}(\mathbf{u}^h) \geq +0.5 \rightarrow \text{white}$  (d).

# Chapter 14

## Examples IV: Fluid - Solid Interaction

In this chapter, numerical examples of fluid-solid interaction are presented. Both the fluid flow and the solid structure are modelled with finite elements.

The choice of appropriate examples is rather difficult for the following reasons: The model problems should be sufficiently complex to demonstrate the capability of the numerical strategy to capture relevant physical phenomena of fluid-solid interaction. They should involve large interface displacements and a two-way coupling of the fluid and the solid. They should test the accuracy, stability and robustness of the solution methodology without requiring complex problem definitions. However, most real problems can not be represented in two dimensions and require the modelling of some physical phenomena which have not been treated in this work, such as turbulent and compressible flow or mechanical contact of the solid structure. The modelling of the latter is, for instance, essential for the realistic simulation of various kinds of valves, the analysis of which is desirable in many areas of mechanical engineering as well as biomechanics (*e. g.* human heart). Furthermore, the closing valve makes remeshing of the fluid domain inevitable. Hence, it is noted that, in contrast to other areas of numerical modelling, very few benchmark problems of fluid-structure interaction have yet been established.

A model problem, which has since been addressed by several researchers, was presented by Wall [127], who simulated the vortex induced oscillations of a flexible beam. The corresponding results, obtained with the methodology presented in this work, are given in Section 14.1. The Sections 14.2 – 14.4 discuss the modelling of flow through a channel with a flexible wall, the fall of a two dimensional parachute at a small Reynolds number and a small water pump based on two valves. Due to the absence of reference solutions, extensive convergence studies have been omitted.

## 14.1 Flow-Induced Oscillations of a Flexible Structure

This model problem has been presented by Wall [127,128] and later by Braess [11], Hübner *et al* [61] and Steindorf [115] to test their numerical solution strategies for fluid-structure interaction problems.

A fixed square rigid body is submerged in incompressible fluid flow. Far away the flow is uniform with the velocity  $u_\infty$ . A flexible thin beam is attached to the rigid body in the centre of the downstream face. In the undeformed configuration the beam is aligned with the far field flow. The vortices, which separate from the corners of the rigid body, generate lift forces which excite oscillations of the flexible beam.

The geometry and the boundary conditions are given in the Figure 14.1. The material parameters of the fluid and the solid are taken from Wall [127] as, respectively,  $\mu_f = 1.82 \cdot 10^{-4}$ ,  $\rho_f = 1.18 \cdot 10^{-3}$  and  $\mu_s = 9.2593 \cdot 10^5$ ,  $K_s = 2.78 \cdot 10^6$ ,  $\rho_s = 0.1$ . The shear and bulk moduli  $\mu_s$  and  $K_s$  correspond to the Young's modulus  $E = 2.5 \cdot 10^6$  and the Poisson's ratio  $\nu = 0.35$ . Plane stress conditions are assumed to hold for the solid. The inflow velocity is chosen as  $u_\infty = 51.3$ . Thus, the Reynolds number is obtained as  $Re = \rho_f D u_\infty / \mu_f = 333$ , whereby  $D = 1$  is the diameter of the square rigid body.

Three different numerical representations of the flexible structure are considered: First, it is discretised with 20 nine noded finite elements of equal size

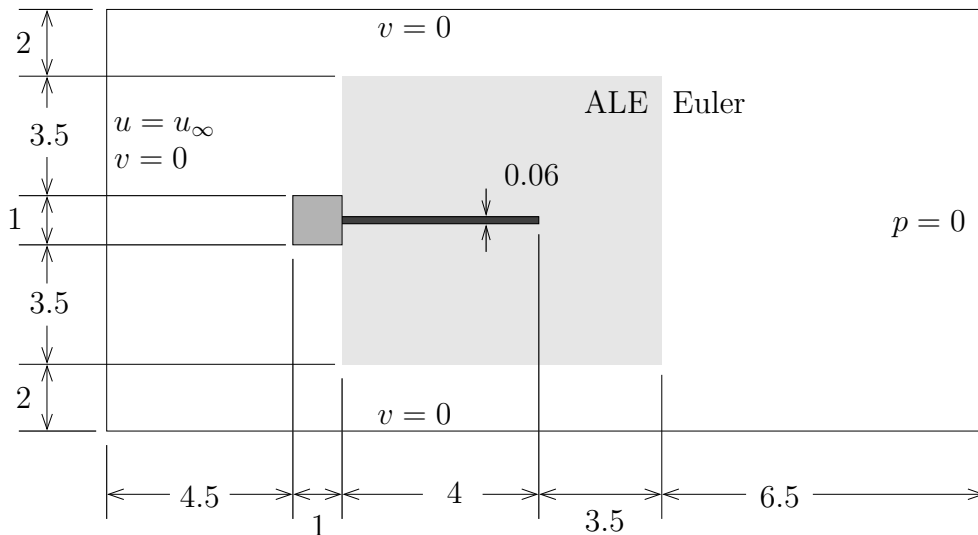


Figure 14.1: Oscillating structure, geometry and boundary conditions.

with only one element in the thickness direction of the beam (plane stress, small strain elasticity, full integration). This corresponds to Wall [127]. The second model differs from the first only by the employment of Neo-Hooke type large strain elasticity. Thirdly, a representation with 20 linear geometrically exact beam elements is considered. For the beam elements, the following parameters can be computed from the problem data:  $E A = 1.5 \cdot 10^5$ ,  $E I = 45.0$  and  $\kappa \mu A = 4.63 \cdot 10^4$ . Details of the solid mechanics finite element formulations are given in Chapter 8.

For the assessment of the numerical results it is necessary to be aware of eventual differences of the behaviour of the three structural models. Therefore, the static response to a point load  $F$  at the tip is computed. Figure 14.2 (a) shows the resulting load-displacement diagram. The dynamic properties are investigated by computing the lowest natural frequency of the beam associated with different loads  $F$ . The results are displayed in Figure 14.2 (b). In both diagrams the responses obtained with the Neo-Hooke elastic continuum elements and the geometrically exact beam elements agree remarkably well.

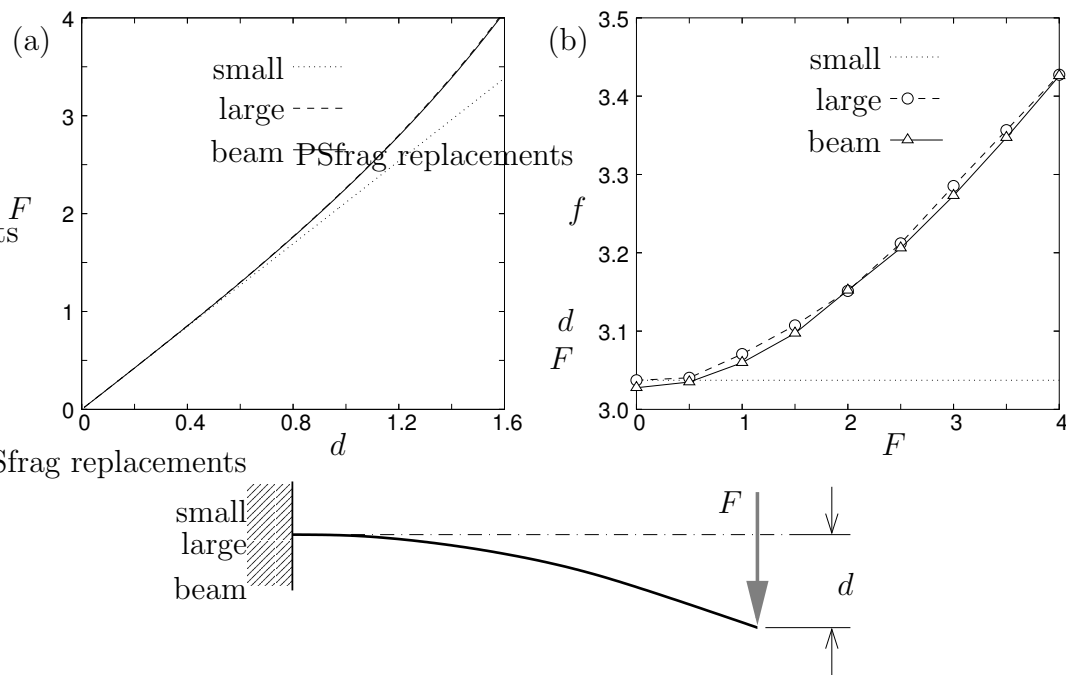


Figure 14.2: Oscillating structure, static and dynamic behaviour of the beam, point load-deflection curve (a), lowest natural frequency  $f$  in deformed configurations (b); the beam is modelled with 20 nine noded plane stress small or large strain finite elements (small, large) or with 20 linear geometrically exact beam elements (beam).

For small loads  $F$ , they coincide with the results of the small strain elastic continuum elements.

With respect to the interface kinematics it should be noted that the continuum model and the beam model of the structure render, respectively, 80 or 20 interface nodes, which shall result in a substantial difference of computational time. The employment of fewer interface nodes for the continuum model is counterproductive, since it results in unwanted stiffening of the thin structure and hence, jeopardises the diagrams in Figure 14.2. Consequently, the beam model seems more attractive.

Due to the neglect of the thickness of the beam elements, different fluid meshes are needed. Therefore, three meshes with 4336, 12,330 (for the interaction with the continuum model of the structure) and 4564 elements (for the interaction with the beam model) are generated. Details of the meshes are displayed in Figure 14.3. The time integration parameters are set to  $\rho_\infty^h = 0.8$  for the fluid and  $\rho_\infty^h = 0.5$  for the solid structure. The update of the positions of the internal nodes of the fluid mesh is performed according to strategy type C. Initially, the fluid and the structure are at rest, and at  $t = 0$  the inflow velocity  $u_\infty$  is applied instantaneously. The simulations are performed for different time step sizes  $\Delta t$ .

The diagrams in the Figures 14.4 – 14.6 show the evolution of the displacement  $d$  of the tip of the flexible structure in time. Some typical flow patterns are displayed in the vorticity diagrams in Figure 14.7. The convergence of the solution procedure is demonstrated in the Tables 14.2 – 14.4.

The following observations are made on the basis of the numerical results:

- Every simulation renders a stable periodic long term response of the flexible structure. The build-up of the oscillations takes approximately 2 time units. For all discretisations considered, the amplitudes of the oscillating tip displacement  $d$  lie between 1.1 and 1.4. The average frequency  $\bar{f}$  is obtained between 2.96 and 3.31 (see Table 14.1). This agrees well with the results obtained by Wall [127], Hübner *et al* [61] and Steindorf [115].
- Figure 14.4 shows that, for the small strain continuum model, the time steps  $\Delta t = 0.02$  and  $0.01$  render pure sinusoidal oscillations of the structure. For  $\Delta t = 0.005$ , however, the amplitude of the oscillation is modulated. Furthermore, one can observe that the oscillation is superimposed with a small amplitude oscillation at a higher frequency. Thus, the time steps considered are too large to illustrate the convergence towards the mesh dependent limit solution as  $\Delta t \rightarrow 0$ . On the contrary, the reduction of the time step size from  $\Delta t = 0.02$  to

$\Delta t = 0.005$  leads to the resolution of more features of the flow and the structural motion, which are otherwise damped out.

Thus, the superimposed low and high frequency oscillations with, respectively, large and small amplitudes, which are obtained for  $\Delta t = 0.005$ , may be associated with the first and second eigenmodes of the structure. In fact, the second eigenfrequency of the small strain structural model corresponds to  $T \approx 0.053$ , which is resolved by  $\Delta t = 0.005$ , but not by  $\Delta t = 0.02$ .

- It is evident from Figure 14.5 and Table 14.1 that the deviation of the responses of the different structural models is small.

Interestingly, the maximum amplitudes of the tip displacement  $d$  of the large strain continuum model and the beam element model coincide (see Table 14.1). They are smaller than the corresponding value of the small strain model. This agrees well with the different structural stiffnesses established in Figure 14.2. Similarly, the fluid mesh with 12,330 elements renders a smaller average amplitude of  $d$  for the large strain than for the small strain model (see Figure 14.6).

The average frequencies  $\bar{f}$  obtained for the large strain and the beam model are slightly larger than the frequency of the oscillation of the small strain model of the structure. This is also consistent with the different dynamic behaviour of the structural models as illustrated in Figure 14.2 (b).

- The combination of the large strain continuum model with the mesh of 12,330 fluid elements renders significant high frequency effects and a strong modulation of the oscillation amplitude, whereas the oscillations of the small strain model, when combined with the dense fluid mesh, are comparatively uniform. This may indicate that the modulation and high frequency effects obtained for the small strain model with 4336 fluid elements and  $\Delta t = 0.005$  are related to the coarse spatial discretisation of the fluid rather than physics.
- Tables 14.2 – 14.4, which are associated with different fluid meshes, different time step sizes and different finite element models of the beam structure, illustrate that the convergence of the absolute residuals of the combined fluid + interface solver and of the subsolvers is asymptotically quadratic.

The details provided by Matthies and Steindorf [82, 115] allow a rough comparison of the computational costs associated with different solution algorithms. Steindorf employs a fluid mesh with approximately

19,700 degrees of freedom and a time step size  $\Delta t = 0.02$ . For a typical time instant, the fluid and solid subsolvers are called 60 to 80 times by the approximate block Newton procedure. Due to the small number of structural finite elements, the solid solver may be neglected. It is thus assumed that, for Steindorf, the computational cost associated with one time step corresponds to roughly 35 calls of the fluid solver.

For the mesh with 4336 fluid elements ( $\approx 6500$  degrees of freedom) and the same time increment  $\Delta t = 0.02$ , the solution strategy developed in this work, requires five iterations per time step. The combined fluid + interface solver takes 19 % of the overall computational time. Due to the unsymmetric matrix pattern, each call is slightly more expensive than that of the pure fluid solver. Consequently, it may be estimated that the computational cost associated with one time step corresponds to 30 to 35 calls of the fluid solver. For the fluid mesh with 12,330 elements ( $\approx 18,400$  degrees of freedom), also five iterations are needed, and 15 % of the computational time are spent in the combined fluid + interface solver. Thus, an estimate of the computational cost of a typical time step is obtained as 35 to 40 calls of the fluid solver. Note that the efficiency of the implementation of the partitioned Newton-Raphson procedure employed here can still be improved.

$\Delta t$	4336 (small)		4336 (large)		4564 (beam)		12330 (small)		12330 (large)	
	$d_{\max}$	$\bar{f}$	$d_{\max}$	$\bar{f}$	$d_{\max}$	$\bar{f}$	$d_{\max}$	$\bar{f}$	$d_{\max}$	$\bar{f}$
0.020	1.26	3.087								
0.010	1.23	3.135								
0.005	1.36	3.180	1.18	3.202	1.18	3.282	1.29	2.967	1.27	3.105
0.001					1.19	3.304				

Table 14.1: Oscillating structure, stable long term response, average frequency  $\bar{f}$  and maxima  $d_{\max} = \max(d)$  of tip displacement for different fluid meshes and structural models.

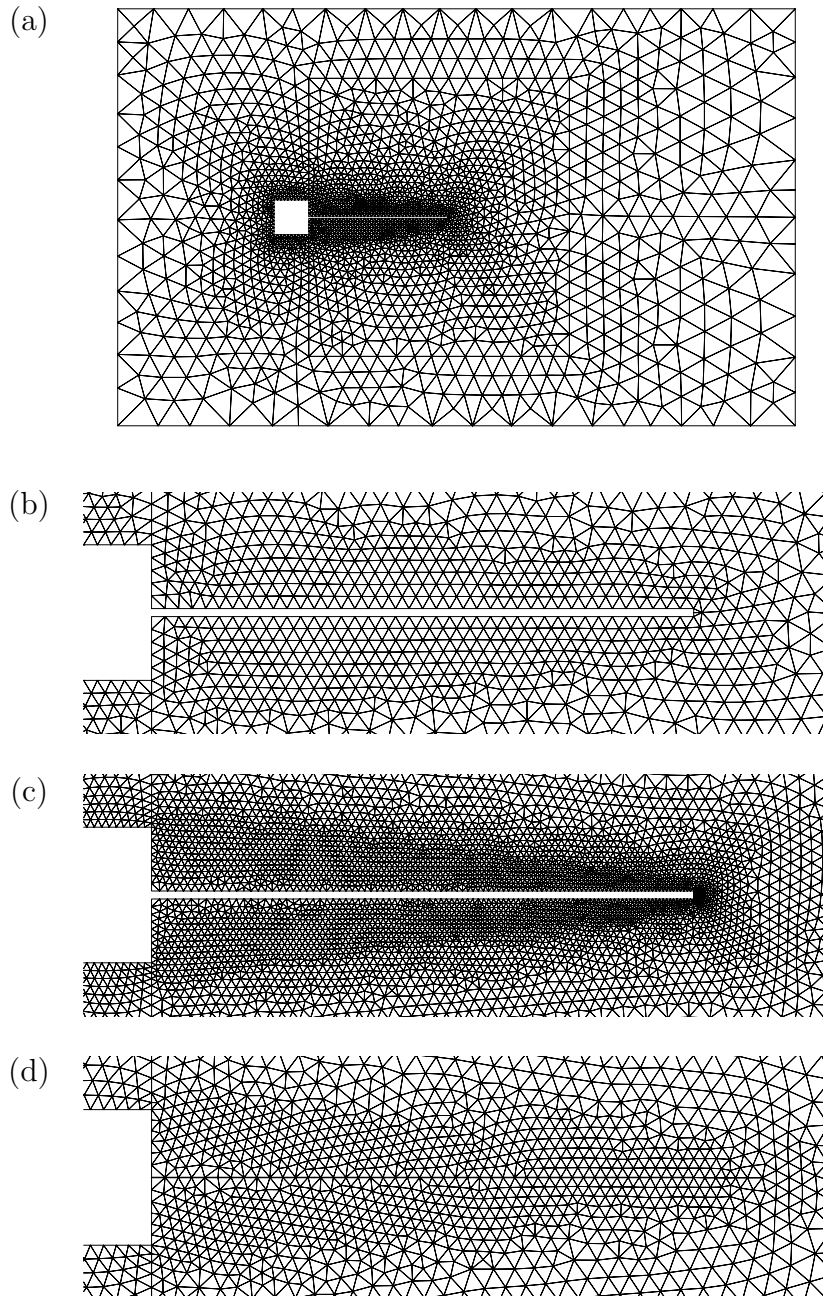


Figure 14.3: Oscillating structure, fluid finite element meshes; mesh with 4336 elements (a), detail of meshes with 4336 (b), 12,330 (c) and 4564 (d) elements; the mesh with 4564 elements is employed for the interaction with beam elements.

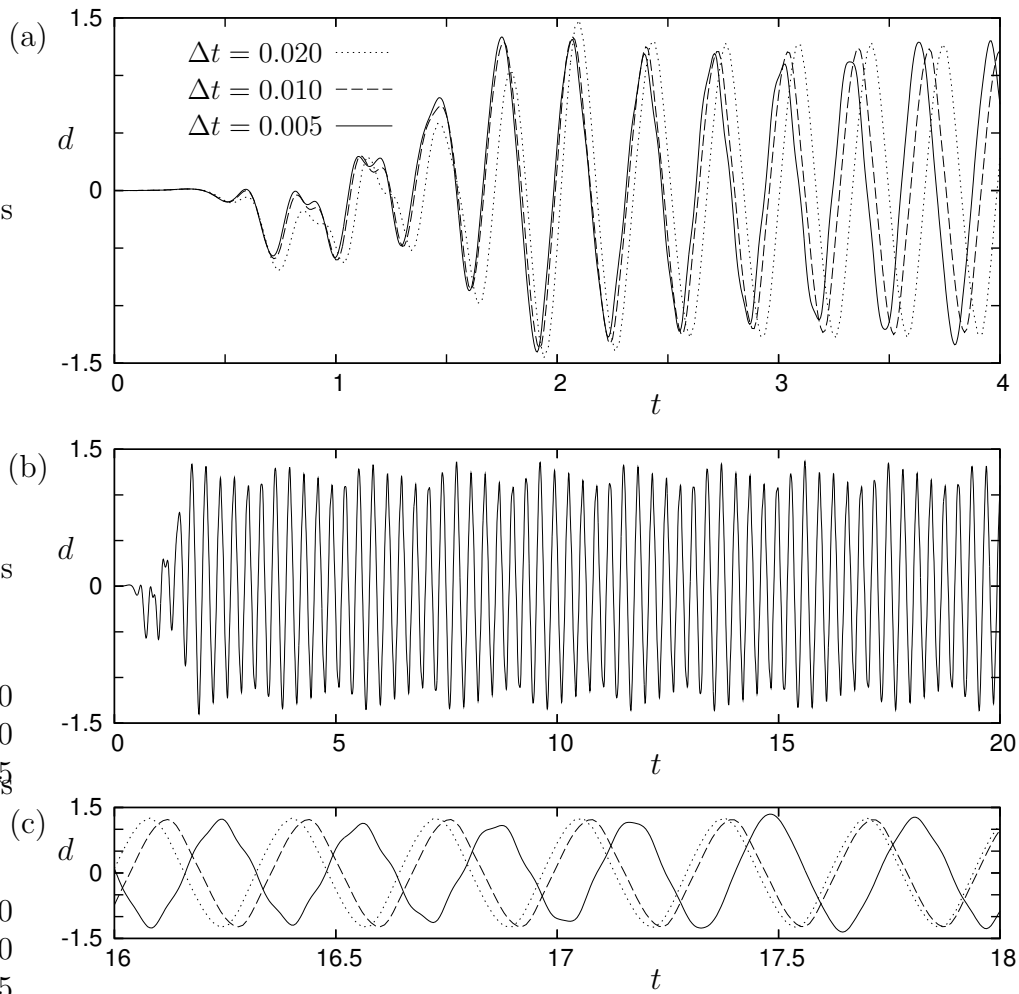


Figure 14.4: Oscillating structure, vertical displacement  $d$  of the tip of the structure; 4336 fluid elements, 20 nine noded small strain solid elements, different time step sizes  $\Delta t$ ; build-up of oscillations from rest (a), oscillations for small time step  $\Delta t = 0.005$  (b), stable long term responses (c).

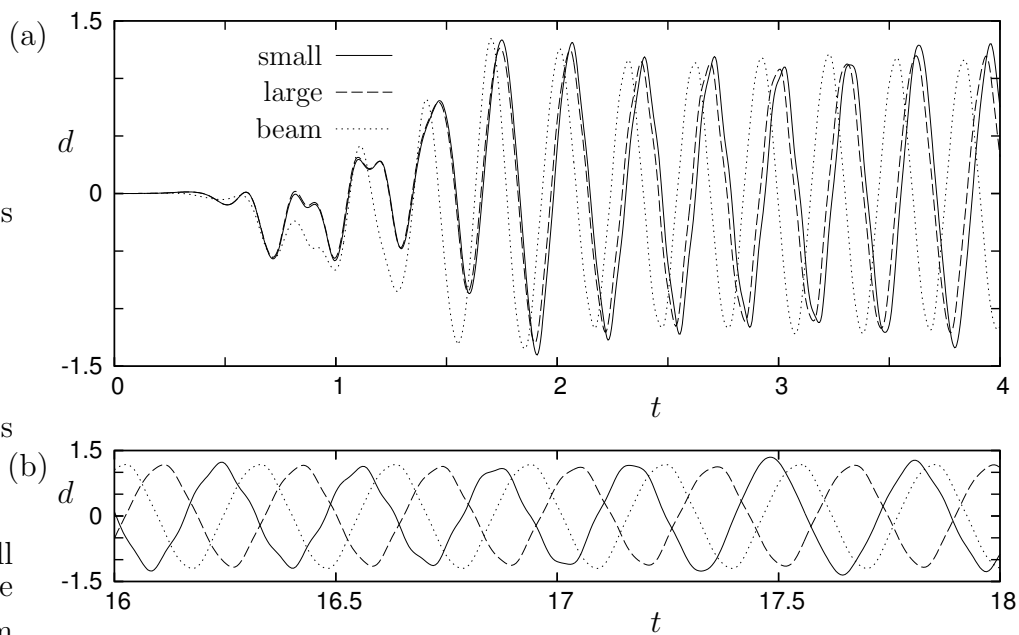


Figure 14.5: Oscillating structure, vertical displacement  $d$  of the tip of the structure;  $\Delta t = 0.005$ ; 4336 fluid elements, 20 nine noded small or large strain solid elements (small,large), 4564 fluid elements, 20 beam elements (beam); build-up of oscillations from rest (a), stable long term responses (b).

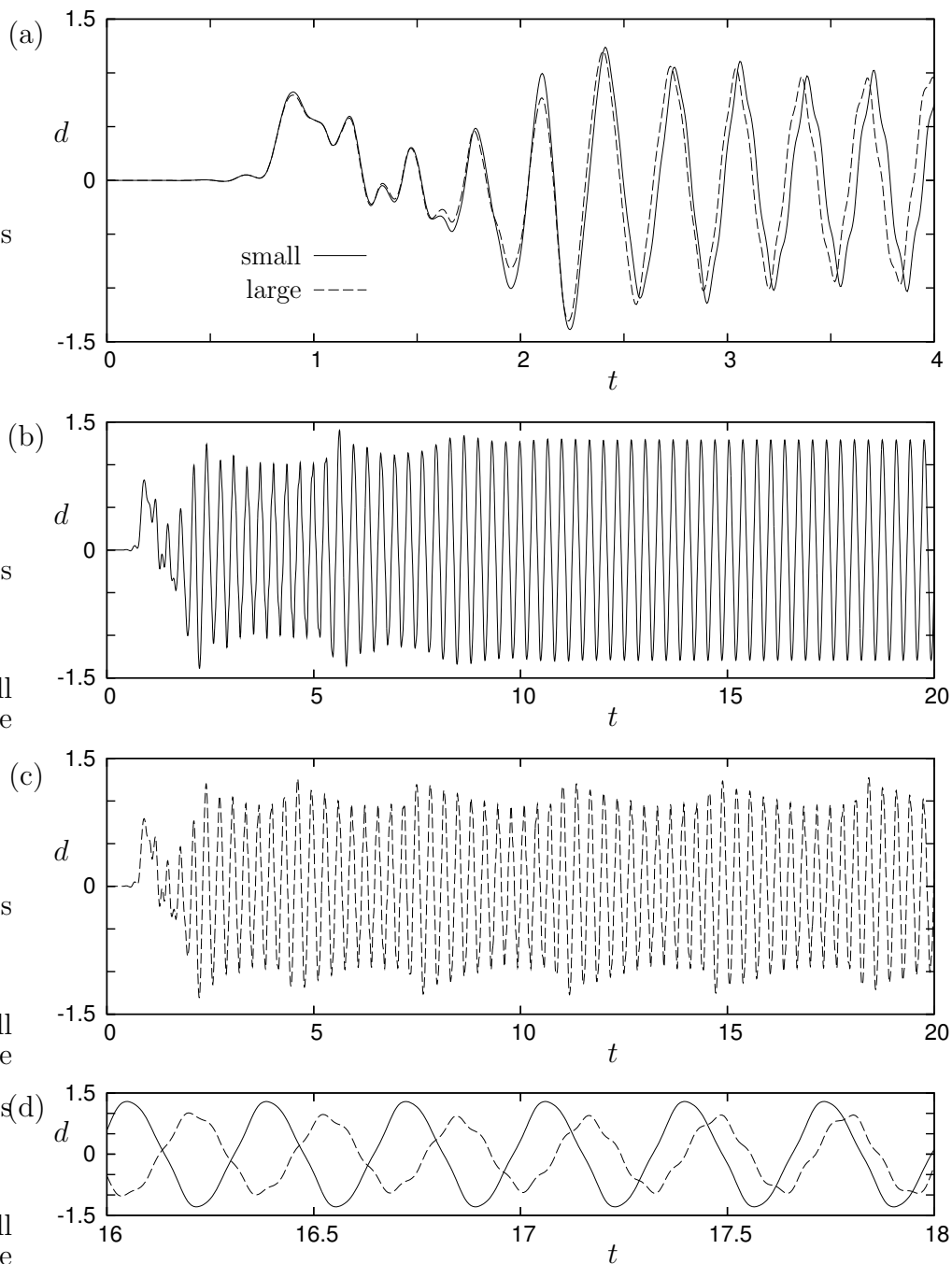


Figure 14.6: Oscillating structure, vertical displacement  $d$  of the tip of the structure;  $\Delta t = 0.005$ ; 12,330 fluid elements, 20 nine noded small or large strain solid elements (small,large); build-up of oscillations from rest (a), oscillations for small strain model (b), oscillations for large strain model (c), stable long term responses (d).

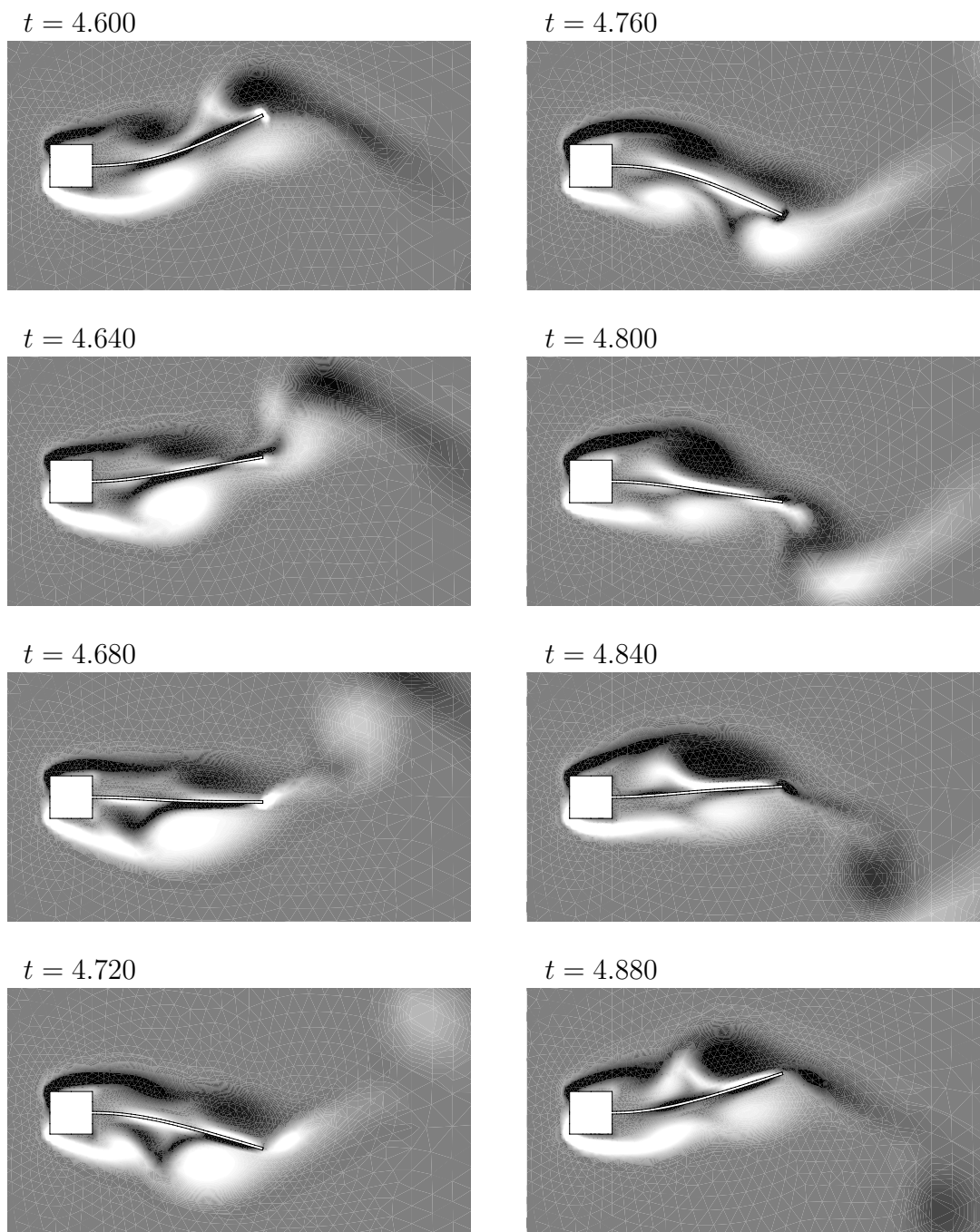


Figure 14.7: Oscillating structure, typical vorticity distribution during stable long term oscillations, 4336 fluid finite elements, 20 small strain solid continuum elements,  $\Delta t = 0.005$ ,  $\text{vort}(\mathbf{u}^h) \leq -150 \rightarrow \text{black}$ ,  $\text{vort}(\mathbf{u}^h) \geq +150 \rightarrow \text{white}$ .

A	B	C	D							
3.		1.00000	no conv.							
		0.50000	no conv.							
		0.25000	no conv.							
		0.12500	no conv.							
		0.06250	no conv.							
		0.03125	8.6E+1	4.4E+1	6.6E+0	2.5E-1	4.2E-4	1.2E-9		
		0.06250	8.5E+1	4.2E+1	6.3E+0	2.3E-1	3.6E-4	9.0E-10		
		0.09375	8.5E+1	4.1E+1	6.0E+0	2.1E-1	3.1E-4	6.7E-10		
		0.12500	8.4E+1	4.0E+1	5.8E+0	2.0E-1	2.7E-4	5.1E-10		
		....	....							
		....	....							
		0.81250	1.5E+2	1.5E+2	4.2E+1	7.2E+0	3.3E-1	8.5E-4	5.6E-9	
		0.87500	1.5E+2	1.4E+2	3.9E+1	6.3E+0	2.6E-1	5.4E-4	2.3E-9	
		0.93750	1.6E+2	1.6E+2	3.7E+1	5.6E+0	2.1E-1	3.4E-4	9.3E-10	
		1.00000	1.6E+2	1.3E+2	3.4E+1	4.9E+0	1.6E-1	2.1E-4	3.7E-10	
4.			4.3E-1	5.2E-9						
5.	1.2E+2									
3.		1.00	no conv.							
		0.50	6.0E+2	4.1E+2	1.5E+2	4.7E+1	8.5E+0	4.2E-1	1.3E-3	1.1E-8
		1.00	6.8E+2	4.7E+2	1.6E+2	5.2E+1	1.0E+1	6.3E-1	2.9E-3	6.4E-8
4.			3.4E+6	4.9E-9						
5.	1.1E+1									
3.		1.00	1.7E+1	8.1E-1	3.4E-3	8.2E-8				
4.			1.5E+5	4.5E-9						
5.	3.3E-1									
3.		1.00	1.2E+0	3.7E-3	7.4E-8					
4.			1.1E+4	4.4E-9						
5.	1.9E-3									
3.		1.00	2.8E-2	2.1E-6	3.1E-11					
4.			2.5E+2	5.3E-9						
5.	2.9E-7									

column A: identifies step in Box 10.1, fluid mesh solver (3.), solid solver (4.), residual of combined fluid + interface solver (5.),

column B: combined fluid + interface residual,

column C: increment cutting in the fluid mesh solver,

column D: residuals of fluid mesh solver and solid solver

Table 14.2: Oscillating structure, stable long term response, typical convergence of the residuals, 4336 fluid elements, 20 small strain solid continuum elements,  $\Delta t = 0.02$ ,  $t = 19.380$ .

A	B	C	D							
3.		1.00	no conv.							
		0.50	no conv.							
		0.25	3.6E+2	1.4E+2	3.7E+1	4.4E+0	1.2E-1	1.0E-4	9.0E-11	
		0.50	3.9E+2	1.5E+2	4.5E+1	5.0E+0	1.4E-1	1.2E-4	1.1E-10	
		0.75	4.3E+2	1.7E+2	5.6E+1	7.7E+0	5.0E-1	2.4E-3	5.1E-8	
		1.00	4.8E+2	1.9E+2	9.8E+1	2.7E+1	3.2E+0	8.5E-2	7.0E-5	7.1E-11
4.			9.1E-1	1.8E-9						
5.	7.4E+1									
3.		1.00	6.9E+0	2.8E-1	5.1E-4	2.0E-9				
4.			2.3E+1	2.5E-5	5.6E-13					
5.	1.1E+0									
3.		1.00	1.9E-1	2.9E-4	5.9E-10					
4.			7.9E-1	2.4E-9						
5.	1.2E-2									
3.		1.00	1.3E-4	1.1E-10						
4.			3.2E-4	5.8E-13						
5.	2.9E-7									

column A: identifies step in Box 10.1, fluid mesh solver (3.), solid solver (4.),  
residual of combined fluid + interface solver (5.),

column B: combined fluid + interface residual,

column C: increment cutting in the fluid mesh solver,

column D: residuals of fluid mesh solver and solid solver

Table 14.3: Oscillating structure, stable long term response, typical convergence of the residuals, 4564 fluid elements, 20 geometrically exact beam elements,  $\Delta t = 0.005$ ,  $t = 19.780$ .

A	B	C	D						
3.		1.0000	no conv.						
		0.5000	no conv.						
		0.2500	no conv.						
		0.1250	no conv.						
		0.0625	6.2E+2	2.6E+2	4.6E+1	2.4E+0	9.4E-3	1.7E-7	6.8E-10
		0.1250	6.2E+2	2.6E+2	4.6E+1	2.4E+0	9.4E-3	1.6E-7	6.8E-10
		0.1875	6.2E+2	2.6E+2	4.6E+1	2.4E+0	9.3E-3	1.6E-7	6.6E-10
		....	....						
		....	....						
		0.6875	6.4E+2	2.6E+2	4.6E+1	2.4E+0	8.8E-3	1.3E-7	6.8E-10
		0.7500	6.4E+2	2.6E+2	4.6E+1	2.4E+0	8.8E-3	1.3E-7	6.7E-10
		0.8125	6.4E+2	2.6E+2	4.6E+1	2.4E+0	8.8E-3	1.3E-7	6.7E-10
		0.8750	6.4E+2	2.6E+2	4.6E+1	2.4E+0	8.8E-3	1.3E-7	6.5E-10
		0.9375	6.4E+2	2.6E+2	4.6E+1	2.4E+0	8.8E-3	1.3E-7	6.6E-10
		1.0000	6.4E+2	2.6E+2	4.6E+1	2.4E+0	8.8E-3	1.2E-7	6.8E-10
4.			1.3E+2	1.0E-5	3.4E-9				
5.	5.9E+3								
3.		1.00	no conv.						
		0.50	2.1E+2	8.5E+1	1.1E+1	2.4E-1	1.2E-4	6.4E-10	
		1.00	2.1E+2	8.5E+1	1.1E+1	2.3E-1	1.1E-4	6.3E-10	
4.			9.3E+4	1.8E+2	2.7E-3	2.0E-9			
5.	1.7E+1								
3.		1.00	5.4E+1	2.3E+0	6.3E-3	6.1E-08			
4.			2.7E+4	7.4E+1	2.2E-3	1.6E-09			
5.	1.6E-1								
3.		1.00	5.6E-1	2.8E-4	6.5E-10				
4.			2.0E+2	6.6E-3	3.0E-9				
5.	4.6E-5								

column A: identifies step in Box 10.1, fluid mesh solver (3.), solid solver (4.), residual of combined fluid + interface solver (5.),

column B: combined fluid + interface residual,

column C: increment cutting in the fluid mesh solver,

column D: residuals of fluid mesh solver and solid solver

Table 14.4: Oscillating structure, stable long term response, typical convergence of the residuals, 12,330 fluid elements, 20 large strain solid continuum elements,  $\Delta t = 0.005$ ,  $t = 19.985$ .

## 14.2 Flow through a Channel with a Flexible Wall

This example is motivated by the work of Heil [57]. It concerns the two dimensional flow through a channel with a flexible wall, *i. e.* a section of the channel wall consists of a Neo-Hooke elastic membrane, otherwise the wall is fixed in space. Similar problems arise in the area of biomechanics, where the objective is to model the blood flow through the veins and arteries of the human body.

At the inflow boundary the prescribed flow profile corresponds to undisturbed Poiseuille flow. The average inflow velocity is chosen as  $\bar{u}_{\text{in}} = 1$ . The geometry and the boundary conditions are given in Figure 14.8. The fluid properties are set to  $\mu_f = 0.002$  and  $\rho_f = 1$ . The Reynolds number is obtained as  $Re = \bar{u}_{\text{in}} D \rho_f / \mu_f = 500$ . The flexible membrane is incompressible and Neo-Hooke elastic with  $\mu_s = 260$ . The relevant stress-strain relation is given by (8.9). The membrane is connected to the points A and B, whereby it is prestressed such that  $\lambda_0 = 1.2$ . The thickness of the prestressed membrane is 0.01 and the density is neglected, *i. e.*  $\rho_s = 0$ . The external pressure, which the membrane has to withstand, is set to  $p_{\text{ext}} = 0.5$ .

The fluid domain is discretised with 8658 elements. A detail of the mesh is given in Figure 14.9. The figure also shows that the membrane is modelled with 25 linear geometrically exact finite elements, the details of which are described in Section 8.2. The time integration parameters are set to  $\rho_\infty^h = 0.8$  for both the fluid and the membrane. First, the equilibrium configuration associated with  $\bar{u}_{\text{in}} = 0$  is computed. It depends only on the external pressure  $p_{\text{ext}}$  and the membrane stiffness. At time instant  $t = 100$ , the inflow velocity is then raised instantaneously from zero to  $\bar{u}_{\text{in}} = 1$ . For  $100 < t < 150$ , the time step size is set to  $\Delta t = 0.1$ , whereas for  $t > 150$  different time step sizes are considered, in order to study the effect of  $\Delta t$  on the long term solution.

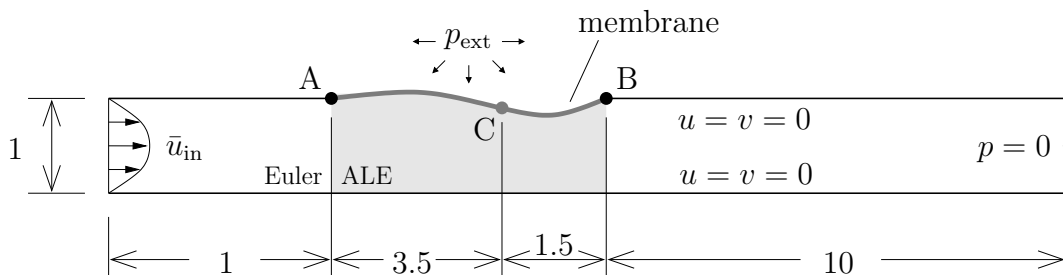


Figure 14.8: Channel with flexible wall, geometry of the problem and boundary conditions.

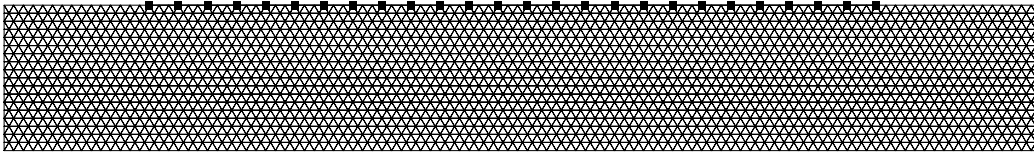


Figure 14.9: Channel with flexible wall, detail of fluid mesh with 8658 and membrane mesh with 25 finite elements.

The diagrams in Figure 14.10 show the evolution of the vertical displacement of point C of the membrane in time. Some vorticity plots are presented in Figure 14.11. The convergence of the residuals for a typical time step is illustrated in Table 14.5.

The following observations are made on the basis of the numerical results:

- The sudden increase of the inflow velocity from zero to  $\bar{u}_{\text{in}}$  causes the propagation of a pressure wave through the channel. The membrane acts like a buffer and temporarily forms a large bubble. The internal forces of the membrane and the external pressure soon reduce the extreme membrane displacements to more moderate values and, at about  $t = 150$ , the fluid flow and the deformation of the membrane seem to take a stable periodic long term response, which is characterised by the periodic necking of the downstream half of the membrane and the separation of vortices from the membrane surface, whenever the necking is maximal. This behaviour is illustrated in the Figures 14.10 and 14.11. A similar solution is obtained by Heil [57], who employs a different, from the solid mechanics points of view, unusual, numerical model for the membrane.
- Figure 14.10 (b) shows that the long term responses obtained for the time step sizes  $\Delta t = 0.02$  and  $\Delta t = 0.50$  deviate only by a small amount.
- For this problem the convergence of the residuals is observed to be very good. Table 14.5 shows the residuals of a typical time instant obtained with the large time increment  $\Delta t = 1.00$ . Note that the table does not display any residuals of the solid solver. This is due to the fact, that all degrees of freedom of the membrane are, in fact, degrees of freedom of the interface. Thus, step 4. in Box 10.1 does not apply, and some expressions in the formula of step 6. vanish. The partitioned Newton-Raphson procedure may be considered to reduce to a monolithic scheme in this special case.

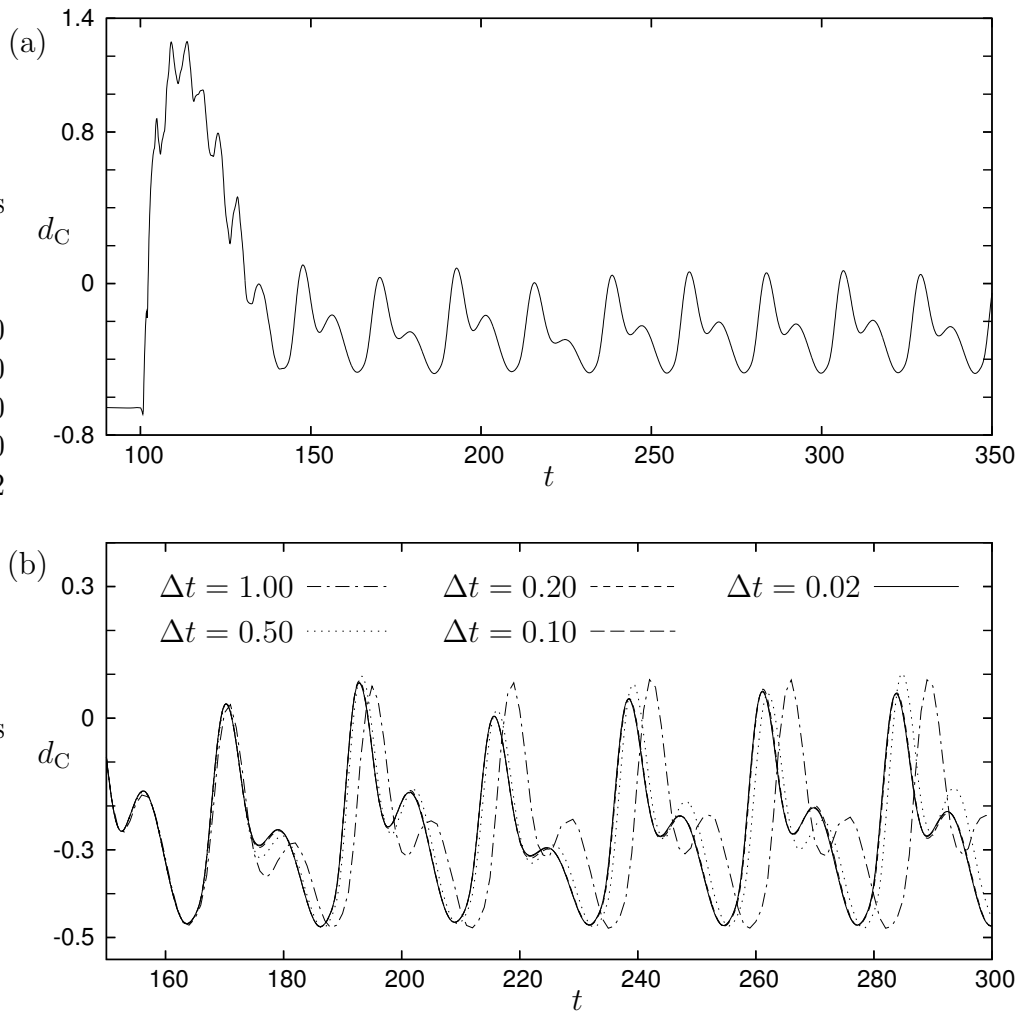


Figure 14.10: Channel with flexible wall, evolution of vertical displacement  $d_C$  of point C of the membrane in time; transition from initial disturbances to stable long term behaviour for  $\Delta t = 0.10$  (a), long term response for different time step sizes (b).

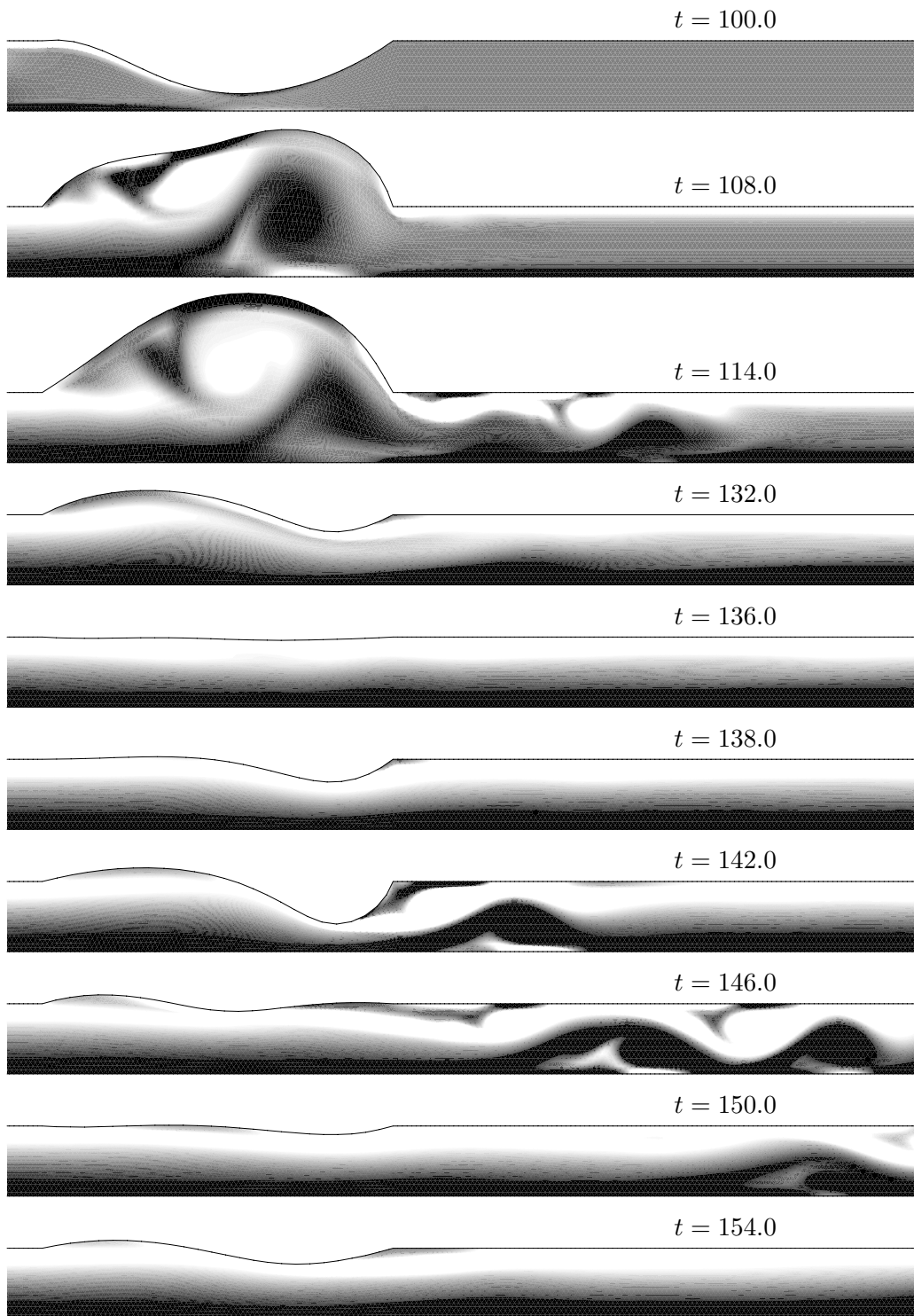


Figure 14.11: Channel with flexible wall, vorticity distribution at different time instants;  $\Delta t = 0.01$ ,  $\text{vort}(\mathbf{u}^h) \leq -3 \rightarrow \text{black}$ ,  $\text{vort}(\mathbf{u}^h) \geq +3 \rightarrow \text{white}$ .

A	B	C	D							
3.		1.000	no conv.							
		0.500	no conv.							
		0.250	1.6E+0	6.9E-1	2.6E-1	6.3E-2	5.3E-3	4.2E-5	2.7E-9	
		0.500	3.0E+0	1.4E+0	6.3E-1	2.7E-1	8.3E-2	1.1E-2	1.8E-4	5.5E-8
		0.625	4.7E-1	1.1E-1	1.1E-2	1.4E-4	2.9E-8			
		0.750	5.0E-1	1.2E-1	1.4E-2	2.4E-4	9.2E-8			
		0.875	5.3E-1	1.4E-1	1.8E-2	4.3E-4	3.1E-7	1.8E-13		
		1.000	5.7E-1	1.6E-1	2.3E-2	7.8E-4	1.1E-6	2.1E-12		
5.	2.4E+0									
3.		1.0	1.5E+0	6.0E-1	2.3E-1	5.1E-2	2.8E-3	8.9E-6	8.6E-11	
5.	4.9E-1									
3.		1.0	4.3E-1	1.0E-1	7.7E-3	6.5E-5	5.4E-9			
5.	4.7E-2									
3.		1.0	1.1E-2	4.2E-5	1.9E-9					
5.	2.7E-4									
3.		1.0	3.7E-5	6.8E-10						
5.	4.5E-9									

column A: identifies step in Box 10.1, fluid mesh solver (3.), residual of combined fluid + interface solver (5.),  
column B: combined fluid + interface residual,  
column C: increment cutting in the fluid mesh solver,  
column D: residuals of fluid mesh solver

Table 14.5: Channel with flexible wall, convergence of the residuals of a typical large time time step,  $\Delta t = 1.0$ ,  $t = 340$ ; note that the solid solver does not need to be evoked since all degrees of freedom of the membrane are interface degrees of freedom.

## 14.3 Parachute at Low Reynolds Number

This example is concerned with the simulation of a model parachute. Clearly, it is impossible to represent realistically the drag of a parachute in air by a two dimensional model, which does not account for the phenomena of turbulent air flow. However, this example may serve as a demonstration of the potential of the numerical strategy developed in this work.

The parachute consists of a membrane and two ropes, which support the load. The load is represented by three heavy trusses, see Figure 14.13. The membrane interacts with the surrounding air flow, whereas the interaction of the air flow with the ropes and the load is ignored. The material of the membrane, the ropes and the trusses is assumed to be incompressible with large elastic moduli. Gravity acts only on the trusses.

The fluid domain is chosen as a large rectangle. No velocity boundary conditions are applied. The pressure is fixed to zero at one point on the boundary. There is no Eulerian region of the domain. The parachute is positioned in the centre of the domain, and a fluid mesh with 4582 finite elements is generated, see Figure 14.13 (a). The membrane, the ropes and the trusses are modelled with 25 membrane elements with different material properties. In order to allow the simulation of a long asymmetric fall, the parachute is shifted, rotated and “closed” as shown in Figure 14.13 (b). The fluid mesh is then adjusted by means of the mesh update strategy type C. Details of the initial configuration of the parachute and the fluid mesh are displayed in Figure 14.13 (b). The time integration parameters are set to  $\rho_{\infty}^h = 0.8$  for the fluid and the solid. Initially, the fluid and the parachute are at rest. At  $t = 0$ , the load is suddenly subjected to gravity and the parachute is dragged downwards. The time step size is chosen as  $\Delta t = 0.1$  and kept constant throughout the simulation. A rough estimate of the vertical limit velocity of the parachute can be made on the basis of the diagram in Figure 14.12 (b) as  $v = 0.6$ . The global Reynolds number then corresponds to  $Re = v \rho_f D / \mu_f = 170$ , where  $D$  is the typical diameter of the parachute.

The evolution in time of the vertical coordinate and the vertical velocity component of the load are displayed in the diagrams in Figure 14.12. Figure 14.14 shows the path of the parachute in the two dimensional plane and the vorticity distribution of the air flow around the parachute at different time instants. The figure also presents details of the fluid mesh around the membrane. The following observations are made:

- The diagrams in Figure 14.12 show the substantial deceleration of the fall, caused by the parachute. The estimate  $v = 0.6$  of the vertical limit velocity allows the evaluation of the drag coefficient. It is obtained as

$C_D = 2 F_D / (\rho_f D v^2) \approx 1.6$ , where  $F_D$  represents the gravity force of the load. The comparison with the three dimensional flow around an open semi-sphere, for which it is known that  $C_D = 1.4$ , shows at least the correct order of magnitude of the numerical results.

Due to its asymmetric initial configuration, the parachute does not fall in a straight line, but oscillates horizontally. The opening process of the parachute causes the superposition of the fall of the load with vertical oscillations, the effects of which may still be observed at  $t = 55$ .

- It is evident from Figure 14.14 that the quality of the fluid finite element mesh near the parachute is excellent. It is remarkable that this is achieved despite the extreme change of the position of the fluid-membrane interface during of the simulation. Note that the vertical displacement of the parachute from  $t = 0$  to  $t = 55$  corresponds to 66 % of the height of the fluid domain.
- The convergence of the residuals of the partitioned Newton-Raphson procedure is asymptotically quadratic. In each time step, the residual of the combined fluid + interface solver typically decreases from 0.5 to less than  $10^{-10}$  in four steps.

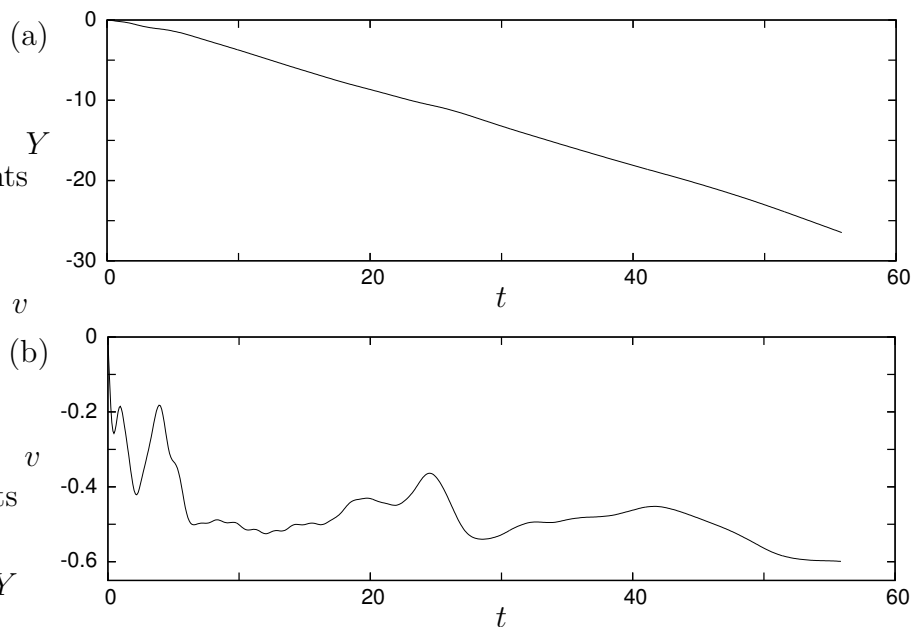


Figure 14.12: Parachute, evolution in time of the vertical position  $Y$  (a) and the vertical velocity  $v$  (b) of the weight.

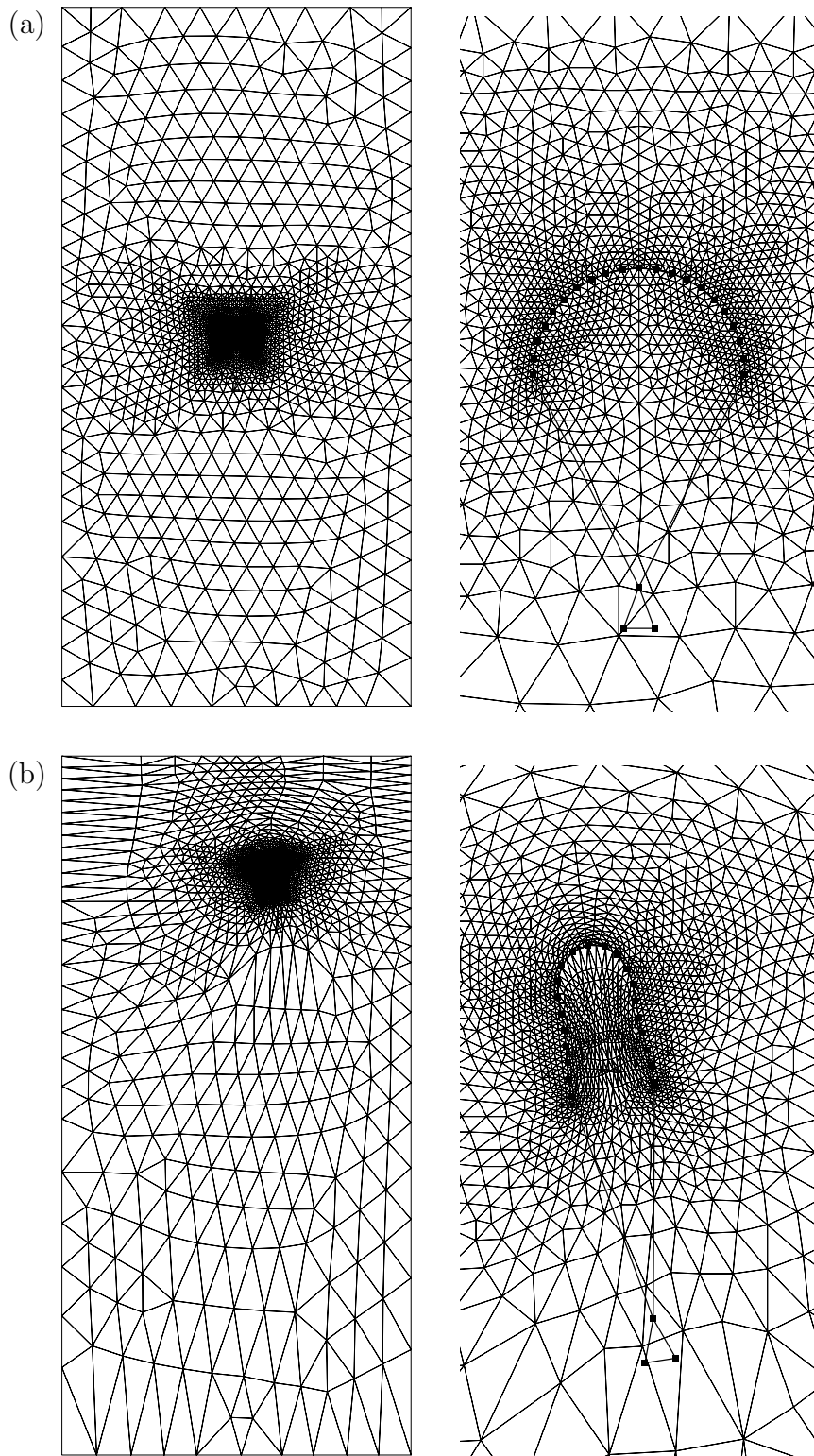


Figure 14.13: Parachute, mesh generated for “nice” geometry (a), deformation of mesh at  $t = 0$  (b).

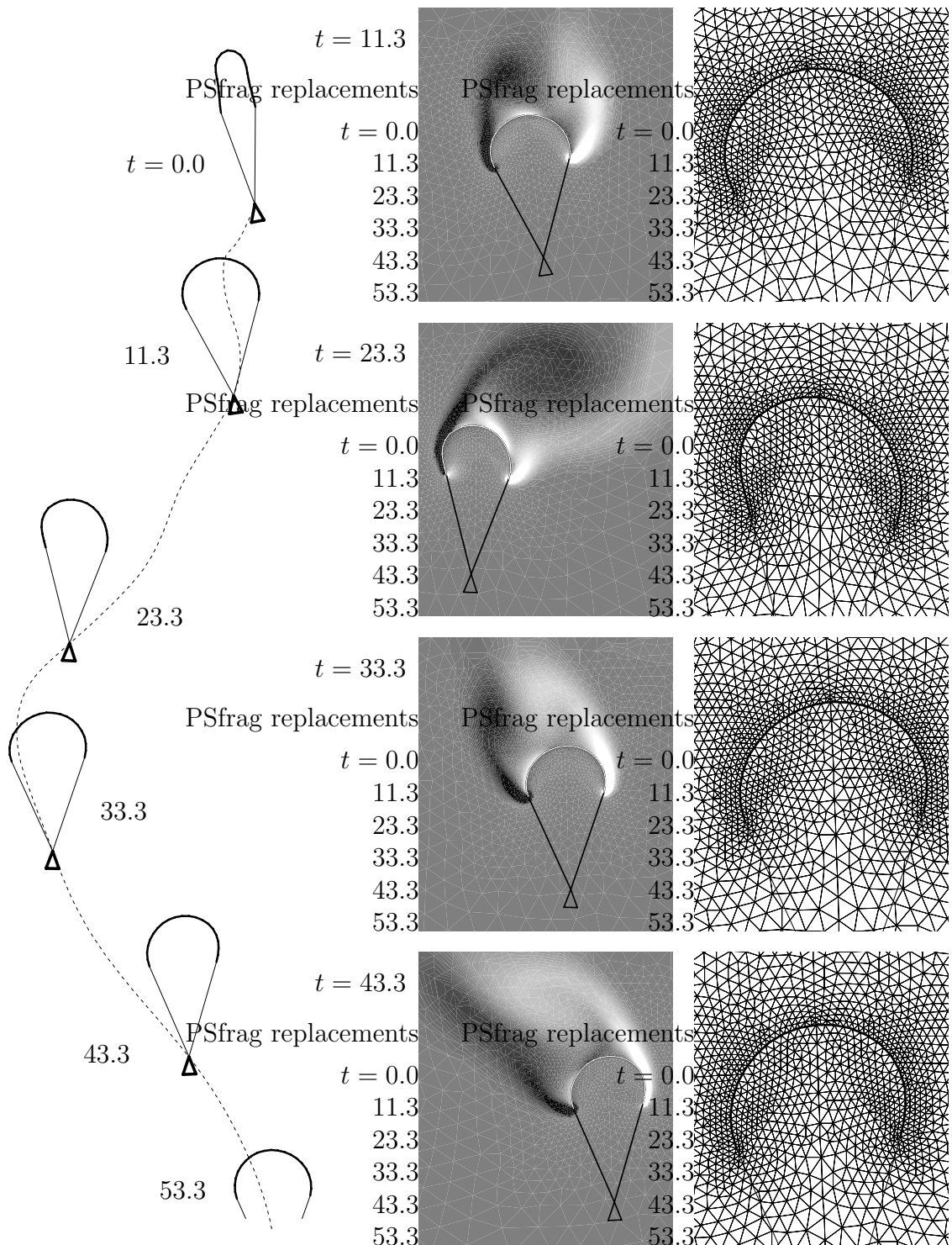


Figure 14.14: Parachute, configuration, vorticity distribution and meshes at different times;  $\text{vort}(\mathbf{u}^h) \leq -2 \rightarrow \text{black}$ ,  $\text{vort}(\mathbf{u}^h) \geq +2 \rightarrow \text{white}$ .

## 14.4 A Pump with Two Valves

Valves are an essential part of various engineering devices. Many pumps are based on the combination of periodically contracting chambers and valves. The most prominent example in the area of biomechanics is clearly the human heart. The modelling of the fluid-structure interaction in valves is a focus of a large body of current research.

In the following, a pump with two valves and one periodically contracting chamber is considered. The valves are based on flexible membranes which deform due to the changes of the fluid pressure. The geometry and the boundary conditions are displayed in Figure 14.15. It is assumed that, due to the symmetry, it suffices to consider only one half of the model. The distance  $h(t)$  is given as

$$h(t) = 0.75 (1 + \cos(2.5 \pi t)) . \quad (14.1)$$

Thus, the chamber contracts and expands periodically with  $T = 0.8$ . The membranes experience large deformations under plane strain conditions. They are assumed to be Neo-Hooke type hyperelastic with  $\mu_s = 800$ ,  $K_s = 50,000$  and the density  $\rho_s = 0.004$ . The ends of the membranes are clamped. The liquid is characterised by  $\mu_f = 10^{-5}$  and  $\rho_f = 0.001$ . Thus, if the units of space, time and mass are assumed to be 1 cm, 1 s and 1 kg, respectively, then the problem under consideration corresponds to a small water pump with rubber membranes.

A coarse and a dense mesh with, respectively, 3428 and 9430 fluid finite elements are generated for  $h = 0.75$ . Each of the membranes is modelled with 40 nine noded finite strain continuum elements under plane strain conditions. A detail of the coarse mesh is shown in Figure 14.16. The entire fluid domain

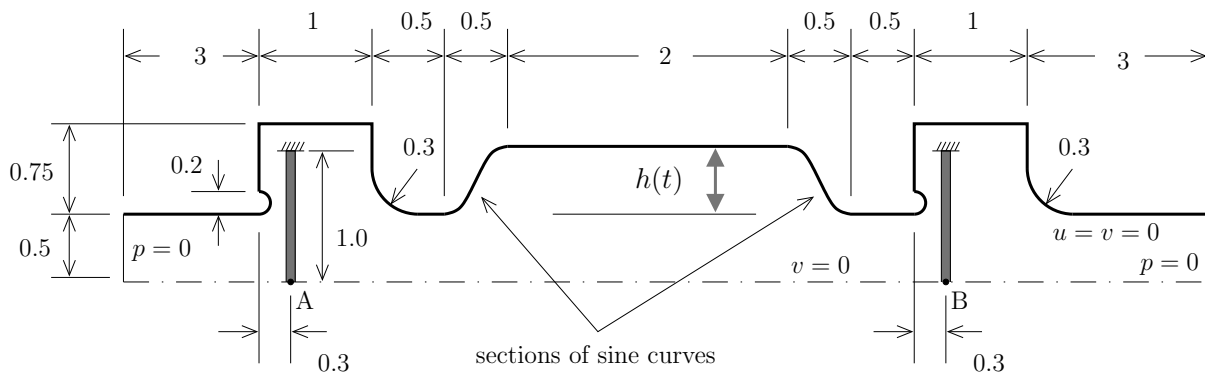


Figure 14.15: Pump with two valves, geometry of the problem and boundary conditions; thickness of the rubber membranes  $H = 0.1$ .

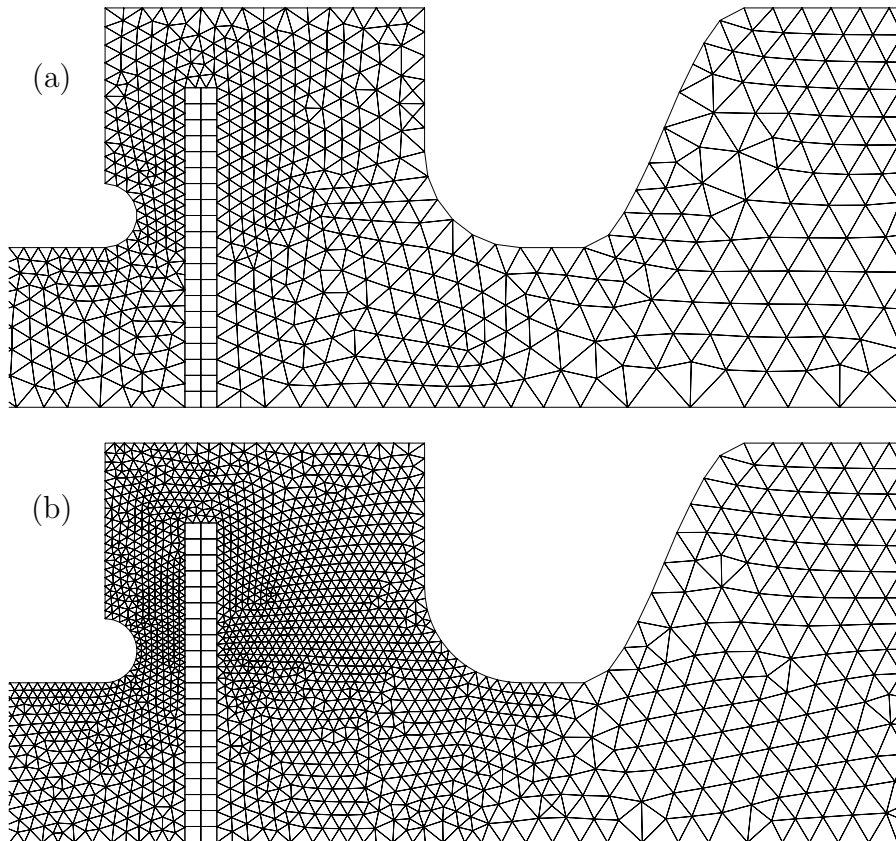


Figure 14.16: Pump with two valves, detail of fluid mesh with 3428 and the membrane mesh with 40 finite elements (a), fluid mesh with 9430 elements (b).

is subject to the ALE strategy, except for two short sections of the inflow and outflow channels, where the mesh is fixed. The nodal positions are updated according to the pseudo-elastic technique A with  $\mu_{\text{mesh}} = 1$  and  $K_{\text{mesh}} = 0$ . The time integration parameters are set to  $\rho_{\infty}^h = 0.8$  for the fluid and  $\rho_{\infty}^h = 0.4$  for the solids. Prior to the simulation, the fluid mesh is adjusted to  $h = 1.5$ . For the dense fluid mesh, the simulation is run with  $\Delta t = 0.0025$ . For the coarse mesh, the time step size is set to  $\Delta t = 0.01$ , but due to convergence failure it sometimes automatically reduces to  $\Delta t = 0.0025$ .

Figure 14.17 (a) shows the evolution of the membrane displacements in the points A and B in time. The flow rates, measured at the left and right hand side open boundaries, are displayed against time in the graph in Figure 14.17 (b). Typical flow patterns are illustrated by the streamline diagrams in Figure 14.18.

The following observations are made on the basis of the numerical results:

- Figure 14.17 (a) and the diagrams in Figure 14.18 show that the membranes deflect substantially, but do not close the valves entirely. If the rubber membranes were softer, or the time period  $T$  was shorter, then the valves would close and the simulation would require to account for the contact between the membranes and the rigid boundaries. In the specific case under consideration, the expansion of the chamber leads to inflow from the left and right hand side, whereas the contraction results in water flowing out at both sides. However, the flow rates are substantially different and thus, in the average, there is a transport of fluid from the left to the right hand side. This is evident from the diagram of the flow rates in Figure 14.17 (b) and also from the different density of the streamlines in Figure 14.18.

The average peak velocity at the open boundaries may be derived from Figure 14.17 (b) as approximately  $10/0.5 = 20$ . By employing one half of the channel width as the characteristic length scale the Reynolds number follows as  $Re = 20 \cdot 0.5 \cdot 0.001/10^{-5} = 1000$ .

- The results obtained with the different fluid meshes agree roughly. Clearly, the denser spatial and temporal discretisation leads to the resolution of significantly more high frequency effects. It is noted that the volume conservation is poor for both meshes. This is due to the high Reynolds number and the extreme complexity of the flow, which is illustrated in the streamline diagrams in Figure 14.18. Under these circumstances, the mesh with 9430 elements may still be regarded as coarse.
- The partitioned Newton-Raphson procedure renders asymptotically quadratic convergence of the residuals.

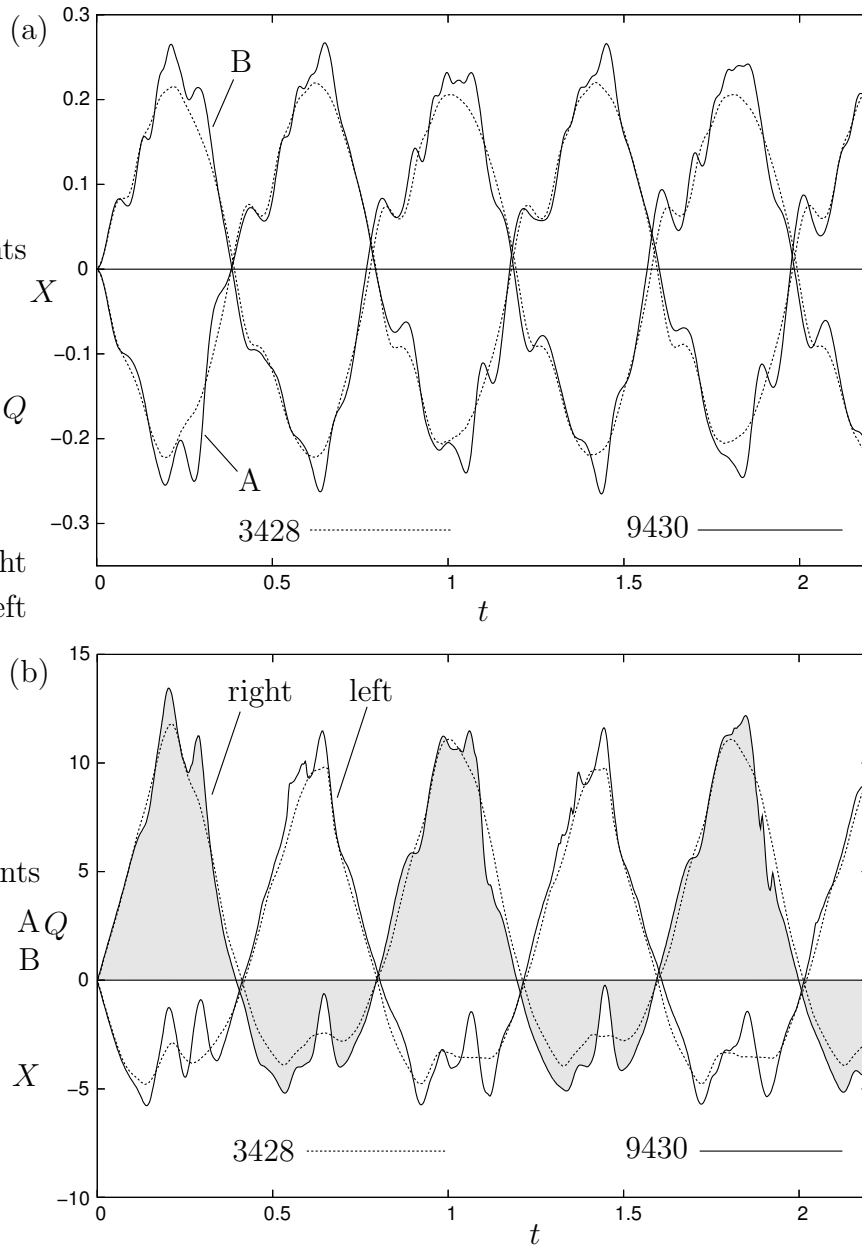


Figure 14.17: Pump with two valves, evolution in time of the membrane displacements in the points A and B (a), evolution in time of inflow and outflow rates (b), whereby the grey areas correspond to the fluid volume which is pumped through the outflow boundary on the right hand side.

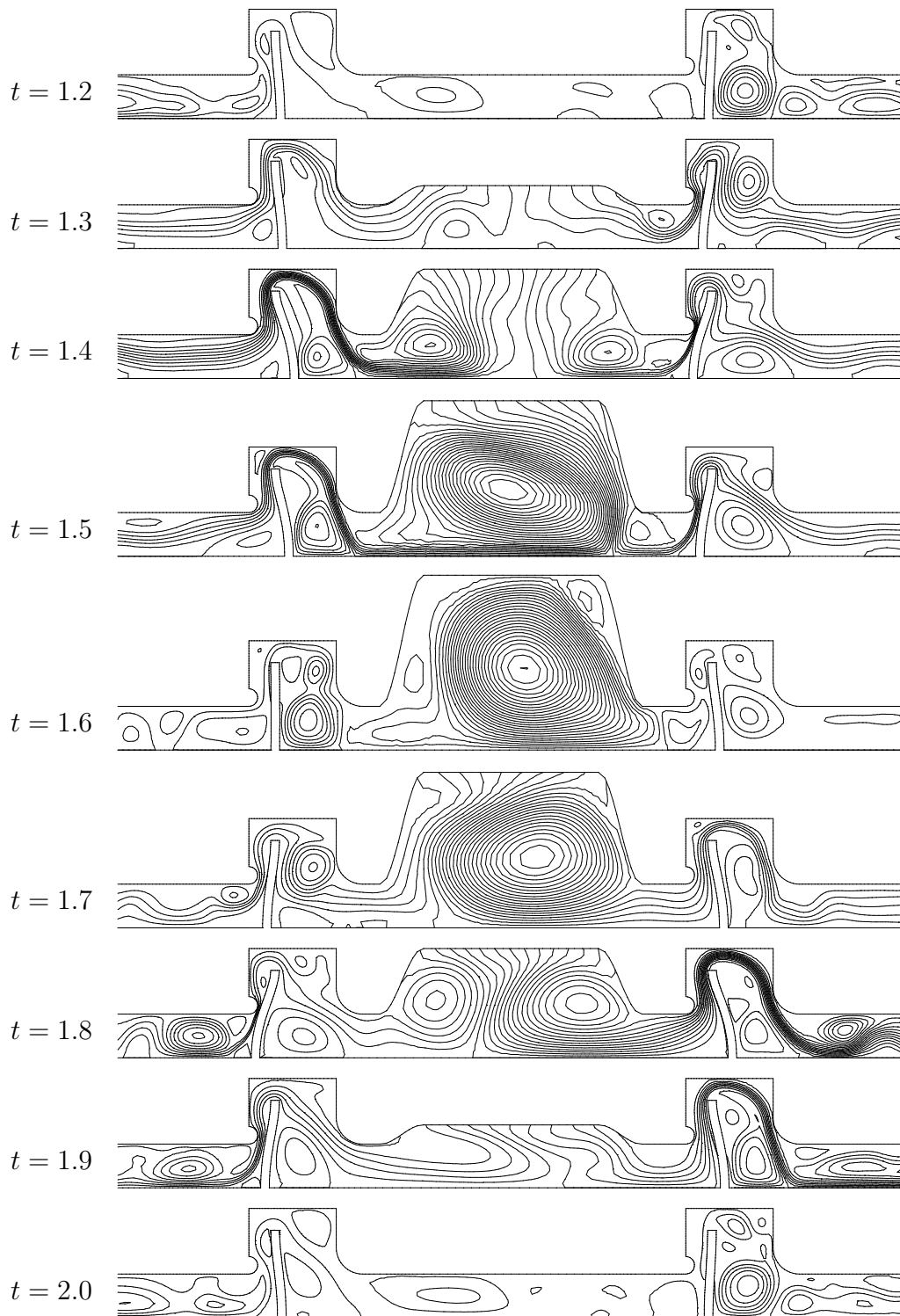


Figure 14.18: Pump with two valves, streamlines at different time instants; 9430 fluid elements.

# Chapter 15

## Conclusions

The aim of this thesis as formulated in Section 1.2 has been achieved. Namely, a numerical model for incompressible Newtonian fluid flow with moving free surfaces and interfaces has been formulated. It is based on the finite element methodology, and captures the interface motion by means of an ALE strategy. The strong coupling is resolved exactly by the partitioned Newton-Raphson procedure developed in this work. Various numerical examples have been presented in detail to demonstrate the robustness, the accuracy and the wide range of applicability of the overall strategy.

In the following, a more detailed list of the achievements and conclusions of this work is provided. The thesis closes with suggestions for future research.

### 15.1 Achievements and Conclusions

*Stabilised finite elements for fluid flow.* The relations between several finite element strategies for the modelling of the incompressible fluid flow have been elucidated. The close relationship between the artificial diffusion, the streamline diffusion, the SUPG, GLS, bubble and multiscale strategies for the stabilisation of advection dominated problems has been shown. Similarly, it has been demonstrated that the PSPG and GLS approaches and the MINI element overcome the numerical problems associated with equal order velocity/pressure interpolations in essentially the same way. The SUPG/PSPG method has then been chosen for the modelling of the incompressible Navier-Stokes equations. Some justification has been provided for the specific choice of the stabilisation parameters.

*Time discretisation.* For the discretisation of time, the discrete generalised- $\alpha$  method has been employed. This choice was motivated by the results of a de-

tailed study and a comparison of semi-discrete and space-time methods. The linear discontinuous time Galerkin method has been shown not to be generally superior to the generalised- $\alpha$  method. In particular, it has been proven that, in the framework of linear spatial interpolations, the stabilisation of the finite element method jeopardises the third order accuracy of the discontinuous Galerkin strategy. The good performance of the overall methodology in the numerical examples of Chapters 11 – 14 justifies the choice of a semi-discrete strategy and of the generalised- $\alpha$  method in particular. It has been suggested that the stabilisation parameters of the finite element formulation should be independent of the time step size.

*Mesh update methods, ALE.* Mesh update methods, based on nonlinear pseudo-elastic and on optimisation strategies, have been considered. They maintain acceptable mesh quality even when the domain geometry becomes severely distorted. Provided that the displacement of the mesh boundary is applied in increments, they allow very large deformations within each time step. In other words, the mesh update strategies employed in this work never impose a restriction on the time step size. The geometrical conservation laws have briefly been addressed. They have been shown not to be violated and are possibly not relevant for the formulation at hand.

*Partitioned Newton-Raphson Procedure.* A solution strategy for the algebraic coupled nonlinear system of equations has been developed. It is based on exact linearisation and follows a Newton-Raphson strategy.

The method computes exactly the dependency of the fluid response on the mesh motion. To the knowledge of the author, this is a novel approach. Clearly, this is achieved at the expense of computational time, and it may also be disputed whether it is necessary to undertake this effort. The response to these possible objections is twofold: First, by employing the exact linearisations the number of iterations is reduced to a minimum. Fewer more expensive iterations need not take longer than many cheap iterations (see Section 14.1). Second, it is pointed out that the most sophisticated alternative solution strategies outlined in Section 10.4 (Matthies and Steindorf [82], Tezduyar [118]) are indeed based on approximations of the off-diagonal terms of the linearisation matrix. In other words, they try to approximate what is computed exactly in this work. Thus, it may be argued that, for some problems, they may require smaller time steps in order to ensure the convergence of the residuals, whereas the methodology at hand still does not impose a restriction on the size of the time increments.

In fact, in the numerical examples presented in the Chapters 11 – 14, the upper limit of the time step size is determined by the time scales of the solution, and possibly by the robustness of the discretisation techniques employed

for the fluid flow or the solid structure, but not by the partitioned Newton-Raphson solution procedure. The examples have also demonstrated that the strategy renders asymptotically quadratic convergence of the residuals.

*Computer implementation.* In the course of this work, the complete solution algorithm has been implemented in a computer program. The decision to write a new program was motivated mainly by the desire to handle simultaneously an arbitrary number of fluid and solid domains, rigid bodies, free surfaces and interfaces, which may then interact. Starting from scratch also allowed to achieve a high degree of modularity.

*Numerical examples.* A variety of numerical examples has been presented and discussed in detail in Chapters 11 – 14. The wide range of applicability of the methodology presented in this work is evident from the physical problems considered, which include the mechanical behaviour of drops as well as the flutter of a bridge deck and the flow through a channel with a flexible wall. The latter may be regarded as a representative for biomechanical applications. Where reference solutions are available, they are well matched by the numerical results. The effect of coarse and dense spatial and temporal discretisations has been studied, whereby good estimates of the solutions have been obtained with coarse spatial meshes and large time steps. In most cases, the spatial and temporal discretisations could be refined independently. All of the computations have been performed on personal computers.

## 15.2 Suggestions for Future Research

The following suggestions are made for future research:

- In order to simulate realistic problems, it clearly is necessary to extend the computer implementation to three dimensions.
- The expressions for the stabilisation parameters of the SUPG/PSPG formulation may still be improved.
- By generalising the fluid model to account for turbulence and for compressibility of the fluid, the methodology can be made applicable to a wider variety of engineering problems.
- The partitioned Newton-Raphson procedure may be made more efficient, without significant deterioration of the rate of convergence, by neglecting certain derivatives. It may, for instance, not be necessary to linearise all fluid residual forces with respect to the mesh motion. The fluid nodes far away from the moving boundary experience only small

displacements and thus, the dependency of their position on the moving free surface or interface may be ignored. Typically, the mesh motion is determined during the first steps of the overall Newton iteration. Hence, towards the end of the iteration, it may suffice to compute the linearisation of the fluid residual forces with respect to the mesh motion only for the element layer directly adjacent to the moving boundary. An intelligent algorithm capable of deciding, which derivatives may be ignored and which are essential for the convergence, is very desirable. It is assumed that significant amounts of computational time may be saved without jeopardising the rate of convergence.

- The methodology should be equipped with a remeshing facility. This seems particularly desirable for the simulation of drops, where the break-up could then be studied in detail. The simulation of the opening of parachutes or complex mixing processes can not be modelled with a pure ALE strategy, either.

# Bibliography

- [1] P. Anagnostopoulos and P. W. Bearman. Response characteristics of a vortex excited cylinder at low reynolds numbers. *Journal of Fluids and Structures*, 6:39–50, 1992.
- [2] D. N. Arnold, F. Brezzi, and M. Fortin. A stable finite element for the Stokes equations. *Calcolo*, 21:337–344, 1984.
- [3] I. Babuska. Error bounds for the finite element method. *Numerische Mathematik*, 16:322–333, 1971.
- [4] P. Z. Bar-Yoseph, S. Mereu, S. Chippada, and V. J. Kalro. Automatic monitoring of element shape quality in 2-d and 3-d computational mesh dynamics. *Computational Mechanics*, 27:378–395, 2001.
- [5] K. J. Bathe. *Finite Element Procedures*. Prentice Hall, New Jersey, 1996.
- [6] M. Behr and T. Tezduyar. The shear-slip mesh update method. *Computer Methods in Applied Mechanics and Engineering*, 174:261–274, 1999.
- [7] T. Belytschko, W. K. Liu, and B. Moran. *Nonlinear Finite Elements for Continua and Structures*. John Wiley & Sons, Chichester, UK, 2000.
- [8] R. B. Bird, W. E. Stewart, and E. N. Lightfoot. *Transport Phenomena*. John Wiley & Sons, 1960.
- [9] R. D. Blevins. *Flow Induced Vibration*. Van Nostrand Reinhold Company, New York, 1977.
- [10] J. Bonet and R. Wood. *Nonlinear Continuum Mechanics for Finite Element Analysis*. Cambridge University Press, Cambridge, UK, 1997.

- [11] H. Braess. *Untersuchungen von Strömungen in zeitlich veränderlichen Gebieten mit der Methode der Finiten Elemente*. PhD thesis, Universität Hannover, Institut für Baumechanik und Numerische Mechanik, 2000.
- [12] H. Braess and P. Wriggers. Arbitrary Lagrangian Eulerian finite element analysis of free surface flow. *Computer Methods in Applied Mechanics and Engineering*, 190:95–109, 2000.
- [13] S. C. Brenner and L. R. Scott. *The Mathematical Theory of Finite Element Methods*. Springer, second edition, 2002.
- [14] F. Brezzi. On the existence, uniqueness and approximation of saddle-point problems arising from lagrange multipliers. *Revue Francaise d'Automatique, d'Informatique et de Recherche Operationnelle. Serie Rouge, Analyse Numerique*, 8:129–151, 1974.
- [15] F. Brezzi, M.-O. Bristeau, L. P. Franca, M. Mallet, and G. Rogé. A relationship between stabilized finite element methods and the Galerkin method with bubble functions. *Computer Methods in Applied Mechanics and Engineering*, 96:117–129, 1992.
- [16] F. Brezzi and M. Fortin. *Mixed and Hybrid Finite Element Methods*. Springer Verlag, New York, 1991.
- [17] F. Brezzi, L. P. Franca, T. J. R. Hughes, and A. Russo.  $b = \int g$ . *Computer Methods in Applied Mechanics and Engineering*, 145:329–339, 1997.
- [18] F. Brezzi, L. P. Franca, and A. Russo. Further considerations on residual-free bubbles for advective-diffusive equations. *Computer Methods in Applied Mechanics and Engineering*, 166:25–33, 1998.
- [19] F. Brezzi and J. Pitkäranta. On the stabilisation of finite element approximations of the Stokes equations. In W. Hackbusch, editor, *Efficient Solutions of Elliptic Systems*, volume 10 of *Notes on Numerical Fluid Mechanics*, Braunschweig, Wiesbaden, 1984.
- [20] A. N. Brooks and T. J. R. Hughes. Streamline-Upwind/Petrov-Galerkin formulations for convection dominated flows with particular emphasis on the incompressible Navier-Stokes equations. *Computer Methods in Applied Mechanics and Engineering*, 32:199–259, 1982.

- [21] A. J. Chorin and J. E. Marsden. *A Mathematical Introduction to Fluid Mechanics*. Springer, New York, USA, 3rd edition, 1997.
- [22] J. Chung and G. M. Hulbert. A time integration algorithm for structural dynamics with improved numerical dissipation: The generalized- $\alpha$  method. *Journal of Applied Mechanics*, 60:371–375, 1993.
- [23] P. G. Ciarlet. *The Finite Element Method for Elliptic Problems*. North-Holland, Amsterdam, 1978.
- [24] R. D. Cook, D. S. Malkus, M. E. Plesha, and R. J. Witt. *Concepts and Applications of Finite Element Analysis*. John Wiley & Sons, fourth edition, 2002.
- [25] M. A. Crisfield. *Non-Linear Finite Element Analysis of Solids and Structures*. John Wiley & Sons, Chichester, UK, 1991.
- [26] I. G. Currie. *Fundamental Mechanics of Fluids*. McGraw-Hill, New York, USA, 1974.
- [27] S. H. Davies. Contact-line problems in fluid mechanics. *Journal of Applied Mechanics*, 50:977–982, 1983.
- [28] C. Degand and C. Farhat. A three-dimensional torsional spring analogy method for unstructured dynamic meshes. *Computers and Structures*, 80:305–316, 2002.
- [29] W. Dettmer and D. Perić. Time integration algorithms for stabilised finite element solutions of incompressible Navier-Stokes equations. Internal Report CR/1029, Department of Civil Engineering, University of Wales Swansea, December 2001.
- [30] W. Dettmer and D. Perić. An arbitrary Lagrangian-Eulerian for the modelling of fluid-solid interaction. In *WCCM V*, Vienna, Austria, July 2002.
- [31] W. Dettmer and D. Perić. An analysis of the time integration algorithms for the finite element solutions of incompressible Navier-Stokes equations based on a stabilised formulation. *Computer Methods in Applied Mechanics and Engineering*, 192:1177–1226, 2003.
- [32] W. Dettmer and D. Perić. A computational framework for free surface fluid flows accounting for surface tension. *accepted for publication in Computer Methods in Applied Mechanics and Engineering*, 2004.

- [33] W. Dettmer and D. Perić. A computational strategy for free surface fluid flows including surface tension effects. In *ECCOMAS*, Jyväskylä, Finland, July 2004.
- [34] W. Dettmer, P. H. Saksono, and D. Perić. A finite element formulation for incompressible newtonian fluid flows on moving domains in the presence of surface tension. In *ACME UK*, Swansea, UK, April 2002.
- [35] W. Dettmer, P. H. Saksono, and D. Perić. On a finite element formulation for incompressible Newtonian fluid flows on moving domains in the presence of surface tension. *Communications in Numerical Methods in Engineering*, 19:659–668, 2003.
- [36] J. Donea. Arbitrary Lagrangian-Eulerian finite element methods. In T. Belytschko and T. J. R. Hughes, editors, *Computational Methods for Transient Analysis*, pages 473–516. Elsevier Science Publishers, 1983.
- [37] J. Donea and A. Huerta. *Finite Element Methods for Flow Problems*. John Wiley & Sons, Chichester, UK, 2003.
- [38] J.-J. Droux and T. J. R. Hughes. A boundary integral modification of the Galerkin/least-squares formulation for the Stokes problem. *Computer Methods in Applied Mechanics and Engineering*, 113:173–182, 1994.
- [39] E. B. Dussan. On spreading of liquids on solid surfaces. Static and dynamic contact lines. *Annual Review of Fluid Mechanics*, 11:371–400, 1979.
- [40] J. Eggers and T. F. Dupont. Drop formulation in a one-dimensional approximation of the Navier-Stokes equation. *Journal for Fluid Mechanics*, 262:205–221, 1994.
- [41] K. Eriksson, D. Estep, P. Hansbo, and C. Johnson. *Computational Differential Equations*. Cambridge University Press, Cambridge, 1996.
- [42] H. Ettinger. *Development of Optimization and Parameterization Techniques Applied to Extrusion Die Design Optimization of PVC Profile Dies*. PhD thesis, University of Wales Swansea, School of Engineering, Civil and Computational Engineering Centre, 2004.
- [43] C. Farhat and M. Lesoinne. Two efficient staggered algorithms for the serial and parallel solution of three-dimensional nonlinear transient aeroelastic problems. *Computer Methods in Applied Mechanics and Engineering*, 182:499–515, 2000.

- [44] C. Farhat, M. Lesoinne, and P. Le Tallec. Load and motion transfer algorithms for fluid/structure interaction problems with non-matching discrete interfaces: Momentum and energy conservation, optimal discretisation and application to aeroelasticity. *Computer Methods in Applied Mechanics and Engineering*, 157:95–114, 1998.
- [45] C. A. Felippa, K. C. Park, and C. Farhat. Partitioned analysis of coupled mechanical systems. *Computer Methods in Applied Mechanics and Engineering*, 190:3247–3270, 2001.
- [46] Y. T. Feng and D. Peric. A time-adaptive space-time finite element method for incompressible Lagrangian flows with free surfaces: Computational issues. *Computer Methods in Applied Mechanics and Engineering*, 190:499–518, 2000.
- [47] J. H. Ferziger and M. Perić. *Computational Methods for Fluid Dynamics*. Springer, Berlin/Heidelberg, Germany, 3rd edition, 2002.
- [48] G. B. Foote. A numerical method for studying liquid drop behaviour: Simple oscillation. *Journal of Computational Physics*, 11:507–530, 1973.
- [49] L. P. Franca, A. Nesliturk, and M. Stynes. On the stability of residual-free bubbles for convection-diffusion problems and their approximation by a two-level finite element method. *Computer Methods in Applied Mechanics and Engineering*, 166:35–49, 1998.
- [50] U. Ghia, K. N. Ghia, and C. T. Shin. High-*re* solutions for incompressible flow using the Navier-Stokes equations and a multigrid method. *Journal of Computational Physics*, 48:387–411, 1982.
- [51] P. M. Gresho, D. K. Dartling, J. R. Torczynski, K. A. Cliffe, K. H. Winters, T. J. Garratt, A. Spence, and J. W. Goodrich. Is the steady viscous incompressible two-dimensional flow over a backward-facing step at  $Re = 800$  stable? *International Journal for Numerical Methods in Fluids*, 17:501–541, 1993.
- [52] P. M. Gresho and R. L. Lee. Don't suppress the wiggles – they're telling you something! In T. R. J. Hughes, editor, *Finite Element Methods for Convection Dominated Flows*, volume 34 of *AMD*, New York, 1979. ASME.
- [53] P. M. Gresho and R. L. Sani. *Incompressible Flows and the Finite Element Method*. John Wiley, Chichester, 1998.

- [54] H. Guillard and C. Farhat. On the significance of the geometric conservation law for flow computations on moving meshes. *Computer Methods in Applied Mechanics and Engineering*, 190:1467–1482, 2000.
- [55] B. Gustafsson, H.-O. Kreiss, and J. Oliger. *Time Dependent Problems and Difference Methods*. John Wiley, New-York, 1995.
- [56] J. P. Den Hartog. *Mechanical Vibrations*. Mc Graw-Hill Book Company, New York, Toronto, London, fourth edition, 1956.
- [57] M. Heil. An efficient solver for the fully coupled solution of large-displacement fluid-structure interaction problems. *Computer Methods in Applied Mechanics and Engineering*, 193:1–23, 2004.
- [58] C. Hirsch. *Numerical Computation of Internal and External Flows*. John Wiley, 1988.
- [59] C. W. Hirt, A. A. Amsden, and J. L. Cook. An arbitrary Lagrangian Eulerian computing method for all flow speeds. *Journal of Computational Physics*, 14:227–253, 1974.
- [60] B. Hübner. *Simultane Analyse von Bauwerk-Wind-Wechselwirkungen*. PhD thesis, Technische Universität Braunschweig, Institut für Statik, 2003.
- [61] B. Hübner, E. Walhorn, and D. Dinkler. Strongly coupled analysis of fluid-structure interaction using space-time finite elements. In *ECCM*, Cracow, Poland, June 2001.
- [62] B. Hübner, E. Walhorn, and D. Dinkler. A monolithic approach to fluid-structure interaction using space-time finite elements. *Computer Methods in Applied Mechanics and Engineering*, 193:2087–2104, 2004.
- [63] A. Huerta and W. K. Liu. Viscous flow with large free surface motion. *Computer Methods in Applied Mechanics and Engineering*, 69:277–324, 1988.
- [64] T. J. R. Hughes. *The Finite Element Method: Linear Static and Dynamic Finite Element Analysis*. Prentice-Hall, New Jersey, 1987.
- [65] T. J. R. Hughes. Multiscale phenomena: Green’s functions, the Dirichlet-to-Neumann formulation, subgrid scale models, bubbles and the origins of stabilized methods. *Computer Methods of Applied Mechanics and Engineering*, 127:387–401, 1995.

- [66] T. J. R. Hughes, G. R. Feijoo, L. Mazzei, and J.-B. Quincy. The variational multiscale method – a paradigm for computational mechanics. *Computer Methods in Applied Mechanics and Engineering*, 166:3–24, 1998.
- [67] T. J. R. Hughes, L. P. Franca, and M. Balestra. A new finite element formulation for computational fluid dynamics: V. Circumventing the Babuska-Brezzi condition: A stable Petrov-Galerkin formulation of the Stokes problem accommodating equal-order interpolations. *Computer Methods in Applied Mechanics and Engineering*, 59:85–99, 1986.
- [68] T. J. R. Hughes, L. P. Franca, and G. M. Hulbert. A new finite element formulation for computational fluid dynamics: VIII. The Galerkin/least-squares method for advective-diffusive equations. *Computer Methods in Applied Mechanics and Engineering*, 73:173–189, 1989.
- [69] T. J. R. Hughes, L. P. Franca, and M. Mallet. A new finite element formulation for computational fluid dynamics: VI. Convergence analysis of the generalized SUPG formulation for linear time dependent multi-dimensional advective-diffusive systems. *Computer Methods in Applied Mechanics and Engineering*, 63:97–112, 1987.
- [70] T. J. R. Hughes, W. K. Liu, and T. K. Zimmermann. Lagrangian-Eulerian finite element formulation for incompressible viscous flows. *Computer Methods in Applied Mechanics and Engineering*, 29:329–349, 1981.
- [71] C. Isenberg. *The Science of Soap Films and Soap Bubbles*. Tieto Ltd., Clevedon, UK, 1978.
- [72] K. E. Jansen, C. H. Whiting, and G. M. Hulbert. A generalized- $\alpha$  method for integrating the filtered Navier-Stokes equations with a stabilized finite element method. *Computer Methods in Applied Mechanics and Engineering*, 190:305–319, 2000.
- [73] C. Johnson. *Numerical Solution of Partial Differential Equations by the Finite Element Method*. Cambridge University Press, Cambridge, 1987.
- [74] C. Johnson, U. Nävert, and J. Pitkäranta. Finite element methods for linear hyperbolic problems. *Computer Methods in Applied Mechanics and Engineering*, 45:285–312, 1984.

- [75] C. Johnson and J. Saranen. Streamline diffusion methods for the incompressible Euler and Navier-Stokes equations. *Mathematics of Computation*, 47(175):1–18, 1986.
- [76] V. Kalro and T. E. Tezduyar. A parallel 3d computational method for fluid-structure interactions in parachute systems. *Computer Methods in Applied Mechanics and Engineering*, 190:321–332, 2000.
- [77] H. Lamb. *Hydrodynamics*. Cambridge University Press, Cambridge, UK, 6th edition, 1932.
- [78] M. Lesoinne and C. Farhat. Geometric conservation laws for flow problems with moving boundaries and deformable meshes, and their impact on aeroelastic computations. *Computer Methods in Applied Mechanics and Engineering*, 134:71–90, 1996.
- [79] R. Löhner, C. Yang, J. Cebal, J. D. Baum, H. Luo, D. Pelessone, and C. Charman. Fluid-structure interaction using a loose coupling algorithm and adaptive unstructured grids. In M. Hafez and K. Oshima, editors, *Computational Fluid Dynamics Review 1995*, Chichester, UK, 1995. John Wiley & Sons.
- [80] A. Masud and T. J. R. Hughes. A space-time Galerkin/least-squares finite element formulation of the Navier-Stokes equations for moving domain problems. *Computer Methods in Applied Mechanics and Engineering*, 146:91–126, 1997.
- [81] H. G. Matthies, R. Niekamp, and J. Steindorf. Algorithms for strong coupling procedures. *preprint*, 2004.
- [82] H. G. Matthies and J. Steindorf. Strong coupling methods. Informatik-bericht 2002-06, Technical University Brunswick, Institute of Scientific Computing, September 2002.
- [83] T. Nomura. ALE finite element computations of fluid-structure interaction problems. *Computer Methods in Applied Mechanics and Engineering*, 112:291–308, 1994.
- [84] T. Nomura and T. R. J. Hughes. An arbitrary Lagrangian-Eulerian finite element method for interaction of fluid and a rigid body. *Computer Methods in Applied Mechanics and Engineering*, 95:115–138, 1992.
- [85] E. Onate. A stabilized finite element method for incompressible viscous flows using a finite increment calculus formulation. *Computer Methods in Applied Mechanics and Engineering*, 182:355–370, 2000.

- [86] T. J. Pedley and K. D. Stephanoff. Flow along a channel with a time-dependent indentation in one wall: The generation of vorticity waves. *Journal of Fluid Mechanics*, 160:337–367, 1985.
- [87] D. Perić and W. Dettmer. Aspects of finite element strategies for large deformation problems on moving meshes. In *USNCCM IIV*, Albuquerque, New Mexico, U.S.A., July 2003.
- [88] D. Perić and S. Slijepčević. Computational modelling of viscoplastic fluids based on a stabilised finite element method. *Engineering Computations*, 18:577–591, 2001.
- [89] S. Piperno and C. Farhat. Partitioned procedures for the transient solution of coupled aeroelastic problems – part ii: Energy transfer analysis and three-dimensional applications. *Computer Methods in Applied Mechanics and Engineering*, 190:3147–3170, 2001.
- [90] C. Pozrikidis. *Introduction to Theoretical and Computational Fluid Dynamics*. Oxford University Press, 1997.
- [91] C. Pozrikidis. *Fluid Dynamics; Theory, Computation, and Numerical Simulation; Accompanied by the Software Library FDLIB*. Kluwer Academic Publishers, 2001.
- [92] R. Radovitzky and M. Ortiz. Lagrangian finite element analysis of Newtonian fluid flows. *International Journal for Numerical Methods in Engineering*, 43:607–619, 1998.
- [93] B. Ramaswamy. Numerical simulation of unsteady viscous free surface flow. *Journal of Computational Physics*, 90:396–430, 1990.
- [94] B. Ramaswamy and M. Kawahara. Arbitrary Lagrangian-Eulerian finite element method for unsteady, convective, incompressible viscous free surface fluid flow. *International Journal for Numerical Methods in Fluids*, 7:1053–1075, 1987.
- [95] B. Ramaswamy and M. Kawahara. Lagrangian finite element analysis applied to viscous free surface fluid flow. *International Journal for Numerical Methods in Fluids*, 7:953–984, 1987.
- [96] B. D. Reddy. *Introductory Functional Analysis*. Springer, 1998.
- [97] E. Reissner. On one-dimensional finite strain beam theory: The plane problem. *Journal of Applied Mathematics and Physics*, 23:795–804, 1972.

- [98] A. Rippl. *Three Dimensional Simulation of Rubber Profile Extrusion on the Basis of In-Line Rheometry*. PhD thesis, University of Wales Swansea, School of Engineering, Civil and Computational Engineering Centre, 2004.
- [99] P. J. Roache. *Computational Fluid Dynamics*. Hermosa Publishers, Albuquerque, 1976.
- [100] I. Robertson, S. J. Sherwin, and P. W. Bearman. A numerical study of rotational and transverse galloping rectangular bodies. *Journal of Fluids and Structures*, 17:681–699, 2003.
- [101] A. Roshko. On the development of turbulent wakes from vortex streets. Technical Report 2913, National Advisory Committee for Aeronautics NACA, 1953.
- [102] P. A. Sackinger, P. R. Schunk, and R. R. Rao. A Newton-Raphson pseudo-solid domain mapping technique for free and moving boundary problems: A finite element implementation. *Journal of Computational Physics*, 125:83–103, 1996.
- [103] P. H. Saksono. *On Finite Element Modelling of Surface Tension Phenomena*. PhD thesis, University of Wales Swansea, Department of Civil Engineering, 2002.
- [104] P. H. Saksono and D. Perić. On finite element modelling of surface tension: Variational formulation and applications – part i: Dynamic problems. *in preparation*, 2004.
- [105] P. H. Saksono and D. Perić. On finite element modelling of surface tension: Variational formulation and applications – part i: Quasi static problems. *in preparation*, 2004.
- [106] J. Sarrate, A. Huerta, and J. Donea. Arbitrary Lagrangian-Eulerian formulation for fluid-rigid body interaction. *Computer Methods in Applied Mechanics and Engineering*, 190:3171–3188, 2001.
- [107] C. Schwab. *p- and hp-Finite Element Methods. Theory and Applications to Solid and Fluid Mechanics*. Oxford University Press, Oxford, 1998.
- [108] F. Shakib and T. J. R. Hughes. A new finite element formulation for computational fluid dynamics: IX. Fourier analysis of space-time Galerkin/least-squares algorithms. *Computer Methods in Applied Mechanics and Engineering*, 87:35–58, 1991.

- [109] J. C. Simo, F. Armero, and C. A. Taylor. Stable and time-dissipative finite element methods for the incompressible Navier-Stokes equations in advection dominated flows. *International Journal for Numerical Methods in Engineering*, 38:1475–1506, 1995.
- [110] S. Slijepčević. *Computational Modelling of Non-Newtonian Fluids Based on the Stabilised Finite Element Method*. PhD thesis, University of Wales Swansea, School of Engineering, Civil and Computational Engineering Centre, 2003.
- [111] A. Soulaïmani, M. Fortin, G. Dhatt, and Y. Ouellet. Finite element simulation of two- and three-dimensional free surface flows. *Computer Methods in Applied Mechanics and Engineering*, 86:265–296, 1991.
- [112] A. Soulaïmani and Y. Saad. An arbitrary Lagrangian-Eulerian finite element method for solving three-dimensional free surface flows. *Computer Methods in Applied Mechanics and Engineering*, 162:79–106, 1998.
- [113] J. H. Spurk. *Fluid Mechanics*. Springer, Berlin/Heidelberg, Germany, 1997.
- [114] E. Stein and F.-J. Barthold. *Elastizitätstheorie, Unterlagen zur Vorlesung*. Institut für Baumechanik und Numerische Mechanik, Universität Hannover, Hannover, Germany, 1995.
- [115] J. Steindorf. *Partitionierte Verfahren für Probleme der Fluid-Struktur Wechselwirkung*. PhD thesis, Technische Universität Braunschweig, Mechanik-Zentrum, 2003.
- [116] N. Sukumar, D. L. Chopp, N. Moës, and T. Belytschko. Modeling holes and inclusions by level sets in the extended finite element method. *Computer Methods in Applied Mechanics and Engineering*, 190:6183–6200, 2001.
- [117] P. Le Tallec and J. Mouro. Fluid structure interaction with large structural displacements. *Computer Methods in Applied Mechanics and Engineering*, 190:3039–3067, 2001.
- [118] T. E. Tezduyar. Finite element methods for flow problems with moving boundaries and interfaces. *Archives of Computational Methods in Engineering*, 8:83–130, 2001.

- [119] T. E. Tezduyar. Computation of moving boundaries and interfaces and stabilization parameters. *International Journal for Numerical Methods in Fluids*, 43:555–575, 2003.
- [120] T. E. Tezduyar. Methods for computation of moving boundaries and interfaces. In P. Neittaanmäki, T. Rossi, S. Korotov, E. O nate, J. Périaux, and D. Knörzer, editors, *ECCOMAS*, Jyväskylä, Finland, 2004.
- [121] T. E. Tezduyar, M. Behr, and J. Liou. A new strategy for finite element computations involving moving boundaries and interfaces – the deforming-spatial-domain/space-time procedure: I. The concept and the preliminary numerical tests. *Computer Methods in Applied Mechanics and Engineering*, 94:339–351, 1992.
- [122] T. E. Tezduyar, M. Behr, and J. Liou. A new strategy for finite element computations involving moving boundaries and interfaces – the deforming-spatial-domain/space-time procedure: II. Computation of free-surface flows, two-liquid flows and flows with drifting cylinders. *Computer Methods in Applied Mechanics and Engineering*, 94:353–371, 1992.
- [123] T. E. Tezduyar, S. Mittal, S. E. Ray, and R. Shih. Incompressible flow computations with stabilized bilinear and linear equal-order-interpolation velocity-pressure elements. *Computer Methods in Applied Mechanics and Engineering*, 95:221–242, 1992.
- [124] T. E. Tezduyar and Y. Osawa. Finite element stabilization parameters computed from element matrices and vectors. *Computer Methods in Applied Mechanics and Engineering*, 190:411–430, 2000.
- [125] T. E. Tezduyar, S. Sathe, and R. Keedy. Space-time techniques for finite element computations of flows with moving boundaries and interfaces. In S. Gallegos, I. Herrera, S. Botello, F. Zarate, and y G. Ayala, editors, *III Congreso Internacional sobre Metodos Numericos en Ingenieria y Ciencias Aplicadas*, Monterrey, Mexico, 2004. CIMNE, Barcelona, Spain.
- [126] V. Thomée. *Galerkin Finite Element Methods for Parabolic Problems*. Springer Verlag, Berlin, Heidelberg, 1997.
- [127] W. A. Wall. *Fluid-Struktur-Interaktion mit stabilisierten Finiten Elementen*. PhD thesis, Universität Stuttgart, Institut für Baustatik, 2000.

- [128] W. A. Wall and E. Ramm. Fluid-structure interaction based upon a stabilized (ALE) finite element method. In S. R. Idelsohn and E. Onate, editors, *Computational Mechanics – New Trends and Applications, 4th World Congress on Computational Mechanics*, Buenos Aires, Brasil, 1998. CIMNE, Barcelona, Spain.
- [129] P. Wriggers. *Nichtlineare Finite-Element-Methoden*. Springer, 2001.
- [130] H. C. Yee, J. R. Torczynski, S. A. Morton, M. R. Visbal, and P. K. Sweby. On spurious behaviour of CFD simulations. *International Journal for Numerical Methods in Fluids*, 30:675–711, 1999.
- [131] Y. Zhang, R. S. Padgett, and O. A. Basaran. Nonlinear deformation and breakup of stretching liquid bridges. *Journal for Fluid Mechanics*, 329:207–245, 1996.
- [132] O. C. Zienkiewicz and R. L. Taylor. *The Finite Element Method*. Butterworth-Heinemann, Oxford, UK, 5th edition, 2000.